3.3.2 Number of research papers published per teacher in the Journals notified on UGC website during the years

2024

S. No.	Title of paper	Name of the author/s	Department of the teacher	Name of journal	Year of publication	ISSN number	Link to website of the Journal	Link to article / paper / abstract of the article	Is it listed in UGC Care list/Scopus/Web of Science/other, mention
								Link to the recognition in UGC enlistment of the Journal /Digital Object Identifier (doi) number	
1	Insights on therapeutic approaches of natural anti Alzheimer agents in thw management of Alzheimer disease A future propective	Rupesh K Gautam	Pharmacology	SAGE Journal	2024	986-024-00800	https://journals.sagepub.com/doi/10.1177/138728772241296557	https://journals.sagepub.com/doi/10.1177/13872877241296557	SCIE
2	Insights on Effective Complementary Strategies in the Management of Urinary Tract Infections	Rupesh K Gautam	Pharmacology	Script Media	2024	55-4970	https://aseestant.ceon.rs/index.php/scriptamed/article/view/49700	https://aseestant.ceon.rs/index.php/scriptamed/article/view/49700/26310	Scopus
3	Forecasting the effects of smoking prevalence scenarios on years of life lost and life expectancy from 2022 to 2050 a systematic analysis for the Global Burden of Disease Study 2021	Rupesh K Gautam	Pharmacology	The Lancet	2024	24-698-725	https://www.thelancet.com/journals/lanpub/article/PIIS2468-2667(24)00166-X/fulltext	https://www.thelancet.com/journals/lanpub/article/PIIS2468-2667(24)00166-X/fulltext	SCIE
4	Global burden of bacterial antimicrobial resistance 1990–2021: a systematic analysis with forecasts to 2050	Rupesh K Gautam	Pharmacology	The Lancet	2024	24-698-725	https://www.thelancet.com/journals/lancet/article/PIIS0140-6736(24)01867-1/fulltext	https://www.thelancet.com/journals/lancet/action/showPdf?pii=S0140-6736%2824%2901867-1	SCIE
	In Vitro Anti-Inflammatory Assays of Synthesized acetophenone	Praveen Sharma,	Pharmacology	AJPS	2024	ISSN : 2663-2187	https://www.afjbs.com/about-the-journal	https://www.afjbs.com/issue-content/in-vitro-anti-inflammatory-assays-of-synthesized-acetophenone-4428	SCIE

Principal
Indore Institute of Pharmacy,
INDORE (M.P.)

#	Title	Author	Subject	Journal	Year	ISSN	Journal Link	Article Link	Index
6	Insights on aspects of apoptosis in neurodegenerative disorders: a comprehensive review	Rupesh K Gautam	Pharmacology	Exploration of Medicine	2024	eISSN 2692-3106	Exploration of Medicine (explorationpub.com)	https://www.explorationpub.com/Journals/em/Article/1001208	SCIE
7	Decoding and Unravelling Mpox, Herpes, and Syphilis Infections: A State of Art Review	Rupesh K Gautam	Pharmacology	Current Pharmaceutical Biotechnology	2024	ISSN (Online) 1873-4316	https://www.eurekaselect.com/article/141790	https://www.eurekaselect.com/article/141790	Scopus
8	Development and validation of spectrohotometric method for simultaneous estimation of atorvastatin calcium and telmisartan in combined dosage form	Vaishali khedekar, Nimita Manocha, Archana Tiwari, PK Dubey	Pharmaceutics	IJPSM	2024	ISSn2519-9889	https://www.afjbs.com/issue-content/formulation-and-evaluation-of-polyherbal-capsules-for-the-treatment-of-poly-cystic-ovarian-syndrome-pcos-2915	https://www.afjbs.com/issue-content/formulation-and-evaluation-of-polyherbal-capsules-for-the-treatment-of-poly-cystic-ovarian-syndrome-pcos-2915	Scopus
9	Preparation And Characterization Of Microspheres Utilizing Rate-Controlling Membranes For The Management Of Diabetes Mellitus	Shreyash Vani, Nimita Manocha, Nadeem A Farooqui	Pharmaceutics	Romanian Journal of Diabetes, Nutrition and Metabolic Diseases	2024	ISSN 1583-8609	Romanian Journal of Diabetes, Nutrition and Metabolic Diseases (jrdiabet.ro)	https://jrdiabet.ro/index.php/RJDNMD/article/view/363/403	Scopus
10	Natural product in the management of neurodegenerative disease	Rupesh K Gautam	Pharmacology	Nutrition and metabolism	2024	26 2024	https://nutritionandmetabolism.biomedcentral.com/articles/10.1186/s12986-024-00800-4	https://nutritionandmetabolism.biomedcentral.com/articles/10.1186/s12986-024-00800-4	Scopus
11	Formulation Development and Hepatoprotective activity of Hydro-alcoholicextract of Abutilon indicum and Phyllanthus niruri against paracetamolinduced liver toxicity in albino rats	Dr. Rekha Bisht	Pharmacology	African Journal of pharmaceutical Science	2024	ISSN 2663-2187	https://mail.google.com/mail/u/0/#inbox?projector=1	https://mail.google.com/mail/u/0/#inbox?projector=1	Scopus
12	Formulation And Evaluation Of Polyherbal Capsules For The Treatment Of Poly Cystic Ovarian Syndrome (Pcos)	Dr Nimita Manocha	Pharmaceutics Chemistry	African Journal Of Biological Sciences	2024	(ISSN: 2663-2187)	https://www.afjbs.com/uploads/paper/41529e811c1156c9beaa898d74848921.pdf	https://www.afjbs.com/uploads/paper/41529e811c1156c9beaa898d74848921.pdf	Scopus
13	Transformative Capsule Technology: A Review Of Tablet-In-Capsule Innovation	Pawan Patel, Isha Dubey, Nayany Sharma, Nadeem Farooqui, Nimita Manocha	Pharmaceutics	Journal of Technology	2024	ISSN 1012-3407	https://journaloftechnology.org/	https://drive.google.com/file/d/1csD7FK0SO_JAtiiabloJP9hApcbjf7Djy/view?usp=sharing	UGC

No.	Title	Authors	Category	Journal	Year	ISSN	Journal (link)	URL	Indexing
14	Development and Optimization of Moxifloxacin-Loaded in-Situ Gel Using Box-Behnken Design for Ophthalmic Drug Delivery	Anjali Kumarawat, Nadeem A. Farooqui, Darshan Jamindar, Nimita Manocha	Pharmaceutics	Journal of Chemical Health Risk	2024	2251-6727	Journal of Chemical Health Risks (jchr.org)	https://jchr.org/index.php/JCHR/article/view/4706	Scopus
15	Theoretical Approaches to Process Validation in Pharmaceutical Manufacturing Process	Richa Shukla, Dr. Nimita Manocha, Dr. Gurmeet Singh Chhabra	Pharmaceutics Chemistry	International Journal of Scientific Research in Science and Technology	2024	Online ISSN 2395-602X	International Journal of Scientific Research in Science and Technology (ijsrst.com)	https://ijsrst.com/index.php/home/article/view/IJSRST152411229	Scopus
16	Formulation and Evaluation of mouth dissolving film of cyclizine hydrochloride	Sakshi Bafna, Nadeem Farooqui, Nimita Manocha, Nayany Sharma	Pharmaceutics	Advance in Research	2024	ISSN 2277-1573	https://soeagra.com/abr_july2024.html	https://www.researchgate.net/publication/235338119_Formulation_and_Evaluation_of_Fast_Dissolving_Oral_Film_ofDicyclomine_as_potential_route_of_Buccal_Delivery	Scopus
17	Optimization, Formulation And Evaluation Of Tablet-In-Capsule: Sodium Bicarbonate Buffer With Pantoprazole Sodium Mini-Tablet	Pawan Patel , Nayany Sharma , Nadeem A. Farooqui , Nimita Manocha	Pharmaceutics	African Journal of Biological Sciences	2024	ISSN 2663-2187	African Journal of Biological Sciences (afjbs.com)	https://www.afjbs.com/issue-content/optimization-formulation-and-evaluation-of-tablet-in-capsule-sodium-bicarbonate-buffer-with-pantoprazole-sodium-mini-tablet-736	Scopus
18	Formulation & Characterization Of Sustained Release Multichambered Tablet Of Losartan Potassium Using Fused Deposition Modelling (FDM) 3D-Printer	Nadeem Farooqui, Nimita Manocha	Pharmaceutics	Journal of Health and Chemical Risk	2024	ISSN 2251-6727	https://jchr.org/index.php/JCHR/article/view/4776/3051	https://jchr.org/index.php/JCHR/article/view/4776/3051	Scopus
19	Global fertility in 204 countries and territories, 1950–2021, with forecasts to 2100: a comprehensive demographic analysis for the Global Burden of Disease Study 2021	Rupesh K. Gautam	Pharmacology	Lancet Infect Dis 2024.	2024	24-698-725	https://www.thelancet.com/action/showPdf?pii=S0140-6736%2824%2900550-6	https://www.thelancet.com/action/showPdf?pii=S0140-6736%2824%2900550-6	SCIE

Principal
Indore Institute of Pharmacy,
INDORE (M.P.)

S.No	Title	Author	Department	Journal Name	Year	Page/Vol	URL 1	URL 2	Indexing
20	Global, regional, and national age-specific progress towards the 2020 milestones of the WHO End TB Strategy: a systematic analysis for the Global Burden of Disease Study 2021	Rupesh K. Gautam	Pharmacology	Lancet Infect Dis 2024,	2024	24-698-725	https://www.thelancet.com/journals/laninf/home	https://www.thelancet.com/journals/laninf/article/showPdf?pii=S1473-3099%2824%2900007-0	SCIE
21	Global, regional, and national burden of disorders affecting the nervous system, 1990–2021: a systematic analysis for the Global Burden of Disease Study 2021	Rupesh K. Gautam	Pharmacology	Lancet Infect Dis 2024,	2024	24-698-725	https://www.thelancet.com/journals/laninf/home	https://www.thelancet.com/journals/laneur/article/PIIS1474-4422%2824%2900038-3/fulltext	SCIE
22	Global burden of 288 causes of death and life expectancy decomposition in 204 countries and territories and 811 subnational locations, 1990–2021: a systematic analysis for the Global Burden of Disease Study 2021	Rupesh K. Gautam	Pharmacology	Lancet Infect Dis 2024,	2024	p2100-2132	https://www.thelancet.com/journals/laninf/article/PIIS0140-6736(24)00367-2/fulltext	https://www.thelancet.com/journals/lancet/article/PIIS0140-6736(24)00367-2/fulltext	SCIE
23	Global age-sex-specific mortality, life expectancy, and population estimates in 204 countries and territories and 811 subnational locations, 1950–2021, and the impact of the COVID-19 pandemic: a comprehensive demographic analysis for the Global Burden of Disease Study 2021	Rupesh K. Gautam	Pharmacology	Lancet Infect Dis 2024,	2024	24-698-725	https://www.thelancet.com/journals/laninf/home	https://www.thelancet.com/journals/lancet/article/PIIS0140-6736(24)00476-8/fulltext	SCIE
24	Unlocking the Immunomodulatory Potential of Rosmarinic Acid Isolated from Punica granatum L. using Bioactivity-Guided Approach: In Silico, In Vitro, and In Vivo Approaches	Rupesh K. Gautam	Pharmacology	Current Medicinal Chemistry	2024	5969 - 5988	https://www.eurekaselect.com/journal/125/about-journal	https://www.eurekaselect.com/article/138960	SCIE
25	Preparation And Characterization Of Microspheres Utilizing Rate-Controlling Membranes For The Management Of Diabetes Mellitus	Rupesh K. Gautam	Pharmacology	Indian Drug	2024	51-56	https://www.indiandrugsonline.org/issuesarticle-details?id=MTU0NA	https://www.indiandrugsonline.org/issuesarticle-details?id=MTU0NA	Scopus
26	Insights on aspects of apoptosis in neurodegenerative disorders: a comprehensive review	Rupesh K. Gautam	Pharmacology	Open Exploration	2024	2024;5:89–100	https://www.explorationpub.com/Journals/em/Article/1001208	https://www.explorationpub.com/Journals/em/Article/1001208	Scopus
27	Unlocking β-cell restoration: The crucial role of PDX1 in diabetes therapy	Rupesh K. Gautam	Pharmacology	Pathology Research and Practice	2024	2024;5:89–100	https://www.sciencedirect.com/science/article/abs/pii/S0344033824000426?via%3Dihub	https://www.sciencedirect.com/science/article/abs/pii/S0344033824000426?via%3Dihub	SCIE

Principal
Indore Institute of Pharmacy,
INDORE (M.P.)

No.	Title	Author	Department	Journal	Year	ISSN	URL	URL	Type
28	Identification and evaluation of antimicrobial and anti- arthritis activities of hydroethanolic extract of rubus ellipticus leaves	Rupesh K. Gautam, Dr. Nadeem Farooqui	Pharmacology	narra J	2024	eISSN: 2692-3106	https://narraj.org/main		Scopus
29	Diuretic activity of Hydoalcoholic extract of Peristrophe bicalyculata Nees Leaves in saline loaded rats	Dr. Gurmeet Chhabra	Pharmaceutics Chemistry	International Journal of Pharmaceutical Quality Assurance	2024	0975 9506	https://ijpqa.com/	https://www.researchgate. net/publication/37743014 1 Diuretic Activity of Hyd roalcoholic Extract of Per istrophe bicalyculata R N ees Leaves in Saline Load ed Rats	Scopus

2023

No.	Title	Author	Department	Journal	Year	ISSN	URL	URL	Type
30	Green Synthetic of Silver Nanoparticles using plants extract for Diabetic wound healing	Navany Sakalle, Mahendra Singh Rathod, Dinesh Kumar Mishra, Shivani Burman	Pharmacy	Journal of the Maharaja Sayajirao University of Baroda	2023	ISSN - 0025-0422	https://www.google. com/search?q=An+i n+vitro+pharmacog nostical+study+on+ gluconeogenesis+an d+glucose&	https://www.google.com/scar ch?q=An+in+vitro+pharmaco gnostical+study+on+gluconeo genesis+and+glucose&	Print
31	Phytotherapeutic Potential of Natural Herbal Medicines for Management of Psoriasis Current Status	Dinesh Kumar Mishra	Pharmacy	Pharmacognosy Research	2023	0974-8490	www.phcogres.com	https://www.phcogres.com/art icle/2023/15/1/105530097484 900261	Web of science
32	Antidiarrhoeal activity zizipus mauritiana leaf extraction in rodents	Rohit Sahu, Pritesh Paliwal & Praveen Sharma	Pharmacy	Journal of the Maharaja Sayajirao University of Baroda	2023	ISSN: 0025-0422	https://www.researc hgate.net/publicatio n289176754_	https://www.researchgate.net/ publication/289176754	UGCapproved
33	An in vitro pharmacognostical study on gluconeogensis and glucose	Praveen Sharma,	Pharmacy	Journal of Advanced Zoology	2023	ISSN NO: 1006-8341	https://www.google. com/search?q=An+i n+vitro+pharmacog nostical+study+on+ gluconeogenesis+an d+glucose&	https://www.google.com/scar ch?q=An+in+vitro+pharmaco gnostical+study+on+gluconeo genesis+and+glucose&	UGCapproved
34	(Knowledge, Attitudes and Practices) Study on Medicine and Health Infrastructure use in Pregnant Women of Rural Areas of Ujjain Madhya Pradesh, India A Cross-Sectional Survey	Sandeep Singh Bhadoriya1*, Prashant Wadaghalkar2, Praveen Sharma3, RekhaBisht3, Nayany Sharma Sakalle3, Amol R Chandelkar4	Pharmacy	Journal of Chemical Health Risks	2023	JCHR (2023) 13(4), 2293-2298 ISSN 2251-6727	file://C:/Users/NIL ESH/Downloads/Sa ndeep_Article_1_p df	file://C:/Users/NILESH/Dow nloads/Sandeep_Article_1_p df	UGCapproved

Principal
Indore Institute of Pharmacy,
INDORE (M.P.)

S.No	Title of paper	Name of author	Department	Journal name	Year	ISSN	Link	Link	Indexed
35	IN SILICO PHARMACOKINETIC, BIOACTIVITY AND TOXICITY STUDIES OF SEVERAL SELECTED ANTI-VIRAL DRUGS	Rohit Kumar Trivedi, Datta Madhavrao Avhad, Rajesh E Jesudasan, Yogesh Tiwari, D.T. Sakhare, Rekha Bisht, Prarthna Lakhera, Jhama Jhamo	Pharmacy Practice	European chemical bulletin	2023	ISSN 2063-5346	https://www.eurchembull.com/issue-content/in-silico-pharmacokinetic-bioactivity-and-toxicity-studies-of-several-selected-anti-viral-drugs-5288	https://www.eurchembull.co m/issue-content/in-silico-pharmacokinetic-bioactivity-and-toxicity-studies-of-several-selected-anti-viral-drugs-5288	UGC approved
36	Phytoconstituent and Pharmacological screening for anti-diabetic activity of Tephrosia villosa	Sheik Nasar I, Azra Aisha, M. Naveen Kumar, Hemant P. Suryawanshi, Rekha Bisht, Sushila Gupta, Yashvardini S., Mohammad Khalid	Pharmacology	European chemical bulletin	2023	ISSN 2063-5346	https://www.eurche mbull.com/issue-content/phytoconstit uent-and-pharmacological-screening-for-anti-diabetic-activity-of-tephrosia-villosa-6881	https://www.eurchembull.co m/issue-content/phytoconstituent-and-pharmacological-screening-for-anti-diabetic-activity-of-tephrosia-villosa-6881	scopus
37	Formulation Development and Evaluation of Herbal Tablet of Diplocyclos palmatus (L.) Jeffry	Sumeet Dwivedi, Devendra S. Lodhi, Deepak Kumawat, Pradeep Golani, Anup K. Chakraborty, Rekha Bisht	Pharmacology	INTERNATIONAL JOURNAL OF DRUGT DELIVERY AND TECHNOLOGY	2023	ISSN 0975 4415	https://ijddt.com/vol ume13issue3/	https://ijddt.com/volume13iss ue3/	UGC approved
38	Reishi (Ganoderma lucidum) A potential Sources of Nutraceuticals and prebiotics	Pritesh Paliwal & Praveen Sharma	Pharmaceutics	Journal of the Maharaja Sayajirao University of Baroda	2023	ISSN. 0025-0422	Print	Print	UGC approved
39	Research progress of small-molecule drugs in targeting telomerase in human cancer and aging	Dinesh K. Mishra5, Rupesh K. Gautam	Pharmacology	Chemico biological Interaction	2023	ISSN NO 1006-8341	https://doi.org/10.10 16/j.cbi.2023.11063 1	https://doi.org/10.1016/j.cbi.2 023.110631	Elsevier
40	Nanomedicine Innovative Strategies and Recent Advances in Targeted Cancer Therapy	Dinesh K. Mishra5, Rupesh K. Gautam	Pharmacology	Current Medicinal Chemistry	2023	0929-8673	Current Medicinal Chemistry, XXXX, XX, 1-00	Current Medicinal Chemistry, XXXX, XX, 1-00	Scopus
41	Phytochemical, Ethnobotanical, and Global Perspectives of Genus Echinacea: A Panoramic Review	Dinesh K. Mishra5, Rupesh K. Gautam	Pharmacology	Current Medicinal Chemistry	2023	2215-0838	Current Medicinal Chemistry, XXXX, XX, 1-01	Current Medicinal Chemistry, XXXX, XX, 1-01	Scopus
42	Review on Nanosuspension as a Novel Drug Delivery System for the Treatment of Fungal Infection	Ritu Kumari1* Nadeem Farooqui1, Dinesh Kumar Mishra1, Arti Majumdar2	Pharmaceutics	Journal For Basic Sciences	2023	ISSN NO : 1006-8341	https://drive.google. com/file/d/1BXEP0 Pgbpo_KXuP2BkL WOd71FWTmOvla/ view?pli=1	https://drive.google.com/file/d /1BXEP0Pgbpo_KXuP2BkL WOd71FWTmOvla/view?pli =1	scopus
43	Celiac disease Pathogenesis, disease management and new insights into the herbal-based treatments	Dinesh K. Mishra5, Rupesh K. Gautam	Pharmacology	Naaraj	2023	875-5550	10.52225/narra.v3i2 .147	10.52225/narra.v3i2.147	scopus
44	Computerized system validation- A Regulatory requirement in pharmaceutical Industry	Niel Ravi Daniel, Dr Gurmeet Singh Chhabra, Gaurav Sarsodiya	Pharmaceutical Chemistry	International Journal of Research and Analytical	2023	2349-5138	www.ijrar.org	Print/online	scopus

Principal
Indore Institute of Pharmacy,
INDORE (M.P.)

No.	Title	Authors	Department	Journal	Year	ISSN	Journal URL	Article URL	Indexing
45	Evaluation of In vitro Antioxidant, Antimicrobial and Cytotoxicity Activities of Orthosiphon Pallidus Royle	Mukesh Kr. Singh, Gurdeep Singh, Ritesh Patel, Amrita Mishra, Arun Kr. Mishra, Sushil Kumar	Pharmaceutical Chemistry	International Journal of Pharmaceutical Sciences and Nanotechnology (IJPSN)	2023	0974-3278	https://www.ijpsnonline.com/	https://www.ijpsnonline.com/index.php/ijpsn/article/view/2619	scopus
46	Mechanism-Based Suppression of Cancer by Targeting DNA-Replicating Enzymes	Rupesh K. Gautam*, Dinesh Kumar Mishra	Pharmacology	Current Protein & Peptide Science	2023	875-5550	https://benthamscience.com/public/journals/current-protein-and-peptide-science	http://dx.doi.org/10.2174/1389203724666230512144011	Scopus, Pubmed/IF-3.118
47	Global, regional, and national burden of diabetes from 1990 to 2021, with projections of prevalence to 2050: a systematic analysis for the Global Burden of Disease Study 2021	Rupesh K. Gautam*	Pharmacology	The Lancet	2023	0140-6736 (print); 1474-547X (web)	https://www.thelancet.com/journals/lancet/home	https://doi.org/10.1016/S0140-6736(23)01301-6	Scopus/ IF-202
48	The unfinished agenda of communicable diseases among children and adolescents before the COVID-19 pandemic, 1990–2019: a systematic analysis of the Global Burden of Disease Study 2019	Rupesh K. Gautam*	Pharmacology	The Lancet	2023	0140-6736 (print); 1474-547X (web)	https://www.thelancet.com/journals/lancet/home	https://doi.org/10.1016/s0140-6736(23)00860-7	Scopus/ IF-202

Principal
Indore Institute of Pharmacy,
INDORE (M.P.)

Insights on Effective Complementary Strategies in the Management of Urinary Tract Infections

Shweta Gandhi

Priya Shah

Rajat Goyal

Rupesh K Gautam
Department of Pharmacology, Indore Institute of Pharmacy, Rau, Indore, India

Hitesh Chopra

ABSTRACT

Urinary tract infections (UTIs) are common health issues that occur frequently in both women and men. These infections occur in the urinary tract, leading to discomfort and potential complications. Prompt medical attention is essential to diagnose and treat UTIs effectively. Aim of this research was to provide an overview of effective complementary strategies in the management of UTIs. This review paper focuses on the current and future treatment strategies for UTI infections. Various natural remedies have been investigated as potential complementary therapies to enhance health outcomes for UTI patients. The efficacy of frequently employed natural products, including cranberry juice/extracts, ascorbic acid, hyaluronic acid, probiotics and multi-component formulations designed for the treatment and prevention of UTIs, has been explored. The probiotics serve to break down food and increase our immunity. Usually, multiple doses of antibiotics are used to treat these infections, but there are many side effects and bacterial resistance rates are increasing. Complementary UTI management strategies, including effective dietary regimens and new formulations, are attaining approvals. Drinking liquids daily significantly suppresses UTI infections. Incorporating daily consumption of cranberry juice may still be regarded as a viable complementary strategy to aid in the management of UTI infections.

REFERENCES

Hudson RE, Job KM, Sayre CL, Krepkova LV, Sherwin CM, Enioutina EY. Examination of complementary medicine for treating urinary tract infections among pregnant women and children. Front Pharmacol. 2022 Apr 27;13:883216. doi: 10.3389/fphar.2022.883216.

Reid G. Potential preventive strategies and therapies in urinary tract infection. World J Urol. 1999;17:359-63. doi: 10.1007/s003450050161.

Braunwald E, Fauci AS, Kasper DL, Hauser SL, Longo DL, Jameson JL. Harrison's principles of internal medicine. In: Harrison's principles of internal medicine-15th edition. New York: McGraw-Hill; 2001. pp. 1187-1187.

Sheerin NS, Glover EK. Urinary tract infection. Medicine. 2019;47(9):546-50. doi: 10.1016/j.mpmed.2019.06.008.

Bhise Sb. Human anatomy and physiology. Pune, India: Pragati Books; 2008.

Mohan H. Textbook of pathology. New Delhi, India: Jaypee Brothers Medical Publishers; 2018.

Auer S, Wojna A, Hell M. Oral treatment options for ambulatory patients with urinary tract infections caused by extended-spectrum-β-lactamase-producing Escherichia coli. Antimicrob Agents Chemother. 2010;54(9):4006-8. doi: 10.1128/aac.01760-09.

Blumberg JB, Camesano TA, Cassidy A, Kris-Etherton P, Howell A, Manach C, et al. Cranberries and their bioactive constituents in human health. Adv Nutr. 2013;4(6):618-32. doi: 10.3945%2Fan.113.004473.

Haverkorn MJ, Mandigers J. Reduction of bacteriuria and pyuria using cranberry juice. JAMA. 1994;272(8):590. doi: 10.1001/jama.272.8.590a.

Kahn HD, Panariello VA, Saeli J, Sampson JR, Schwartz E. Effect of cranberry juice on urine. J Am Diet Assoc. 1967 Sep;51(3):251-4. PMID: 6035629

Howell AB, Reed JD, Krueger CG, Winterbottom R, Cunningham DG, Leahy M. A-type cranberry proanthocyanidins and uropathogenic bacterial anti-adhesion activity. Phytochemistry. 2005;66(18):2281-91. doi: 10.1016/j.phytochem.2005.05.022.

Lynch DM. Cranberry for prevention of urinary tract infections. Am Fam Physician. 2004 Dec 1;70(11):2175-7. PMID: 15606066

Schmidt DR, Sobota AE. An examination of the anti-adherence activity of cranberry juice on urinary and nonurinary bacterial isolates. Microbios. 1988;55(224-225):173-81. PMID: 3063927.

Principal
Indore Institute of Pharmacy,
INDORE (M.P.)

Log in

Search for...

⤓ Download Full Issue

Forecasting the effects of smoking prevalence scenarios on years of life lost and life expectancy from 2022 to 2050: a systematic analysis for the Global Burden of Disease Study 2021

GBD 2021 Tobacco Forecasting Collaborators

Affiliations & Notes ∨   Article Info ∨

Summary

Background

Smoking is the leading behavioural risk factor for mortality globally, accounting for more than 175 million deaths and nearly 4·30 billion years of life lost (YLLs) from 1990 to 2021. The pace of decline in smoking prevalence has slowed in recent years for many countries, and although strategies have recently been proposed to achieve tobacco-free generations, none have been implemented to date. Assessing what could happen if current trends in smoking prevalence persist, and what could happen if additional smoking prevalence reductions occur, is important for communicating the effect of potential smoking policies.

Methods

In this analysis, we use the Institute for Health Metrics and Evaluation's Future Health Scenarios platform

Download PDF   Outline   Share   More

Principal
Indore Institute of Pharmacy,
INDORE (M.P.)

2

scenario forecasts what could occur if past smoking prevalence and other risk factor trends continue, the Tobacco Smoking Elimination as of 2023 (Elimination-2023) scenario quantifies the maximum potential future health benefits from assuming zero percent smoking prevalence from 2023 onwards, whereas the Tobacco Smoking Elimination by 2050 (Elimination-2050) scenario provides estimates for countries considering policies to steadily reduce smoking prevalence to 5%. Together, these scenarios underscore the magnitude of health benefits that could be reached by 2050 if countries take decisive action to eliminate smoking. The 95% uncertainty interval (UI) of estimates is based on the 2·5th and 97·5th percentile of draws that were carried through the multistage computational framework.

Findings

- Global age-standardised smoking prevalence was estimated to be 28·5% (95% UI 27·9–29·1) among males and 5·96% (5·76–6·21) among females in 2022. In the reference scenario, smoking prevalence declined by 25·9% (25·2–26·6) among males, and 30·0% (26·1–32·1) among females from 2022 to 2050. Under this scenario, we forecast a cumulative 29·3 billion (95% UI 26·8–32·4) overall YLLs among males and 22·2 billion (20·1–24·6) YLLs among females over this period. Life expectancy at birth under this scenario would increase from 73·6 years (95% UI 72·8–74·4) in 2022 to 78·3 years (75·9–80·3) in 2050. Under our Elimination-2023 scenario, we forecast 2·04 billion (95% UI 1·90–2·21) fewer cumulative YLLs by 2050 compared with the reference scenario, and life expectancy at birth would increase to 77·6 years (95% UI 75·1–79·6) among males and 81·0 years (78·5–83·1) among females. Under our Elimination-2050 scenario, we forecast 735 million (675–808) and 141 million (131–154) cumulative YLLs would be avoided among males and females, respectively. Life expectancy in 2050 would increase to 77·1 years (95% UI 74·6–79·0) among males and 80·8 years (78·3–82·9) among females.

Interpretation

Existing tobacco policies must be maintained if smoking prevalence is to continue to decline as forecast by the reference scenario. In addition, substantial smoking-attributable burden can be avoided by accelerating the pace of smoking elimination. Implementation of new tobacco control policies are crucial in avoiding additional smoking-attributable burden in the coming decades and to ensure that the gains won over the past three decades are not lost.

Funding

Introduction

years of life lost (YLLs) were attributable to smoking in 2021.[1] Smoking also has important effects on health-care costs, productivity, and health disparities.[3-5] As a result, tobacco control is an enduring policy and public health priority, with enormous potential to improve population health.

Research in context

Evidence before this study

Smoking is widely recognised as a major global health risk with extensive supporting literature. The Global Burden of Diseases, Injuries, and Risk Factors Study serves as the most comprehensive source for smoking prevalence and all-cause and cause-specific attributable burden across 204 countries and territories, by age and sex. However, fewer studies have focused on forecasting tobacco use and burden. We searched PubMed on July 9, 2024, using the following search terms: (("smok*"[All Fields] OR "tobacco"[All Fields]) AND ("forecast*"[All Fields] OR "scenario*"[All Fields] OR "projection*"[All Fields]) AND ("prevalence"[All Fields] OR "burden"[All Fields] OR "disease"[All Fields])). We restricted the search to articles published in the past 10 years. The search yielded 1098 studies. Many studies have forecasted smoking prevalence in the status quo, as well as under various policy scenarios, for specific countries. A 2024 WHO report forecasts global smoking prevalence will be 30·6% among males and 5·7% among females in 2030. Previous studies have also estimated future disease burden from smoking, although these studies typically focus on all causes combined or a small subset of smoking-related causes. Our search did not identify any studies that have estimated the future burden of smoking for all countries and all smoking-related health conditions.

Added value of this study

Our study contributes a comprehensive set of estimates of future health burden under three smoking prevalence scenarios for 204 countries and 365 diseases and injuries, disaggregated by 5-year age group and sex. Methodologically, we have developed a forecasting framework that incorporates smoking prevalence, intensity, duration, and risk reduction from cessation. Furthermore, by leveraging the Institute for Health Metrics and Evaluation's Future Health Scenarios platform, our forecasts integrate dynamic changes in demographics and other determinants of health.

4

The current evidence underscores the substantial potential for health gains through more aggressive tobacco control policies, worldwide. Although a continuation of the existing decline in smoking prevalence will undoubtedly yield health benefits, our analysis quantifies the substantial increase in life expectancy and decrease in years of life lost that could result from accelerated efforts in tobacco control.

After a period of accelerated progress following the adoption of WHO's Framework Convention on Tobacco Control, progress has slowed in recent years.[6,7] Although global prevalence of smoking continues to decline, the pace of decline fluctuates and has slowed in many countries. Renewed efforts are required to overcome the tobacco industry's attempts to maintain a market. The concept of a tobacco endgame, in which focus shifts from controlling the tobacco epidemic to eliminating the tobacco epidemic, has been discussed for more than 10 years in the academic literature.[8,9] Countries and organisations around the world have set goals to reduce smoking prevalence to less than 5% in the coming years.[10–13]

Strategies to reach a tobacco-free future work together to eliminate the initiation of tobacco use among youth while steadily phasing out tobacco use in the adult population. Despite promising policy proposals in some countries, including the UK,[14] the political commitment to implement and enforce the measures necessary to realise a tobacco-free future largely remains elusive. New Zealand's transformational legislation that would have prohibited the sale of tobacco to anyone born on or after Jan 1, 2009, was recently repealed to fund other tax cuts. Similarly, Malaysia's generational smoking ban was dropped from their recent tobacco control bill.[15,16] Forecasts of the health effects of potential smoking policy scenarios provide quantitative evidence on the costs of inaction that can aid decision makers.

Previous studies have simulated the effects of reducing smoking prevalence in selected countries.[17–29] These studies find large population health benefits that accrue over time, the potential for health-care cost savings, and reductions in smoking-attributable health disparities.[30,31] Although many prospective policy simulation studies exist for some countries, such analyses do not exist for all countries. Furthermore, previous studies have not systematically disaggregated impacts by disease, which can aid health system planning and prioritisation of medical innovation. Finally, health forecasting is a dynamic process that reflects simultaneous changes across many determinants of health and feedback between changes in health determinants and changes in demography. Our study adds to existing evidence by providing comprehensive country-specific and disease-specific estimates under three smoking prevalence scenarios using a dynamic forecasting framework.

With the use of the Institute for Health Metrics and Evaluation's Future Health Scenarios platform, we aim to forecast all-cause and cause-specific YLLs for all countries from 2022 to 2050, as well as life expectancy

future health benefits from smoking elimination. The third scenario, Tobacco Smoking Elimination by 2050 (Elimination-2050), which includes a generational ban beginning in 2023 and a steady reduction of smoking prevalence to 5% among older cohorts by 2050, provides insight into what gains could be realised by countries considering policies to reach endgame targets. Together, these scenarios underscore the magnitude of health benefits, benefits that will continue to grow beyond 2050, which could be achieved if countries take action to end the global tobacco epidemic. This manuscript was produced as part of the GBD Collaborator Network and in accordance with the GBD Protocol.

Methods

Overview

We used the Future Health Scenarios platform to forecast YLLs under three smoking prevalence scenarios, for 204 countries and territories as well as 365 diseases and injuries by 5-year age group and sex from 2022 to 2050. In the following sections, we focus primarily on methods specific to this analysis of the effects of smoking prevalence reductions. The methods used to forecast population, fertility, and all-cause mortality have been reported elsewhere.[32–35] Methods and accompanying estimates for smoking-specific inputs, including smoking prevalence, continuous measures of intensity of exposure, and dose-response relative risks for 32 health outcomes have also been previously published.[1] In this analysis, we only report the direct effects from smoking tobacco, which do not include the health effects from second-hand smoke, smokeless tobacco use, or electronic nicotine delivery systems. This study adheres to the Guidelines for Accurate and Transparent Health Estimates Reporting statement (appendix 1 pp 16–17).[36]

Forecasting framework
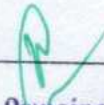
We obtained estimates of independent drivers of health, including over 70 risk factor summary exposure values from the Global Burden of Diseases, Injuries, and Risk Factors Study (GBD), interventions such as vaccines and antiretroviral therapy coverage, and covariates such as Socio-demographic Index (a composite measure of income, education, and fertility under age 25 years) from GBD 2021, for every location, age, and sex, from 1990 to 2019. These independent variables were then forecasted to 2050, mostly using a generalised ensemble model that includes past annual rates of change and relationship with Socio-demographic Index to predict future trends (appendix 1 p 13).

Once we have a complete time series from 1990 to 2050 for each of the independent variables, we use them to forecast cause-specific mortality rates up to 2050. Future mortality is estimated using three components: underlying (risk-deleted) mortality, a risk factor scalar, and latent trends predicted with an autoregressive integrated moving average (0,1,0) model.[35] These cause-specific mortality estimates are aggregated to obtain all-cause mortality.[33] We used the methods published in Vollset and colleagues' study[33] to obtain life tables and population estimates to 2050. Briefly, age-specific and sex-specific future

6

enabling us to capture the effects of differing mortality rates on population age structure and size. YLLs were then computed for each scenario using demographically aggregated mortality forecasts and the GBD reference life table.[33] Details on validation of our forecasting model can be found in previous studies.[32,33,35]

Smoking scenario definitions

We forecast cause-specific and all-cause mortality under three scenarios, which we refer to as the reference, Elimination-2023, and Elimination-2050 scenarios. The reference scenario assumes that past independent health driver trends and relationships between drivers and health outcomes persist into the future. To estimate an upper bound on the effect of reducing smoking prevalence, we constructed the Elimination-2023 scenario, under which past trends persist across all inputs except current smoking prevalence, which is reduced to zero from 2023 onwards. Finally, we constructed the Elimination-2050 scenario, under which past trends persist across all inputs except smoking prevalence, which is linearly reduced to 5% between 2023 and 2050. The Elimination-2050 scenario provides a benchmark that falls between the reference scenario and Elimination-2023 scenario.

For all scenarios, we use GBD 2021 estimates of distributions of cigarette-equivalents smoked per day and pack-years among current smokers, distributions of years since quitting among former smokers, and cause-specific relative risk estimates for both current and former smokers. We assumed the 2022 age-specific distributions of cigarette-equivalents smoked per day and pack-years among current smokers remained constant into the future. In the reference scenario, we similarly assumed the 2022 age-specific distributions of years since quitting among former smokers remained constant into the future. In the alternative scenarios, we shifted the 2022 years since quitting distributions for former smokers who quit in 2022 or earlier forward with every future year and created uniform distributions to model the years since quitting for former smokers who quit in 2023 or later. We then used these inputs, and scenario-specific prevalence forecasts for current smokers, former smokers, and never smokers, to compute population attributable fractions for smoking between 2020 and 2050, which in turn were used to compute smoking summary exposure values. The population attributable fraction calculation was adapted from the GBD study, with additional terms added to capture the burden among recent quitters (appendix 1 p 12).
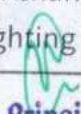
Reference scenario forecast

The reference scenario is a probabilistic forecast that allows historical trends of drivers of health to continue into the future and holds the past relationship between drivers and health outcomes constant. To forecast smoking prevalence in this scenario, we first obtained current smoking and former smoking prevalence estimates for every location, sex, 5-year age group, and year from 1990 to 2019 from GBD 2021.[1] We then used an ensemble model to forecast current and former smoking prevalence from 2020 to 2050.[35] Briefly, the ensemble models consisted of six submodels that used annualised rates of change to forecast prevalence to 2050 based on past smoking trends. Each submodel had a recency-weighting parameter

Alternative smoking prevalence scenarios

The Elimination-2023 scenario was constructed with the reference scenario's current and former smoking prevalence values from 2020 to 2022, setting current smoking prevalence to 0% from 2023 onwards. We considered the population of current smokers in 2022 to be former smokers from 2023 onwards and tracked their years since quitting for every year from 2023 to 2050. For the population of existing former smokers that quit smoking between 1990 and 2022, we held the distribution of years since quitting constant and extended it into the future (ie, if for a given cohort the mean years since quitting was 10 in 2022, the mean years since quitting for that cohort would be 15 in 2027).

The Elimination-2050 scenario was constructed similarly. We created the scenario by setting smoking prevalence to zero for birth cohorts of ages 0–19 years in 2023. For older cohorts, we linearly reduced current smoking prevalence starting in 2023 to 5% by 2050. For older cohorts with current smoking prevalence rates below 5% in 2022, we held that prevalence rate constant to 2050. As in the Elimination-2023 scenario, we held the distribution of years since quitting constant and logically extended it into the future for the population of existing former smokers that quit smoking between 1990 and 2022. We used a uniform distribution of years since quitting for the population of former smokers that quit during or after 2023, since the proportion of people quitting between 2023 and 2050 was constant.

To account for the effects of different mortality rates between people who currently, formerly, and never smoked, we estimated the all-cause relative risks of mortality for each smoking status. First, we computed exposure-weighted relative risks by location, age, sex, and cause in 2022. We then aggregated these cause-specific relative risks across all causes to generate an all-cause relative risk of mortality. Finally, we computed the mortality rate among people who never smoked and used each of the mortality rates to adjust our prevalence estimates in every future year. As a result, the share of current and former smokers in the population decreased over time in each of the alternative scenarios.

Uncertainty estimation

Uncertainty intervals (UIs) were computed from distributions for each estimate generated by propagating 500 draws through the multistage computational pipeline. The 95% uncertainty interval of estimates is based on the 2·5th and 97·5th percentile of draws. We report results with the mean and UI for all three scenarios in the main text and tables, and only for the reference scenario in figures. We did all analyses using R (version 4.2.2) and Python (version 3.10.13).

Role of the funding source

The funders of the study had no role in study design, data collection, data analysis, data interpretation, or writing of the report.

Download PDF

Principal
Indore Institute of Pharmacy,
INDORE (M.P.)

8

Smoking prevalence forecasts

The age-standardised prevalence of current smoking declined globally from 1990 to 2022, from 40·8% (95% UI 40·4–41·1) to 28·5% (27·9–29·1) among males aged 10 years and older, and from 9·94% (9·77–10·15) to 5·96% (5·76–6·21) among females aged 10 years and older (figure 1). We forecast that this decline will continue, albeit at a slower pace, with an age-standardised prevalence of 21·1% (20·6–21·6) among males and 4·18% (3·98–4·48) among females in 2050, a 25·9% (25·2–26·6) and 30·0% (26·1–32·1) decline relative to 2022, respectively. By 2050, the age-standardised prevalence among males is forecasted to range between 3·18% (2·95–3·47) in Brazil and 63·2% (60·6–65·6) in the Federated States of Micronesia, and among females between 0·50% (0·36–0·68) in Nigeria and 38·5% (35·2–41·8) in Serbia (appendix 2 pp 3–9). Despite a forecasted increase of the global population of 1·44 billion (95% UI 1·07–1·84) or 18·1% (95% UI 13·6–23·0) between 2022 and 2050, as well as population ageing, the number of current smokers is also forecast to decline. Globally, we forecast 1040 million (95% UI 980–1110) male smokers and 201 million (187–220) female smokers by 2050. The largest relative decline in the number of current smokers is forecasted to occur in Tropical Latin America and the largest increase in central sub-Saharan Africa for both sexes. Population growth is the largest factor responsible for increases in current smoking populations in most regions.

Figure 1 Annual change in global smoking

Show full caption ∨

(A) Changes in current and former smoking prevalence over time, age standardised. (B) Number of current and former smokers over time for all ages. Estimates for 1990–2019 were obtained from GBD 2021 for (A) and (B). The solid lines in (A) and (B) indicate the mean estimate, whereas the shaded areas reflect the 95% uncertainty interval. (C) Decomposition of forecasted change in number of smokers from 2023 to 2050 due to population ageing, population growth, and changes in the prevalence rate

10

forecast year). The black dots in (C) indicate the overall percentage change in the number of smokers from 2023 to 2050.

Global age-standardised prevalence of former smoking among those aged 20 years and older is forecast to stay relatively constant from 14·3% (95% UI 13·9–14·6) in 2022 to 14·2% (13·9–14·6) in 2050 among males and from 5·81% (5·60–6·05) to 5·50% (5·28–5·72) among females. The forecasted age-standardised prevalence of former smoking among males in 2050 ranges between 3·80% (3·44–4·17) in Benin and 56·9% (54·1–59·1) in Tanzania, and among females between 0·47% (0·39–0·56) in Libya and 46·9% (42·9–51·5) in Tanzania. Due to a combination of population growth, ageing, and increases in the prevalence of former smoking, the number of former smokers is forecasted to increase by 28·5% (23·0–34·6) by 2050. Compared with 800 million (95% UI 771–835) former smokers in 2022, we forecast 1030 million (973–1090) former smokers in 2050. The number of former smokers is forecast to increase in most GBD regions, apart from central Europe among males and eastern Europe, central Europe, and western Europe among females. In these regions, declines in the population between 2022 and 2050 offset any increases in former smoking prevalence. Population growth and ageing are the largest factors responsible for increases in the former smoking population in the regions with an increasing number of former smokers.

YLLs under the reference scenario

YLLs represent the number of life-years lost due to premature death. Globally, there were 1020 million (95% UI 942–1090) YLLs among males and 757 million (705–810) among females in 2022 (figure 2). Under our reference scenario, we project that there will be 1040 million (932–1190) YLLs among males and 816 million (720–953) YLLs among females in 2050, for a cumulative total of 51·5 billion (47·3–56·9) future YLLs between 2022 and 2050. Although large, these global increases are a product of population growth and ageing. The global age-standardised rate of YLLs is forecast to decrease from 26 530·9 (24 623·2–28 614·0) per 100 000 among males in 2022 to 17 113·2 (14 553·3–20 949·3) per 100 000 in 2050, and from 18 919·3 (17 608·9–20 322·8) per 100 000 to 12 448·6 (10 282·1–16 034·6) per 100 000 among females. In our reference scenario non-communicable diseases comprise the majority of future YLLs, accounting for 68·1% (95% UI 64·9–70·8) of cumulative YLLs among females and 64·3% (61·8–66·3) among males (figure 3). Non-communicable diseases are also responsible for the largest age-standardised YLL rates, accounting for 11 273·6 (10 328·7–12 498·2) YLLs per 100 000 between 2022 and 2050 among males and 7760·4 (7007·3–8602·8) per 100 000 among females. Cardiovascular diseases and cancers are the leading causes of non-communicable diseases YLLs in this scenario, accounting for 12·3 billion (95% UI 10·8–14·1) and 9·05 billion (8·13–9·92) cumulative future YLLs, respectively.

Principal
Indore Institute of Pharmacy,
INDORE (M.P.)

11

Global burden of bacterial antimicrobial resistance 1990–2021: a systematic analysis with forecasts to 2050

GBD 2021 Antimicrobial Resistance Collaborators*

GBD Ⓦ Ⓡ
GrossMark

oa

Summary

Background Antimicrobial resistance (AMR) poses an important global health challenge in the 21st century. A previous study has quantified the global and regional burden of AMR for 2019, followed with additional publications that provided more detailed estimates for several WHO regions by country. To date, there have been no studies that produce comprehensive estimates of AMR burden across locations that encompass historical trends and future forecasts.

Methods We estimated all-age and age-specific deaths and disability-adjusted life-years (DALYs) attributable to and associated with bacterial AMR for 22 pathogens, 84 pathogen–drug combinations, and 11 infectious syndromes in 204 countries and territories from 1990 to 2021. We collected and used multiple cause of death data, hospital discharge data, microbiology data, literature studies, single drug resistance profiles, pharmaceutical sales, antibiotic use surveys, mortality surveillance, linkage data, outpatient and inpatient insurance claims data, and previously published data, covering 520 million individual records or isolates and 19 513 study-location-years. We used statistical modelling to produce estimates of AMR burden for all locations, including those with no data. Our approach leverages the estimation of five broad component quantities: the number of deaths involving sepsis; the proportion of infectious deaths attributable to a given infectious syndrome; the proportion of infectious syndrome deaths attributable to a given pathogen; the percentage of a given pathogen resistant to an antibiotic of interest; and the excess risk of death or duration of an infection associated with this resistance. Using these components, we estimated disease burden attributable to and associated with AMR, which we define based on two counterfactuals; respectively, an alternative scenario in which all drug-resistant infections are replaced by drug-susceptible infections, and an alternative scenario in which all drug-resistant infections were replaced by no infection. Additionally, we produced global and regional forecasts of AMR burden until 2050 for three scenarios: a reference scenario that is a probabilistic forecast of the most likely future; a Gram-negative drug scenario that assumes future drug development that targets Gram-negative pathogens; and a better care scenario that assumes future improvements in health-care quality and access to appropriate antimicrobials. We present final estimates aggregated to the global, super-regional, and regional level.

Findings In 2021, we estimated 4·71 million (95% UI 4·23–5·19) deaths were associated with bacterial AMR, including 1·14 million (1·00–1·28) deaths attributable to bacterial AMR. Trends in AMR mortality over the past 31 years varied substantially by age and location. From 1990 to 2021, deaths from AMR decreased by more than 50% among children younger than 5 years yet increased by over 80% for adults 70 years and older. AMR mortality decreased for children younger than 5 years in all super-regions, whereas AMR mortality in people 5 years and older increased in all super-regions. For both deaths associated with and deaths attributable to AMR, meticillin-resistant *Staphylococcus aureus* increased the most globally (from 261 000 associated deaths [95% UI 150 000–372 000] and 57 200 attributable deaths [34 100–80 300] in 1990, to 550 000 associated deaths [500 000–600 000] and 130 000 attributable deaths [113 000–146 000] in 2021). Among Gram-negative bacteria, resistance to carbapenems increased more than any other antibiotic class, rising from 619 000 associated deaths (405 000–834 000) in 1990, to 1·03 million associated deaths (909 000–1·16 million) in 2021, and from 127 000 attributable deaths (82 100–171 000) in 1990, to 216 000 (168 000–264 000) attributable deaths in 2021. There was a notable decrease in non-COVID-related infectious disease in 2020 and 2021. Our forecasts show that an estimated 1·91 million (1·56–2·26) deaths attributable to AMR and 8·22 million (6·85–9·65) deaths associated with AMR could occur globally in 2050. Super-regions with the highest all-age AMR mortality rate in 2050 are forecasted to be south Asia and Latin America and the Caribbean. Increases in deaths attributable to AMR will be largest among those 70 years and older (65·9% [61·2–69·8] of all-age deaths attributable to AMR in 2050). In stark contrast to the strong increase in number of deaths due to AMR of 69·6% (51·5–89·2) from 2022 to 2050, the number of DALYs showed a much smaller increase of 9·4% (–6·9 to 29·0) to 46·5 million (37·7 to 57·3) in 2050. Under the better care scenario, across all age groups, 92·0 million deaths (82·8–102·0) could be cumulatively averted between 2025 and 2050, through better care of severe infections and improved access to antibiotics, and under the Gram-negative drug scenario, 11·1 million AMR deaths (9·08–13·2) could be averted through the development of a Gram-negative drug pipeline to prevent AMR deaths.

Interpretation This study presents the first comprehensive assessment of the global burden of AMR from 1990 to 2021, with results forecasted until 2050. Evaluating changing trends in AMR mortality across time and location is necessary
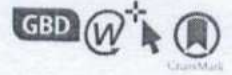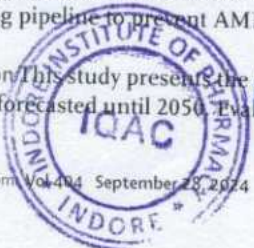
12

to understand how this important global health threat is developing and prepares us to make informed decisions regarding interventions. Our findings show the importance of infection prevention, as shown by the reduction of AMR deaths in those younger than 5 years. Simultaneously, our results underscore the concerning trend of AMR burden among those older than 70 years, alongside a rapidly ageing global community. The opposing trends in the burden of AMR deaths between younger and older individuals explains the moderate future increase in global number of DALYs versus number of deaths. Given the high variability of AMR burden by location and age, it is important that interventions combine infection prevention, vaccination, minimisation of inappropriate antibiotic use in farming and humans, and research into new antibiotics to mitigate the number of AMR deaths that are forecasted for 2050.

Introduction

In 2014, the Review on Antimicrobial Resistance (AMR) projected that 10 million deaths caused by AMR could occur by 2050.[1] This estimate, while the subject of scientific criticism,[2] helped position AMR as one of the most pressing threats to health of the 21st century.[1] In the years since, WHO committed to the 2015 AMR global action plan, AMR was the focus of a high-level UN general assembly in 2016, and an AMR-specific indicator was included as a Sustainable Development Goal: to reduce the percentage of bloodstream infection due to selected antimicrobial-resistant organisms (indicator 3.d.2). Despite the attention AMR has received at the global level, the implementation and funding of national action plans[4] has been uneven, leading to uncertain progress in attenuating the burden of AMR.[3]

The Review on Antimicrobial Resistance[1] acknowledged its broad brush estimates would be strengthened by more robust work from academic researchers.[5] In the decade since its publication, however, global AMR estimates have been sparse. One recent step forward in AMR epidemiology was a global estimate of the burden of bacterial AMR in 2019,[6] which found that of the roughly 8·9 million deaths due to bacterial infections that year, 1·27 million deaths were attributable to AMR and 4·95 million deaths were associated with AMR.[6,7] While this estimate has been used to inform research and policy priorities, such as the 2024 WHO Bacterial Priority Pathogens List,[8] it provides only a cross-section of burden, limiting the ability to understand the historical trend of AMR and evaluate policies implemented to reduce its impact. So far, time trends in AMR have been limited to select high-income locations for a small number of pathogen–drug combinations. These include estimates from the US Centers for Disease Control and Prevention, which evaluated 18 AMR threats in 2013 and 2019, and from Cassini and colleagues,[9] who produced AMR estimates for the European Union and European Economic Area in 2007 and 2015 for 16 pathogen–drug combinations. Recent estimates indicate that the highest burdens attributable to, and associated with, AMR are in

sub-Saharan Africa and south Asia;[6] however, these are locations without any historical estimates. Identifying the regions with increasing AMR burden would enable the global health community to better target locations with the most urgent need. Documenting the evolving nature of AMR, including the trends in resistance to critical antibiotic classes, such as the carbapenems, can guide antimicrobial stewardship, infection prevention measures, and prioritisation of drug and vaccine development to combat this growing threat.

A recent *Lancet* series on AMR highlighted current paediatric vaccines, investment in water, sanitation, and hygiene (WASH) infrastructure, and infection control practices as strategies to curtail AMR-related deaths in low-income and middle-income countries (LMICs). Previously published global estimates reported a 53% decline in age-standardised sepsis-related deaths from 1990 to 2017.[10] Much of this was driven by reductions in child mortality[11] and the prevention of deaths due to lower respiratory infection[12] and diarrhoea,[13] causes of death that are often avertable with access to WASH and vaccines.[14] While this decrease in sepsis mortality might be expected to reduce AMR-related deaths due to sepsis, research suggests demographic shifts over the next century will produce an ageing population,[15] leading to increasing prevalence of comorbidities and immunosenescence, resulting in a population at greater risk of sepsis related deaths and AMR mortality. Furthermore, the continued overuse of antimicrobials, both in human health and in agriculture, produces an environment that selects for increasingly resistant bacteria.[16] It is currently unknown how the convergence of these factors might affect future AMR burden because no recent global AMR burden forecasts have been produced. Characterising these trends and producing forecasts of estimates into the future, with alternative scenarios based on policy-related interventions, are needed to better understand the nature of AMR, and to inform research and public health priorities for decades to come.

In this study, we present the first global and regional estimates of AMR mortality over the past three decades, from 1990 to 2021, for 22 pathogens and 16 antimicrobials

13

Research in context

Evidence before this study

In 2014, the review on antimicrobial resistance (AMR) was established to assess the global issue of rising drug resistance, understand its magnitude, and define steps to address it. The AMR review published an influential analysis in 2016, forecasting that 10 million people could die annually from AMR by 2050. Since then, estimates of the burden of drug-resistant infections covering several pathogens have been published for the USA, Thailand, the EU, and the European Economic Area. No studies, however, provided comprehensive estimates covering all locations and a broad range of pathogen–drug combinations until the global burden of AMR in 2019 study was published. The study estimated that 4·95 million deaths associated with bacterial AMR and 1·27 million deaths attributable to bacterial AMR occurred in 2019. This research was followed by additional studies that detailed more granular country estimates published for the WHO regions of Europe, the Americas, and Africa, showing that deaths from AMR are unevenly distributed among populations. Each regional study, and the larger global study, have provided an essential snapshot of the magnitude of AMR burden for 2019. A 2024 *Lancet* Series on antimicrobial resistance used findings from some of these studies and others to summarise the current state of antibiotic resistance and recommended several global targets to combat the rise of AMR, including a target for 10% reduction in AMR mortality from the 2019 baseline by 2030.

Added value of this study

Ascertaining the time trends of AMR burden is of considerable importance to improve our understanding of its current and future threat. Multidecade temporal trends allow us to observe how patterns of AMR mortality are changing and for which populations it may be worsening. Such temporal analyses are essential for monitoring progress towards targeted reductions in AMR burden, for informing prioritisation of AMR interventions, and for assessing the long-term effectiveness of national action plans for tackling AMR. Existing time trends of AMR are limited to select high-income countries and do not include a comprehensive set of pathogen–drug combinations. We provide estimates of deaths and disability-adjusted life-years (DALYs) for 22 pathogens and 11 infectious syndromes for 204 countries and territories from 1990 to 2021. We produced estimates of deaths and DALYs attributable to

AMR and associated with AMR. The attributable burden is defined using a counterfactual in which all drug-resistant infections are replaced by equivalent drug-susceptible infections. The associated burden is defined using a counterfactual in which all drug-resistant infections are replaced by no infection. Additionally, using the Global Burden of Disease Study (GBD) 2021 forecasting framework, we produced reference forecasts (the most likely future) for burden attributable to or associated with AMR, and the wider impact of alternative scenarios on disease burden to 2050. This study represents our most robust estimates of AMR burden to date, including updates to our input data, estimates of AMR by time and more granular age groups, and improvements to our statistical models. We build our analysis on estimates of disease, incidence, prevalence, and mortality from GBD, allowing for comparability of deaths from AMR to other leading causes of death and disability throughout the world.

Implications of all the available evidence

Our analysis greatly expands the evidence base for time trends of AMR mortality. We show that global mortality from AMR increased minimally between 1990 and 2019, followed by a small decline that occurred during the COVID-19 pandemic. Our reference scenario indicates that deaths from AMR will increase by 2050 if remediation measures are not in place. Our analysis of trends in AMR mortality by age suggests that there is a need for interventions to tackle the increasing burden of AMR in older age groups going forward. Findings from this study provide evidentiary support to policy measures that combat AMR and have the potential to save lives, by adopting strategies that decrease risk of infections through new vaccines, improved quality of health care in hospitals and health centres, improved access to antibiotics and promotion of antibiotic stewardship. The development of new antimicrobials for Gram-negative bacteria should be prioritised, given the large increase in carbapenem-resistance highlighted in this study. New prevention efforts to address AMR must remain a priority for global health policy makers. Our time trend analyses and the methodology used lay the foundation for additional studies to continue forecasting future AMR trends and track the progress of implemented measures in our ongoing efforts to mitigate this important global health challenge. Our forecasts of alternative scenarios show the potential to avert large numbers of deaths over the next quarter century.

using two counterfactual scenarios: the counterfactuals of no infection (ie, deaths or disability-adjusted life-years [DALYs] associated with a drug-resistant infection) and drug-sensitive infection (ie, deaths or DALYs directly attributable to the drug resistance of an infection). The Global Burden of Diseases, Injuries, and Risk Factors Study (GBD) forecasting framework allowed us to produce forecasts of AMR burden and impact of alternative scenarios on disease burden. We

present global and regional forecasts of AMR burden to 2050 for a reference scenario (the most likely future), a scenario assuming future drug development targeting Gram-negative pathogens (Gram-negative drug scenario), and a scenario assuming future improvements in health-care quality for sepsis and access to appropriate antimicrobials (better care scenario). This Article was produced as part of the GBD Collaborator Network and in accordance with the GBD protocol.

Principal
Indore Institute of Pharmacy,
INDORE (M.P.)

1201

14

Methods

Overview

To estimate AMR burden, we used the same broad methodological approach as the global burden of AMR in 2019 study. The detailed methods of that study are published elsewhere[6] and are summarised here, along with important methodological improvements.

We developed an approach for estimating the burden of AMR that builds on death and select incidence estimates for different underlying conditions from GBD 2021 (appendix 1 pp 16–74, 80).[19] First, we collected data from multiple sources, ensuring that we included information available by year, age, and location across our ten estimation steps wherever possible. We estimated the AMR burden associated with and attributable to 11 of the 22 modelled infectious syndromes (bloodstream infections; meningitis; lower respiratory infections; endocarditis; peritoneal and intra-abdominal infections; diarrhoea; urinary tract infections and pyelonephritis; infections of bones, joints, and related organs; infections of the skin and subcutaneous systems; tuberculosis; and typhoid, paratyphoid, and invasive non-typhoidal *Salmonella*), 22 bacterial pathogens, 16 drug categories or combinations of drugs for which there is resistance, and 84 pathogen–drug combinations (appendix 1 pp 51–52). We modelled all-age and age-specific deaths and DALYs for 204 countries and territories, and we present aggregated estimates globally and for each of the seven GBD super-regions and 21 GBD regions.[20] For a complete list of GBD locations by region see appendix 2 (pp 18–35).

Input data

We sought the widest possible range of data using several data collection strategies. Through our large collaborator networks and through standard data seeking as part of the GBD, we obtained datasets not previously available for AMR research, including multiple cause of death data, hospital discharge, microbiology data with and without patient outcome, studies published in scientific journals, reports from networks that monitor bacteria resistant to antibiotics, pharmaceutical sales, antibiotic use surveys, mortality surveillance, linkage data, outpatient and inpatient linked insurance claims data, and publicly available data.[21] Each component of our estimation processes had distinct data requirements and the input data used for each step thus differed (table 1). The diverse data sought included the following sources: (1) pharmaceutical companies that run surveillance networks, diagnostic laboratories, and clinical trials; (2) researchers including large, multisite research collaborations; smaller studies; and well established research institutes based in LMICs; (3) public and private hospitals and public health institutes doing diagnostic testing; and (4) global surveillance networks; enhanced surveillance systems; national surveillance systems; and surveillance systems for specific organisms such as *Mycobacterium tuberculosis* and *Neisseria*

gonorrhoeae. All sources are listed by data type in appendix 1 (pp 7–16).

Table 1 shows a summary of the distinct data types gathered and for which model component each data type was used. Also shown is the number of unique study-location-years and individual records or isolates available for each data type. Location-years of data refer to unique GBD locations and years for which we have records or isolates. In total, there were 520 million individual records or isolates covering 19 513 study-location-years used as input data to the AMR estimation process. An additional 702 million deaths informed the underlying cause-specific mortality envelope from the GBD that we leveraged when calculating our sepsis mortality envelope. Table 2 shows the number of individual records or isolates used and the number of countries covered in each primary modelling step separately by GBD region. Three of five component models include data from every GBD region, and two of five include data from 13 and 20 of the 21 GBD regions. Our models of sepsis and infectious syndrome fractions of underlying causes are the most geographically sparse, covering 23 countries from 13 regions; the results of which are then applied to the GBD cause-specific mortality envelope informed by data covering 195 countries from all 21 regions.

All data inputs for the models used in steps 1–10 (appendix 1 p 80) were empirical data, not modelled estimates, with the exception of a custom meta-analysis of vaccine probe data that we did to estimate the fraction of pneumonia caused by *Streptococcus pneumoniae* (appendix 1 pp 40–41). All study-level covariates for models, such as age and sex, were extracted from empirical data. All country-level covariates were modelled estimates that were produced previously for GBD[22,32] and the Antimicrobial Collaborators Network,[7] or modelled using a method previously described in Browne and colleagues.[34] Data inputs for each estimation step are described in greater detail below and in appendix 1 (pp 17–20, 32, 36, 50–51, 60). Data input citations are available online.

Sepsis and infectious syndromes (steps 1 and 2)

First, to define the number of sepsis deaths, we used GBD 2021 cause of death estimates[14] to determine the number of deaths by age, sex, and location where the pathway to death on the death certificate included sepsis. Sepsis was defined as life-threatening organ dysfunction due to a dysregulated host response to infection.[35] The methods used to estimate infectious underlying causes of death and sepsis have been previously published[10] and are summarised in appendix 1 (pp 17–20).

In modelling step one (appendix 1 p 80), multiple cause of death data covering 139 million deaths, 10·1 million hospital discharges with discharge status of death, 288 315 multiple cause of death records linked to hospital records from ten countries and territories, as well as 1805 deaths from Child Health and Mortality Prevention Surveillance sites across seven countries

	1990–2009		2010–2021		Sample size units
	Number of study-GBD location-years	Sample size	Number of study-GBD location-years	Sample size	
Multiple cause of death	1996	71766533	1503	66804957	Deaths
Hospital discharge	508	5052412	805	4999065	Discharges
Outpatient and Inpatient insurance claims	0	0	8	20991554	Visits and admissions
Microbial or laboratory data with outcome	359	1325029	995	17646602	Isolates
Microbial or laboratory data without outcome	1038	13681797	3009	97863850	Isolates
Literature studies	3321	4400616	1545	3010191	Isolates
Single drug resistance profiles	816	49563600	1482	161875741	Cases or isolates
Pharmaceutical sales	883	883	829	829	Isolates
Antibiotic use among children younger than 5 years who reported illness	134	57171	207	200498	Study-country-years
Mortality surveillance (minimally invasive tissue sampling from Child Health and Mortality Prevention Surveillance)	0	0	37	2460	Households surveyed
Linkage (mortality only)	27	204736	11	83579	Isolates
Cause of death input data	5130	469412517	1436	232349574	Deaths
					Deaths

Table 1: Data inputs by source type, 1990–2009 and 2009–2021, sample size, and study location years

(appendix 1 pp 18–20) were used in mixed effects logistic regression models to predict the fraction of sepsis occurring in each of the 195 GBD underlying causes of death. This approach follows the methods validated by many studies on the epidemiology of sepsis[26–29] and was used by Rudd and colleagues.[10] We then multiplied the fraction of sepsis predicted from the logistic regression models onto GBD cause-age-sex-year-specific and location-specific mortality estimates to determine the mortality envelope for our analysis. Our mortality envelope consisted of all sepsis deaths in non-infectious underlying causes, plus all explicit sepsis deaths with an infectious underlying cause in GBD (appendix 1 pp 22–24). COVID-19 contributed to the sepsis mortality envelope but did not contribute to our estimation of AMR burden.

In modelling step two, details on the pathways of disease provided in the multiple cause of death data or hospital discharge data were used in a second stage of mixed effects logistic regression models to further subdivide sepsis deaths into 22 major infectious syndromes, of which 11 had both bacterial aetiologies for which we estimate AMR burden and sufficient data available for pathogen modelling (appendix 1 p 21). These regressions predicted the fraction of sepsis-related deaths that were caused by a given infectious syndrome, separately for each GBD underlying cause of death, location, age, sex, and year. We used this fraction to subdivide sepsis deaths in non-infectious underlying causes into specific infectious syndromes. For underlying causes of death that are themselves infectious, all deaths were assigned to a single corresponding infectious syndrome (eg, GBD cause "lower respiratory infections" was assigned to infectious syndrome "lower respiratory infections"; appendix 1 pp 22–24).

Case fatality rates and pathogen distribution for deaths and incident cases (steps 3 and 4)

For analytical step three (appendix 1 p 80), we took data that linked pathogen-specific disease incidence to deaths to develop models for pathogen-specific case-fatality ratios (CFRs) that varied by age, year, location, and infectious syndrome. Depending on data quality and availability, we used four levels of granularity per pathogen-syndrome, estimating (from most detail to least): a unique model for that pathogen-syndrome, a unique intercept for that pathogen-syndrome in a model with data for all pathogens, a pooled model for each given infectious organism type (eg, bacteria, fungus, parasite, and virus), or a pooled model using all data. CFR models were implemented with the RegMod[30] regression model environment and generated CFRs as a function of the Healthcare Access and Quality (HAQ) Index and various bias-adjusting covariates (appendix 1 pp 32–35).[23] We then used CFR results to estimate implied cases for each pathogen from mortality-only data sources that otherwise reported useful information on pathogen distributions. In total, the pathogen distribution models leveraged 24 million isolates and cases from 142 countries and territories to estimate the pathogen distribution of each infectious syndrome by age, year, and location, with each dataset including a unique spectrum of pathogens and groups of pathogens. To incorporate these heterogeneous data, we used the multinomial estimation with partial and composite observations modelling environment, which allows for the inclusion of covariates in the network analysis[11] and for Bayesian priors to be incorporated. To model the infectious syndrome pathogen distribution comprehensively, we estimated, where applicable, the incidence and death proportions attributable to viral, fungal, parasitic, and bacterial pathogens; however, AMR burden was calculated
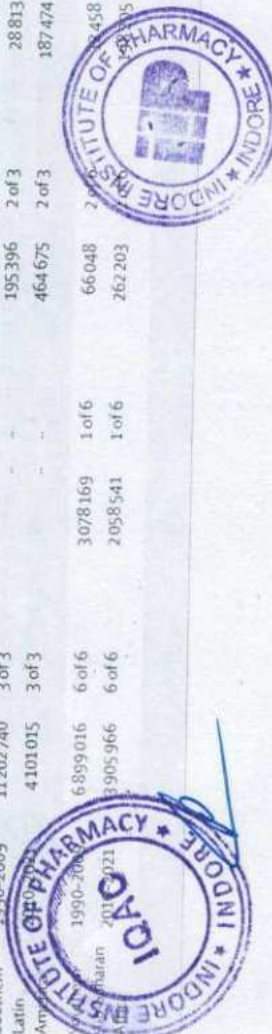
Principal
Indore Institute of Pharmacy,
INDORE (M.P.)

16

Region	Years	GBD cause of death database (step 0)* Number of deaths	Fraction of countries represented	Sepsis and infection syndrome models (step 1) Number of deaths	Fraction of countries represented	Case fatality rate (step 2) Number of cases	Fraction of countries represented	Pathogen distribution (step 3) Number of cases
Andean Latin America	1990–2009	3 820 911	3 of 3	··	··	3480	2 of 3	63 243
	2010–2021	1 465 590	3 of 3	··	··	80	1 of 3	2365
Australasia	1990–2009	4 528 250	2 of 2	149 697	1 of 2	80 275	1 of 2	25 998
	2010–2021	1 622 390	2 of 2	167 840	1 of 2	277 427	2 of 2	398 308
Caribbean	1990–2009	455 782	19 of 19	··	··	19 251	2 of 19	62 456
	2010–2021	1 418 887	19 of 19	··	··	8432	3 of 19	6102
Central Asia	1990–2009	11 961 820	9 of 9	66 771	3 of 9	4887	1 of 9	81 972
	2010–2021	3 794 666	9 of 9	··	··	··	··	2234
Central Europe	1990–2009	33 212 410	13 of 13	··	··	1 171 088	10 of 13	3 797 792
	2010–2021	11 429 450	13 of 13	··	··	275 296	10 of 13	114 245
Central Latin America	1990–2009	23 751 460	9 of 9	2 987 071	2 of 9	525 174	9 of 9	76 286
	2010–2021	11 011 570	9 of 9	11 787 179	2 of 9	1 453 094	8 of 9	1 467 114
Central sub-Saharan Africa	1990–2009	4120	5 of 6	··	··	··	··	430
	2010–2021	1213	5 of 6	··	··	··	··	··
East Asia	1990–2009	13 921 440	3 of 3	249 992	1 of 3	154 863	2 of 3	66 516
	2010–2021	53 581 700	3 of 3	1 079 267	1 of 3	907 562	2 of 3	530 432
Eastern Europe	1990–2009	71 077 680	7 of 7	··	··	470 286	5 of 7	203 816
	2010–2021	25 203 530	7 of 7	··	··	33 732	3 of 7	18 594
Eastern sub-Saharan Africa	1990–2009	228 636	14 of 15	··	··	1003	1 of 15	7610
	2010–2021	27 948	14 of 15	625	3 of 15	19 466	4 of 15	43 724
High-income Asia Pacific	1990–2009	33 180 280	4 of 4	··	··	417 693	3 of 4	194 837
	2010–2021	15 927 180	4 of 4	··	··	97 050	2 of 4	20 951
High-income North America	1990–2009	73 876 250	3 of 3	56 181 023	1 of 3	1 808 900	2 of 3	3 296 180
	2010–2021	29 459 200	3 of 3	28 502 039	1 of 3	29 965 525	2 of 3	3 894 238
North Africa and Middle East	1990–2009	4 450 410	21 of 21	62 401	2 of 21	700 309	13 of 13	490 458
	2010–2021	8 233 307	21 of 21	··	··	55 919	7 of 21	13 807
Oceania	1990–2009	82 070	11 of 18	··	··	··	··	102
	2010–2021	30 422	11 of 18	··	··	2212	1 of 18	255
South Asia	1990–2009	14 574 240	5 of 5	22 834	3 of 5	276 726	4 of 5	360 479
	2010–2021	2 238 041	5 of 5	··	··	52 332	2 of 5	113 838
Southeast Asia	1990–2009	16 095 170	13 of 13	89 276	1 of 13	662 017	8 of 13	364 423
	2010–2021	10 140 950	13 of 13	··	··	45 912	7 of 13	20 488
Southern Latin America	1990–2009	11 202 740	3 of 3	··	··	195 396	2 of 3	28 813
	2010–2021	4 101 015	3 of 3	··	··	464 675	2 of 3	187 474
Southern sub-Saharan Africa	1990–2009	6 899 016	6 of 6	3 078 169	1 of 6	66 048	1 of 6	··458
	2010–2021	5 995 966	6 of 6	2 058 541	1 of 6	262 203	··	··

(Table continued)

17

	Years	GRD cause of death database (step 0)*		Sepsis and infectious syndrome models (step 1)		Case fatality rate (step 2)		Pathogen distribution (step 3)		Prevalence of resistance (step 4)		Relative risk (step 5)	
		Number of deaths	Fraction of countries represented	Number of deaths	Fraction of countries represented	Number of cases	Fraction of countries represented	Number of cases	Fraction of countries represented	Number of cases	Fraction of countries represented	Number of cases	Fraction of countries represented
Andean Latin America	1990–2009	3820911	3 of 3			3480	2 of 3	63243	3 of 3	121066	3 of 3	65964	3 of 3
	2010–2021	1465590	3 of 3			80	1 of 3	2365	2 of 3	227755	3 of 3	26900	3 of 3
Australasia	1990–2009	4528250	2 of 2	149697	1 of 2	80275	1 of 2	25998	2 of 2	216474	2 of 2	150952	2 of 2
	2010–2021	1622390	2 of 2	167840	1 of 2	277427	2 of 2	398308	2 of 2	3396867	2 of 2	592851	2 of 2
Caribbean	1990–2009	4558782	19 of 19			19251	2 of 19	62456	5 of 19	173074	5 of 19	133113	5 of 19
	2010–2021	1418887	19 of 19			8432	3 of 19	6102	4 of 19	60279	6 of 19	30272	5 of 19
Central Asia	1990–2009	11961820	9 of 9	66771	3 of 9	4887	1 of 9	81972	6 of 9	101408	3 of 9	59934	3 of 9
	2010–2021	3794666	9 of 9					2234	2 of 9	5949	5 of 9	4596	2 of 9
Central Europe	1990–2009	33212410	13 of 13			1171088	10 of 13	3797792	10 of 13	3120201	12 of 13	3628021	12 of 13
	2010–2021	11429450	13 of 13			275296	10 of 13	114245	10 of 13	880145	10 of 13	1066039	8 of 13
Central Latin America	1990–2009	23751460	9 of 9	2987071	2 of 9	525174	9 of 9	76286	8 of 9	1046062	9 of 9	466049	9 of 9
	2010–2021	11011570	9 of 9	11787179	2 of 9	1453094	8 of 9	1467114	9 of 9	22822424	9 of 9	1615835	9 of 9
Central sub-Saharan Africa	1990–2009	4120	5 of 6					430	4 of 6	28331	5 of 6	24855	4 of 6
	2010–2021	1213	5 of 6							1734	3 of 6	139	2 of 6
East Asia	1990–2009	13921440	3 of 3	249992	1 of 3	154863	2 of 3	66516	2 of 3	1501542	2 of 3	860165	2 of 3
	2010–2021	53581700	3 of 3	1079267	1 of 3	907562	2 of 3	530432	2 of 3	2152800	2 of 3	1738085	2 of 3
Eastern Europe	1990–2009	71077680	7 of 7			470286	5 of 7	203816	6 of 7	669146	7 of 7	876947	7 of 7
	2010–2021	25203530	7 of 7			33732	3 of 7	18594	5 of 7	157873	7 of 7	168981	4 of 7
Eastern sub-Saharan Africa	1990–2009	228636	14 of 15			1003	1 of 15	7610	10 of 15	133681	11 of 15	88268	8 of 15
	2010–2021	27948	14 of 15	625	3 of 15	19466	4 of 15	43724	11 of 15	354548	13 of 15	273361	12 of 15
High-income Asia Pacific	1990–2009	33180280	4 of 4			417693	3 of 4	194837	3 of 4	121845396	4 of 4	121983482	4 of 4
	2010–2021	15927180	4 of 4			97050	2 of 4	20951	3 of 4	1325127	4 of 4	1343243	4 of 4
High-income North America	1990–2009	73876250	3 of 3	56181023	1 of 3	1808900	2 of 3	3296180	2 of 3	1326754	2 of 3	1288451	2 of 3
	2010–2021	29459200	3 of 3	28502039	1 of 3	29965525	2 of 3	3894238	2 of 3	51880035	2 of 3	38539427	2 of 3
North Africa and Middle East	1990–2009	4450410	21 of 21	62401	2 of 21	700309	13 of 21	490458	19 of 21	2962227	21 of 21	3003646	21 of 21
	2010–2021	8233307	21 of 21			55919	7 of 21	13807	18 of 21	117890	18 of 21	93792	16 of 21
Oceania	1990–2009	82070	11 of 18					102	2 of 18	664	2 of 18	599	2 of 18
	2010–2021	30422	11 of 18			2212	1 of 18	255	2 of 18	5092	2 of 18	3237	1 of 18
South Asia	1990–2009	14574240	5 of 5	22834	3 of 5	276726	4 of 5	360479	4 of 5	4972848	5 of 5	4541180	5 of 5
	2010–2021	2238041	5 of 5			52332	2 of 5	113838	4 of 5	1122319	4 of 5	971269	3 of 5
Southeast Asia	1990–2009	16695170	13 of 13	89276	1 of 13	662017	8 of 13	364423	8 of 13	3471130	9 of 13	2478300	9 of 13
	2010–2021	10140950	13 of 13			45912	7 of 13	20488	8 of 13	44819274	10 of 13	44534172	8 of 13
Southern Latin America	1990–2009	11202740	3 of 3			195396	2 of 3	28813	2 of 3	315381	3 of 3	101458	3 of 3
	2010–2021	4101015	3 of 3			464675	2 of 3	187474	2 of 3	1610206	3 of 3	1496431	3 of 3
Western sub-Saharan Africa	1990–2009	6899016	6 of 6	3078169	1 of 6	66048	1 of 6	30458	4 of 6	371099	4 of 6	39088	4 of 6
	2010–2021	5905966	6 of 6	2058541	1 of 6	262203	1 of 6		6 of 6	789849	6 of 6	535563	6 of 6

(Table 2 continues on next page)

18

Years	GBD cause of death database (step 0)*		Sepsis and infectious syndrome models (step 1)		Case fatality rate (step 2)		Pathogen distribution (step 3)		Prevalence of resistance (step 4)		Relative risk (step 5)	
	Number of deaths	Fraction of countries represented	Number of deaths	Fraction of countries represented	Number of cases	Fraction of countries represented	Number of cases	Fraction of countries represented	Number of cases	Fraction of countries represented	Number of cases	Fraction of countries represented
(Continued from previous page)												
1990–2009*	27322900	2 of 2	18530993	1 of 2	238892	1 of 2	369451	2 of 2	264189	2 of 2	339079	2 of 2
2010–2021	12692420	2 of 2	9211493	1 of 2	46175	1 of 2	101524	1 of 2	86099	2 of 2	30973	2 of 2
Europe 1990–2009	114548600	24 of 24	5166236	2 of 24	1716285	19 of 24	1491426	21 of 24	4367966	20 of 24	4728278	22 of 24
2010–2021	36034880	24 of 24	9610507	2 of 24	8303874	19 of 24	6104507	20 of 24	41382029	21 of 24	43421657	21 of 24
Western sub-Saharan Africa 1990–2009	115334	19 of 19	409	2 of 19	3605	2 of 19	11950	10 of 19	138332	14 of 19	74493	9 of 19
2010–2021	29247	19 of 19			76886	6 of 19	6551	13 of 19	282917	15 of 19	269633	14 of 19
Total 1990–2021	701762090	195 of 204	149002363	23 of 204	50864030	104 of 204	24251653	142 of 204	322576481	161 of 204	296231257	154 of 204

*We multiplied our results from estimation step 1 on the CoDCorrect estimates from the GBD, which are produced using data from the GBD's Cause of Death database, outlined in this table as step 0.

Table 2: Data (cases or deaths) included in each primary modelling step by region and the fraction of countries represented in each region

only for selected bacteria for which resistance is clinically relevant and sufficient data are available. More details on this approach are provided in appendix 1 (pp 36–50).

Prevalence of resistance by pathogen (steps 5 to 7)

The 84 pathogen–antibiotic class combinations were selected by first creating an exhaustive list of all clinically relevant combinations for which we had data, and then eliminating combinations that did not meet minimum data availability and computational feasibility require-ments for accurate statistical modelling (appendix 1 p 70). We supplemented microbial datasets from collaborators with aggregate data from systematic reviews and published surveillance reports. The number of isolates assessed for resistance for each pathogen–drug combination is shown in appendix 1 (pp 121–124).

When classifying resistance, we used two categories, susceptible and non-susceptible, the latter of which included dose-dependent, intermediate, and resistant interpretations. We excluded combinations of antibiotics to which bacteria have intrinsic resistance (appendix 1 pp 51–55). Two-thirds of datasets used in the prevalence of resistance modelling reported a laboratory susceptibility interpretation rather than quantitative test values. Data providers used several guidelines (and therefore breakpoints) to interpret test results, which potentially introduced bias. Information on the minimum inhibitory concentration of antibiotics was available in the remaining third of microbiology data sources. This information was used both to categorise bacterial isolates into susceptible and non-susceptible based on the 2023 Clinical and Laboratory Standard Institute (CLSI) breakpoints (our gold standard), and to infer the relationship between proportions of resistance when classifying our data using other versions of CLSI and the European Committee on Antimicrobial Susceptibility Testing guidelines. These relationships were then used to create adjustment factors and correct the data that only reported laboratory interpretations as described in appendix 1 (pp 51–55). Additionally, to account for bias in resistance data provided by tertiary care facilities, we adjusted tertiary rates of resistance by crosswalking them to data from non-tertiary and mixed facilities (appendix 1 pp 51–55).

After adjustments, we employed a two-stage spatiotemporal modelling framework to estimate the prevalence of resistance in each pathogen–drug combination by location-year for 1990–2021. First, we fit a stacked ensemble model between the input data and selected covariates from the list of plausible and health-related covariates available in GBD (appendix 1 pp 56, 102–108). As a second stage, the estimates from the stacked ensemble model were then input into a spatiotemporal Gaussian process regression[17] model to smooth the estimates in space and time. The exceptions to this modelling approach were made for tuberculosis (both extensively drug-resistant tuberculosis and
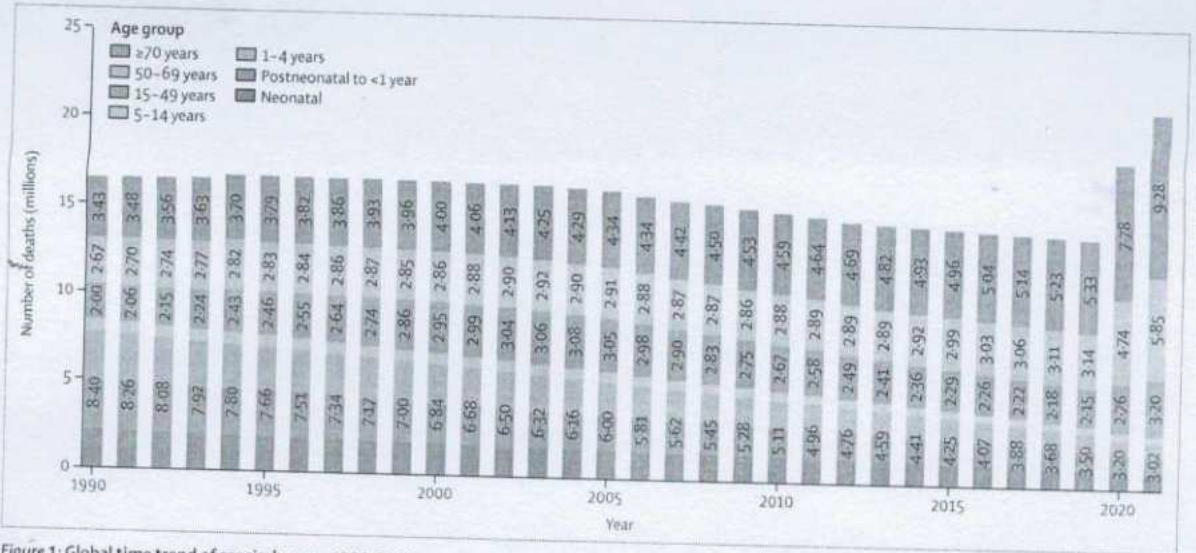
Principal
Indore Institute of Pharmacy,
INDORE (M.P.)

Figure 1: Global time trend of sepsis, by age, 1990–2021
Bar labels represent the number of sepsis deaths in a given year for people aged 0–14 years, 15–49 years, 50–69 years, and ≥70 years. Values for the age group of 0–14 years represent the sum of sepsis deaths among neonates, postneonates to <1 year, 1–4 years, and 5–14 years.

multidrug-resistant excluding extensively drug-resistant tuberculosis), for which published GBD 2021 estimates were already available.[19]

Given the strong relationship between antibiotic consumption levels and the proliferation of resistance, we modelled antibiotic consumption at the national level to use as a covariate in the stacked ensemble model of prevalence of resistance. Data from 65 Demographic and Health Surveys and 138 Multiple Indicator Cluster Surveys were analysed using model-based geostatistics to quantify antibiotic usage in LMICs. This was combined with pharmaceutical sales data from IQVIA, WHO, and the European Centre for Disease Prevention and Control: using an ensemble spatiotemporal Gaussian process regression model.[24] Antibiotic use and sales data for 1990–2018 were used to produce a location-year covariate on antibiotic consumption for all 204 countries and territories between 1990 and 2021 included in this study (appendix 1 pp 32–35, 56, 80).[24]

To account for multidrug resistance, we used line-level microbiology data that tested the same isolate for resistance to multiple antibiotics to produce both marginal frequency of resistance and pairwise co-occurrences for each pair of antibiotics. Using the marginal and co-occurrence information, we then found the 'best' multinomial distribution that matched available data in the least square sense. The method (appendix 1 p 56) reframes the optimisation problem over the space of multivariate probability measures as a least squares optimisation problem over the space of n-dimensional probability simplices, using the marginal and pairwise co-occurrence information as data. The method is guaranteed to find a solution even if observations are noisy, or mutually inconsistent. In case of inconsistent observations, the method still provides

the multinomial distribution that approximately matches the margins, best in the least squares sense. The approach was applied for every location-year combination of resistance to the antibiotics analysed (appendix 1 p 56).

Relative risk of death for drug-resistant infection compared with drug-sensitive infections (steps 8 and 9)
Using data from 1238 sources representing 296 million samples from patients with outcome and resistance, we estimated the relative risk of death for each pathogen–drug combination for a resistant infection compared with a drug-sensitive infection using the meta-regression—Bayesian, regularised, trimmed tool (appendix 1 p 80). Because of data sparsity, we estimated the relative risk by antibiotic class, pathogen, and infectious syndrome; we assumed that risk did not vary by location and age, which is consistent with the assumptions made by Cassini and colleagues.[9] We used a two-stage modelling approach with a mixed effects binomial logistic regression and a mixed effects meta-regression model to estimate relative risk of death for each pathogen–drug combination (appendix 1 pp 60–65). For the non-fatal excess risk, we estimated the relative increase in length of stay associated with a resistant infection compared with a susceptible infection of the same kind (appendix 1 p 80). Data on length of stay were available from 309 sources representing 38 million admissions. We used a similar modelling framework for excess length of stay as we used for relative risk of death with a two-stage nested mixed effects meta-regression model. Due to data sparsity associated with drug-resistant N gonorrhoeae, we only produced a non-fatal estimate for this pathogen. To produce burden estimates of multiple pathogen–drug

20

combinations that were mutually exclusive within a given pathogen (and thus could be added), we produced a population attributable fraction (PAF) for each resistance profile with resistance to at least one drug (appendix 1 pp 65–72).

Computing burden attributable to drug resistance and burden associated with drug-resistant infections (step 10)

We computed two counterfactuals to estimate the drug-resistant burden: the burden attributable to bacterial AMR based on the counterfactual of drug-sensitive infection and the burden associated with bacterial AMR based on the counterfactual of no infection. These methods are described in greater detail in appendix 1 (pp 65–72). Briefly, to estimate the burden attributable to AMR, we first calculated the deaths attributable to resistance by taking, for each underlying cause, the product of cause-specific deaths, the fraction of these deaths co-occurring with sepsis, the fraction of sepsis deaths attributable to each infectious syndrome, the fraction of infectious syndrome deaths attributable to each pathogen, and the mortality PAF for each resistance profile. We used standard GBD methods[19] to convert age-specific deaths into years of life lost (YLLs) using the standard counterfactual life expectancy at each age.[11] To calculate attributable years lived with disability (YLDs), we took the product of the infectious syndrome incidence (appendix 1 pp 27–32), the fraction of infectious syndrome incident cases attributable to each pathogen, YLDs per incident case, and the non-fatal

PAF. For resistance profiles that had resistance to more than one antibiotic class, we redistributed burden to the individual antibiotic classes proportionally based on excess risk, providing a mutually exclusive burden for each pathogen–drug combination (appendix 1 pp 65–72). To calculate DALYs, we took the sum of YLLs and YLDs. To estimate the overall AMR burden of the drug-sensitive counterfactual, we summed the burden estimates of every pathogen–drug combination. The approach for calculating the fatal burden associated with AMR was identical except we replaced the mortality PAF for each resistance profile with the prevalence of resistance in deaths (appendix 1 pp 65–72).

Decomposition of the factors contributing to change in AMR associated deaths

To better understand the relative contributions of various factors to the overall change in deaths associated with AMR, we did a 6-factor decomposition analysis, drawing from methods developed by Das Gupta.[34,35] This decomposition accounted for the following factors: (1) population growth, (2) the population age structure, (3) the sepsis mortality rate, (4) the proportion of sepsis deaths associated with AMR syndromes, (5) the proportion of AMR syndrome deaths associated with AMR bacteria, and (6) the proportion of AMR bacteria deaths associated with resistance. The decomposition was done for global and GBD super-region level estimates comparing 1990 to 2019. For a detailed description of the methods see appendix 1 (pp 70–72).

	Associated death counts (thousands)				Associated death rates per 100 000				Attributable death counts (thousands)				Attributable death rate per 100 000			
	1990	2019	2021	2050	1990	2019	2021	2050	1990	2019	2021	2050	1990	2019	2021	2050
Global	4780 (4000–5550)	4940 (4430–5450)	4710 (4230–5190)	8220 (6850–9650)	89·6 (75·0–104)	63·8 (57·2–70·4)	59·7 (53·6–65·7)	87·7 (73·2–104)	1060 (841–1270)	1200 (1050–1350)	1140 (1000–1280)	1910 (1560–2260)	19·8 (15·8–23·9)	15·5 (13·6–17·4)	14·5 (12·7–16·2)	20·4 (16·6–24·2)
Central Europe, Eastern Europe, and Central Asia	285 (240–330)	281 (252–310)	265 (235–295)	360 (297–420)	67·8 (57·1–78·4)	67·1 (60·1–74·0)	63·4 (56·2–70·6)	90·5 (76·3–106)	63·0 (49·5–76·6)	68·6 (59·2–78·0)	64·0 (55·2–72·8)	82·9 (67·1–98·7)	15·0 (11·8–18·2)	16·4 (14·1–18·6)	15·3 (13·2–17·4)	20·8 (17·0–24·8)
High-income	477 (385–568)	579 (513–644)	553 (489–618)	883 (674–1040)	52·5 (42·4–62·5)	53·3 (47·3–59·3)	50·7 (44·8–56·6)	78·1 (59·8–92·2)	108 (82·9–133)	131 (115–146)	125 (110–140)	192 (146–225)	11·9 (9·12–14·7)	12·0 (10·6–13·5)	11·4 (10·1–12·8)	17·0 (12·9–19·9)
Latin America and Caribbean	247 (210–284)	339 (305–372)	322 (285–360)	650 (520–808)	63·3 (53·8–72·8)	57·9 (52·2–63·6)	54·2 (47·9–60·6)	96·7 (78·0–119)	55·7 (44·4–67·0)	82·4 (72·4–92·5)	78·1 (67·7–88·6)	148 (117–185)	14·3 (11·4–17·2)	14·1 (12·4–15·8)	13·2 (11·4–14·9)	22·1 (17·5–27·2)
North Africa and Middle East	264 (219–310)	243 (211–274)	226 (194–259)	525 (430–641)	78·0 (64·5–91·4)	40·0 (34·8–45·2)	36·3 (31·1–41·5)	61·4 (49·2–73·9)	63·0 (49·4–76·7)	64·7 (54·4–75·1)	60·2 (50·1–70·3)	133 (107–161)	18·6 (14·6–22·6)	10·7 (8·97–12·4)	9·66 (8·05–11·3)	15·5 (12·3–19·0)
South Asia	1400 (1170–1630)	1350 (1200–1500)	1260 (1110–1420)	2400 (1910–2980)	128 (107–149)	74·7 (66·5–83·0)	68·5 (60·2–76·8)	114 (91·3–141)	308 (249–367)	356 (303–408)	335 (282–387)	604 (463–743)	28·2 (22·8–33·6)	19·7 (16·8–22·6)	18·1 (15·3–21·0)	28·8 (22·5–35·6)
Southeast Asia, East Asia, and Oceania	1110 (916–1310)	1140 (995–1290)	1150 (1010–1290)	1940 (1580–2370)	65·8 (54·2–77·5)	52·8 (46·0–59·5)	52·7 (46·3–59·1)	92·0 (75·0–113)	250 (195–304)	271 (235–307)	270 (237–304)	428 (348–511)	14·8 (11·5–18·0)	12·5 (10·9–14·2)	12·4 (10·8–13·9)	20·3 (16·4–24·5)
Sub-Saharan Africa	990 (797–1180)	1010 (811–1200)	923 (732–1110)	1470 (1140–1860)	202 (162–241)	93·2 (75·1–111)	81·5 (64·6–98·4)	69·3 (53·7–87·5)	210 (158–262)	227 (179–276)	209 (161–257)	323 (245–416)	42·8 (32·2–53·3)	21·0 (16·5–25·5)	18·5 (14·2–22·7)	15·3 (11·5–19·5)

Table 3: Deaths (in counts and all-age rates) associated with and attributable to bacterial antimicrobial resistance, globally, by GBD super-region, for 1990, 2019, 2021 and 2050

21

	Associated DALY counts (thousands)				Associated DALY rates per 100 000				Attributable DALY counts (thousands)				Attributable DALY rates per 100 000			
	1990	2019	2021	2050	1990	2019	2021	2050	1990	2019	2021	2050	1990	2019	2021	2050
Global	281 000 (232 000–331 000)	196 000 (170 000–221 000)	178 000 (154 000–202 000)	201 000 (165 000–245 000)	5270 (4350–6200)	2530 (2190–2860)	2250 (1950–2550)	2140 (1750–2630)	60 900 (47 700–74 100)	46 800 (39 800–53 700)	42 600 (36 100–49 000)	46 500 (37 700–57 300)	1140 (895–1390)	604 (514–693)	539 (458–621)	496 (399–613)
Central Europe, Eastern Europe, and Central Asia	10 500 (8770–12 100)	7840 (7010–8670)	7190 (6380–8000)	7310 (6010–8680)	2480 (2080–2880)	1870 (1670–2070)	1720 (1530–1920)	1840 (1530–2180)	2310 (1790–2840)	1940 (1650–2230)	1760 (1500–2030)	1700 (1380–2060)	550 (426–674)	464 (394–533)	422 (359–485)	428 (348–516)
High income	11 100 (9090–13 100)	11 700 (10 700–12 700)	11 200 (10 200–12 200)	12 800 (10 500–14 600)	1220 (1000–1450)	1080 (988–1170)	1030 (937–1120)	1130 (931–1290)	2560 (1970–3140)	2700 (2450–2960)	2590 (2340–2830)	2810 (2280–3220)	281 (217–345)	249 (225–273)	237 (214–260)	248 (203–285)
Latin America and Caribbean	13 700 (11 500–15 900)	10 400 (9260–11 400)	9600 (8420–10 800)	12 600 (10 200–15 600)	3510 (2960–4070)	1770 (1580–1950)	1620 (1420–1810)	1880 (1530–2300)	3030 (2390–3670)	2540 (2220–2860)	2350 (2030–2680)	2910 (2330–3620)	776 (612–940)	434 (380–488)	396 (341–451)	433 (347–537)
North Africa and Middle East	17 600 (14 300–20 900)	10 100 (8470–11 600)	8770 (7350–10 200)	13 100 (10 400–16 700)	5190 (4210–6170)	1660 (1400–1920)	1410 (1180–1640)	1530 (1210–1930)	4140 (3190–5090)	2670 (2180–3160)	2330 (1900–2760)	3330 (2590–4280)	1220 (940–1500)	441 (360–522)	374 (305–443)	390 (303–493)
South Asia	96 400 (79 300–113 000)	59 200 (51 200–67 100)	52 200 (44 900–59 400)	57 700 (44 900–72 400)	8810 (7250–10 400)	3270 (2840–3710)	2830 (2430–3220)	2750 (2170–3500)	20 800 (16 500–25 000)	15 000 (12 600–17 300)	13 300 (11 100–15 500)	14 400 (10 900–18 200)	1900 (1510–2290)	828 (696–959)	721 (602–839)	687 (527–881)
Southeast Asia, East Asia, and Oceania	58 500 (47 300–69 700)	32 400 (28 700–36 000)	31 400 (28 000–34 800)	35 200 (29 300–42 800)	3460 (2800–4120)	1500 (1330–1670)	1440 (1280–1590)	1670 (1410–2020)	12 700 (9750–15 600)	7710 (6760–8660)	7430 (6560–8300)	7870 (6580–9480)	751 (577–924)	356 (312–400)	340 (300–380)	374 (311–453)
Sub-Saharan Africa	73 400 (58 000–88 900)	64 100 (49 900–78 300)	57 300 (43 400–71 200)	62 100 (43 100–86 000)	14 900 (11 800–18 100)	5940 (4620–7260)	5060 (3830–6280)	2930 (2100–4160)	15 400 (11 400–19 400)	14 200 (10 900–17 600)	12 800 (9450–16 100)	13 500 (9210–18 800)	3140 (2320–3950)	1320 (1010–1630)	1130 (834–1420)	637 (448–899)

Table 4: DALYs (in counts and all-age rates) associated with and attributable to bacterial antimicrobial resistance, globally, by GBD super-region, for 1990, 2019, 2021 and 2050

AMR forecasts

IHME's Future Health Scenarios framework produces forecasts of disease burden by cause, age, sex and location from 2022–2050. These estimates of disease burden were combined with forecasts of AMR to forecast the future burden attributable to and associated with AMR. Detailed methods for the Future Health Scenarios framework are described in detail by Vollset and colleague.[17]

Forecasting AMR population attributable fractions
We used the historical estimates of deaths due to AMR (attributable deaths) by GBD cause and computed 19 PAFs for GBD Level 2 causes with AMR attributable death counts. We then used a Generalized Ensemble Model to forecast the fraction of cause-specific deaths due to AMR. This model used two main modelling approaches: the weighted annualised rate of change and a two-stage spline model based on the meta-regression—Bayesian, regularised, trimmed tool[11] to generate 12 difference sub-models (appendix 1 pp 73–74). We then obtained the final AMR PAFs ensemble forecasts by taking a mean over these submodels using the sampling weights from the out-of-sample experiments. Finally, we applied these PAF forecasts to our reference cause-specific forecasts of mortality.[17]

Computing future attributable and associated burden
For computing attributable AMR burden, we first multiplied our reference mortality and YLL forecasts for 19 cause groups at the age-sex-location level by the forecasted AMR PAFs described in the section above. Afterwards, we computed AMR-attributable YLDs by applying a scalar to the attributable YLLs using the global ratio of YLL:YLD AMR deaths in 2019.[6] Finally, we computed AMR-attributable DALYs by taking the sum of AMR-attributable YLLs and YLDs.

For computing associated AMR burden, first, we computed the ratio of AMR-associated deaths to AMR-attributable deaths for 19 cause groups by age-sex-location in 2021. We then multiplied our AMR PAFs by the resulting ratio to calculate associated burden forecasts for each measure using the same methods as computing attributable burden.

Developing AMR scenarios
The reference scenario provides a probabilistic forecast of the most likely future. In addition to a reference scenario, we produced two alternative scenarios: the Gram-negative drug scenario and the better care scenario. We developed the Gram-negative drug scenario under the assumption that a regular release of new, potent antibiotics targeting Gram-negative bacteria would lead to decreases in AMR burden. To simulate this, we calculated the fraction of AMR burden caused by Gram-negative pathogens and linearly reduced it by 50% of the value observed from 2021 to 2036 (appendix 1 p 74). For the better care scenario, we

In Vitro Anti-Inflammatory Assays of Synthesized acetophenone

PDF (https://www.afjbs.com/uploads/paper/48885e13b877839e4dd66735423372b4.pdf)

Nisha Choudhary,Neeraj Sharma, Amit Modi, Mo.Imran, Shruti Rathore, Praveen Sharma

Abstract

At 1600µg/ml, the greatest percentage of denaturation of egg albumin was inhibited by synthesized acetophenone (89.16±0.38%). At the greatest concentration, the synthesized acetophenone showed a significant effect of obstructing protein denaturation in a dose-dependent manner. It was investigated whether the synthesized acetophenone could keep BSA from becoming denaturated. Synthesized acetophenone demonstrated the greatest percentage denaturation of BSA to be 76.59±0.56% at 1600µg/ml. The RBC membrane was stabilized by the synthesized acetophenone in a dose-dependent manner, with the maximum stability occurring at 1600 µg/ml. At 1600 µg/ml, the greatest percentage inhibition of RBC membrane lysis (91.15±0.31%) was observed, in contrast to DS (90.01±0.02%) and piroxicam (80.34±0.29%). The highest and lowest levels of trypsinase activity hindrance were seen at 1600µg/ml and 50µg/ml, respectively, for the synthesized acetophenone. The greatest percentage of trypsinase activity suppression was found to be 83.94±0.24.

Issue

Submit Your Article Here. (https://www.afjbs.com/submit-article)

Principal
Indore Institute of Pharmacy,
INDORE (M.P.)

23

AFJBS African Journal of Biological Sciences

Search for title, author, doi.   Search

Principal
Indore Institute of Pharmacy,
INDORE (M.P.)

24

Open Access (cc) (i) Review

Insights on aspects of apoptosis in neurodegenerative disorders: a comprehensive review

Rajat Goyal [1] (https://orcid.org/0000-0001-5702-0932),
Kashish Wilson [1] (https://orcid.org/0000-0002-4784-6383),
Anjali Saharan [2],
Rupesh K. Gautam [3*] (mailto:rupeshgautammmu@gmail.com),
Hitesh Chopra [4] (https://orcid.org/0000-0001-8867-7603),
Sumeet Gupta [1] (https://orcid.org/0000-0003-2980-7791),
Mohammad Amjad Kamal [4,5,6,7,8]
(https://orcid.org/0000-0003-0088-0565)

Abstract

Nerve cell death is the central aspect of human neurodegenerative disorders. Neuronal death in results leads to the onset of various human neurological disorders such as Alzheimer's disease, Parkinson's disease, Huntington's disease, amyotrophic lateral sclerosis, and stroke. In developing neurons, apoptosis is assumed to provide a counterbalance to overexuberant cell replication. Numerous signals may induce apoptosis in neurons, such as the absence of neurotrophic factor support, increased levels of metabolic and oxidative stress, and overstimulation of glutamate receptors (leading to the calcium influx). Cell death and neurological disorders have been related to oxidative stress, which creates an imbalance between antioxidant defenses and free radical production. In this paper, a summary of the engrossment of oxidative stress, neuronal apoptosis, and mitochondrial dysfunction in neurodegenerative disorders has been discussed. Antioxidant therapy's potential assistance for neurodegenerative illnesses in human beings is still up for dispute, despite encouraging pre-clinical research findings. One elucidation for this disparity could be the non-existence of an accurate way to assess oxidative stress in the brain. The explosion in research on apoptosis in neurodegeneration has stemmed from the conception that persuading neuronal apoptotic death may be crucial to the progression of a disease and that anti-apoptotic approaches may be useful in the prevention of neurodegenerative processes. A deeper understanding of the role that apoptosis plays in neurodegenerative processes will serve as the foundation for future research into the development of focused, effective treatment modalities.

Submit a Manuscript (https://mc03.manuscript

Aims and Scope (https://www.explorationp

Editorial Board (https://www.explorationp

Author Instructions (https://www.explorationp

PDF   XML

Citation   Cite this

RIS   Article

Article Metrics

View: 1247

Download: 31

Times Cited: 2

(https://www.explorationpub.com/Journals/CitingArticleList/1152)

Sections

Abstract

Keywords

Introduction

Prompts of apoptosis: oxidative stress and Ca²⁺

Pathogenesis of neurogenerative disorders

Apoptosis involvement in NDs

Introduction

Apoptosis is a phenomenon of programmed cell death, in which cells die sequentially at the end. The central nervous system is at fatal risk during both acute and chronic neurodegenerative disorders (NDs) [1]. The onset and prevalence of NDs such as Parkinson's disease (PD), Alzheimer's disease (AD), and stroke lead to an alarming rate of increase in the number of people suffering from it. These disorders cause the degeneration of neurons oxidative stress and excessive cell-mediated proteolysis [2].

Degenerating neurons exhibit oxidative stress and excessive calcium-mediated proteolysis at the cellular level, which eventually results in apoptosis. In apoptosis, the cell and nucleus shrink and form blebbing, causing chromatin fragmentation, loss of adhesion, and rapid engulfment by phagocytosis [3]. Apoptosis also causes several biochemical changes along with morphological alterations such as DNA fragmentation, plasma membrane depolarization, lysosome permeability, and enhanced formation of reactive oxygen species (ROS) [4]. Induction of apoptosis is achieved by many methods depending on their pathways such as internal and external stimuli. Internal stimuli are triggered by activating intrinsic pathways such as abnormalities in the DNA and external stimuli are activated by cytokines such as extrinsic signaling pathways [5]. The description of normal apoptotic pathways by Guerin et al. [6] is depicted in Figure 1.

Display full size

Figure 1.
The description of the general apoptosis pathway of a cell

The apoptosis pathways elaborated in Figure 1 show different phases such as shrinking of the cell, membrane blebbing, the collapse of the nucleus, normal apoptotic body, and at the end leads to lysis of the apoptotic body. The descriptive pathways include two different methods of apoptosis such as intrinsic and extrinsic pathways for cascades, as depicted in Figure 2.

Display full size

Figure 2.

26

cytochrome c

Intrinsic apoptosis

The non-receptor-mediated intracellular signals that are part of the intrinsic signaling pathway for programmed cell death include the numerous mitochondrial processes that start apoptosis [7]. The intrinsic pathway for programmed cell death can also be activated by damage to cellular DNA. Pro-apoptotic proteins set off caspases, which then regulate several cell death pathways. These proteins also enter the cellular nucleus where they trigger apoptosis and DNA damage. The removal of growth factor supplements from culture media, exposure to ultraviolet (UV) light, or cell stressors are examples of situations that can start the intrinsic pathway (for instance osmotic or metabolic). In the end, these circumstances result in DNA cell damage. When exposed to UV radiation, thymine base pairs adsorb UVB photon, which then joins together to generate pyrimidine dimers. ROS production may rise in response to growth factor withdrawal or other stressful circumstances. ROS can harm DNA through several mechanisms, including base modification [8].

The literature has reported that several diseases, including hypoxia, irreversible DNA damage, oxidative stress, and viral infections are triggered by intrinsic pathways, which will cause the alteration in the release of cytochrome from mitochondria, and form the complexes with the apoptotic protease activating factor-1 (Apaf-1) and procaspase [9].

Extrinsic apoptosis

Transmembrane death receptors, which are the products of the tumor necrosis factor (TNF) receptor gene, are a component of the extrinsic signaling cascade that results in apoptosis [10]. These receptors interact with extrinsic ligands to bind and translate intracellular signals that lead to cell death. It works on the active receptor and subsequently l binds procaspase-8 and TNF R1 (receptor type 1). Procaspase-8 is activated by this multiprotein complex, which starts apoptosis, or the process of cell death. Several caspases, which are proteases with specific biological targets, are involved in the signal transduction of the extrinsic pathway. The activation of caspases affects a variety of cellular processes and plays a significant part in the process that results in cell death [11].

Prompts of apoptosis: oxidative stress and Ca^{2+}

Oxidative stress

A high level of ROS such as hydrogen peroxide radicals ($\cdot H_2O_2$), hydroxyl radicals ($\cdot OH$), and superoxide anion and an imbalance of antioxidant enzymes contribute to oxidative stress, which is a detrimental factor in memory dysfunctions [12]. Oxidative stress may be associated with cell membrane mutilation from lipid peroxidation, vicissitudes in protein structure and function, and structural damage to DNA. As the brain is one of the most metabolically active organs in the body, it is particularly susceptible to oxidative stress for the reasons listed below: First, its high oxygen demand (20% of the body's oxygen intake). Second, the brain is full of redox-active metals like copper and iron, which constantly accelerate ROS production. Third, the membranes of brain cells contain substantial amounts of polyunsaturated fatty acids, that act as substrates for lipid peroxidation. Fourth, the brain has comparatively low levels of GSH, which functions as an endogenous antioxidant that helps in eliminating ROS [13].

It was evident from a research study that showed a prompt increase in oxidative stress levels as compared to neurologically impaired patients with aging factors. From the immunohistological examination, it was evident the increased protein oxidation, and lipid peroxidation in brain areas having neurofibrillary tangles and plaques. In AD, the cerebrospinal fluid had increased lipid peroxidation levels such as 4-hydroxynonenal [14]. Variations in the antioxidant enzymes catalase, Cu/Zn-superoxide dismutase (SOD), and Mn-SOD are caused by the increased oxidative stress in AD. These enzymes present in the neurons in the membrane cause lipid peroxidation with an increase in the secretion of toxic aldehydes such as 4-hydroxynonenal or malondi-aldehyde. These aldehydes disturb cellular Ca^{2+} homeostasis by interfering with the

glutamate transporters. Oxidative stress accumulation leads to the generation of ROS, which causes mitochondrial dysfunctions [15].

Nitric oxide (NO), which functions as a second messenger and can combine with superoxide anion to generate peroxynitrite [ONOO(-)], produces an interesting concept concerning oxidative stress in neurons. It has been demonstrated that ONOO(-) is neurotoxic and induces apoptosis in leukemic cells [16]. Several substances including vitamin E, estrogens, uric acid, and glutathione, are utilized to alleviate oxidative stress. They have been reported to prevent cellular injury, and membrane lipid or protein damage. Through the tumor protein (p53), poly(ADP-ribose) polymerase (PARP), or the ataxia telangiectasia mutant (ATM), ROS can cause DNA damage, which triggers lethal apoptotic signaling [17]. It was evident that oxidative stress in AD has scavenging free radicals which are used as a neuroprotective therapy for the disease. Moreover, prophylactic treatment with free radical scavengers such as vitamin E may reduce the risk of AD.

Perturbed Ca^{2+} homeostasis

The alteration and dysfunction in the Ca^{2+} regulation have been reported in various clinical studies on patients with AD. The neurofibrillary changes are exhibited by calpain-II which gets activated by the activation of Ca^{2+}-dependent protease [18]. The oxidative stress or greater intracellular calcium levels can activate cysteine proteases called caspases, such as calpain linked to neuronal cell death. Some conditions, such as cerebral ischemia, epilepsy, and traumatic brain injury, affect the calcium homeostasis of neurons and overstimulate capillaries [19].

To maintain cellular ion homeostasis and cell viability, calpain depends on a variety of substrates, including membrane receptors, kinases, phosphatases, cytoskeletal proteins, and transporters. Increased levels of calpains or the endogenous calpain inhibitor, calpastatin, have been connected to neuron loss in several neurodegenerative illnesses, including amyotrophic lateral sclerosis (ALS), PD, and AD [20]. Calpain inhibitors inhibited neuronal cell death in a variety of experimental scenarios, supporting the idea that calpains are crucial in the regulation of apoptosis and necrosis. The existence of higher Ca^{2+} binding proteins such as calretinin and calbindin, which are resistant to neurofibrillary degeneration, has been found to promote neurodegeneration in AD illness [21].

It is widely known that the cytotoxic buildup of intracellular calcium plays a crucial role in neuronal cell death as well as other stress conditions like toxicity. The cytotoxic intracellular Ca^{2+} is mediated via the stimulation of glutamate receptors. This strengthens the voltage-dependent Ca^{2+} channels, metabotropic glutamate receptors, and Ca^{2+} permeable α-amino-3-hydroxy-5-methyl-4-isoxazole propionic acid (AMPA) receptors [22]. The lethal accumulation of Ca^{2+} in apoptotic cells is caused due to the over-activation of glutamate receptors. This fatal result arises due to the cleavage of ion pumps due to variability in the physiological environment which supports the pumping out of Ca^{2+} to maintain a stable state of cytosolic calcium [23]. On exposure to apoptotic damage, the caspases or calpains become activated and cleave the ion pumps. This lets the Ca^{2+} ion pump remove huge amounts of calcium that have accumulated in the cytosol. Because of this, calcium homeostasis is upset, which ultimately causes apoptotic signaling to change to necrosis.

It reveals that the signaling pathways of apoptosis are crucial for the development and control of illness. There are still a large number of proteins that are unknown and are involved in various signaling pathways. The purpose of that unidentified protein would be as a linker protein, which would be able to treat or stop the aberrant loss of neural cells in neurodegenerative illnesses. One of the key goals of current science is to understand the mechanism of proteins in the signaling pathways of apoptosis and anti-apoptosis [24].

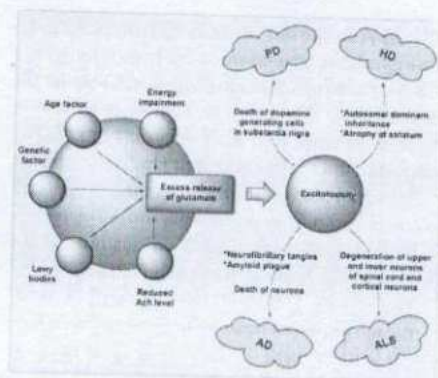## Pathogenesis of neurogenerative disorders

Proteopathies are diseases in which some proteins develop aberrant structural characteristics, which are aggregated at various cellular levels and in tissues causing the interruption of their activities [25]. The proteopathies comprise several NDs in which peculiarly accumulated proteins seem to play a vital role [26]. When the misfolded or atypical proteins accumulate in the nuclear, cytoplasmic, and extracellular enclosures, it leads to disruption of

via oxidative stress, disruption of calcium homeostasis, and metabolic impairment, at the cellular level. The anti-apoptotic or neuroprotective signaling pathways comprising neurotrophic factors, cytokines, and conditioning responses may offset the aging effects and hereditary predisposition in the experimental models of NDs [27].

Free radical production, activation of the pathway for NO synthesis, disruption of cellular calcium homeostasis, and programmed cell death are all factors that contribute to the progression of neurodegenerative illnesses associated with glutamatergic dysfunction [28, 29]. These methods may induce mutilation of proteins, nucleic acids, and lipids, as well as open the pores of mitochondrial permeability transition, which may increase the ROS generation, energy failure degeneration, and proclamation of proapoptotic substances like Cyt c in the cytoplasm [30]. The overproduction of ROS and downregulation of antioxidant defense cause the death of NDs' neuronal cells [31]. A variety of neurodegenerative illnesses are linked to inappropriate regulation of Wnt/β-catenin (WβC) signaling [32]. Degenerative nerve diseases are thought to contribute to the deterioration of various vital bodily functions, including memory, breathing, balance, speech, movement, and heartbeat [29]. The factors for the pathogenesis of neurogenerative disorders by Mehta et al. [33] are illustrated in Figure 3.

Display full size

Figure 3.
Pathogenesis of NDs. HD: Huntington's disease

Apoptosis involvement in NDs

Apoptosis is a fundamental physiologic process that contributes to cellular homeostasis. Apoptosis (programmed cell death) is a type of physiological cellular suicide that occurs in several biological processes, including immune response, synaptogenesis, embryogenesis, and normal tissue and organ involvement. Normal brain development depends on programmed cell death. It affects the quantity and type of cells in the growing brain and spinal cord and is essential for the development of a functional neural network. In pathological circumstances, it is also partly accountable for physiological aging and the death of neurons linked to NDs [27]. Apoptotic cell death is well characterized via a sequence of morphological variations that comprise attenuation of nuclear and cytoplasmic compartments, condensation of chromatin, DNA degradation into fragments of oligonucleosomes, and an assortment of nuclear material into the vesicular apoptotic bodies [34].

Neurodegenerative disorders cause neuronal death at the cellular level as a result of oxidative stress, DNA damage as a result of endoplasmic reticulum (ER) stress, and disruption of cellular calcium homeostasis. The apparent upsurge in the lifespan of individuals and the normal age of the population is tactlessly allied to a liberal intensification in the vast number of persons having NDs [35]. Apoptosis induction via pathogenic proteins of NDs by Yang et al. [36] is described in Figure 4.

Principal
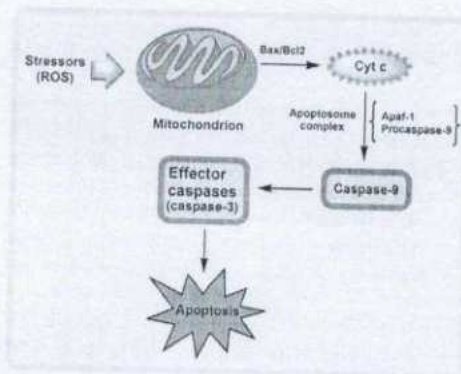Indore Institute of Pharmacy,
INDORE (M.P.)

29
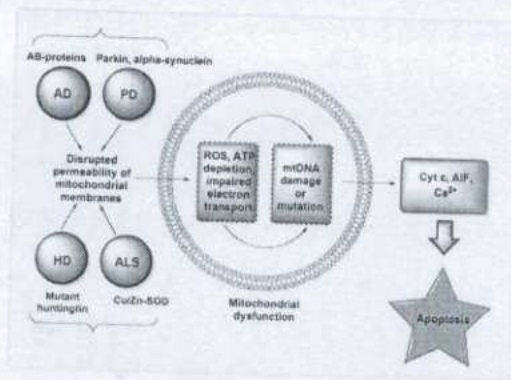
Display full size

Figure 4.
Induction of apoptosis by pathogenic proteins of NDs. ATP: adenosine triphosphate; mtDNA: mitochondrial DNA; AIF: apoptosis-inducing factor

Mitochondrial apoptotic signaling

Mitochondrial dysfunction plays a crucial role in the etiology of NDs. Numerous fragments of data suggest that NDs have profoundly impaired mitochondrial activity. The mitochondria are highly vulnerable to oxidative stress as it has the primary organelles for the production of ATP and are the main source of ROS generation [37]. The release of Cyt c, which occupies center stage as the starting point and mediator of the apoptosis cascade, is the major paradigm in mitochondria-mediated apoptotic signaling. Cyt c acts as a molecular adaptor that couples the procaspase-9 and Apaf-1 to produce the apoptosome complex during the activation of the death protease, caspase-3. Cyt c is released from the mitochondria into the cytosol either by non-specifically expanding and rupturing the mitochondria or by opening a particular channel or permeability transition pore in the mitochondrial membrane. Members of the pro- and anti-apoptotic subfamilies of B-cell lymphoma 2 (Bcl-2) are the guardians of channel-mediated Cyt c release within mitochondria. This ROS mechanism of apoptosis signaling is probably going to be crucial in reperfusion-induced neuronal cell death since post-ischemic mitochondria can produce more ROS [34]. This mitochondrial pathway of cellular apoptosis is illustrated in Figure 5.

Display full size

Figure 5.
The mitochondrial pathway of cellular apoptosis. Bax: Bcl-2-associated X protein

Novel strategies for preventing neuronal apoptosis/anti-apoptotic strategies

The apoptosis induction in tumor cells affects the anti-tumor efficacy of radiotherapy and chemotherapy. However, the significant adverse impact of those pro-apoptotic therapies has prompted researchers to seek out other ways to promote tumor

Principal
Indore Institute of Pharmacy,
INDORE (M.P.)

30

reduce neuronal death in NDs. Anti-inflammatory medicines and caspase inhibitors are also being utilized. The biology of neural stem cells and the "anti-aging" enzyme telomerase have also been utilized to create two distinct strategies for avoiding apoptosis and replacing damaged or dead neurons. The six-base DNA repeat sequence (TTAGGG) is added to chromosomal ends by the telomerase reverse transcriptase (TERT) enzyme, which has recently attracted a lot of attention due to its purported "anti-aging" capabilities. TERT may assist an anti-apoptotic activity in neurons by suppressing the TERT expressions or activity, which makes them more vulnerable to oxidative and excitotoxic stimuli. Conversely, overexpression of TERT protects the neurons from apoptosis [39].

Acetylcholine (Ach) is a parasympathetic neurotransmitter that also enhances synaptogenesis in living cells to influence memory and learning in people. With three approved medications (donepezil, galantamine, and rivastigmine), acetylcholinesterase inhibitors (AChEIs) are the most well-researched medications and the first-choice treatment for NDs globally. Nevertheless, the AChEIs are less valuable in the advanced stages as they necessitate a higher dose which also upsurges the risk of adverse effects. Over the years, many potential candidates like metrifonate and tesofensine came under clinical trial as AChEIs but failed at certain stages mainly due to their safety profile. Altogether, this evidence indicates an awful and unmet necessity for the development of novel AChEIs [40].

Some potent apoptotic medications used for the treatment of NDs are described in Table 1.

Table 1.

Some potent apoptotic medications used for the treatment of NDs

Sr. No.	Drugs	Mechanism of action	Model use
1.	Minocycline	Inhibition of the generation of free radicals and the neurotoxicity caused by 6-OHDA in rat CGN.	Cultured r CGN
2.	Rasagiline	This causes MAO-B inhibition, which may decrease oxidation and the buildup of free radicals while simultaneously increasing the amount of monoamines in the brain through the suppression of their catabolism.	Aged male C57Bl/6J mice

Display full size

(https://www.explor

ationpub.com/Journ

als/Tables/1001208/t

1)

Sr. No.: serial number; 6-OHDA: 6-hydroxydopamine; CGN: cerebellar granule neurons; MAO-B: monoamine oxidase B; P13K: phosphoinositide 3-kinase; C57Bl/6J: parentral substrain of mice; Nrf2: nuclear factor erythroid 2–related factor 2; PQ: paraquat; iNOS: inducible NO synthase; MPTP: 1-methyl-4-phenyl-1,2,3,6-tetrahydropyridine

Principal
Indore Institute of Pharmacy,
INDORE (M.P.)

31

When subjected to excessive oxidative stress, neurons may respond adaptively to overcome the stress, or they may activate a programmed cell death pathway called apoptosis. Alterations in the ER and mitochondria, as well as the activation of cysteine proteases known as caspases, are the characteristics of apoptosis. There is mounting evidence that neurodegenerative diseases cause malfunction and neuronal death due to apoptotic biochemical pathways. Indeed, the notion that neuronal apoptotic death induction plays a crucial role in the progression of the disease, the recent advances in basic apoptosis research, and the recognition that apoptosis has a broad range of clinical applications, have prompted much of the research into investigations of intervention tactics directed at the apoptosis control or apoptosis induction in the neuronal apoptotic death program. Potential remedies can be inferred from the hypothesis that oxidative stress is shared by multiple illnesses involving increasing cell death. Among these, using neurotrophic growth factors and antioxidant molecules could be a common strategy to shield neurons from oxidative damage.

Conclusions

The field of apoptosis research has recently gained exciting additional insights into the mechanics of cell death programs that may perhaps contribute to the degeneration and death of neurons after acute brain trauma and the evolution of neurodegenerative diseases. The focus of this review paper will be on contemporary ideas that are important for comprehending the apoptotic death program, the mediators and regulators of cellular apoptosis, and the connection between aberrant apoptosis and the emergence of neurodegenerative illnesses. A deeper comprehension of the mechanisms underlying apoptosis may open the door to more advanced therapeutic approaches and treatment modalities that aim to regulate the neuronal apoptotic death pathway. To date, caspases and the Bcl-2 protein family are two members of the apoptotic machinery that have been the subject of much investigation. Future treatment modalities that emerge from research to more precisely identify the redox-sensitive molecular components of the neuronal apoptotic death machinery and their regulation in the various acute and chronic neurodegenerative pathologies should be challenged by the successes of these current approaches. More apoptotic inhibitors will probably be added to physicians' daily toolkits in the coming years for treating neurologic conditions involving caspase-mediated cell malfunction and cell death.

Abbreviations

6-OHDA:	6-hydroxydopamine
AChEIs:	acetylcholinesterase inhibitors
AD:	Alzheimer's disease
ALS:	amyotrophic lateral sclerosis
Apaf-1:	apoptotic protease activating factor-1
Bcl-2:	B-cell lymphoma 2
Cyt c:	cytochrome c
DNA:	deoxyribonucleic acid
NDs:	neurodegenerative disorders
NO:	nitric oxide
PD:	Parkinson's disease
ROS:	reactive oxygen species
SOD:	superoxide dismutase
TERT:	telomerase reverse transcriptase
UV:	ultraviolet

Declarations

Acknowledgments

Author contributions

Principal
Indore Institute of Pharmacy,
INDORE (M.P.)

to conceiving this paper and participated in its revisions. All authors read and approved the final manuscript.

Conflicts of interest

The authors declare that they have no conflicts of interest.

Ethical approval

Not applicable.

Consent to participate

Not applicable.

Consent to publication

Not applicable.

Availability of data and materials

Not applicable.

Funding

Not applicable.

Copyright

References

1. Sankari SL, Masthan KM, Babu NA, Bhattacharjee T, Elumalai M. Apoptosis in cancer-an update. Asian Pac J Cancer Prev. 2012;13:4873–8. [DOI (https://doi.org/10.7314/apjcp.2012.13.10.4873)] [PubMed (https://pubmed.ncbi.nlm.nih.gov/23244073)]

2. Rahman MA, Sultan MT, Islam MR. Apoptosis and cancer: insights molecular mechanisms and treatments. Int J Biomol Biomed. 2012;2:1–6.

3. Cheung HH, Liu X, Rennert OM. Apoptosis: reprogramming and the fate of mature cells. Int Sch Res Not. 2012;2012:685852.

4. Rahbar Saadat Y, Saeidi N, Zununi Vahed S, Barzegari A, Barar J. An update to DNA ladder assay for apoptosis detection. Bioimpacts. 2015;5:25–8. [DOI (https://doi.org/10.15171/bi.2015.01)] [PubMed (https://pubmed.ncbi.nlm.nih.gov/25901294)] [PMC (https://www.ncbi.nlm.nih.gov/pmc/articles/PMC4401164)]

5. Shirjang S, Mansoori B, Asghari S, Duijf PH, Mohammadi A, Gjerstorff M, et al. MicroRNAs in cancer cell death pathways: apoptosis and necroptosis. Free Radic Biol Med. 2019;139:1–15. [DOI (https://doi.org/10.1016/j.freeradbiomed.2019.05.017)] [PubMed (https://pubmed.ncbi.nlm.nih.gov/31102709)]

6. Guerin MB, McKernan DP, O'Brien CJ, Cotter TG. Retinal ganglion cells: dying to survive. Int J Dev Biol. 2006;50:665–74. [DOI (https://doi.org/10.1387/ijdb.062159mg)] [PubMed (https://pubmed.ncbi.nlm.nih.gov/17051476)]

7. Kim MA, Lee HE, Lee HS, Yang HK, Kim WH. Expression of apoptosis-related proteins and its clinical implication in surgically resected gastric carcinoma. Virchows Archiv. 2011;459:503–10. [DOI (https://doi.org/10.1007/s00428-011-1150-6)] [PubMed (https://pubmed.ncbi.nlm.nih.gov/21947931)]

8. Franklin JL. Redox regulation of the intrinsic pathway in neuronal apoptosis. Antioxid Redox Signal. 2011;14:1437–48. [DOI (https://doi.org/10.1089/ars.2010.3596)] [PubMed (https://pubmed.ncbi.nlm.nih.gov/20812874)] [PMC (https://www.ncbi.nlm.nih.gov/pmc/articles/PMC3061193)]

9. Loreto C, La Rocca G, Anzalone R, Caltabiano R, Vespasiani G, Castorina S, et al. The role of intrinsic pathway in apoptosis activation and progression in Peyronie's disease. Bio Med Res Int. 2014;2014:616149. [DOI (https://doi.org/10.1155/2014/616149)] [PubMed (https://pubmed.ncbi.nlm.nih.gov/25197653)] [PMC (https://www.ncbi.nlm.nih.gov/pmc/articles/PMC4147380)]

10. Nair P, Lu M, Petersen S, Ashkenazi A. Apoptosis initiation through the cell-extrinsic pathway. Methods Enzymol. 2014;544:99–128. [DOI (https://doi.org/10.1016/B978-0-12-417158-9.00005-4)] [PubMed

Principal
Indore Institute of Pharmacy,
INDORE (M.P.)

cancer: lessons learned and future directions. J Clin Invest. 2015;125:487–9. [DOI (https://doi.org/10.1172/JCI80420)] [PubMed (https://pubmed.ncbi.nlm.nih.gov/25642709)] [PMC (https://www.ncbi.nlm.nih.gov/pmc/articles/PMC4319431)]

12. Tripathi PN, Srivastava P, Sharma P, Tripathi MK, Seth A, Tripathi A, et al. Biphenyl-3-oxo-1, 2, 4-triazine linked piperazine derivatives as potential cholinesterase inhibitors with anti-oxidant property to improve the learning and memory. Bioorg Chem. 2019;85:82–96. [DOI (https://doi.org/10.1016/j.bioorg.2018.12.017)] [PubMed (https://pubmed.ncbi.nlm.nih.gov/30605887)]

13. Kim GH, Kim JE, Rhie SJ, Yoon S. The role of oxidative stress in neurodegenerative diseases. Exp Neurobiol. 2015;24:325–40. [DOI (https://doi.org/10.5607/en.2015.24.4.325)] [PubMed (https://pubmed.ncbi.nlm.nih.gov/26713080)] [PMC (https://www.ncbi.nlm.nih.gov/pmc/articles/PMC4688332)]

14. Giorgi C, Baldassari F, Bononi A, Bonora M, De Marchi E, Marchi S, et al. Mitochondrial Ca^{2+} and apoptosis. Cell Calcium. 2012;52:36–43. [DOI (https://doi.org/10.1016/j.ceca.2012.02.008)] [PubMed (https://pubmed.ncbi.nlm.nih.gov/22480931)] [PMC (https://www.ncbi.nlm.nih.gov/pmc/articles/PMC3396846)]

15. Tian H, Qu S, Wang Y, Lu Z, Zhang M, Gan Y, et al. Calcium and oxidative stress mediate perillaldehyde-induced apoptosis in *Candida albicans*. Appl Microbiol Biotechnol. 2017;101:3335–45. [DOI (https://doi.org/10.1007/s00253-017-8146-3)] [PubMed (https://pubmed.ncbi.nlm.nih.gov/28224196)]

16. Gorman AM, McGowan A, O'Neill C, Cotter T. Oxidative stress and apoptosis in neurodegeneration. J Neurol Sci. 1996;139:45–52. [DOI (https://doi.org/10.1016/0022-510x(96)00097-4)] [PubMed (https://pubmed.ncbi.nlm.nih.gov/8899658)]

17. Ly LD, Xu S, Choi SK, Ha CM, Thoudam T, Cha SK, et al. Oxidative stress and calcium dysregulation by palmitate in type 2 diabetes. Exp Mol Med. 2017;49:e291. [DOI (https://doi.org/10.1038/emm.2016.157)] [PubMed (https://pubmed.ncbi.nlm.nih.gov/28154371)] [PMC (https://www.ncbi.nlm.nih.gov/pmc/articles/PMC5336562)]

18. Resende R, Pereira C, Agostinho P, Vieira AP, Malva JO, Oliveira CR. Susceptibility of hippocampal neurons to Aβ peptide toxicity is associated with perturbation of Ca^{2+} homeostasis. Brain Res. 2007;1143:11–21. [DOI (https://doi.org/10.1016/j.brainres.2007.01.071)] [PubMed (https://pubmed.ncbi.nlm.nih.gov/17336275)]

19. Giorgi C, Bonora M, Sorrentino G, Missiroli S, Poletti F, Suski JM, et al. p53 at the endoplasmic reticulum regulates apoptosis in a Ca^{2+}-dependent manner. Proc Natl Acad Sci. 2015;112:1779–84. [DOI (https://doi.org/10.1073/pnas.1410723112)] [PubMed (https://pubmed.ncbi.nlm.nih.gov/25624484)] [PMC (https://www.ncbi.nlm.nih.gov/pmc/articles/PMC4330769)]

20. Cook NL, Viola HM, Sharov VS, Hool LC, Schöneich C, Davies MJ. Myeloperoxidase-derived oxidants inhibit sarco/endoplasmic reticulum Ca^{2+}-ATPase activity and perturb Ca^{2+} homeostasis in human coronary artery endothelial cells. Free Radic Biol Med. 2012;52:951–61. [DOI (https://doi.org/10.1016/j.freeradbiomed.2011.12.001)] [PubMed (https://pubmed.ncbi.nlm.nih.gov/22214747)] [PMC (https://www.ncbi.nlm.nih.gov/pmc/articles/PMC3736816)]

21. Vergun O, Keelan J, Khodorov BI, Duchen MR. Glutamate-induced mitochondrial depolarisation and perturbation of calcium homeostasis in cultured rat hippocampal neurones. J Physiol. 1999;519:451–66. [DOI (https://doi.org/10.1111/j.1469-7793.1999.0451m.x)] [PubMed (https://pubmed.ncbi.nlm.nih.gov/10457062)] [PMC (https://www.ncbi.nlm.nih.gov/pmc/articles/PMC2269520)]

22. Florea AM. Toxicity of alkylated derivatives of arsenic, antimony, and tin *in vitro*: cellular uptake, cytotoxicity, genotoxic effects, perturbation of Ca^{2+} homeostasis, and cell death [dissertation]. Essen: University of Duisburg-Essen; 2005

Principal
Indore Institute of Pharmacy,
INDORE (M.P.)

homeostasis identified by inference of kinetic model parameters from live single cells perturbed by siRNA. Sci Signal. 2013;6:ra56. [DOI (https://doi.org/10.1126/scisignal.2003649)] [PubMed (https://pubmed.ncbi.nlm.nih.gov/23838183)] [PMC (https://www.ncbi.nlm.nih.gov/pmc/articles/PMC3897207)]

24. Zhou X, Hao W, Shi H, Hou Y, Xu Q. Calcium homeostasis disruption-a bridge connecting cadmium-induced apoptosis, autophagy and tumorigenesis. Oncol Res Treat. 2015;38:311–5. [DOI (https://doi.org/10.1159/000431032)] [PubMed (https://pubmed.ncbi.nlm.nih.gov/26045029)]

25. Luheshi LM, Crowther DC, Dobson CM. Protein misfolding and disease: from the test tube to the organism. Current Opin Chem Biol. 2008;12:25–31. [DOI (https://doi.org/10.1016/j.cbpa.2008.02.011)] [PubMed (https://pubmed.ncbi.nlm.nih.gov/18295611)]

26. Xilouri M, Stefanis L. Autophagy in the central nervous system: implications for neurodegenerative disorders. CNS Neurol Disord Drug Targets. 2010;9:701–19. [DOI (https://doi.org/10.2174/187152710793237421)] [PubMed (https://pubmed.ncbi.nlm.nih.gov/20942791)]

27. Ghavami S, Shojaei S, Yeganeh B, Ande SR, Jangamreddy JR, Mehrpour M, et al. Autophagy and apoptosis dysfunction in neurodegenerative disorders. Prog Neurobiol. 2014;112:24–49. [DOI (https://doi.org/10.1016/j.pneurobio.2013.10.004)] [PubMed (https://pubmed.ncbi.nlm.nih.gov/24211851)]

28. Maragakis NJ, Rothstein JD. Mechanisms of disease: astrocytes in neurodegenerative disease. Nat Clin Pract Neurol. 2006;2:679–89. [DOI (https://doi.org/10.1038/ncpneuro0355)] [PubMed (https://pubmed.ncbi.nlm.nih.gov/17117171)]

29. Lee HG, Zhu X, Casadesus G, Pallàs M, Camins A, O'Neill MJ, et al. The effect of mGluR2 activation on signal transduction pathways and neuronal cell survival. Brain Res. 2009;1249:244–50. [DOI (https://doi.org/10.1016/j.brainres.2008.10.055)] [PubMed (https://pubmed.ncbi.nlm.nih.gov/19026996)] [PMC (https://www.ncbi.nlm.nih.gov/pmc/articles/PMC2698437)]

30. Nicholls DG. Mitochondrial dysfunction and glutamate excitotoxicity studied in primary neuronal cultures. Current Mol Med. 2004;4:149–77. [DOI (https://doi.org/10.2174/1566524043479239)] [PubMed (https://pubmed.ncbi.nlm.nih.gov/15032711)]

31. Farooqui T, Farooqui AA. Aging: an important factor for the pathogenesis of neurodegenerative diseases. Mech Ageing Dev. 2009;130:203–15. [DOI (https://doi.org/10.1016/j.mad.2008.11.006)] [PubMed (https://pubmed.ncbi.nlm.nih.gov/19071157)]

32. Ramakrishna K, Nalla LV, Naresh D, Venkateswarlu K, Viswanadh MK, Nalluri BN, et al. WNT-β catenin signaling as a potential therapeutic target for neurodegenerative diseases: current status and future perspective. Diseases. 2023;11:89. [DOI (https://doi.org/10.3390/diseases11030089)] [PubMed (https://pubmed.ncbi.nlm.nih.gov/37489441)] [PMC (https://www.ncbi.nlm.nih.gov/pmc/articles/PMC10366863)]

33. Mehta A, Prabhakar M, Kumar P, Deshmukh R, Sharma PL. Excitotoxicity: bridge to various triggers in neurodegenerative disorders. Eur J Pharmacol. 2013;698:6–18. [DOI (https://doi.org/10.1016/j.ejphar.2012.10.032)] [PubMed (https://pubmed.ncbi.nlm.nih.gov/23123057)]

34. Ekshyyan O, Aw TY. Apoptosis: a key in neurodegenerative disorders. Curr Neurovasc Res. 2004;1:355–71. [DOI (https://doi.org/10.2174/1567202043362018)] [PubMed (https://pubmed.ncbi.nlm.nih.gov/16181084)]

35. Culmsee C, Landshamer S. Molecular insights into mechanisms of the cell death program: role in the progression of neurodegenerative disorders. Curr Alzheimer Res. 2006;3:269–83. [DOI (https://doi.org/10.2174/156720506778249461)] [PubMed (https://pubmed.ncbi.nlm.nih.gov/17017859)]

Principal
Indore Institute of Pharmacy,
INDORE (M.P.)

damage and repair in neurodegenerative disorders. DNA Repair. 2008;7:1110–20. [DOI (https://doi.org/10.1016/j.dnarep.2008.03.012)] [PubMed (https://pubmed.ncbi.nlm.nih.gov/18463003)] [PMC (https://www.ncbi.nlm.nih.gov/pmc/articles/PMC2442166)]

37. Rai SN, Singh C, Singh A, Singh MP, Singh BK. Mitochondrial dysfunction: a potential therapeutic target to treat Alzheimer's disease. Mol Neurobiol. 2020;57:3075–88. [DOI (https://doi.org/10.1007/s12035-020-01945-y)] [PubMed (https://pubmed.ncbi.nlm.nih.gov/32462551)]

38. Mazarakis ND, Edwards AD, Mehmet H. Apoptosis in neural development and disease. Arch Dis Child Fetal Neonatal Ed. 1997;77:F165–70. [DOI (https://doi.org/10.1136/fn.77.3.f165)] [PubMed (https://pubmed.ncbi.nlm.nih.gov/9462183)] [PMC (https://www.ncbi.nlm.nih.gov/pmc/articles/PMC1720726)]

39. Mattson MP, Duan W, Pedersen WA, Culmsee C. Neurodegenerative disorders and ischemic brain diseases. Apoptosis. 2001;6:69–81. [DOI (https://doi.org/10.1023/a:1009676112184)] [PubMed (https://pubmed.ncbi.nlm.nih.gov/11321043)]

40. Srivastava P, Tripathi PN, Sharma P, Rai SN, Singh SP, Srivastava RK, et al. Design and development of some phenyl benzoxazole derivatives as a potent acetylcholinesterase inhibitor with antioxidant property to enhance learning and memory. Eur J Med Chem. 2019;163:116–35. [DOI (https://doi.org/10.1016/j.ejmech.2018.11.049)] [PubMed (https://pubmed.ncbi.nlm.nih.gov/30503937)]

41. Kim HS, Suh YH. Minocycline and neurodegenerative diseases. Behav Brain Res. 200;196:168–79. [DOI (https://doi.org/10.1016/j.bbr.2008.09.040)] [PubMed (https://pubmed.ncbi.nlm.nih.gov/18977395)]

42. Lin S, Wei X, Xu Y, Yan C, Dodel R, Zhang Y, et al. Minocycline blocks 6-hydroxydopamine-induced neurotoxicity and free radical production in rat cerebellar granule neurons. Life Sci. 2003;72:1635–41. [DOI (https://doi.org/10.1016/s0024-3205(02)02442-6)] [PubMed (https://pubmed.ncbi.nlm.nih.gov/12551752)]

43. Youdim MB, Bar Am O, Yogev-Falach M, Weinreb O, Maruyama W, Naoi M, et al. Rasagiline: neurodegeneration, neuroprotection, and mitochondrial permeability transition. J Neurosci Res. 2005;79:172–9. [DOI (https://doi.org/10.1002/jnr.20350)] [PubMed (https://pubmed.ncbi.nlm.nih.gov/15573406)]

44. Weinreb O, Badinter F, Amit T, Bar-Am O, Youdim MB. Effect of long-term treatment with rasagiline on cognitive deficits and related molecular cascades in aged mice. Neurobiol Aging. 2015;36:2628–36. [DOI (https://doi.org/10.1016/j.neurobiolaging.2015.05.009)] [PubMed (https://pubmed.ncbi.nlm.nih.gov/26142126)]

45. Khan MM, Ahmad A, Ishrat T, Khan MB, Hoda MN, Khuwaja G, et al. Resveratrol attenuates 6-hydroxydopamine-induced oxidative damage and dopamine depletion in rat model of Parkinson's disease. Brain Res. 2010;1328:139–51. [DOI (https://doi.org/10.1016/j.brainres.2010.02.031)] [PubMed (https://pubmed.ncbi.nlm.nih.gov/20167206)]

46. Allard JS, Perez EJ, Fukui K, Carpenter P, Ingram DK, de Cabo R. Prolonged metformin treatment leads to reduced transcription of Nrf2 and neurotrophic factors without cognitive impairment in older C57BL/6J mice. Behav Brain Res. 2016;301:1–9. [DOI (https://doi.org/10.1016/j.bbr.2015.12.012)] [PubMed (https://pubmed.ncbi.nlm.nih.gov/26698400)] [PMC (https://www.ncbi.nlm.nih.gov/pmc/articles/PMC4823003)]

47. Choi H, Park HH, Koh SH, Choi NY, Yu HJ, Park J, et al. Coenzyme Q10 protects against amyloid beta-induced neuronal cell death by inhibiting oxidative stress and activating the P13K pathway. Neurotoxicology. 2012;33:85–90. [DOI (https://doi.org/10.1016/j.neuro.2011.12.005)] [PubMed (https://pubmed.ncbi.nlm.nih.gov/22186599)]

Principal
Indore Institute of Pharmacy,
INDORE (M.P.)

Insights on therapeutic approaches of natural anti-Alzheimer's agents in the management of Alzheimer's disease: A future perspective

Kalpesh Mahajan[1], Sanjay Sharma[2] ⓘ, Rupesh K Gautam[3], Rajat Goyal[4], Dinesh Kumar Mishra[5] and Rajeev K Singla[6,7] ⓘ

Abstract

In the current scenario, Alzheimer's disease is a complex, challenging, and arduous health issue, and its prevalence, together with comorbidities, is accelerating around the universe. Alzheimer's disease is becoming a primary concern that significantly impacts an individual's status in life. The traditional treatment of Alzheimer's disease includes some synthetic drugs, which have numerous dangerous side effects, a high risk of recurrence, lower bioavailability, and limited treatment. Hence, the current article is a detailed study and review of all known information on plant-derived compounds as natural anti-Alzheimer's agents, including their biological sources, active phytochemical ingredients, and a possible mode of action. With the help of a scientific data search engine, including the National Center for Biotechnology Information (NCBI/PubMed), Science Direct, and Google Scholar, analysis from 2001 to 2024 has been completed. This article also described clinical studies on phytoconstituents used to treat Alzheimer's disease. Plant-derived compounds offer promising alternatives to synthetic drugs in treating Alzheimer's disease, with the potential for improving cognitive function and slowing down the progression of the disease. Further research and clinical trials are needed to fully explore their therapeutic potential and develop effective strategies for managing this complex condition.

Keywords

Alzheimer's disease, management, natural anti-Alzheimer's agents, neurodegenerative diseases, neurological disorders, phytochemicals

[1]School of Pharmacy and Technology Management, SVKMS NMIMS Maharashtra, Shirpur, India
[2]Shobhaben Pratapbhai Patel School of Pharmacy & Technology Management, SVKMs NMIMS, Mumbai, Maharashtra, India
[3]Department of Pharmacology, Indore Institute of Pharmacy, Rau, Indore, India
[4]MM College of Pharmacy, Maharishi Markandeshwar (Deemed to be University), Mullana-Ambala, India
[5]Department of Pharmacy, Guru Ghasidas Vishwavidyalaya (A Central University) Koni, Bilaspur (C.G.), India
[6]Department of Pharmacy and Institutes for Systems Genetics, Center for High Altitude Medicine, Frontiers Science Center for Disease-related Molecular Network, West China Hospital, Sichuan University, Chengdu, Sichuan, China
[7]School of Pharmaceutical Sciences, Lovely Professional University, Phagwara, Punjab, India

Corresponding authors:
Sanjay Sharma, Shobhaben Pratapbhai Patel School of Pharmacy & Technology Management, SVKMs NMIMS, V.L. Mehta Road, Vile Parle (W), Mumbai, Maharashtra 400056, India.
Email: sanjaysharma.qa@gmail.com

Rupesh K Gautam, Department of Pharmacology, Indore Institute of Pharmacy, IIST Campus, Opposite IIM Indore, Indore 453331, MP, India.
Email: drrupeshgautam@gmail.com

Rajeev K Singla, Department of Pharmacy and Institutes for Systems Genetics, Center for High Altitude Medicine, Frontiers Science Center for Disease-related Molecular Network, West China Hospital, Sichuan University, Chengdu, Sichuan 610041, China.
Emails: rajeevsingla26@gmail.com; rajeevkumar@scu.edu.cn

Handling Associate Editor: Rekha Khandia

Principal
Indore Institute of Pharmacy,
INDORE (M.P.)

37

Introduction

Neurodegenerative diseases are characterized by the progressive loss of both the structural and functional elements of the peripheral nervous system and the central nervous system.[1] Neuronal death leads to the onset of various neurodegenerative diseases such as Alzheimer's disease (AD), Parkinson's disease, Huntington's disease, amyotrophic lateral sclerosis, and stroke.[2] AD is the most observable form of dementia in aged people,[3] characterized by the progressive deterioration of memory and other cognitive functions.[4] Memory loss is the key symptom of AD.[5] Major hypotheses for AD include amyloid and cholinergic hypotheses and additional risk factors like genetic problems, aging, head injuries, infections, vascular disorders, and environmental factors.[6] Recent research has demonstrated that the genesis of AD is significantly influenced by the inhibition of oxidative stress and target enzymes like cholinesterase, β-secretase, and monoamine oxidase, as well as by the suppression of tau protein hyperphosphorylation and amyloid-β (Aβ) plaque aggregation, inflammatory responses, and unfolded protein responses.[7] The comorbidities due to AD include hypertension, depression, osteoarthritis, diabetes mellitus, cerebrovascular disease, and others.

The FDA-approved medications for the treatment of AD are cholinesterase inhibitors (donepezil, galantamine, rivastigmine), glutamate regulators (memantine), and orexin receptor antagonists (suvorexant), and novel anti-amyloid antibodies (aducanumab).[8] The availability of these pharmaceuticals and their potentially hazardous side effects restrict their usage. As a result, developing an effective, safe, economical, and cost-efficient drug is essential. Recent studies indicate that natural products might exert therapeutic potential against AD and recommend that herbal drugs are alternatives to synthetic drugs in managing AD.[9] The efficacious usage of these herbal drugs will enhance anti-AD effects by acting on numerous targets associated with AD with lower side effects.[10] Therefore, herbal plants and their derivatives are practical approaches to treating AD.

In recent years, researchers have found many active compounds in herbs, and such bioactives have targeted the therapeutic potential of herbal products against AD with fewer adverse effects than conventional drugs.[11] This review highlights the recent research contributions from different academics worldwide in herbal-based AD treatment. The present study covers the trends in epidemiological data, pathogenesis, and herbs with their phytochemicals and mechanism of action against AD. This review also discusses the country-wise research carried out from 2001 to 2021. Figure 1 depicts the workflow for the literature selection process.

Epidemiology of Alzheimer's disease

AD is the most familiar and common type of dementia, accounting for 60 to 70% of all cases, and around 5 million new cases are found annually. Dementia affects more than 50 million people in the world today, and by 2050, the total figure of patients is expected to triple, the majority of whom have AD.[12,13] Turkey, Lebanon, Libya, and Finland have higher death rates because of AD as compared to other countries in the world.

Pathophysiology of Alzheimer's disease

AD is characterized by a complex interplay of pathological processes contributing to its pathophysiology. Key factors involved in AD include the deposition of extracellular Aβ, tau protein abnormalities, oxidative neuronal damage, intracellular neurofibrillary tangles (NFTs), neuroinflammation, genetic mutations, dysregulation of neurotransmitters, and various molecular and cellular pathways; represented in Figure 2. Deposition of the extracellular Aβ due to neurotoxicity is the main reason for AD.[14–16]

Extracellular deposition of Aβ plays a central role in AD. Aβ peptides are derived from the cleavage of amyloid-β protein precursor (AβPP) and can aggregate to form insoluble plaques. These plaques disrupt normal neuronal function and activate inflammatory responses. Aβ oligomers, intermediate forms of Aβ aggregation, are particularly toxic to neurons and contribute to synaptic dysfunction and neurotoxic cascades. Tau protein abnormalities contribute to intracellular NFT formation. Tau is a microtubule-associated protein involved in maintaining neuronal structure and transport. In AD, tau becomes hyperphosphorylated, leading to its detachment from microtubules and aggregation into NFTs. These tangles disrupt neuronal integrity, impair axonal transport, and contribute to cognitive decline.

Oxidative stress is a prominent feature of AD pathophysiology. Excessive production of reactive oxygen species overwhelms the antioxidant defense mechanisms, leading to neuron oxidative damage. Mitochondrial dysfunction, Aβ-induced oxidative stress, and inflammation contribute to reactive oxygen species generation. Oxidative stress results in lipid peroxidation, protein oxidation, DNA damage, and mitochondrial dysfunction, further exacerbating neuronal injury and synaptic dysfunction.

Neuroinflammation plays a significant role in AD. Microglial cells, the brain's immune cells, are activated in response to Aβ accumulation and NFT formation. Activated microglia release pro-inflammatory cytokines, contributing to Aβ production, tau pathology, and neuronal damage. Peripheral immune cells are also recruited, amplifying the inflammatory response and contributing to neuroinflammation.

Genetic mutations are implicated in familial forms of AD. Mutations in genes such as *APP*, *PSEN1*, and *PSEN2* affect Aβ production or metabolism, directly contributing to AD pathology. Risk factors such as advanced age, the *APOE* ε4 allele, and lifestyle factors influence AD susceptibility and disease progression. Dysregulation of neurotransmitters is observed in AD. Cholinergic

Flowchart of the literature selection process

Identification

Records identified through NCBI (PubMed) database by searching various keywords including the names of plants, families and phytochemicals in Alzheimer's disease etc. from time interval: 2001-2024
(n=231)

Additional records were identified through other sources like Google Scholar, Scince direct etc.
(n=89)

Screening

Records after duplicates removed
(n=277)

Records screened
(n=254)

Records excluded
(n=28)

Eligibility

Full-text articles assessed for eligibility
(n=226)

Full-text articles excluded, with no relevant data of interest
(n=23)

Studies included in qualitative analysis of plants in management of Alzheimer's disease
(n=203)

Included

Studies included in quantitative analysis of plants in management of Alzheimer's disease
(n=197)

Figure 1. Flowchart of the literature selection process.

dysfunction, characterized by the degeneration of cholinergic neurons and reduced acetylcholine levels, contributes to cognitive impairment. Other neurotransmitter systems, including glutamate and serotonin, are also affected, leading to excitotoxicity, synaptic dysfunction, and behavioral and psychiatric symptoms.
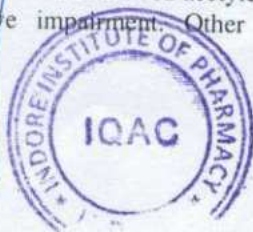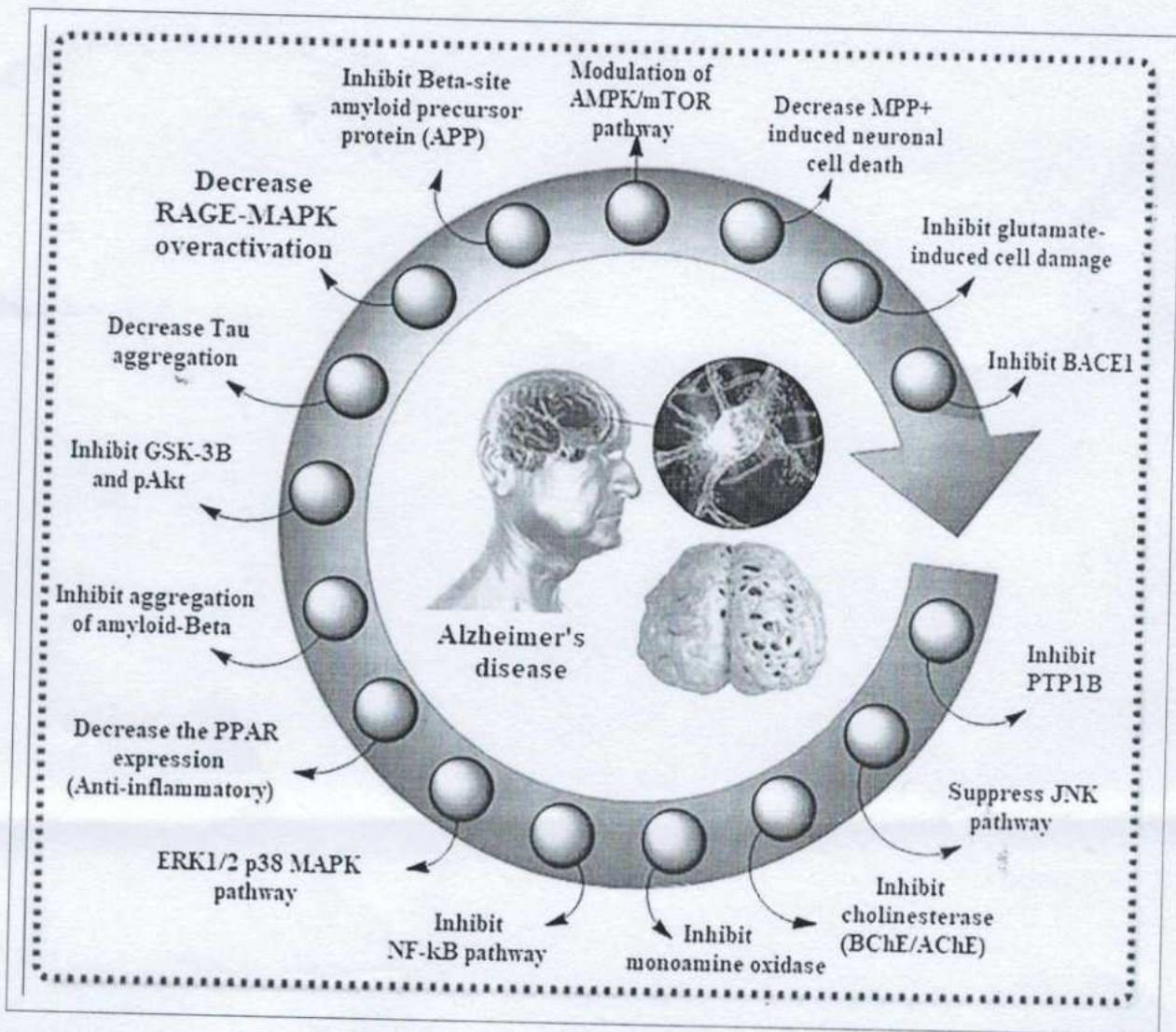
Figure 2. Various pathways involved in the pathogenesis of Alzheimer's disease.

AD involves various molecular and cellular pathways, including factor nuclear factor-kappa B (NF-κB), extracellular regulated kinases (ERK1/2), p38 mitogen-activated protein kinases (MAPK), AMP-activated protein kinase (AMPK)/mTOR, extracellular regulated kinases (ERK1/2), and c-Jun N-terminal kinase (JNK), along with others. Dysregulated AβPP processing leads to the production of different Aβ species with varying degrees of aggregation and neurotoxicity. Tau kinases, such as glycogen synthase kinase-3β, contribute to abnormal tau phosphorylation and NFT formation. Disrupted calcium homeostasis, impaired insulin signaling, compromised autophagy, lysosomal degradation, and altered synaptic plasticity contribute to AD pathophysiology.

Emerging pathways and mechanisms have gained attention in AD research. Mitochondrial dysfunction, vascular abnormalities, epigenetic modifications, and the gut-brain axis are emerging areas of investigation. Mitochondrial dysfunction affects energy production and increases oxidative stress. Vascular abnormalities lead to reduced cerebral blood flow and metabolic disturbances. Epigenetic modifications influence gene expression patterns and may contribute to AD development. The gut-brain axis involves bidirectional communication between the gut microbiota and the brain and has been implicated in AD pathophysiology.[17,18]

Trends based upon natural anti-AD agents

The present study is based on a colossal numeral of literature gathered from scientifically authenticated sources like NCBI/PubMed, Science Direct, and Google Scholar.

Table I. Various representative herbs and their parts used, pharmacological action, and active phytoconstituents.

Sr. no.	Biological source	Family	Active constituents	Part use	Pharmacological action (mechanism)	Type of extract	Method/assay/animal model	References
1.	Abies holophylla	Pinaceae	Firmanoic acid, mangiferonic acid, and terpenoids	Trunk	Suppress JNK signaling pathway, inhibit NO production, prostaglandin E2, tumor necrosis factor, and interleukins (anti-euro-inflammatory)	Ethanol and ethanol extract (chloroform- and hexane-soluble fractions)	Murine microglial cells	19,20
2.	Acorus calamus	Araceae	α- and β-asarone and phenylpropanoids	Rhizome	Inhibition of AChE and decreased ROS production	Hydroalcoholic extract and essential oil	96 well microplate reader (Ellman's method)	21-23
3.	Allium sativum	Liliaceae	Allicin	Clove	Inhibit cholinesterase, decrease Aβ induced toxicity	Hydroalcoholic extract	Intra hippocampal rat model	23,24
4.	Angelica decursiva	Apiaceae	Umbelliferone, 6-formyl umbelliferone and coumarin	Whole plant	Inhibit AChE and BChE	Methanolic extract	BACE1 and ChE enzyme Assay	25,26
5.	Artemisia annua	Asteraceae	Artemisinin (Sesquiterpene lactone), chrysosplenetin and scopoletin	Leaves	Inhibit AChE, inhibit NO production, and decrease the oxidative stress	Ethanolic extract	264.7 macrophages cell line and Ellman's colorimetric method	27,28
6.	Ferula assafoetida	Apiaceae	Ferulic acid and umbelliferone	Resins	Decrease Aβ-induced neurotoxicity and oxidative stress, inhibit AChE	Aqueous extract	Mice	29,30
7.	Azadirachta indica	Meliaceae	Nimbin, salannin, limonoids, and terpenoids	Fruits	Inhibits tau aggregation, anti-inflammatory	Methanolic extract	HEK293T cell line, Thioflavin S fluorescence,	31,32
8.	Bacopa monnieri	Scrophulariaceae	Bacopasaponi, pseudo jujubogenin, bacopaside and brahmine	Arial parts	Improve aceetylcholine and cerebral blood flow, and inhibit superoxide anion formation (antioxidant)	Alcoholic extract	Male Wistar rats, Morris water maze test	33
9.	Berberis darwinii	Berberidaceae	Berberine (alkaloid)	Stem, bark	Inhibit AChE	Methanolic extract	Anti-AChE assay	34
10.	Boletinus asiaticus	Suillaceae	Asiaticusinols C, asiachromenic acid, asiaticusin A, and terpenoids	Fruits	Inhibit BACE1	Chloroform and methanolic extract	BACE1 FRET Assay	35
11.	Caesalpinia crista	Leguminosae	Polyphenol	Leaves	Inhibit the Aβ-aggregation, anti-amyloidogenic	Aqueous extract	Thioflavin-T assay and Transmission electron microscopy study	36
12.	Camellia sinensis	Theaceae	L-Theanine	Leaves	Inhibit NK-κB, ERK1/2 and p38 MAPK pathway, antioxidant	Pure form	Human neuroblastoma cells (dopaminergic and nondopaminergic cells)	37,38

(continued)

41

Table I. Continued.

Sr. no.	Biological source	Family	Active constituents	Part use	Pharmacological action (mechanism)	Type of extract	Method/assay/animal model	References
13.	Cannabis sativa	Cannabaceae	Cannabidiol, cannabielsoin, cannabigerol, cannabitriol, cannabinoid	Flowers	Prevent toxicity of Aβ-induced increase in $[Ca^{2+}]$, inhibit AChE and BChE, neuroprotection, antioxidant	Methanol: chloroform (9:1) extract and pure Cannabidiol	Rat pheochromocytoma PC12 cells, In vitro ChE inhibitory test	39,40
14.	Carica papaya	Caricaceae	Carpaine (alkaloid)	Leaves	Inhibit BChE	Ethanolic extract	Ellman's microplate assay	41
15.	Cassia obtusifolia	Leguminosae	Rubrofusarin-6-O-D-gentiobioside, and Nor-rubrofusarin-6-O-D-glucoside	Seeds	Inhibit AChE, BChE, AβPP and BACEI	Methanolic extract	Ellman's colorimetric method	42
16.	Catharanthus roseus	Apocynaceae	Serpentine (alkaloid)	Roots	Inhibit AChE	Aqueous extract	Male Wistar rat	43
17.	Centella asiatica	Apiaceae	Asiatic acid (triterpenoids), asiaticoside (saponins glycoside)	Leaves	Decreases Aβ, decreases lipid peroxidation, inhibits AChE and BChE	Aqueous extract	B103 cell cultures, rat embryonic cortical primary cell culture	44
18.	Chrysanthemum indicum	Asteraceae	Acaciin, 3,5-diarylpyrazole, acacetin-7-O-beta-D-galactopyranoside (Flavonoid)	Flowers	Inhibits AChE, reduces Aβ aggregation	Ethanolic extract	96 well microplate reader (Ellman's method) hippocampal slices	45,46
19.	Cinnamomum zeylanicum	Lauraceae	Cinnamaldehyde	Barks	Inhibit AChE and antioxidant	Aqueous extract	Male Wistar rats	47
20.	Cissampelos sympodialis	Menispermaceae	Phanostenin, aporphine (Alkaloids)	Roots	Inhibit AChE, antioxidant	Methanolic extract	96-well plates	48
21.	Citrus limon	Rutaceae	Neoeriocitrin, isonaringin, naringin, hesperidin, neohesperidin, limonin	Peels	Inhibit AChE, antioxidant	Pure form	PC12 cell cultures, 96-well plates	49,50
22.	Commiphora whighitii / C. berryil / C. caudatal / C. pubescens	Burseraceae	Guggulsterone, myrrhterpenoids K, Myrrterpenoid N (Terpenoid)	Barks and leaves	Inhibit AChE, lipid peroxidation, and neuroprotective effect against MPP+-induced neuronal cell death (antioxidant)	Ether extract	Ellman's assay, 96-well plates, human neuroblastoma cell line SH-SYSY	51
23.	Convolvulus pluricaulis	Convolvulaceae	Not clear	Roots	Decrease AβPP, tau, Aβ and activate PI3K/Akt signaling pathway	Aqueous extract	Male Wistar rats	52,53

(continued)

Principal
Indore Institute of Pharmacy,
INDORE (M.P.)

Table I. Continued.

Sr. no.	Biological source	Family	Active constituents	Part use	Pharmacological action (mechanism)	Type of extract	Method/assay/animal model	References
24.	Coptidis rhizoma	Ranunculaceae	Berberine, jateorrhizine palmatine, epiberberine, coptisine, and groenlandicine	Rhizomes	Inhibit cholinesterase and Aβ development, antioxidants, reduce Aβ accumulation and tau phosphorylation.	1-Butanol fraction of extract	BACE1 enzyme assay, 96-well plates, male Wistar rats	54,55
25.	Coptis chinensis	Berberidaceae	Berberine, palmatine, jatrorrhizine	Rhizomes	Inhibit monoamine oxidase A and B	Methanolic extract	Rat brain mitochondrial fraction	56,57
26.	Coreopsis lanceolata	Asteraceae	Caffeic acid, cinnamic acid	Flowers	Antioxidant, neuroprotective, and anti-inflammatory effects	Ethanolic and aqueous extracts	PC12 neuronal cells and mice	58
27.	Coriandrum sativum	Apiaceae	Caffeic acid, protocatechuic acid, and glycitin	Aerial parts	Antioxidants	Aqueous ethanolic extract	Diphenylpicrylhydrazyl radical, 15-lipoxygenase, and Fe^{2+} induced porcine brain phospholipid peroxidation assay	59
28.	Corni fructus	Cornaceae	Ursolic acid, p-coumaric acid	Fruits	Inhibit BACE1	Ethanolic extract	α- and β-secretase, chymotrypsin, and trypsin enzyme assay	60
29.	Cornus officinalis	Cornaceae	Cornuside (tannin)	Fruits	Inhibit cholinesterase and BACE1	Not clear	Cholinesterase (Ellman's) and BACE1 enzyme assay	61
30.	Corydalis cava	Fumariacea	Corycavamine, corynoline, protoberberine (alkaloid)	Tubers	Inhibit BACE1	Ethanolic extract	BACE1 fluorescence resonance energy transfer, glycogen synthase kinase-3β, and casein kinase-1δ assays	62
31.	Corydalis tuber	Papaveraceae	Berberine, pseudo dehydrocorydaimine, pseudocoptisine (Alkaloid)	Tubers	Inhibit AChE and BuChE	Ethanolic extract	Ellman's assay	63
32.	Crocus sativus	Iridaceae	Crocin (Carotenoid)	Stigma	Inhibit Aβ-aggregation, inflammatory process, apoptosis, beta-amyloid aggregation, tauopathy, and antioxidant.	Hydroalcoholic extract	Trolox equivalent antioxidant capacity (TEAC), thioflavin T, DNA binding shift assay	64,65
33.	Cullen corylifolium	Leguminosae	Isobavachalcone, bavachromene (chalcone) and kanzonol B	Seeds	Block I-kBα and NF-kB pathway, inhibit NO, PGE2 (anti-inflammatory and antioxidant)	Methanolic extract	BV-2 microglial cells	66

(continued)

Principal
Indore Institute of Pharmacy,
INDORE (M.P.)

43

Table 1. Continued.

Sr. no.	Biological source	Family	Active constituents	Part use	Pharmacological action (mechanism)	Type of extract	Method/assay/animal model	References
34.	Curcuma longa	Zingiberaceae	Curcumin (curcuminoids)	Rhizomes	Inhibit Aβ deposition	Methanolic extract	PC12 rat pheochromocytoma and usual human umbilical vein endothelial (HUVEC) cells	67,68
35.	Dioscorea bulbifera	Dioscoreaceae	Diosgenin, stigmasterol, (saponin glycoside)	Tubers	Neuroprotective, antioxidants	Not clear	HT-22 mouse hippocampal cells	69
36.	Emblica officinalis	Euphorbiaceae	3,6-di-O-galloyl-d-glucose, myricetin (flavonoid), chebulagic acid (tannin)	Fruits	Inhibit AChE, BuChE, cytosolic cytochrome c, pTau, GSK-3β, and pAkt, antioxidant	Methanolic extract	2,2-diphenyl-1-picrylhydrazyl scavenging activity, AChE, and BuChE assay, rodents	70
37.	Esenbeckia leiocarpa	Rutaceae	Leptomerine, galanthamine, skimmianine (Alkaloid)	Stem	Inhibit cholinesterase	Ethanolic extract	96-well microplate method	71
38.	Eucommia ulmoides Oliv	Eucommiaceae	Geniposidic acid (glucoside)	Bark, leaves, and seeds	Prevent Aβ-induced Ca^{2+} intake and protective effect against Aβ-induced cytotoxicity, anti-inflammatory.	Aqueous extract	Rat pheochromocytoma PC-12 cell line, cell number TCR 3	72,73
39.	Eugenia aromatica	Myrtaceae	Eugenol	Buds	Enhance learning-memory ability and antioxidant effect	Pure form	Sprague Dawley rats	74,75
40.	Evolvulus alsinoides	Convolvulaceae	β-Sitosterol (aglycone), kaempferol (flavonoid)	Aerial parts	Acts against tau-proteins	Aqueous extract	Not mentioned	76
41.	Ficus racemosa	Moraceae	Racemosic acid, quercetin, kaempherol	Bark	Inhibit AChE, antioxidant, anti-inflammatory	Aqueous extract	Male Wistar rats	77,78
42.	Pinus pinaster	Pinaceae	Not clear	Bark	Decrease amyloid plaques, antioxidant	Not clear	APP-transgenic mice	79,80
43.	Galanthus nivalis	Amaryllidaceae	Galanthamine (alkaloid)	Bulb	Inhibit AChE	Methanolic extract	TLC bioautographic method	81
44.	Garcinia mangostana	Guttiferae	α-Mangostin, 8-deoxy gartanin, garcinone C, garcinone D, gartanin, garciniafuran, and xanthones	Pericarp	Inhibits Aβ agglomeration, glutamate-induced cell damage, BACE1, and AChE, and reduces NF-κB.	Ethanolic extract (xanthones are purified from the extract)	Ellman's assay Thioflavin T, DPPH radical scavenging, Cu21-chelating ability assay, HT22 murine hippocampal neuronal cells	82,83
45.	Gardenia jasminoides	Rubiaceae	Geniposide (glycosides)	Fruits	Inhibit AChE, ChAT expression, blocking of RAGE-MAPK over-activation, Aβ accumulation.	Pure form	mPrP-APPswe/PS1dE9 doubly transgenic mice and littermate wild-type mice	84,85

(continued)

Principal
Indore Institute of Pharmacy,
INDORE (M.P.)

44

Table I. Continued.

Sr. no.	Biological source	Family	Active constituents	Part use	Pharmacological action (mechanism)	Type of extract	Method/assay/animal model	References
34.	Curcuma longa	Zingiberaceae	Curcumin (curcuminoids)	Rhizomes	Inhibit Aβ deposition	Methanolic extract	PC12 rat pheochromocytoma and usual human umbilical vein endothelial (HUVEC) cells	67,68
35.	Dioscorea bulbifera	Dioscoreaceae	Diosgenin, stigmasterol, (saponin glycoside)	Tubers	Neuroprotective, antioxidants	Not clear	HT-22 mouse hippocampal cells	69
36.	Emblica officinalis	Euphorbiaceae	3,6-di-O-galloyl-d-glucose, myricetin (flavonoid), chebulagic acid (tannin)	Fruits	Inhibit AChE, BuChE, cytosolic cytochrome c, pTau, GSK-3β, and pAkt, antioxidant	Methanolic extract	2,2-diphenyl-1-picrylhydrazyl scavenging activity, AChE, and BuChE assay, rodents	70
37.	Esenbeckia leiocarpa	Rutaceae	Leptomerine, galanthamine, skimmianine (Alkaloid)	Stem	Inhibit cholinesterase	Ethanolic extract	96-well microplate method	71
38.	Eucommia ulmoides Oliv	Eucommiaceae	Geniposidic acid (glucoside)	Bark, leaves, and seeds	Prevent Aβ-induced Ca^{2+} intake and protective effect against Aβ-induced cytotoxicity, anti-inflammatory.	Aqueous extract	Rat pheochromocytoma PC-12 cell line, cell number TCR 3	72,73
39.	Eugenia aromatica	Myrtaceae	Eugenol	Buds	Enhance learning-memory ability and antioxidant effect	Pure form	Sprague Dawley rats	74,75
40.	Evolvulus alsinoides	Convolvulaceae	β-Sitosterol (aglycone), kaempferol (flavonoid)	Aerial parts	Acts against tau-proteins	Aqueous extract	Not mentioned	76
41.	Ficus racemosa	Moraceae	Racemosic acid, quercetin, kaempherol	Bark	Inhibit AChE, antioxidant, anti-inflammatory	Aqueous extract	Male Wistar rats	77,78
42.	Pinus pinaster	Pinaceae	Not clear	Bark	Decrease amyloid plaques, antioxidant	Not clear	APP-transgenic mice	79,80
43.	Galanthus nivalis	Amaryllidaceae	Galanthamine (alkaloid)	Bulb	Inhibit AChE	Methanolic extract	TLC bioautographic method, Ellman's assay	81
44.	Garcinia mangostana	Guttiferae	α-Mangostin, 8-deoxy gartanin, garcinone C, garcinone D, gartanin, garciniafuran, and xanthones	Pericarp	Inhibits Aβ agglomeration, glutamate-induced cell damage, BACEI, and AChE, and reduces NF-κB.	Ethanolic extract (xanthones are purified from the extract)	Thioflavin T, DPPH radical scavenging, Cu21-chelating ability assay, HT22 murine hippocampal neuronal cells	82,83
45.	Gardenia jasminoides	Rubiaceae	Geniposide (glycosides)	Fruits	Inhibit AChE, ChAT expression, blocking of RAGE-MAPK over-activation, Aβ accumulation.	Pure form	mPrP-APPswe/PS1dE9 doubly transgenic mice and littermate wild-type mice	84,85

(continued)

Table I. Continued.

Sr. no.	Biological source	Family	Active constituents	Part use	Pharmacological action (mechanism)	Type of extract	Method/assay/animal model	References
46.	Ginkgo biloba (L)	Ginkgoaceae	Ginkgolide B, quercetin (glycosides)	Leaves	Modulate phosphorylation of tau protein, restrict Aβ peptide-induced mitochondrial dysfunction, activation of ERK1/2, JNK, and Akt pathway.	Acetone extract	Embryonic brain tissue was harvested from E15 NMRI mice	86,87
47.	Glycine max	Leguminosae	Genistein (isoflavones)	Seeds	Inhibit pro-inflammatory mediators ICAM-1, TNF-α, MCP-1, IL-1β (cytokines), IL-8 (chemokines), (anti-inflammatory). inhibit AChE.	Ethanolic extract	Ellman's method, male Wistar rats	88,89
48.	Glycyrrhiza glabra	Leguminosae	Glabridin (flavonoid)	Roots	Inhibit cholinesterase, anti-inflammatory, antioxidant, and stimulate PI3K-Akt signaling pathway.	Acetone extract (Glabridin isolated in pure form)	Male Kunming mice	90,91
49.	Hizikia fusiformis	Sargassaceae	Glycyrrhizin (saponin), 18a-glycyrrhetinic acid, 18b-glycyrrhetinic acid	Seaweed	Inhibit BACE1	Methanolic extract	Ellman's method, FRET assay	92
50.	Huperzia serrate	Huperziaceae	Huperzine A (alkaloid)	Whole plant	Inhibit AChE, neuroprotective activity against hydrogen peroxide, Aβ and glutamate (antioxidant)	Pure form	Rat and human model	93,94
51.	Hypericum perforatum	Hypericaceae	hyperforin, tetrahydrohyperforin, hypericin, chlorogenic acid	Aerial parts	Inhibit AChE, BuChE, and DPPH radical scavenging activity (antioxidant)	Acetate, methanol, and aqueous extract	Ellman's method, dopachrome method, DPPH, N,N-dimethyl-p-phenylene-diamine, superoxide, Nitric oxide radical scavenging assay, ferric-reducing antioxidant power assay, Phosphomolibdenum-reducing antioxidant power assay	95

(continued)

Table 1. Continued.

Sr. no.	Biological source	Family	Active constituents	Part use	Pharmacological action (mechanism)	Type of extract	Method/assay/animal model	References
52.	Ilex paraguariensis	Aquifoliaceae	Chlorogenic acid caffeine, theophylline, and theobromine (alkaloid)	Leaves	Reduce AChE activity, reduce Aβ-induced toxicity	Hydroalcoholic extract	Transgenic worms CL2006	96
53.	Juglans regia	Juglandaceae	Phenol and flavonoid contents	Leaves and fruits	Neuroprotective, antioxidant, inhibits BChE	Dichloromethane, ethyl acetate, acetone, methanol, and aqueous extract	AChE and BuChE, DPPH, DMPD, superoxide, NO, and hydrogen peroxide radicals ferric ion-chelating capacity assay	97
54.	Juniperus chinensis	Cupressaceae	α-methyl artoflavanocoumarin, 5,7,4'-trihydroxy-2-styrylchromone, vanillic acid, taxifolin	Heartwood	Inhibit BACE1	Methanolic extract	Ellman's and BACE1 enzyme assay	98
55.	Lavandula angustifolia	Lamiaceae	Linalool and linalyl acetate	Leaves and flowers	Increase clearance of Aβ plaque, antioxidant	Aqueous extract	Rats	99
56.	Lepidium meyenii	Brassicaceae	Quercetin (anthocyanins)	Hypocotyls	Inhibit AChE and antioxidant	Aqueous extract	Female mice	100
57.	Liriope platyphylla	Asparagaceae	Spicatoside A, (saponin)	Roots	Stimulate PI3-kinase/Akt and ERK1/2 pathways, decrease production and aggregation of Aβ42 peptides, increase nerve growth factor, anti-inflammatory	Aqueous extract	Tg2576 mice	101,102
58.	Maclura pomifera	Moraceae	Osajin, pomiferi (isoflavones)	Fruits	Inhibit cholinesterase			
59.	Magnolia obovate	Magnoliaceae	Obovatol (lignan)	Fruits	Inhibit NF-kB pathway, Aβ generation, BACE1, and AChE	Methanolic extract Methanolic extract (Obovatol isolated in pure form)	Ellman method Mice	103 104
60.	Magnolia officinalis	Magnoliaceae	4-O-methylhonokiol (lignan)	Bark	Decreased activity of AβPP, BACE1, inhibits cytokine release and NF-kB pathway, decreases Aβ toxicity.	Ethanolic extract	Transgenic C57BL/6 mouse model	105–107
61.	Melia toosendan	Meliaceae	1-O-Tigloyl-1-O-deacetyl-nimbolinin B, limonoids	Fruits	Suppress NF-κβ and JNK pathway, iNOS, TNF-α, IL-1β, and COX-2 (anti-inflammatory)	Pure form	BV-2 microglia cells	108

(continued)

Principal
Indore Institute of Pharmacy,
INDORE (M.P.)

Table 1. Continued.

Sr. no.	Biological source	Family	Active constituents	Part use	Pharmacological action (mechanism)	Type of extract	Method/assay/animal model	References
62.	Melissa officinalis	Lamiaceae	Rosmarinic acid, gallic acid, isomenthone, c-caryophyllene, neral/geranial, citronellal, ursolic acid	Leaves	Inhibit AChE, matrix metalloproteinase-2, antiagitation properties, antioxidant	Aqueous and ethanolic extract	AChE and DPPH assay	109
63.	Morinda Officinalis	Rubiaceae	Alizarin-1-methyl ether, scopoletin, b-sitosterol, 1-hydroxy-3-hydroxymethyl (anthraquinone)	Roots	Inhibit AChE, BChE, and BACEI	Methanolic extract	AChE, BChE, and BACEI inhibition assay	110
64.	Moringa oleifera	Moringaceae	β-carotene, kaempferol, rutin	Leaves, seeds, roots, flowers, and bark	Antioxidant	Methanolic extract	Rats	111
65.	Morus alba	Moraceae	Quercetin (flavonoid), Artoindonesianin flavone	Root bark, fruits, and leaves	Inhibit BACEI, AChE, attenuates Aβ-induced toxicity, blocks oligomer Aβ4	Methanolic extract	BACE FRET assay	112,113
66.	Murraya koenigii	Rutaceae	Mahanimbine, koenimbine, mahanine, bispyrayafoline	Leaves	Improve the level of acetylcholine, inhibit BACEI, and nootropic effect	Methanolic extract	Male Swiss Albino mice	114,115
67.	Myrica pensylvanica	Myricaceae	Myricetin, myricitrin (Flavonol), myricanol	Berry	Decrease level of tau proteins	Aqueous extract	M17 neuroblastoma cells, HeLa cell line, human IMR32 cell line, H4 neuroglioma cells, IMR32 cells	116
68.	Myristica fragrans	Myristicaceae	{[(7S)-8-(4-hydroxy-3-methoxyphenyl)-7-hydroxypropyl]benzene-2,4- diol}. [(8R,8S)-7-(3,4-methylenedioxyphenyl)-8,8-dimethyl-7- (3,4-dihydroxyphenyl)-butane]	Seeds	Inhibit AChE and BACEI	Methanolic extract	Ellman method	117
69.	Nelumbo nucifera embryos	Nelumbonaceae	Cycloartenol, p-hydroxybenzoic acid, vanilloloside, nuciferoside, and 5-O-methyladenosine	Stamen	Inhibit AChE and BChE	Methanolic extract	Ellman method, BACEI enzyme assay	118

(continued)

Principal
Indore Institute of Pharmacy,
INDORE (M.P.)

Table I. Continued.

Sr. no.	Biological source	Family	Active constituents	Part use	Pharmacological action (mechanism)	Type of extract	Method/assay/animal model	References
70.	Nicotiana tobaccum	Solanaceae	Anatabine (alkaloid)	Leaves	Inhibit NFκB pathway, Aβ production, BACE-I, decrease Aβ	Pure form	Transgenic mice, HEK293 cells, SHSY-5Y cells, 7 W CHO cells overexpressing wild-type human APP	119–121
71.	Ocimum sanctum	Lamiaceae	Ursolic acid and oleanolic acid	Leaves	Inhibit AChE, immunostimulant property	Alcoholic and aqueous extract	Male albino Wistar rats	122,123
72.	Olea europaea	Oleaceae	Oleuropein (glucoside)	Leaves	Prevents Aβ aggregation, reduces amyloid aggregates, and modulates the AMPK/mTOR pathway	Pure Oleuropein extracted from olive oil	Mouse brain endothelial cells	124,125
73.	Paeonia lactiflora	Ranunculaceae	Paeoniflorin (glycoside)	Roots	Decreases ROS production and mitochondrial membrane potential and upsurges Bax/Bcl-2 ratio, activation of caspases, and cytochrome c release	Pure form	Rat model, SH-SY5Y cell	126
74.	Passiflora edulis	Passifloraceae	C dideoxyhexosyl (flavonoid)	Stem and leaves	Antioxidant	Acetone extract	PC12 cells	127,128
75.	Physostigma venenosum	Leguminosae	Physostigmine (alkaloid)	Seeds	Inhibit AChE and BuChE	Pure form	Human and animal models	129,130
76.	Pimpinella brachycarpa	Apiaceae	Quinic acid derivatives	Aerial parts	Anti-neuroinflammatory, inhibits NO production (antioxidant)	Methanolic extract	Murine microglial cell line	131
77.	Pistacia atlantica	Anacardiaceae	Digallic acid, trigallic acid and depsidones	Leaves	Inhibit AChE, antioxidant	Aqueous extract	TLC bioautography and DPPH assay	132
78.	Pistacia integerrima	Anacardiacea	Pistagremic acid, terpene	Galls	Inhibit BACEI	Methanolic extract	BACEI inhibition assay	133
79.	Pongamia pinnata	Leguminosae	Pongaglabol methyl ether, lonchocarpin, and glabrachromene II	Seeds and stems	Neuroprotective, anti-inflammatory, decrease NO production	Dichloride methane extract	BV-2 cells	134
80.	Psoralea corylifolia	Leguminosae	Bakuchiol, psoralen, neocorylinbavachromen, isobavachromene, bavachalcone, isobavachalcone	Seeds	Inhibit BACEI and decrease NO production	Methanolic extract	FRET assay	135,136

(continued)

Table I. Continued.

Sr. no.	Biological source	Family	Active constituents	Part use	Pharmacological action (mechanism)	Type of extract	Method/assay/animal model	References
81.	Psoralea fructus	Leguminosae	Bavachin, bavachinin, bavachalcone, and isobavachalcone (flavonoid)	Fruits	Inhibit amyloid -peptide 42, glycogen synthase kinase 3β, β-secretase, and AChE.	Ethanolic aqueous extract	BV-2 microglial cell line, BACE-I, AChE and GSK-3β assay	137,138
82.	Pteridium aquilinum	Dennstaedtiaceae	Pteroside N (Glycoside), Pterosinone (terpene)	Whole plant	Inhibit cholinesterase enzymes	Aqueous extract	BACE1, FRET assay, and Ellman method	139
83.	Pterocarpus santalinus	Leguminosae	Pterostilbene (stilbenoid)	Heartwood, bark	Down-regulate NF-kB, JNK pathway, inhibit cholinesterase	Methanolic extract	Swiss Albino mice and Ellman method	140,141
84.	Ptychopetalum olacoides	Olacaceae	Not clear	Roots	Inhibit AChE	Ethanolic extract	Male adult Albino mice, Ellman method	142,143
85.	Pueraria lobata	Leguminosae	Lupeol, Lupenone, genistein, biochanin A, triterpenoids, and polyphenol	Roots	Inhibit BACE1, reduce Aβ induce toxicity	Aqueous extract	BACE1, FRET assay	144,145
86.	Punica granatum	Punicaceae	Punicalgin, quercetin, gallic acid, cyanidin-3-glucoside	Leaves	Inhibit BACE1, 5-lipoxygenase (5-LOX), AChE, and BuChE	Hexane, dichloromethane, ethyl acetate, ethanol, methanol, and hydroalcoholic extract	Recombinant human BACE assay, DPPH, 2,20-azinobis-3-ethylbenzothiazoline-6 sulphonate, and Ellman's method	146,147
87.	Rabdosia japonica	Lamiaceae	Glaucocalyxin A	Aerial parts	Suppress NF-κB, anti-inflammatory	Methanolic extract (Glaucocalyxin A further isolated from this extract)	Primary microglia and BV-2 cell	148
88.	Rabdosia rubescens	Lamiaceae	Oridonin (terpenoid)	Leaves	Inhibited the NF-kB pathway, decreased the release of inflammatory cytokines, and Aβ deposition	Pure form	Transgenic mice	149
89.	Rauvolfia reflexa	Apocynaceae	Isorespiline and rescinnamine	Bark	Inhibit cholinesterase	Methanolic extract	Ellman's microplate assay	150
90.	Reseda luteola	Resedaceae	Luteolin	Aerial part	Suppress BACE1, NF-κB, MAPK pathway interleukin (anti-inflammatory), and antioxidant	Aqueous extract	Sprague–Dawley rats	151,152
	Rhodiola rosea	Crassulaceae	Salidroside, gossypetin-7-O-L-rhamnopyranoside, rhodioflavonoside	Roots	Activation of PI3K/Akt, decreased Aβ deposition and inhibited AChE.	Ethanolic extract (Salidroside is in pure form)	Transgenic Drosophila AD model, Ellman's method	153,154

(continued)

Table 1. Continued.

Sr. no.	Biological source	Family	Active constituents	Part use	Pharmacological action (mechanism)	Type of extract	Method/assay/animal model	References
92.	Rosa damascene	Rosaceae	Docosahexaenoic acid, polyunsaturated fatty acid	Buds	Decrease Aβ-induced atrophy and cell death	Chloroform extract	Embryos of Sprague-Dawley rats	155,156
93.	Salix alba	Salicaceae	Salicin (glucoside), procyanidins	Bark	Inhibit AChE and shows the antioxidant effect	Hydroalcoholic extract	2,2'-azino-bis(3-ethylbenzothiazoline-6-sulphonic acid, DPPH test, Ellman's method	157,158
94.	Salvia miltiorrhiza	Lamiaceae	Tanshinone	Roots	Protect from Aβ-induced toxicity, antioxidant, inhibit ROS, inhibit PTP1B generation, prevention of lipid peroxidation, decrease the release of cytochrome c	Alcoholic extract	Sprague Dawley rats, cell viability assay	159,160
95.	Salvia officinalis	Lamiaceae	Isorosmanol, 7a-methoxy rosmanol, terpenoid glycosides	Aerial parts	Inhibit AChE	Methanolic extract	Ellman's method	161
96.	Schisandra chinensis	Schisandraceae	Gomisin A, C, D & G schisandrol B, (lignan)	Fruits	Inhibit AChE	Hexane extract	Ellman's method	162
97.	Scutellaria baicalensis	Lamiaceae	Baicalin, baicalein, wogonin, and chrysin	Roots	Anti-inflammatory, inhibit BACE1, and AChE	Aqueous, n-hexane, ethanol, and methanol extract	BACE1, AChE, TACE, trypsin, chymotrypsin, elastase, MTT assay, mouse monocyte/macrophage cell line	163,164
98.	Sorghum bicolor	Poaceae	Quercetin, quercetrin, rutin, caffeic and chlorogenic acid	Stem	Inhibit AChE, ecto-5'-nucleotidase activities, and increased Na^+/K^+-ATPase activity	Methanol: 1 N HCl (1:1, v/v) extract	Albino rats, modified colorimetric method	165
99.	Stephania tetrandra	Menispermaceae	Tetrandrine (alkaloid)	Roots	Inhibit NF-κB activation, down-regulation of TNF-α and IL-1β	Pure form	Male Sprague–Dawley rats, Morris water maze test	166,167
100.	Symphyocladia latiuscula	Rhodomelaceae	2,3,6-tribromo-4,5-dihydroxybenzyl methyl ether; 2,3-tribromo-4,5-dihydroxybenzyl alcohol, and bis-(2,3,6-tribromo-4,5-dihydroxybenzyl) ether bromophenols	Alga	Inhibit AChE and BChE, GSK-3β, and BACE1, antioxidant	Methanolic extract	Human recombinant β-secretase and a BACE1 fluorescence resonance energy transfer, GSK-3β enzyme inhibition, self-induced $Aβ_{25-35}$ aggregation inhibition assay	168,169

(continued)

Table I. Continued.

Sr. no.	Biological source	Family	Active constituents	Part use	Pharmacological action (mechanism)	Type of extract	Method/assay/animal model	References
101.	Tabernaemontana pandacaqui	Apocynaceae	Astragalin (flavonoid)	Flowers	Inhibit AChE	Methanolic extract	^{g}Ellman's method	170
102.	Terminalia chebula	Combretaceae	Ethyl N-(N-benzyloxycarbonyl-beta-l-aspartyl)-beta-d-glucosaminide	Fruits	Inhibit AChE, antioxidant	Ethyl acetate extract	Ellman's method, DPPH radical scavenging assay	171
103.	Tinospora cordifolia	Menispermaceae	Tinosporide and 8-hydroxytinosporide	Stem	Inhibit AChE and BuChE	Methanolic extract	Ellman's method, AChE inhibition assay method	172
104.	Uncaria rhynchophylla	Rubiaceae	Rhynchophylline and isorhynchophylline (alkaloid)	Stem	Inhibit Aβ-generated neurotoxicity, intracellular calcium overloading, and tau protein hyperphosphorylation. Prevent Aβ protein aggregation, mitraphylline amyloid protein	Hydroalcoholic extract	Rat pheochromocytoma cells, MTT method	173,174
105.	Uncaria tomentosa	Rubiaceae	Mitraphylline (alkaloid)	Root bark		Aqueous extract	Aβ protein fragment 1–40	175
106.	Valeriana officinalis	Valerianaceae	Volvalerenal acid	Roots	Inhibit AChE	Ethanolic extract	Ellman's method, Seventy-five Class SPF APPswe/PS1E9 double-transgenic dementia mice, Morris water maze	176,177
107.	Vitis vinifera	Vitaceae	Resveratrol (stilbenoid)	Grapes/berry	Decrease aggregation and toxicity of Aβ peptides, stimulation of regulation by AMPK-dependent signaling pathways, mTOR inhibition, inhibit cholinesterase, transcription factor (NF-κB), and cellular autophagy stimulation.	Pure form	Rodent model	178
108.	Withania somnifera	Solanaceae	Withanolides (steroid)	Roots	Decreases Aβ$_{1-42}$-induced toxicity	Chloroform extract	Adult male Wistar rats	179,180
109.	Xanthoceras sorbifolia	Sapindaceae	Xanthoceraside	Fruits, husk	Inhibits tau hyperphosphorylation, PI3K/Akt-dependent	Pure form	Adult male and female Wistar rats	181

(continued)

Principal
Indore Institute of Pharmacy
INDORE (M.P.)

52

Table I. Continued.

Sr. no.	Biological source	Family	Active constituents	Part use	Pharmacological action (mechanism)	Type of extract	Method/assay/animal model	References
110.	Zingiber officinale	Zingiberaceae	6-shogaol	Rhizomes	GSK-3β signaling pathway, and increases the activity of phosphatases. Inhibit $A\beta_{1-42}$ induced activation of astrocytes and microglial cells, TNF-α, iNOS, NO, and COX-2 inflammatory gene PGE2, prompt NGF and modulate NF-κB pathway (anti-inflammatory)	Methanolic extract	Adults Sprague–Dawley rats, DPPH, FRAP assay, Ellman's method	182,183
111.	Zizyphus jujuba var. spinosa	Rhamnaceae	Jujuboside A, and jujuboside B	Seeds	Improve Aβ-induced synaptic dysfunction and increase the level of BDNF and TrkB	Ethanolic extract	Male CD-1 mice	184

AChE: acetylcholinesterase; AβPP: amyloid-β protein precursor; Aβ: amyloid-β; BACE1: β secretase; BChE: butyrylcholinesterase; BDNF: brain-derived neurotrophic factor; ChAT: choline acetyltransferase; ChE: cholinesterase; COX-2: cyclooxygenase-2; DMPD: dimethyl-4-phenylenediamine; DPPH: 2,2-diphenyl-1-picrylhydrazyl; ERK: extracellular regulated kinases; FRAP: ferric reducing antioxidant power; FRET: fluorescence resonance energy transfer; GSK-3β: glycogen synthase kinase-3β; ICAM: intercellular adhesion molecule; IL: Interleukin; iNOS: inducible nitric oxide synthase; JNK: c-Jun N-terminal kinase; MAPK: mitogen-activated protein kinase; MCP-1: monocyte chemoattractant protein-1; NF-κB: nuclear factor kappa-light-chain-enhancer of activated B cells; NGF: nerve growth factor; NO: nitric oxide; PGE2: prostaglandin E2; PI3K: phosphatidylinositide 3-kinase; pTau: phospho-Tau; PTP1B: protein tyrosine phosphatase IB; RAGE: receptor of advanced glycation end products; ROS: reactive oxygen species; TACE: TNF-α-converting enzyme; TLC: thin layer chromatography; TNF: tumor necrosis factor; TrkB: tropomyosin-related kinase B.

Principal
Indore Institute of Pharmacy.
INDORE (M.P.)

53

Table 1 depicts some significant advancements in natural medicinal development in treating AD. It includes a list of natural anti-Alzheimer's agents and information on their biological sources, families, chemical composition, parts used, and potential mode of action.

According to this review, there are 64 families of herbal plants, and around 23 parts demonstrated anti-AD activity. The families, including Leguminosae, Lamiaceae, Apiaceae, Rubiaceae, and Moraceae, devote a large number of anti-AD agents (Figure 3). More than 15 different anti-AD mechanisms have been discovered in phyto-constituents from these plants. The plants from the Leguminosae family inhibit the Aβ aggregation, AChE, BChE, AβPP, and BACE1, anti-amyloidogenic, blockage of NF-kB pathway, NO, PGE2 (anti-inflammatory and anti-oxidant), pro-inflammatory mediators, TNF-α, IL-8, MCP-1, IL-1β (cytokines), and ICAM-1, along with others. The most common mechanism behind the anti-AD activity is inhibiting the cholinesterase enzyme (BChE/AChE); the second most common mechanism is the antioxidant-mediated effect. Only a few researchers, however, have focused on the particular molecular mechanism responsible for anti-AD action. As a result, the expanding threat of AD to world health has prompted experts and researchers to devote more time and exercise to identifying an effective molecular mode of action.

It is observed from Figure 4 that Korea is first, China is second, India is third in phytochemical research against AD, followed by Iran, Brazil, and Japan. It has been noted that research efforts are gradually growing day by day for the evaluation of potent anti-AD phytochemicals in the management of AD. Research done in the year 2021 is more than in other years, indicating a growing interest of researchers in investigating the therapeutic application of plant-derived compounds in treating AD (Figure 5).

Figure 6 illustrates phytochemicals derived from various plant parts exhibiting anti-AD activity, and analysis reveals that phytochemicals obtained from leaves exhibit the highest and most significant therapeutic potential against AD, followed by roots, fruits, bark, and seeds. This information holds valuable implications for selecting specific plant parts for further investigation in herbal plant research related to AD. However, there is another aspect that we should not miss: the common observation that not all plant parts have been explored for all the medicinal plants. So, in the present case, it would be more appropriate to indicate leaves as the most explored plant part for anti-AD potential.

Figure 7 summarizes the different modes of action by which various plants demonstrated their anti-AD activity. Most plants showed anti-AD activity by inhibiting the cholinesterase enzyme (BChE/AChE), followed by antioxidant activity.

As data is given in Figure 8, alkaloids play a vital role in treating AD, followed by flavonoids, terpenoids, glycosides, and many more. We could also mention alkaloids
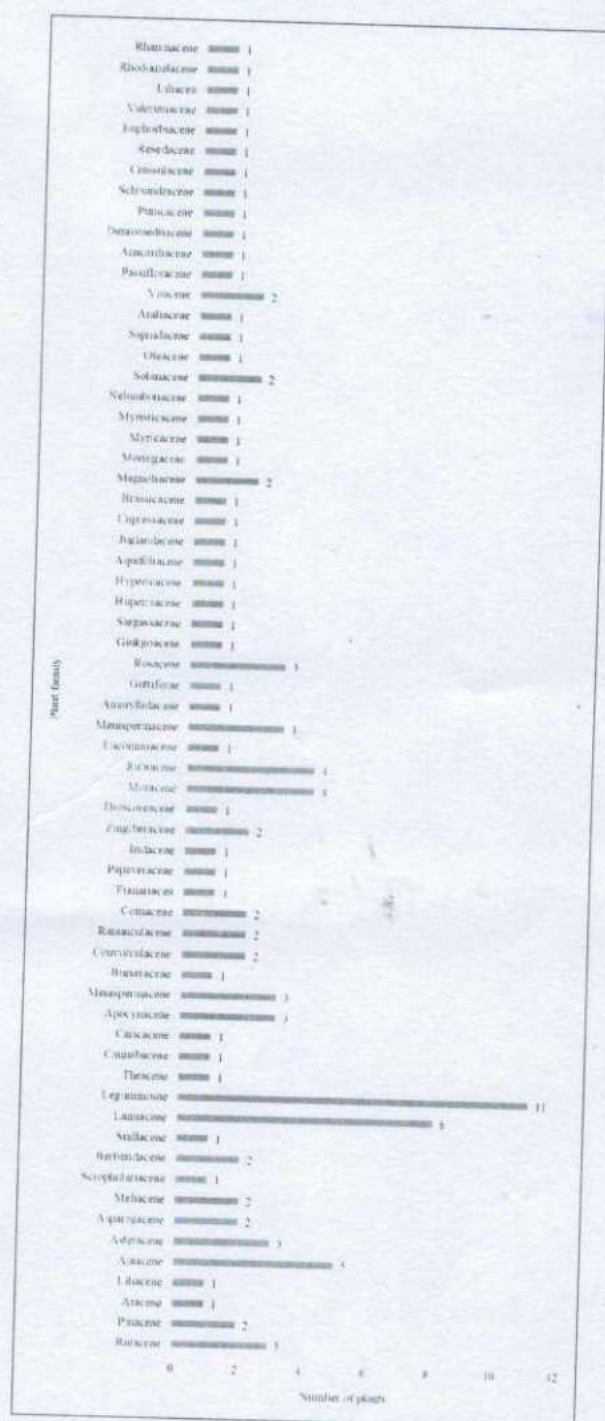
Figure 3. Plants associated with several families having anti-AD action.

are the most explored phytochemical class in evaluating anti-AD potential.

Clinical studies

Clinical trials have been conducted recently to assess their therapeutic efficacy and potential side effects. Nicotine
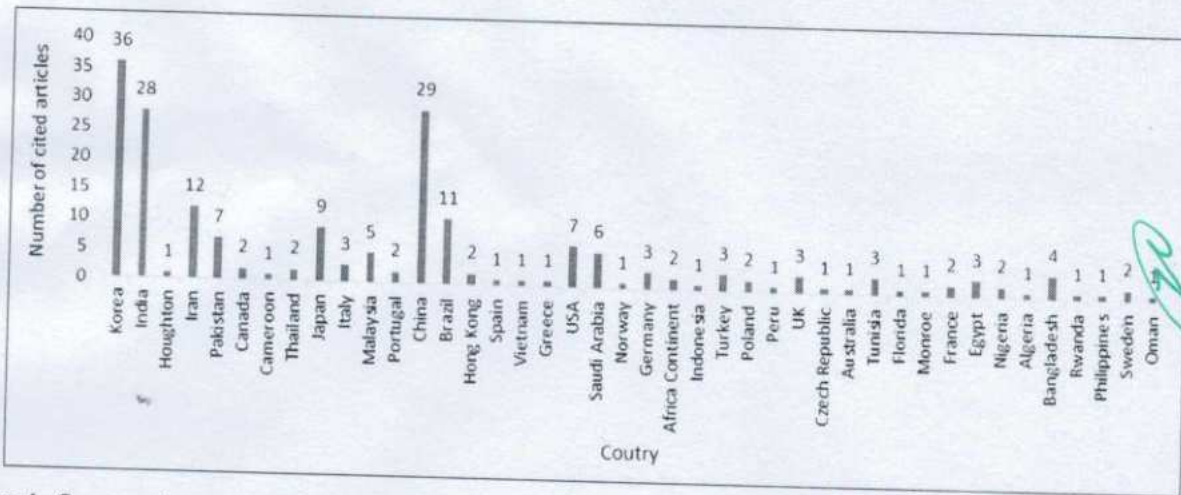
Figure 4. Country-wise research trends.
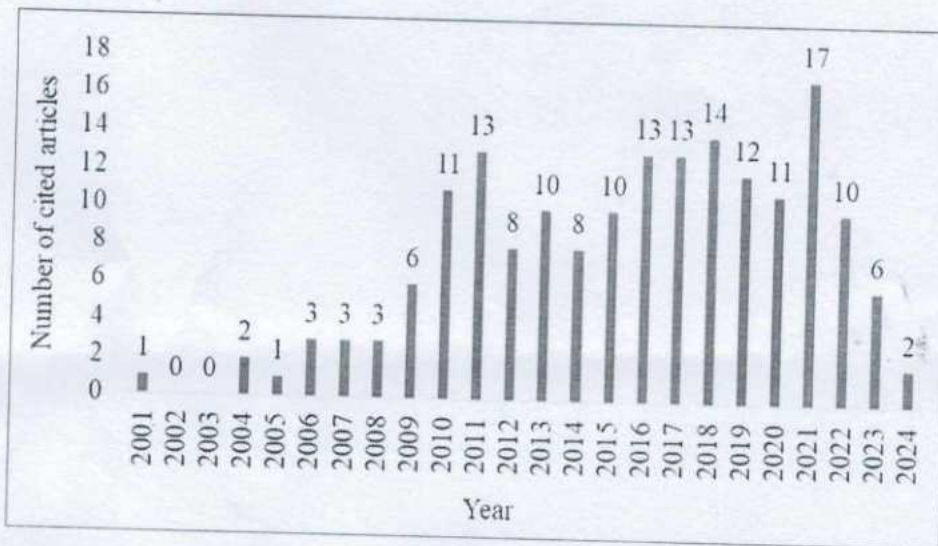
Figure 5. Year-wise research was done to estimate trends of natural anti-AD agents.
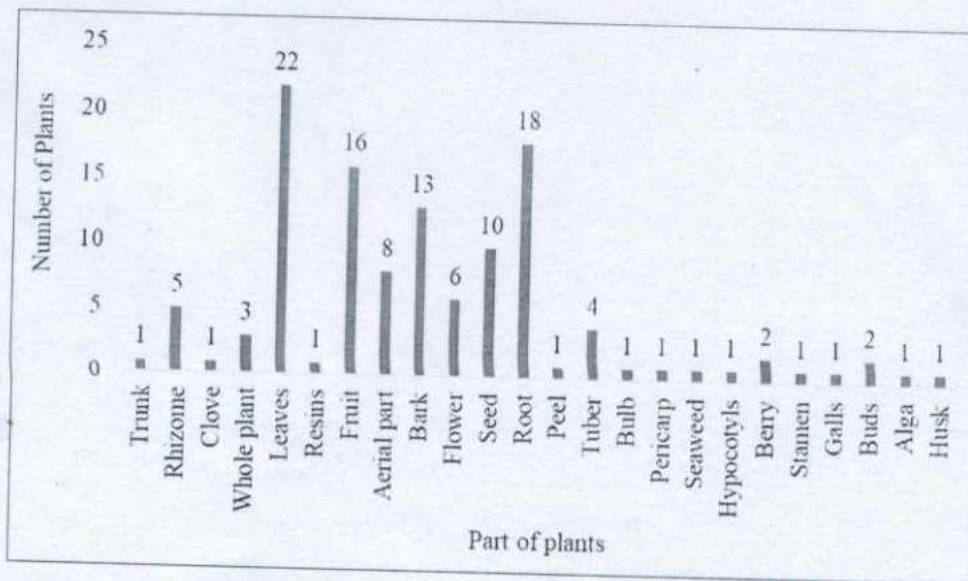
Figure 6. Different parts of the plants have anti-AD activity.
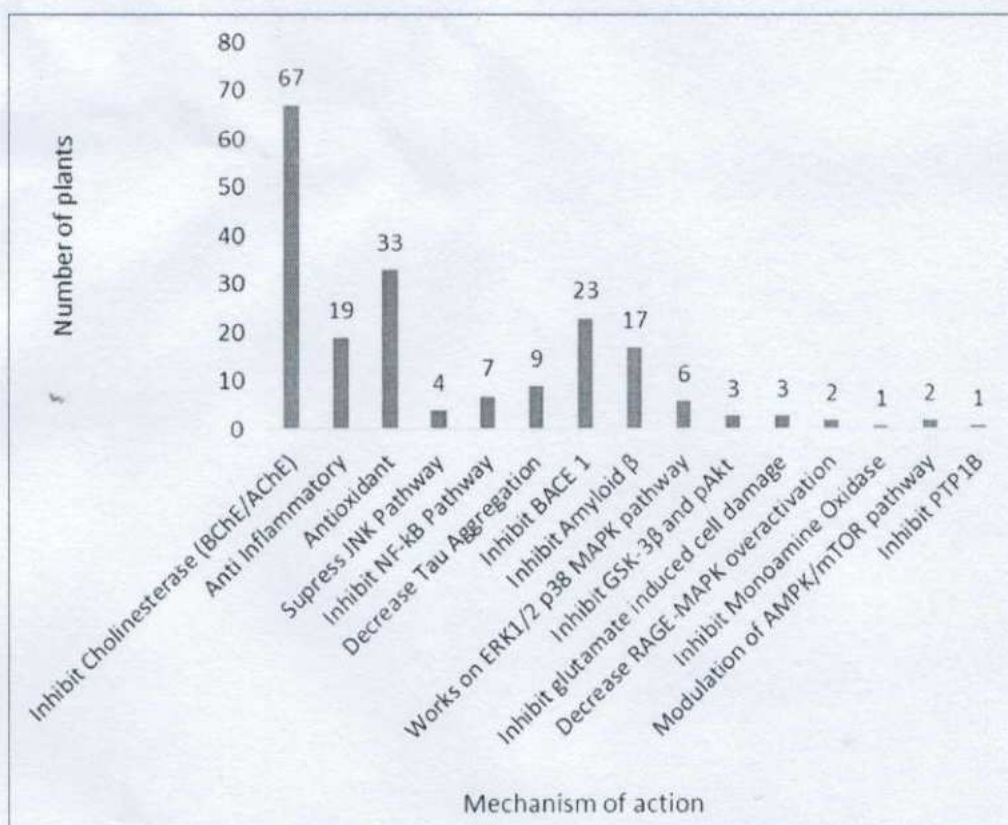
Figure 7. Graphical representation of different modes of action shown by various natural anti-AD phytochemicals.
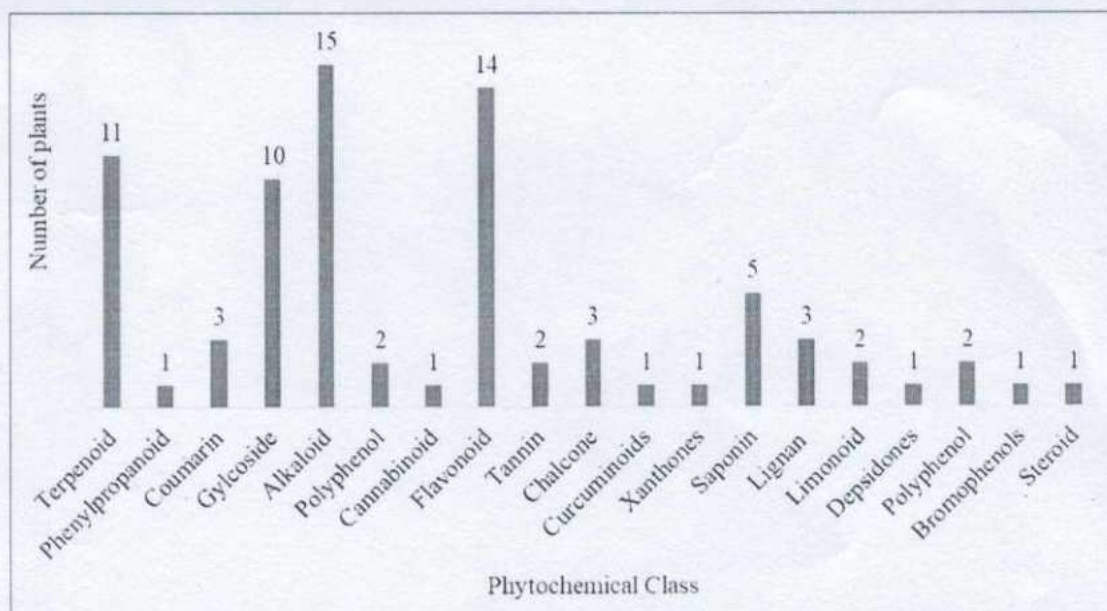
Figure 8. The different phytochemical classes responsible for anti-AD activity.

was the first natural product studied in a clinical trial study in 1992. Several other compounds, such as vitamins, were studied in clinical trials for AD therapy during the 1990s.[185] The use of natural products in clinical trials has recently gained popularity. Through a webinar in 2017, the National Centre for Complementary and Integrative

56
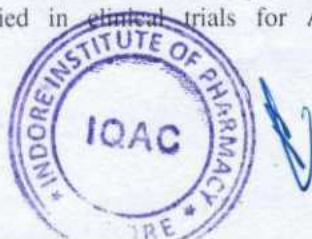
Table 2. Natural products that were used in the clinical trial studies for AD.

S. no.	Natural Products	Condition of Participants	Dose	Route of administration	Number of subjects	Duration	Outcomes	References
1.	Curcumin	AD	1–4 gm/day	Oral	34	Six months	Safer and well-tolerated	[187]
2.	Nicotine	AD	5–10 mg/day	Transdermal	8	Ten weeks	Enhancement of attentional performance	[188]
			0.4–0.8 mg/day	Subcutaneous	70	Two weeks	Enhancement of visual and perceptual attentional deficits	[189]
3.	Resveratrol	Mild to moderate AD	500–1000 mg/ twice a day	Oral	119	52 weeks	Side effects, no effectiveness in the reduction of biomarker levels	[190]
4.	Saffron	Mild to moderate AD	30 mg/day	Oral	46	16 weeks	Safe, improvement of memory and cognitive functions	[191]
5.	Blueberry	Early memory failures	Not mentioned	Oral	9	12 weeks	Reduction of depressive symptoms and enhancement of learning	[192]
6.	Huperzine A	Mild to moderate AD	200–400 μg BID/day	Not mentioned	177	16 weeks	Safer and well-tolerated, improvement of cognitive functions	[193]
		AD	50–100 mg/day	Oral	60	60 days	Safer and well-tolerated, reduction of oxidative stress	[194]
7.	Ginkgo biloba	Mild cognitive impairment	240 mg/day	Oral	160	24 weeks	Safer and well-tolerated, improvement of cognitive functions	[195]
		Mild to moderate dementia	240 mg/day	Oral	410	24 weeks	Safe, improvement of neuropsychiatric symptoms	[196]
		AD or vascular dementia	240 mg/day	Oral	404	24 weeks	Improvement of cognitive functions and functional abilities, improvement of neuropsychiatric symptoms	[197]

Health (NCCIH) announced new funding opportunities for natural product clinical trials.[186]

A detailed report of clinical trial studies on natural products used to treat AD is described in Table 2.

Conclusion

AD is expanding at a frightening rate worldwide in old age people. AD and its comorbidities are generally lethal if not treated. Thus, to effectively manage and treat AD, numerous countries focus on research and development activities. Natural anti-Alzheimer's agents derived from plants might be promising alternatives to synthetic drugs in managing and treating AD. These plant-derived compounds have shown potential for improving cognitive function and slowing down the progression of the disease. However, it is essential to ensure the safety and efficacy of these phytoconstituents through rigorous toxicological studies and clinical trials. Additionally, further research is needed to elucidate the molecular mechanisms underlying the anti-Alzheimer's activity of these natural compounds,

allowing for the development of more targeted and effective therapies. The exploration of plant-derived compounds in AD treatment will continue to be an area of significant interest and focus of future research, with the ultimate goal of providing improved care and management options for individuals affected by AD.

ORCID iDs

Sanjay Sharma https://orcid.org/0000-0003-3662-4635
Rajeev K Singla https://orcid.org/0000-0002-3353-7897

Statements and declarations

Author contributions

Kalpesh Mahajan (Data curation; Formal analysis; Investigation; Visualization; Writing – original draft); Sanjay Sharma (Conceptualization; Formal analysis; Project administration; Supervision; Validation; Writing – review & editing); Rupesh K

Gautam (Conceptualization; Formal analysis; Project administration; Supervision; Writing – review & editing); Rajat Goyal (Data curation; Formal analysis; Investigation; Visualization; Writing – original draft); Dinesh Kumar Mishra (Formal analysis; Validation; Writing – review & editing); Rajeev K Singla (Conceptualization; Formal analysis; Project administration; Supervision; Writing – review & editing).

Declaration of conflicting interests

The authors declared no potential conflicts of interest with respect to the research, authorship, and/or publication of this article.

References

1. Goyal R, Mittal P, Gautam RK, et al. Natural products in the management of neurodegenerative diseases. *Nutr Metab* 2024; 21: 26.
2. Goyal R, Wilson K, Saharan A, et al. Insights on aspects of apoptosis in neurodegenerative disorders: a comprehensive review. *Explor Med* 2024; 5: 89–100.
3. Migliore L and Coppedè F. Genetics, environmental factors and the emerging role of epigenetics in neurodegenerative diseases. *Mutat Res* 2009; 667: 82–97.
4. Onyango IG, Jauregui GV, Čarná M, et al. Neuroinflammation in Alzheimer's disease. *Biomedicines* 2021; 9: 524.
5. Gregory J, Vengalasetti YV, Bredesen DE, et al. Neuroprotective herbs for the management of Alzheimer's disease. *Biomolecules* 2021; 11: 543.
6. Anwal L, Chandakavate S, Lalitha S, et al. A comprehensive review on Alzheimer's disease. *World J Pharm Pharm Sci* 2021; 10: 1170.
7. Pandey J. Flavonoid-based derivatives for modulating various targets of Alzheimer's disease. In: A Sharma and GP Modi (eds) *Natural product-based synthetic drug molecules in Alzheimer's disease*. Singapore: Springer, 2023, pp.267–315.
8. Wang J-H, Wu Y-J, Tee BL, et al. Medical comorbidity in Alzheimer's disease: a nested case-control study. *J Alzheimers Dis* 2018; 63: 773–781.
9. Noori T, Dehpour AR, Sureda A, et al. Role of natural products for the treatment of Alzheimer's disease. *Eur J Pharmacol* 2021; 898: 173974.
10. Wang Z-Y, Liu J-G, Li H, et al. Pharmacological effects of active components of Chinese herbal medicine in the treatment of Alzheimer's disease: a review. *Am J Chin Med* 2016; 44: 1525–1541.
11. Wu T-Y, Chen C-P and Jinn T-R. Traditional Chinese medicines and Alzheimer's disease. *Taiwan J Obstet Gynecol* 2011; 50: 131–135.
12. Qiu C, Kivipelto M and von Strauss E. Epidemiology of Alzheimer's disease: occurrence, determinants, and strategies toward intervention. *Dialog Clin Neurosci* 2022; 11: 111–128.
13. Zhang XX, Tian Y, Wang ZT, et al. The epidemiology of Alzheimer's disease modifiable risk factors and prevention. *J Prev Alzheimers Dis* 2021; 8: 313–321.
14. Imbimbo BP, Lombard J and Pomara N. Pathophysiology of Alzheimer's disease. *Neuroimaging Clin N Am* 2005; 15: 727–753.
15. Guo T, Zhang D, Zeng Y, et al. Molecular and cellular mechanisms underlying the pathogenesis of Alzheimer's disease. *Mol Neurodegener* 2020; 15: 40.
16. Kumar Thakur A, Kamboj P, Goswami K, et al. Pathophysiology and management of Alzheimer's disease: an overview. *J Anal Pharm Res* 2018; 9: 226–235.
17. Heneka MT, Carson MJ, Khoury JE, et al. Neuroinflammation in Alzheimer's disease. *Lancet Neurol* 2015; 14: 388–405.
18. Wong-Guerra M, Calfio C, Maccioni RB, et al. Revisiting the neuroinflammation hypothesis in Alzheimer's disease: a focus on the druggability of current targets. *Front Pharmacol* 2023; 14: 1161850.
19. Subedi L and Yumnam S. Terpenoids from Abies holophylla attenuate LPS-induced neuroinflammation in microglial cells by suppressing the JNK-related signaling pathway. *Int J Mol Sci* 2021; 22: 965.
20. Shal B, Ding W, Ali H, et al. Anti-neuroinflammatory potential of natural products in attenuation of Alzheimer's disease. *Front Pharmacol* 2018; 9: 548.
21. Mukherjee P, Kumar V, Mal M, et al. In vitro acetylcholinesterase inhibitory activity of the essential oil from Acorus calamus and its main constituents. *Planta Med* 2007; 73: 283–285.
22. Mikami M, Takuya O, Yoshino Y, et al. Acorus calamus extract and its component α-asarone attenuate murine hippocampal neuronal cell death induced by l-glutamate and tunicamycin. *Biosci Biotechnol Biochem* 2021; 85: 493–501.
23. Ghajarbeygi P, Hajhoseini A, Hosseini M-S, et al. An in vitro and in vivo cholinesterase inhibitory activity of Pistacia khinjuk and Allium sativum essential oils. *J Pharmacopunct* 2019; 22: 231–238.
24. Saini N, Kadian M, Khera A, et al. Therapeutic potential of Allium Sativum against the abeta((1–40))-induced oxidative stress and mitochondrial dysfunction in the Wistar rats. *Am J Neurodegener Dis* 2021; 10: 13–27.
25. Ali M, Seong S, Reddy M, et al. Kinetics and molecular docking studies of 6-formyl umbelliferone isolated from Angelica decursiva as an inhibitor of cholinesterase and BACE1. *Molecules* 2017; 22: 1604.
26. Ali MY, Seong SH, Jannat S, et al. Ethnobotany, phytochemistry, and pharmacology of Angelica decursiva Fr. et Sav. *Nat Prod Sci* 2019; 25: 181–199.
27. Chougouo RDK, Nguekeu YMM, Dzoyem JP, et al. Anti-inflammatory and acetylcholinesterase activity of extract, fractions and five compounds isolated from the leaves and twigs of Artemisia annua growing in Cameroon. *Springerplus* 2016; 5: 1525.
28. Zhou W-S, Silva M, Yang C, et al. Mechanism and molecular targets of a water-soluble extract of Artemisia annua on the treatment of Alzheimer's disease based on network

pharmacology and experimental validation. *Am J Chin Med* 2023; 51: 595–622.

29. Bagheri SM and Dashti-R MH. Influence of Asafoetida on prevention and treatment of memory impairment induced by d-Galactose and NaNO2 in mice. *Am J Alzheimers Dis Other Demen* 2015; 30: 607–612.

30. Bagheri SM, Allahtavakoli M and Moradi A. Acetylcholinesterase inhibitory activity of Ferula plants and their potential for treatment of Alzheimer's disease. *J Complement Integr Med.* DOI: 10.1515/jcim-2022-0284

31. Gorantla NV, Das R, Mulani FA, et al. Neem derivatives inhibits tau aggregation. *J Alzheimers Dis Rep* 2019; 3: 169–178.

32. Sandhir R, Khurana M and Singhal NK. Potential benefits of phytochemicals from Azadirachta indica against neurological disorders. *Neurochem Int* 2021; 146: 105023.

33. Uabundit N, Wattanathorn J, Mucimapura S, et al. Cognitive enhancement and neuroprotective effects of Bacopa monnieri in Alzheimer's disease model. *J Ethnopharmacol* 2010; 127: 26–31.

34. Habtemariam S. The therapeutic potential of Berberis darwinii stem-bark: quantification of berberine and in vitro evidence for Alzheimer's disease therapy. *Nat Prod Commun* 2011; 6: 1089–1090.

35. Yatsu G, Kino Y, Sasaki H, et al. Meroterpenoids with BACE1 inhibitory activity from the fruiting body of Boletinus asiaticus. *J Nat Prod* 2019; 82: 1797–1801.

36. Ramesh BN, Indi SS and Rao KSJ. Anti-amyloidogenic property of leaf aqueous extract of Caesalpinia crista. *Neurosci Lett* 2010; 475: 110–114.

37. Jo M-R, Park M-H, Choi D-Y, et al. Neuroprotective effect of L-theanine on Aβ-induced neurotoxicity through antioxidative mechanisms in SK-N-SH and SK-N-MC cells. *Biomol Ther (Seoul)* 2011; 19: 288–295.

38. Vishnoi H, Bodla R, Kant R, et al. Green tea (Camellia Sinensis) and its antioxidant property: a review article. *Int J Pharm Sci Res* 2018; 9: 1723.

39. Iuvone T, Esposito G, Esposito R, et al. Neuroprotective effect of cannabidiol, a non-psychoactive component from Cannabis sativa, on β-amyloid-induced toxicity in PC12 cells. *J Neurochem* 2004; 89: 134–141.

40. Karimi I, Yousofvand N and Hussein BA. In vitro cholinesterase inhibitory action of Cannabis sativa L. Cannabaceae and in silico study of its selected phytocompounds. *In Silico Pharmacol* 2021; 9: 13.

41. Khaw K-Y, Chear NJY, Maran S, et al. Butyrylcholinesterase inhibitory activity and GC-MS analysis of Carica papaya leaves. *Nat Prod Sci* 2020; 26: 165–170.

42. Jung HA, Ali MY, Jung HJ, et al. Inhibitory activities of major anthraquinones and other constituents from Cassia obtusifolia against β-secretase and cholinesterases. *J Ethnopharmacol* 2016; 191: 152–160.

43. Pereira DM, Ferreres F, Oliveira JMA, et al. Pharmacological effects of Catharanthus roseus root alkaloids in acetylcholinesterase inhibition and cholinergic neurotransmission. *Phytomedicine* 2010; 17: 646–652.

44. Gohil K, Patel J and Gajjar A. Pharmacological review on Centella asiatica: A potential herbal cure-all. *Indian J Pharm Sci* 2010; 72: 546–556.

45. Jeung SK, Yim HJ, Kim HM, et al. Isolation of acetylcholinesterase inhibitors from the flowers of Chrysanthemum indicum Linne. *Food Sci Biotechnol* 2007; 16: 265–269.

46. Wu T, Jiang C, Wang L, et al. 3,5-diarylpyrazole Derivatives obtained by ammonolysis of the total flavonoids from Chrysanthemum indicum extract show potential for the treatment of Alzheimer's disease. *J Nat Prod* 2015; 78: 1593–1599.

47. Malik J, Munjal K and Deshmukh R. Attenuating effect of standardized lyophilized Cinnamomum zeylanicum bark extract against streptozotocin-induced experimental dementia of Alzheimer's type. *J Basic Clin Physiol Pharmacol* 2015; 26: 275–285.

48. Mendes J, Camilo CJ, de Carvalho NKG, et al. In vitro antioxidant and acetylcholinesterase inhibitory properties of the alkaloid fraction of Cissampelos sympodialis Eichler. *S Afr J Bot* 2021; 141: 99–104.

49. Liu C, Hou W, Li S, et al. Extraction and isolation of acetylcholinesterase inhibitors from Citrus limon peel using an in vitro method. *J Sep Sci* 2020; 43: 1531–1543.

50. Ben Hsouna A, Ben Halima N, Smaoui S, et al. Citrus lemon essential oil: chemical composition, antioxidant and antimicrobial activities with its preservative effect against Listeria monocytogenes inoculated in minced beef meat. *Lipids Health Dis* 2017; 16: 146.

51. Dhivya PS, Selvamani P, Latha S, et al. In vitro evaluation of acetylcholinesterase inhibitory and neuroprotective activity in Commiphora species: a comparative study. *Pharmacogn J* 2020; 12: 1223–1231.

52. Bihaqi S, Singh A and Tiwari M. Supplementation of Convolvulus pluricaulis attenuates scopolamine-induced increased tau and amyloid precursor protein (AβPP) expression in rat brain. *Indian J Pharmacol* 2012; 44: 593–598.

53. Hannan MA, Sultana A, Rahman MH, et al. Protective mechanisms of nootropic herb shankhpushpi (Convolvulus pluricaulis) against dementia: network pharmacology and computational approach. *Evid Based Complement Alternat Med* 2022; 2022: 1015310.

54. Jung HA, Min B-S, Yokozawa T, et al. Anti-Alzheimer and antioxidant activities of coptidis rhizoma alkaloids. *Biol Pharm Bull* 2009; 32: 1433–1438.

55. Ye X-w, Wang H-l, Cheng S-q, et al. Network pharmacology-based strategy to investigate the pharmacologic mechanisms of coptidis rhizoma for the treatment of Alzheimer's disease. *Front Aging Neurosci* 2022; 14: 890046.

56. Wang Y, Qin W, Yang Y, et al. A study on the processing technology for Rhizoma coptidis. *BMC Biotechnol* 2022; 22: 3.

57. Das T, Saha SC, Sunita K, et al. Promising botanical-derived monoamine oxidase (MAO) inhibitors:
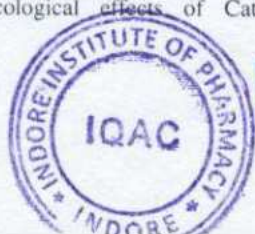
pharmacological aspects and structure-activity studies. *S Afr J Bot* 2022; 146: 127–145.

58. Kim HD, Lee JY, Park J-Y, et al. Neuroprotective effects of Coreopsis lanceolata flower extract against oxidative stress-induced apoptosis in neuronal cells and mice. *Antioxidants* 2021; 10: 951.

59. Asgarpanah J. Phytochemistry, pharmacology and medicinal properties of Coriandrum sativum L. *African J Pharm Pharmacol* 2012; 6: 2340–2345.

60. Youn K and Jun M. Inhibitory effects of key compounds isolated from Corni fructus on BACE1 activity. *Phytother Res* 2012; 26: 1714–1718.

61. Bhakta HK, Park CH, Yokozawa T, et al. Potential anti-cholinesterase and β-site amyloid precursor protein cleaving enzyme 1 inhibitory activities of cornuside and gallotannins from Cornus officinalis fruits. *Arch Pharm Res* 2017; 40: 836–853.

62. Chlebek J, De Simone A, Hošťálková A, et al. Application of BACE1 immobilized enzyme reactor for the characterization of multifunctional alkaloids from Corydalis cava (Fumariaceae) as Alzheimer's disease targets. *Fitoterapia* 2016; 109: 241–247.

63. Hung TM, Thuong PT, Nhan NT, et al. Cholinesterase inhibitory activities of alkaloids from Corydalis tuber. *Nat Prod Sci* 2011; 17: 108–112.

64. Papandreou MA, Kanakis CD, Polissiou MG, et al. Inhibitory activity on amyloid-β aggregation and antioxidant properties of Crocus sativus stigmas extract and its crocin constituents. *J Agric Food Chem* 2006; 54: 8762–8768.

65. Talebi M, Talebi M and Samarghandian S. Association of Crocus sativus with cognitive dysfunctions and Alzheimer's disease: a systematic review. *Biointerface Res Appl Chem* 2020; 11: 7468–7492.

66. Kim D, Li H, Han Y, et al. Modulation of inducible nitric oxide synthase expression in LPS-stimulated BV-2 microglia by prenylated chalcones from Cullen corylifolium (L.) Medik. through inhibition of I-κBα degradation. *Molecules* 2018; 23: 109.

67. Mukhopadhyay CD, Ruidas B and Chaudhury SS. Role of curcumin in treatment of Alzheimer disease. *Int J Neurorehabil* 2017; 4: 1000274.

68. Kim DSHL, Park S-Y and Kim J-Y. Curcuminoids from Curcuma longa L. (Zingiberaceae) that protect PC12 rat pheochromocytoma and normal human umbilical vein endothelial cells from βA(1–42) insult. *Neurosci Lett* 2001; 303: 57–61.

69. Kundu BB, Vanni K, Farheen A, et al. Dioscorea bulbifera L. (Dioscoreaceae): a review of its ethnobotany, pharmacology and conservation needs. *S Afr J Bot* 2021; 140: 365–374.

70. Husain I, Zameer S, Madaan T, et al. Exploring the multifaceted neuroprotective actions of Emblica officinalis (Amla): a review. *Metab Brain Dis* 2019; 34: 957–965.

71. Cardoso-Lopes EM, Maier JA, Silva M, et al. Alkaloids from stems of Esenbeckia leiocarpa Engl. (Rutaceae) as

potential treatment for Alzheimer disease. *Molecules* 2010; 15: 9205–9213.

72. Zhou Y, Liang M, Li W, et al. Protective effects of Eucommia ulmoides Oliv. bark and leaf on amyloid β-induced cytotoxicity. *Environ Toxicol Pharmacol* 2009; 28: 342–349.

73. Tang J-J, Zhao N, Gao Y-Q, et al. Phytosterol profiles and iridoids of the edible Eucommia ulmoides Oliver seeds and their anti-inflammatory potential. *Food Biosci* 2021; 43: 101295.

74. Liu Z, Niu W, Yang X, et al. Effects of combined acupuncture and eugenol on learning-memory ability and antioxidation system of hippocampus in Alzheimer disease rats via olfactory system stimulation. *J Tradit Chin Med* 2013; 33: 399–402.

75. Nisar MF, Khadim M, Rafiq M, et al. Pharmacological properties and health benefits of eugenol: a comprehensive review. *Oxid Med Cell Longev* 2021; 2021: 2497354.

76. Vanaja D and Yellamma K. Molecular docking studies on Evolvulus Alsinoides compounds against tau protein in Alzheimer's disease. *Int J Scic Res* 2012; 3: 21–24.

77. Ahmed F, Manjunath S and Narendra Sharath Chandra JN. Acetylcholine and memory-enhancing activity of Ficus racemosa bark. *Pharmacognosy Res* 2011; 3: 246–249.

78. Pahari N, Majumdar S, Karati D, et al. Exploring the pharmacognostic properties and pharmacological activities of phytocompounds present in Ficus racemosa linn.: a concise review. *Pharmacol Res Modern Chinese Med* 2022; 4: 100137.

79. Paarmann K, Prakash SR, Krohn M, et al. French Maritime pine bark treatment decelerates plaque development and improves spatial memory in Alzheimer's disease mice. *Phytomedicine* 2019; 57: 39–48.

80. Maimoona A, Naeem I, Saddiqe Z, et al. A review on biological, nutraceutical and clinical aspects of French maritime pine bark extract. *J Ethnopharmacol* 2011; 133: 261–277.

81. Sibanyoni MN, Chaudhary SK, Chen W, et al. Isolation, in vitro evaluation and molecular docking of acetylcholinesterase inhibitors from South African Amaryllidaceae. *Fitoterapia* 2020; 146: 104650.

82. Wang SN, Li Q, Jing MH, et al. Natural xanthones from Garcinia mangostana with multifunctional activities for the therapy of Alzheimer's disease. *Neurochem Res* 2016; 41: 1806–1817.

83. Muniroh M, Nindita Y, Karlowee V, et al. Effect of Garcinia mangostana pericarp extract on glial NF-κB levels and expression of serum inflammation markers in an obese-type 2 diabetes mellitus animal model. *Biomed Rep* 2021; 15: 63.

84. Zhao C, Zhang H, Li H, et al. Geniposide ameliorates cognitive deficits by attenuating the cholinergic defect and amyloidosis in middle-aged Alzheimer model mice. *Neuropharmacology* 2017; 116: 18–29.

85. Phatak RS. Phytochemistry, pharmacological activities and intellectual property landscape of Gardenia jasminoides Ellis: a review. *Pharmacognosy J* 2015; 7: 254–265.

86. Shi C, Liu J, Wu F, et al. Ginkgo biloba extract in Alzheimer's disease: from action mechanisms to medical practice. *Int J Mol Sci* 2010; 11: 107–123.

87. Bader BM, Jügelt K, Schultz L, et al. Ginkgo biloba L. (Ginkgoaceae) leaf extract medications from different providers exhibit differential functional effects on mouse frontal cortex neuronal networks. *Front Pharmacol* 2018; 9: 848.

88. Ahmad A, Hayat I, Arif S, et al. Mechanisms involved in the therapeutic effects of soybean (Glycine Max). *Int J Food Prop* 2014; 17: 1332–1354.

89. Mandegary A, Sharififar F, Sheibani V, et al. Ameliorating effect of standardized extract from textured soy protein (Glycine max L.) on memory deficit and learning insufficiency in scopolamine-induced amnesia. *Basic Clin Neurosci J* 2022; 13: 501–510.

90. Cui Y-M, Ao M-Z, Li W, et al. Effect of glabridin from Glycyrrhiza glabra on learning and memory in mice. *Planta Med* 2008; 74: 377–380.

91. Pei H, He L, Shi M, et al. PI3K-Akt Signaling pathway based on network pharmacology for the anti-Alzheimer's disease effect of licorice stem flavonoids. *Aging* 2023; 15: 3381–3393.

92. Wagle A, Seong SH, Zhao BT, et al. Comparative study of selective in vitro and in silico BACE1 inhibitory potential of glycyrrhizin together with its metabolites, 18α- and 18β-glycyrrhetinic acid, isolated from Hizikia fusiformis. *Arch Pharm Res* 2018; 41: 409–418.

93. Ma X and Gang DR. In vitro production of huperzine A, a promising drug candidate for Alzheimer's disease. *Phytochemistry* 2008; 69: 2022–2028.

94. Wu Q and Gu Y. Quantification of huperzine A in Huperzia serrata by HPLC-UV and identification of the major constituents in its alkaloid extracts by HPLC-DAD-MS-MS. *J Pharm Biomed Anal* 2006; 40: 993–998.

95. Altun ML, Yılmaz BS, Orhan IE, et al. Assessment of cholinesterase and tyrosinase inhibitory and antioxidant effects of Hypericum perforatum L. (St. John's wort). *Ind Crops Prod* 2013; 43: 87–92.

96. Machado ML, Arantes LP, da Silveira TL, et al. Ilex paraguariensis extract provides increased resistance against oxidative stress and protection against Amyloid beta-induced toxicity compared to caffeine in Caenorhabditis elegans. *Nutr Neurosci* 2019; 24: 697–709.

97. Orhan I, Şenol FS, Kartal M, et al. Cholinesterase inhibitory effects of the extracts and compounds of Maclura pomifera (Rafin.) Schneider. *Food Chem Toxicol* 2009; 47: 1747–1751.

98. Jung HJ, Jung HA, Min B-S, et al. Anticholinesterase and β-site amyloid precursor protein cleaving enzyme 1 inhibitory compounds from the heartwood of Juniperus chinensis. *Chem Pharm Bull* 2015; 63: 955–960.

99. Prusinowska R and Śmigielski KB. Composition, biological properties and therapeutic effects of lavender (Lavandula angustifolia L). A review. *Herba Polonica* 2014; 60: 56–66.

100. Rubio J, Qiong W, Liu X, et al. Aqueous extract of black Maca (Lepidium meyenii) on memory impairment induced by ovariectomy in mice. *Evide Based Complement Alternat Med* 2011; 2011: 253958.

101. Choi S-I, Go J, Kim J-E, et al. Precautionary effects of RedLiriope platyphyllaon NGF secretion and Aβ42 deposition under the preclinical stage of Alzheimer's disease in Tg2576 mice. *Lab Anim Res* 2013; 29: 212–220.

102. Park HR, Lee H, Park H, et al. Neuroprotective effects of Liriope platyphylla extract against hydrogen peroxide-induced cytotoxicity in human neuroblastoma SH-SY5Y cells. *BMC Complement Altern Med* 2015; 15: 171.

103. Orhan IE, Suntar IP and Akkol EK. In vitroneuroprotective effects of the leaf and fruit extracts ofJuglans regiaL. (walnut) through enzymes linked to Alzheimer's disease and antioxidant activity. *Int J Food Sci Nutr* 2011; 62: 781–786.

104. Eric WCC, Wong S-K and Hung TC. A short review on the chemistry, pharmacological properties and patents of obovatol and obovatal (Neolignans) from Magnolia obovata. *Nat Prod Sci* 2021; 27: 141–150.

105. Lee YJ, Choi DY, Han SB, et al. Inhibitory effect of ethanol extract of Magnolia officinalis on memory impairment and amyloidogenesis in a transgenic mouse model of Alzheimer's disease via regulating β-secretase activity. *Phytother Res* 2012; 26: 1884–1892.

106. Lee JW, Lee YK, Lee BJ, et al. Inhibitory effect of ethanol extract of Magnolia officinalis and 4-O-methylhonokiol on memory impairment and neuronal toxicity induced by beta-amyloid. *Pharmacol Biochem Behav* 2010; 95: 31–40.

107. Zhu S, Liu F, Zhang R, et al. Neuroprotective potency of neolignans in Magnolia officinalis cortex against brain disorders. *Front Pharmacol* 2022; 13: 857449.

108. Tao L, Zhang F, Hao L, et al. 1-O-Tigloyl-1-O-deacetyl-nimbolinin B inhibits LPS-stimulated inflammatory responses by suppressing NF-κB and JNK activation in microglia cells. *J Pharmacol Sci* 2014; 125: 364–374.

109. Shakeri A, Sahebkar A and Javadi B. Melissa officinalis L. – A review of its traditional uses, phytochemistry and pharmacology. *J Ethnopharmacol* 2016; 188: 204–228.

110. Lee Y, Bang H, Oh J, et al. Bioassay-guided isolated compounds from Morinda officinalis inhibit Alzheimer's disease pathologies. *Molecules* 2017; 22: 1638.

111. Singh AK, Rana HK, Tshabalala T, et al. Phytochemical, nutraceutical and pharmacological attributes of a functional crop Moringa oleifera Lam: an overview. *S Afr J Bot* 2020; 129: 209–220.

112. Kuk EB, Jo AR, Oh SI, et al. Anti-Alzheimer's disease activity of compounds from the root bark of Morus alba L. *Arch Pharm Res* 2017; 40: 338–349.

113. Rebai O, Belkhir M, Fattouch S, et al. Phytochemicals from mulberry extract (Morus sp.): antioxidant and neuroprotective potentials. *J Appl Pharm Sci* 2017; 7: 217–222.

114. Mani V, Ramasamy K, Ahmad A, et al. Protective effects of total alkaloidal extract from Murraya koenigii leaves on experimentally induced dementia. *Food Chem Toxicol* 2012; 50: 1036–1044.

115. Tan MA, Sharma N and An SSA. Multi-target approach of Murraya koenigii leaves in treating neurodegenerative diseases. *Pharmaceuticals* 2022; 15: 188.

116. Jones JR, Lebar MD, Jinwal UK, et al. The diarylheptanoid (+)-aR,11S-myricanol and two flavones from bayberry (Myrica cerifera) destabilize the microtubule-associated protein tau. *J Nat Prod* 2010; 74: 38–44.

117. Cuong TD, Hung TM, Han HY, et al. Potent acetylcholinesterase inhibitory compounds from Myristica fragrans. *Nat Prod Commun* 2014; 9: 499–502.

118. Jung HA, Jung YJ, Hyun SK, et al. Selective cholinesterase inhibitory activities of a new monoterpene diglycoside and other constituents from Nelumbo nucifera stamens. *Biol Pharm Bull* 2010; 33: 267–272.

119. Paris D, Beaulieu-Abdelahad D, Bachmeier C, et al. Anatabine lowers Alzheimer's Aβ production in vitro and in vivo. *Eur J Pharmacol* 2011; 670: 384–391.

120. Holscher C, Verma M, Beaulieu-Abdelahad D, et al. Chronic anatabine treatment reduces Alzheimer's disease (AD)-like pathology and improves socio-behavioral deficits in a transgenic mouse model of AD. *PLoS One* 2015; 10: e0128224.

121. Mali RR and Rawat A. Phytochemical properties and pharmcological activities of Nicotiana tabacum: a review. *Indian J Pharm Biol Res* 2013; 1: 74–82.

122. Giridharan VV, Thandavarayan RA, Mani V, et al. Ocimum sanctum Linn. leaf extracts inhibit acetylcholinesterase and improve cognition in rats with experimentally induced dementia. *J Med Food* 2011; 14: 912–919.

123. Kushwah S, Maurya NS, Kushwaha S, et al. Herbal therapeutics for Alzheimer's disease: ancient Indian medicine system from the modern viewpoint. *Curr Neuropharmacol* 2023; 21: 764–776.

124. Abuznait AH, Qosa H, Busnena BA, et al. Olive-oil-derived oleocanthal enhances β-amyloid clearance as a potential neuroprotective mechanism against Alzheimer's disease: in vitro and in vivo studies. *ACS Chem Neurosci* 2013; 4: 973–982.

125. Otero DM, Lorini A, Oliveira FM, et al. Leaves of Olea europaea L. as a source of oleuropein: characteristics and biological aspects. *Res Soc Dev* 2021; 10: e185101321130.

126. Manayi A, Omidpanah S, Barreca D, et al. Neuroprotective effects of paeoniflorin in neurodegenerative diseases of the central nervous system. *Phytochem Rev* 2017; 16: 1173–1181.

127. Xu F, Wang C, Yang L, et al. C-dideoxyhexosyl flavones from the stems and leaves of Passiflora edulis Sims. *Food Chem* 2013; 136: 94–99.

128. Rudnicki M, de Oliveira MR, Veiga Pereira T, et al. Antioxidant and antiglycation properties of Passiflora alata and Passiflora edulis extracts. *Food Chem* 2007; 100: 719–724.

129. Wasef L, Shaheen H, Beshbishy AM, et al. Physostigmine: a plant alkaloid isolated from Physostigma venenosum: a review on pharmacokinetics, pharmacological and toxicological activities. *J Drug Deliv Ther* 2020; 10: 187–190.

130. Konrath EL, Passos C, Klein-Júnior LC, et al. Alkaloids as a source of potential anticholinesterase inhibitors for the treatment of Alzheimer's disease. *J Pharm Pharmacol* 2013; 65: 1701–1725.

131. Lee SY, Moon E, Kim SY, et al. Quinic acid derivatives from Pimpinella brachycarpa exert anti-neuroinflammatory activity in lipopolysaccharide-induced microglia. *Bioorganic Med Chem Lett* 2013; 23: 2140–2144.

132. Benamar H, Marouf A and Bennaceur M. Phytochemical composition, antioxidant and acetylcholinesterase inhibitory activities of aqueous extract and fractions of Pistacia atlantica subsp. atlantica from Algeria. *J Herbs Spices Med Plants* 2018; 24: 229–244.

133. Rauf A, Uddin G, Khan A, et al. Pistagremic acid, a novel β-secretase enzyme (BACE1) inhibitor from Pistacia integerrima Stewart. *Nat Prod Res* 2015; 29: 1735–1738.

134. Li J, Jiang Z, Li X, et al. Natural therapeutic agents for neurodegenerative diseases from a traditional herbal medicine Pongamia pinnata (L.) Pierre. *Bioorg Med Chem Lett* 2015; 25: 53–58.

135. Choi Y, Yon G, Hong K, et al. In vitro BACE-1 inhibitory phenolic components from the seeds of Psoralea corylifolia. *Planta Med* 2008; 74: 1405–1408.

136. Patel DK. Therapeutic application of bavachalcone in chronic diseases: a concise report on medicinal importance and pharmacological activities. *Curr Chin Sci* 2022; 2: 257–262.

137. Xu Q-X, Hu Y, Li G-Y, et al. Multi-target anti-Alzheimer activities of four prenylated compounds from Psoralea fructus. *Molecules* 2018; 23: 614.

138. Zhou Y-T, Zhu L, Yuan Y, et al. Effects and mechanisms of five psoralea prenylflavonoids on aging-related diseases. *Oxid Med Cell Longev* 2020; 2020: 2128513.

139. Choi Y-H, Choi CW, Kim JK, et al. (−)-Pteroside N and pterosinone, new BACE1 and cholinesterase inhibitors from Pteridium aquilinum. *Phytochem Lett* 2018; 27: 63–68.

140. Kosuru R, Rai U, Prakash S, et al. Promising therapeutic potential of pterostilbene and its mechanistic insight based on preclinical evidence. *Eur J Pharmacol* 2016; 789: 229–243.

141. Vaddi D, Bulle S, Reddyvari H, et al. Therapeutic potential of Pterocarpus santalinus L.: an update. *Pharmacogn Rev* 2016; 10: 43–49.

142. Figueiro M, Pochmann D, Porciuncula LO, et al. Inhibition of ptychopetalum olacoides on acetylcholinesterase isoforms in brain of mice. *Chin Herb Med* 2012; 04: 189–194.
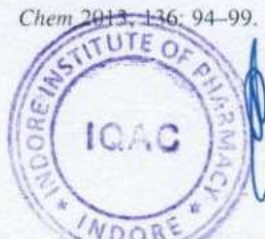
143. Ahmed S, Khan ST, Zargaham MK, et al. Potential therapeutic natural products against Alzheimer's disease with reference of acetylcholinesterase. *Biomed Pharmacother* 2021; 139: 111609.

144. Koirala P, Seong SH, Jung HA, et al. Comparative molecular docking studies of lupeol and lupenone isolated from Pueraria lobata that inhibits BACE1: probable remedies for Alzheimer's disease. *Asian Pac J Trop Med* 2017; 10: 1117–1122.

145. Choi Y-h, Hong SS, Shin YS, et al. Phenolic compounds from Pueraria lobata protect PC12 cells against Aβ-induced toxicity. *Arch Pharm Res* 2010; 33: 1651–1654.

146. Bekir J, Mars M, Souchard JP, et al. Assessment of antioxidant, anti-inflammatory, anti-cholinesterase and cytotoxic activities of pomegranate (Punica granatum) leaves. *Food Chem Toxicol* 2013; 55: 470–475.

147. Kwak H-M, Jeon S-Y, Sohng B-H, et al. β-Secretase (BACE1) inhibitors from pomegranate (Punica granatum) husk. *Arch Pharm Res* 2005; 28: 1328–1332.

148. Block ML, Kim B-W, Koppula S, et al. Regulation of microglia activity by glaucocalyxin-A: attenuation of lipopolysaccharide-stimulated neuroinflammation through NF-κB and p38 MAPK signaling pathways. *PLoS One* 2013; 8: e55792.

149. Owona BA and Schluesener HJ. Molecular insight in the multifunctional effects of oridonin. *Drugs R&D* 2015; 15: 233–244.

150. Fadaeinasab M, Basiri A, Kia Y, et al. New indole alkaloids from the bark of Rauvolfia reflexa and their cholinesterase inhibitory activity. *Cell Physiol Biochem* 2015; 37: 1997–2011.

151. Daily JW, Kang S and Park S. Protection against Alzheimer's disease by luteolin: role of brain glucose regulation, anti-inflammatory activity, and the gut microbiota-liver-brain axis. *Biofactors* 2020; 47: 218–231.

152. Kim SS, Seo JY, Lim SS, et al. Neuroprotective effect of Reseda luteola L. extract in a mouse neuronal cell model. *Food Sci Biotechnol* 2015; 24: 333–339.

153. Chen S-D, Zhang B, Wang Y, et al. Neuroprotective effects of salidroside through PI3K/Akt pathway activation in Alzheimer's disease models. *Drug Design Devel Ther* 2016; 10: 1335–1343.

154. Hillhouse B, Ming DS, French C, et al. Acetylcholine esterase inhibitors in Rhodiola rosea. *Pharm Biol* 2008; 42: 68–72.

155. Awale S, Tohda C, Tezuka Y, et al. [Retracted] protective effects of Rosa damascena and its active constituent on aβ(25–35)-induced neuritic atrophy. *Evid Based Complement Alternat Med* 2011; 2011: 131042.

156. Beigom Hejaziyan L, Hosseini SM, Taravati A, et al. Effect of Rosa damascena extract on rat model Alzheimer's disease: a histopathological, behavioral, enzyme activities, and oxidative stress study. *Evid Based Complement Alternat Med* 2023; 2023: 4926151.

157. Zaiter A, Becker L, Petit J, et al. Antioxidant and antiacetyl-cholinesterase activities of different granulometric classes of Salix alba (L.) bark powders. *Powder Technol* 2016; 301: 649–656.

158. Maistro EL, Terrazzas PM, Perazzo FF, et al. Salix alba (white willow) medicinal plant presents genotoxic effects in human cultured leukocytes. *J Toxicol Environ Health A* 2020; 82: 1223–1234.

159. Liu T, Jin H, Sun Q-R, et al. The neuroprotective effects of tanshinone IIA on β-amyloid-induced toxicity in rat cortical neurons. *Neuropharmacology* 2010; 59: 595–604.

160. Kim DH, Paudel P, Yu T, et al. Characterization of the inhibitory activity of natural tanshinones from Salvia miltiorrhiza roots on protein tyrosine phosphatase 1B. *Chem Biol Interact* 2017; 278: 65–73.

161. Sallam A, Mira A, Ashour A, et al. Acetylcholine esterase inhibitors and melanin synthesis inhibitors from Salvia officinalis. *Phytomedicine* 2016; 23: 1005–1011.

162. Hung TM, Na M, Min BS, et al. Acetylcholinesterase inhibitory effect of lignans isolated fromSchizandra chinensis. *Arch Pharm Res* 2007; 30: 685–690.

163. Han J, Ji Y, Youn K, et al. Baicalein as a potential inhibitor against BACE1 and AChE: mechanistic comprehension through in vitro and computational approaches. *Nutrients* 2019; 11: 2694.

164. Yingrui W, Zheng L, Guoyan L, et al. Research progress of active ingredients of Scutellaria baicalensis in the treatment of type 2 diabetes and its complications. *Biomed Pharmacother* 2022; 148: 112690.

165. Oboh G, Adewuni TM, Ademosun AO, et al. Sorghum stem extract modulates Na+/K+-ATPase, ecto-5′-nucleotidase, and acetylcholinesterase activities. *Comp Clin Pathol* 2016; 25: 749–756.

166. He F-Q, Qiu B-Y, Zhang X-H, et al. Tetrandrine attenuates spatial memory impairment and hippocampal neuroinflammation via inhibiting NF-κB activation in a rat model of Alzheimer's disease induced by amyloid-β(1–42). *Brain Res* 2011; 1384: 89–96.

167. Jiang Y, Liu M, Liu H, et al. A critical review: traditional uses, phytochemistry, pharmacology and toxicology of Stephania tetrandra S. Moore (Fen Fang Ji). *Phytochem Rev* 2020; 19: 449–489.

168. Paudel P, Seong SH, Zhou Y, et al. Anti-Alzheimer's disease activity of bromophenols from a red alga, Symphyocladia latiuscula (Harvey) Yamada. *ACS Omega* 2019; 4: 12259–12270.

169. Nogueira CCR, de Palmer Paixão ICN and Teixeira VL. Antioxidant activity of natural products isolated from red seaweeds. *Nat Prod Commun* 2014; 9: 1031–1036.

170. Athipornchai A, Ketpoo P and Saeeng R. Acetylcholinesterase inhibitor from Tabernaemontana pandacaqui flowers. *Nat Prod Commun* 2020; 15. DOI: 10.1177/1934578X20911488.

171. Govindaraju A, Natarajan S, Rajmohamed M, et al. Antioxidant and cholinesterase inhibitory activities of

ethyl acetate extract of Terminalia chebula: cell-free in vitro and in silico studies. *Pharmacogn Mag* 2017; 13(Suppl 3): S437–S445.

172. Adib M, Islam R, Ahsan M, et al. Cholinesterase inhibitory activity of tinosporide and 8-hydroxytinosporide isolated from Tinospora cordifolia: in vitro and in silico studies targeting management of Alzheimer's disease. *Saudi J Biol Sci* 2021; 28: 3893–3900.

173. Xian Y-F, Lin Z-X, Mao Q-Q, et al. Bioassay-guided isolation of neuroprotective compounds from Uncaria rhynchophylla against beta-amyloid-induced neurotoxicity. *Evid Based Complement Alternat Med* 2012; 2012: 802625.

174. Ndagijimana A, Wang X, Pan G, et al. A review on indole alkaloids isolated from Uncaria rhynchophylla and their pharmacological studies. *Fitoterapia* 2013; 86: 35–47.

175. Frąckowiak T, Bączek T, Kaliszan R, et al. Binding of an oxindole alkaloid from Uncaria tomentosa to amyloid protein (Aβ1-40). *Z Naturforsch C J Biosci* 2006; 61: 821–826.

176. Chen H-W, He X-H, Yuan R, et al. Sesquiterpenes and a monoterpenoid with acetylcholinesterase (AchE) inhibitory activity from Valeriana officinalis var. latiofolia in vitro and in vivo. *Fitoterapia* 2016; 110: 142–149.

177. Arya A, Chahal R, Rao R, et al. Acetylcholinesterase inhibitory potential of various sesquiterpene analogues for Alzheimer's disease therapy. *Biomolecules* 2021; 11: 350.

178. Gomes BAQ, Silva JPB, Romeiro CFR, et al. Neuroprotective mechanisms of resveratrol in Alzheimer's disease: role of SIRT1. *Oxid Med Cell Longev* 2018; 2018: 8152373.

179. Kuboyama T, Tohda C and Komatsu K. Effects of Ashwagandha (roots of Withania somnifera) on neurodegenerative diseases. *Biol Pharm Bull* 2014; 37: 892–897.

180. Sehgal N, Gupta A, Valli RK, et al. Withania somnifera reverses Alzheimer's disease pathology by enhancing low-density lipoprotein receptor-related protein in liver. *Proc Natl Acad Sci U S A* 2012; 109: 3510–3515.

181. Liu P, Zou L-B, Wang L-H, et al. Xanthoceraside attenuates tau hyperphosphorylation and cognitive deficits in intracerebroventricular-streptozotocin injected rats. *Psychopharmacology* 2013; 231: 345–356.

182. Moon M, Kim HG, Choi JG, et al. 6-Shogaol, An active constituent of ginger, attenuates neuroinflammation and cognitive deficits in animal models of dementia. *Biochem Biophys Res Commun* 2014; 449: 8–13.

183. Mathew M and Subramanian S. In vitro evaluation of anti-Alzheimer effects of dry ginger (Zingiber officinale roscoe) extract. *Indian J Exp Biol* 2014; 52: 606–612.

184. Kwon H, Jung IH, Yi JH, et al. The seed of Zizyphus jujuba var. spinosa attenuates Alzheimer's disease-associated hippocampal synaptic deficits through BDNF/TrkB signaling. *Biol Pharm Bull* 2017; 40: 2096–2104.

185. Andrade S, Ramalho MJ, Loureiro JA, et al. Natural compounds for Alzheimer's disease therapy: a systematic review of preclinical and clinical studies. *Int J Mol Sci* 2019; 20: 2313.

186. Pohl F and Kong Thoo Lin P. The potential use of plant natural products and plant extracts with antioxidant properties for the prevention/treatment of neurodegenerative diseases: in vitro, in vivo and clinical trials. *Molecules* 2018; 23: 3283.

187. Baum L, Lam CWK, Cheung SK-K, et al. Six-month randomized, placebo-controlled, double-blind, pilot clinical trial of curcumin in patients with Alzheimer disease. *J Clin Psychopharmacol* 2008; 28: 110–113.

188. White HK and Levin ED. Four-week nicotine skin patch treatment effects on cognitive performance in Alzheimer's disease. *Psychopharmacology* 1999; 143: 158–165.

189. Jones GMM, Sahakian BJ, Levy R, et al. Effects of acute subcutaneous nicotine on attention, information processing and short-term memory in Alzheimer's disease. *Psychopharmacology* 1992; 108: 485–494.

190. Turner RS, Thomas RG, Craft S, et al. A randomized, double-blind, placebo-controlled trial of resveratrol for Alzheimer disease. *Neurology* 2015; 85: 1383–1391.

191. Akhondzadeh S, Shafiee Sabet M, Harirchian MH, et al. A 22-week, multicenter, randomized, double-blind controlled trial of Crocus sativus in the treatment of mild-to-moderate Alzheimer's disease. *Psychopharmacology* 2009; 207: 637–643.

192. Krikorian R, Shidler MD, Nash TA, et al. Blueberry supplementation improves memory in older adults. *J Agric Food Chem* 2010; 58: 3996–4000.

193. Rafii MS, Walsh S, Little JT, et al. A phase II trial of huperzine A in mild to moderate Alzheimer disease. *Neurology* 2011; 76: 1389–1394.

194. Xu SS, Cai ZY, Qu ZW, et al. Huperzine-A in capsules and tablets for treating patients with Alzheimer disease. *Zhongguo Yao Li Xue Bao* 1999; 20: 486–490.

195. Gavrilova SI, Preuss UW, Wong JWM, et al. Efficacy and safety of Ginkgo biloba extract EGb 761® in mild cognitive impairment with neuropsychiatric symptoms: a randomized, placebo-controlled, double-blind, multi-center trial. *Int J Geriatr Psychiatry* 2014; 29: 1087–1095.

196. Hoerr R, Bachinskaya N and Ihl R. Alleviating neuropsychiatric symptoms in dementia: the effects of Ginkgo biloba extract EGb 761. Findings from a randomized controlled trial. *Neuropsychiatr Dis Treat* 2011; 7: 209–215.

197. Ihl R, Tribanek M and Bachinskaya N. Efficacy and tolerability of a once daily formulation of Ginkgo biloba extract EGb 761® in Alzheimer's disease and vascular dementia: results from a randomised controlled trial. *Pharmacopsychiatry* 2011; 45: 41–46.
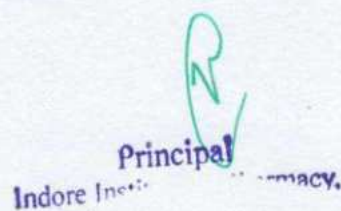
BENTHAM SCIENCE

Current Pharmaceutical Biotechnology

Back   Journal ▼   Subscribe

Review Article

Decoding and Unravelling Mpox, Herpes, and Syphilis Infections: A State of Art Review

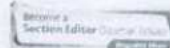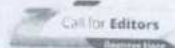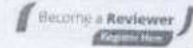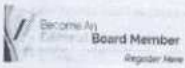In Press, (this is not the final "Version of Record") Available online 19 July, 2024

Author(s): Jiao Wang, Rajat Goyal, Rupesh K. Gautam, Kajal Garg, Shaheen Husain, Hitesh Chopra, Ankit Kumar Dubey, Rehab A. Rayan, Mohammad Amjad Kamal, Dinesh Kumar Mishra, Rohit Gundamaraju, Bairong Shen and Rajeev K. Singla*

Price: $95

Purchase PDF

Become An Editorial Board Member   Become a Reviewer   Call for Editors   Become a Section Editor

Article Metrics

PDF

Note! Please note that this article is currently in the "Article in Press" stage and is not the final "Version of record". While it has been accepted, copy-edited, and formatted, however, it is still undergoing proofreading and corrections by the authors. Therefore, the text may still change before the final publication. Although "Articles in Press" may not have all bibliographic details available, the DOI and the year of online publication can still be used to cite them. The article title, DOI, publication year, and author(s) should all be included in the citation format. Once the final "Version of record" becomes available the "Article in Press" will be replaced by that.

FIND YOUR INSTITUTION

Journal Information

> About Journal

> Editorial Board

> Current Issue

> Volumes /Issues

Abstract

As the world recovers from the COVID-19 pandemic, a resurgence in MPXV cases is causing serious concern. The early clinical similarity of MPXV to common ailments like the flu and cold, coupled with the resemblances of its progressing rash to other infections, underscores the importance of prompt and accurate diagnosis. Among the infections, smallpox is clinically closest to MPXV, and rashes similar to MPXV stages also appear in syphilis and varicella zoster. A comprehensive review of MPXV, herpes, and syphilis was carried out, including structural and morphological features, origins, transmission modes, and computational studies. PubMed literature search on MPXV, using MeSH key terms, yielded 1904 results, with the analysis revealing prominent links to sexually transmitted diseases. More in-depth exploration of MPXV, Herpes Simplex Virus (HSV), and Syphilis revealed further disease interconnections and geographical correlations. These findings emphasize the need for a holistic understanding of these interconnected infectious agents for better control and management.

Keywords: MPXV virus, syphilis, herpes, comparative studies, computational, transmission mode, MPXV.

For Authors

For Editors

For Reviewers

Explore Articles

Open Access

Mark Item   Purchase PDF   Rights & Permissions   Print   Cite

For Visitors

Call for Papers in Thematic Issues

Submission closes on : 31 December, 2025

Artificial Intelligence in Bioinformatics

Submission closes on : 31 December, 2025

Latest Advancements in Biotherapeutics.

Principal
Indore Institute of Pharmacy,
INDORE (M.P.

IQAC

65

Development and Validation of Spectrophotometric Method for Simultaneous Estimation of Atorvastatin Calcium and Telmisartan in Combined Dosage Form

Vaishali Gadekar*[1]; Nimita Manocha[1]; Archana Tiwari[1]; PK Dubey[1]

[1]Swami Vivekanand College of Pharmacy, Indore, M.P., India

ABSTRACT: A simple, reproducible, economical, accurate, and precise UV spectrophotometric method for simultaneous estimation of Atorvastatin Calcium (ATC) and Telmisartan (TEL) in tablet dosage form has been developed. The absorption maxima at 246 nm and 273 nm were used for the estimation of Atorvastatin Calcium and Telmisartan respectively. A calibration curve was plotted over a degree range of 2-20 µg/ml for Atorvastatin Calcium and 1-6 µg/ml for Telmisartan respectively. Recovary was found at 90.14%for ATR and TEL 99.05 % using proposed UV spectrophotometric Telmisartan. The method was validated according to International Conference on Harmonization (ICH) guidelines with respect to linearity, recovery, precision, LOD, and LOQ. The validation study statistically significant as all the statistical parameters are within the acceptance range (%RSD < 2%). The developed method is simple, inexpensive, and accurate

KEYWORDS: UV spectroscopy, Simultaneous Estimation method, Atrovastatin, Telmisartan

INTRODUCTION

Atorvastatin is a dihydroxy monocarboxylic acid that is a member of the drug class known as statins, used primarily for lowering blood cholesterol and for preventing cardiovascular diseases. It has a role as an environmental contaminant and a xenobiotic. It is an aromatic amide, a member of monofluorobenzenes, a statin (synthetic), a dihydroxy monocarboxylic acid and a member of pyrroles. It derives from a heptanoic acid. It is a conjugate acid of an atorvastatin (1))

Principal
Indore Institute of Pharmacy,
INDORE (M.P.)

66

Telmisartan is a member of the class of benzimidazoles used widely in the treatmentof hypertension. It has a role as an antihypertensive agent, an angiotensin receptor antagonist, (peptidyl-dipeptidase A) inhibitor, a xenobiotic and an environmental contaminant. It is a member of biphenyls, a member of benzimidazoles and a carboxybiphenyl.(2)

MATERIAL AND METHOD:

Chemical and reagents

Atrovastatin and Telmisartan standard materials obtainedas gift from cipla pharma.indore. tablets (Telista plus) make Verdant life science . Containing Atrovastatin (10 mg) and telmisartan (40 mg) were purchased from locak market.

Instrumentation

A double beam UV Spectrophotometer using Shimadzu UV-1800 (Shimadzu Corp. Japan). With spectral width of 2 nm quartz cell (1.0cm path) was employed to measure absorbance of solutions. On the basis of solubility study Ethanol was selected as the solvent for dissolving Atrovastatin and Telmisartan .(3)

Preparation of standard stock solution

A. Prepration of standard stock solutions Accurately weighed (10 mg) each of standard Atorvastatin Calcium (10 mg) and Telmisartan (10 mg) were transferred to two separate 100 mL calibrated volumetric flasks (100 mL) dissolved in Ethanol which were further diluted with the Ethanol to obtain standard solutions of Atorvastatin Calcium and Telmisartan (100 µg/mL)(4)

B. Selection of working wavelength

Working standard stock solutions of both the drugs were diluted to obtain final concentration of Atorvastatin Calcium (10 µg/mL) and Telmisartan (10 µg/mL). Solutions were scanned in the wavelength range of 200 - 400 nm. wavelength range of 210 -236, 237-246 nm were selected for the analysis(4)

C. Preparation of calibration curve of Atorvastatin Calcium and Telmisartan

A. calibration curve was plotted over a degree range of 2-20 µg/ml for Atorvastatin Calcium and 1-6 µg/ml for Telmisartan. Accurately measured standard stock solution of Atorvastatin Calcium (2, 4, 8, 12, 16 & 20 ml) and standard stock solution of Telmisartan (1, 2, 3, 4, 5 & 6 ml) were transferred to a separate series of 10 ml of volumetric flasks and diluted to the mark with Ethanol. The absorbance of each solution was measured at the wavelengths 246 nm and 273 nm.Calibration curves were constructed for Atorvastatin Calcium and Telmisartan by plotting absorbance versus concentrations at both wavelengths. (5)

Simultaneous estimation of atorvastatin calcium and telmisartan by simultaneous equation method

Standard Stock solutions of ATR and TEL in the concentration range 1-10 µg/mL and 220µg/ml were made in the water and absorbance of these solutions was measured at 246nm and 273nm. Calibration curves were plotted to confirm the Beer"s law and the absorptivity values calculated at the respective wavelengths for both the drugs. Two simultaneous equations as below were formed using these absorptivity values

A (1%, 1 cm)

$\lambda 1 \ A1 = ax1bCx + ay1bCy$ .... (1)

$\lambda 2A2 = ax2bCx + ay2 \ bCy$ .... (2)

For measurements in 1 cm cells b=1 Rearrange eq. (2) Cy= A2- ax2Cx/ ay2

Substituting for Cy in eq (1) and rearranging

$Cx = A2ay1 - A1 \ ay2 / ax2 \ ay1 - ax1 \ ay2$ .... (3)

$Cy = A1ax2 - A2 \ ax1 / ax2 \ ay1 - ax1 \ ay2$ .... (4)

Where Cx and Cy are the concentration of ATR and TEL, respectively, A1 and A2 are absorbance at 246 nm and 273 nm respectively, ax1 and ax2 are absorptivities of ATR at 246 nm and 273 nm respectively; ay1 and ay2 are absorptivities TEL of at 246 nm and 273 nm

Principal
Indore Institute of Pharmacy,
INDORE (M.P.)

68

respectively. By solving the two simultaneous equations, the concentrations of ATR and TEL in sample solutions were obtained.(6)

Analysis of tablets formulation

Twenty tablets of (Telistaplus 40 tablet) each contained 10mg of ATC and 40 mg Accurately weighed. their average weight determined .they was crushed to fine powder The powder equivalent to 10mg ofamount of drug combination(10 mg ATC+ 40 mg TEL) was weighed and dissolved in 10 mg Of ethanol with the aid of ultrasonication for 5 min. The solution was filtered through Whatman Filter paperno.41 to get sample stock solution . 0.1 ml of this solution was further diluted with 10 ml distilled water to get required concentration in the liner range the absorbance was measured at the selected wavelength for the drug the absorbance of the solution was measured at 246 nm and 273 nm.(7)

Validation of proposed method

The method was validated according to ICH guidelines for validation of analytical procedures in order to determine linearity, sensitivity, accuracy and precision for each analyte

Linearity

The linearity of the method is its ability to elicit test results that are directly proportional to the concentration of the analyte in samples. The calibration curve was taken in the range of 1-6 µg/ml for Telmisartan and 2-20 µg/mL for Atorvastatin Calcium at the respective λmax (8)

Accuracy

10 mg of Atorvastatin Calcium, standard drugs of Atorvastatin calcium and Telmisartan were added at 80%, 100% and 120% levels. This was extracted diluted and reanalyzed as per the formulation procedure. Absorbance was noted at respective wavelength.(8)

Precision

The intraday and interday precisions of the proposed spectrophotometric methods were determined by estimating t he corresponding response 3 times on the same day and on 3 different days over a period of 1 week for 3 different concentrations of TEL (1, 2, 3 µg/mL) and ATR (2, 4, 8 µg/mL) and the results are reported in terms relative standard deviation (RSD)52. The

developed method was found to be precise as the %RSD value for intermediate precision studies(9)

Limit of Detection

It is the lowest amount of analyst in a sample that can be detected but not necessarily quantitated under the stated experimental conditions. Limit of detection can be calculated using following equation as per ICH guidelines(10)

LOD = 3.3 × N/S

Where, N = Standard deviation of the response and S = Slope of the corresponding calibration curve

Limit of quantification

It is the lowest concentration of analyte in a sample that can be determined with the acceptable precision and accuracy under stated experimental conditions. Limit of quantification can be calculated using following equation as per ICH guideline(10)

LOQ = 10 × N/S

Where, N = Standard deviation of the response and S = Slope of the corresponding calibration curve. Slope of the corresponding calibration curve.

RESULTS AND DISCUSSION

In the present study, we have to develop UV-vis spectrophotometric method for the simultaneous estimation of Atrovastatin and Telmisartan in combined dosage form. The developed method was validated as per the ICH guidelines. Linearity was evaluated by analysis of working standard solution of Atorvastatin Calcium and Telmisartan at six different concentrations. TEL found to be linear within conc. range of 1-6 µg/ml with regression coefficient of 0.998 and ATR was found to be linear within conc. range of 2-20 µg/ml with regression coefficient of 0.999 the results of regression The Absorptivity were found approximately same for all the concentrations hence both drugs obeyed Beer Lambert's law in indicated concentration range. The high value of correlation coefficient (R2) also indicates good linearity for both the drugs. The absorbances

Principal
Indore Institute of Pharmacy,
INDORE (M.P.)

70

were measured at the selected wavelengths and absorptivities for both drugs were determined at both wavelengths

Table 1: Absorptivity Values Of ATR and TEL at 246.0 nm and 273.0 nm

Concentration (Mcg/ml)		Absorptivity (246.0nm)		Absorptivity (273.0nm)	
ATR	TEL	ATR	TEL	ATR	TEL
2	1	0.44	0.79	0.051	0.116
4	2	0.043	0.089	0.046	0.115
8	3	0.036	0.108	0.034	0.112
12	4	0.034	0.115	0.03	0.11
16	5	0.033	0.126	0.025	0.112
20	6	0.032	0.133	0.022	0.11
Mean		0.103	0.226	0.034	0.096
SD		Ax1=0.023	Ay1=0.055	Ax2=0.002	Ay2=0.032

Table 2: Analysis of drug formulation

Sr. No	Concentration of Drug taken (equipment weight) mg/ml		Absorbance	
			At Lambda Max	At Lambda Max
			1(246nm)	2 (273nm)
	TEL	ATC	A1	A2
1	40	10	0.079	0.11
2	40	10	0.11	0.112
3	40	10	0.115	0.116

Principal
Indore Institute of Pharmacy,
INDORE (M.P.)

71

IJPSM

Vaishali Gadekar *et al*, International Journal of Pharmaceutical Sciences and Medicine (IJPSM), Vol.9 Issue. 6, June- 2024, pg. 51-60

4	40	10	0.117	0.118
5	40	10	0.12	0.12
Mean			0.115	0.116

PRECISION

The repeatability is expressed as percentage relative standard deviations (% RSD) for the ATR at the concentration of 2, 4 and 8 µg/ml and their average % RSD value were 0.350, 0.168 and 0.286 while for the TEL the concentration of 1,2 and 3 µg/ml and their average % RSD value were 0.387, 0.170 and 0.282.

TABLE 3: Result of intraday precision studies

S.no	Parameters	% Amt. found (Atorvastatin Calcium)			% Amt. found (Telmisartan)		
		2 µg/ml	4 µg/ml	8µg/ml	1µg/ml	2 µg/ml	3 µg/ml
1.	Morning	99.89	99.65	99.48	99.93	99.56	99.35
2.	Afternoon	99.69	99.69	100.05	99.66	99.97	99.98
3.	Evening	99.21	99.21	99.72	99.28	99.22	99.78
4.	Mean	99.59	99.79	99.75	99.48	99.84	99.76
5.	S.D.	0.349	0.168	0.286	0.385	0.170	0.282
6.	% R.S.D.	0.350	0.168	0.286	0.387	0.170	0.282

Accuracy: The accuracy was assessed by the standard addition method of three replicate determinations of three different solutions containing 8, 10 and 12 µg/ml of TEL and ATR. The average % recoveries for three different concentrations were found to be 90.14% for ATR and

57

Principal
Indore Institute of Pharmacy,
INDORE (M.P.)

72

TEL 99.05 % using proposed UV spectrophotometric method. The higher values indicate that the proposed method is accurate for the determination of ATR and TEL in pharmaceutical dosage form

Table 4 Recovery (Accuracy) analysis for Atorvastatin Calcium and Telmisartan

S.no	Recovery Level	Standard Conc. µg/ml	Conc. added µg/ml	Conc. Found	%Recovery	% Mean Recovery
			Atorvastatin Calcium			
1.	80 %	10	8	7.96	99.50	
2.	100%	10	10	9.86	98.60	99.14
3.	120%	10	12	11.92	99.33	
			Telmisartan			
1.	80 %	10	8	7.94	99.25	
2.	100%	10	10	9.90	99.00	99.05
3	120 %	10	12	11.87	98.90	

LOD and LOQ: The limit of detection and limit of quantification were found to be 0.31µg/ml and 0.1023µg/ml for Atorvastatin Calcium and 0.2805µg/ml and 0.85µg/ml for Telmisartan respectively by proposed UV spectrophotometric method. Results of LOD and LOQ are summarized in Table 5 limit of detection (LOD) and limit of quantification (LOQ) of Atorvastatin Calcium and Telmisartan.

S.no	Parameters	Method(Simultaneous estimation method)	
		Atorvastatin Calcium	Telmisartan
1.	LOD(µg/ml)	0.1023	0.2805
2.	LOQ(µg/ml)	0.31	0.85

IQAC

Principal
Indore Institute of Pharmacy,
INDORE (M.P.)
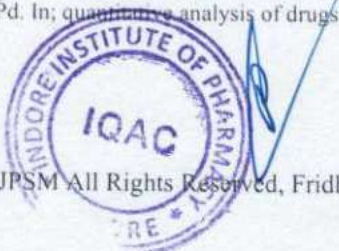
CONCLUSION: The validation procedure followed were as per the ICH guidelines study. The
linearity was achieved with Ethanol solvent, Linearity, Accuracy and precision were satisfactory
and the limit of detection (LOD), limit of quantitation achieved was also satisfactory. Hence we
conclude that the simple, rapid, less-time consuming, cost effective and precise method was
developed and validated by UV-spectroscopy with the simultaneous estimation of Atorvastatin
Calcium & Telmisartan.

REFERENCES

[1]. http://pubchem.ncbi.nlm.nih.gov/compound/Telmisartan

[2]. https://pubchem.ncbi.nlm.nih.gov/compound/Atorvastatin-calcium

[3]. Tomlesh B.deshmukh, Sujata s.deo,farhin s.inam. simultaneous estimation of atrovastatin calcium and telmisartan in tablet dosage form by spectrophotomery

[4]. http://en.wikipedia.org/wiki/Atrovastatin

[5]. http://en.wikipedia.org/wiki/Telmisartan

[6]. S K. masthannamma, ISTejaswini , P saidulu and G Rambabu .simultanious eqution method and absorption corrrection method for the estimation of perindopril Erbumine and Amlodipino Besylate in bulk and in combined tablet dosagr for using uv Spectrometry

[7]. sandip s chaudhari and swapnil d phalak development and validation of uv spectrophotometric method for simultaneous equation of aspirin and omeprazole in tablet dosage form pharmaceuticaanalyticaacta research article - (2020) volume 11, issue 1

[8]. S.K. Rathi S.V. Samantaray and S.C. Dinda Development And Validation Of New Analytical Method For The Estimation Of Atorvastatin Calcium Hydrate Residue By Using Uv Spectrophotometer International Journal of Pharmaceutical Sciences and Research 2013; Vol. 4(9): 3416-3425

[9]. sapan shah, dineshkawade development and validation of a simple uv spectrophotometric method for the determination of antihyperlipidemic drugs both in bulk and marketed dosage formulations international journal of chemical science volume 1; issue 2; november 2017; page no. 32-35

[10]. J.S. Rajawat,P Dadeech,A.D.Ankalgi M.S.Ranawat,MS.Panwar , method development of telmisartan and atrovastatin calcium capsule by using simultaneous equation method and absorbance Ratio method Asian journal of pharmaceutics oct-dec 2014

[11]. http://go.drugbank.com/salts/DBSALT00001

[12]. SethiPd. In; quantitative analysis of drugs in pharmaceutical formulations. Unique publishers, delhi.1999: 5.

Principal
Indore Institute of Pharmacy,
INDORE (M.P.)

74

CONCLUSION: The validation procedure followed were as per the ICH guidelines study. The linearity was achieved with Ethanol solvent, Linearity, Accuracy and precision were satisfactory and the limit of detection (LOD), limit of quantitation achieved was also satisfactory. Hence we conclude that the simple, rapid, less-time consuming, cost effective and precise method was developed and validated by UV-spectroscopy with the simultaneous estimation of Atorvastatin Calcium & Telmisartan.

REFERENCES

[1]. http://pubchem.ncbi.nlm.nih.gov/compound/Telmisartan

[2]. https://pubchem.ncbi.nlm.nih.gov/compound/Atorvastatin-calcium

[3]. Tomlesh B.deshmukh, Sujata s.deo,farhin s.inam. simultaneous estimation of atrovastatin calcium and telmisartan in tablet dosage form by spectrophotomery

[4]. http://en.wikipedia.org/wiki/Atrovastatin

[5]. http://en.wikipedia.org/wiki/Telmisartan

[6]. S K. masthannamma, ISTejaswini , P saidulu and G Rambabu .simultanious eqution method and absorption corrrection method for the estimation of perindopril Erbumine and Amlodipino Besylate in bulk and in combined tablet dosagr for using uv Spectrometry

[7]. sandip s chaudhari and swapnil d phalak development and validation of uv spectrophotometric method for simultaneous equation of aspirin and omeprazole in tablet dosage form pharmaceuticaanalyticaacta research article - (2020) volume 11, issue 1

[8]. S.K. Rathi S.V. Samantaray and S.C. Dinda Development And Validation Of New Analytical Method For The Estimation Of Atorvastatin Calcium Hydrate Residue By Using Uv Spectrophotometer International Journal of Pharmaceutical Sciences and Research 2013; Vol. 4(9): 3416-3425

[9]. sapan shah, dineshkawade development and validation of a simple uv spectrophotometric method for the determination of antihyperlipidemic drugs both in bulk and marketed dosage formulations international journal of chemical science volume 1; issue 2; november 2017; page no. 32-35

[10]. J.S. Rajawat,P Dadeech,A.D.Ankalgi M.S.Ranawat,MS.Panwar , method development of telmisartan and atrovastatin calcium capsule by using simultaneous equation method and absorbance Ratio method Asian journal of pharmaceutics oct-dec 2014

[11]. http://go.drugbank.com/salts/DBSALT00001

[12]. SethiPd. In; quantitative analysis of drugs in pharmaceutical formulations. Unique publishers. delhi.1999; 5[.

Principal
Indore Institute of Pharmacy,
INDORE (M.P.)

[13].Beckett ah and stenlakeJb. In; practical pharmaceutical chemistry. 4thedn, vol.ii, cbs publishers and distributors, new delhi.1988: 284.

[14].Lakshmana Rao A1,*, Prasanthi T2 , Anusha J3 , Prasanna MR4 , Jyothi P Method development and validation for simultaneous determination of Telmisartan and Telmisartan by UV Spectrophotometry Indian Journal of Pharmacy and Pharmacology, October-December 2016;3(4);221-224

[15].Vinitchavhan and minalghante stability indicating uv spectrophotometric method development and validation of simvastatin in bulk and tablet dosage form j app pharm vol. 6; issue 2: 235 -246; april, 2014

[16].Varshabalkrishna mane, surekhaBabar, nitakulkarni. Development of UV spectrophotometric method for the simultaneous estimation of simvastatine and ezetimibe in tablet dosage form by simultaneous equation and absorbance ratio method. International journal of pharmtech research vol.3, no.3, pp 1459-1466, july-sept 2011

[17].Prashnath nallavelli, Sharath,komuwadi veleti.Development and validation for the simultaneous estimation of telmisartan and atrovastatin in bulk and tablet dosage form international journal of applied pharmaceutical sciences and research vol 5 issue January March 2020

[18].Bangaruthalli , Harini u, Divya m, Sushma p. Simultaneous estimation of telmisartan and atrovastatin calcium in API and tablet dosage form. journal of drug delivery and therapeutics 2019(9)175-179

[19].vinit chavhan, Rohini lawande, Jyoti salunke,minal ghate,supriya jagtap. UV spectrophotomeric method development and validation for telmisartan in bulk and tablet dosage form. Asian pharm.cimres,vol6 ,issue 4,2013,19-21

[20].J.S. Rajawat,P Dadeech,A.D.Ankalgi M.S.Ranawat,MS.Panwar , method development of telmisartan and atrovastatin calcium capsule by using simultaneous equation method and absorbance Ratio method Asian journal of pharmaceutics oct-dec 2014

[21].http://go.drugbank.com/salts/DBSALT00001

Principal
Indore Institute of Pharmacy,
INDORE (M.P.)

INDIAN DRUGS

Article Details

PREPARATION AND CHARACTERIZATION OF MICROSPHERES UTILIZING RATE-CONTROLLING MEMBRANES FOR THE MANAGEMENT OF DIABETES MELLITUS

Niti Pandiac, Nadeem A. Farooquib, Darshan Jamwadacd, Dinesh K. Mishrae, Rajat Goyalc, Hitesh Chopratd and Rupesh K. Gautama

a Department of Pharmaceutics, Indore Institute of Pharmacy, IIST Campus, Rau-Indore–453 331, Madhya Pradesh, India.
b Department of Pharmaceutics, Madhyanchal Professional University, Bhopal – 462 044, Madhya Pradesh, India.
c Department of Pharmacy, Guru Ghasedas Vishwavidyalaya, Bilaspur-495 009, Chhattisgarh, India
d MM College of Pharmacy, Maharishi Markandeshwar (Deemed to be University), Mullana-Ambala -133 207, Haryana, India
e Department of Biosciences, Saveetha School of Engineering, Saveetha Institute of Medical and Technical Sciences, Chennai-602 105, Tamil Nadu, India
For Correspondence, E-mail: drrupeshgautam@gmail.com

ABSTRACT

The present research work aimed at the formulation of film-coated microspheres incorporating glibenclamide drug and their evaluation for the management of diabetes mellitus (DM). Microspheres were prepared by solvent evaporation methodology by the usage of ethyl cellulose as polymer, ethanol and dichloromethane as solvents and Tween 80® as a non-ionic surfactant. The film-coated membrane was prepared by pan coating method, incorporating ethyl cellulose, isopropyl alcohol, diethyl phthalate and sodium lauryl sulfate. This film membrane was coated on microspheres with the help of a spray gun. The efficiency of entrapment of the film coated microspheres of F5* batch, among different formulations, is highest and comes out to be in the range of 76.65±0.58. The percentage yield was observed to be 73.32±0.14. Morphological studies conducted by scanning electron microscope show spherical microspheres of uniform size. In vitro drug release study conducted of the coated microspheres of glibenclamide shows the highest amount of release of 97.44% in the F5*batch. The best-fit model was determined by the highest R2 value. Further, the developed formulation helps in reduction in dose dumping, with better patient compliance, and also masks the bitter taste of the drug

DOWNLOAD ARTICLE

Quick Contact

Go

Principal
Indore Institute of Pharmacy,
INDORE (M.P.)

77

Formulation and Evaluation of Polyherbal Capsules for the Treatment of Poly Cystic Ovarian Syndrome (Pcos)

Dr Nimita Manocha[1], Dr Pankaj Agrawal[2], Rahul Singh[3], Dr. Md Sajid Ali[4], Dr. Sandeep Gupta[5], Poonam Arora[6], Dr. Anjali ganjare[7], Dr. M. Vijaya Jyothi[8*]

[1]Principal, Indore Institute of Pharmacy.
[2]Project Director (Center of Excellence in Pharmaceutical Sciences and University School of Medicine and   Allied), Guru Gobind Singh Indraprastha University Govt of NCT of Delhi Sector 16C Dwarka New Delhi 110078
[3]Assistant Professor, Maharana Pratap College Of Pharmacy, Kanpur UP
[4]Assistant Professor, Department of pharmaceutics, College of Pharmacy, Jazan University, Jazan, Kingdom of Saudi Arabia, Postal code- 45142
[5]Principal, LCIT College of Pharmacy, Bodri, Bilaspur (CG) 49522
[6]SGT College of Pharmacy, SGT University, Gurugram , Haryana. India. 122505
[7]Assistant Professor, Central India college of Pharmacy.

*Corresponding Author:
Dr. M. Vijaya Jyothi[8*]
[8*]Professor, Raghavendra Institute of Pharmaceutical Education and Research K. R. Palli cross, Chiyyedu post Anantapur District Andhra Pradesh PIN-515721.
Email: drmvjyothiriper@gmail.com

Article Info

ABSTRACT:

Poly Cystic Ovarian Syndrome (PCOS) is a gynecological disorder with increasing presence in the women belonging to the reproductive age group with about 75% occurrence. With various studies, PCOS has shown impact on metabolic functioning also which was earlier only limited to reproductive functioning of women. The Objective of this study is to formulate herbal capsules using the herbal extract prepared by different herbs for the treatment of Poly Cystic Ovarian Syndrome. The capsules were formulated and then further evaluated. The collected herbs were first extracted using ethanol solvent and then further the extract was mixed with several excipients in different ratios based on increasing the ratio of the disintegrating agent to get fine granules. These granules were further made into the final end product which is the polyherbal capsules. These capsules were evaluated and tested. All the performed tests were evaluated and compiled. The performed tests showed all the parameters were in compliance as per the standard pharmacopoeias. The current research study was based on the role of medicinal herbs, namely, Bauhinia variegata, Emblica officinalis, Terminalia belerica, Terminalia chebula, Commiphora wightii, Cinnamon Cassia, Tribulus Terrestris, Hypericum perforatum, Commiphora molmol, Nigella sativa in the treatment of Poly Cystic Ovarian Syndrome. The study includes all the Phytochemical, Pharmacognostic, Rheological evaluation of the herbs and preparation of the end product polyherbal capsules. Also, the prepared formulation complies with all the standards as per Indian Pharmacopoeia and Ayurvedic Formulary.

Keywords: Poly cystic ovarian syndrome, polyherbal capsules, infertility, toxicity studies.

Principal
Indore Institute of Pharmacy,
INDORE (M.P.)

78

1. Introduction

Poly Cystic Ovarian Syndrome (PCOS) is a gynecological disorder with increasing prevalence, and an ovulatory infertility is a big concern which is almost 75% in women. PCOS now has shown an impact on metabolic functioning of the syndrome with recent researches, but earlier, PCOS was limited only as a reproductive or gynecological disorder. [1] PCOS occurs in women of the reproductive age group or the child-bearing age and is found to affect mostly the endocrine system. Ovaries tend to enlarge in the medical condition of PCOS with the accumulation of a large amount of fluid in it. Several clinical conditions of PCOS include irregular menstrual cycle, hair growth, the problem of acne, obesity, in the long-run problem of infertility, etc. The follicular growth is impaired during the ovarian cycle, which leads to cysts formation as follicles remain in contact with the ovary the underlying condition is due to hormonal imbalance. The anterior pituitary secretes luteinizing hormone (LH) & follicle-stimulating hormone (FSH), which is the major underlying cause of the disease. [2]

The major challenge of women suffering from PCOS includes irregular and impaired estrogen, androgen metabolism, and, also production of androgen control is impaired. The premenopausal and women of reproductive age group are most commonly affected by the disease. The major focus is on normalizing the functions of the ovary. [3]

The Gonadotropin-releasing hormone is secreted by the hypothalamus, and the LH & FSH is secreted by the gonadotrophs in return. The major functions of LH & FSH include reproductive, growth, and, menstrual regulation. This imbalance between the LH, FSH, and their ratio of increased serum concentration is the underlying cause of the diseased condition in women of the reproductive age group. [4]

Both environmental, as well as hereditary factors are the underlying factors for PCOS. Lack of proper physical exercise, obesity which might further cause insulin resistance comes under the environmental factors. Several diagnostic parameters of PCOS include Cushing's syndrome, secreting tumors of adrenal androgen and ovarian, in some cases hypothyroidism, etc. [5] It is believed, slight changes in the lifestyle including proper exercise, walking, weight management might help in the management of the disease by regulating several problems symptoms of PCOS like weight gain, the regularity of the menstrual cycle, hair growth in excess, etc. [6] For the treatment of PCOS, various methods and procedures have been used like changing or modifying the lifestyle, several surgeries, use of Vitamin D, induction of ovulation, etc. [7,8] Various synthetic drugs such as metformin for insulin resistance during PCOS have been prescribed to women; Clomiphene Citrate too was used for ovulation stimulation. But, these drugs showed several side-effects. Therefore, the role of herbal drugs has increased in the treatment of the disease. Various studies suggest that herbs have been useful in the treatment of PCOS. The steroidogenic property is seen in the case of herbs and provides several benefits with the treatment of PCOS. [9] One of the major benefits of using herbs in combination is that it provides a synergistic or potentiating effect. [10] The herbs selected for the study are Bauhinia variegata, Emblica officinalis, Terminalia belerica, Terminalia chebula, Commiphora wightii, Cinnamon Cassia, Tribulus Terrestris, Hypericum perforatum, Commiphora molmol, and, Nigella sativa. As per a study, the use of Ayurvedic herbs such as Bauhinia variegata (Kanchnar Guggul) is an effective way for the treatment of PCOS. The herb shows no adverse drug reaction or risks and can be used to treat hormonal imbalance, minimize the ovaries with polycystic appearance, menstrual irregularities, the problem of acne, and pain improvement. [11] The combination of medicinal herbs, namely, Terminalia chebula (Harad), Emblica officinalis (Amla), and Terminalia bellirica (Baheda) is collectively called Triphala. These are the most common Ayurvedic preparations with

significant effect. The plant part with great medicinal significance is the fruit. Due to the presence of vitamin C and anti-oxidant effects in fruits like Amla, these are considered useful in treating the condition of menorrhagia. [12] Due to the scavenging of free radicals, Amla also helps in detoxifying as well as helps to improve the hormonal imbalance in the body. [10] The next drug used for the study is Commiphora wightii (Guggul), and as per a study, the ethanolic extract of Guggul is used as a potent medicinal herb to the treatment of PCOS. Commiphora wightii plays a significant role in normalizing hormone levels and reducing ovarian follicle abnormalities. [13] Cinnamon Cassia is another herb used for research. Insulin resistance is one of the common factors gathered by the researchers in the pathogenesis of PCOS which leads to hyperinsulinemia. Cinnamon cassia is seen to have a sensitizing effect on PCOS-induced hyperinsulinemia. Also, the study states that Cinnamon has a vital role in improving the menstrual cycle and effective in the treatment of PCOS. [14] Another medicinal herb selected for the study is Tribulus terrestris. As per a research study, the ethanolic extract of Tribulus terrestris in a pre-clinical PCOS study showed the effect on body mass, synthesis of androgen, etc. The treatment of Tribulus terrestris extract showed a positive effect on the growth of healthy follicles and minimizing the cystic follicles in number. Thus, Tribulus terrestris has a significant on women with PCOS. It has a role in improving lipid, estrogenic, insulin-sensitizing, and hyperandrogenic profile. [1] Hypericum perforatum or St. John wort's is another medicinal plant used in PCOS to modulate the serotonin levels in the body. Mood swings or depression are the signs of illness due to PCOS. Thus, Hypericum perforatum modulates the levels of serotonin. [15] St. John Wort is useful in treating depression or mood swings during PCOS. [16] Commiphora molmol or Myrrh is another medicinal plant chosen for the research. Myrrh is used in PCOS as an Amenorrhea agent, generally given with iron compounds so as to induce menstruation. Another role in PCOS is as a Menorrhagia, which helps to prevent excessive loss of blood during the menstrual cycle. Myrrh also helps in painful or irregular menstruation. [17] The medicinal herb, Nigella sativa or Kalaunji, is used in the study as it is used in PCOS to decrease menstrual irregularities in women. The severity of menstrual bleeding also tends to stabilize by the use of Nigella sativa. The herb acts on oligomenorrhea or irregular menstrual bleeding which is a common symptom of PCOS by the anti-oxidant and anti-inflammatory mechanisms. [18]

2. Methods and Materials

Selection and Collection of Plant Material:

The bark of Bauhinia variegata, fruit of Emblica officinalis, seeds of Terminalia bellerica, Terminalia chebula, Tribulus Terrestris, and Nigella sativa, resin of Commiphora wightii, Commiphora molmol, sticks of Cinnamon Cassia and seeds of flowers of Hypericum perforatum, were procured from the botanical garden of Pranveer Singh Institute of Technology (PSIT), Kanpur.

They were dried and grounded properly in a mixer grinder. Further, it was passed through sieve number 60. The polyherbal powder was then mixed in a fixed ratio with a maximum of Commiphora wightii and the remaining in the total amount of Commiphora wightii was mixed.

Table 1 List of Plant Parts Used.

S.No.	Plant part used
1.	Bark of Bauhinia variegate

Princlpal
Indore Institute of Pharmacy,
INDORE (M.P.)

80

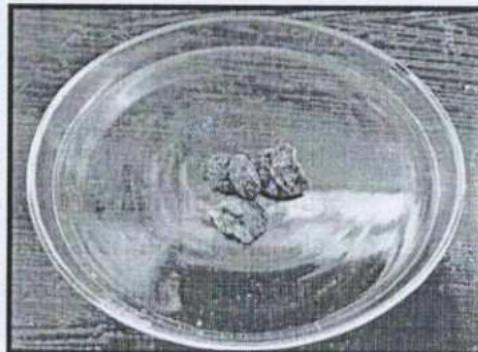| 2.		Fruit part of Emblica officinalis
3.		Seeds of Terminalia bellirica
4.		Seeds of Terminalia chebula
5.		Resin of Commiphora wightii
6.		Sticks of Cinnamon Cassia
7.		Seeds of Tribulus Terrestris
8.		Flowers of Hypericum perforatum
9.		Resin of Commiphora molmol
10.		Seeds of Nigella sativa
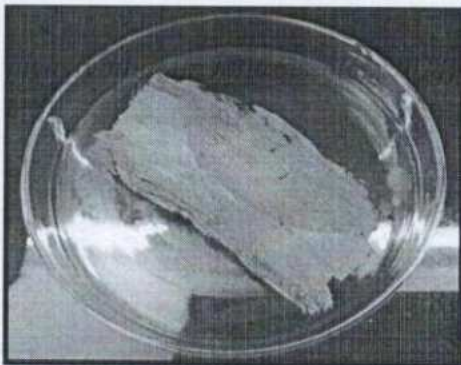
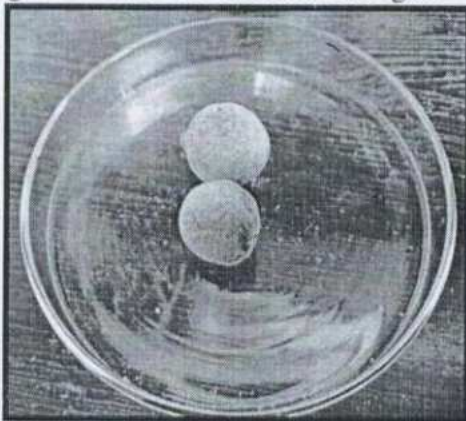Figure 1 Bark of Bauhinia variegata　　　　Figure 2 Fruit of Emblica officinalis

Figure 3 Seeds of Terminalia belerica　　　　Figure 4 Seeds of Terminalia chebula
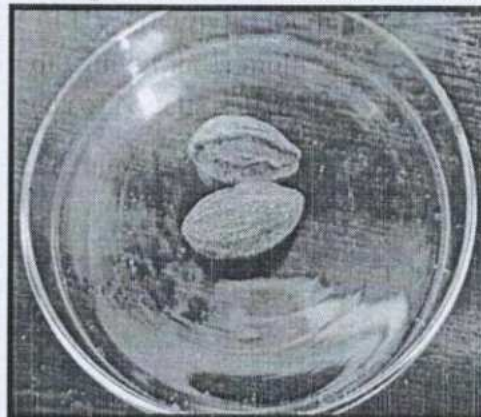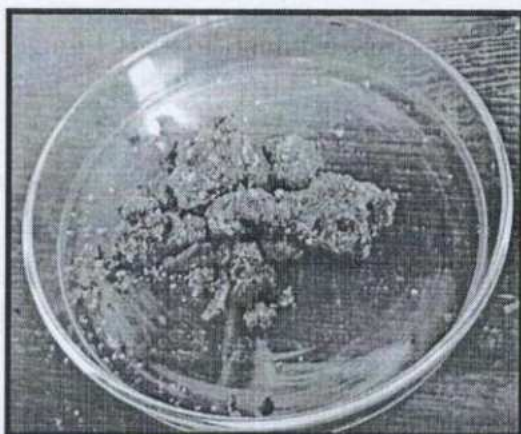
Figure 5 Resin of Commiphora wightii　　　　Figure 6 Sticks of Cinnamon cassia
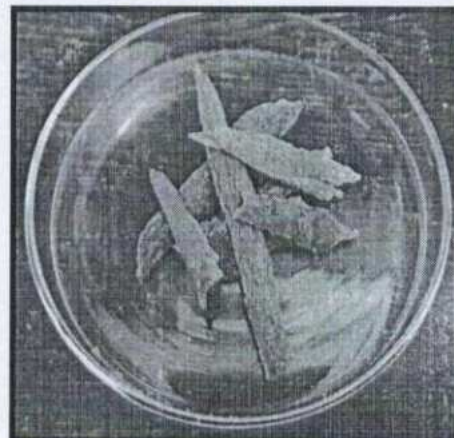
Principal
Indore Institute of Pharmacy,
INDORE (M.P.)

81

Figure 7 Seeds of Tribulus terrestris
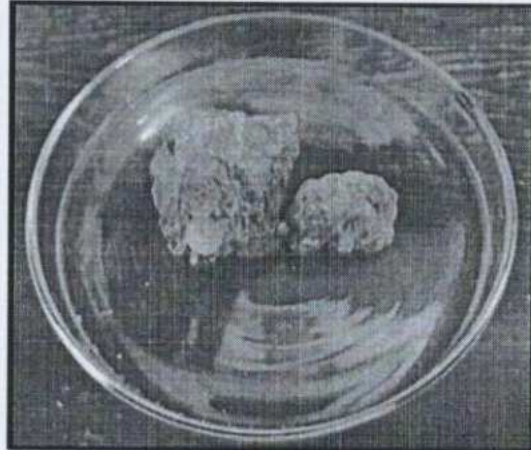
Figure 8 Resin of Commiphora molmol
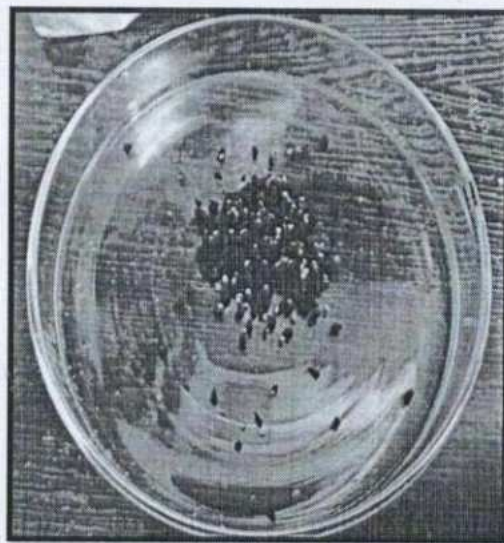
Figure 9 Seeds of Nigella sativa
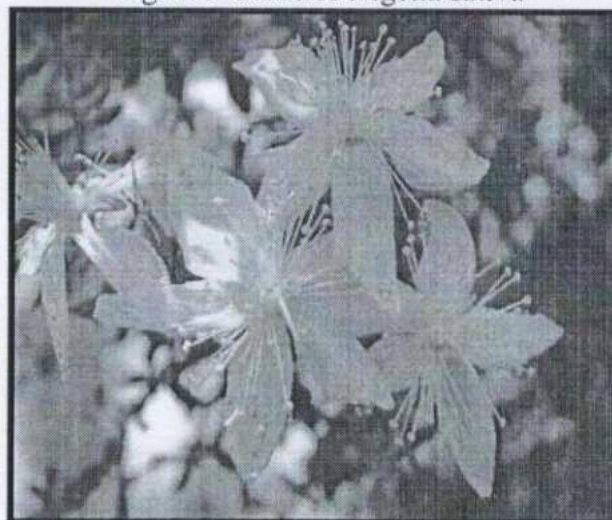
Figure 10 Flower of Hypericum perforatum

Preparation of the Polyherbal Powder (PHP)

PHP was prepared by mixing the selected 10 herbs in a particular ratio. The ratio selected for the preparation of PHP was in the ratio of 2.5:1.0:0.10:0.10:0.10:0.5:0.83:0.83:0.5:0.5 which

Principal
Indore Institute of Pharmacy,
INDORE (M.P.)

82

includes herbs in the order Guggul, Kanchanar, Harad, Baheda, Amla, Dalchini, Gokhru, Myrrh, Kalaunji, and St. John's wort respectively.

The selected herbs were first properly washed, and shade dried and then they were blend into a fine powder using mixer grinder. The obtained PHP was then made to get fine and homogenous particles by using sieve of 60 mesh size.

Determination of Drug Excipients Interaction: [20]

The drug excipients interaction testing was done through the isothermal method. About 100 mg of the PHP was taken and separately excipients including lactose, starch, talc, magnesium stearate, sodium benzoate, microcrystalline cellulose, and sodium starch glycolate were weighed individually, 100 mg each. Sample 1 was PHP; sample (2-7) was the individual excipients and combination of drug- excipients samples (8-14) was in the combination of PHP and excipient combination.

The samples were placed in clean glass vials along with ultra pure water 10 μL with the help of micropipette was added separately into each glass vials and mixed using capillary without touching the sample. The glass vials, were labeled, and sealed properly to avoid any contamination and kept in the hot air oven for a period of 4 weeks at 40-50°C. After the end of the fourth week, the samples were analyzed using FTIR. The bands were studied and the drug- excipient interaction was studied.

Preparation of the extract by Soxhelation Method [21]

The powdered herbs were extracted using ethanol solvent by the Soxhelation process. The herbs were extracted in the fixed ratio and extracted for the active constituents. For the process of soxhelation, about 200 grams of powdered herbs were extracted in about 800 ml of ethanol. The process was carried out at around 40-50°C. The obtained extract was concentrated with the rotary evaporator till the extract gets concentrated.

Preparation of the Granules [22]

The method used for the preparation of the granules was Wet Granulation Method. The extract was weighed 500 mg and mixed with 500 mg of excipients. The excipients selected include lactose, talc, magnesium stearate, starch, microcrystalline cellulose, sodium benzoate, and sodium starch glycolate.

The extract was first mixed with lactose to form a mass which is less sticky in nature. After that, other excipients were added in successive order till the extract starts forming a uniform mass. Starch, then talc in very less quantity (2-3%), magnesium stearate, cellulose, sodium benzoate, and sodium starch glycolate at the last. The concentration of sodium starch glycolate was varied in the formulation (1%-5%).

Sodium starch glycolate is used as a super disintegrant in the formulation, which helps in faster disintegration of the granules. The granules were then dried in desiccator to remove moisture. The granules were then sieved through sieve no. 44 and then sieve no. 60 to get even finer particles. The prepared granules were then tested as per the flow properties and other factors like microscopy, pH, moisture content, reaction of granules with different reagents, drug interaction test, and Differential scanning colorimetry.

Table 2 Formulation of granules in different concentrations

S. No.	Extract (500 mg)	Lactose (mg)	Starch (mg)	Talc (mg)	Mag. Stearate (mg)	Sodium Benzoate (mg)	Cellulose (MCC) (mg)	Sodium starch glycolate (mg)
F1	500	300	100	30	30	0.5	40	

83

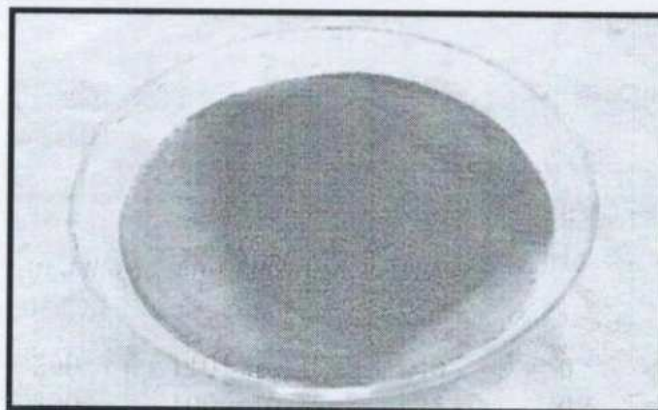| F2	500	290	110	25	40	0.5	25	10
F3	500	300	100	25	25	0.5	30	20
F4	500	280	100	30	40	0.5	20	30
F5	500	260	100	30	35	0.5	35	40
F6	500	270	100	25	35	0.5	20	50

Figure 11 Prepared granules

Evaluation of the prepared granules: [22]
Determination of the flow properties of the prepared granules:
The prepared granules were prepared in bulk for the determination of the flow properties. The granules were tested for Bulk density, Carr's index, Tapped density, Angle of repose, and Hausner's ratio.

Bulk density: It was estimated for flow of the granules by weighing it 25 grams and placed in 100 ml of graduated cylinder without disturbing to get the exact space covered by granules. Bulk density can be calculated by: Bulk density= weight of granules (gm)/ volume occupied by the powder in the measuring cylinder (ml)

Tapped density: The tapped density of the prepared granules was calculated by placing 25 grams of granules in 100 ml of measuring cylinder and tapping the cylinder 2 inches above the ground till no deviation in measurement is seen. It is calculated by: Tapped Density= weight of the prepared granules (gm)/ space occupied by the measuring cylinder after tapping (ml). [23]

The Carr's Index:
It is the abbreviation used for the calculation of compressibility of the prepared granules. Tapped density and bulk density are the two parameters used for the calculation.
Formula for Carr's Index is = (bulk Density- tapped Density/ Tapped Density) * 100.

Hausner's Ratio:
Hauser's ratio is the property used to define how fine the granules are in terms of Flowability. It can be calculated by:
Hauser's ratio= Tapped density/ Bulk density [24]

Angle of Repose: The property for granules was calculated after placing a funnel at a fixed height of 10 mm from the ground and paper was placed beneath it. Pouring of granules done using funnel and the height and diameter of the circle formed on plain paper were noted. The formula for angle of repose is:

Principal
Indore Institute of Pharmacy,
INDORE (M.P.)

84

Angle of repose (θ) = tan-1 h/r; where, h is observed height, r is the radius formed by the base of cone, and tan θ is height. [25]

Moisture content evaluation: [26]

The moisture content of the prepared granules was evaluated by placing 10 grams of the granules into a petri dish and kept in oven for drying at 100-105 °C for about 4-5 hours till no change in weight is observed. The weigh was taken periodically to check the difference of the weight. The percentage of it is given as: % moisture content= [(weight initial- weigh final/weight of granules taken]* 100)

pH determination: The pH for the granules was calculated using pH meter. The pH meter was calibrated by using capsules of pH 4 and 7. Then around 1gram of the granules was properly dissolved in 100 ml demineralised water with the help using sonicator. The pH was measured for same.

Granules disintegration test: The disintegration test of the granules was done to check if the granules disintegrate in as given set of time. The test was performed in a digital disintegration assembly. The granules were weighed and put into the disintegrating tubes covered with the disc. The temperature was maintained to room temperature 37±5°C. The time for granules to permeate through the mesh was observed and noted.

Microscopical Evaluation of the granules: [27] The structure of the prepared granules was observed under the compound microscope for the evaluation of the granule structure. The prepared granules were placed on the glass slide and several staining dyes like Phloroglucinol in combination with conc. HCl was used to observe the granule structure. Glycerin was also used with saffranine or any other staining dye to observe the structure distinctly. Other staining dyes used include Iodine solution, and Sudan III. The slide was covered using cover slip without applying much pressure and in proper light, the slide was observed using the microscope.

Assessment of physical nature of granules by using different reagents: [28] The granules were assessed based on their physical nature by testing them with different reagents. The change in color of the granules after a time interval of 5, 10, 15, and 30 minutes was observed. The reagents used for the estimation include n-hexane, iodine solution, chloroform, ferric chloride, acetone, and methanol. The results were observed and noted.

Formulation of the capsules [28]

The prepared granules were further converted to capsule formulation. The capsules include equal amount of extract (500mg) and excipients. The granules were filled into the herbal capsule shells of size 000 by using hand operated capsule filling machine with accuracy. The prepared capsules were then further evaluated based on various evaluation parameters like weight variation, drug uniformity content, disintegration, dissolution, thermal evaluation of the formulation by Differential scanning colorimetry (DSC).

Principal
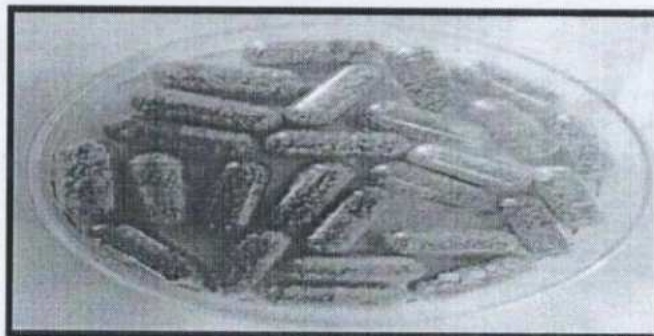Indore Institute of Pharmacy,
INDORE (M.P.)

85

Figure 12 Prepared herbal capsules

Evaluation of the prepared capsules:

The capsules were evaluated based on weight variation, drug uniformity content, disintegration, dissolution, thermal evaluation of the formulation by Differential scanning colorimetry.

Maximum wavelength (λ_{max}) estimation: [28]

Exactly measured 10 mg of the herbal extract was mixed properly in 10 ml of the phosphate buffer with pH 6.8. The prepared stock mixture is 1000 μg/ml in concentration. The solution was further diluted to 100 μg/ml solution. The wavelength determination was done was done using Ultra violet spectrophotometer in the range between 200-400 nm.

Preparation of buffer pH 6.8: [29]

The phosphate buffer preparation is done by disodium hydrogen phosphate and potassium dihydrogen phosphate to produce 1000ml of the buffer. 28.80grams of disodium hydrogen phosphate and potassium dihydrogen phosphate comprise of 11.45 grams. The solutions were mixed thoroughly with the help of sonicator till mixing is done. The prepared buffer was checked on pH meter and filtered.

Preparation of the calibration curve for the polyherbal formulation: [28]

The curve standard was initiated mixing 10 mg of the herbal extract in 10ml of phosphate buffer with pH 6.8. The prepared concentration of the stock solution is 1000 μg/ml. It was again diluted as 100μg/ml, 200μg/ml, 300μg/ml, 400μg/ml, 500μg/ml. The calibration of UV spectrophotometer was done by running the initial baseline by placing the phosphate buffer in both the cuvette; after the calibration, the prepared dilutions were placed serially in one cuvette. The maximum wavelength of 275.20 nm was observed and the absorbance was noted. The process was continued interday and intraday to get accurate readings.

Determination of Weight Variation of Capsules:

The weight variation test is done to establish the uniformity of weight in the capsules. The weight of the prepared capsules must fall in the particular range to avoid deviations. The process includes selecting exact twenty capsules from the batch randomly and the average of these twenty capsules is compared to the weight of the individual capsule. This process is done as per Indian Pharmacopoeia, 2010. The deviation in the weight should not fall under 90% and should not exceed 110% of the amount calculated. The limit should not exceed ±5% for capsule more than 300mg.

Disintegration test:

Principal
Indore Institute of Pharmacy,
INDORE (M.P.)

The disintegrating test of the capsules was performed on the disintegration apparatus. The test is generally done on the conventional dosage forms. The disintegration rate is defined as the rate or time with which the prepared formulation breaks or disintegrates into the smaller particles and reaches the site of action, the gastrointestinal tract. The disintegration test was performed on the randomly selected six capsules from the lot. The required conditions are 1000ml of beaker and 37±5 ℃ temperature of the apparatus. Each capsule was kept in the six tubes of the assembly separately with dissolution medium. The time taken by the particles to cross the mesh at a particular time is the disintegration time.

Dissolution test/ Invitro Release [30]
The dissolution test of the capsules was done as per USP type-I apparatus that is, rotating basket type assembly. The assembly was set at 37±5 ℃ and at rpm of 100± 5. The capsule was weighed and then kept in the basket then fitted to assembly. 1000ml beaker in the assembly was poured with 900 ml of the phosphate buffer with pH 6.8. The sample was withdrawn at an interval of 10 mins. 2ml of the sample was withdrawn and then volume was made up with 2ml of buffer in the assembly. The volume of the sample was diluted so that it can be observed under ultra violet spectrophotometer. The sample was observed under UV, and absorbance was noted. This absorbance was then calculated for the concentration and % drug release. The standard calibrated curve was used for the determination.

Drug content uniformity analysis:
The test for drug content was done as per the specifications mentioned in Indian Pharmacopoeia, 2007. About twenty capsules were taken and emptied its content in mortar pestle. Accurately weighed 500 mg of the granules were mixed with the phosphate buffer pH 6.8. Ultraviolet spectrophotometer was used for the estimation of drug content in each capsule at 275.20 nm wavelength.

Formulation characterization
Prepared formulation FTIR analysis [31]
The prepared six types of granules were analyzed by FTIR analysis. The drug and excipients showed no signs of drug interaction. The Perkin Elmer FTIR spectrum was used to scan the range of 4000 to 400 cm^{-1}.
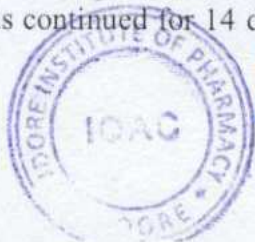
Differential Scanning colorimetry [32]
The sample which can be analyzed based on the changes in temperature is called differential scanning colorimetry. The breakdown of heat gives information about the various processes. DSC (SDT Q600) model has been used for the estimation. The estimation has been done in the nitrogen based environment.

Toxicity Studies [33]
Acute toxicity study (OECD Guidelines)
The 14 day study was accomplished by with the aqueous extract of the prepared polyherbal extract. The testing of the herbal extract was done on female rats in dose of 500, 1000mg/kg. The dosing was done with compliance of Organization for Economic Development (OECD) guidelines. OECD Guideline 425 was followed. The female Wistar rats were weighed and the extract was dissolved in distilled water as per the body weight. The extract was given orally to the rats. The rats were observed for any irritation for the first 15 minutes and monitored for the starting 4 hours. The next 48 hours the animals were monitored on daily basis. The study was continued for 14 days in which the rats were monitored for any changes like irritation in

Principal
Indore Institute of Pharmacy,
INDORE (M.P.)

87

African Journal of Biological Sciences

Journal homepage: http://www.afjbs.com

Research Paper

Open Access

Formulation Development and Hepatoprotective activity of Hydro-alcoholic extract of *Abutilon indicum* and *Phyllanthus niruri* against paracetamol induced liver toxicity in albino rats

Sujit Appasaheb Jadhav[1], Vikas Gupta[2], Aditi Omprakash Jyotishi[3], Pankaj Sahu[4], Rekha Bisht[5], Pravin Kumar Sharma[6]* and Sumeet Dwivedi[6]

1, R.G. Sapkal College of Pharmacy, Nashik, Maharashtra, India

2, Kailash Narayan Patel College of Pharmacy, Bhopal, Madhya Pradesh, India

3, Dr. Vedprakash Patil College of Pharmacy, Aurangabad, Maharashtra, India

4, Department of Botany, Govt. S.S.P. College, Waraseoni, Balaghat, Madhya Pradesh, India

5, Indore Institute of Pharmacy, Indore, Madhya Pradesh, India

6, Acropolis Institute of Pharmaceutical Education and Research, Indore, Madhya Pradesh, India

*Corresponding Author

E.mail: praveensharma910@gmail.com

Abstract

The term "hepatic disease" refers to a broad category of conditions that affect the human liver's tissues, structures, and cells. The liver performs a great deal of vital processes, therefore there are many opportunities for anything to go wrong. Inflammation is one of the most frequent causes of liver illness and is frequently brought on by alcohol abuse, a bad diet, or even malnourishment. The most significant health concern that affects the drug control board, the pharmaceutical industry, and medical professionals is medication-induced liver damage or dysfunction. The United States Acute Liver Failure Study Group states that over half of cases of acute liver failure are due to drug-induced liver injury, which includes paracetamol overdose-induced hepatotoxicity. The present paper deals with the formulation of polyherbal tablet containing hydro-alcoholic extract of *Abutilon indicum* Leaves and *Phyllanthus niruri* Fruits. The formulated tablet was evaluated and screened for Hepatoprotective activity against paracetamol induced liver toxicity in albino rats. The results indicate that prepared polyherbal tablet showed significant hepatoprotective activity as compared to the hepatotoxic control.

Keywords: Liver disorders, Medicinal Plants, Paracetamol induced

Introduction

The field of herbal medicine has grown exponentially in the past several years, and due to their natural origins and low side effects, these medications are becoming more and more popular in both developed and developing nations. Medicinal plants, minerals, and organic materials are the source of many commonly used traditional medications. Many medicinal plants known as rasayana, which have been utilised for over a millennium, are included in herbal remedies used in Indian traditional medical systems. The majority of medical professionals in Indian systems create and administer their own concoctions. 21,000 plants are registered by the World Health Organisation (WHO) as being used medicinally worldwide. Of these 2500 species, 150 are employed commercially on a somewhat regular basis in India.. [1-3]

Indian Indigenous medicinal plants are most widely used for the treatment of several diseases either in alone or in combination in raw as well as their extract. Synthetic hepatoprotective agents can produce several serious effects and also they are not suitable to use during pregnancy. In this light herbals are preferred in the treatment of liver disorders. Ancient ayurvedic literature reveals that the selected plants i.e., *Abutilon indicum* (Leaves) and *Phyllanthus niruri* (Fruits) have been widely used in the treatment of liver disorders. These plants have been extensively used in ayurveda and traditional system of medicine for the treatment of liver disorders and found to be efficient and inexpensive as compared to synthetic drugs and not evaluated scientifically in combination as polyherbal tablet. Therefore, it was worthwhile to investigate the hepatoprotective activity of polyherbal tablet containing hydr0oalcoholic extract of *Abutilon indicum* (Leaves) and *Phyllanthus niruri* (Fruits).

Material and Methods

Collection of herbs and their authentication

Abutilon indicum (Leaves) and *Phyllanthus niruri* (Fruits) were collected from local sites of Malwa region of Madhya Pradesh, India during October 2023 and identified morphologically, microscopically and compared with standard pharmacopoeial monograph and authenticated by Dr. S. N. Dwivedi, Retd. Prof. and Head, Department of Botany, Janata PG College, Visiting Professor, A.P.S. University, Rewa, (M.P.) and was deposited in our Laboratory. Voucher specimen No. J/Bot./AI-L/12; J/Bot/PN-F/13 were allotted to the selected plant parts.

Extraction of selected herbs

The shade dried coarsely powdered plant material (250 gms) of plant viz., *Abutilon indicum* (Leaves) and *Phyllanthus niruri* (Fruits) were loaded in Soxhlet apparatus and was extracted with ethanol: water for 48 hour. After completion of extraction, the solvent was removed by evaporation. The extracts were dried using rotator evaporator. The residue was then stored in dessicator and percentage yield were determined. [8-9]

Pharmacological screening

Acute Toxicity Studies of Extracts & Procurement of experimental animals

The mice were used for acute toxicity study as per OECD guidelines 423. The animals were fed with standard pellet diet (Hindustan lever Ltd. Bangalore) and water *ad libitum*. All the animals were housed in polypropylene cages. The animals were kept under alternate cycle of 12 hours of darkness and light. The animals were acclimatized to the laboratory condition for 1 week before starting the experiment. The experimental protocols were approved by Institutional Animal Ethics Committee after scrutinization. IEAC approval.

Development of Polyherbal Formulation

Preparation of Polyherbal formulation (Tablet)

Polyherbal formulations table (PFT) containing hydro-alcoholic extract of plant *Abutilon indicum* (Leaves) and *Phyllanthus niruri* (Fruits) was prepared by wet granulation method using

IQAC

Principal
Indore Institute of Pharmacy,
INDORE (M.P.)

89

suitable excipients like microcrystalline cellulose, starch, crospovidone, aerosil and magnesium stearate.[7-8] The composition of PFT was given in table 1.

Table 1: Composition of Polyherbal formulation (Tablet)

Ingredients	Quantity
HAEAIL	100
HAEPNF	100
Microcrystalline Cellulose	125
Starch	50
Crospovidone	20
Granulation	
Water	q.s.
Prelubrication	
Starch	25
Aerosil	10
Talc	15
Lubrication	
Magnesium Sterate	5
Total weight (mg)	500

Evaluation of polyherbal formulation (Tablet) [7-9]

Appearance
The prepared herbal tablets were evaluated for their color and appearance. In this study color, odor, taste were noted down.

Hardness
Randomly five tablets were taken out from each batch and crushing strength was determined using Monsanto tablet hardness tester.

Friability
Randomly 25 tablets were taken and weighed out and was placed in Electrolab friabilator and was rotated at 25 rpm for 4 mts to determine the frability. The percentage friability was calculated by using formula

$$\%F = (1-WI/WF)*100$$

Where, WI=Initial weight of the 25 tablets; WF=Final weight of 25 tablets

Weight Variation
Randomly selected 20 tablets were evaluated for weight variation as per IP 2018.

Disintegration Time
Randomly 6 tablets were taken from each batch and were placed in USP disintegration apparatus using 0.1 N HCl at 37^0C. The time was noted down when the tablet get disintegrates completely.

Hepatoprotective activity of Polyherbal Formulatio (Tablet)

Experimental Animal
Albino rats (200-250 g) used in the present studies was procured. The animals were fed with standard pellet diet (Hindustan lever Ltd. Bangalore) and water *ad libitum*. All the animals were acclimatized for a week before use.

90

Paracetamol Induced Model

The rats were divided into 7 groups of 6 animals in each. [18-19]

S/No.	Group	Treatments
1.	Group I (Normal)	Received vehicle gum acacia (5mg/kg p.o) for 7 days
2.	Group II (Control)	Received vehicle gum acacia (5 mg/kg p.o) for 7 days once daily and paracetamol 500mg/kg once daily
3.	Group III (Standard)	Received silymarin as standard (50 mg/kg) for 7 days once daily and paracetamol 500mg/kg once daily
4.	Group IV	Received PFT (100 mg/kg) once daily and paracetamol 500mg/kg once daily
5.	Group V	Received PFT (200 mg/kg) once daily and paracetamol 500mg/kg once daily

On the seventh day, the blood samples were collected via orbital sinus puncture for the estimation of biochemical marker enzymes and allowed to clot and serum was separated by centrifuge at 2500 rpm for 15 min and analyzed for various biochemical parameters. Then the liver was carefully isolated and cleaned off extraneous tissue and preserved in 10% neutral formalin and then subjected to histopathological studies. [13-14]

Statistical Analysis

All the values ware statistically analyzed by one-way analysis of variance (ANOVA) followed by Dunnette multiple Comparisons test. Statistically significance of * $P<0.01$, ** $P<0.001$, when compared with respective control. All values are expressed as mean ± SEM.

Results and Discussion

The hydroalcoholic extracts of *Abutilon indicum* (Leaves) and *Phyllanthus niruri* (Fruits) were screened for acute toxicity study by OECD guideline no. 423 for determination of LD_{50}. The LD_{50} was 2000 mg/kg, therefore, ED_{50} was 200 mg/kg. Polyherbal formulation (tablet) containing hydroalcoholic extracts of *Abutilon indicum* (Leaves) and *Phyllanthus niruri* (Fruits), were evaluated for appearance, hardness, friability, weight variation and disintegration time. The physical appearances of PFT were given in table 2. The results obtained suggest that formulation do not have any tablet defects. The evaluation parameters of PFT were shown in table 3. The results obtained indicates that the data obtained are within the limit as per IP.

Rats treated with silymarin, PFT (at the dose of 100 & 200 mg/kg bw respectively) formulations showed noticeable improvement in histopathological parameters. The results were presented in table 4. The results were found to be more promising at the dose of 100 mg/kg bw than 200 mg/kg bw in pacarematol induced liver toxicity when compared to standard drug silymarin. Hence the formulations have prominent action on paracetamol-induced liver damage. Moreover, at necropsy, livers of rats treated with paracetamol appeared degeneration in hepatocytes, hepatic cell injury, focal necrosis, congestion in central vein, vascular swelling, and Kupffer cell proliferation. Furthermore, no gross pathological findings were noted in the livers of the other groups of rats.

Principal
Indore Institute of Pharmacy,
INDORE (M.P.)

91

Table 2: Physical Parameters (Appearance) of Polyherbal Formulation Tablet

Formulation Code	Physical Parameters (Appearance)			
	Color	Odor	Taste	Shape
PFT	Light green	Characteristic	Characteristic	Circular biconvex

Table 3: Evaluation Parameters of Polyherbal Formulation Tablet

Formulation Code	Parameters			
	Weight variations (%)	Hardness (kg/cm^2)	Friability (%)	Disintegration time (mts)
PFT-1	±3.52	4.74±0.08	0.31±0.24	8.66±0.02

Note: All values are expressed in Mean±SD, n=3

Table 4: Effect of Polyherbal formulation table on Biochemical Parameters in Paracetamol Induced Hepatic Injury in Rats

Treatment	Total Bilirubin (mg %)	Direct Bilirubin (mg %)	SGOT (μ/min/l)	SGPT (μ/min/l)	ALP (μ/min/l)
Normal	0.44 ± 0.21	0.43 ± 0.64	183.02 ± 2.1	77.40 ± 2.43	192.0 ± 6.2
Induced (PCM 2g/kg)	8.61 ± 2.46	7.45 ± 8.60	345.41± 10.42	153.7± 8.44	358.22±8.85
Standard (Silymarin 50mg/kg)	0.53 ±4.39[**]	0.49 ±0.19[**]	197.07±9.43[**]	88.07±8.79[**]	199.21 ±10.61[**]
PFT-1 (100 mg/kg)	0.58 ±0.01[**]	0.55 ±0.22[**]	203.14± 6.10[**]	94.02±6.01[**]	204.02± 8.32[**]
PFT-1 (200 mg/kg)	0.61 ±0.11[**]	0.59 ±0.27[**]	207.27± 8.39[**]	100.12±8.11[**]	206.13± 8.01[**]

Note: Values are mean ±SEM, n= 6. (One way ANOVA Followed by Dunnette multiple Comparisons test). Statistically significance of * $P<0.01$, ** $P<0.001$, when compared with respective control.

Conclusion

The liver disorders are very common and alarming. In the present work formulation development, evaluation and hepatoprotective activity of *Abutilon indicum* (Leaves) and *Phyllanthus niruri* (Fruits) against paracetamol induced liver toxicity in albino rats were investigated and the results the formulated polyherbal tablet at the test dose of 100 mg.kg bw showed significant hepatoprotective activity

Principal
Indore Institute of Pharmacy.
INDORE (M.P.)

92
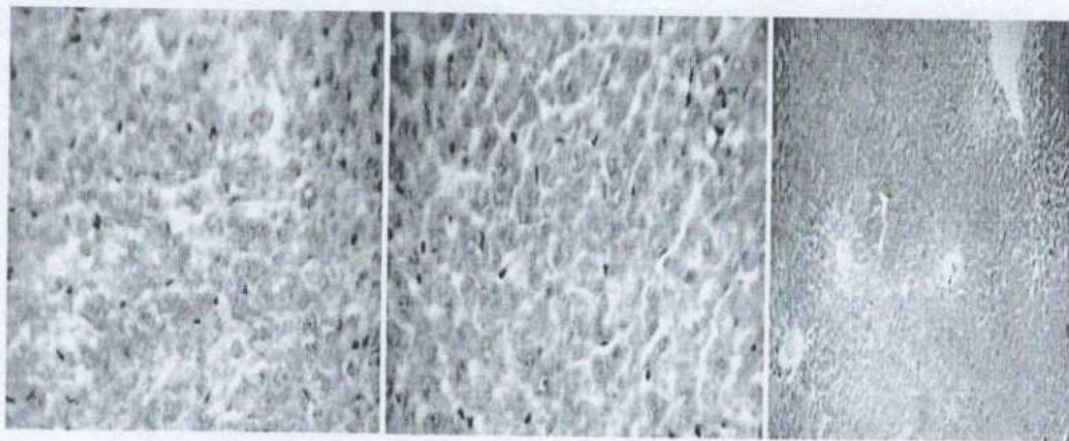
Normal Paracetamol induced (500mg/kg) Silymarin (50mg/kg)
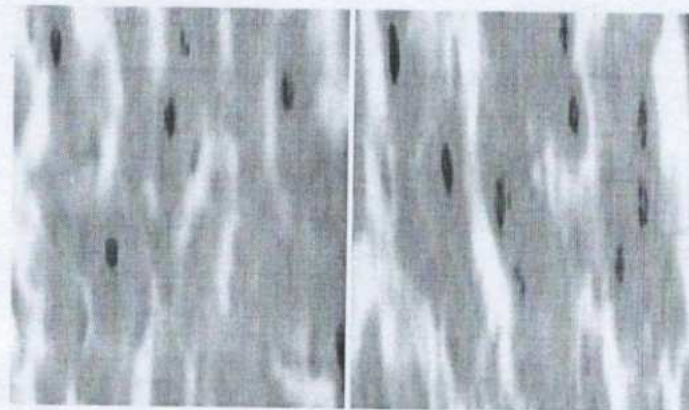
PFT 100 mg/kg   PFT 200 mg/kg

Fig. 1: Histopathologic Section of Liver of Rats in Paracetamol induced Hepatotoxicity of Normal, Control, Standard, PHT

References

1. Lipinski B. Pathophysiology of oxidative stress in diabetes mellitus. J. Diabet. Complications., 15:203–210, 2001;
2. Grover J.K., Yadav S., Vats V. Medicinal plants of India with antidiabetic potential. J. Ethnopharmacol. 81:81–100, 2002.
3. Seth S.D., Sharma B. Medicinal plants of India. Indian J. Med. Res., 120:9–11, 2004.
4. Sharma A., Sharma R.A. and Singh H., Phytochemical and Pharmacological Profile of Abutilon Indicum L. Sweet : A Review, Int. J. Pharm. Sci. Rev. Res., 20(1), May – Jun; 20, 120-127, 2013.
5. Narendra K., Swathi J., Sowjanya K. M. and Krishna Satya A., Phyllanthus niruri: A Review on its Ethno Botanical, Phytochemical and Pharmacological Profile, Journal of Pharmacy Research,5(9),4681-4691, 2012.
6. Mithun NM, Shashidhara S and Vivek Kumar R, Eclipta alba (L.) A Review on its Phytochemical and Pharmacological Profile, Pharmacologyonline, 1: 345-357, 2011.

Principal
Indore Institute of Pharmacy,
INDORE (M.P.)

93

7. Singh S., Prasad R. and Rai N.P., Phytochemical and pharmacological review on rasona (Allium sativum Linn.): a potential Herb, International Journal of Phytopharmacy Research, Vol 6(2), 53-58, 2015.

8. *Divakar M. C., Plant drug evaluation-a laboratory guide, published by, CD remedies, 2nd Ed., 84-92, 2002.*

9. Kokate C. K., *Practical Pharmacognosy*, Vallabh Prakashan, Delhi., 4th Edition, 107 – 111, 1997.

10. Rasheed R. A., Ali B.H. and Bashir A.K., Effect of *Teucrium stocksianum* on Paracetamol-induced Hepatoxicity in Mice. J Pharmacol, 26(2): 297-301, 1995

11. Jafri, M.A., Subhani, M., Jalis, Javed, Kalim. and Singh, S.., Hepatoprotective activity of leaves of *Cassia occidentails* against paracetamol and ethyl alcohol intoxication in rats. J Ethnopharmacol., 66(3): 355-361, 1999.

Principal
Indore Institute of Pharmacy,
INDORE (M.P.)

94
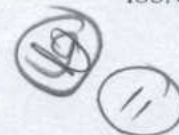
TRANSFORMATIVE CAPSULE TECHNOLOGY: A REVIEW OF TABLET-IN-CAPSULE INNOVATIONS

Pawan Patel[1*], Isha Dubey[2], Nayany Sharma[3], Nadeem A. Farooqui[4], Nimita Manocha[4]

[1*]Department of Pharmaceutics, Indore Institute of Pharmacy, Pithampur road, Opposite Indian Institute of Management, Rau, 453331, Indore, Madhya Pradesh, India.
[2]Department of Quality Assurance, Indore Institute of Pharmacy, Pithampur road, Opposite Indian Institute of Management, Rau, 453331, Indore, Madhya Pradesh, India.
[3]Faculty of Pharmacy, Indore Institute of Pharmacy, Pithampur road, Opposite Indian Institute of Management, Rau, 453331, Indore, Madhya Pradesh, India.
[4] Faculty of Pharmacy and Principal, Indore Institute of Pharmacy, Pithampur road, Opposite Indian Institute of Management, Rau, 453331, Indore, Madhya Pradesh, India.

*Corresponding Author: Pawan Patel

Institution Name: Indore Institute of Pharmacy, Pithampur road, Opposite Indian Institute of Management, Rau Indore, Madhya Pradesh, 453331.

Orcid ID: 0009-0004-3224-8390

Principal
Indore Institute of Pharmacy,
INDORE (M.P.)

95

" TRANSFORMATIVE CAPSULE TECHNOLOGY: A REVIEW OF TABLET-IN-CAPSULE INNOVATIONS"

ABSTRACT

This review explores the revolutionary tablet-in-capsule technology, a novel approach transforming oral drug delivery systems. Oral administration remains the most favored method for therapeutic agents, encompassing a range of pharmaceutical dosage forms such as tablets, capsules, suspensions, and solutions. Solid dosage forms, particularly tablets, stand out as the preferred class of products, widely embraced by pharmaceutical manufacturers, physicians, and patients alike. Capsules, defined as solid dosage forms encapsulating drugs within gelatin shells, serve as versatile containers for both powder and non-powder fillings, including tablets and pellets. The past few decades have witnessed significant advancements in drug delivery systems, setting the stage for the emergence of tablet-in-capsule technology. Tablet in capsule represents a multifunctional and multiple unit system, featuring versatile mini-tablets enclosed in a hard-gelatin capsule. The formulation of this system offers tremendous flexibility, allowing for tailored solutions to specific therapeutic needs. Mini-tablets, a novel trend in solid dosage form design, aim to overcome therapeutic obstacles providing benefits such as dose flexibility and combined release patterns. This review explores the key aspects of this technology, including formulation possibilities, manufacturing processes and general evaluation tests.

KEYWORDS- Minitablet, Capsule, Tablet-in-capsule, Oral drug delivery, Solid dosage form

INTRODUCTION

Oral drug delivery is one of the most common and preferred methods for administering pharmaceutical substances to patients. [1]

Solid oral dosage forms are prescribed to produce a therapeutic impact either locally in the oral cavity, throat, or digestive tract, or to induce a systemic effect in the body following absorption through oral or gastrointestinal pathways. [2]

This route of drug administration offers several advantages, such as ease, patient-conformity, and cost-effective, manufacture in go-to choose for a wide range of therapeutic interventions. [3]

Oral drug delivery system is the most desirable, preferable and suitable route for the ad-ministration of therapeutic and pharmaceutical agents for administration. [4]

Medications are commonly delivered via the oral-route in a radius of pharmaceutical dosage forms with capsules, tablets, suspensions, and diverse pharmaceutical solutions being the most prevalent choices.

It involves intake of medications in the form of tab, cap, syrups, or other solid or liquid formulations, with the drugs being ab-sorbed through the gastro-intestinal-tract into the blood-stream.

Solid oral dosage forms are the favorable categories in pharmaceutical products for oral-administration. They offer versatility, allow for a wide range of dosage strengths, exhibiting stability, and pose fewer challenges in terms of formulation and packaging. Additionally, they are suitable to formulate, reserve, and dispense. Solid oral dosage forms provide optimal protection for medications against factors like light, oxygen, temperature, humidity, and transportation-related stress. Among these solid oral dosage forms, tablet & capsule have their widespread usage. [5]

Principal
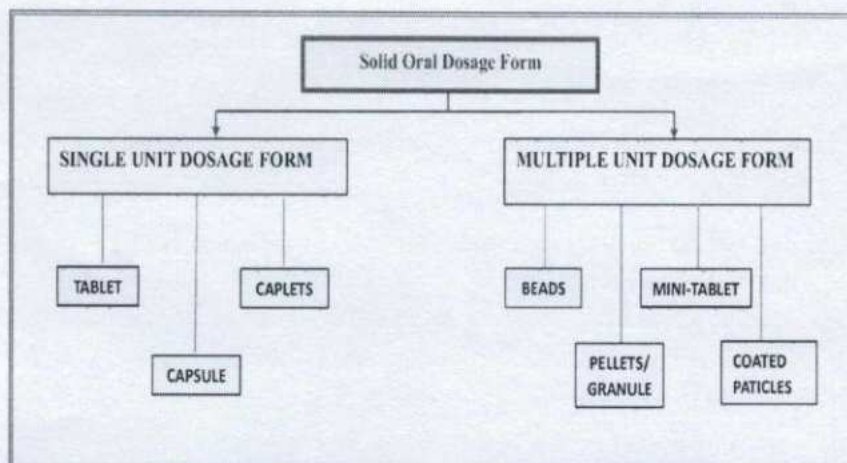Indore Institute of Pharmacy,
INDORE (M.P.)   PAGE NO: 292

96

Figure 1: Solid oral dosage form chart[6]

Novel Tablet Technologies

In recent years, there has been a significant development in various novel tablet technologies aimed at enhancing product performance and providing more effective drug delivery solutions.[7] These technologies include fast-disintegrating tablets, matrix tablets, tablet-in-tablet systems, tablet-in-capsule systems, multi-layered tablets, and multi-particulate systems has been developed to benefit product performance.[8]

Tab-in-Tab Systems:

- Tab-in-tab systems involve embedding one tablet within another.

- This approach can be used for combination therapies, where two different drugs are released at different rates or for drugs with incompatible stability requirements.

- It allows for separate release profiles within a single dosage form.[9]

Tab-in-Cap Systems:

- Tablet-in-capsule systems combine the benefits of tablet and capsule.

- Tablets or tablet segments are enclosed within a capsule, offering protection to the tablet and controlled release when the capsule dissolves.

- This approach can be useful for drugs with specific release requirements or stability concerns.

Table- 1: Capsule size chart

Capsule Size	Volume [Theoretical]			External Diameter	Weight
From Largest to smallest	{ml}	Tolerance		{mm}	+/- 10% {mg}
		Component			
000	1.37	Cap		9.91	163
		Body		9.55	
00	0.95	Cap		8.53	118
		Body		8.18	
0	0.68	Cap		7.65	96
		Body		7.34	
1	0.50	Cap		6.91	76
		Body		6.63	
2	0.37	Cap		6.35	61
		Body		6.07	
3	0.30	Cap		5.82	48
		Body		5.56	

Principal
Indore Institute of Pharmacy,
INDORE (M.P.)

97

4	0.21	Cap	5.31	38
		Body	5.05	
5	0.13	Cap	4.91	28
		Body	4.68	

Tablet – In – Capsule Technology

This innovative and distinctive system is referred to as a "TABs-in-CAP device." The resulting capsule device is comprised of an impermeable capsule body and a soluble capsule.

Figure 2: Tab-in-Cap

Impermeable Capsule Body:

The impermeable capsule body is the outer shell or Encasing of the device. It is designed to be completely sealed and impervious to external factors, such as moisture, air, or other environmental conditions. This is important to safeguarding the contents of the capsule and maintain their stability.

Soluble Capsule:

The soluble capsule is an inner component of the device. Unlike the impermeable capsule body, the soluble capsule is designed to dissolve or disintegrate in a specific environment or under certain conditions. This dissolution is a controlled process and is typically triggered by factors like exposure to moisture, changes in pH, or specific physiological conditions within the body. [10]

The TAB-in-CAP system encompasses filling and sealing of single or multiple tabs-in-caps. Targeted drug delivery or controlled drug release rate is attained by confining multiple tabs

with different separated coatings within a capsule.

Mini-Tablets

Mini-tabs are typically flat or gently curved tablets of a diameter ranging from 1.0 to 3.0 mm. [11]

These mini-tabs are commonly introduced within capsule, occasionally compressed into more substantial tablets, or on occasion, enclosed in sachets to facilitate administration.

Manufactured by conventional tablet presses equipped with a multiple tooling system. This production process resembles that of regular tablets but necessitates exceptional powder flow due to the smaller die size, precise control of process parameters, and careful assembly of the tablet press to prevent tool damage. [12]

Mini-tabs, which can be either coated or uncoated and are formulated as single unit or multiple-unit systems, and are primarily designed as patient-friendly result for pediatric and geriatric patients, as well as for personalized medicine. They enhance ease of

98

swallowing and offer flexible dosing options, allowing for the combination of various release kinetics, dosage strengths, and active ingredients within a single system. Mini-tabs can also effectively serve as multiple-unit modified release systems, including extended release, delayed-colon release, pulsatile release, bi-modal release, and gastro-retentive systems, thereby enhancing drug bioavailability compared to single-unit systems.[13]

Mini-Tablet for TAB-in-CAP- technology:

Controlled release caps, frequently comprising multiple coated pellets, constitute another class of solid oral formulations that provide similar therapeutic benefits. [14] A more recent approach that has emerged combines the characteristics of both controlled release tablets and modified release capsule within a single dosage form.[15] This system is designed to offer precise and versatile drug release profiles by encapsulating various types of tablets within an impermeable capsule body sealed with a water-soluble capsule. Let's elaborate on this system:

Formulation of Mini Tab-In-Cap System

The process of formulating mini-tablet-in-capsule systems can be broken down into three essential stages:

1. Creating/producing the mini-tabs.

2. Applying the suitable coating-polymer to these mini-tabs.[16]

3. Placing the coated mini-tabs into hard gelatin or hydroxy propyl methyl cellulose capsules. (Mini-tabs-in-capsule systems).[17]

he administration of mini tabs can occur through the subsequent approaches:

a. Administered directly as an individual unit dosage form.

b. Encapsulated within hard gelatin capsules. (single or multiple mini tabs).

c. utilization of an automated dose dispensing device.[18]

Administered directly as a unitary dosage form:

a. Mini-tablets can be administered directly.

b. The prescribed dosage can be easily consumed, hence, these are packaged in bottles.

c. At times, compressed mini tablets undergo additional compression to form tablets of regular size.[18]

Encapsulated in hard gelatin capsules (HGC)

Due to the challenge of managing mini-tabs, they are typically enclosed in hard gelatin capsules hard gelatin capsules before administration.[19]

Marketed Formulation of Tab-In-Cap

Table-2: Marketed formulation of tab-in-cap

Brand name	Drug name	Indication	Manufacturer	Dosage form
Rythmol SR	Propafenone HCL	Antiarrhythmic	GlaxoSmithKline	Capsule
Polycap	Simvastatin, ramipril, atenol, hydrochlorothiazide, aspirin	Heart attack, stroke	Cadila pharmaceutical	Capsule
Ramitorva	Atorvastatin, Aspirin, Ramipril	Heart attack, stroke	Zydus Cadila	Capsule
Polytorva 5kit	Atorvastatin, Aspirin, Ramipril	Heart attack, stroke	USV ltd.	Capsule
Unigel	Omega 3 fatty acid, Atorvastatin	Improve cholesterol	Procaps	Capsule
Pantafol-DSR	Domperidone + Pantoprazole	Acid reflux, Indigestion	Daniel Pasteur	Capsule
Rasodan-DSR	Rabeprazole + Domperidone	Anti-ulcer	Daniel Pasteur	Capsule
Rabex DSR	Domperidone + Rabeprazole	Anti-ulcer	Apotex Pharmachem India Pvt Ltd	Capsule

Principal
Indore Institute of Pharmacy,
INDORE (M.P.)

99

Silrab-D	Domperidone + Rabeprazole	Acid reflux	Ascent Therapeuticals	Capsule
Midezole	Omeprazole + domperidone	Gastroesophageal reflux disease	Life vision Healthcare	Capsule
XOM DSR	Domperidone + Omeprazole	Gastroesophageal reflux disease	Novogen Captab	Capsule

Evaluation of Tab-In-Cap Technology

Evaluation of tabs-in-capsules involves specific tests to assess the quality, safety, and performance of this drug delivery system.

The most common evaluation tests and their associated procedures for tab-in-cap:[20-22]
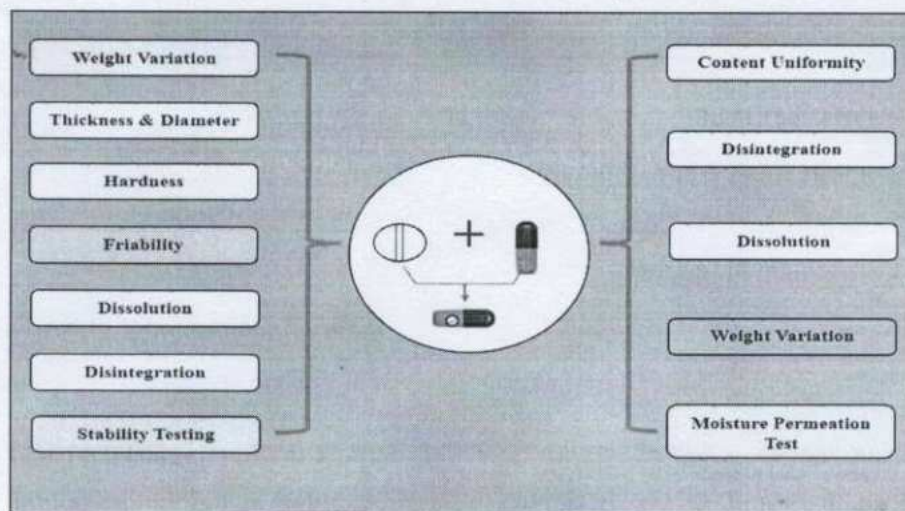
Figure 3: Evaluation of Tab-in-Cap

Future Prospective Of Tablet In Capsule

The future prospects of mini tablets in capsules (commonly known as "mini-tabs-in-a-capsule" technology) are promising and may lead to significant advancements in drug delivery and therapeutic strategies. Here are some potential future developments and prospects for this innovative drug delivery system:

Customized Drug Release Profiles:

Mini-tabs-in-a-capsule technology allows for precise control of drug release. In the future, we can expect even more customization of release profiles to meet the specific needs of various medications. This could include the development of complex multi-particulate systems within a single capsule, each with a different release profile to optimize treatment.

Improved Patient Compliance:

The convenience of taking a single capsule with multiple mini-tabs can enhance patient compliance. In the future, this approach may be further optimized to simplify complex dosing regimens, especially for patients who require multiple medications.

Combination Therapies:

Mini-tabs-in-a-capsule systems are well-suited for combination therapies. Future developments may focus on combining multiple drugs with different release profiles, improving the management of complex medical conditions.

Drug Delivery:

Advances in drug formulation and encapsulation within mini-tabs may result in more accurate and targeted drug delivery. This could include strategies for site-specific drug release within the body, enhancing the treatment of various conditions.

Biological Rhythm Alignment:

Principal
Indore Institute of Pharmacy,
INDORE (M.P.)

100

The chrono-pharmaceutical approach, which aligns drug delivery with biological rhythms, can be further explored. Future mini-tabs-in-a-capsule systems may be designed to release drugs at specific times of day to optimize treatment efficacy based on the body's natural rhythms.

Centric Drug Delivery:

Future developments may focus on improving patient-centric drug delivery, taking into account factors like age, lifestyle, and patient preferences. Personalized medicine could be integrated with mini-tabs-in-a-capsule technology for tailored treatment.

Advanced Materials and Formulations:

Continued research and development in materials science and pharmaceutical formulation can lead to the creation of more stable, biocompatible, and biodegradable components for mini-tabs and capsules.

Regulatory Approvals:

As these innovative drug delivery systems gain popularity, regulatory agencies may establish clear guidelines and approval pathways for mini-tabs-in-a-capsule technology, ensuring safety, efficacy, and quality standards.

Research and Collaboration:

Ongoing research and collaboration between pharmaceutical companies, research institutions, and healthcare providers are likely to drive the evolution of this technology. New discoveries and innovations will continue to expand its capabilities.

lobal Accessibility:

As mini-tabs-in-a-capsule technology matures, it may become more accessible and cost-effective, benefiting patients in various healthcare settings worldwide.

The future of mini-tabs in capsules holds the potential to transform drug delivery, making treatments more effective, convenient, and patient-centered. As research and development efforts progress, we can expect to see a wider range of applications and increased adoption of this technology across various medical specialties.

List Of Patents In Tab-In-Cap

Table 3: Tab-in-Cap Patents.[23-28]

Patent number	Title	Inventor name	Publication date
US-20230062872-A1	Pharmaceutical Formulation	Cavatur; Raghu et al.	2023-03-02
US20210145817A1	Apixaban Formulations	Sherif Ibrahim Farag Badawy	2019-04-15
US9̶ ̶0704B2	Composite formulation comprising a tablet encapsulated in a hard capsule	Kyeong Soo KimKi Young Jang Seung Jae Park Yong Il KimJae Hyun Park Jong Soo Woo	2018-07-06
US-20170304210-A1	Pharmaceutical capsule containing at least two tablets	Ahlgren; Nils William et al.	2017-10-26
WO2014002015A1	Pharmaceutical composition comprising dutasteride	Sumit Madan Ravinder Singh Vinod Kumar Arora	2014-01-03
US-7378102-B2	Diclofenac sodium oral pharmaceutical	Ishibashi; Nobuyuki	2008-05-27

CONCLUSION

The conclusion of this review delves deeply into the evolving landscape of tablet-in-capsule technology, providing nuanced insights into its ongoing advancements and the exciting potential for future developments. The synergistic integration of versatile formulation, cutting-edge mini-tablet technology, and the innovative encapsulation approach marks a promising frontier in oral drug delivery.

Principal
Indore Institute of Pharmacy,
INDORE (M.P.)

101

This multifaceted approach not only addresses existing challenges in drug delivery but also holds the key to significantly enhancing therapeutic outcomes. The comprehensive exploration of tablet-in-capsule technology in this review signifies its transformative impact on the field, ushering in a new era of tailored and efficient oral drug delivery systems.

ACKNOWLEDGEMENT

CONFLICT OF INTEREST

No conflict of interests.

References:

1. Kaur G, Arora M, Ravi Kumar MNV. Oral drug delivery technologies-a decade of developments. *J Pharmacol Exp Ther* 2019;370(3):529-43. doi: 10.1124/jpet.118.255828
2. Lou J, Duan H, Qin Q, Teng Z, Gan F, Zhou X, et al. Advances in oral drug delivery systems: Challenges and opportunities. *Pharmaceutics* 2023;15(2). doi: 10.3390/pharmaceutics15020484
    Darji MA, Lalge RM, Marathe SP, Mulay TD, Fatima T, Alshammari A, et al. Excipient stability in oral solid dosage forms: A review. *AAPS PharmSciTech* 2018;19(1):12-26. doi: 10.1208/s12249-017-0864-4
4. Jiang L, Sun Y, Lu A, Wang X, Shi Y. Ionic liquids: Promising approach for oral drug delivery. *Pharm Res* 2022;39(10):2353-65. doi: 10.1007/s11095-022-03260-8
5. Allen LV, Ansel HC,2013. Ansel's Pharmaceutical Dosage Forms and Drug Delivery Systems. 10th ed., New York, Lippincott Williams and Wilkins, Philadelphia, PA. pp. 2-781.
6. Strickley RG. Pediatric oral formulations: An updated review of commercially available pediatric oral formulations since 2007. *J Pharm Sci* 2019;108(4):1335-65. doi: 10.1016/j.xphs.2018.11.013
7. Janczura M, Sip S, Cielecka-Piontek J. The development of innovative dosage forms of the fixed-dose combination of active pharmaceutical ingredients. *Pharmaceutics* 2022;14(4):1-22. doi: 10.3390/pharmaceutics14040834
8. Sohail Arshad M, Zafar S, Yousef B, Alyassin Y, Ali R, AlAsiri A, et al. A review of emerging technologies enabling improved solid oral dosage form manufacturing and processing. *Adv Drug Deliv Rev* 2021;178:1-28. doi: 10.1016/j.addr.2021.113840
9. Gaikwad SS, Kshirsagar SJ. Review on tablet in tablet techniques. *Beni-Suef University Journal of Basic and Applied Sciences* 2020;9(1):1-7. doi: 10.1186/s43088-019-0027-7
10. Zou H, Jiang X, Kong L, Gao S. Design and gamma-scintigraphic evaluation of a floating and pulsatile drug delivery system based on an impermeable cylinder. *Chem Pharm Bull (Tokyo)* 2007;55(4):580-5. doi: 10.1248/cpb.55.580
11. Comoglu T, Dilek Ozyilmaz E. Orally disintegrating tablets and orally disintegrating mini tablets - novel dosage forms for pediatric use. *Pharm Dev Technol* 2019;24(7):902-14. doi: 10.1080/10837450.2019.1615090
12. Lopes CM, Lobo JM, Pinto JF, Costa P. Compressed mini-tablets as a biphasic delivery system. *Int J Pharm* 2006;323(1-2):93-100. doi: 10.1016/j.ijpharm.2006.05.063
13. Spomer N, Klingmann V, Stoltenberg I, Lerch C, Meissner T, Breitkreutz J. Acceptance of uncoated mini-tablets in young children: Results from a prospective exploratory cross-over study. *Arch Dis Child* 2012;97(3):283-6. doi: 10.1136/archdischild-2011-300958
14. Obara S, Quadir A, Kokubo H.,2016. Chapter-10 Application of HPMC and HPMCAS to Aqueous Polymeric Coatings for Pharmaceutical Dosage Forms. 4th ed., CRC Press,Taylor and Francis group, Boca Raton, pp. 247-284. DOI: https://doi.org/10.1201/9781315369938
15. Syed SM. Mini-tablet: A review. *Advances in Bioresearch* 2016;7:5-10. doi: 10.15515/abr.0976-4585.7.2.510
16. El-Zahaby SA, Kassem AA, El-Kamel AH. Design and evaluation of gastroretentive levofloxacin floating mini-tablets-in-capsule system for eradication of helicobacter pylori. *Saudi Pharmaceutical Journal* 2014;22(6):570-9. doi: https://doi.org/10.1016/j.jsps.2014.02.009
17. Tan YTF, Heng PWS, Wan LSC. Mixed polymer coating for modified release from coated spheroids. *Pharm Dev Technol* 1999;4(4):561-70. doi: 10.1081/pdt-100101395
18. Chauhan V, Global Institute of Pharmaceutical E, Research KUI. Fast dissolving tablets: A promising approach for drug delivery. *Univers J Pharm Res* 2017;2(4):58-64. doi: 10.22270/ujpr.v2i4.rw4
19. Priyanka P, Teotia D. A comprehensive review on pharmaceutical mini tablets. *Journal of Drug Delivery and Therapeutics* 2018;8:382-90. doi: 10.22270/jddt.v8i6.2060
20. Gowthami B, Krishna SVG, Rao DS. Formulation of tablets in capsule system: Statistical optimization for chronotherapeutic drug delivery of propranolol hydrochloride. *Journal of Drug Delivery Science and Technology* 2021;63:1-9. doi: https://doi.org/10.1016/j.jddst.2021.102398

Principal
Indore Institute of Pharmacy,
INDORE (M.P.)

102

Development and Optimization of Moxifloxacin-Loaded in-Situ Gel Using Box-Behnken Design for Ophthalmic Drug Delivery

Anjali Kumarawat[1]*, Nadeem A. Farooqui[2], Darshan Jamindar[3], Nimita Manocha[4]

Department of Pharmaceutics, Indore Institute of Pharmacy, Pithampur Road, Opp. IIM, Rau, Indore-453331(M.P.) India.

*Corresponding author- Anjali Kumarawat, Department of Pharmaceutics, Indore Institute of Pharmacy, Pithampur Road, Opp. IIM, Rau, Indore-453331(M.P.) India.

ABSTRACT:

Objective: This research aims to develop, optimize and characterize the sustained release *in situ* ocular gel containing moxifloxacin hydrochloride. **Material and Method:** Box-Behnken design was applied to optimize the formulation. The independent variables were (X_1) concentration of sodium alginate (%w/v), (X_2) concentration of carbopol 934 (%w/v) and (X_3) concentration of HPMC K100M (%w/v) while the (Y_1) drug release (%) was the dependent variable.

Evaluation: Further the optimized formulation was evaluated for appearance, pH, viscosity, gelling capacity, drug content estimation, sterility testing and spreadability of formulated gel.

Result: The optimized formula of moxifloxacin *in situ* gel containing sodium alginate (1.5 %w/v), Carbopol 934 (1%w/v) and HPMC K100M (0.625%w/v) was found to be clear, pH was found to be in range (6.8-7.4) and showed maximum drug release of 96.45% upto 8 hours. These results concluded that *in situ* gels can be used as an alternative of traditional eye drops.

Introduction

Ocular drug delivery is a challenging task for the pharmaceutical scientists because of the protective mechanism of eyes such as rapid precorneal elimination of drug, tear turnover and poor drug bioavailability.[1] Conventional drug delivery system such as eye drops shows poor ocular bioavailability (<5%). To overcome these factors, the designing of a novel approach for simple, safe, and effective drug delivery has been investigated.[2] Over the past decades several novel approaches have been developed among which *in-situ* gels has attained a great attention which were investigated by researchers to enhance retention time, bioavailability and therapeutic efficacy of the topically administered drugs.[3]

When the polymer chain is cross-linked, either chemically (chemical cross-linking) or non-covalently (physical cross-linking), the polymeric solution transforms into the gel. An additional mechanism known as physiologic stimuli are also responsible for the formulation of *in-situ* gel, these stimuli include those that are triggered by temperature and pH. [4] Numerous natural and synthetic polymers such as alginic acid, gellan gum, xanthum gum, xyloglucan, pectin, chitosan, poly (DL lactic acid), poly (DL-lactide-co-glycolide), and poly-caprolactone are employed in the formulation and development of *in-situ* gel drug delivery systems.[4]

The formulation adopted is a sodium alginate solution containing carbopol 934 and HPMC K 100 M (viscosity enhancer) which complexes with the Ca^{2+} ions present the lachrymal fluid. Free calcium ions interact with

1254

sodium alginate, leading to cross-linking of polymer chains and forming a matrix structure. Gelation involves the formation of double helical junction zones and reassembly of helical segments, creating a three-dimensional network via cation complexation and hydrogen bonding with water.

Moxifloxacin acts as an antibacterial agent by targeting and inhibiting the functions of DNA gyrase (also known as topoisomerase II) and topoisomerase IV. These enzymes are crucial for bacterial DNA processes, including replication, translation, repair, and recombination. By binding to these enzymes, Moxifloxacin disrupts the survival mechanisms of bacteria, making it an effective concentration-dependent, bactericidal anti-infective medication.[6]

Materials and Methods

Materials

Moxifloxacin Hydrochloride was obtained from MSN Pharmachem Private Limited, Hyderabad as a gift sample. Sodium alginate was procured from Sisco Research Laboratory Pvt. Ltd. Maharashtra. Carbopol 934 was purchased from Loba Chemie Pvt Ltd. Mumbai. HPMC K100M was procured from Chemdyes Corporation, Rajkot Gujarat. Other ingredients and reagents were used of analytical grade.

Methods

Drug-Polymer Compatibility Studies

Fourier Transform Infrared Spectroscopy (FTIR)

The FTIR spectra for moxifloxacin hydrochloride in its pure form alongside a mixture containing moxifloxacin hydrochloride, carbopol 934, and HPMC K100M were recorded with the use of an FTIR Spectrophotometer. To evaluate the physicochemical interactions between the drug and its excipients, analysis through FTIR was conducted utilizing the Potassium bromide disk technique.[7]

Method of Preparation of *In-situ* Gel

The composition of *in-situ* gel containing moxifloxacin hydrochloride was prepared by employing Box-Behnken design presented in Table 2. To prepare these formulations, Sodium alginate combined with Carbopol® 934 and HPMC K100M was utilized using the dispersion method. Initially, 75 ml of distilled water was preheated to 70°C to dissolve sodium alginate, followed by the addition of HPMC K100M, and Carbopol® 934 into the solution. This mixture was left at room temperature overnight to allow for polymer hydration. Separately, moxifloxacin hydrochloride (0.5%w/v) was dissolved in 25 mL of distilled water and then added to the polymeric solution. The mixture was stirred until a uniform solution was achieved. The final product was then filled into sterile amber-colored bottles and sterilized in an autoclave at 121°C for 15 minutes. Subsequently, the prepared formulations were stored in a refrigerator at 4°C until further use.[6],[8]

Formula Optimization using Design Expert Software

Computer-aided modeling-

Box–Behnken statistical design with 3-factors, 3-levels, and 15 runs was implemented for the optimization study using Design-Expert software (version 13). Concentration of sodium alginate (%w/v) (X1), concentration of carbopol 934 (%w/v) (X2) and Concentration of HPMC K100M (%w/v) (X3) were selected as independent variables and they were set at low, medium and high levels. Table no.1 summarizes the coded values of different variables. In accordance with the design, 15 *in-situ* gel formulations were prepared and characterized for *in-vitro* % drug release (Y1) which was chosen as response parameter. This design explains the main effects and interaction effects of the independent variables on the formulation characteristics. The objective function for the present study was to enhance the retention time of the formulation and sustained drug release of the product.

$$Y1 = b_0 + A - B - C$$
(Equation 1)

Where, b_0 is arithmetic mean response of 15 runs. A, B, and C are the independent variables.

Table1. Levels and Constrains of Independent and Dependent Variables

Levels and Constrains of Independent and Dependent Variables				
Independent Variables	Levels			Constrains
	Low (-1)	Medium (0)	High (+1)	
A: Concentration of Sodium Alginate	0.5	1	1.5	
B: Concentration of Carbopol 934	0.25	0.625	1	
C: Concentration of HPMC K100M	0.25	0.625	1	
Dependent Variables	Drug Release upto 8 hours (%)			>95%

Data analysis and validation of model

Box–Behnken design was particularly selected, because it needs fewer runs than a central composite design, in cases of three or four variables. Analysis of variance (ANOVA) was used to establish the statistical validation of the polynomial equations generated by Design Expert software. All the responses observed were simultaneously fitted to linear (first order), and quadratic models. Various feasibilities were conducted over the experimental domain to find the compositions of the optimized *in-situ* gel formulation. 2D and 3D response surface plots (fig.4 and fig.5) were generated by the Design Expert software. The resultant experimental values of the responses were quantitatively compared to that of the predicted values.[9]

Characterization of Moxifloxacin loaded *in-situ* gel

1. Physical Appearance

The formulated *in-situ* gel solutions were tested for clarity by visual appearance against black and white background in bright light. The pH of the prepared in-situ gel was measured by digital pH meter (Labtech DPH-115 PM, Chennai).[10]

2. Gelling Capacity

The ability of the formulation to form a gel was evaluated by adding several drops of it into a vial with 2 ml of simulated tear fluid, freshly prepared and with a pH of 7.4. Observation was made visually to determine the duration needed for gel formation.[11]

3. Rheological Studies

The viscosity estimation was carried out using Brookfield viscometer (DV-E, USA model). The *in-situ* gel formulations were placed in a beaker. The samples were analyzed at 27°C. Spindle number 61 was dropped perpendicularly into the solution in a beaker. The angular velocity of the spindle was increased from 10 rpm to 30 rpm and the rheological behaviour of the formulation was noted at the end of 30 seconds.[12]

4. Spreadability

To determine the spread ability of in-situ gel, transfer 1g of gel to the centre of a glass plate (10cm × 10cm) at 32 ± 0.5°C and cover this plate by another glass plate of same size. Apply some weight (125g) on the upper slide to evenly spread the gel. After one minute remove the weight and measure the diameter of the gel spread area (cm). Perform this determination test in triplicates. The mathematical formula expressed as:

$$S = M \times L / T$$

Where S is spreadability, M is weight tied to the upper glass slide, L is length of the glass slide and T is time taken to spread the gel.[13]

5. Drug Content Estimation

The % drug content estimation was carried out by diluting prepared formulation equivalent to 50mg in 50 ml of distilled water and analyzed after further dilution

1256

Principal
Indore Institute of Pharmacy,
INDORE (M.P.)

105

using UV-visible spectrophotometer (Shimadzu UV-1800, Shimadzu Corporation, Japan) at 289 nm. The experiment was performed in triplicates.[14]

6. *In-vitro* Dissolution Studies

The in vitro release of moxifloxacin hydrochloride from the formulated preparation was investigated using a Franz diffusion cell apparatus, comprising two compartments: a donor compartment and an acceptor compartment. The acceptor compartment was filled with freshly prepared simulated tear fluid (pH 7.4), maintained at a temperature of 37°C±1°C with continuous stirring using a magnetic stirrer. Subsequently, the donor compartment, containing a cellophane membrane soaked overnight, was securely attached to the acceptor compartment. A 2 ml volume of the prepared solution was then added to the donor compartment. At predetermined time intervals, 1 ml aliquots were withdrawn from the acceptor compartment and replaced with fresh simulated tear fluid. All samples were collected in triplicate. The amount of drug released was quantified using a UV-visible spectrophotometer at 289 nm, with simulated tear fluid at pH 7.4 serving as the blank control.[15]

7. Sterility Test

To ensure the sterility of ocular products, it is essential to conduct sterility testing. In this process, the chosen formulation is transferred into a sterile fluid thioglycolate medium under aseptic conditions. The mixture is then incubated for a minimum of 14 days at 35°C to monitor bacterial growth. Sterility is assessed by visually inspecting the clarity of the medium over the 14-day period.[16]

Result and Discussion

Drug-Polymer Compatibility Studies

Fourier Transform Infrared Spectroscopy (FTIR)

An infrared analysis was conducted to investigate potential interactions between the pure drug and additives. Figure 1 depicts the FTIR spectra of moxifloxacin hydrochloride along with physical mixture.

The spectra of pure moxifloxacin hydrochloride (MH) displayed distinct peaks, including C=O stretching vibrations at 1710 cm^{-1}, N-H stretching vibrations at 2928 cm^{-1}, and O-H stretching vibration at 3527 cm^{-1}. In FTIR spectra of physical mixture, primary absorption bands of moxifloxacin hydrochloride were evident, showing no notable alterations compared to pure drug spectrum. This observation indicates no apparent interaction between the drug and polymers.
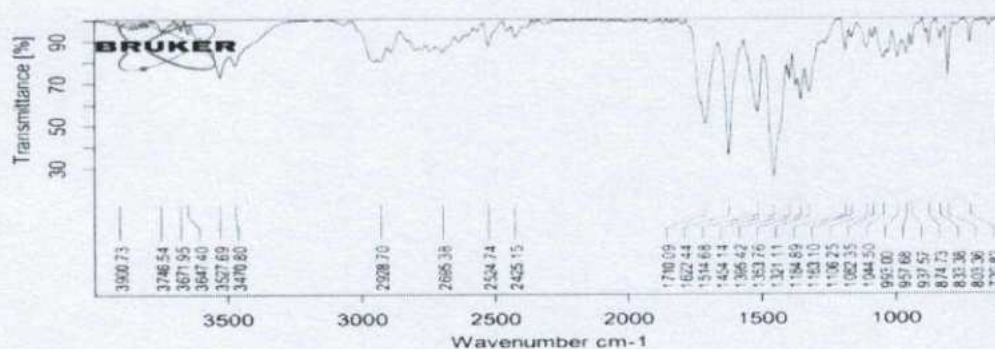

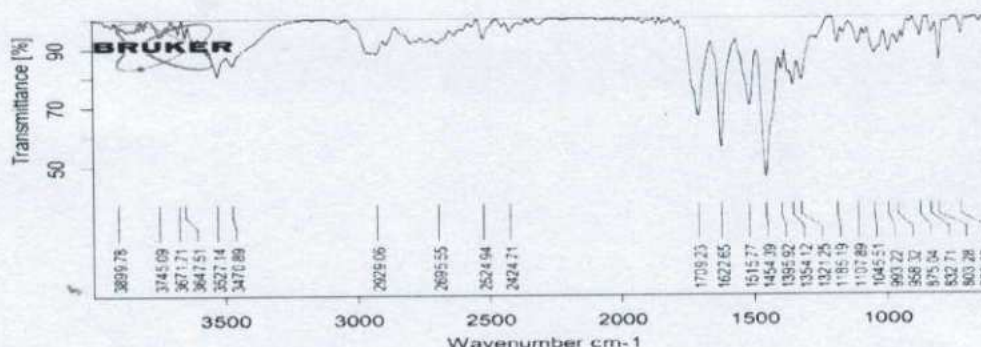Fig.1 FTIR spectra of pure moxifloxacin hydrochloride (API)

Fig.2 FTIR spectra of physical mixture of moxifloxacin hydrochloride and polymers

Formula Optimization using Design Expert Software

Box–Behnken statistical design with 3-factors, 3-levels, and 15 runs was employed for the optimization study using the Design Expert software (version 13). In accordance with the design, 15 *in-situ* gel formulations were prepared and characterized for *in-vitro* % drug release (Y1) which was chosen as response parameter. (Table 2)

Table 2. Experimental run by design expert software

Std	Run	Factor 1 A:Concentration of Sodium Alginate	Factor 2 B:Concentration of Carbopol 934	Factor 3 C:Concentration of HPMC K100M	Response 1 Drug Release upto 8 hours
		%w/v	%w/v	%w/v	%
1	1	0.5	0.25	0.625	78.67
15	2	1	0.625	0.625	85.94
9	3	1	0.25	0.25	82.74
13	4	1	0.625	0.625	87.01
12	5	1	1	1	89.54
3	6	0.5	1	0.625	80.02
4	7	1.5	1	0.625	96.45
11	8	1	0.25	1	85.26
14	9	1	0.625	0.625	85.71
5	10	0.5	0.625	0.25	77.63
10	11	1	1	0.25	88.35
2	12	1.5	0.25	0.625	93.54
7	13	0.5	0.625	1	80.92
6	14	1.5	0.625	0.25	94.32
8	15	1.5	0.625	1	95.02

1258

Data Analysis and Optimization

Response Y1: Drug Release upto 8 hours

The high value of the correlation coefficient indicates a good fit between the independent variables, and the dependent variable. The linear model was found to be significant as shown in (Table 3) and the P value is less than < 0.05. This result clearly demonstrates that this selected independent variable have a statistically significant influence on the drug release.[17]

Table 3. Analysis of Variance (ANOVA for Linear model)

Source	Sum of Squares	Degree of Freedom	Mean Square	F-value	p-value	
Model	514.34	3	171.45	193.47	< 0.0001	significant
A-Concentration of Sodium Alginate	481.90	1	481.90	543.79	< 0.0001	
B-Concentration of Carbopol 934	25.03	1	25.03	28.24	0.0002	
C-Concentration of HPMC K100M	7.41	1	7.41	8.36	0.0147	
Residual	9.75	11	0.8862			
Lack of Fit	8.79	9	0.9761	2.03	0.3737	not significant
Pure Error	0.9626	2	0.4813			
Cor Total	524.08	14				

The Model F-value of 193.47 implies the model is significant. There is only a 0.01% chance that an F-value this large could occur due to noise.

P-values less than 0.0500 indicate model terms are significant. In this case A, B, and C are significant model terms. Values greater than 0.1000 indicate the model terms are not significant. If there are many insignificant model terms (not counting those required to support hierarchy), model reduction may improve your model.

The Lack of Fit F-value of 2.03 implies the Lack of Fit is not significant relative to the pure error. There is a 37.37% chance that a Lack of Fit F-value this large could occur due to noise. Non-significant lack of fit is good -- we want the model to fit.

Table 4. Showing Fit Statistics of linear model (ANOVA)

Fit Statistics of linear model (ANOVA)			
Std. Dev.	0.9414	R²	0.9814
Mean	86.74	Adjusted R²	0.9763
C.V. %	1.09	Predicted R²	0.9635
		Adeq Precision	39.2084

The Predicted R² of 0.9635 is in reasonable agreement with the Adjusted R² of 0.9763; i.e. the difference is less than 0.2.

1259

Adeq Precision measures the signal to noise ratio. A ratio greater than 4 is desirable. Your ratio of 39.208 indicates an adequate signal. This model can be used to navigate the design space.

Final Equation in Terms of Actual Factors

Drug release $(Y1) = 66.66675 + 15.52250*A + 4.71667*B + 2.56667*C$

The design expert software suggested that 1.49% of sodium alginate, 0.85% of carbopol 934 and 0.983% of HPMC K100 shows optimum drug release upto 8 hours. All response graphs showing desirability and drug release at different independent variables are shown in figure 3. Contour plot and three dimensional response surface plot of optimized formulation as shown in figure 4 and 5 respectively shows the interaction effects of the factors on response. When the experimental data of response (Y1) of 15 runs was fitted into different models of Box-Behnken design. linear model was found to be best fitted model.
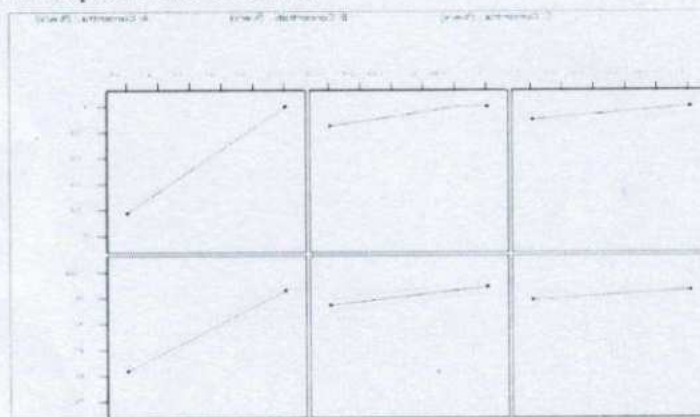
Fig.3 All response graphs showing desirability and drug release at different independent variables
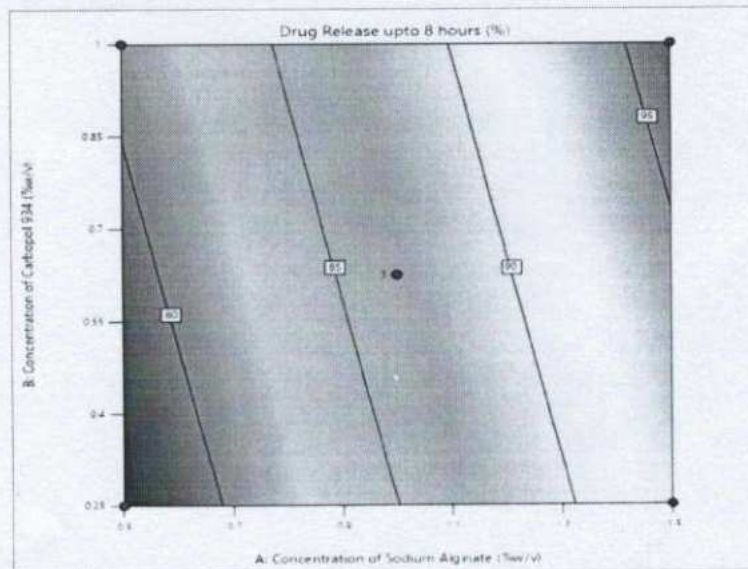
Fig.4 The Contour plot for Y_1 (% Drug release upto 8 hours)

Principal
Indore Institute of Pharmacy,
INDORE (M.P.)

109
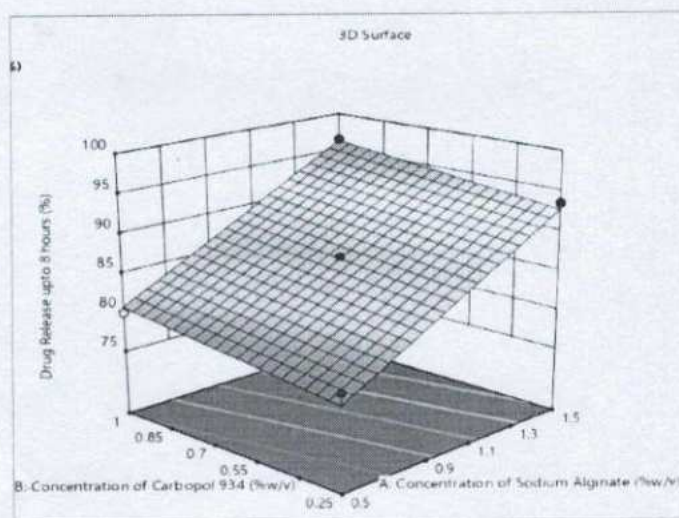
Fig.5 The 3D response surface plot showing effect of independent variable on Y_1 (% Drug release upto 8 hours)

Evaluation of *in-situ* gel

Physical Parameter

The optimized prepared formulation of *in-situ* gel (F7) was found to be transparent and clear. The pH of the formulation was found to be in range between 6.8 and 7.4 when noted in triplicates (n=3).

Gelling capacity

Stiff gel of optimized formula F7 is formed immediately and remained for extended period of time (more than 8 hours).

Rheological studies

Viscosity of the ophthalmic *in-situ gel* is an important parameter to determine the residence period of drug into the eyes. The viscosity of polymeric solution was found to be 580cp±0.84 before conversion into gel and the viscosity of *in-situ gel* was found to be 1450cp±0.57 after becoming the gel which comes under the preferred range.

Spreadability

The spreadability of optimized *in situ* gel was found to be 13.95±0.43 g.cm/sec which was in the acceptable range. Spreadability is inversely proportional to viscosity. Increase in concentration of any polymer can decrease the spreadability of the formulation.

Drug content

The drug content of optimized *in situ* gel was analyzed in triplicates by UV-Visible spectrophotometer (Shimadzu UV-1800, Shimadzu Corporation, Japan) at 289nm and the drug content was found to be 97.47±0.2 %.

In-vitro dissolution studies

This study was performed by Franz diffusion cell for 8 hours. By this study it was concluded that an increase in the concentration of polymers shows the release retarding property of the polymer.

Table 5. *In-vitro* drug release studies of optimized batch

S.No.	Time (hours)	% Drug Release		
		F7 (Optimized)	F14	F15
1	0	0	0	0
2	1	3.62±0.02	3.16±0.15	3.46±0.05

Principal
Indore Institute of Pharmacy,
INDORE (M.P.)

110

3	2	20.52±0.32	16.41±0.81	14.6±0.12
4	3	34.78±0.45	33.28±0.32	31.77±0.67
5	4	48.22±0.27	42.92±0.25	40.51±0.82
6	5	67.74±0.32	58.89±0.41	56.78±0.16
7	6	78.09±0.12	70.93±0.23	68.52±0.90
8	7	83.59±0.83	82.08±0.68	80.57±0.24
9	8	96.45±0.91	95.03±0.24	94.31±0.54
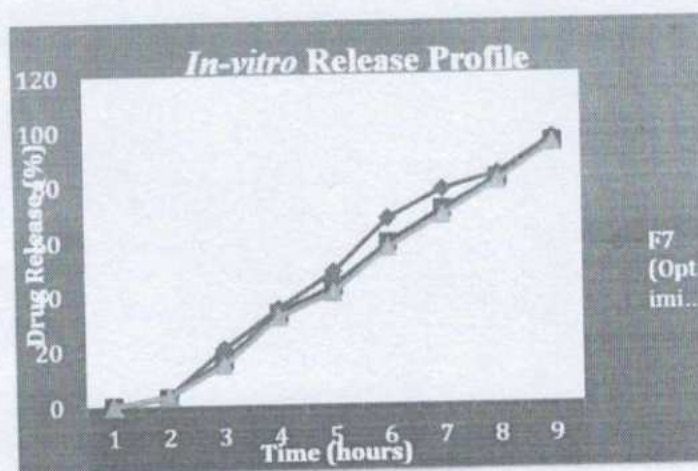
Fig.6 *In vitro* release profile of optimized moxifloxacin hydrochloride *in-situ* gel (F7, F14 and F15)

Data Analysis via Drug release Kinetics Studies

The formulation of moxifloxacin *in-situ* gel was subjected to drug release studies using Franz Diffusion Cell apparatus containing simulated tear fluid (pH 7.4) and cellophane membrane. The fitting of drug dissolution profile against kinetics models were analyzed using Microsoft Excel. It was observed that the optimized batch F7 followed First Order Release Kinetics as the plot showed linearity.
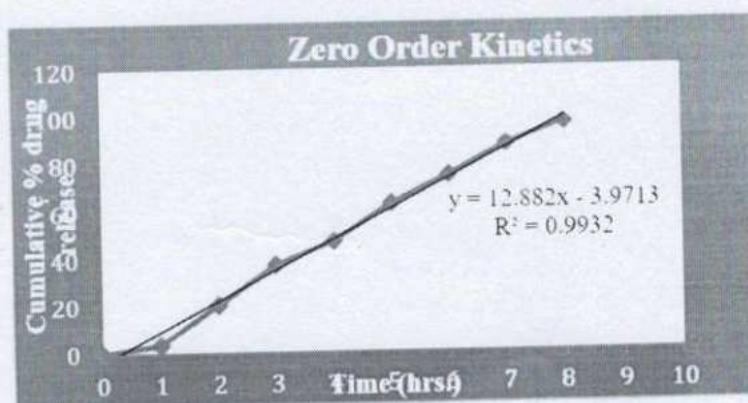
Fig.7 Zero Order Release Kinetics of Optimized formulation (F7)

1262

111

Sterility Test

To ensure the sterility of ocular products, it is essential to conduct sterility testing. In this process, the chosen formulation F7 was transferred into a sterile fluid thioglycolate medium under aseptic conditions. The mixture was then incubated for a minimum of 14 days at 35°C to monitor bacterial growth. Sterility was assessed by visually inspecting the clarity of the medium over the 14-day period.
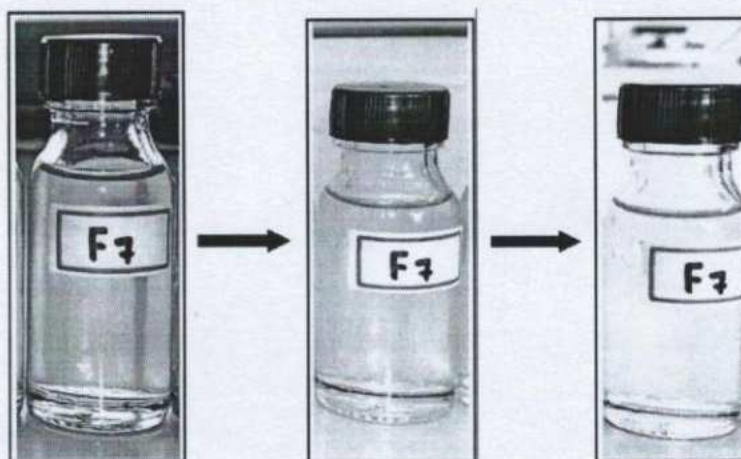
Fig.7 Sterility testing of optimized formulation F7 from day 1 to day 14.

Conclusion

The present study demonstrate that the optimized *in-situ* gel of moxifloxacin hydrochloride was prepared successfully using sodium alginate, carbopol 934 and HPMC K100M for ophthalmic drug delivery that showed sustained drug release for more than 8 hours and enhanced retention time. Certainly Commercialization of a dosage form requires both preclinical and clinical studies. To optimize an in situ ophthalmic gel, a Box-Behnken design was employed. The optimization analysis determined that a batch comprising 1.5%w/v sodium alginate, 1%w/v carbopol 934 and 0.625% HPMC K100M exhibited the longest residence time and improved efficacy. On the basis of all evaluation parameters it was concluded that ophthalmic *in-situ* gel shows potential as a promising delivery system for ophthalmic drugs, offering enhanced bioavailability.

Acknowledgement

Conflict Of Interest

The authors declare no conflict of interest.

Reference

1. Gaudana, R.; Jwala, J.; Boddu, S. H. S.; Mitra, A. K. Recent Perspectives in Ocular Drug Delivery. *Pharm. Res.* **2009,** *26* (5), 1197.

2. Araújo, J.; Gonzalez, E.; Egea, M. A.; Garcia, M. L.; Souto, E. B. Nanomedicines for Ocular NSAIDs: Safety on Drug Delivery. *Nanomedicine Nanotechnol. Biol. Med.* **2009,** *5* (4), 394–401.

3. Paul, S.; Majumdar, S.; Chakraborty, M. Revolutionizing Ocular Drug Delivery: Recent Advancements in in Situ Gel Technology. *Bull. Natl. Res. Cent.* **2023,** *47* (1), 154.

4. Vigani, B.; Rossi, S.; Sandri, G.; Bonferoni, M. C.; Caramella, C. M.; Ferrari, F. Recent Advances in the Development of In Situ Gelling Drug Delivery Systems for Non-Parenteral Administration Routes. *Pharmaceutics* **2020,** *12* (9), 859.

5. Sabale, A. S.; Kulkarni, A. D.; Sabale, A. S. Nasal In Situ Gel: Novel Approach for Nasal Drug

1263

Principal
Indore Institute of Pharmacy,
INDORE (M.P.)

Delivery. *J. Drug Deliv. Ther.* **2020**, *10* (2-s), 183–197.

6. Dholakia, M.; Dave, R.; Thakkar, V.; Rana, H.; Gohel, M.; Patel, N. Newer Ophthalmic In Situ Gel Of Moxifloxacin Hydrochloride: Optimization Using Box Behnken Statistical Design. *Int. J. Pharm. Pharm. Sci.* **2018**, *10* (12), 5.

7. Kalaria, V. J.; Saisivam, S.; Alshishani, A.; Aljariri Alhesan, J. S.; Chakraborty, S.; Rahamathulla, M. Design and Evaluation of *in Situ* Gel Eye Drops Containing Nanoparticles of Gemifloxacin Mesylate. *Drug Deliv.* **2023**, *30* (1), 2185180.

8. Mandal, S.; Prabhushankar, G.; Thimmasetty, M.; Geetha, M. Formulation and Evaluation of an in-situ Gel-Forming Ophthalmic Formulation of Moxifloxacin Hydrochloride. *Int. J. Pharm. Investig.* **2012**, *2* (2), 78.

9. Baig, M. S.; Ahad, A.; Aslam, M.; Imam, S. S.; Aqil, Mohd.; Ali, A. Application of Box–Behnken Design for Preparation of Levofloxacin-Loaded Stearic Acid Solid Lipid Nanoparticles for Ocular Delivery: Optimization, in Vitro Release, Ocular Tolerance, and Antibacterial Activity. *Int. J. Biol. Macromol.* **2016**, *85*, 258–270.

10. Jain, D.; Kumar, V.; Singh, S.; Mullertz, A.; Shalom, D. B. Newer Trends in In Situ Gelling Systems for Controlled Ocular Drug Delivery. *J. Anal. Pharm. Res.* **2016**, *2* (3), 98–111.

11. Kaur, H.; Loyee, S. L.; Garg, R. Formulation and Evaluation of In-Situ Ocular Gel of Gatifloxacin. *Int. J. Pharma Res. Health Sci.* **2016**, *4* (5), 1365–1370.

12. Kondepati, H. V.; Kulyadi, G. P.; Tippavajhala, V. K. A Review on In Situ Gel Forming Ophthalmic Drug Delivery Systems. *Res. J. Pharm. Technol.* **2018**, *11* (1), 380.

13. Chaudhary, B.; Verma, S. Preparation and Evaluation of Novel *In Situ* Gels Containing Acyclovir for the Treatment of Oral Herpes Simplex Virus Infections. *Sci. World J.* **2014**, *2014*, 1–7.

14. Kolawole, O. M.; Cook, M. T. In Situ Gelling Drug Delivery Systems for Topical Drug Delivery. *Eur. J. Pharm. Biopharm.* **2023**, *184*, 36–49.

15. Makwana, S. B.; Patel, V. A.; Parmar, S. J. Development and Characterization of In-Situ Gel for Ophthalmic Formulation Containing Ciprofloxacin Hydrochloride. *Results Pharma Sci.* **2016**, *6*, 1-6.

16. Sheshala, R.; Ming, N. J.; Kok, Y. Y.; Raj Singh, T. R.; Dua, K. Formulation and Characterization of pH Induced in Situ Gels Containing Sulfacetamide Sodium for Ocular Drug Delivery: A Combination of Carbopol® HPMC Polymer. *Indian J. Pharm. Educ. Res.* **2019**, *53* (4), 654–662.

17. Fukuda, I. M.; Pinto, C. F. F.; Moreira, C. D. S.; Saviano, A. M.; Lourenço, F. R. Design of Experiments (DoE) Applied to Pharmaceutical and Analytical Quality by Design (QbD). *Braz. J. Pharm. Sci.* **2018**, *54*.

Figure Legends

Fig.1 FTIR spectra of pure moxifloxacin hydrochloride (API)

Fig.2 FTIR spectra of physical mixture of moxifloxacin hydrochloride and polymers

Fig.3 All response graphs showing desirability and Drug release at different independent variables

Fig.4 The response Contour plot for Y_1 (% Drug release upto 8 hours)

Fig.5 The response Contour plot for Y_1 (% Drug release upto 8 hours)

Fig.6 *In vitro* release profile of optimized moxifloxacin hydrochloride *in-situ* gel (F7, F14 and F15)

Fig.7 Zero Order Release Kinetics of Optimized formulation (F7)

Fig.8 Sterility testing of optimized formulation F7 from day 1 to day 14.

Table Legends

Table1. Levels and Constrains of Independent and Dependent Variables

Table 2. Experimental run by design expert software

Table 3. Analysis of Variance (ANOVA for Linear model)

Table 4. Showing Fit Statistics of linear model (ANOVA)

Table 5. *In-vitro* drug release studies of optimized batch

Principal
Indore Institute of Pharmacy,
INDORE (M.P.)

Table 1 Neurological diseases: pathogenesis, genetic basis, disease mechanism and manifestations

Alzheimer's disease (AD) is a chronic and progressive neurodegenerative disorder that predominantly distorts the human brain's vast cerebral cortex and hippocampus regions. The disease is characterized by a range of symptoms, including mental and memory impairments, cognitive decline, and personality changes, and it predominantly affects the elderly population, especially in patients above 65 years [36]. It is distinguished by two key neuropathological features i.e., (i) intracellular accretion of hyperphosphorylated tau- proteins, which form NFTs in the brain, and (ii) extracellular development and deposition of amyloid-beta (Aβ) plaques [3]. Parkinson's disease (PD) is another most common NDs that significantly impair the eminence of life and dependency and increase the menace of premature death in affected individuals [11, 16]. This disease is instigated via substantial damage to dopaminergic nigrostriatal neurons, leading to reduced motor function and induced symptoms i.e., bradykinesia, resting tremor, postural imbalance, and muscular rigidity. PD are distinguished by the accretion of protein aggregates, Lewy neurites, and Lewy bodies, primarily composed of aggregated and misfolded forms of pre-synaptic protein α-synuclein [42]. Amyotrophic lateral sclerosis (ALS) is a devastating ND characterized by substantial degeneration and demise of both lower and upper motor neurons,

Principal
Indore Institute of Pharmacy,
INDORE (M.P.)

114

Nutrition & Metabolism

Home   About   Articles   Submission Guidelines   Submit manuscript

Download PDF   Download ePub ↓

Natural products in the management of neurodegenerative diseases

Rajat Goyal, Pooja Mittal, Rupesh K. Gautam ✉, Mohammad Amjad Kamal, Asma Perveen, Vandana Garg, Athanasios Alexiou, Muhammad Saboor, Shafiul Haque, Aisha Farhana, Marios Papadakis ✉ & Ghulam Md Ashraf ✉

Nutrition & Metabolism 21, Article number: 26 (2024)

Abstract

Neurodegenerative diseases represent one of the utmost imperative well-being health issues and apprehensions due to their escalating incidence of mortality. Natural derivatives are more efficacious in various preclinical models of neurodegenerative illnesses. These natural compounds include phytoconstituents in herbs, vegetables, fruits, nuts, and marine and freshwater flora, with remarkable efficacy in mitigating neurodegeneration and

115

enhancing cognitive abilities in preclinical models. According to the latest research, the therapeutic activity of natural substances can be increased by adding phytoconstituents in nanocarriers such as nanoparticles, nanogels, and nanostructured lipid carriers. They can enhance the stability and specificity of the bioactive compounds to a more considerable extent. Nanotechnology can also provide targeting, enhancing their specificity to the respective site of action. In light of these findings, this article discusses the biological and therapeutic potential of natural products and their bioactive derivatives to exert neuroprotective effects and some clinical studies assessing their translational potential to treat neurodegenerative disorders.

Graphical Abstract

Common mechanisms, therapeutic targets, and molecular pathogenesis of neurodegeneration. It is focused on the biological and therapeutic potential of natural products and their bioactive derivatives to exert a neuroprotective effect on the pathologies of neurodegenerative diseases.

Principal
Indore Institute of Pharmacy,
INDORE (M.P.)

116
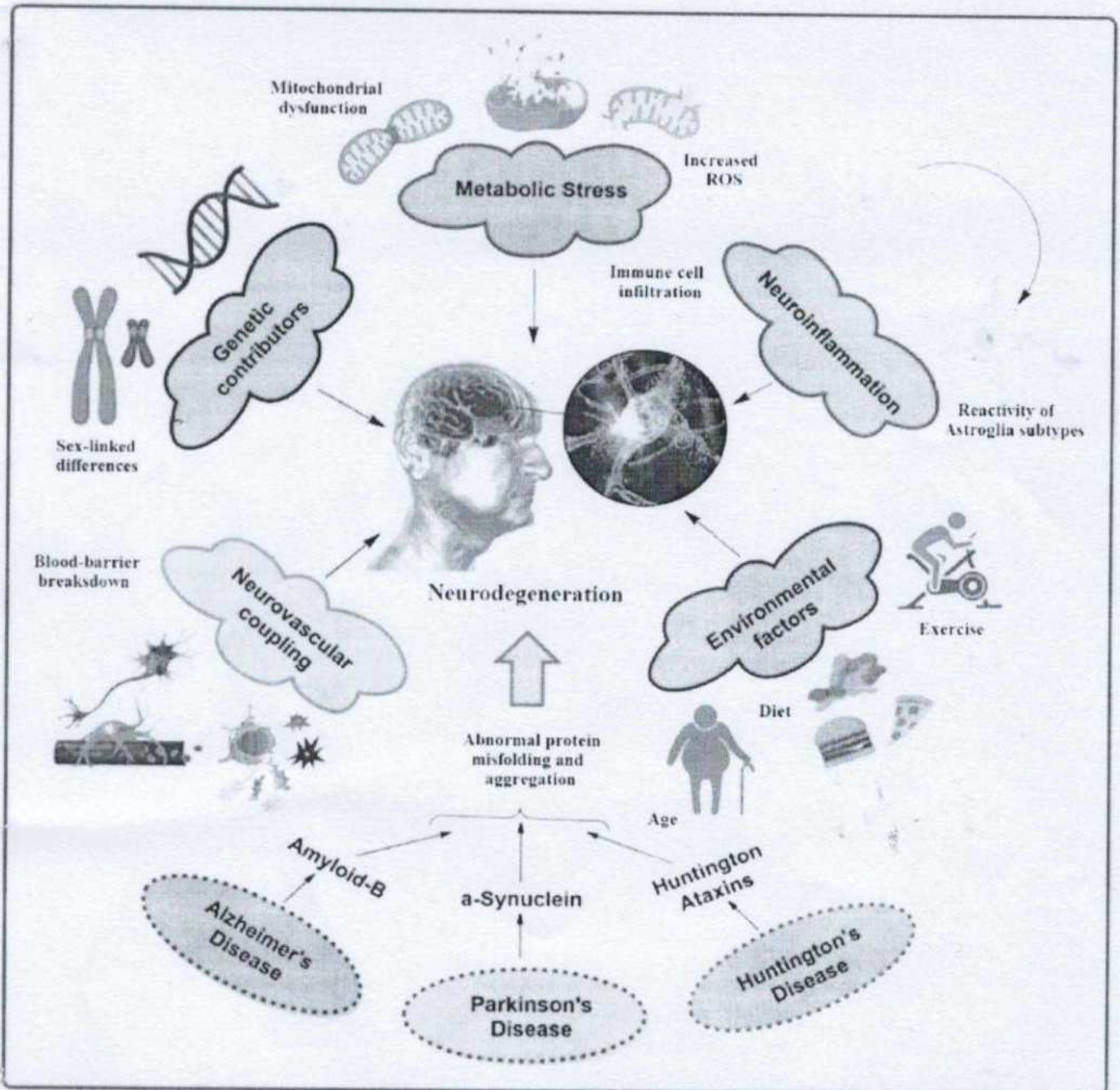
Introduction

Neurodegenerative diseases (NDs), comprising a diverse array of disorders, are typified by the progressive degeneration of both the structural and functional components of either the central nervous system (CNS) or peripheral nervous system (PNS). Among the most prevalent of these maladies are Alzheimer's disease (AD), Parkinson's disease (PD),

Principal
Indore Institute of Pharmacy,
INDORE (M.P.)

117
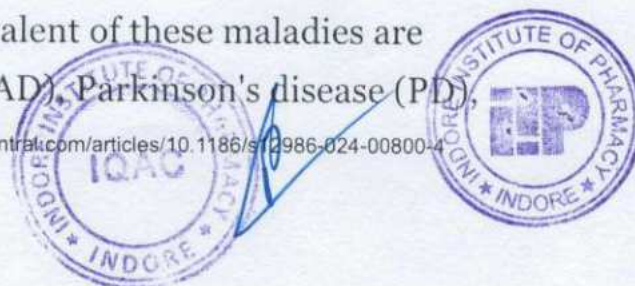
and spinal cord injury, which typically afflict individuals beyond the age of 60 years [57]. These debilitating conditions engender a prodigious burden on individuals and society, as the progressive loss of structural features and functions marks them. However, the root causes of several NDs remain obscure within the current healthcare system [41]. These NDs often present with a range of biological phenomena, including neuroinflammation, oxidative stress, cognitive decline, the accumulation of neurofibrillary tangles (NFTs), abnormal deposition of amyloid-β peptide (Aβ), diminution, or inadequate amalgamation of neurotransmitters and abnormal ubiquitination are linked to the progression of NDs [43]. Nevertheless, the role of aging in NDs is crucial, given their irreversible nature, the attendant social and economic burdens, and the paucity of efficacious therapeutic interventions [9].

Acute neurodegeneration is a clinical condition characterized by rapid damage resulting from abrupt insult or traumatic events, i.e., strokes, traumatic brain injuries, head injuries, ischemic brain damage, subarachnoid, or cerebral hemorrhage. Conversely, chronic neurodegeneration represents a protracted ailment in which neurons undergo a neurodegenerative process that typically commences gradually and exacerbates progressively due to various aspects, ultimately causing the irreversible devastation of specific neuron populations. Chronic neurodegenerative disorders comprise a variety of conditions, including ADs, PDs, Huntington's disease (HD), and amyotrophic lateral sclerosis (ALS) [42]. Other neurological disorders, such as spinal muscular

118

atrophy, Cockayne's syndrome, Coffin-lowry
syndrome, Triple-A syndrome, and Rett syndrome,
also fall within the purview of chronic NDs [35],
described in Fig. 1 and summarized in Table 1.

Fig. 1
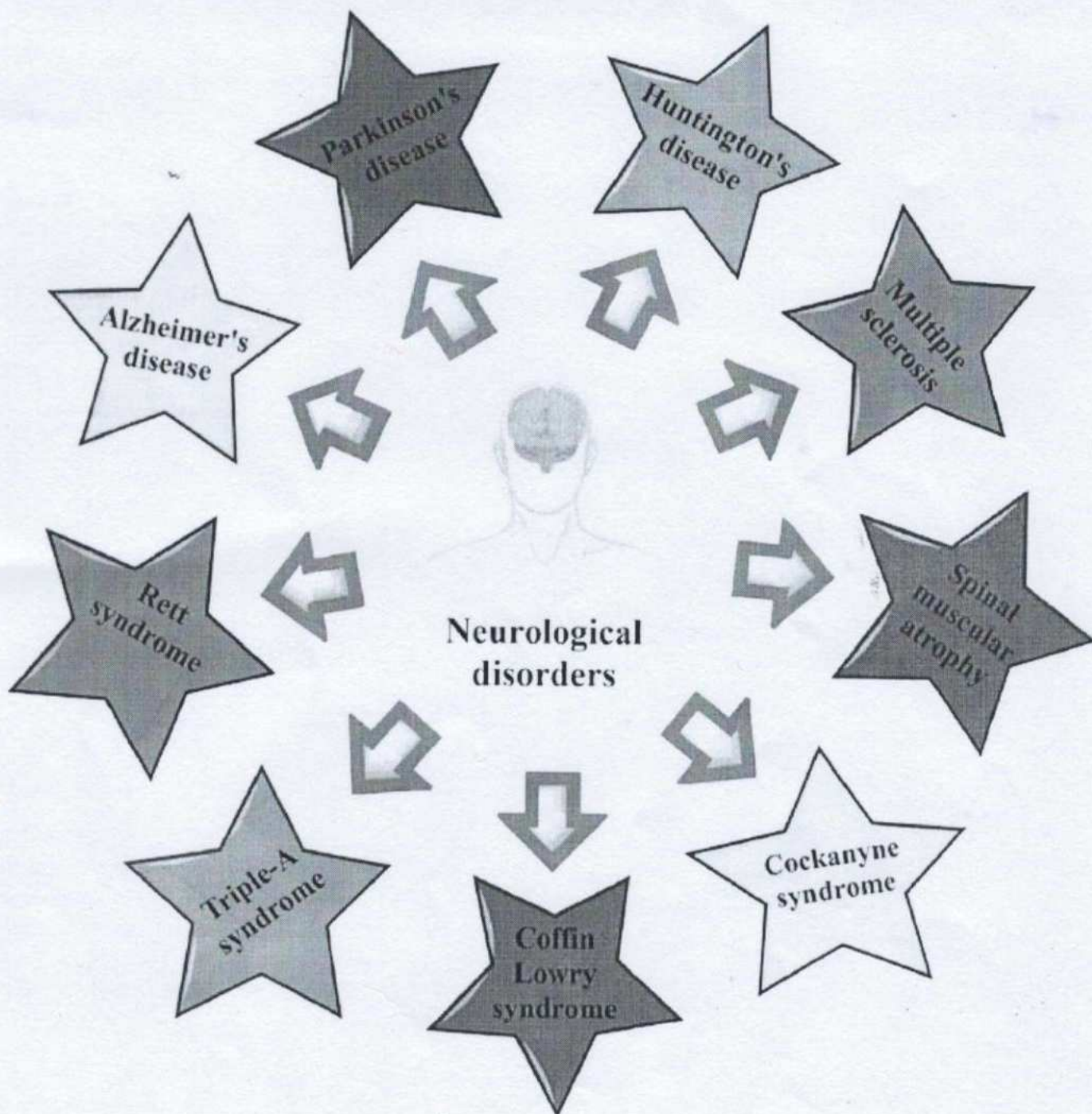
Neurological disorders

119

dosage forms: a review", Int. Research Journal of pharmacy; 2012, 3(4).

[20] Sharad K, Chethan T P , Kavya , Abhishek Singh, Rishu Yadav, Lax-mi Yadav, Samruddhi Phansekar, Shailendra Gupta, Shubham Yadav "process validation of azifast tablet", Journal of Advances in Pharmacy and Healthcare Research; 2011, 1(2).

[21] Alka N Choudhary, Tanya Sehgal, "A review on pharmaceutical validation and its implications", Journal of medical pharmaceutical and allied sciences, Volume 10 - Issue 6, 1927, 2021, Page – 3951-3959.

[22] Ketaki S. Shinde, Dr. R. C. Doijad1, Dr. J. S. Mulla1 and Sachin S. Mali, "Basic Aspects of Pharmaceutical Process Vali-dation of Solid Dosage Forms: Quality Assurance Point Of View", European Journal of Pharmaceutical and Medical Re-search, Vol 9, Issue 3, 2022

[23] Tushar Humbe, Tushar Kale, Dhairyasheel Gund, Vijaya Barge, Amit Kasbe, "Review Article on Process Validation and Its Types and Theoretical Approaches", international Journal of Pharmacy and Pharmaceutical Research, 2021; Vol. 21 (3): 544-557.

[24] Importance of Validation Qualification In Pharmaceutical Industries; url-https://www.researchgate.net publication 304 038382_Importance_Of_Validation_Qualificat ion_In_Pharmaceutical_Industries.

[25] Validation and Qualification in Pharma Facilities url-https://www.pharmamanufacturing.com articl es 2016 validation-and-qualification-in-pharma-facilities

Principal
Indore Institute of Pharmacy,
INDORE (M.P.)

120

Pharmaceutical Research Scholars (IJPRS) V-3, I-3, 2014 ISSN No: 2277 – 7873

[2] Singh Asheesh, Singour Pradeep, Singh Parul Computer system vali-dation in the perspective of the pharmaceutical industry Journal of Drug Delivery and Therapeutics 2018; 8(6-s):359-365 ISSN: 2250-1177

[3] Swarupa Vijay Jadhav, Swamini Subhash Wagchaure , Dr. S. Z. Che-mate3 . International Journal of Creative Research Thoughts (IJCRT) Volume 9, Issue 6 June 2021 | ISSN: 2320-2882

[4] Raul S., Padhy G., Mahapatra A., Alekha Charan S.; An Overview of concept of Pharmaceutical Validation Research Journal of Pharmacy and Technology.2014; 7(9): 1081- 1090.

[5] Mohankumar M., Sivakamasundari G.; A Review on Pharmaceutical Validation and Its Importance and Imputation. International Research Journal of Pharmacy. 2021; 12 (10): 23-26.

[6] Telange D.; Bioanalytical Method Validation: A Review Article. Journal of Analytical & amp; Bioanalytical Techniques. 2010; 1(1): 88-93.

[7] Swati R., Mansi P., and Aditya P.; Analytical Method Development and Validation: A Concise Review. International Journal of Pharmacy and Biological Sciences, 2021; 11(1): 9-16.

[8] Choudharya A.; A Review on Pharmaceutical Validation and Its Implications. Journal of Medical Pharmaceutical and Allied Sciences. 2021; 10(6): 3951-3961.

[9] Manish Kumar Mishra., Pooja Kumari, "A review on pharmaceutical process validation", The Pharma Innovation Journal 2019; 8(6): 950-958.

[10] Pandita Rachna., Rana AC, Seth Nimrata, Bala Rajni, "Introduction and General Overview of Pharmaceutical Process Validation: A Review" International Research Journal Of Pharmacy 2012; 3 (6).

[11] Shruthi N. K., N. Vishal Gupta, Raghunandan H V, U Nitin-Kashyap, "USFDA Guidelines on Process Validation - A Re-view", International Journal of PharmTech Research 2014; 6(3), pp 920-923.

[12] Guidance for Industry Process Validation: General Princi-ples and Practices U.S. Department of Health and Human Ser-vicesFood and Drug Administration, Center for Drug Evalua-tion and Research (CDER), Center for Biologics Evaluation and Research (CBER), Center for Veterinary Medicine (CVM), Janu-ary 2011, Current Good Manufacturing Practices (CGMP), Revision 1.

[13] Swathi Sree Karumuri., A. Karthikeyan, "Process Valida-tion of Griseofulvin Tablets", 2012; 1-101.

[14] Kaur Harpreet., Singh Gurpreet, Seth Nimrata, "Pharmaceutical Process Validation: A Review", Journal of Drug Delivery & Therapeu-tics; 2013, 3(4), 189-194.

[15] Sharma Sumeet, Singh Gurpreet, "Process Validation in Pharmaceu-tical Industry: An Overview", Journal of Drug Delivery & Therapeutics; 2013, 3(4), 184-188.

[16] Good Manufacturing Practices for Pharmaceutical Products, WHO Pharm. 93.562 Annex: Guidelines on Validation of Manufacturing Process. Geneva: WHO.

[17] Food and Drug Administration, 21 CFR parts 210 and 211, Pro-posed Rule, Federal Register, May 3, 1996.

[18] World Health Organization 2003. Committee on specifications for pharmaceutical preparations, GMP for pharmaceutical products. WHO Tech Report. 82, 14-79.

[19] Singh H, A.C. Rana, Seema Saini, Gurpreet Singh, "industrial pro-cess validation of solid

Principal
Indore Institute of Pharmacy,
INDORE (M.P.)

121

11) Sampling locations, sampling procedures, stages, and plans.

12) The statistical instruments should be applied to data analysis.

13) The processing operators' training needs.

14) Test strategies that have been proven to work for both process and final product testing.

15) Details regarding test procedures, raw ingredients, and packaging.

16) The charts and forms that will be used to record the outcomes.

17) Format for presenting findings, recording conclusions, and endorsing research findings. [21,22]

C. **Validation Report:** Following the conclusion of the validation, a documented report ought to be made available. Should it be deemed appropriate, it ought to be permitted and approved (signed and dated). It ought to draw conclusions about the process's validation status and provide the required advice for regular procedures. Following the execution of batches, a validation report must be created to evaluate adherence to the protocol. During execution, data might be gathered in a format that has been preplanned. The formulation order of the validation batch processing records must be compared with the actual yield that was attained at various stages.

At minimum, the following should be included in the report:

1) The study's title and goal.

2) A mention of protocol.

3) Specifics of the content.

4) Tools.

5) Cycles and programs utilized.

6) Specifics of protocols and testing techniques.

7) Outcomes (weighed against acceptance standards).

8) Suggestions regarding the upper limit and future application criteria. [13]

XI. CONCLUSION

In pharmaceutical companies, the practice of process validation is crucial. It is essential to ensuring that the quality objectives are fulfilled. Understanding of the product and process will be enhanced, and waste, rejections, lead times, and other failures will be decreased, by conducting validation in accordance with USFDA process validation guidelines. Throughout the course of the product life cycle, this guideline also aids in the validation process' ongoing improvement. Prior to receiving approval, a novel medication must undergo a thorough and dependable evaluation to determine its safety and efficacy for the intended use and intended patient population.

To guarantee that the drug product will meet or set pharmaceutical standards for identity, strength, quality, purity, stability, assessment safety, and efficacy, pharmaceutical validation and process control are required when the drug is approved.

Under the more expansive statutory CGMP provisions of section 501(a)(2)(B) of the Federal Food, Drug and Cosmetic Act, validation of manufacturing processes is deemed an enforceable element of current good manufacturing practice for active pharmaceutical ingredients (APIs). Validation of manufacturing processes is a requirement of the Current Good Manufacturing Practice (CGMP) regulations for finished pharmaceuticals (21 CFR 211.100 and 211.110). There is a high degree of exact assurance that a manufacturing process that has been validated will consistently yield acceptable items. Thus, process validation is a scientific way of proving that a process can reliably produce high-quality results.

REFERENCE

[1] Todkar VS, Lade MS, Patil KS, D'souza JI Computerized System Valida-tion: Introduction Implementation and Regulations - A Review Interna-tional Journal for

Principal
Indore Institute of Pharmacy,
INDORE (M.P.)

122

	study at maximum speed	& near end of hopper
		Individual weight variation
		Thickness
		Hardness
		Friability
		Disintegration time
		Content uniformity
Coating	Inlet temp. Exhaust temp. Pan speed atomization pressure, spray rate gun distance	Weight build up
		At the end of coating
		LOD
		Dissolution profile at 15, 20, 30, 45 & 60 minutes
Blister packing	Machine speed, forming and sealing temperature	Blister appearance and quality, leak test and impurity

X. Documents

A. **Validation Master Plan:** The purpose of this document is to demonstrate to the Federal Department of Agriculture (FDA) inspectors that the company has a very well-organized validation program. Included in the format and content should be:

1) Introduction: scope, location, schedule, and validation policy.

2) Organizational structure: duties assigned to employees.

3) Plant, process, or product description: justification for additions or deletions, as well as the scope of validation.

4) Particular process factors that need special attention and are crucial.

5) A matrix-formatted list of the systems, processes, and products that need to be validated, along with the validation methodology.

6) Key acceptance criteria, real status, and revalidation operations.

7) Format for documentation.

8) Making use of the necessary SOPs.

9) Schedules for every validation project and its subsidiary projects. [19, 20]

B. **Validation Protocol:** To guarantee that the process is sufficiently validated, comprehensive procedures are necessary for carrying out validations. The following components must to be included in validation protocols:

1) The goals and extent of the validation study's coverage.

2) The composition, credentials, and duties of the validation team.

3) Validation types include prospective, contemporaneous, retrospective, and re-validation.

4) The quantity and choice of batches to be included in the validation research.

5) A list with the typical and worst-case operating parameters for every piece of equipment that will be used.

6) IQ and OQ results for essential equipment.

7) Requirements for all measurement instruments' calibration.

8) Important process variables and the tolerances that apply to them.

9) Process characteristics and variables that are likely to cause risk should be noted.

10) A copy of the product's master documents is used to describe the processing processes.

123

IX. Process Validation of Manufacturing Process (Eg., Solid Dosage Form) [13]

addition of active excipients, or raw ingredients

↓

Pre-blending with a granulator and high-speed mixer

↓

High-speed mixer granulator for granulating

↓

Fluid-bed dryer for drying

↓

Sizing (mill/sieve)

↓

addition of raw materials (disintegrants and lubricants)

↓

V-blender for blending

↓

Tableting (precompression combined with high-speed rotary)
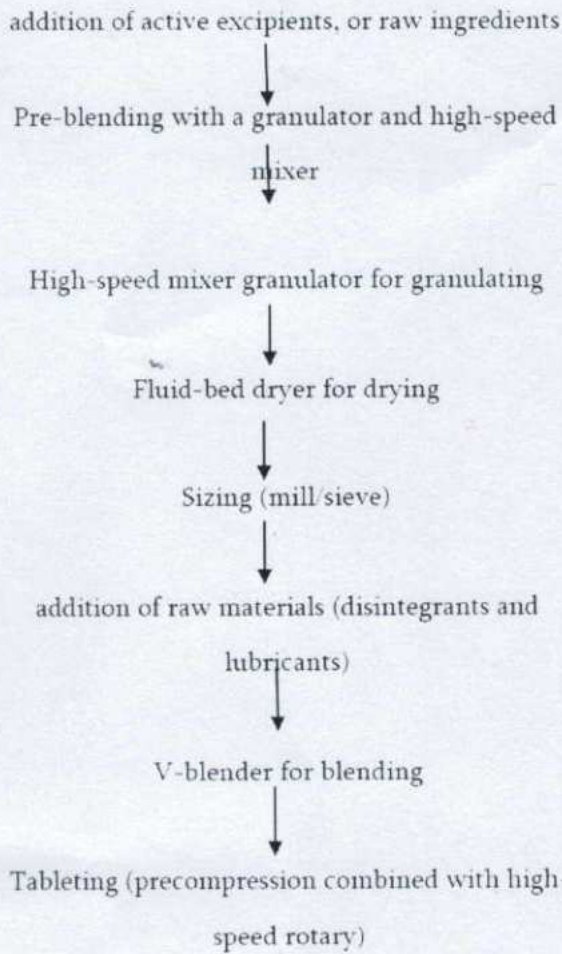
Fig. 5. Synopsis of Process

TABLE III. Parameters performed during process validation.

Stage	Process variables	Tests performed
Dry mixing	Mixing time	Uniformity of content, Bulk density, moisture content, sieve analysis
Granulation	Mixing time impeller reading	

Stage	Process variables	Tests performed
	during mixing	
Drying	Inlet & outlet temperature drying time	Final drying, Loss on drying moisture content
Blending	Blending time	Uniformity of content & RSD
		Bulk density, sieve analysis & compressibility index
Compression	Pre compression studies	Optimum speed-Dissolution at lower & higher thickness
Compression	Machine speed (10 - 30 rpm)	At different speeds
		Appearance
		Group weight variation
		Individual weight variation
		Thickness
		Hardness
		Friability
		Disintegration time
		Dissolution
		Content uniformity
		Assay
Compression	Hopper	Full hopper, middle of hopper

124

of all process-related documentation, including validation audit report backs. At this point, the validation team additionally guarantees that there haven't been any modifications or deviations that should have led to revalidation and requalification. [11, 12, 13]
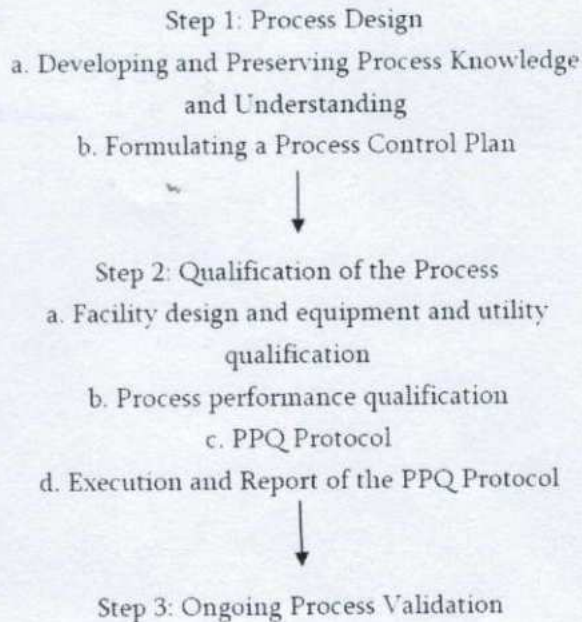
Step 1: Process Design

a. Developing and Preserving Process Knowledge and Understanding

b. Formulating a Process Control Plan

↓

Step 2: Qualification of the Process

a. Facility design and equipment and utility qualification

b. Process performance qualification

c. PPQ Protocol

d. Execution and Report of the PPQ Protocol

↓

Step 3: Ongoing Process Validation

Fig. 3. Methods for Validating Processes

VII. Types of Process Validation

A. **Prospective validation** is the practice of conducting validation before a new product or one created using an altered manufacturing process—a process that may have an impact on the product's characteristics—is distributed. FDA validation is performed prior to the regular production of goods meant for retail distribution.

B. **Concurrent validation** is the process of validating products that are routinely produced with the intention of selling them.

C. **Retrospective validation** is the process of validating a product's manufacturing procedure using data from production, testing, and control that has already been distributed. (FDA) Process validation for a product that has been sold using data gathered from manufacture, testing, and control batches.

D. **Re-Validation**: A repeat of the process validation to guarantee that equipment or process modifications made in compliance with change control procedures won't negatively impact the process's characteristics or its output quality. [14]

VIII. Validation Life Cycle

The process of validation is ongoing and dynamic. Its scope includes training, process and system maintenance, and revision control for documentation. Validation evidence ought to be visible at the corporate level and show up in the management hierarchy. One technique for establishing and preserving quality is validation. [15]
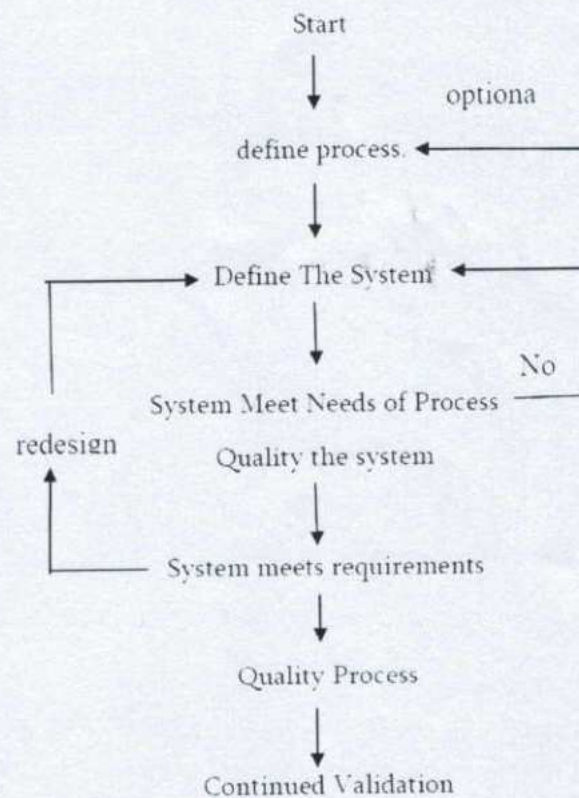
Start

↓

optiona

define process. ←

↓

→ Define The System ←

↓

System Meet Needs of Process — No

redesign   Quality the system

↓

System meets requirements

↓

Quality Process

↓

Continued Validation

Fig. 4. Life Cycle of Validation

Principal
Indore Institute of Pharmacy,
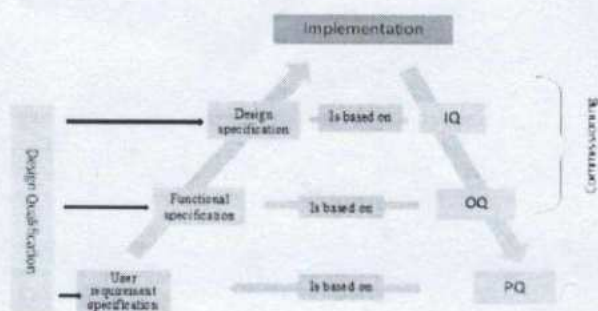INDORE (M.P.)

125

Fig. 2. V-Model for Validation

V. Process Validation

European Commission: The validation process, known as the "Act of Proving, in Compliance with GMPs that Any," genuinely yields the anticipated outcomes. 2000: "Documented evidence that the process can perform effectively and reproducibly to produce a medicinal product meeting its predetermined specifications and quality attributes when operated within established parameters."

According to USFDA 1987, "a high degree of assurance that a specified process will consistently produce a product meeting its pre-determined specifications and quality characteristics" is provided by documented evidence.

According to ICH, "Process Validation is the process of verifying and supplying documented proof that processes operating within the parameters of their designated designs are able to consistently and dependably produce a final product of the necessary quality."

According to the WHO, "the documented act of proving that any procedure, process, piece of machinery, substance, activity, or system actually produces the desired outcome."

USFDA (2011) - Process validation is the process of gathering and analyzing data to demonstrate scientifically that a process can consistently create high-quality products, starting from the process design stage and continuing through commercial production. [10]

TABLE II. The most recent definition of process validation is provided in this table.

1987 Definition	2011 Definition
"Determining documented proof that offers a high level of assurance that a particular process will consistently yield a product that satisfies its predetermined specifications and quality characteristics"	"The process design stage through production data collection and evaluation that establishes scientific evidence that a process is capable of consistently delivering quality products"

VI. Process Validation Stages

A. stage 1: Process Design: Using the knowledge gathered from development and scale-up activities, the commercial process is defined at this step. It includes all of the following: creating stability conditions; storing and managing in-process and finished dosage forms; equipment qualification; installation qualification; master production documents; operational qualification; process capability; formulations; pilot batch studies; scaleup studies; and the transfer of technology to commercial scale batches.

B. Stage 2: Process Qualification: In this phase, the process design's suitability for repeatable commercial manufacturing is verified. This stage is designed to confirm that all of the important process parameter limits that have been defined are valid and that good products are frequently generated even in the worst-case scenario. It stands for the specific research or experiments carried out to demonstrate.

C. Stage 3: Ongoing Process Verification: During regular production, continuous assurance is obtained that the process stays under control. In order to ensure that there are no deviations, failures, or changes to the assembly process, as well as that all SOP, including the change control procedure, are followed, this phase necessitates periodic evaluation

Principal
Indore Institute of Pharmacy,
INDORE (M.P.)

126

There are four forms of process validation depending on the stage of manufacturing. These are as follows:

The four types of validation are

1) Retro specific,

2) concurrent,

3) prospective, and

4) revalidation.

C. **Cleaning validation**: Cleaning validation is a recorded setup that offers a high level of assurance that a specific system, piece of equipment, or quality of clean-up is regularly carried out to acceptable limits and established quality. A wide range of pollutants, including lubricants, airborne contaminants, prepared product residues, and microorganisms, can contaminate pharmaceutical goods. Therefore, preventing contamination and cross-contamination requires a thorough cleaning process.

D. **Equipment validation**: Equipment validation is the established, documented setup that demonstrates that any equipment functions as intended and produces results that are accurate and acceptable (predetermined result). The idea that equipment needs to be built, maintained, and modified in order to carry out the intended tasks is the basis of the equipment validation process. Since equipment is the fundamental element of the pharmaceutical industry, it is crucial to provide equipment validation (recorded evidence of equipment) prior to carrying out any process in the sector. [9]

IV. Validation Approaches

1) Manufacturers ought to design and arrange validation in a way that guarantees the efficacy, safety, and quality of their products over the duration of their life cycles.

2) Risk management concepts ought to serve as the foundation for the range and depth of qualification and validation.

3) When applicable, statistical computations should be used to support scientific claims that a system,

process, or other relevant element has been suitably validated.

4) Qualification and validation should be carried out in compliance with established processes, and the outcomes suitably recorded, for example, in reports.

5) The administration and organization of validation should be ensured by a suitable and efficient quality system.

6) Senior management is in charge of making sure there are enough resources available to complete validation tasks quickly.

7) The task of completing validation should fall to individuals who possess the necessary training and expertise.

8) A defined timetable or program should be in place to assist with the organizing and carrying out of validation tasks.

9) In accordance with the established protocols and procedures, validation should be carried out in an organized manner.

10) Qualification and validation should be carried out: whenever new facilities, machinery, utilities, systems, processes, and procedures are introduced; if changes are made, contingent upon the results of the risk assessment; and whenever required or recommended by the results of the periodic review.

11) The results of the validation should be documented in writing.

12) As stated in the World Health Organization (WHO) guidelines on quality risk management, the breadth and depth of validation should be determined by knowledge, experience, and the application of quality risk management principles. Worst-case scenarios or particular challenge tests, such as stress load and volume verification in computer system validation, should be taken into consideration when adding to the validation as needed.

13) The V-model provides an illustration of a qualification and validation strategy. [22]

127

3) Raw material requirements

4) Operating procedures for processes.

5) The requirements for handling materials.

6) Change control procedures.

7) Education.

8) The role of equipment control.

9) The process's short-term stability and capabilities (latitude studies or control charts).

10) Worst-case scenarios, action levels, and probable failure modes.

11) In order to optimize the procedure, statistically sound methods like screening experiments may be applied at this stage. [6]

D. **Performance Qualification (PQ):** Installation and operational qualification should be successfully completed before moving on to performance qualification (PQ).

PQ factors consist of the following:

1) Real product and process specifications and guidelines set forth in OQ.

2) The product's acceptability.

3) Guarantee of process capability according to OQ standards.

4) Long-term stability and repeatability of the process.

5) Tests that incorporate an upper and lower operating limit condition, or circumstances that encompass both. [7]

E. **Re-qualification:** Any equipment modification or relocation must be approved by the change control procedure after a thorough evaluation and approval process. It is recommended that the equipment be requalified as part of this official examination. Modest alterations or those that don't directly affect the quality of the finished or in-process product should be managed using the preventive maintenance program's documentation system.[8]
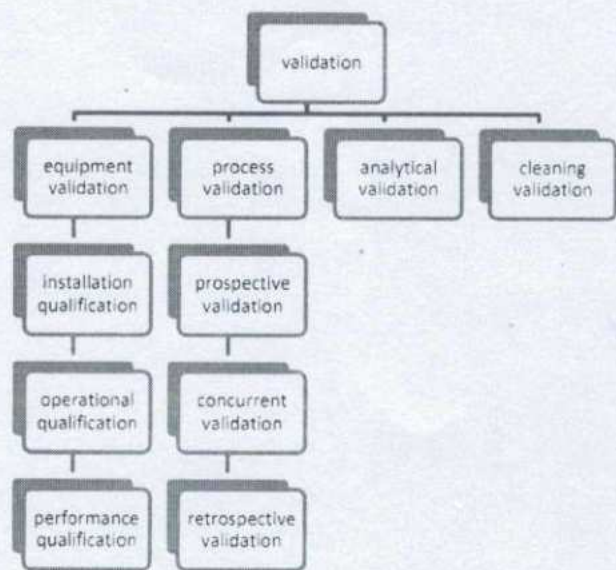
III. Types

Fig. 1. Types of validation

A. **Analytical method validation:** This process aims to confirm that the chosen analytical technique will produce accurate results sufficient for the intended use. The validation of analytical methods encompasses various parameters. These are listed in the following order:

1) Accuracy

2) Detection limit;

3) range;

4) linearity;

5) precision;

6) repeatability;

7) reproducibility;

8) specification;

9) The quantity limit.

B. **Process validation:** This kind of validation presents written evidence, which offers a higher level of assurance that the procedure will reliably result in a product that satisfies all predefined quality standards and attributes. In addition to ensuring process repeatability and lowering the possibility of manufacturing issues, process validation also increases output of a set quality.

577

Principal
Indore Institute of Pharmacy.
INDORE (M.P.)

128

4) Quality controls: Evaluate protocols, conduct contracts validation testing, and provide reports as required.

5) Research & development: This field addresses product design.

6) Department of Engineering: Installs, certifies, and maintains plant, facilities, equipment, and support systems. [24, 22]

D. Validation Team and Its Responsibilities

Validation investigations are generally carried out and supervised by a diverse team. Individuals possessing training and experience in a pertinent field may carry out these kinds of investigations.

Among the validation team's many duties are:

1) Updates, evaluates, and approves each project's validation deliverables and plans.

2) Verifies that the project validation plan and the company validation master plan are followed for validation.

3) Coordinates, carries out, and validates VMP components.

4) Gives advice, assesses, and approves modifications.

5) Examines and authorizes IQ/OQ/PQ plans and processes.

6) Examines test findings and offers suggestions for publication.

7) Evaluates potential threats and creates backup plans. [25, 22]

II. Phases of Validation

A. **Design Qualification (DQ):** Design qualification may be the initial step in validating new buildings, systems, or equipment (DQ). The design's adherence to GMP requirements needs to be proven and recorded. It is an official confirmation of the production facilities' and equipment's designs.

DQ factors include:

1) Legal requirements and good manufacturing procedures.

2) Criteria for performance.

3) Dependability and effectiveness.

4) Access to and maintenance of vital instruments and equipment.

5) Impact on the environment and safety.

6) Pressure engines, movement flow, and air flow within the facility. [5]

B. **Installation Qualification (IQ):** is the process of proving, by objective evidence, that every important detail of the installation of the process equipment and ancillary systems complies with the manufacturer's approved specification and that the equipment supplier's recommendations are appropriately taken into account. Equipment, systems, and facilities that are new or updated need to undergo installation qualification.

IQ factors include:

1) Features of equipment design (e.g., cleanability of construction materials, etc.)

2) Installation circumstances (utility, functionality, wiring, etc.)

3) Cleaning schedules, calibration, and preventative maintenance.

4) Security elements.

5) Prints, drawings, and manuals from suppliers.

6) Documentation for software.

7) List of spare parts.

8) Environmental factors (including humidity, temperature, and clean room requirements).

9) Equipment description.

10) Functional specifications for the facility.

11) Operational premise.

C. **Operational Qualification (OQ):** An approved protocol should be followed when conducting an operational qualification (OQ). At the OQ stage, the crucial operational parameters for the systems and equipment should be determined.

OQ factors include:

1) Process control constraints (time, temperature, pressure, line speed, setup conditions, etc.) are among the OQ factors to be taken into account.

2) Parameters of the software.

129

preliminary evidence that the process design yields the desired product quality through commercial batch manufacturing.

A. Goals

1) Equipment validation is necessary for both the manufacturing process and the individual pieces of equipment.

2) The objective is to develop a strong manufacturing process that reliably yields a pharmaceutical product that satisfies purity, identification, and potency quality standards with little fluctuation.

3) Any process or system's validation results in the determination of process parameters and controls.

4) It assists in identifying potential hazards and worst-case scenarios during the production of high-quality goods.

Examining variations that occur during the process is beneficial.

6) Validation enables in-depth analysis and comprehension of the system and its components.

7) Following validation, the risk of regulatory noncompliance is reduced.

8) Less process control and final product testing are needed throughout a validation process.

9) There is less fluctuation from batch to batch.

10) Lowers the cost of production.

11) Boosts manufacturing facility output as a result of less rejection and rework.

12) Reduces the likelihood that batches may fail. [1]

B. Requirements

1) Experience

2) Planning

3) Resources

4) Communication and Understanding

5) Instruction

6) Standard Operating Procedures, Tools, and Techniques

7) Master Plan for Validation

8) Information Evaluation

9) Report on Validation [1]

TABLE I. Difference Between Validation and Qualification.

Validation	Qualification
1) The act of demonstrating and recording that a process, method, or procedure genuinely and reliably produces the desired outcomes.	1) Ensuring that equipment or auxiliary systems are installed correctly, function as intended, and produce the desired outcomes through documentation and provision of this information.
2) System, procedure, or process validation is carried out.	2) Equipment qualification is carried out as a component of validation.
3) Documentary proof that the procedure will reliably result in the intended result.	3) Done on a specific process element to verify its functionality and ascertain whether it possesses the necessary characteristics to generate a predetermined result.

C. Departments Responsible for Validation:

The following departments hold primary responsibility for validation:

1) Site validation committee: Create a plan for the master validation of the site.

2) The manufacturing section is responsible for preparing the batches as if they were regular production batches. to help in data collection.

3) Quality assurance: Verify that all procedures, documentation, and compliance are in place. approves reports and procedures. Examining the documentation for validation. to give the procedure approval.

Principal
Indore Institute of Pharmacy,
INDORE (M.P.)

130

I. INTRODUCTION

Validation is a crucial component of quality assurance that ensures the equipment, manufacturing process, software, and testing are all of the highest caliber.

Validation ensures that, within predetermined manufacturing process limitations, items with particular quality features and qualities can be produced consistently.

Documented evidence that offers a high level of assurance that a particular procedure will consistently result in a product that satisfies its planned specifications and quality attributes is known as validation. [1,16]

To maintain and enhance the quality of pharmaceutical products, the Food and Drug Administration (FDA) adopted Good Manufacturing Practices. [2]

The portion of quality assurance known as GMP makes ensuring that products are regularly manufactured and managed to the standards of quality appropriate for their intended use and as mandated by the marketing authorization.

The primary guidelines of GMP include correct facility and equipment design and construction, ongoing facility and equipment monitoring, and recurring audits.

Good practices, such as good manufacturing practices (GMP) and good clinical practices (GCP), depend on validation. Thus, it is a component of the system for ensuring pharmaceutical quality. [2,3,17]

Validation entails certification and ought to be used throughout a system's, equipment's, product's, process', or method's life.

The general principles of qualification and validation, as well as tasks like computerized systems, analytical methodologies, process validation, cleaning validation, and other related operations, are covered in these guidelines.[3]

Pharmaceutical facilities use a variety of processes, all of which need to be precise in order to guarantee a high-quality final product. Although the focus of validation is mostly on processes, when the same methodology is used on a machine or piece of equipment rather than a process, it is known as a qualification. [1,4]

In an effort to raise the caliber of medications, Ted Byers and Bud Loftus, two FDA officials, originally put out the idea of validation in the middle of the 1970s. The documented proof that offers a high level of assurance to a desired outcome with planned conformity is the validation process. The word "valid or validity," which meaning "legally defined," is the source of this phrase.

The US FDA and other food, drug, and pharmaceutical regulatory bodies, as well as their good manufacturing practices recommendations, mandate validation. [18]

Precise and accurate measurement of analytical data depends on the calibration of analytical instruments. Everything else that depends on using that instrumentation is dubious if it is not certified to ensure that the results shown are reliable. For the purposes of this paper, it will be assumed that well-qualified instrumentation forms the basis of the validation and verification work that will come after. The process of proving through laboratory testing that an analytical procedure's performance characteristics satisfy the demands of the planned analytical applications is known as validation. [1,2]

A manufacturer must to be able to validate the manufacturing process with appropriate design and dependable methods to transfer process knowledge from development to commercial production. Within a quality system, process validation offers

Principal
Indore Institute of Pharmacy,
INDORE (M.P.)

131

Theoretical Approaches to Process Validation in Pharmaceutical Manufacturing Process

Richa Shukla*[1], Dr. Nimita Manocha[2], Dr. Gurmeet Singh Chhabra[3]

[1]Department of Quality Assurance, Indore Institute of Pharmacy, Indore, Madhya Pradesh, India
[2]Department of Pharmaceutical Chemistry (Principal), Indore Institute of Pharmacy, Indore, Madhya Pradesh, India
[3]Department of Quality Assurance (HOD), Indore Institute of Pharmacy, Indore, Madhya Pradesh, India

ARTICLEINFO	ABSTRACT
	Under the more general statutory CGMP provisions of section 501(a)(2)(B) of the Federal Food, Drug and Cosmetic Act, validation of manufacturing processes is deemed a legal part of current good manufacturing practice for active pharmaceutical ingredients (APIs). Validation of manufacturing processes is required by the Current Good Manufacturing Practice (CGMP) regulations for finished pharmaceuticals (21 CFR 211.100 and 211.110). A medication should be created that is suitable for its intended purpose, according to the fundamental tenet of quality assurance. Procedure Validation is the collection and estimation of data that proves a process can reliably produce high-quality goods, starting with process design and continuing through commercial production. Three stages of validation are suggested by the 2011 USFDA process validation guideline - Process design, Process qualification, Continued Process qualification. An introduction and broad review of process validation in the pharmaceutical manufacturing process, specifically in the tablet manufacturing process, are provided in this article. Process validation ensures that a process will consistently create a product that meets its predefined quality features and qualities. It is a crucial step in the design, prototyping, and manufacturing processes. Since quality is always a necessary precondition for any product, pharmaceuticals must be produced to the greatest standards of quality. Furthermore, end-product testing does not ensure the product's quality on its own; rather, quality assurance methods need to be applied to incorporate the product's quality throughout the whole process, rather than only testing it at the conclusion. **Keywords** – GMP, Food and Drug Administration, QA, Validation, Validation Master Plan, Re-Qualification.

573

132

suitable dilutions with buffer, the absorbance was measured at 225 nm and the drug content was calculated by the standard curve drawn. (9)

Percentage Moisture Loss: % moisture loss of the film was determined by keeping the films in desiccator for three days containing silica gel and then the before and after weight of three days was noted and moisture loss was evaluated. (10)

% Moisture Loss = (Initial Weight – Final Weight) × 100

Initial Weight

In-Vitro Disintegration Test: The disintegration of the film was conducted by putting the film of every formulation in beaker containing 25ml of distilled water and the time was recorded when the film starts break or disintegrates. (11)

In-Vitro Dissolution Study: Dissolution study of film was carried out by using USP type II apparatus having 300ml of buffer solution (6.8pH) rotated at 50 rpm and temperature-maintained 37±0.5°C. The solution was withdrawn at every 15 sec and replace by the fresh solution, the withdrawn sample as filtered and then absorbance was recorded at 225nm.

Kinetic Study: In order to analyze kinetic release or drug release parameter the data was fitted in different orders zero-order, First-order and Higuchi model, Korsmeyer-Peppas Model, Hixson model.(12)

In-Vitro Permeation Release: In-Vitro permeation release was conducted with the help of Franz diffusion cell, in which the cellophane membrane of 3cm was mounted between the receptor and donor compartment, receptor compartment was filled with 6.8 pH buffer (37±0.2°C) solution for maintaining dynamics magnetic bead was kept and the formulation (film) was moistened with same buffer solution and was held on donor compartment. After a fixed interval of time solution was withdrawn from the receptor compartment and replace by the 6.8 pH buffer. The % amount of drug release or permeated was determined by checking absorbance in UV spectrophotometry.(13)

RESULTS AND DISCUSSION
Evaluation of Mouth Dissolving Film of Cyclizine Hydrochloride

Table 2.Physical Appearance of the Film

Property	Observation
Color	White
Odor	Odorless
Shape	Rectangular

Thickness of MDF

The thickness of the film was measured with the help of vernier caliper. As the concentration of the polymer increase the thickness of the film also increases gradually. The thicknesses of the formulations are ranged from 0.030±0.00057 to 0.047± 0.00057 as shown in table 3.

Weight Variation

The average weight of the formulations was determined and was in the range of 43.4±0.057 to 84.2±0.057 and is shown in table 3.

Table 3. Evaluation of thickness, weight variation, folding endurance and surface pH of MDF

Formulation Code	Thickness (mm) (*Mean±SD)	Weight Variation(mg) (*Mean±SD)	Folding Endurance (*Mean±SD)	Surface pH (*Mean±SD)
F1	0.032±0.001	43.4±0.057	40±1.15	7.02±0.005
F2	0.035±0.0011	47.5±0.057	53±0.57	6.95±0.01
F3	0.039±0.0011	53.7±0.1	62±0.57	6.92±0.01
F4*	0.030±0.00057	59.4±0.057	74±1.0	6.82±0.005
F5	0.032±0.001	66.4±0.152	80±1.52	6.90±0.015
F6	0.041±0.00057	71.8±0.057	82±0.57	6.93±0.017
F7	0.043±0.00057	78.5±0.115	83±1.0	6.99±0.10
F8	0.047±0.00057	84.2±0.057	85±1.52	6.96±0.015

Values are represented as mean ± SD and n = 3

Folding Endurance

The value of folding was in the range of 40±1.15 to 85± 1.52. It was observed that with the increase in the concentration of the polymer folding endurance also increases and hence the chance of film rupturing decreases as shown in table 3 of films.

Principal
Indore Institute of Pharmacy,
INDORE (M.P.)

MATERIAL AND METHODS

Materials

Cyclizine hydrochloride was obtained as a gift sample from Tooba Pharmaceutical Private Limited, MIDC Paithan, Aurangabad, India, Aspartame from Oxford Lab fine chem LLP, Maharashtra, India; Gelatin from Merck Specialities Pvt. Ltd, Mumbai, PEG 400, Tween 80, Citric acid, Ethanol were supplied by Lobachemiepvt. Ltd.Mumbai, Maharashtra, India.

Method to Prepare MDF

The most appropriate and convenient method for the formation of film is solvent casting method. In this method water soluble polymer was dissolved in water on magnetic stirrer and the drug and other ingredients were dissolved in appropriate solvent after dissolving the solutions separately both the solutions were mixed and stirred to get an homogenous solution then after degassing, poured the solution in petriplate, dry the films so that they are ready to cut in desired shape and dimensions. (4)

Table 1: Formulation of mouth dissolving film of cyclizine hydrochloride

Ingredients	F1	F2	F3	F4	F5	F6	F7	F8
Cyclizine Hydrochloride (mg)	25	25	25	25	25	25	25	25
Gelatin (mg)	700	750	800	850	900	950	1000	1050
PEG 400 (mg)	90	90	90	90	90	90	90	90
Citric Acid (mg)	30	30	30	30	30	30	30	30
Tween 80 (mg)	0.6	0.6	0.6	0.6	0.6	0.6	0.6	0.6
Aspartame (mg)	30	30	30	30	30	30	30	30
Water (ml)	9	9	9	9	9	9	9	9
Ethanol (ml)	1	1	1	1	1	1	1	1

Dose Calculations

Width of the plate = 8cm

Length of the plate = 15cm

No. of 3×2 cm^2 films present whole plate = 20

Each film contains 25mg of drug

20 no. of films contains mg of drug = 25×20

$$= 500 \text{ mg}$$

Evaluation of MDF

Organoleptic Evaluation: The external appearance of film like transparency, color, odor and shape was observed visually and recorded.

Folding Endurance: Folding endurance of the film was estimated manually by folding the film continuously from the same position till the films get break. For experimental purpose the formulated dosage form of 3×2 cm^2 film was taken and folded at a same point again and again till it breaks.(5)

Thickness of Film: The thickness of the film was measured by vernier calipers so that accurate thickness of the film was observed and recorded. The thickness is measured by repeating the process approximately 3 times at different positions and get average thickness of the film.

Weight Variation: For determining the weight of the individual film 3-4 film of every formulation were weigh by digital weighing balance and average was recorded. (6)

Surface pH: The pH of the film was tested by moistened the film with the help of water and then the electrode was kept in contact with film for 1 min and pH was recorded by observing on three film, the mean was obtained. (7)

Tensile Strength: Tensile strength of the film is the test used to determine that at what maximum load the film get break. For this the film of 3×2cm^2 was placed longitudinal between the grips of tensile tester and load at breakage was recorded.

Tensile strength = Load at Breakage × Strip Width

Strip Thickness

Percentage Elongation: The % elongation of the film was determined by dividing the Increase in the length to the original length.(8)

% Elongation = Increase in Length × 100

Original Length

Drug Content Uniformity: Drug Content Uniformity: The film was transferred into a graduated flask, dissolved in 100 ml 6.8 pH buffer and the flask was shaken continuously. The solution was filtered after

Principal
Indore Institute of Pharmacy,
INDORE (M.P.)

134

Advances
in
Bioresearch

ORIGINAL ARTICLE

Formulation and Evaluation of Mouth Dissolving Film of Cyclizine Hydrochloride

Sakshi Bafna[1]*, Nadeem A. Farooqui[2], Nayany Sharma[3], Nimita Manocha[4]

Department of Pharmaceutics, Indore Institute of Pharmacy,Pithampur Road,Opposite Indian Institute of Management, Rau, Indore, Madhya Pradesh

*Correspondence author's Email:sakshi.bafnampharm2022@indoreinstitute.com

ABSTRACT

The aim of the present research work was to formulate the Mouth Dissolving Film, to minimize the current and future problems of engulfing the oral dosage form like tablets, capsules and less patient compliance especially of pediatric and geriatric. Therefore, to overcome the problems like dysphagia, bedridden and comatose patient and to improve the bioavailability of the drug mouth dissolving film can be a better option. The preparation of mouth dissolving film was carried out by simple method that was solvent casting method, the homogeneity and the thickness of the film obtained by this method was good. The film was tested for thickness, surface pH, weight variation, folding endurance, % moisture loss, ex vivo permeation study, tensile strength, % elongation, drug content uniformity, in-vitro dissolution studies and in-vitro disintegration test. The best formulation was F4 as it releases 99.17% of drug in 2 minutes, the drug release of the best formulation (F4) followed zero-order kinetics and the Correlation Coefficient R^2 was 0.993and ex-vivo permeation study of F4 formulation showed a drug release of 87.62% within 2 minutes. The study reveals that the formulation can be very useful for the treatment of the disease which requires quick-onset of action.
Keywords: Mouth Dissolving Film, Natural Polymer, Solvent-Casting Method, Cyclizine Hydrochloride, Oral Mucosal Absorption.

How to cite this article:
Sakshi B, Nadeem A. F, Nayany S , Nimita M. Formulation and Evaluation of Mouth Dissolving Film of Cyclizine Hydrochloride. Adv. Biores. Vol 15 [4] July 2024. 72-78

INTRODUCTION

The common pharmaceutical dosage form like tablets, capsule, syrup are maximally used in market to deliver the dose and give therapeutic effect but the geriatric, pediatric and dysphagia patients have choking and swallowing problem so to overcome this problems mouth dissolving oral film are formed. Mouth dissolving oral film is the novel approach to deliver the dose in appropriate manner to enhance activity and making more convenient, they can be manufactured by different types of technologies like: solvent casting method, hot melt extrusion, semisolid casting method, rolling method and solid dispersion extrusion. The major advancement of this system is no requirement of water, painless and can be administered by ourselves (1). MDF (Mouth Dissolving Film) by pass the hepatic first pass metabolism so there is no or less chance of drug degradation and increase the bioavailability of the drug, the drug incorporated in MDF is used in less amount therefore it reduces the side-effects. This dosage form is the best option for the diseases which requires quick on-set of action like: high blood pressure, cardiac problems, allergic condition, shortness of breath, nausea, epilepsy, for comatose patients, accidental patients and in various disease or conditions in which patients are unable to engulf the tablets or pills or any other dosage forms(2).MDF are the dosage form which get adhere to the surface of oral mucosal layer and delivering the drug through polymeric layer achieved a greater success in the field of pharmaceutical science. When the films are placed on tongue it releases the active pharmaceutical ingredients as soon as it gets hydrated by saliva. First MDF was Listerine and Pfizer was the first company who manufactured it for mouth freshening purpose(3).

Principal
Indore Institute of Pharmacy,
INDORE (M.P.)

135

8. Roy H, Shaik AR. Box-Behnken Design for Optimization of Formulation Variables for Fast Dissolving Tablet of Urapidil. AJP. 12(3).

9. Venkata Srikanth M, Sreenivasa Rao N, Ambedkar Sunil S, Janaki Ram B, Kolapalli VRM. Statistical design and evaluation of a propranolol HCl gastric floating tablet. Acta Pharmaceutica Sinica B. 2012 Feb;2(1):60–9.

10. Kim D, Park MS, Yoo BW, Hong T, Park SJ, Kim CO. The safety, pharmacodynamics, and pharmacokinetics of immediate-release formulation containing esomeprazole 20 mg/sodium bicarbonate 800 mg in healthy adult male. DDDT. 2019 Sep;Volume 13:3151–9.

11. Abdallah MH. BOX-BEHNKEN DESIGN FOR DEVELOPMENT AND OPTIMIZATION OF ACETAZOLAMIDE MICROSPHERES. IJPSR. 5(4):1228–39.

12. India, Indian Pharmacopoeia Commission, editors. Indian pharmacopoeia, 2010. Sixth edition. Ghaziabad: Indian Pharmacopoeia Commission; 2010. 3 p.

13. Khar RK, Vyas SP, Ahmad FJ, Jain GK. Lachman/Lieberman's the theory and practice of industrial pharmacy. 4th ed. New Delhi: CBS Publishers & Distributor; 2015.

14. Kumari M, Jain NP. Formulation Development & Evaluation of Buffered Tablet of Proton Pump Inhibitors Drug Rabeprazole Sodium. J Drug Delivery Ther. 2019 Aug 15;9(4-s):315–21.

15. Gowthami B, Krishna SVG, Rao DS. Formulation of Tablets in Capsule system: Statistical optimization for chronotherapeutic drug delivery of propranolol hydrochloride. Journal of Drug Delivery Science and Technology. 2021 Jun;63:102398.

16. Kurakula M, Naveen NR. In Situ Gel Loaded with Chitosan-Coated Simvastatin Nanoparticles: Promising Delivery for Effective Anti-Proliferative Activity against Tongue Carcinoma. Marine Drugs. 2020 Apr 9;18(4):201.

17. Liu S, Ho PC. Formulation optimization of scutellarin-loaded HP-β-CD/chitosan nanoparticles using response surface methodology with Box–Behnken design. Asian Journal of Pharmaceutical Sciences. 2017 Jul;12(4):378–85.

136

Conclusion

In conclusion, this study successfully formulated and optimized a Tablet-in-Capsule containing sodium bicarbonate and pantoprazole sodium using response surface methodology, specifically the Box-Behnken Design, to enhance the performance of pantoprazole sodium mini-tablets. The precise determination of the sodium bicarbonate dose via Digital pH meter measurements ensured accurate control over the alkalizing capacity of the formulation. Utilizing a desirability plot, a highly desirable D value of 0.995 confirmed the effectiveness of the optimized formulation. Evaluation of the formulation revealed excellent characteristics, including appropriate thickness, minimal weight variation, satisfactory hardness, and minimal friability, crucial for tablet integrity and patient compliance. Moreover, the formulation achieved a disintegration time of 5.5 minutes and 99.11% drug release within 50 minutes, indicating robust performance in drug delivery. This comprehensive approach highlights the potential of Tablet-in-Capsule technology to improve the therapeutic outcomes of pantoprazole sodium, offering promising avenues for enhanced patient treatment and compliance in managing gastroesophageal reflux disease.

CONFLICT OF INTEREST

No conflict of interests.

REFERENCE

1. Kaur G, Arora M, Ravi Kumar MNV. Oral Drug Delivery Technologies—A Decade of Developments. J Pharmacol Exp Ther. 2019 Sep;370(3):529–43.

2. Lou J, Duan H, Qin Q, Teng Z, Gan F, Zhou X, et al. Advances in Oral Drug Delivery Systems: Challenges and Opportunities. Pharmaceutics. 2023 Feb 1;15(2):484.

3. Sohail Arshad M, Zafar S, Yousef B, Alyassin Y, Ali R, AlAsiri A, et al. A review of emerging technologies enabling improved solid oral dosage form manufacturing and processing. Advanced Drug Delivery Reviews. 2021 Nov;178:113840.

4. Ramakrishnan K, Salinas RC. Peptic ulcer disease. Am Fam Physician. 2007 Oct 1;76(7):1005–12.

5. Pandey S, Mehta P, Patel H, Shah R, Gupta A, Mishra A. Novel time and site specific "tablets in capsule" system for nocturnal asthma treatment. Journal of Pharmaceutical Investigation. 2014 Oct;44(5):381–90.

6. Abdel Hamid H. Modified PPIs (a search for the better). Al-Azhar Assiut Med J. 2016;14(1):8.

7. Duangjit S, Kraisit P. Optimization of orodispersible and conventional tablets using simplex lattice design: Relationship among excipients and banana extract. Carbohydrate Polymers. 2018 Aug;193:89–98.
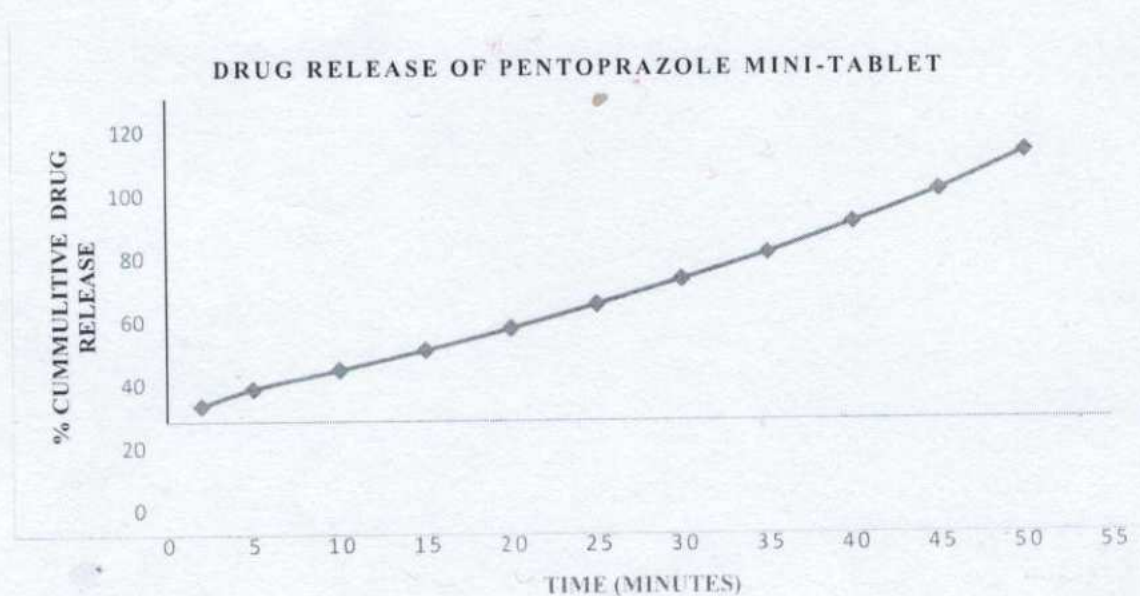
Principal
Indore Institute of Pharmacy,
INDORE (M.P.)

Angle of repose	32.8	Good
Carr's index	20±2	Fair
Hausner's ratio	1.25±0.25	Fair

PARAMETER	RESULTS
Thickness	3.65±0.10 mm
Hardness	6.9±0.70 kg/cm^2
Weight variation	195.71±4.8 mg
friability	0.51±0.02%
Disintegration	5.5±0.15 min
In-vitro drug release	99.11±0.15 %

Dissolution Profile

DRUG RELEASE OF PENTOPRAZOLE MINI-TABLET

The kinetic parameters revealed that release data of optimized formula showed r^2 value of 0.989 which is close to 1 indicating that release of drug follows **zero** order **kinetics** and the release are independent of concentration.

Principal
Indore Institute of Pharmacy,
INDORE (M.P.)
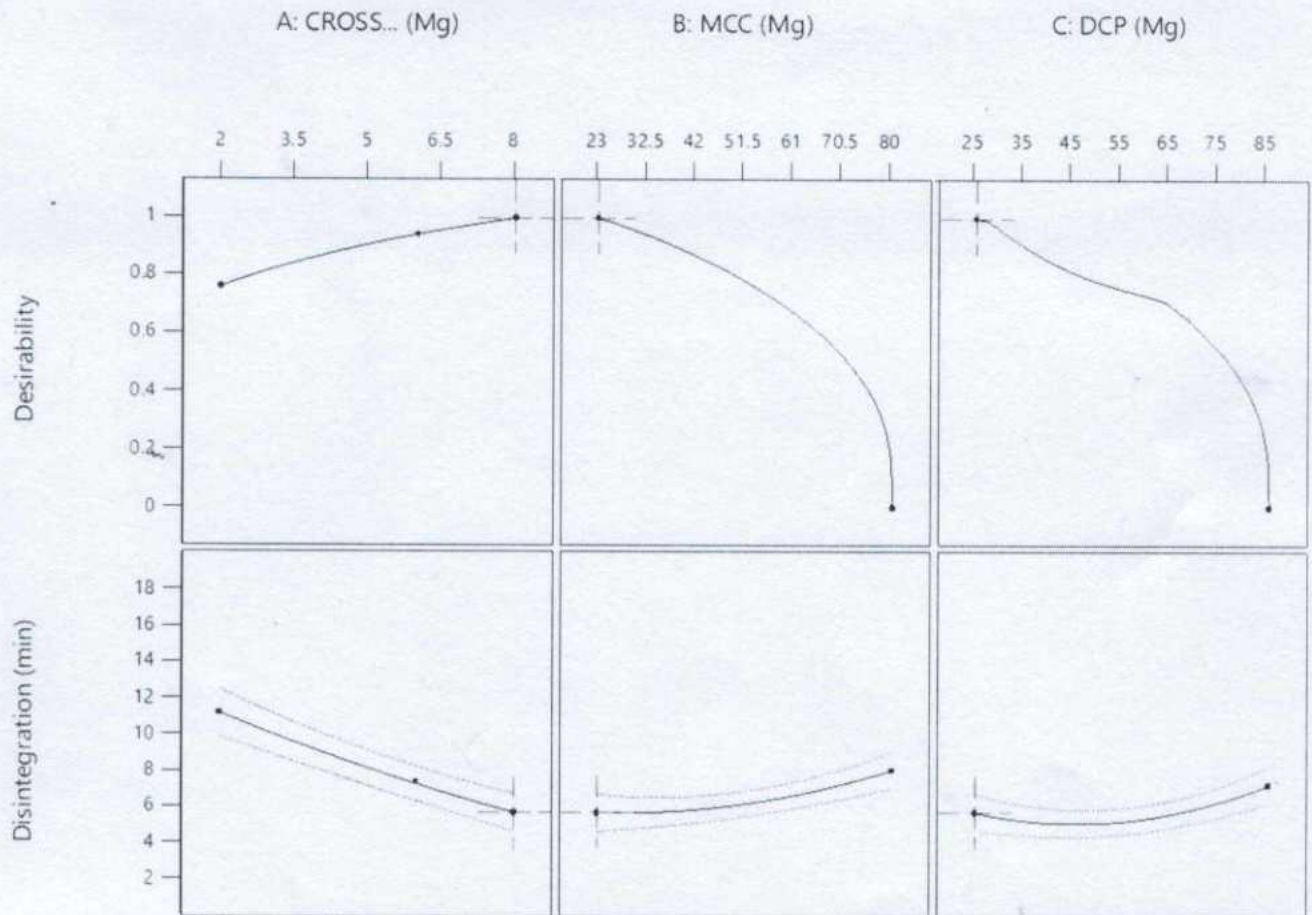
Figure 04: All factor interaction for desirability

Preparation of Pantoprazole sodium tablets

Pre-compression and post-compression parameters: Powder blend of mini-tablet is evaluated for pre-compression parameters. Obtained results were compared with standard values to confirm the flow characteristics. Formulation blend of tablet shows the Hausner's ratio of 1.25 and Carr's index as 20%. The maximum angle of repose was found to be 32.8θ. All these results confirm the good to fair flow property. Prepared mini-tablet formulations were found to be flat, oval with thickness in the range of 3.65 mm. Hardness and thickness for mini-tablet was maintained as 6.9 kg/cm^2 and 3.65mm. Weight variation for mini-tablet was found to be within the acceptable range i.e., 195.71mg. Percentage friability for mini-tablet is 0.51% which shows good mechanical strength. Desired formulation was selected on the basis of disintegration profile and according to global desirability function. Drug release profile of the optimized formulation was found to be 99.11%.

PARAMETER	RESULTS	FLOW CHARACTERISTICS
Bulk density	0.36±0.021	-
Tapped density	0.45±0.2	-

Principal
Indore Institute of Pharmacy,
INDORE (M.P.)

139
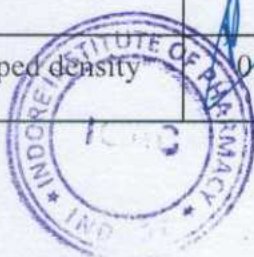
conclusion, formulation with Croscarmellose concentration of 8mg, MCC concentration of 23 mg and DCP concentration of 25mg and total tablet weight of 200 mg, can accomplish the prerequisites of optimum formulation and the use of such combination will achieve CDH at 5.5 min which matches with the optimized result.

Factor Coding: Actual

All Responses
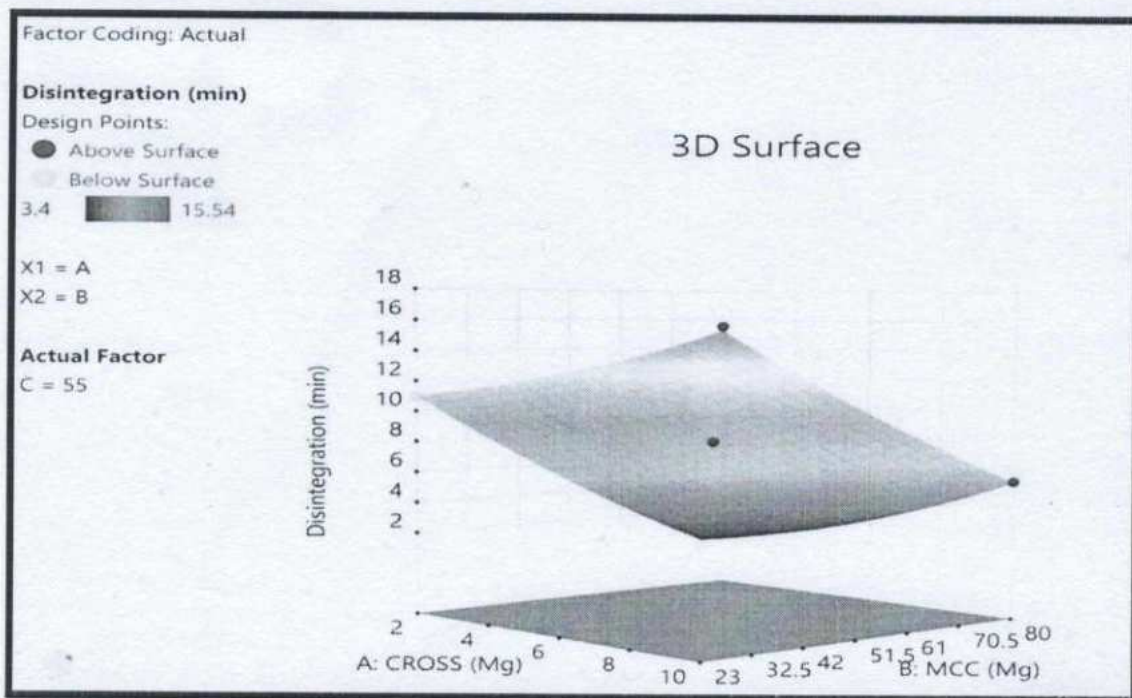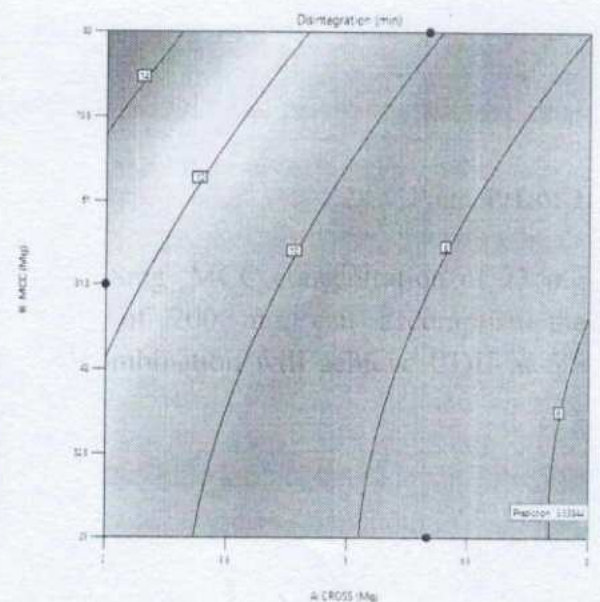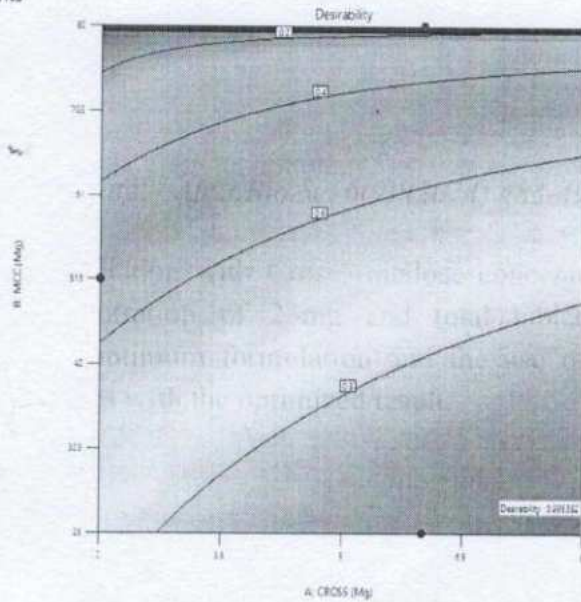- Design Points

0 ▬▬ 1

X1 = A
X2 = B

Actual Factor
C = 25.0001

Factor Coding: Actual

Disintegration (min)
Design Points:
- Above Surface
- Below Surface

3.4 ▬▬ 15.54

X1 = A
X2 = B

Actual Factor
C = 55

3D Surface

Figure 03: Normal probability plots of the residuals and model residuals

straight line, they affirm the accuracy of the quadratic modelling.

ANOVA results (Table 4) reinforce the model's reliability, with a significant Model F-value of 215.13 and a non-significant Lack of Fit value, indicating the model's adequacy in representing the data. Polynomial equations, derived from multiple regression analysis, enable the estimation of variable effects on selected responses, with significant factors determined by p-values less than 0.0500. (16)

In particular, Response I is significantly influenced by both the antagonistic effect of factors A and B (p < 0.001) and the synergistic effect of the interaction term AB and the polynomial term of A (with p-values of 0.0007 and 0.0012, respectively). Notably, factor B exhibits the highest magnitude of impact on Response I among all significant factors. **Table 4: Disintegration**

Source	Sum of Squares	df	Mean Square	F-value	p-value	
Model	182.51	9	20.28	90.76	< 0.0001	significant
A-CROSS	145.35	1	145.35	650.56	< 0.0001	
B-MCC	18.39	1	18.39	82.32	< 0.0001	
C-DCP	6.90	1	6.90	30.89	0.0009	
AB	1.35	1	1.35	6.02	0.0438	
AC	0.2116	1	0.2116	0.9471	0.3629	
BC	0.0072	1	0.0072	0.0323	0.8624	
A^2	0.9651	1	0.9651	4.32	0.0763	
B^2	2.01	1	2.01	9.00	0.0199	
C^2	6.44	1	6.44	28.80	0.0010	
Residual	1.56	7	0.2234			
Lack of Fit	0.3640	3	0.1213	0.4044	0.7585	not significant
Pure Error	1.20	4	0.3000			
Cor Total	184.08	16				

Factor coding is **Coded**.
Sum of squares is **Type III - Partial**
The Model F-value of 90.76 suggests that the model is highly significant. The probability of such a large F-value occurring due to noise is only 0.01%.(17)
P-values less than 0.0500 indicate that model terms are significant, implying their influence on the response. In this case, factors A, B, C, AB, B^2, and C^2 are all found to be significant model terms. Conversely, values greater than 0.1000 suggest that the model terms lack significance. Additionally, a polynomial equation can be employed to predict the response at any given level of the factor. Utilizing response surface methodology enables the elucidation and analysis of the effects of factors on selected responses. Visual representations such as contour plots and 3-dimensional (3-D) response surface graphs (RSG) provide a clear illustration of calculated responses.

Final Equations in Terms of Coded Factors

$15.0969 + -1.05725 * A + -0.00666205 * B + -0.111199 * C + -0.00508772 * AB + -0.00191667 * AC + 4.97076e-05 * BC + 0.0299219 * A^2 + 0.000851031 * B^2 + 0.00137361 * C^2$

Principal
Indore Institute of Pharmacy,
INDORE (M.P.)

GLOBAL DESIRABILITY FUNCTION
Optimization of the process can be done by setting the goal for every response then the Global desirability function (D) was applied simultaneously. Response I was targeted to 5.5 min. On basis of these criteria, the desirability plot was generated with a D value of 0.995 (Fig. 3).

was assured that pH should not shift too much alkaline that it impacts the digestion process.
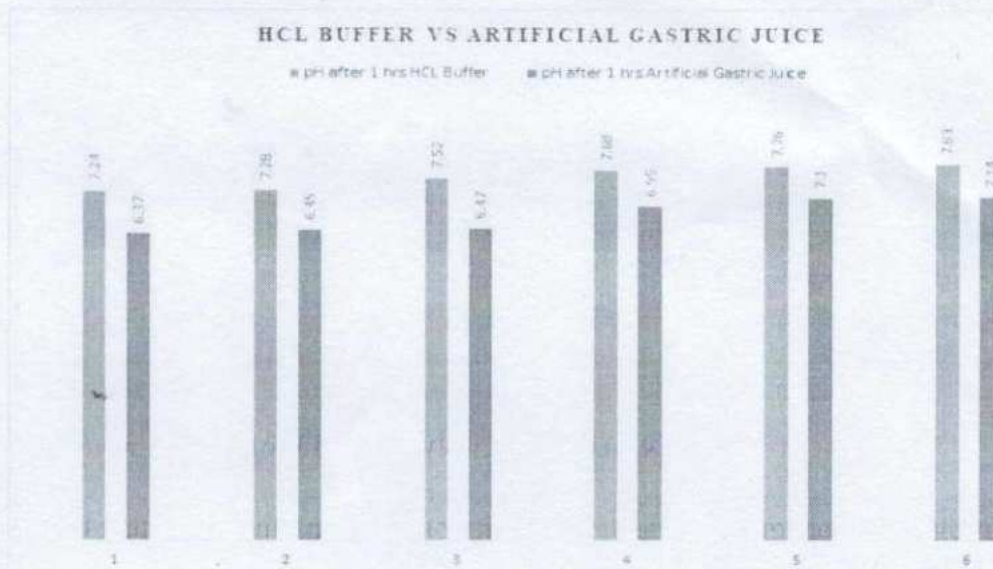

Figure 01: pH profile of the formulation.

Optimization data analysis and validation of Optimization model:

Box-Behnken design was used to study the optimal levels of independent variables. As shown in Table 1, a total of 17 anticipated runs were observed. The sequential model sum of squares [Type III] confirms the highest fit Statistics. The **Predicted R²** of 0.9582 is in reasonable agreement with the **Adjusted R²** of 0.9806; i.e. the difference is less than 0.2.

The sequential p value for the Quadratic model was found to be 0.0018, which is below the level of significance (< 0.001). The Predicted R² of 0.9582 is in reasonable agreement with the Adjusted R² of 0.9806; i.e. the difference is less than 0.2. Fig. 02.
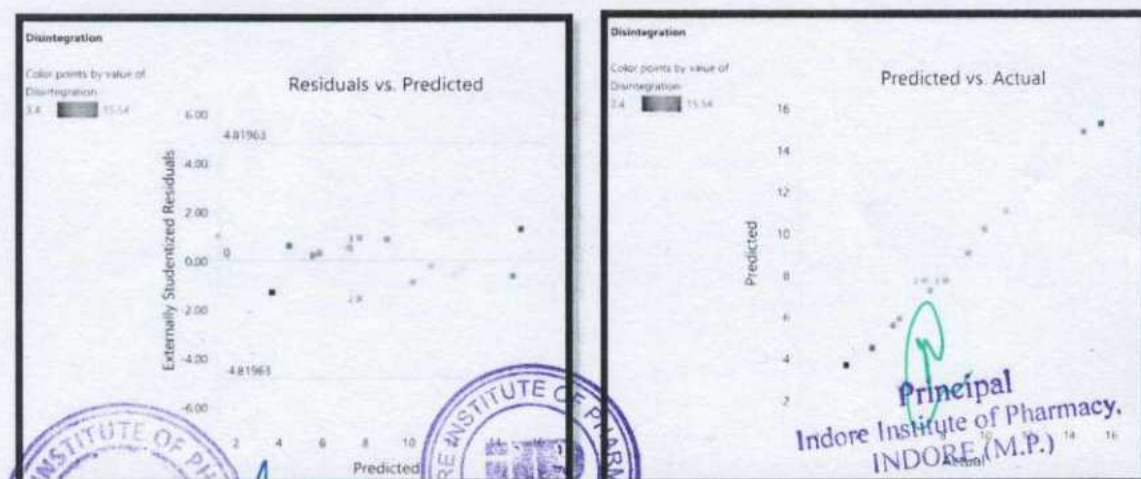
Figure 02: Drug release profiles of Mini tablet formulations

Adequate precision, as assessed by the signal-to-noise ratio, is essential for ensuring model reliability. A ratio exceeding 4 is considered desirable, and our ratio of 31.880 indicates a robust signal, underscoring the model's efficacy for navigating the design space (refer to Table 2). The quadratic model, characterized by a precision ratio of 31.8578, signifies satisfactory signal strength for exploration within the design space. This is further bolstered by a relatively low coefficient of variation (CV) of 2.42%. Although studentized results displayed slight deviation from the

142

from the batch are sampled, and their average thickness is calculated. Acceptable thickness falls within ±5% variation of the standard value.(14)

Friability Test

The friability test, conducted with a friabilator, presents results as a percentage (%). Twenty tablets from each batch are weighed individually (Wt. Initial) and subjected to 100 revolutions at 25 rpm in the friabilator. Subsequently, the tablets are reweighed (Wt. Final), and the percentage friability (F) is calculated using a specified formula.

Weight Variation Test

The weight variation test selects twenty tablets from the lot, weighs each to find the average weight, and calculates the percent deviation from this average. Acceptable weight ranges, as per pharmacopeial standards, determine maximum and minimum allowable weights for the tablets. The batch passes if no more than 2 tablets exceed the specified limit.

Drug Content Uniformity

Drug Content Uniformity ensures that each unit dose of a drug product contains the correct amount of active pharmaceutical ingredient (API) within acceptable limits. Randomly select 30 tablets from the batch for testing. Out of which 10 tablets were assayed individually.

The batch is considered to pass the test if 9 out of 10 tablets contain not less than 85% and not more than 115% of the labelled drug content, and the 10th tablet must also contain not less than 75% and not more than 125% of the labelled drug content. Should these conditions not be met, the remaining 20 tablets are assayed individually, and none may fall outside of the 85%-115% range.

Disintegration Test

Disintegration test was carried out using disintegration test apparatus. It assesses the time taken for a dosage form to break down into smaller particles or disintegrate into its individual components when exposed to a specified medium under standard conditions.

Randomly 6 tablets were selected from the batch for testing in water as disintegration medium at 37 ± 0.5 °C and recorded the time taken for each unit to completely disintegrate. Compare the observed disintegration times of the dosage units to the pharmacopeial standards. If all units meet the specified disintegration time, the batch passes the test.

In-vitro drug release studies

In vitro drug release studies of the formulation were conducted in 900 ml of 6.8 phosphate buffer as the dissolution media using a USP type 1 dissolution apparatus. The apparatus was maintained at 50 rpm and 37 ± 0.5 °C for 1 hour. During the dissolution test, samples were withdrawn at appropriate time interval and replaced with equivalent volume of fresh medium to maintain sink condition. The samples were filtered, diluted appropriately and then analysed spectrophotometrically for Pantoprazole sodium at 285nm.(15)

Results and Discussion
Estimation of Acid Neutralizing Capacity of Sodium Bicarbonate

Sodium bicarbonate was taken at doses spanning 300mg to 800mg in HCl buffer and artificial gastric juice. The objective was to assess its ability to neutralize acidity within the stomach, potentially safeguarding pantoprazole sodium mini-tablets from degradation by altering pH levels from acidic to alkaline conditions. The optimum dose i.e., 400mg was selected on the basis of ANC and its ability to maintain the pH at or above 5.5 for 1 hour. figure 1 While selecting the optimum dose, it

143

15.0969 + -1.05725 * A + -0.00666205 * B + -0.111199 * C + -0.00508772 * AB + -0.00191667 * AC + 4.97076e-05 * BC + 0.0299219 * A^2 + 0.000851031 * B^2 + 0.00137361 * C^2

Where, A=CROSS, B= MCC, C=DCP

Evaluation
Pre-Compression Parameters

The flow characteristics of powders play a crucial role and are vital for optimizing tabletting efficiency. Efficient tabletting relies on good powder flow for effective mixing and uniform tablet weight. Common flow property measurements, such as Bulk Density, Tapped Density, Compressibility Index, Hausner's Ratio, and Angle of Repose, inform the selection of compression techniques by assessing material flow characteristics. The flow property measurements of drug and blend, guides the selection of Compression method based on the flow characteristics of materials.(12)

Bulk Density

Bulk density is crucial in tablet manufacturing as it influences blend homogeneity, tablet weight uniformity, compression behaviour, tablet hardness, disintegration, dissolution, and manufacturing efficiency.

Tapped Density

Tapped density in tablet manufacturing ensures optimal powder compaction, uniform tablet weight, and consistent tablet hardness.

Angle of Repose

Angle of repose in tablet manufacturing determines powder flow properties and influences manufacturing processes such as blending, filling, and compaction.

Carr's Index

Carr's index in tablet manufacturing assesses powder compressibility, aiding in formulation optimization and ensuring consistent tablet quality.

Hausner's Ratio

Hausner's ratio in tablet manufacturing evaluates powder flowability, indicating potential processing challenges and affecting tablet compression efficiency.

POST-COMPRESSION PARAMETERS

Post-compression parameters such as hardness, thickness, weight variation, friability, disintegration time, and dissolution rate are vital for ensuring the quality, efficacy, and safety of pharmaceutical tablets. These parameters directly influence the tablet's strength, uniformity, durability, and drug release properties, crucial for its performance in treating patients. Hence, meticulous control and monitoring of these parameters are essential to uphold product quality and comply with regulatory standards.(13)

Hardness Test

The tablets prepared underwent hardness testing carried out using a monsanto hardness tester and results were expressed in kg/cm2.

Thickness Test

Thickness is measured by the tablet diameter using micrometres or vernier calliper.Twenty tablets

Principal
Indore Institute of Pharmacy,
INDORE (M.P.)

144
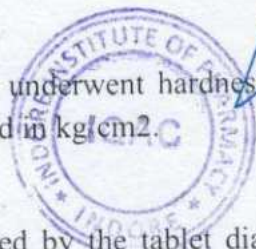
Factor	Name	Units	Type	SubType	Minimum	Maximum	Coded Low	Coded High	Mean	Std. Dev.
A	CROSS	Mg	Numeric	Continuous	2.00	10.00	-1 ↔ 2.00	+1 ↔ 10.00	6.00	2.83
B	MCC	Mg	Numeric	Continuous	23.00	80.00	-1 ↔ 23.00	+1 ↔ 80.00	51.50	20.15
C	DCP	Mg	Numeric	Continuous	25.00	85.00	-1 ↔ 25.00	+1 ↔ 85.00	55.00	21.21

Table: 2 Experimental run Project:

Std	Run	Factor 1 A:CROSS mg	Factor 2 B:MCC mg	Factor 3 C:DCP mg	Response 1 Disintegration min
17	1	6	51.5	55	8.12
15	2	6	51.5	55	8.12
1	3	2	23	55	11
9	4	6	23	25	7.38
6	5	10	51.5	25	4.63
14	6	6	51.5	55	7.12
16	7	6	51.5	55	7.12
5	8	2	51.5	25	12.46
7	9	2	51.5	85	14.7
2	10	10	23	55	3.4
12	11	6	80	85	12
11	12	6	23	85	9.23
10	13	6	80	25	9.98
4	14	10	80	55	5.62
8	15	10	51.5	85	5.95
3	16	2	80	55	15.54
13	17	6	51.5	55	8.12

Table 3: Fit Statistics:

Std. Dev.	0.4727	R^2	0.9915
Mean	8.85	Adjusted R^2	0.9806
C.V. %	5.34	Predicted R^2	0.9582
		Adeq Precision	31.8803

Quadratic Coded Equation:
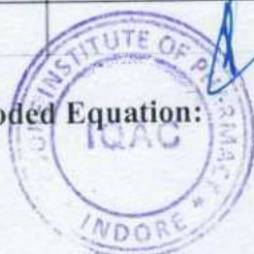
Estimation of Alkalizing Power of Sodium Bicarbonate

The study determined the acid-neutralizing capacity of sodium bicarbonate within a dosage range of 300-800mg, alkalizing capacity within this range was investigated using a digital pH meter for one hour and the investigation was conducted in two media: HCl buffer and artificial gastric juice.(10)

Formulation Development of Pantoprazole Sodium Mini-Tablets

The mini-tablets were fabricated using the direct compression method using Croscarmellose sodium used as a Disintegrating agent, Microcrystalline cellulose used as binder, Mannitol & Dicalcium Phosphate used as a filler. Magnesium stearate used as a glidant and talc used as a lubricant.

An ideal mixture was directly punched into tablets weighing about 200 mg containing 40 mg of pantoprazole sodium sesquihydrate, using rotary tablet compression machine using 5.6 mm diameter concave punches. The different batches of pantoprazole tablets were collected and stored in air tight containers.

Optimization of Mini Tablet:

Three formulation factors, namely CROSS (Croscarmellose sodium), MCC (Microcrystalline cellulose), and DCP (Dicalcium Phosphate), exerted significant influence on powder flowability, compressibility, and consequently, the characteristics of compressed tablets via direct compression. Table 1 outlines the levels for each variable determined in preliminary studies. Disintegration time (DT), cited in Table 2, served as the selected response variable.

A five-level three-factor BB experimental design assessed the impact of chosen independent variables on enhancing flowability, compressibility, characterizing drug release, and optimizing procedures.

This design enables exploration of quadratic response surfaces and construction of second-order polynomial models, facilitating process optimization with minimal experimental runs. In the three-level three-factor BB experimental design, 17 experimental runs were conducted, as indicated in Table 2. Tablets were assessed for physiochemical properties, with disintegration time (DT) measured as the response variable. Polynomial regression equations were derived and tested for significance. Subsequently, the process was optimized to determine levels of A, B, and C that yield optimal Y values under constrained conditions.

To confirm these values, a new formulation was created following the anticipated levels of A, B, and C. Subsequently, tablets were manufactured based on the optimized values and compared with the predicted values, as illustrated in Table 3. (11)

Table 1: Composition of Tablet:

146
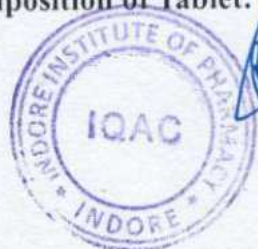
Introduction

The oral route of drug administration plays a crucial role in healthcare delivery as it is the most common and natural form of drug delivery offering numerous benefits including convenience, patient-centered care, and cost-effectiveness, making it a preferred choice for a diverse array of therapeutic interventions.(1) Oral drug delivery stands out as the most favored and preferred approach for administering therapeutic agents to achieve systemic effects. Tablets and capsules are solid dosage forms commonly used for drug delivery. They offer convenience, precise dosing, and easy administration. Tablets are compressed powders or granules, while capsules consist of gelatin shells enclosing drug formulations. Both tablets and capsules are available in various sizes, shapes, and formulations to accommodate diverse therapeutic needs.(2) Tablet-in-Capsule, a novel approach that combines the advantages of both tablet and capsule dosage forms. This amalgamation offers precise dosing, ease of administration, and improved drug stability. Gastrointestinal (GIT) diseases encompass a range of conditions affecting the digestive tract.(3)

Common gastrointestinal conditions encompass GERD (Gastroesophageal Reflux Disease), peptic ulcer disease, IBD (Inflammatory Bowel Disease), IBS (irritable bowel syndrome), gastroenteritis, and more.

Proton pump inhibitors (PPIs) are commonly used to treat such gastric conditions by inhibiting the proton pump enzyme in the stomach lining, which is responsible for producing acid.(4) By reducing acid production, PPIs help to relieve symptoms and promote healing of gastric conditions. But the acidic environment in stomach, leads to degradation of the drug molecules of PPI's. To mitigate the degradation of PPIs and ensure their efficacy, tablet-in-capsule technology is employed.(5) So, the current frontier in PPI therapy is immediate-release mini-tablet of Pantoprazole sodium combined with Sodium bicarbonate acting as buffering agent which prevents the degradation of drug by neutralizing the pH of stomach before absorption and protect the drug from low pH. (6)

Computer-aided modelling:

The mathematical relationship, expressed as a polynomial equation and visualized using the Box-Behnken design, was plotted to represent the measured responses. This was achieved using the statistical package of Design Expert V.13. (7)

Box-Behnken Experimental Design

For the optimization of mini tablet, three independent variables representing different concentrations of excipients were utilized. Design Expert 13, specifically employing the Box-Behnken design, facilitated this optimization process. Each numeric factor was set to three levels, allowing for a comprehensive exploration of the design space. The Box-Behnken design was duplicated for every combination of the categorical factor levels, ensuring thorough coverage of the parameter space.(8,9)

MATERIALS AND METHOD

Materials

Pantoprazole sodium was obtained as sample from IPCA Labs, Pithampur, Indore. Croscarmellose sodium and micro crystalline cellulose was obtained from Sisco Research Laboratories pvt. ltd., Mumbai, India.

Sodium bicarbonate, Potassium dihydrogen phosphate, disodium hydrogen phosphate, sodium bicarbonate, talc, magnesium stearate was obtained from LOBA Chemie pvt. Ltd.
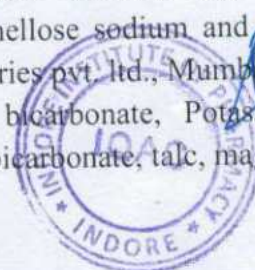
147

Research Paper   **Open Access**

Optimization, Formulation And Evaluation Of Tablet-In-Capsule: Sodium Bicarbonate Buffer With Pantoprazole Sodium Mini-Tablet

Pawan Patel[1*], Nayany Sharma[2], Nadeem A. Farooqui[3], Nimita Manocha[4]

Department of Pharmaceutics, Indore Institute of Pharmacy, Pithampur road, Opposite Indian Institute of Management, Rau Indore, Madhya Pradesh, 453331.

Corresponding author- Pawan Patel

Address: Department of Pharmaceutics, Indore Institute of Pharmacy, Pithampur road, Opposite Indian Institute of Management, Rau Indore, Madhya Pradesh, 453331. **Email:** pawan.patelmpharm2022@indoreinstitute.com

Orchid ID:0009-0004-3224-8390

ABSTRACT

Objective: This study aimed to formulate and optimize a Tablet-in-Capsule containing sodium bicarbonate and pantoprazole sodium using response surface methodology to optimize pantoprazole sodium mini-tablets.

Methods: Mini-tablets were prepared via the direct compression method, utilizing Croscarmellose sodium as a disintegrating agent, Microcrystalline cellulose as a binder, Mannitol & Dicalcium Phosphate as fillers. Magnesium stearate was used as a glidant and talc as a lubricant.
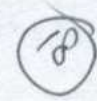
Results: The sodium bicarbonate dose was determined via Digital pH meter measurements for one hour. Mini-tablet formulation aimed for a disintegration time of 5.5 minutes. Subsequently, a desirability plot yielded a D value of 0.995. The optimized formulation was evaluated for thickness (3.65±0.10mm), weight variation (195.71±4.8 mg), hardness (6.9±0.70 kg/cm2), friability (0.51±0.02%), disintegration (5.5±0.15 min), and dissolution(99.11±0.15%).

Conclusion: A formulation containing sodium bicarbonate (400mg) and pantoprazole sodium mini-tablets with concentrations of pantoprazole sodium (40mg) Croscarmellose sodium (8mg), Dicalcium Phosphate (25mg), Microcrystalline cellulose (23mg) ,Mannitol (98mg) talc (2mg) magnesium stearate (4mg) with a total tablet weight of 200 mg, met the prerequisites of optimum formulation. This combination yielded a disintegration time of 5.5 minutes and 99.11% drug release in 50 minutes, aligning with the optimized result.
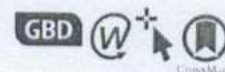
KEYWORDS: Pantoprazole sodium, Sodium bicarbonate, tablet-in-capsule, optimization, design expert, formulation.

148

Global fertility in 204 countries and territories, 1950–2021, with forecasts to 2100: a comprehensive demographic analysis for the Global Burden of Disease Study 2021

GBD 2021 Fertility and Forecasting Collaborators*

Summary

Background Accurate assessments of current and future fertility—including overall trends and changing population age structures across countries and regions—are essential to help plan for the profound social, economic, environmental, and geopolitical challenges that these changes will bring. Estimates and projections of fertility are necessary to inform policies involving resource and health-care needs, labour supply, education, gender equality, and family planning and support. The Global Burden of Diseases, Injuries, and Risk Factors Study (GBD) 2021 produced up-to-date and comprehensive demographic assessments of key fertility indicators at global, regional, and national levels from 1950 to 2021 and forecast fertility metrics to 2100 based on a reference scenario and key policy-dependent alternative scenarios.

Methods To estimate fertility indicators from 1950 to 2021, mixed-effects regression models and spatiotemporal Gaussian process regression were used to synthesise data from 8709 country-years of vital and sample registrations, 1455 surveys and censuses, and 150 other sources, and to generate age-specific fertility rates (ASFRs) for 5-year age groups from age 10 years to 54 years. ASFRs were summed across age groups to produce estimates of total fertility rate (TFR). Livebirths were calculated by multiplying ASFR and age-specific female population, then summing across ages 10–54 years. To forecast future fertility up to 2100, our Institute for Health Metrics and Evaluation (IHME) forecasting model was based on projections of completed cohort fertility at age 50 years (CCF50; the average number of children born over time to females from a specified birth cohort), which yields more stable and accurate measures of fertility than directly modelling TFR. CCF50 was modelled using an ensemble approach in which three sub-models (with two, three, and four covariates variously consisting of female educational attainment, contraceptive met need, population density in habitable areas, and under-5 mortality) were given equal weights, and analyses were conducted utilising the MR-BRT (meta-regression—Bayesian, regularised, trimmed) tool. To capture time-series trends in CCF50 not explained by these covariates, we used a first-order autoregressive model on the residual term. CCF50 as a proportion of each 5-year ASFR was predicted using a linear mixed-effects model with fixed-effects covariates (female educational attainment and contraceptive met need) and random intercepts for geographical regions. Projected TFRs were then computed for each calendar year as the sum of single-year ASFRs across age groups. The reference forecast is our estimate of the most likely fertility future given the model, past fertility, forecasts of covariates, and historical relationships between covariates and fertility. We additionally produced forecasts for multiple alternative scenarios in each location: the UN Sustainable Development Goal (SDG) for education is achieved by 2030; the contraceptive met need SDG is achieved by 2030; pro-natal policies are enacted to create supportive environments for those who give birth; and the previous three scenarios combined. Uncertainty from past data inputs and model estimation was propagated throughout analyses by taking 1000 draws for past and present fertility estimates and 500 draws for future forecasts from the estimated distribution for each metric, with 95% uncertainty intervals (UIs) given as the 2·5 and 97·5 percentiles of the draws. To evaluate the forecasting performance of our model and others, we computed skill values—a metric assessing gain in forecasting accuracy—by comparing predicted versus observed ASFRs from the past 15 years (2007–21). A positive skill metric indicates that the model being evaluated performs better than the baseline model (here, a simplified model holding 2007 values constant in the future), and a negative metric indicates that the evaluated model performs worse than baseline.

Findings During the period from 1950 to 2021, global TFR more than halved, from 4·84 (95% UI 4·63–5·06) to 2·23 (2·09–2·38). Global annual livebirths peaked in 2016 at 142 million (95% UI 137–147), declining to 129 million (121–138) in 2021. Fertility rates declined in all countries and territories since 1950, with TFR remaining above 2·1—canonically considered replacement-level fertility—in 94 (46·1%) countries and territories in 2021. This included 44 of 46 countries in sub-Saharan Africa, which was the super-region with the largest share of livebirths in 2021 (29·2% [28·7–29·6]). 47 countries and territories in which lowest estimated fertility between 1950 and 2021 was below replacement experienced one or more subsequent years with higher fertility; only three of these locations rebounded above replacement levels. Future fertility rates were projected to continue to decline worldwide, reaching a global TFR of 1·83 (1·59–2·08) in 2050 and 1·59 (1·25–1·96) in 2100 under the reference scenario. The number of countries and territories with fertility rates remaining above replacement was forecast to be 49 (24·0%) in 2050 and

149

only six (2·9%) in 2100, with three of these six countries included in the 2021 World Bank-defined low-income group, all located in the GBD super-region of sub-Saharan Africa. The proportion of livebirths occurring in sub-Saharan Africa was forecast to increase to more than half of the world's livebirths in 2100, to 41·3% (39·6–43·1) in 2050 and 54·3% (47·1–59·5) in 2100. The share of livebirths was projected to decline between 2021 and 2100 in most of the six other super-regions—decreasing, for example, in south Asia from 24·8% (23·7–25·8) in 2021 to 16·7% (14·3–19·1) in 2050 and 7·1% (4·4–10·1) in 2100—but was forecast to increase modestly in the north Africa and Middle East and high-income super-regions. Forecast estimates for the alternative combined scenario suggest that meeting SDG targets for education and contraceptive met need, as well as implementing pro-natal policies, would result in global TFRs of 1·65 (1·40–1·92) in 2050 and 1·62 (1·35–1·95) in 2100. The forecasting skill metric values for the IHME model were positive across all age groups, indicating that the model is better than the constant prediction.

Interpretation Fertility is declining globally, with rates in more than half of all countries and territories in 2021 below replacement level. Trends since 2000 show considerable heterogeneity in the steepness of declines, and only a small number of countries experienced even a slight fertility rebound after their lowest observed rate, with none reaching replacement level. Additionally, the distribution of livebirths across the globe is shifting, with a greater proportion occurring in the lowest-income countries. Future fertility rates will continue to decline worldwide and will remain low even under successful implementation of pro-natal policies. These changes will have far-reaching economic and societal consequences due to ageing populations and declining workforces in higher-income countries, combined with an increasing share of livebirths among the already poorest regions of the world.

Introduction

Characterising trends in key demographic indicators of fertility and projecting estimates into the future are essential to understand the impact of changing birth rates on social, economic, and geopolitical systems, both now and in the coming century. Dynamics in fertility patterns are central to the well established concept of the demographic transition,[1,2] which classically holds that societies will passage from a condition of high fertility and high mortality with more young than old people to a state of low fertility and low mortality with an increasingly older population. Some theorists have proposed the concept of a demographic dividend, whereby declining fertility rates lead temporarily to higher proportions of working adults available to generate resources and capital, potentially stimulating economic growth and eventual rebounds in fertility rates.[3] Demographic data in the 5 years preceding 2021 demonstrate that the total fertility rate (TFR) in some countries has fallen below replacement levels—the minimum rate necessary for generational replacement of the population assuming no migration—with no evidence of this predicted rebound.[4-7] The replacement level is generally accepted to be a TFR of at least 2·1, although the true replacement level depends on the specific mortality rate and sex ratio at birth in a population.[8] Low levels of fertility have the potential over time to result in inverted population pyramids with growing numbers of older people and declining working-age populations. These changes are likely to place increasing burdens on health care systems, transform labour and consumer markets, and

alter patterns of resource use. Accurate estimates and future forecasts of fertility rates and their impact on population age structures are therefore essential to anticipate potential economic and geopolitical consequences and to inform the development of effective health, environmental, and economic policies.

At present, an important source of fertility estimates and future forecasts for countries and areas throughout the world has been the Population Division of the UN Department of Economic and Social Affairs, which most recently produced the 2022 Revision of World Population Prospects (WPP 2022).[5] The UN Population Division estimates of past fertility are not compliant with the Guidelines on Accurate and Transparent Health Estimates Reporting (GATHER) statement in important respects; notably, they do not provide all code for statistical models or explicit details on criteria for exclusion or adjustment of primary data sources. Furthermore, the validity of UN Population Division projections has been questioned due to the assumptions applied in countries experiencing low post-transition fertility dropping below replacement level.[9,10] Previous UN Population Division forecasts have assumed that, in such circumstances, fertility rates will increase towards replacement levels,[11-13] and WPP 2022 assumes convergence to a rate that is a combination of country-specific historical rates and the mean rate in low-fertility countries that have experienced fertility increases.[14] The WPP 2022 projects gradual increases in TFR even in countries that have shown no evidence of fertility rate increases, such as South Korea and Thailand.[6,14-17] Additionally, UN Population Division

150

Research in context

Evidence before this study

Since the 1950s, global and national estimates and projections of key fertility indicators have been produced and regularly updated by the Population Division of the UN Department of Economic and Social Affairs, with the most recent iteration being the 2022 Revision of World Population Prospects. Assessments of fertility at national and subnational levels worldwide have also been conducted by the US Census Bureau since the 1960s, with estimates reported in the Bureau's International Database. More recently, fertility estimates and projections have been generated by the Wittgenstein Centre for Demography and Global Human Capital and by the Global Burden of Diseases, Injuries, and Risk Factors Study (GBD), an ongoing, large-scale research enterprise that systematically analyses worldwide data to assess global health trends. Past estimates of fertility have been produced as part of GBD since 2017, and future forecasts based on GBD findings were first published in 2020.

Added value of this study

Of the existing large-scale efforts to estimate worldwide trends in fertility, only GBD analyses are compliant with the Guidelines on Accurate and Transparent Health Estimates Reporting (GATHER) statement. This study also incorporates several important innovations introduced by the GBD population forecasting study by Vollset and colleagues in 2020 that support forecasting accuracy assessment and provide a framework by which to explore the impact of various policy scenarios on fertility patterns. These methods include: basing the GBD forecasting model on a measure of cohort fertility (completed cohort fertility at age 50 years, CCF50) that reflects the number of children born over time to females from a specific cohort, which better captures long-term choices people make about childbearing—such as delaying having children—than does the classic period-based measure of total fertility rate; and incorporating measures of female education and met need for modern contraceptives as covariates, which improves accuracy and allows for modelling alternative scenarios by changing levels of these indicators. In contrast to other models that assume rates in countries currently experiencing low fertility will tend to increase over time, or those that base their projections on expert

judgements, GBD fertility forecasting methods are grounded in existing, real-world evidence about fertility patterns in long-term cohorts of females and in data on related evidence-based covariates such as education and contraception. GBD 2021 has further improved the estimation of past, current, and future fertility in four important ways. First, an additional 147 surveys, 21 censuses, and 634 country-years of vital and sample registration data were added for estimation of past fertility trends. Second, smoothing parameters for estimating past fertility trends were updated to better fit available data. Third, to further improve specificity and accuracy of future fertility projections, two additional covariates were included that account for urbanicity (defined here as population density in habitable areas) and under-5 mortality in the CCF50 model. Fourth, we added a pro-natal alternative scenario to help policy makers plan interventions in countries with fertility rates below replacement level. Based on a skill metric designed to evaluate forecasting accuracy, the model presented here performed better across all age groups compared with a constant prediction.

Implications of all the available evidence

Our past estimates and future forecasts indicate that fertility rates are declining everywhere and are projected to continue to decrease over the coming century. By 2100, we estimate that fertility rates will be below replacement level in more than 95% of the world's countries and territories but that marked disparities in rates will remain. Our forecasts also suggest that, by 2100, the largest concentrations of livebirths will shift to low-income settings, particularly a subset of countries and territories in sub-Saharan Africa, which are among the most vulnerable to economic and environmental challenges. Extreme shifts in the global distribution of livebirths can be partially ameliorated by improved female education and met need for modern contraception. Outside of this subset of low-income areas, most of the world's countries will experience the repercussions of low fertility, with ageing populations, declining workforces, and inverted population pyramids, which are likely to lead to profound fiscal, economic, and social consequences. National policy makers and the global health community must plan to address these divided sets of demographic challenges emerging worldwide.

models are based on TFR, which is a period measure and therefore does not account for change over time in fertility behaviours. For example, in settings where fertility rates in older women increase due to choices to delay births, TFR would underestimate fertility forecasts. Reliance on TFR can also lead to short-term fluctuations in estimated fertility forecasts that are especially impactful in countries with low fertility rates.[18] Moreover, their projections forecast TFR solely as a function of time and do not include other covariates to inform the models, which disregards potential explanatory data and precludes investigating the effects

of alternative policy-related scenarios or other drivers of fertility. The US Census Bureau International Database has also provided worldwide fertility estimates and projections, currently in 227 countries, since the 1960s, but country-specific updates are not performed on a regular basis.[19] Since the 1990s, global and regional fertility forecasts have also been generated by the World Population Program of the International Institute for Applied Systems Analysis,[20] with country-level projections more recently produced by an affiliated group, the Wittgenstein Centre for Demography and Global Human Capital.[21,22] These forecasts rely on

assumptions informed by expert opinions from demographic scientists to predict future fertility rates.[21–23]

The Global Burden of Diseases, Injuries, and Risk Factors Study (GBD) is an ongoing, large-scale research enterprise that characterises the state of global health by estimating key health metrics at global, regional, and national levels.[24] Beginning with the 2017 GBD cycle, past and current fertility estimates generated as part of the GBD analytic framework were published;[25] before that, estimates from the UN Population Division were used as inputs to GBD analytic processes.[26,27] For GBD 2019, past and current fertility estimates were reported jointly with mortality, life expectancy, and population measures in a publication focused on overall demographic estimates,[28] and GBD-based forecasts of population and fertility up to 2100 were reported separately by Vollset and colleagues in 2020.[3] GBD fertility estimates are based on clear data and methods applying a standardised approach, providing publicly available code. Vollset and colleagues addressed some of the existing issues regarding the use of TFR in the modelling process by developing an Institute for Health Metrics and Evaluation (IHME) forecasting model based instead on completed cohort fertility at age 50 years (CCF50: the average number of children born over time to females from a specified birth cohort)[29] to capture change over time in fertility behaviours, which yields more stable and accurate fertility estimates. Vollset and colleagues[4] also included covariates representing female educational attainment and contraceptive met need (a measure of the proportion of females of reproductive age whose need for contraception has been met with modern contraceptive methods) to better inform fertility estimates and facilitate exploration of alternative future scenarios associated with achievement of UN Sustainable Development Goals (SDGs) related to education and contraception.

The present GBD 2021 study focuses on fertility metrics, presenting past estimates (1950–2021) along with forecasts up to 2100. Results were improved since GBD 2019 and the 2020 study by Vollset and colleagues by incorporating newly available demographic data and through key methodological advances. This paper provides a high-level overview of our findings. We anticipate that the results will provide insights for policy makers and will be used as a tool to help plan and shape future policies to better prepare for profound changes in global fertility.

This paper was produced as part of the GBD Collaborator Network and in accordance with the GBD Protocol.[30]

Methods

Overview

For each subsequent GBD round, newly available data and updated methods are used to update the full time series of estimates from 1950 up to the latest year of

analysis. As a consequence, GBD 2021 estimates supersede all previous estimates. GBD 2021 estimated key fertility metrics in females between ages 10 years and 54 years in 204 countries and territories grouped into 21 regions and seven super-regions. GBD regions are made up of countries and territories that are geographically close and epidemiologically similar.[31] These regions are then grouped into super-regions based on cause of death patterns. The full GBD location hierarchy is shown in appendix 1 (table S1). GBD 2021 drew on the expertise of more than 11000 collaborators across more than 160 countries and territories. The GBD 2021 fertility analysis framework produced estimates for every year from 1950 to 2021 and forecasts up to 2100.

The methods used to produce fertility estimates from 1950 to 2021 closely followed those of GBD 2019.[28] Methods used to generate fertility forecasts to 2100 were based on a modified and revised version of the modelling approach used in the 2020 study by Vollset and colleagues.[4] These methods have been peer-reviewed over previous GBD rounds and as part of the peer-review process for GBD 2021. Here we provide an overview of the methods with an emphasis on the main changes since GBD 2019 and the 2020 study by Vollset and colleagues;[4,28] a more comprehensive description of the analytical methods for GBD 2021 is provided in appendix 1. Additional details on specific data inputs are accessible through the GBD Sources Tool.

Data sources and processing

We systematically searched for accurate and complete data on livebirths reported according to the age of mothers. In many high-income countries and territories, these data were available from high-quality vital registration systems, but in many lower-income countries, birth registries were incomplete, interrupted, or delayed; in these instances, we instead relied on complete and summary birth histories in censuses and household surveys. Fertility rates from vital registration data were calculated as observed births divided by population estimates. Complete and summary birth history data were collapsed from the available microdata and sample weights applied to calculated age-specific fertility rates (ASFRs) and number of children ever born, respectively. A full description of data seeking and synthesis is provided in appendix 1 (section 2.1). In total, we compiled 58072 unique location-source-years of data for females aged 10–54 years for the period between 1950 and 2021 (number of sources by location and by year can be found in appendix 1 tables S3 and S4). At the national level, we obtained 8680 unique country-source-years of vital registration data, with an additional 29 country-source-years of data from sample registration systems. We additionally extracted data on period ASFR, or average number of children ever born from surveys and censuses that yielded 735 complete birth histories,

879 summary birth histories, and 28 unclassified forms of birth histories (details are in appendix 1 tables S3 and S4).

Throughout the forecasting modelling processes, we used female education, under-5 mortality, met need for contraceptive use, and population density in habitable areas as covariates. Details of these covariates are available in appendix 1 (section 3.1).

Fertility from 1950 to 2021

GBD 2021 estimates of fertility metrics between 1950 and 2021 were based on a systematic synthesis of all available data for all GBD locations. The fertility estimation process was closely connected to parallel, concordant modelling of population and mortality, with population estimates used iteratively to generate inputs to fertility estimation models and vice versa.[28] GBD methods are designed to account for the diversity of data available and the different biases inherent in various data sources, with customised data processing and data synthesis steps implemented to account for known biases, missing data, and heterogeneous measurement metrics used across data sources. Estimation of fertility rates between 1950 and 2021 for females ages 10–54 years largely followed the methods used in GBD 2019.[28] First, ASFRs were estimated for 5-year age groups between 15 years and 49 years only using age-specific vital registration and complete birth history data. These results were used to split all-age data from vital registration, summary birth history, and other sources into ASFRs, and then another model was fit to estimate ASFRs using the original age-specific ASFR data from vital registration and complete birth history along with these age-split data. Next, we extended these estimates to the age groups of 10–14 years and 50–54 years using data from these ages and adjacent age groups. Finally, ASFR estimates were used to calculate TFR. A summary of these methods follows, with a comprehensive description provided in appendix 1 (section 2).

To estimate ASFRs by 5-year age groups for females aged 15–49 years, we implemented mixed-effects regression models using bounded logit(ASFR) as the outcome. The 20–24-years age group was estimated first, and these estimates were used to model the remaining age groups. Both sets of models were fit separately for the high-income, sub-Saharan Africa, and central Europe, eastern Europe, and central Asia super-regions to account for differences in the relationships between the ASFR of the 20–24-years age group and that of other age groups. ASFRs in the 20–24-years age group were modelled with female educational attainment as a covariate and random intercepts for each location source. Then, we separately modelled ASFRs in the remaining age groups between 15 years and 49 years using a linear spline on the logit(ASFR) in the 20–24-years age group. The selection of spline knots varied by super-region and age group. These models also included female educational

attainment as a covariate, except in the high-income super-region, and random intercepts for each location source. After running these mixed-effects models, we corrected for systematic differences across data sources by selecting a reference source for each location and adjusting other sources based on their discrepancy from the reference source. Last, a spatiotemporal Gaussian process regression (ST-GPR) was used to smooth ASFRs across location and time, producing final point estimates and uncertainty intervals (UIs).

First-round ASFR estimates were generated from this modelling approach using age-specific vital registration and complete birth history data. To split total birth data from vital registration data, summary birth histories, and other sources into ASFRs, we calculated the ratio of the parity implied by each total birth data source to the parity estimated in this first-round ASFR model. This ratio was then multiplied by the estimated ASFRs from the first-round model. These age-split data were incorporated into a second round of estimation for each location using the same modelling approach described earlier. To generate estimates for ages 10–14 years and 50–54 years, we estimated the ratio of ASFR to the adjacent age group using all available data, then applied these ratios to the second-round ASFR estimates. We used a mixed-effects regression model to estimate location-specific ratios for ages 10–14 years, whereas we calculated the average ratio across all locations for ages 50–54 years. Finally, TFR was calculated by multiplying the ASFRs from each 5-year age group by five and summing.

Fertility forecasting

We produced forecasts of fertility using an updated modelling framework (appendix 1 section 3) that improved on the methods in the 2020 study by Vollset and colleagues.[4] In our updated methods, we used not only estimates of female educational attainment and contraceptive met need as covariates, but also estimates of under-5 mortality and population density in habitable areas to account for a larger variation in CCF50 across all countries in the sub-models (appendix 1 section 3.1, appendix 2 figure S2). Similar to Vollset and colleagues, we continued to forecast fertility with CCF50 rather than TFR, because modelling in cohort space is more stable than in period space. For this analysis, we used past CCF50 estimates for birth cohorts from 1945 to 1972 to forecast CCF50 up to the 2085 birth cohort of females, followed by predicting ASFR for each 5-year age interval as a proportion of CCF50. CCF50 was defined as the average number of children born to an individual female from an observed birth cohort (indexed by year of birth) if she lived to the end of her reproductive lifespan (ages 15–49 years). CCF50 was forecast using an ensemble modelling approach with three equally weighted sub-models (with five, three, and four covariates) in which each sub-model utilised the MR-BRT (meta-regression—Bayesian, regularised, trimmed) tool.[34] For example, the

2061

153

four-covariate sub-model was represented by the following equation:

$$logit_{(0.7,10)}(CCF50_{lc})=\beta_0+ spline(education_{lc}) \times \beta_1$$
$$+ met\ need_{lc} \times \beta_2$$
$$+ under\text{-}5\ mortality_{lc} \times \beta_3$$
$$+ population\ density\ per\ habitable\ area_{lc} \times \beta_4$$
$$+ \varepsilon_{lc.}$$

where CCF50 is scaled from more than 0·7 to less than 10 and modelled in logit space for location (*l*) and cohort (*c*), β_0 is an intercept, β_1 is a vector of the spline coefficients of female educational attainment covariate, β_2 is a slope on proportion of met need for contraception, β_3 is a slope on under-5 mortality, β_4 is a slope on population density in habitable areas, and ε is a residual term. Further details are provided in appendix 1 (section 3.2, figure S1).

From forecast CCF50, we then derived ASFR forecasts for the years 2022 to 2100 using a combination of a linear mixed-effects model, spline interpolation, and an autoregressive integrated moving average (ARIMA) model (1,0,0) on residuals to estimate the age pattern of fertility for each cohort. Once ASFR values for ages 15–49 years were obtained, we inferred the ASFR values for the 10–14-years and 50–54-years age groups based on their ratios to the rest of the age pattern during the last observed year (2021). Single-year age interval ASFRs were summed over all ages to yield the TFR for each calendar year (appendix 1 section 3.3).

We also produced fertility forecasts for four alternative scenarios applied to all 204 countries and territories. These scenarios explore shifting forecast values of two known drivers of fertility (education and met need for contraceptives) as well as a proxy pro-natal policy. More specifically, the scenarios included were: the UN SDG target 4.1 for education is achieved by 2030; the contraceptive met need SDG target 3.7 is achieved by 2030; pro-natal policies are enacted that create supportive environments for those who give birth; and the previous three scenarios combined (more details are provided in appendix 1 section 3.4). For the education SDG scenario, the forecasts assume that by 2030, all people will have 12 years or more of education by the age of 25 years and then maintains the same rate of change as the reference scenario up to 2100. For the contraceptive met need scenario, to reflect the SDG scenario of universal access, the forecasts assumed a linear increase in contraceptive coverage to reach 100% by 2030 and then stay constant up to 2100.

In the pro-natal scenario, we assumed a country will introduce pro-natal policies, such as childcare subsidies, extended parental leave, insurance coverage expansion for infertility treatment,[11] and other forms of support to parents to afford high-quality child-care services once TFR decreases to less than 1·75. We then made three

assumptions on the effects of such policies. First, we assumed the full effect of pro-natal policies will be to increase TFR by 0·2. Second, it will take 5 years after the policy is introduced for the full increase in TFR to occur, and TFR will rise linearly over that time span. Last, we assumed that both the policies and the increase in TFR by 0·2 will endure for the remainder of the century. For each pro-natal year, the TFR increase was distributed proportionally among the single-year ages according to their reference forecast ASFR values. The pro-natal scenario parameters were drawn from previously observed increases in TFR that coincided with pro-natal policies and broader empirical evidence regarding effects of pro-natal policies in low-fertility contexts. Further details on the pro-natal scenario can be found in appendix 1 (section 3.4.3).

In the combined scenario, we applied the aforementioned changes to the covariate forecasts simultaneously without assigning any weights because these covariates were already embedded in our model and the coefficients for each covariate were calculated based on the observed data.

GBD 2021 updates

To estimate ASFRs from 1950 to 2021, GBD 2021 added 147 surveys, 21 censuses, and 634 country-years of vital and sample registration data compared with GBD 2019, for a total of 1455 surveys and censuses, 8709 country-years of vital and sample registration data, and 150 other sources. Methods were updated for GBD 2021 by changing the time weight in ST-GPR to use a beta density function, in which hyperparameters were assigned based on quality of available data sources and the number of available datapoints. This better accounted for increased data availability, which improved precision and produced more plausible time trends compared with GBD 2019.

Updates to the fertility forecasting methods first introduced in the 2020 study by Vollset and colleagues[4] included the incorporation of two new covariates in the CCF50 model—namely, under-5 mortality and population density in habitable areas—in addition to those previously used (ie, female educational attainment and contraceptive met need). Furthermore, the current iteration of the IHME model employed a linear fixed-effect model to forecast 5-year ASFRs, which were interpolated to 1-year estimates using an ARIMA model on the residuals to quantify variation not explained by the covariates.

Comparison with other models

We evaluated the IHME fertility forecasting model performance based on out-of-sample predictions during the validation period 2007–21. We used the following skill metric[14] for model evaluation and comparison (see appendix 1 section 3.6 for more details):

$$= 1 - \frac{RMSE(Model)}{RMSE(Baseline\ Model)},$$

154

	Total fertility rate					Livebirths (thousands)					Net reproductive rate, 2021
	1950	1980	2021	2050	2100	1950	1980	2021	2050	2100	
Global	4·84 (4·63–5·06)	3·61 (3·53–3·69)	2·23 (2·09–2·38)	1·83 (1·59–2·08)	1·59 (1·25–1·96)	92675·8 (88663·5–96630·8)	122004·7 (119441·0–124623·8)	129383·6 (121382·9–138206·0)	112073·6 (93598·4–133329·8)	73386·8 (40812·5–118843·5)	1·0 (1·0–1·1)
Central Europe, eastern Europe, and central Asia	3·01 (2·91–3·11)	2·24 (2·21–2·28)	1·81 (1·72–1·92)	1·68 (1·56–1·81)	1·57 (1·42–1·73)	7452·5 (7227·2–7699·6)	7113·3 (7020·5–7211·4)	4906·1 (4635·7–5195·7)	3874·8 (3409·2–4396·4)	2344·9 (1739·5–3067·1)	0·9 (0·8–0·9)
Central Asia	4·45 (4·32–4·59)	3·73 (3·65–3·80)	2·79 (2·68–2·91)	2·31 (2·16–2·47)	1·95 (1·76–2·13)	1016·0 (986·0–1046·1)	1676·9 (1642·3–1709·2)	2073·1 (1990·1–2158·2)	1913·2 (1629·7–2201·3)	1418·0 (1007·6–1927·4)	1·3 (1·3–1·4)
Armenia	4·14 (3·95–4·33)	2·49 (2·39–2·61)	1·68 (1·53–1·84)	1·45 (1·27–1·65)	1·24 (1·01–1·49)	49·0 (46·8–51·1)	76·5 (73·2–79·9)	35·0 (31·6–38·5)	16·9 (11·9–22·2)	6·7 (3·5–11·3)	0·8 (0·7–0·9)
Azerbaijan	4·38 (4·09–4·69)	3·33 (3·18–3·48)	1·75 (1·55–1·95)	1·51 (1·27–1·76)	1·29 (1·01–1·59)	107·5 (100·2–114·9)	162·2 (155·0–169·6)	138·7 (123·5–154·9)	93·5 (69·0–122·7)	38·3 (17·9–69·8)	0·8 (0·7–0·9)
Georgia	2·60 (2·42–2·79)	2·21 (2·07–2·33)	2·05 (1·92–2·18)	1·80 (1·65–1·96)	1·52 (1·34–1·71)	84·2 (78·4–90·3)	91·8 (86·3–96·9)	45·2 (42·4–48·1)	36·1 (28·7–43·7)	21·3 (14·2–30·4)	1·0 (0·9–1·0)
Kazakhstan	3·94 (3·79–4·11)	3·02 (2·93–3·11)	3·02 (2·85–3·20)	2·43 (2·21–2·65)	1·94 (1·69–2·19)	253·8 (244·5–264·1)	365·1 (353·6–376·9)	424·9 (400·9–448·7)	392·9 (325·0–461·4)	261·4 (147·7–409·6)	1·4 (1·4–1·5)
Kyrgyzstan	4·19 (4·03–4·35)	4·12 (3·98–4·27)	2·92 (2·66–3·21)	2·35 (2·05–2·70)	1·95 (1·63–2·33)	57·9 (55·6–60·2)	111·9 (107·3–116·3)	159·2 (145·4–175·1)	139·1 (104·2–181·6)	72·0 (21·5–145·6)	1·4 (1·3–1·5)
Mongolia	5·09 (4·78–5·41)	5·76 (5·55–5·97)	3·16 (2·86–3·49)	2·46 (2·02–2·88)	1·87 (1·35–2·35)	30·2 (28·4–32·1)	61·9 (59·7–64·1)	80·0 (72·4–88·0)	100·9 (76·4–124·5)	104·2 (46·7–179·1)	1·5 (1·4–1·6)
Tajikistan	6·65 (6·33–6·96)	5·65 (5·47–5·84)	3·40 (3·17–3·64)	2·66 (2·33–2·97)	2·13 (1·75–2·49)	86·2 (82·6–89·9)	159·7 (154·8–164·5)	286·4 (268·0–306·6)	301·0 (229·2–381·8)	243·2 (101·7–421·6)	1·6 (1·5–1·7)
Turkmenistan	4·82 (4·63–5·01)	4·75 (4·55–4·94)	2·83 (2·54–3·15)	2·25 (1·87–2·66)	1·81 (1·38–2·28)	48·7 (46·7–50·5)	96·4 (92·9–99·8)	110·5 (99·4–122·7)	105·2 (80·2–139·0)	75·9 (33·1–146·2)	1·3 (1·2–1·5)
Uzbekistan	5·68 (5·32–6·06)	4·58 (4·47–4·69)	2·87 (2·66–3·10)	2·34 (2·08–2·62)	1·97 (1·69–2·27)	298·6 (280·9–316·6)	555·5 (526·2–564·1)	793·1 (733·6–848·3)	727·6 (491·2–993·0)	595·0 (307·1–992·9)	1·3 (1·2–1·4)
Central Europe	3·22 (3·13–3·30)	2·21 (2·18–2·24)	1·48 (1·36–1·61)	1·34 (1·19–1·50)	1·21 (1·03–1·41)	2336·9 (2276·3–2399·1)	2085·5 (2056·7–2113·8)	1038·3 (954·3–1129·1)	668·1 (567·7–786·3)	283·6 (185·8–412·4)	0·7 (0·7–0·8)
Albania	5·88 (5·63–6·13)	3·44 (3·31–3·58)	1·50 (1·33–1·69)	1·34 (1·10–1·61)	1·17 (0·86–1·50)	48·0 (45·9–50·0)	71·4 (68·8–74·3)	27·9 (24·7–31·4)	16·4 (11·6–22·4)	6·3 (2·9–12·3)	0·7 (0·6–0·8)
Bosnia and Herzegovina	3·68 (3·31–4·08)	2·21 (1·97–2·46)	1·33 (1·20–1·46)	1·16 (0·99–1·35)	0·95 (0·71–1·19)	92·6 (83·8–102·1)	79·0 (70·7–87·8)	26·7 (24·2–29·4)	12·4 (8·8–16·8)	3·5 (1·7–6·2)	0·6 (0·6–0·7)
Bulgaria	2·77 (2·65–2·91)	2·07 (2·02–2·12)	1·58 (1·47–1·70)	1·43 (1·29–1·59)	1·26 (1·08–1·45)	167·6 (160·5–175·7)	127·8 (124·7–130·8)	58·1 (53·7–62·4)	36·6 (29·6–44·0)	13·9 (8·5–21·6)	0·8 (0·7–0·8)
Croatia	2·89 (2·78–3·00)	1·83 (1·78–1·87)	1·37 (1·22–1·53)	1·27 (1·08–1·46)	1·14 (0·92–1·38)	90·2 (87·0–93·5)	67·4 (65·9–69·2)	34·8 (31·0–38·9)	16·8 (12·3–22·0)	3·2 (0·3–7·2)	0·7 (0·6–0·7)
Czechia	2·81 (2·69–2·94)	2·08 (2·03–2·13)	1·74 (1·57–1·93)	1·54 (1·34–1·76)	1·36 (1·13–1·60)	186·6 (178·6–194·9)	152·3 (148·6–155·8)	105·9 (95·4–117·6)	82·1 (67·2–98·5)	44·9 (27·3–68·3)	0·8 (0·8–0·9)
Hungary	2·58 (2·43–2·72)	1·89 (1·84–1·94)	1·56 (1·40–1·75)	1·42 (1·22–1·65)	1·29 (1·06–1·55)	193·1 (182·7–203·9)	147·0 (143·1–151·2)	87·9 (78·5–98·4)	77·0 (61·9–94·7)	51·6 (32·1–78·9)	0·8 (0·7–0·8)
Montenegro	4·12 (3·89–4·37)	2·22 (2·13–2·30)	1·72 (1·61–1·83)	1·56 (1·43–1·70)	1·40 (1·23–1·58)	12·5 (11·8–13·2)	10·5 (10·1–10·9)	7·0 (6·5–7·4)	4·5 (3·7–5·4)	1·6 (0·9–2·5)	0·8 (0·8–0·9)
North Macedonia	3·62 (3·26–4·02)	2·45 (2·21–2·71)	1·23 (1·16–1·30)	1·10 (1·01–1·20)	0·97 (0·84–1·09)	37·6 (34·0–41·5)	39·9 (36·0–44·0)	18·7 (17·7–19·8)	9·4 (7·3–11·9)	1·8 (0·9–3·0)	0·6 (0·6–0·6)
Poland	3·63 (3·53–3·72)	2·28 (2·24–2·32)	1·37 (1·22–1·53)	1·21 (1·04–1·40)	1·07 (0·87–1·29)	757·4 (737·3–776·6)	693·3 (680·1–706·4)	342·0 (304·9–381·1)	206·2 (163·3–254·7)	74·4 (43·4–116·7)	0·7 (0·6–0·7)

(Table 1 continues on next page)

155

	Total fertility rate					Livebirths (thousands)					Net reproductive rate, 2021
	1950	1980	2021	2050	2100	1950	1980	2021	2050	2100	
(Continued from previous page)											
Romania	3·02 (2·84–3·22)	2·32 (2·25–2·39)	1·70 (1·57–1·84)	1·48 (1·32–1·66)	1·26 (1·06–1·48)	415·0 (390·9–442·4)	387·3 (375·7–399·2)	177·6 (163·6–192·6)	114·9 (89·2–143·0)	37·7 (18·8–62·7)	0·8 (0·8–0·9)
Serbia	3·31 (3·22–3·40)	2·22 (2·17–2·28)	1·08 (0·99–1·16)	1·01 (0·90–1·11)	0·96 (0·82–1·09)	183·9 (179·1–188·1)	157·5 (153·3–161·7)	61·6 (56·8–66·7)	34·0 (27·8–40·6)	10·5 (7·1–14·6)	0·5 (0·5–0·6)
Slovakia	3·65 (3·56–3·75)	2·32 (2·27–2·36)	1·63 (1·53–1·73)	1·46 (1·34–1·59)	1·31 (1·16–1·46)	99·6 (97·1–102·2)	94·6 (92·9–96·3)	56·3 (52·9–59·8)	40·0 (34·2–45·7)	20·9 (15·1–27·4)	0·8 (0·7–0·8)
Slovenia	2·86 (2·54–3·20)	2·01 (1·97–2·06)	1·63 (1·53–1·74)	1·51 (1·39–1·64)	1·38 (1·24–1·54)	32·3 (28·8–36·2)	29·5 (28·8–30·1)	18·8 (17·6–20·0)	17·9 (15·7–20·5)	13·2 (10·3–16·9)	0·8 (0·7–0·8)
Eastern Europe	2·70 (2·59–2·82)	1·91 (1·88–1·95)	1·38 (1·27–1·49)	1·28 (1·15–1·42)	1·19 (1·05–1·35)	4099·6 (3935·2–4285·2)	3350·8 (3289·2–3418·5)	1794·7 (1651·3–1949·2)	1293·5 (1082·3–1534·3)	643·2 (456·2–881·7)	0·7 (0·6–0·7)
Belarus	3·00 (2·83–3·18)	2·01 (1·94–2·09)	1·42 (1·23–1·64)	1·29 (1·06–1·55)	1·19 (0·95–1·47)	192·3 (181·8–203·2)	156·4 (150·9–162·4)	82·5 (70·6–95·6)	59·8 (43·0–80·3)	30·5 (16·3–53·1)	0·7 (0·6–0·8)
Estonia	2·30 (2·18–2·43)	2·06 (2·01–2·11)	1·60 (1·49–1·71)	1·37 (1·24–1·50)	1·21 (1·06–1·36)	20·1 (19·1–21·2)	22·5 (21·9–23·1)	13·1 (12·2–14·0)	9·4 (8·0–11·2)	4·2 (2·8–5·9)	0·8 (0·7–0·8)
Latvia	1·98 (1·84–2·14)	1·90 (1·86–1·94)	1·52 (1·35–1·71)	1·35 (1·16–1·56)	1·22 (1·01–1·49)	32·9 (30·7–35·5)	35·6 (34·9–36·4)	16·8 (14·9–18·9)	9·7 (7·5–12·4)	3·9 (2·7–6·6)	0·7 (0·6–0·8)
Lithuania	2·92 (2·78–3·10)	2·00 (1·95–2·05)	1·40 (1·30–1·51)	1·23 (1·11–1·35)	1·09 (0·96–1·25)	58·6 (55·7–62·0)	51·3 (49·9–52·6)	23·6 (21·9–25·4)	12·4 (10·0–15·4)	4·2 (2·7–6·1)	0·7 (0·6–0·7)
Moldova	3·77 (3·61–3·92)	2·46 (2·38–2·54)	1·18 (1·06–1·33)	1·09 (0·94–1·25)	1·03 (0·87–1·24)	84·7 (81·4–88·0)	86·1 (83·4–88·9)	28·4 (25·4–32·0)	9·5 (5·6–13·4)	2·7 (1·3–4·7)	0·6 (0·5–0·6)
Russia	2·77 (2·62–2·95)	1·87 (1·83–1·93)	1·48 (1·37–1·60)	1·33 (1·20–1·47)	1·21 (1·06–1·37)	2819·9 (2671·0–2995·4)	2232·6 (2184·0–2299·0)	1352·4 (1251·9–1464·1)	1053·8 (871·5–1239·4)	562·8 (408·0–758·1)	0·7 (0·7–0·8)
Ukraine	2·44 (2·33–2·55)	1·95 (1·90–2·01)	1·05 (0·94–1·18)	1·01 (0·88–1·16)	0·98 (0·83–1·16)	891·1 (853·1–930·3)	761·3 (739·2–783·2)	277·9 (246·7–311·8)	138·8 (104·8–185·4)	34·9 (19·2–60·5)	0·5 (0·4–0·6)
High income	**2·85 (2·78–2·92)**	**1·88 (1·86–1·90)**	**1·51 (1·41–1·61)**	**1·43 (1·30–1·56)**	**1·37 (1·22–1·53)**	**13626·1 (13275·0–13959·1)**	**12483·6 (12339·3–12633·7)**	**10399·8 (9728·0–11116·3)**	**9387·4 (8381·2–10552·0)**	**6961·9 (5348·6–8941·5)**	**0·7 (0·7–0·8)**
Australasia	3·13 (3·06–3·21)	1·93 (1·90–1·97)	1·64 (1·48–1·80)	1·45 (1·35–1·68)	1·33 (1·08–1·59)	251·9 (246·1–258·0)	278·2 (273·0–283·7)	357·9 (324·6–393·9)	404·9 (338·5–481·9)	363·9 (250·1–516·0)	0·8 (0·7–0·9)
Australia	3·06 (2·98–3·14)	1·92 (1·88–1·97)	1·64 (1·47–1·82)	1·45 (1·23–1·70)	1·32 (1·06–1·61)	202·2 (196·9–207·7)	227·7 (222·7–232·9)	299·3 (268·5–332·1)	339·1 (278·3–411·8)	307·8 (204·0–447·8)	0·8 (0·7–0·9)
New Zealand	3·49 (3·41–3·57)	1·96 (1·92–2·00)	1·62 (1·53–1·72)	1·45 (1·33–1·58)	1·35 (1·20–1·51)	49·7 (48·7–50·8)	50·5 (49·4–51·6)	58·6 (55·2–62·0)	65·7 (57·4–74·2)	56·1 (42·5–72·1)	0·8 (0·7–0·8)
High-income Asia Pacific	3·72 (3·59–3·86)	1·94 (1·89–2·00)	1·12 (1·03–1·22)	1·14 (1·00–1·30)	1·14 (0·96–1·35)	3059·8 (2947·5–3174·6)	2467·7 (2400·6–2541·4)	1169·5 (1075·7–1275·1)	908·3 (784·1–1047·7)	499·8 (348·5–707·9)	0·5 (0·5–0·6)
Brunei	6·41 (6·24–6·57)	3·87 (3·65–4·10)	1·65 (1·43–1·88)	1·40 (1·08–1·78)	1·25 (0·87–1·71)	5·8 (5·4–6·1)	6·4 (5·6–7·3)	5·5 (5·6–7·3)	3·4 (2·4–4·7)	1·0 (0·2–2·5)	0·8 (0·7–0·9)
Japan	3·27 (3·12–3·42)	1·69 (1·64–1·76)	1·26 (1·14–1·41)	1·26 (1·09–1·45)	1·32 (1·06–1·61)	1573·3 (1518·2–1636·1)	837·0 (754·0–933·3)	667·4 (555·1–790·8)	560 (44·0–70·8)	387·8 (259·2–572·2)	0·6 (0·5–0·7)
Singapore	6·03 (5·75–6·31)	1·77 (1·66–1·88)	1·20 (1·05–1·39)	1·15 (0·93–1·41)	1·35 (1·20–1·51)	42·0 (39·2–44·8)	55·5 (48·5–64·0)	45·3 (28·5–69·5)	56·0 (44·0–70·8)	45·3	0·6 (0·5–0·7)
South Korea	5·72 (5·37–6·08)	2·56 (2·48–2·64)	0·82 (0·71–0·95)	0·82 (0·71–0·92)	1·12 (0·88–1·41)	402·3 (397·9–412·4·2)	846·6 (822·3–873·2)	269·6 (246·4–294·2)	181·5 (155·9–209·6)	65·6 (28·5–69·5)	0·4 (0·4–0·6)
High-income North America	3·10 (3·03–3·18)	1·78 (1·75–1·81)	1·63 (1·53–1·73)	1·51 (1·38–1·64)	1·43 (1·27–1·60)	4023·2 (3927·9–4124·2)	3948·6 (3866·5–4026·4)	4014·6 (3772·1–4278·3)	3732·8 (3300·8–4245·6)	2967·3 (2256·1–3805·1)	0·7 (0·7–0·8)

(Table 1 continues on next page)

Formulation & Characterization of Sustained Release: Multichambered Tablet of Losartan Potassium Using Fused Deposition Modelling (FDM) 3D-Printer

Shalini Bhattacharya[1*], Nadeem Farooqui[2], Nimita Manocha[3]

Indore Institute of Pharmacy, Indore, Pincode: 453331

ABSTRACT:

Introduction: The Aim of present research work was to formulate and characterize Sustained release: Multichambered Tablet Using Fused Deposition Modelling (FDM) 3D-Printer, the drug candidate used in this project was Losartan Potassium, is an Angiotensin receptor Type -II blocker.

Objectives: By altering the shell thickness and infill density %, sustained release action of tablet using API Losartan Potassium had been achieved.

Methods: The Novel method had been used for fabricating Tablet called "Pause and fill Method". Tablets was prepared using FDM 3D-printer with three different batches (FI, FII and FIII) by creating variation in infill-density and inner wall thickness: 0.5mm, 1mm and 1.5 mm respectively using poly vinyl alcohol (PVA) filament. As half-life of Losartan is 1.5–2hrs (Indian Pharmacopoeia, 2018) with poor bioavailability, sustained release tablet enhanced the bioavailability of the drug, the *in-vitro* drug release from the tablet drug is extended upto 270mins (approx.).

Results: From the Results it concluded that the FIII batch of tablet is the optimized batch with drug release about 99.23 % for 270 mins, whereas FII shows 98.69 % for 240 mins and FI shows 97.71% for 210 mins. The data when used to evaluate the kinetic studies, states that the coefficient 'r' indicated the drug release from the tablet which was followed by zero order release kinetics.

Conclusions: The work conclude that the FDM 3D printing process was capable for producing rapid and sustained release tablets on the basis of different thickness. This work also helps to decrease the side effects of drugs by providing sustained release of drugs & increase the safety and efficacy and avoid incompatible between APIs by developing drug release characteristics. The printer software enabled easy fabrication of oral drug delivery devices with different wall or chamber thickness.

1. Introduction

Novel Drug delivery systems are the techniques which are day by day getting more developed and more accurate for delivering of therapeutic doses, which are tailored according to the patient need or requirement. Additive manufacturing technology includes various types of 3D-printing methods are as follows: Stereolithography (SLA), selective laser sintering (SLS), inkjet-based 3D-printing and Fused deposition modelling (FDM). Such novel methods can be used in choosing the doses i.e, flexibility in selection of amount of drug or API, shape and size of the dosage, etc [1-3] A Rapid proto-typing technology, due to it's cheapest printing costs, high printing quality, and well capacity to employ drug-loaded filaments via hot-melt extrusion (HME), Fused deposition modelling (FDM) is one of the additive

Principal
Indore Institute of Pharmacy,
INDORE (M.P.)
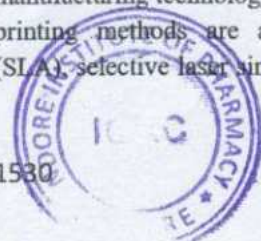
manufacturing techniques that is most oftenly researched or used for formulating dosage forms, or even in case of bioprinting in medical emergencies [4,5].

The "three Ds of 3D printing" refers to the overall procedure of 3D-printing method. These are (i) Design, (ii) Development and (iii) Dispense. This technique is only now beginning to be adopted by the pharmaceutical sector. There aren't any significant companies in the pharmaceutical sector creating drugs for regular use. Chuck Hull's stereolithography apparatus (SLA) received the first patent in 1986, which is when 3D printing initially emerged. He is regarded as the originator of 3D printing technology as well printing in the biomedical and pharmaceutical industries or field had been introduced in the year of 2015 [6-8]. Numerous firms are investigating this possibility, including Teva and Aprecia Pharmaceuticals. A high medication load, up to 1,000 mg, may be delivered in a single dosage thanks to ZipDose Technology. By administering even the highest concentrations of levetiracetam with only a sip of drink, "SPRITAM" was authorized by the US Food and Drug Administration (FDA) on year August 3, 2015, to treat partial-onset, myoclonic, and generalized tonic-clonic seizures improves the patient experience. Using 3DP technology, which was developed at Massachusetts Institute of Technology, Aprecia created its ZipDose Technology platform [9-11]

An appropriate polymer is chosen, melted, and then pushed or introduced through a heated nozzle out that may be moved. The polymer is applied layer by layer along all three following axis i.e, (x, y, and z axis), and when it get solidified, it takes on the precise shape as per the computer-aided design (CAD) models had intended into machine [12-14]. The invention and experiments using 3D -printing method had been described illustratively in **Figure 1**
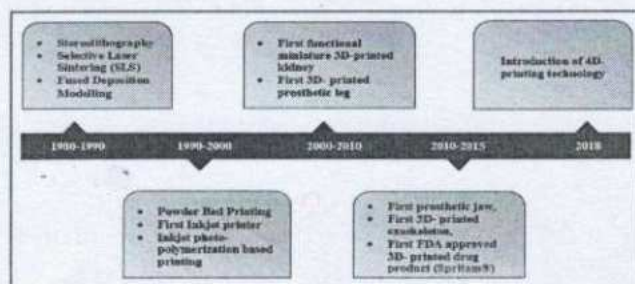
Figure 1: Inventions & Experiments using 3D-Printing

2. Objectives

The aim of this research work is that the FDM 3D printing process was capable for producing rapid and sustained release tablets on the basis of different thickness. This work also helps to decrease the side effects of drugs by providing sustained release of drugs & increase the safety and efficacy and avoid incompatible between APIs by developing drug release characteristics. The printer software enabled easy fabrication of oral drug delivery devices with different wall or chamber thickness. DSC and HPLC are carried to check the identification and purity of drug. All results are within the acceptance range. DSC data showed that the Losartan Potassium drug was unaffected by the printing and that there were no detectable interactions. PVA compartments are designed by the use of CAD software (Auto-CAD) in two steps. First printing of the tablet upto 75% and then paused, again after the API filling manually the rest part of the body building up. PVA reservoir were fabricated in three different batches on the basis of different thickness of inner most walls and difference in infill densities (FI, FII, FIII).

The 3D printed tablets were evaluated for Size and shape, hardness, weight variation, dye test and drug release test. All results are within acceptable range as defined by Indian Pharmacopoeia. In drug release performance we found the best result from FIII batch because it showed up for longest period of time amongst the three batches of formulation i.e, sustained release action upto 270 mins (approx.) In this system the drug resent in the outer compartment or chamber with thin wall is released first and release of the drug in the thick layer of compartment only commences when the thin lay er is practically dissolved. Drug release kinetic data of the 3D printed (FIII) batch of tablet analyzed and found to be fitted into zero order drug release kinetics. First order, Higuchi and korsmeyer-peppas model. Almost all formulations were well fitted in zero-order drug release kinetics with the highest linearity

3. Methods

Model Designing of 3D- Tablet

The tablet model had been designed using CAD software (Auto-CAD), then the STL file is further sliced using Cura-Ultimaker and converted into G-code format file i.e, Machine readable format. The filament which was used

for the fabrication of the sustained release multi-chambered tablets namely Poly-vinyl Alcohol (PVA) filament. PVA is a water- soluble, biodegradable Polymer which is widely used by the researchers in the preparation or fabrication of the Pharmaceutical Formulation using 3D- Printer, due to its flexibility and physiochemical properties. **Figure 2** provides brief working of 3D- printing process[15].

This section outlines plan and how the process had been carried out. In this study "Pause and fill method". The structure was printed by a single-nozzled (0.4 mm in diameter) FDM 3D printer (3D-Prototyperz, DEX 200, Indore, India). The filament which is used to fabricate the Tablet is Poly vinyl alcohol (PVA) which is a water-soluble and biodegradable polymer. This Tablet is having 2 hollow chambers in which the drug (API) is to be filled shown in **Figure 3** The outer most chamber wall is having thickness of 1.5mm and the inner-most wall thickness is about 1.0 mm. The command had been given to the 3D-Printer using SD card in which the design of the tablet is saved in the format of g-code. The g-code file must be containing the command of stop i.e; after the completion of 75-80 % of the printing of tablet the machine will automatically be paused and then the desired dose will be poured into the different cavities or chambers of the tablet as per the need, then again just "press" print again and the remaining portion of the tablet will be printed successfully.

The printer parameter was adjusted by the 3D slicing software namely "Auto-CAD software" are as follows: a layer height of 0.1 mm, printing speed 10 mm/sec., infill density of 40%, 75% and 100% (FI, FII, FIII) respectively. The nozzle temperature were set to be at temperature 210 ˚C and the bed or printer tray temperature at 60 ˚C [16,17].
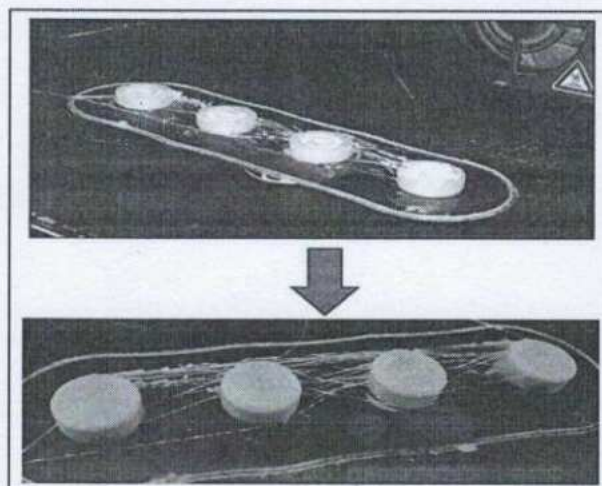

Figure 3: Printing procession of Tablet (After completion of 75% the nozzle is moved back, for the filling of the API)

4. Results

Losartan Potassium loaded Sustained Release: Multi-chambered Tablet were prepared successfully using Fused Deposition Modelling 3D- Printing method. The three batches of tablets had been prepared with different infill densities and inner-wall thickness, FI, FII and FIII with 40%, 75% and 100% infill density respectively. And the results were evaluated and observed as follows – **Size, Height, mass, width:**

The shape of the tablet fabricated was circular containing chambers or cavities in the form of different layers vertically. The Diameter of the tablet was found to be 13 mm and height 0.5 mm. Three batches of the formulation were formulated i.e, FI, FII and FIII with different infill densities are as followed – 40%, 75% and 100% enlisted in **Table no. 1**

Figure 2: Flow chart showing processing of 3D- Printing of object
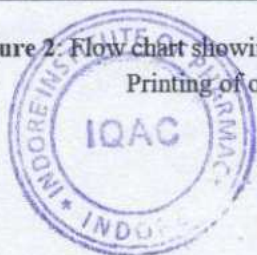
Table 1: Size and shape of 3D- Printed tablets

S. No.	Diameter (mm)	Height (mm)	Infill density (%)	Inner chamber wall thickness (mm)
1.	13mm	5mm	40	0.5 mm
2.	13mm	5mm	75	1 mm
3.	13mm	5mm	100	1.5 mm

The thickness and the difference in the infill density of the tablet so the weight of the tablet found to be consequently increasing i.e, FI – 0.11% < FII – 0.27% <FIII – 0.39%. All the tablet batches were passed the weight variation test and within the acceptable limit (less than ±5 %) according to USP weight variation limit.

Differential scanning calorimeter (DSC)

DSC study was carried out to check the compatibility between Losartan Potassium and PVA filament used in the formulation. It is carried out to confirm that there should be complete physical compatibility of drug and filament with no mutual interaction. DSC thermogram of Losartan Potassium exhibited an endothermic peak at 278 °C followed by **Figure 4**
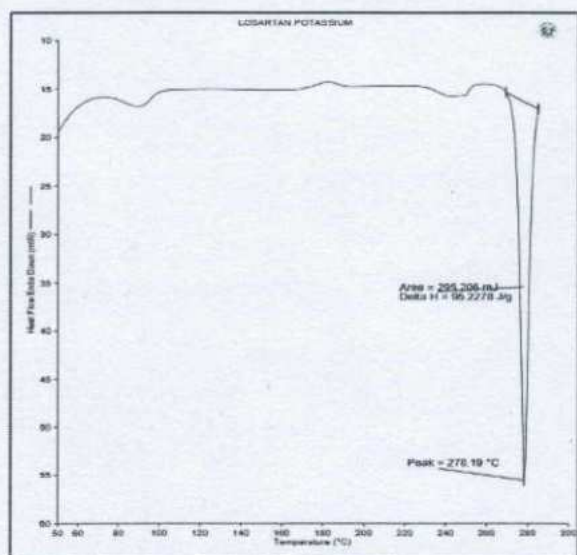
Figure 4: DSC report of Losartan Potassium

Whereas, the mixture of drug (Losartan) and polymer (PVA filament) was kept in an accelerated condition of 40 °C/ 75% RH for 10 days and subjected to DSC analysis. The mixture exhibits endothermic peak which was found approx. 275.34

°C, which suggested clearly that there was no interaction between Losartan Potassium and PVA filament and the drug Losartan Potassium was existed in it's unchanged form **Figure 5**
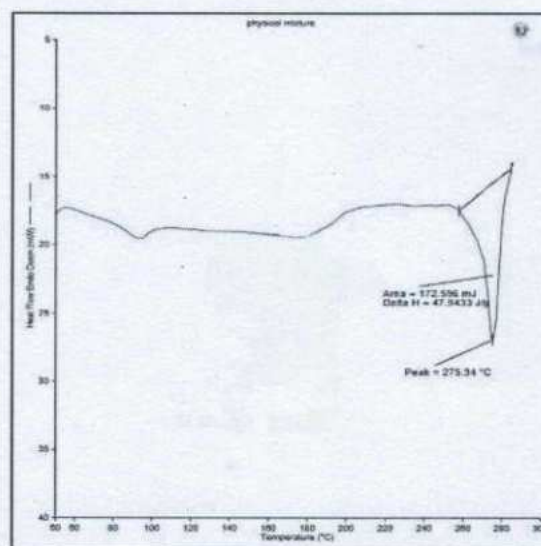

Figure 5: DSC report of mixture of PVA and Losartan Potassium

High Performance Liquid Chromatography (HPLC)

The chromatographic separation was performed using C_{18} column (250mm x 4.6mm x 5.0µm) including a Rheodyne injector with 10 µl fixed loop. Empower software had been used for the data analysis and interpretation. The mobile phase consists of 2 solvents: 0.1% Ortho-phosphoric acid (OPA) considered as mobile phase (A) and Acetonitrile (ACN) as, mobile phase (B) in ratios 75:25, 10:90, 75:25, 75:25 followed by I.P, 2018 edition. Run time of the method was set at 55 mins. The flow rate of the sample was 1ml/min. The readings are – *ref.* **Table 2 and Figure 6 & 7**

Table 2: - HPLC report conc./area

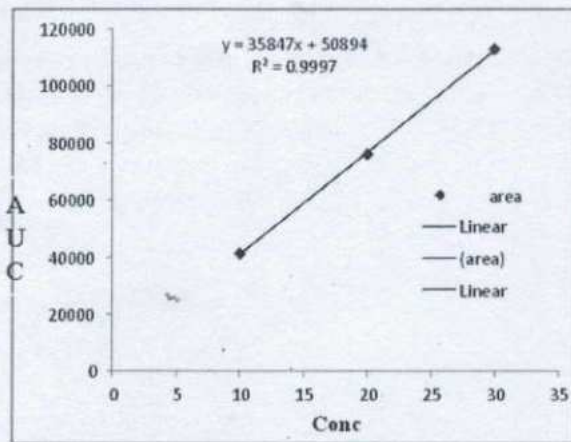| S. No.	Concentration (ppm)	Area (AUC)
1.	10	413061
2.	20	760424
3.	30	1129993

160
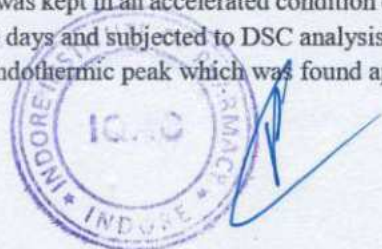
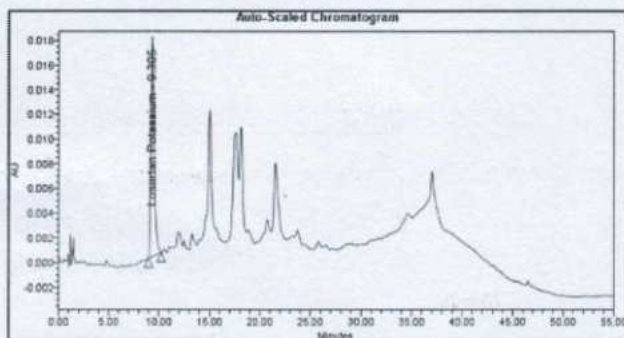**Figure 6:** Graph of Losartan Potassium showing linearity Conc. (ppm)/AUC

Figure 7: HPLC spectrum of Losartan potassium

Hardness Determination

The hardness measured of the tablet of each batch between 5-6.5 kg/cm². According to Indian pharmacopoeia 5.5 ± 0.06 and 7.5 ± 0.06 kg/cm² is the hardness limit of the matrix tablet which depicts good mechanical strength of tablet. It was due to the plasticity nature of the PVA. Hardness of the 3D- Printed Tablet is shown in **Table no- 3**

Table 3: - Hardness of 3D- Printed tablets (n=3)

Formulation	Hardness (kg/cm²)			Average Hardness (kg/cm²)
FI	5.8	6.2	5.9	5.9 ±0.61
FII	6.0	5.5	6.2	5.9 ±0.13
FIII	5.5	6.5	6.4	6.1 ±0.33

Dye Test

The results of Dye test reveals that the methyl orange starts releasing between 30 mins to 120 mins i.e, The outer chamber wall started dissolving between 30-120mins. whereas, inner chambers wall start dissolving and the methylene blue start releasing between 180 mins. to 270 mins. as shown in **Figure 8**
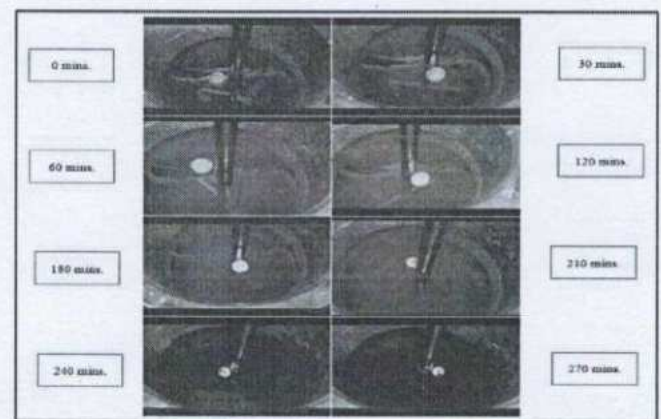

Figure 8: Photographs of dye test

In-vitro Drug release

Dissolution study had been carried out at 0.1 N HCl medium at 205nm by maintaining the temperature about 37 ˚C ± 0.5 ˚C of the medium to mimic human stomach environment for all the three batches of tablet and the results clearly shows that the drug percentage release profile of the batch three i.e, FIII with infill density 100% and inner chamber wall thickness upto 1.5mm is having extended time duration and better drug release profile comparatively to the other two batches (FI and FII) of formulations shown in **Figure 9**-
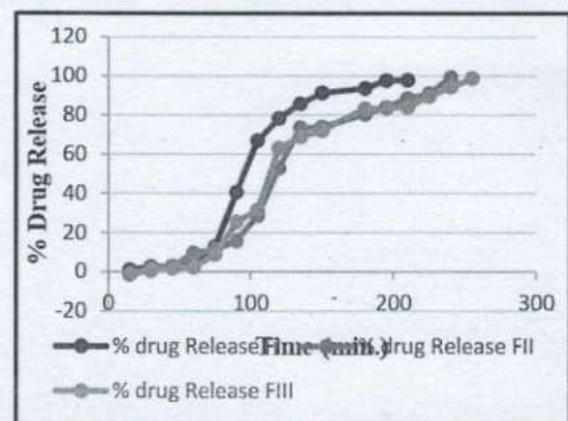

**Figure 9:** Percentage Drug release of 3D- Printed Tablet

1534

161

Drug release kinetics mechanism study

The kinetics of *in-vitro* drug release was calculated by applying the data of drug released to various kinetic model such as Zero order, First order, Higuchi and Korsmeyer – peppas. And the result obtained is shown in **Table 4**. From the results of kinetic studies, the coefficient 'r' indicated that the drug release followed zero order release kinetics. It was found that the value of 'r' for zero order ranged from 0.9651 to 0.9902, which is near to 1 when compared to first order ranged from 0.8089 to 0.9123. So, it was understood to be following zero order release pattern followed by all three formulations shown in **Figure 10** and **11-**
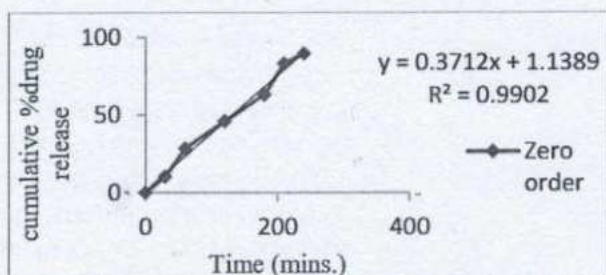
(a)

(b)

(c)
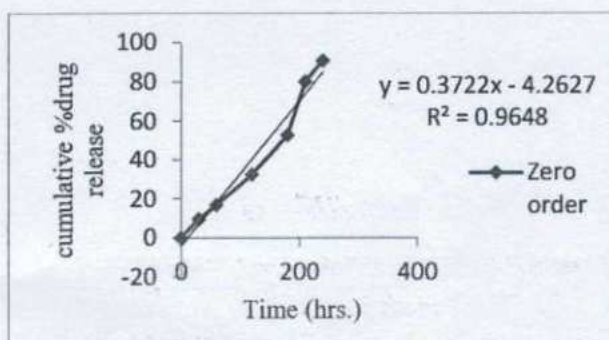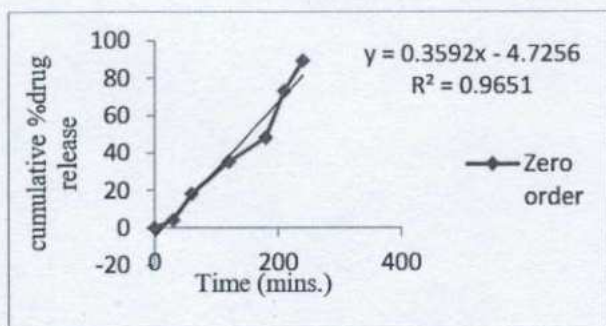
Figure 10: Graph between cumulative % drug release v/s time of Losartan Potassium (a) Formulation -I, (b) Formulation – II, (c) Formulation – III

Table 4: - Kinetic data of 3D- printed Tablet

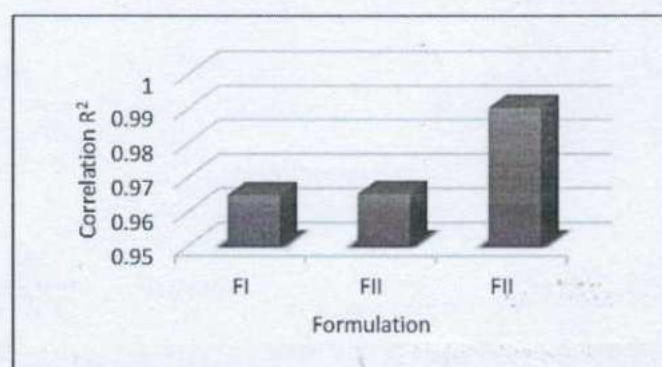| Formulation	Zero order (r^2)
FI (40 %)	0.9648
FII (75%)	0.9651
FIII (100%)	0.9902

Figure 11: Chart showing the increase in R^2 value of zero order for all batches of formulation

5. Discussion

In conventional dosage form drugs, which are Amorphous nature, flocculent and low-density character is difficult to compress into a tablet. Hygroscopic drugs are not suitable for compressed tablets. Some limitations and problems like poor patient compliance, dose variation etc. Conventional dosage form has drawbacks like poor bioavailability and fluctuations in plasma drug level and are unable to achieve sustained release. Conventional oral dosage forms such as tablets or capsules undergo many production steps eg, granulation, compaction, size reduction, tableting or coating. In other hand, 3D printing reduces production to one or two steps, depending if there is pharmaceutical material in filament from available. 3D printing can revolutionize the world. 3D printing used to modify medicines as per the patient requirement involving the potentially to select optimal dose, appearances and release profile. Fused deposition modelling (FDM) is one of the most widely used 3D printing techniques to make solid dosages and offers accurate dosage by adjusting the parameters in CAD.

Principal
Indore Institute of Pharmacy,
INDORE (M.P.)

1535

162

This paper aim was to formulate and evaluate 3D printed Sustained Release: Multi-chambered Tablet using Fused Deposition Modelling (FDM) technology. The 3D printer uses a fixed amount of drug and polymer to print which minimizes the dose variation of the drug. Result accurate and precision dosing of the drug to the patients. Keeping in view of the above benefits, our aim was to explore 3D printing technology for formulation suitable dosage form of drug which may lead to reduce the dosing frequency, manufacturing cost and increase the patient compliance.

6. Acknowledgement

References

1. Beg, S.; Almalki, W. H.; Malik, A.; Farhan, M.; Aatif, M.; Rahman, Z.; Alruwaili, N. K.; Alrobaian, M.; Tarique, M.; Rahman, M. 3D Printing for Drug Delivery and Biomedical Applications. *Drug Discovery Today* 2020, 25 (9), 1668–1681.

2. Lee, T. C.; Shahrubudin, N.; Ramlan, R. An Overview on 3D Printing Technology: Technological, Materials, and Applications. *Procedia Manufacturing* 2019, 35, 1286–1296.

3. Mandloi, N.; Vinchurkar, K.; Mishra, D. K.; Dixit, P. 3D Printing for Drug Delivery and Its Pharmaceutical Applications – Recent Findings and Challenges. *PCI-Approved-IJPSN* 2022, 15 (2), 5922–5931.

4. Mathew, E.; Pitzanti, G.; Larrañeta, E.; Lamprou, D. A. 3D Printing of Pharmaceuticals and Drug Delivery Devices. *Pharmaceutics* 2020, 12 (3), 266.

5. Wang, S.; Chen, X.; Han, X.; Hong, X.; Li, X.; Zhang, H.; Li, M.; Wang, Z.; Zheng, A. A Review of 3D Printing Technology in Pharmaceutics: Technology and Applications, Now and Future. *Pharmaceutics* 2023, 15 (2), 416.

6. Bhattacharya, S.; Singh, S.; Shrestha, S.; Baghel, Y. Recent Findings and Development of 3D Printing Technology in Pharmaceutical Formulation Development: An Extensive Review. *International Journal of Drug Development and Research* 2019, Volume 11, Issue 4 (2019), Volume 11(4): 1-14 (2019)-01-Volume 11(4): 1-14 (2019)-14.

7. Jamróz, W.; Szafraniec, J.; Kurek, M.; Jachowicz, R. 3D Printing in Pharmaceutical and Medical Applications – Recent Achievements and Challenges. *Pharm Res* 2018, 35 (9), 176.

8. O Oyewumi, M. 3D Printing Technology in Pharmaceutical Drug Delivery: Prospects and Challenges. *J Biomol Res Ther* 2015, 04 (04).

9. Chakka, L. R. J.; Chede, S. 3D Printing of Pharmaceuticals for Disease Treatment. *Front. Med. Technol.* 2023, 4, 1040052.

10. Jose, P. A.; Christoper GV, P. 3D PRINTING OF PHARMACEUTICALS – A POTENTIAL TECHNOLOGY IN DEVELOPING PERSONALIZED MEDICINE. *Asian Journal of Pharmaceutical and Development* 2018, No. 2018;6 (3):46-54, 46–54.

11. Kun, K. Reconstruction and Development of a 3D Printer Using FDM Technology. *Procedia Engineering* 2016, 149, 203–211.

12. Abaci, A.; Gedeon, C.; Kuna, A.; Guvendiren, M. Additive Manufacturing of Oral Tablets: Technologies, Materials and Printed Tablets. *Pharmaceutics* 2021, 13 (2), 156.

13. Ali, A.; Ahmad, U.; Akhtar, J. 3D Printing in Pharmaceutical Sector: An Overview. In *Pharmaceutical Formulation Design - Recent Practices*; Ahmad, U., Akhtar, J., Eds.; IntechOpen, 2020.

14. Jandyal, A.; Chaturvedi, I.; Wazir, I.; Raina, A.; Ul Haq, M. I. 3D Printing – A Review of Processes, Materials and Applications in Industry 4.0. *Sustainable Operations and Computers* 2022, 3, 33–42.

15. Maroni, A.; Melocchi, A.; Parietti, F.; Foppoli, A.; Zema, L.; Gazzaniga, A. 3D Printed Multi-Compartment Capsular Devices for Two-Pulse Oral Drug Delivery. *Journal of Controlled Release* 2017, 268, 10–18.

16. Skowyra, J.; Pietrzak, K.; Alhnan, M. A. Fabrication of Extended-Release Patient-Tailored Prednisolone Tablets via Fused Deposition Modelling (FDM) 3D Printing. *European Journal of Pharmaceutical Sciences* 2015, 68, 11–17.

Principal
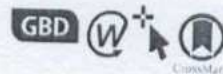Indore Institute of Pharmacy,
INDORE (M.P.)

163

17. Goyanes, A.; Chang, H.; Sedough, D.; Hatton, G. B.; Wang, J.; Buanz, A.; Gaisford, S.; Basit, A. W. Fabrication of Controlled-Release Budesonide Tablets via Desktop (FDM) 3D Printing. *International Journal of Pharmaceutics* **2015**, *496* (2), 414–420.

18. Al-Majed, A.-R. A.; Assiri, E.; Khalil, N. Y.; Abdel-Aziz, H. A. Losartan. In *Profiles of Drug Substances, Excipients and Related Methodology*; Elsevier, 2015; Vol. 40, pp 159–194.

19. Patel, N. G.; Serajuddin, A. T. M. Development of FDM 3D-Printed Tablets with Rapid Drug Release, High Drug-Polymer Miscibility and Reduced Printing Temperature by Applying the Acid-Base Supersolubilization (ABS) Principle. *International Journal of Pharmaceutics* **2021**, *600*, 120524.

20. Zhao, X.; Wei, W.; Niu, R.; Li, Q.; Hu, C.; Jiang, S. 3D Printed Intragastric Floating and Sustained-Release Tablets with Air Chambers. *Journal of Pharmaceutical Sciences* **2022**, *111* (1), 116–123.

21. Qian, H.; Chen, D.; Xu, X.; Li, R.; Yan, G.; Fan, T. FDM 3D-Printed Sustained-Release Gastric-Floating Verapamil Hydrochloride Formulations with Cylinder, Capsule and Hemisphere Shapes, and Low Infill Percentage. *Pharmaceutics* **2022**, *14* (2), 281.

164

Global fertility in 204 countries and territories, 1950–2021, with forecasts to 2100: a comprehensive demographic analysis for the Global Burden of Disease Study 2021

GBD 2021 Fertility and Forecasting Collaborators*

Summary

Background Accurate assessments of current and future fertility—including overall trends and changing population age structures across countries and regions—are essential to help plan for the profound social, economic, environmental, and geopolitical challenges that these changes will bring. Estimates and projections of fertility are necessary to inform policies involving resource and health-care needs, labour supply, education, gender equality, and family planning and support. The Global Burden of Diseases, Injuries, and Risk Factors Study (GBD) 2021 produced up-to-date and comprehensive demographic assessments of key fertility indicators at global, regional, and national levels from 1950 to 2021 and forecast fertility metrics to 2100 based on a reference scenario and key policy-dependent alternative scenarios.

Methods To estimate fertility indicators from 1950 to 2021, mixed-effects regression models and spatiotemporal Gaussian process regression were used to synthesise data from 8709 country-years of vital and sample registrations, 1455 surveys and censuses, and 150 other sources, and to generate age-specific fertility rates (ASFRs) for 5-year age groups from age 10 years to 54 years. ASFRs were summed across age groups to produce estimates of total fertility rate (TFR). Livebirths were calculated by multiplying ASFR and age-specific female population, then summing across ages 10–54 years. To forecast future fertility up to 2100, our Institute for Health Metrics and Evaluation (IHME) forecasting model was based on projections of completed cohort fertility at age 50 years (CCF50; the average number of children born over time to females from a specified birth cohort), which yields more stable and accurate measures of fertility than directly modelling TFR. CCF50 was modelled using an ensemble approach in which three sub-models (with two, three, and four covariates variously consisting of female educational attainment, contraceptive met need, population density in habitable areas, and under-5 mortality) were given equal weights, and analyses were conducted utilising the MR-BRT (meta-regression—Bayesian, regularised, trimmed) tool. To capture time-series trends in CCF50 not explained by these covariates, we used a first-order autoregressive model on the residual term. CCF50 as a proportion of each 5-year ASFR was predicted using a linear mixed-effects model with fixed-effects covariates (female educational attainment and contraceptive met need) and random intercepts for geographical regions. Projected TFRs were then computed for each calendar year as the sum of single-year ASFRs across age groups. The reference forecast is our estimate of the most likely fertility future given the model, past fertility, forecasts of covariates, and historical relationships between covariates and fertility. We additionally produced forecasts for multiple alternative scenarios in each location: the UN Sustainable Development Goal (SDG) for education is achieved by 2030; the contraceptive met need SDG is achieved by 2030; pro-natal policies are enacted to create supportive environments for those who give birth; and the previous three scenarios combined. Uncertainty from past data inputs and model estimation was propagated throughout analyses by taking 1000 draws for past and present fertility estimates and 500 draws for future forecasts from the estimated distribution for each metric, with 95% uncertainty intervals (UIs) given as the 2·5 and 97·5 percentiles of the draws. To evaluate the forecasting performance of our model and others, we computed skill values—a metric assessing gain in forecasting accuracy—by comparing predicted versus observed ASFRs from the past 15 years (2007–21). A positive skill metric indicates that the model being evaluated performs better than the baseline model (here, a simplified model holding 2007 values constant in the future), and a negative metric indicates that the evaluated model performs worse than baseline.

Findings During the period from 1950 to 2021, global TFR more than halved, from 4·84 (95% UI 4·63–5·06) to 2·23 (2·09–2·38). Global annual livebirths peaked in 2016 at 142 million (95% UI 137–147), declining to 129 million (121–138) in 2021. Fertility rates declined in all countries and territories since 1950, with TFR remaining above 2·1—canonically considered replacement-level fertility—in 94 (46·1%) countries and territories in 2021. This included 44 of 46 countries in sub-Saharan Africa, which was the super-region with the largest share of livebirths in 2021 (29·2% [28·7–29·6]). 47 countries and territories in which lowest estimated fertility between 1950 and 2021 was below replacement experienced one or more subsequent years with higher fertility; only three of these locations rebounded above replacement levels. Future fertility rates were projected to continue to decline worldwide, reaching a global TFR of 1·83 (1·59–2·08) in 2050 and 1·59 (1·25–1·96) in 2100 under the reference scenario. The number of countries and territories with fertility rates remaining above replacement was forecast to be 49 (24·0%) in 2030,

2057

165

only six (2·9%) in 2100, with three of these six countries included in the 2021 World Bank-defined low-income group, all located in the GBD super-region of sub-Saharan Africa. The proportion of livebirths occurring in sub-Saharan Africa was forecast to increase to more than half of the world's livebirths in 2100, to 41·3% (39·6–43·1) in 2050 and 54·3% (47·1–59·5) in 2100. The share of livebirths was projected to decline between 2021 and 2100 in most of the six other super-regions—decreasing, for example, in south Asia from 24·8% (23·7–25·8) in 2021 to 16·7% (14·3–19·1) in 2050 and 7·1% (4·4–10·1) in 2100—but was forecast to increase modestly in the north Africa and Middle East and high-income super-regions. Forecast estimates for the alternative combined scenario suggest that meeting SDG targets for education and contraceptive met need, as well as implementing pro-natal policies, would result in global TFRs of 1·65 (1·40–1·92) in 2050 and 1·62 (1·35–1·95) in 2100. The forecasting skill metric values for the IHME model were positive across all age groups, indicating that the model is better than the constant prediction.

Interpretation Fertility is declining globally, with rates in more than half of all countries and territories in 2021 below replacement level. Trends since 2000 show considerable heterogeneity in the steepness of declines, and only a small number of countries experienced even a slight fertility rebound after their lowest observed rate, with none reaching replacement level. Additionally, the distribution of livebirths across the globe is shifting, with a greater proportion occurring in the lowest-income countries. Future fertility rates will continue to decline worldwide and will remain low even under successful implementation of pro-natal policies. These changes will have far-reaching economic and societal consequences due to ageing populations and declining workforces in higher-income countries, combined with an increasing share of livebirths among the already poorest regions of the world.
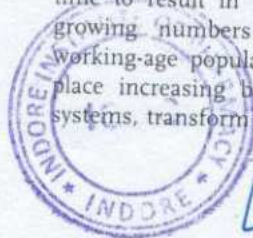
Introduction

Characterising trends in key demographic indicators of fertility and projecting estimates into the future are essential to understand the impact of changing birth rates on social, economic, and geopolitical systems, both now and in the coming century. Dynamics in fertility patterns are central to the well established concept of the demographic transition,[1,2] which classically holds that societies will passage from a condition of high fertility and high mortality with more young than old people to a state of low fertility and low mortality with an increasingly older population. Some theorists have proposed the concept of a demographic dividend, whereby declining fertility rates lead temporarily to higher proportions of working adults available to generate resources and capital, potentially stimulating economic growth and eventual rebounds in fertility rates.[3] Demographic data in the 5 years preceding 2021 demonstrate that the total fertility rate (TFR) in some countries has fallen below replacement levels—the minimum rate necessary for generational replacement of the population assuming no migration—with no evidence of this predicted rebound.[4,2] The replacement level is generally accepted to be a TFR of at least 2·1, although the true replacement level depends on the specific mortality rate and sex ratio at birth in a population.[8] Low levels of fertility have the potential over time to result in inverted population pyramids with growing numbers of older people and declining working-age populations. These changes are likely to place increasing burdens on health care and social systems, transform labour and consumer markets, and

alter patterns of resource use. Accurate estimates and future forecasts of fertility rates and their impact on population age structures are therefore essential to anticipate potential economic and geopolitical consequences and to inform the development of effective health, environmental, and economic policies.

At present, an important source of fertility estimates and future forecasts for countries and areas throughout the world has been the Population Division of the UN Department of Economic and Social Affairs, which most recently produced the 2022 Revision of World Population Prospects (WPP 2022).[5] The UN Population Division estimates of past fertility are not compliant with the Guidelines on Accurate and Transparent Health Estimates Reporting (GATHER) statement in important respects; notably, they do not provide all code for statistical models or explicit details on criteria for exclusion or adjustment of primary data sources. Furthermore, the validity of UN Population Division projections has been questioned due to the assumptions applied in countries experiencing low post-transition fertility dropping below replacement level.[9,10] Previous UN Population Division forecasts have assumed that, in such circumstances, fertility rates will increase towards replacement levels,[11-13] and WPP 2022 assumes convergence to a rate that is a combination of country-specific historical rates and the mean rate in low-fertility countries that have experienced fertility increases.[13] The WPP 2022 projects gradual increases in TFR even in countries that have shown no evidence of fertility rate increases, such as South Korea and Thailand.[6,14-17] Additionally, UN Population Division

166

Research in context

Evidence before this study
Since the 1950s, global and national estimates and projections of key fertility indicators have been produced and regularly updated by the Population Division of the UN Department of Economic and Social Affairs, with the most recent iteration being the 2022 Revision of World Population Prospects. Assessments of fertility at national and subnational levels worldwide have also been conducted by the US Census Bureau since the 1960s, with estimates reported in the Bureau's International Database. More recently, fertility estimates and projections have been generated by the Wittgenstein Centre for Demography and Global Human Capital and by the Global Burden of Diseases, Injuries, and Risk Factors Study (GBD), an ongoing, large-scale research enterprise that systematically analyses worldwide data to assess global health trends. Past estimates of fertility have been produced as part of GBD since 2017, and future forecasts based on GBD findings were first published in 2020.

Added value of this study
Of the existing large-scale efforts to estimate worldwide trends in fertility, only GBD analyses are compliant with the Guidelines on Accurate and Transparent Health Estimates Reporting (GATHER) statement. This study also incorporates several important innovations introduced by the GBD population forecasting study by Vollset and colleagues in 2020 that support forecasting accuracy assessment and provide a framework by which to explore the impact of various policy scenarios on fertility patterns. These methods include: basing the GBD forecasting model on a measure of cohort fertility (completed cohort fertility at age 50 years, CCF50) that reflects the number of children born over time to females from a specific cohort, which better captures long-term choices people make about childbearing—such as delaying having children—than does the classic period-based measure of total fertility rate; and incorporating measures of female education and met need for modern contraceptives as covariates, which improves accuracy and allows for modelling alternative scenarios by changing levels of these indicators. In contrast to other models that assume rates in countries currently experiencing low fertility will tend to increase over time, or those that base their projections on expert judgements, GBD fertility forecasting methods are grounded in existing, real-world evidence about fertility patterns in long-term cohorts of females and in data on related evidence-based covariates such as education and contraception. GBD 2021 has further improved the estimation of past, current, and future fertility in four important ways. First, an additional 147 surveys, 21 censuses, and 634 country-years of vital and sample registration data were added for estimation of past fertility trends. Second, smoothing parameters for estimating past fertility trends were updated to better fit available data. Third, to further improve specificity and accuracy of future fertility projections, two additional covariates were included that account for urbanicity (defined here as population density in habitable areas) and under-5 mortality in the CCF50 model. Fourth, we added a pro-natal alternative scenario to help policy makers plan interventions in countries with fertility rates below replacement level. Based on a skill metric designed to evaluate forecasting accuracy, the model presented here performed better across all age groups compared with a constant prediction.

Implications of all the available evidence
Our past estimates and future forecasts indicate that fertility rates are declining everywhere and are projected to continue to decrease over the coming century. By 2100, we estimate that fertility rates will be below replacement level in more than 95% of the world's countries and territories but that marked disparities in rates will remain. Our forecasts also suggest that, by 2100, the largest concentrations of livebirths will shift to low-income settings, particularly a subset of countries and territories in sub-Saharan Africa, which are among the most vulnerable to economic and environmental challenges. Extreme shifts in the global distribution of livebirths can be partially ameliorated by improved female education and met need for modern contraception. Outside of this subset of low-income areas, most of the world's countries will experience the repercussions of low fertility, with ageing populations, declining workforces, and inverted population pyramids, which are likely to lead to profound fiscal, economic, and social consequences. National policy makers and the global health community must plan to address these divided sets of demographic challenges emerging worldwide.

models are based on TFR, which is a period measure and therefore does not account for change over time in fertility behaviours. For example, in settings where fertility rates in older women increase due to choices to delay births, TFR would underestimate fertility forecasts. Reliance on TFR can also lead to short-term fluctuations in estimated fertility forecasts that are especially impactful in countries with low fertility rates.[18] Moreover, their projections forecast TFR solely as a function of time and do not include other covariates to inform the models, which disregards potentially explanatory data and precludes investigating the effects

of alternative policy-related scenarios or other drivers of fertility. The US Census Bureau International Database has also provided worldwide fertility estimates and projections, currently in 227 countries, since the 1960s, but country-specific updates are not performed on a regular basis.[19] Since the 1990s, global and regional fertility forecasts have also been generated by the World Population Program of the International Institute for Applied Systems Analysis,[20] with country-level projections more recently produced by an affiliated group, the Wittgenstein Centre for Demography and Global Human Capital.[21,22] These forecasts rely on

2059

167

assumptions informed by expert opinions from demographic scientists to predict future fertility rates.[21-23]

The Global Burden of Diseases, Injuries, and Risk Factors Study (GBD) is an ongoing, large-scale research enterprise that characterises the state of global health by estimating key health metrics at global, regional, and national levels.[24] Beginning with the 2017 GBD cycle, past and current fertility estimates generated as part of the GBD analytic framework were published;[25] before that, estimates from the UN Population Division were used as inputs to GBD analytic processes.[26,27] For GBD 2019, past and current fertility estimates were reported jointly with mortality, life expectancy, and population measures in a publication focused on overall demographic estimates,[28] and GBD-based forecasts of population and fertility up to 2100 were reported separately by Vollset and colleagues in 2020.[5] GBD fertility estimates are based on clear data and methods applying a standardised approach, providing publicly available code. Vollset and colleagues addressed some of the existing issues regarding the use of TFR in the modelling process by developing an Institute for Health Metrics and Evaluation (IHME) forecasting model based instead on completed cohort fertility at age 50 years (CCF50: the average number of children born over time to females from a specified birth cohort)[29] to capture change over time in fertility behaviours, which yields more stable and accurate fertility estimates. Vollset and colleagues[4] also included covariates representing female educational attainment and contraceptive met need (a measure of the proportion of females of reproductive age whose need for contraception has been met with modern contraceptive methods) to better inform fertility estimates and facilitate exploration of alternative future scenarios associated with achievement of UN Sustainable Development Goals (SDGs) related to education and contraception.

The present GBD 2021 study focuses on fertility metrics, presenting past estimates (1950–2021) along with forecasts up to 2100. Results were improved since GBD 2019 and the 2020 study by Vollset and colleagues by incorporating newly available demographic data and through key methodological advances. This paper provides a high-level overview of our findings. We anticipate that the results will provide insights for policy makers and will be used as a tool to help plan and shape future policies to better prepare for profound changes in global fertility.

This paper was produced as part of the GBD Collaborator Network and in accordance with the GBD Protocol.[30]

Methods
Overview
For each subsequent GBD round, newly available data and updated methods are used to update the full time series of estimates from 1950 up to the latest year of

analysis. As a consequence, GBD 2021 estimates supersede all previous estimates. GBD 2021 estimated key fertility metrics in females between ages 10 years and 54 years in 204 countries and territories grouped into 21 regions and seven super-regions. GBD regions are made up of countries and territories that are geographically close and epidemiologically similar.[11] These regions are then grouped into super-regions based on cause of death patterns. The full GBD location hierarchy is shown in appendix 1 (table S1). GBD 2021 drew on the expertise of more than 11000 collaborators across more than 160 countries and territories. The GBD 2021 fertility analysis framework produced estimates for every year from 1950 to 2021 and forecasts up to 2100.

The methods used to produce fertility estimates from 1950 to 2021 closely followed those of GBD 2019.[28] Methods used to generate fertility forecasts to 2100 were based on a modified and revised version of the modelling approach used in the 2020 study by Vollset and colleagues.[4] These methods have been peer-reviewed over previous GBD rounds and as part of the peer-review process for GBD 2021. Here we provide an overview of the methods with an emphasis on the main changes since GBD 2019 and the 2020 study by Vollset and colleagues;[28] a more comprehensive description of the analytical methods for GBD 2021 is provided in appendix 1. Additional details on specific data inputs are accessible through the GBD Sources Tool.
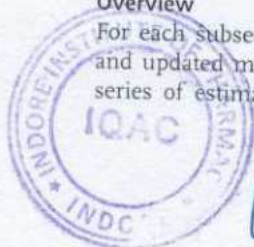
Data sources and processing
We systematically searched for accurate and complete data on livebirths reported according to the age of mothers. In many high-income countries and territories, these data were available from high-quality vital registration systems, but in many lower-income countries, birth registries were incomplete, interrupted, or delayed; in these instances, we instead relied on complete and summary birth histories in censuses and household surveys. Fertility rates from vital registration data were calculated as observed births divided by population estimates. Complete and summary birth history data were collapsed from the available microdata and sample weights applied to calculated age-specific fertility rates (ASFRs) and number of children ever born, respectively. A full description of data seeking and synthesis is provided in appendix 1 (section 2.1). In total, we compiled 58072 unique location-source-years of data for females aged 10–54 years for the period between 1950 and 2021 (number of sources by location and by year can be found in appendix 1 tables S3 and S4). At the national level, we obtained 8680 unique country-source-years of vital registration data, with an additional 29 country-source-years of data from sample registration systems. We additionally extracted data on period ASFR, or average number of children ever born from surveys and censuses that yielded 735 complete birth histories.

879 summary birth histories, and 28 unclassified forms of birth histories (details are in appendix 1 tables S3 and S4).

Throughout the forecasting modelling processes, we used female education, under-5 mortality, met need for contraceptive use, and population density in habitable areas as covariates. Details of these covariates are available in appendix 1 (section 3.1).

Fertility from 1950 to 2021

GBD 2021 estimates of fertility metrics between 1950 and 2021 were based on a systematic synthesis of all available data for all GBD locations. The fertility estimation process was closely connected to parallel, concordant modelling of population and mortality, with population estimates used iteratively to generate inputs to fertility estimation models and vice versa.[28] GBD methods are designed to account for the diversity of data available and the different biases inherent in various data sources, with customised data processing and data synthesis steps implemented to account for known biases, missing data, and heterogeneous measurement metrics used across data sources. Estimation of fertility rates between 1950 and 2021 for females ages 10–54 years largely followed the methods used in GBD 2019.[28] First, ASFRs were estimated for 5-year age groups between 15 years and 49 years only using age-specific vital registration and complete birth history data. These results were used to split all-age data from vital registration, summary birth history, and other sources into ASFRs, and then another model was fit to estimate ASFRs using the original age-specific ASFR data from vital registration and complete birth history along with these age-split data. Next, we extended these estimates to the age groups of 10–14 years and 50–54 years using data from these ages and adjacent age groups. Finally, ASFR estimates were used to calculate TFR. A summary of these methods follows, with a comprehensive description provided in appendix 1 (section 2).

To estimate ASFRs by 5-year age groups for females aged 15–49 years, we implemented mixed-effects regression models using bounded logit(ASFR) as the outcome. The 20–24-years age group was estimated first, and these estimates were used to model the remaining age groups. Both sets of models were fit separately for the high-income, sub-Saharan Africa, and central Europe, eastern Europe, and central Asia super-regions to account for differences in the relationships between the ASFR of the 20–24-years age group and that of other age groups. ASFRs in the 20–24-years age group were modelled with female educational attainment as a covariate and random intercepts for each location source. Then, we separately modelled ASFRs in the remaining age groups between 15 years and 49 years using a linear spline on the logit(ASFR) in the 20–24-years age group. The selection of spline knots varied by super-region and age group. These models also included female educational

attainment as a covariate, except in the high-income super-region, and random intercepts for each location source. After running these mixed-effects models, we corrected for systematic differences across data sources by selecting a reference source for each location and adjusting other sources based on their discrepancy from the reference source. Last, a spatiotemporal Gaussian process regression (ST-GPR) was used to smooth ASFRs across location and time, producing final point estimates and uncertainty intervals (UIs).

First-round ASFR estimates were generated from this modelling approach using age-specific vital registration and complete birth history data. To split total birth data from vital registration data, summary birth histories, and other sources into ASFRs, we calculated the ratio of the parity implied by each total birth data source to the parity estimated in this first-round ASFR model. This ratio was then multiplied by the estimated ASFRs from the first-round model. These age-split data were incorporated into a second round of estimation for each location using the same modelling approach described earlier. To generate estimates for ages 10–14 years and 50–54 years, we estimated the ratio of ASFR to the adjacent age group using all available data, then applied these ratios to the second-round ASFR estimates. We used a mixed-effects regression model to estimate location-specific ratios for ages 10–14 years, whereas we calculated the average ratio across all locations for ages 50–54 years. Finally, TFR was calculated by multiplying the ASFRs from each 5-year age group by five and summing.

Fertility forecasting

We produced forecasts of fertility using an updated modelling framework (appendix 1 section 3) that improved on the methods in the 2020 study by Vollset and colleagues.[4] In our updated methods, we used not only estimates of female educational attainment and contraceptive met need as covariates, but also estimates of under-5 mortality and population density in habitable areas to account for a larger variation in CCF50 across all countries in the sub-models (appendix 1 section 3.1, appendix 2 figure S2). Similar to Vollset and colleagues, we continued to forecast fertility with CCF50 rather than TFR, because modelling in cohort space is more stable than in period space. For this analysis, we used past CCF50 estimates for birth cohorts from 1945 to 1972 to forecast CCF50 up to the 2085 birth cohort of females, followed by predicting ASFR for each 5-year age interval as a proportion of CCF50. CCF50 was defined as the average number of children born to an individual female from an observed birth cohort (indexed by year of birth) if she lived to the end of her reproductive lifespan (ages 15–49 years). CCF50 was forecast using an ensemble modelling approach with three equally weighted sub-models (with two, three, and four covariates) in which each sub-model utilised the MR-BRT (meta-regression—Bayesian, regularised, trimmed) tool.[12] For example, the

2061

Principal
Indore Institute of Pharmacy,
INDORE (M.P.)

four-covariate sub-model was represented by the following equation:

$$logit_{(0.7,10)}(CCF50_{lc}) = \beta_0 + spline(education_{lc}) \times \beta_1$$
$$+ met\ need_{lc} \times \beta_2$$
$$+ under-5\ mortality_{lc} \times \beta_3$$
$$+ population\ density\ per\ habitable\ area_{lc} \times \beta_4$$
$$+ \varepsilon_{lc}$$

where CCF50 is scaled from more than 0·7 to less than 10 and modelled in logit space for location (l) and cohort (c), β_0 is an intercept, β_1 is a vector of the spline coefficients of female educational attainment covariate, β_2 is a slope on proportion of met need for contraception, β_3 is a slope on under-5 mortality, β_4 is a slope on population density in habitable areas, and ε is a residual term. Further details are provided in appendix 1 (section 3.2, figure S1).

From forecast CCF50, we then derived ASFR forecasts for the years 2022 to 2100 using a combination of a linear mixed-effects model, spline interpolation, and an autoregressive integrated moving average (ARIMA) model (1,0,0) on residuals to estimate the age pattern of fertility for each cohort. Once ASFR values for ages 15–49 years were obtained, we inferred the ASFR values for the 10–14-years and 50–54-years age groups based on their ratios to the rest of the age pattern during the last observed year (2021). Single-year age interval ASFRs were summed over all ages to yield the TFR for each calendar year (appendix 1 section 3.3).

We also produced fertility forecasts for four alternative scenarios applied to all 204 countries and territories. These scenarios explore shifting forecast values of two known drivers of fertility (education and met need for contraceptives) as well as a proxy pro-natal policy. More specifically, the scenarios included were: the UN SDG target 4.1 for education is achieved by 2030; the contraceptive met need SDG target 3.7 is achieved by 2030; pro-natal policies are enacted that create supportive environments for those who give birth; and the previous three scenarios combined (more details are provided in appendix 1 section 3.4). For the education SDG scenario, the forecasts assume that by 2030, all people will have 12 years or more of education by the age of 25 years and then maintains the same rate of change as the reference scenario up to 2100. For the contraceptive met need scenario, to reflect the SDG scenario of universal access, the forecasts assumed a linear increase in contraceptive coverage to reach 100% by 2030 and then stay constant up to 2100.

In the pro-natal scenario, we assumed a country will introduce pro-natal policies, such as childcare subsidies, extended parental leave, insurance coverage expansion for infertility treatment,[¹] and other forms of support for parents to afford high-quality child-care services, once TFR decreases to less than 1·75. We then made three

assumptions on the effects of such policies. First, we assumed the full effect of pro-natal policies will be to increase TFR by 0·2. Second, it will take 5 years after the policy is introduced for the full increase in TFR to occur, and TFR will rise linearly over that time span. Last, we assumed that both the policies and the increase in TFR by 0·2 will endure for the remainder of the century. For each pro-natal year, the TFR increase was distributed proportionally among the single-year ages according to their reference forecast ASFR values. The pro-natal scenario parameters were drawn from previously observed increases in TFR that coincided with pro-natal policies and broader empirical evidence regarding effects of pro-natal policies in low-fertility contexts. Further details on the pro-natal scenario can be found in appendix 1 (section 3.4.3).

In the combined scenario, we applied the aforementioned changes to the covariate forecasts simultaneously without assigning any weights because these covariates were already embedded in our model and the coefficients for each covariate were calculated based on the observed data.

GBD 2021 updates

To estimate ASFRs from 1950 to 2021, GBD 2021 added 147 surveys, 21 censuses, and 634 country-years of vital and sample registration data compared with GBD 2019, for a total of 1455 surveys and censuses, 8709 country-years of vital and sample registration data, and 150 other sources. Methods were updated for GBD 2021 by changing the time weight in ST-GPR to use a beta density function, in which hyperparameters were assigned based on quality of available data sources and the number of available datapoints. This better accounted for increased data availability, which improved precision and produced more plausible time trends compared with GBD 2019.

Updates to the fertility forecasting methods first introduced in the 2020 study by Vollset and colleagues[⁴] included the incorporation of two new covariates in the CCF50 model—namely, under-5 mortality and population density in habitable areas—in addition to those previously used (ie, female educational attainment and contraceptive met need). Furthermore, the current iteration of the IHME model employed a linear fixed-effect model to forecast 5-year ASFRs, which were interpolated to 1-year estimates using an ARIMA model on the residuals to quantify variation not explained by the covariates.

Comparison with other models

We evaluated the IHME fertility forecasting model performance based on out-of-sample predictions during the validation period 2007–21. We used the following skill metric[¹⁴] for model evaluation and comparison (see appendix 1 section 3.6 for more details):
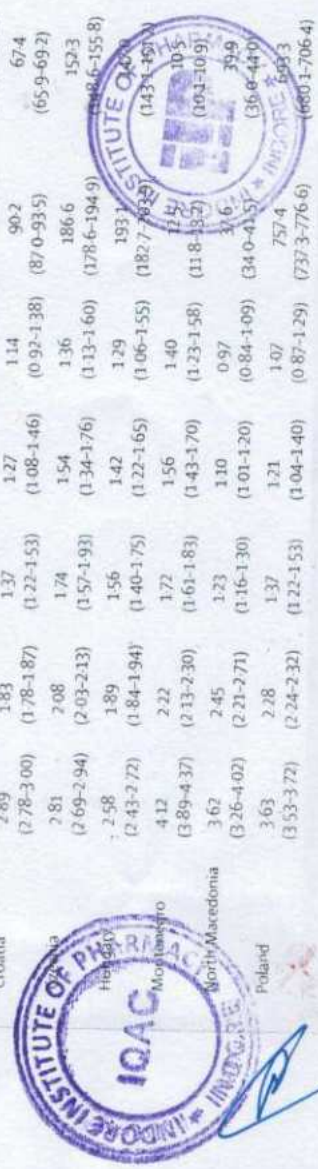
$$skill = 1 - \frac{RMSE(Model)}{RMSE(Baseline\ Model)}$$

Principal
Indore Institute of Pharmacy,
INDORE (M.P.)

170

	Total fertility rate					Livebirths (thousands)					Net reproductive rate, 2021
	1950	1980	2021	2050	2100	1950	1980	2021	2050	2100	
Global	4·84 (4·63–5·06)	3·61 (3·53–3·69)	2·23 (2·09–2·38)	1·83 (1·59–2·08)	1·59 (1·25–1·96)	92675·8 (88663·5–96630·8)	122023·7 (119441·0–124623·8)	129383·6 (121382·9–138206·0)	112073·6 (93698·4–133329·8)	72386·8 (40812·5–118843·5)	1·0 (1·0–1·1)
Central Europe, eastern Europe, and central Asia	3·01 (2·91–3·11)	2·24 (2·21–2·28)	1·81 (1·72–1·92)	1·68 (1·56–1·81)	1·57 (1·42–1·73)	7452·5 (7227·2–7699·6)	7113·3 (7020·5–7211·4)	4906·1 (4635·7–5195·7)	3874·8 (3409·2–4396·4)	2744·9 (1739·5–3067·1)	0·9 (0·8–0·9)
Central Asia	4·45 (4·32–4·59)	3·73 (3·65–3·80)	2·79 (2·68–2·91)	2·31 (2·16–2·47)	1·95 (1·76–2·13)	1016·0 (986·0–1046·1)	1676·9 (1642·3–1709·2)	2073·1 (1990·1–2158·2)	1913·2 (1629·7–2201·3)	1418·0 (1007·6–1927·4)	1·3 (1·3–1·4)
Armenia	4·14 (3·95–4·33)	2·49 (2·39–2·61)	1·68 (1·53–1·84)	1·45 (1·27–1·65)	1·24 (1·01–1·49)	49·0 (46·8–51·1)	76·5 (73·2–79·9)	35·0 (31·6–38·5)	16·9 (11·9–22·2)	6·7 (3·5–11·3)	0·8 (0·7–0·9)
Azerbaijan	4·38 (4·09–4·69)	3·33 (3·18–3·48)	1·75 (1·55–1·95)	1·51 (1·27–1·76)	1·29 (1·01–1·59)	107·5 (100·2–114·9)	162·2 (155·0–169·6)	138·7 (123·5–154·9)	93·5 (69·0–122·7)	38·3 (17·9–69·8)	0·8 (0·7–0·9)
Georgia	2·60 (2·42–2·79)	2·21 (2·07–2·33)	2·05 (1·92–2·18)	1·80 (1·65–1·96)	1·52 (1·34–1·71)	84·2 (78·4–90·3)	91·8 (86·3–96·9)	45·2 (42·4–48·1)	36·1 (28·7–43·7)	21·3 (14·2–30·4)	1·0 (0·9–1·0)
Kazakhstan	3·94 (3·79–4·11)	3·02 (2·93–3·11)	3·02 (2·85–3·20)	2·43 (2·21–2·65)	1·94 (1·69–2·19)	253·8 (244·5–264·1)	365·1 (353·6–376·9)	424·9 (400·9–448·7)	392·9 (325·0–461·4)	261·4 (147·7–409·6)	1·4 (1·4–1·5)
Kyrgyzstan	4·19 (4·03–4·35)	4·12 (3·98–4·27)	2·92 (2·66–3·21)	2·35 (2·05–2·70)	1·95 (1·62–2·33)	57·9 (55·6–60·2)	111·9 (107·3–116·3)	159·2 (145·4–175·1)	139·1 (104·2–181·6)	72·0 (21·5–145·6)	1·4 (1·3–1·5)
Mongolia	5·09 (4·78–5·41)	5·76 (5·55–5·97)	3·16 (2·86–3·49)	2·46 (2·02–2·88)	1·87 (1·35–2·35)	30·2 (28·4–32·1)	61·9 (59·7–64·1)	80·0 (72·4–88·0)	100·9 (76·4–124·5)	104·2 (46·7–179·1)	1·5 (1·4–1·6)
Tajikistan	6·65 (6·33–6·96)	5·65 (5·47–5·84)	3·40 (3·17–3·64)	2·66 (2·33–2·97)	2·13 (1·75–2·49)	86·2 (82·6–89·9)	159·7 (154·8–164·5)	286·4 (268·0–306·6)	301·0 (229·2–381·8)	243·2 (101·7–421·6)	1·6 (1·5–1·7)
Turkmenistan	4·82 (4·63–5·01)	4·75 (4·55–4·94)	2·83 (2·54–3·15)	2·25 (1·87–2·66)	1·81 (1·38–2·28)	48·7 (46·7–50·5)	96·4 (92·9–99·8)	110·5 (99·4–122·7)	105·2 (80·2–139·0)	75·9 (33·1–146·2)	1·3 (1·2–1·5)
Uzbekistan	5·68 (5·32–6·06)	4·58 (4·47–4·69)	2·87 (2·66–3·10)	2·34 (2·08–2·62)	1·97 (1·69–2·27)	298·6 (280·9–316·8)	551·5 (538·2–564·1)	793·1 (733·9–854·3)	727·6 (491·2–993·0)	595·0 (307·1–992·9)	1·3 (1·2–1·4)
Central Europe	3·22 (3·13–3·30)	2·21 (2·18–2·24)	1·48 (1·36–1·61)	1·34 (1·19–1·50)	1·21 (1·03–1·41)	2336·9 (2276·3–2399·1)	2085·5 (2056·7–2113·8)	1038·3 (954·3–1129·1)	668·1 (567·7–786·3)	283·6 (185·8–412·4)	0·7 (0·7–0·8)
Albania	5·88 (5·63–6·13)	3·44 (3·31–3·58)	1·50 (1·33–1·69)	1·34 (1·10–1·61)	1·17 (0·86–1·50)	48·0 (45·9–50·0)	71·4 (68·8–74·3)	27·9 (24·7–31·4)	16·4 (11·6–22·4)	6·3 (2·9–12·3)	0·7 (0·6–0·7)
Bosnia and Herzegovina	3·68 (3·31–4·08)	2·21 (1·97–2·46)	1·33 (1·20–1·46)	1·16 (0·99–1·35)	0·95 (0·71–1·19)	92·6 (83·8–102·1)	79·0 (70·7–87·8)	26·7 (24·2–29·4)	12·4 (8·8–16·8)	3·5 (1·7–6·2)	0·6 (0·6–0·7)
Bulgaria	2·77 (2·65–2·91)	2·07 (2·02–2·12)	1·58 (1·47–1·70)	1·43 (1·29–1·59)	1·26 (1·08–1·45)	167·6 (160·5–175·7)	127·8 (124·7–130·8)	58·1 (53·7–62·4)	36·6 (29·6–44·0)	13·9 (8·5–21·6)	0·8 (0·7–0·8)
Croatia	2·89 (2·78–3·00)	1·83 (1·78–1·87)	1·23 (1·16–1·30)	1·10 (1·01–1·20)	0·97 (0·84–1·09)	90·2 (87·0–93·5)	67·4 (65·9–69·2)	34·8 (31·0–38·9)	16·8 (12·3–22·0)	3·2 (0·3–7·2)	0·7 (0·6–0·7)
Czechia	2·81 (2·69–2·94)	2·08 (2·03–2·13)	1·74 (1·57–1·93)	1·54 (1·34–1·76)	1·36 (1·13–1·60)	186·6 (178·6–194·9)	152·3 (148·6–155·8)	105·9 (95·4–117·6)	82·1 (67·2–98·5)	44·9 (27·3–68·3)	0·8 (0·8–0·9)
Hungary	2·58 (2·43–2·72)	1·89 (1·84–1·94)	1·56 (1·40–1·75)	1·42 (1·22–1·65)	1·29 (1·06–1·55)	193·3 (182·7–203·?)	143·1 (143·1–150·?)	87·9 (78·5–98·4)	77·0 (61·9–94·7)	51·6 (32·1–78·9)	0·8 (0·7–0·8)
Montenegro	4·12 (3·89–4·37)	2·22 (2·13–2·30)	1·72 (1·61–1·83)	1·56 (1·43–1·70)	1·40 (1·23–1·58)		10·5 (10·1–10·9)	7·0 (6·5–7·4)	4·5 (3·7–5·4)	1·6 (0·9–2·5)	0·8 (0·8–0·9)
North Macedonia	3·62 (3·26–4·02)	2·45 (2·21–2·71)	1·27 (1·08–1·46)	1·14 (0·92–1·38)		39·9 (36·8–44·0)	18·7 (17·7–19·8)	9·4 (7·3–11·9)	1·8 (0·9–3·0)	0·7 (0·6–0·7)
Poland	3·63 (3·53–3·72)	2·28 (2·24–2·32)	1·37 (1·22–1·53)	1·21 (1·04–1·40)	1·07 (0·87–1·29)	757·4 (737·3–776·6)	693·3 (668·1–706·4)	342·0 (304·9–381·1)	206·2 (163·3–254·7)	74·4 (43·4–116·7)	0·7 (0·6–0·7)

171

	Total fertility rate					Livebirths (thousands)					Net reproductive rate, 2021
	1950	1980	2021	2050	2100	1950	1980	2021	2050	2100	
(Continued from previous page)											
Romania	3·02 (2·84–3·22)	2·32 (2·25–2·39)	1·70 (1·57–1·84)	1·48 (1·32–1·66)	1·26 (1·06–1·48)	415·0 (390·9–442·4)	387·3 (375·7–399·2)	177·6 (163·6–192·6)	114·9 (89·2–143·0)	37·7 (18·7–62·7)	0·8 (0·8–0·9)
Serbia	3·31 (3·22–3·40)	2·22 (2·17–2·28)	1·08 (0·99–1·16)	1·01 (0·90–1·11)	0·96 (0·82–1·09)	183·9 (179·1–188·1)	157·5 (153·3–161·7)	61·6 (56·8–66·7)	34·0 (27·8–40·6)	10·5 (7·1–14·6)	0·5 (0·5–0·6)
Slovakia	3·65 (3·56–3·75)	2·32 (2·27–2·36)	1·63 (1·53–1·73)	1·46 (1·34–1·59)	1·31 (1·16–1·46)	99·6 (97·2–102·2)	94·6 (92·9–96·3)	56·3 (52·9–59·8)	40·0 (34·2–45·7)	20·9 (15·1–27·4)	0·8 (0·7–0·8)
Slovenia	2·86 (2·54–3·20)	2·01 (1·97–2·06)	1·63 (1·53–1·74)	1·51 (1·39–1·64)	1·38 (1·24–1·54)	32·3 (28·8–36·2)	29·5 (28·8–30·1)	18·8 (17·6–20·0)	17·9 (15·7–20·5)	13·2 (10·3–16·9)	0·8 (0·7–0·8)
Eastern Europe	2·70 (2·59–2·82)	1·91 (1·88–1·95)	1·38 (1·27–1·49)	1·28 (1·15–1·42)	1·19 (1·05–1·35)	4099·6 (3935·2–4285·2)	3350·8 (3289·2–3418·5)	1794·7 (1651·3–1949·2)	1293·5 (1082·3–1534·3)	643·2 (456·2–881·7)	0·7 (0·6–0·7)
Belarus	3·00 (2·83–3·18)	2·01 (1·94–2·09)	1·42 (1·23–1·64)	1·29 (1·06–1·55)	1·19 (0·95–1·47)	192·3 (181·8–203·2)	156·4 (150·9–162·4)	82·5 (70·6–95·6)	59·8 (43·0–80·3)	30·5 (16·3–53·1)	0·7 (0·6–0·8)
Estonia	2·30 (2·18–2·43)	2·06 (2·01–2·11)	1·60 (1·49–1·71)	1·37 (1·24–1·50)	1·21 (1·06–1·36)	20·1 (19·1–21·2)	22·5 (21·9–23·1)	13·1 (12·2–14·0)	9·4 (8·0–11·2)	4·2 (2·8–5·9)	0·8 (0·7–0·8)
Latvia	1·98 (1·84–2·14)	1·90 (1·86–1·94)	1·52 (1·35–1·71)	1·35 (1·16–1·56)	1·22 (1·01–1·49)	32·9 (30·7–35·5)	35·6 (34·9–36·4)	16·8 (14·9–18·9)	9·7 (7·5–12·4)	3·9 (2·2–6·6)	0·7 (0·6–0·8)
Lithuania	2·92 (2·78–3·10)	2·00 (1·95–2·05)	1·40 (1·30–1·51)	1·23 (1·11–1·35)	1·09 (0·96–1·25)	58·6 (55·7–62·0)	51·3 (49·9–52·6)	23·6 (21·9–25·4)	12·4 (10·0–15·4)	4·2 (2·7–6·1)	0·7 (0·6–0·7)
Moldova	3·77 (3·61–3·92)	2·46 (2·38–2·54)	1·18 (1·06–1·33)	1·09 (0·94–1·25)	1·03 (0·87–1·24)	84·7 (81·4–88·0)	86·1 (83·4–88·9)	28·4 (25·4–32·0)	9·5 (5·6–13·4)	2·7 (1·3–4·7)	0·6 (0·5–0·6)
Russia	2·77 (2·62–2·95)	1·87 (1·83–1·93)	1·48 (1·37–1·60)	1·33 (1·20–1·47)	1·21 (1·06–1·37)	2819·9 (2671·0–2995·4)	2237·6 (2184·0–2299·0)	1352·4 (1251·9–1464·1)	1053·8 (871·5–1239·4)	562·8 (408·0–758·1)	0·7 (0·7–0·8)
Ukraine	2·44 (2·33–2·55)	1·95 (1·90–2·01)	1·05 (0·94–1·18)	1·01 (0·88–1·16)	0·98 (0·83–1·16)	891·1 (853·1–930·3)	761·3 (739·2–783·2)	277·9 (246·7–311·8)	138·8 (104·8–185·4)	34·9 (19·2–60·5)	0·5 (0·4–0·6)
High income	2·85 (2·78–2·92)	1·88 (1·86–1·90)	1·51 (1·41–1·61)	1·43 (1·30–1·56)	1·37 (1·22–1·53)	13626·1 (13275·0–13959·1)	12483·6 (12339·3–12633·7)	10399·8 (9728·0–11116·3)	9387·4 (8381·2–10552·0)	6961·9 (5348·6–8941·5)	0·7 (0·7–0·8)
Australasia	3·13 (3·06–3·21)	1·93 (1·90–1·97)	1·64 (1·48–1·80)	1·45 (1·25–1·68)	1·33 (1·08–1·59)	251·9 (246·1–258·0)	278·2 (273·0–283·7)	357·9 (324·6–393·9)	404·9 (338·5–481·9)	363·9 (250·1–516·0)	0·8 (0·7–0·9)
Australia	3·06 (2·98–3·14)	1·92 (1·88–1·97)	1·64 (1·47–1·82)	1·45 (1·23–1·70)	1·32 (1·06–1·61)	202·2 (196·9–207·7)	227·7 (222·7–232·9)	299·3 (268·5–332·1)	339·1 (278·3–411·8)	307·8 (204·0–447·8)	0·8 (0·7–0·9)
New Zealand	3·49 (3·41–3·57)	1·96 (1·92–2·00)	1·62 (1·53–1·72)	1·45 (1·33–1·58)	1·35 (1·20–1·51)	49·7 (48·7–50·8)	50·5 (49·4–51·6)	58·6 (55·2–62·0)	65·7 (57·4–74·2)	56·1 (42·5–72·1)	0·8 (0·7–0·8)
High-income Asia Pacific	3·72 (3·59–3·86)	1·94 (1·89–2·00)	1·12 (1·03–1·22)	1·14 (1·00–1·30)	1·14 (0·96–1·35)	3059·8 (2947·5–3174·6)	2467·7 (2400·6–2541·4)	1169·5 (1075·7–1275·1)	908·3 (784·1–1047·7)	499·8 (348·5–707·9)	0·5 (0·5–0·6)
Brunei	6·41 (6·24–6·57)	3·87 (3·65–4·10)	1·65 (1·43–1·88)	1·40 (1·08–1·78)	1·25 (0·87–1·70)	2·7 (2·6–2·7)	5·8 (5·4–6·1)	6·4 (5·6–7·3)	3·4 (2·4–4·7)	1·0 (0·2–2·5)	0·8 (0·7–0·9)
Japan	3·27 (3·12–3·42)	1·69 (1·64–1·76)	1·26 (1·14–1·41)	1·26 (1·09–1·45)	1·21 (1·00–1·43)	2188·1 (2087·3–2289·4)	1573·3 (1518·2–1626·1)	838·0 (754·0–933·3)	667·4 (555·1–790·8)	387·8 (259·2–572·2)	0·6 (0·5–0·7)
Singapore	6·03 (5·75–6·31)	1·77 (1·66–1·88)	1·20 (1·05–1·39)	1·15 (0·93–1·41)	1·12 (0·88–1·41)	48·0 (45·7–50·3)	41·9 (39·2–44·8)	55·5 (48·5–64·0)	56·0 (44·0–70·8)	45·3 (28·5–69·5)	0·6 (0·5–0·7)
South Korea	5·72 (5·37–6·08)	2·56 (2·48–2·64)	0·82 (0·75–0·89)	0·82 (0·73–0·92)	0·82 (0·71–0·95)	821·1 (774·1–869·0)	845·6 (822·3–873·2)	269·6 (246·4–294·2)	181·5 (155·9–209·6)	65·6 (45·4–90·3)	0·5 (0·5–0·7)
High-income North America	3·10 (3·03–3·18)	1·78 (1·75–1·81)	1·63 (1·53–1·73)	1·51 (1·38–1·64)	1·43 (1·27–1·60)	4023·2 (3927·9–4124·...)	3948·6 (3866·5–4035·4)	4014·6 (3772·1–4278·3)	3732·8 (3300·8–4245·6)	2967·3 (2256·1–3805·1)	0·8 (0·7–0·8)

(Table 1 continues on next page)

	Total fertility rate					Livebirths (thousands)					Net reproductive rate, 2021
	1950	1980	2021	2050	2100	1950	1980	2021	2050	2100	
(Continued from previous page)											
Canada	3·31 (3·23–3·40)	1·65 (1·62–1·69)	1·46 (1·31–1·62)	1·39 (1·21–1·58)	1·32 (1·12–1·54)	361·9 (353·0–370·7)	357·7 (350·4–365·1)	361·6 (324·1–401·3)	442·0 (374·4–521·9)	415·5 (299·8–570·6)	0·7 (0·6–0·8)
Greenland	5·62 (5·37–5·87)	2·32 (2·21–2·43)	1·94 (1·78–2·13)	1·84 (1·60–2·10)	1·67 (1·36–2·00)	1·0 (0·9–1·0)	1·0 (0·9–1·0)	0·8 (0·7–0·9)	0·7 (0·5–0·8)	0·5 (0·3–0·7)	0·9 (0·8–1·0)
USA	3·08 (3·01–3·17)	1·79 (1·76–1·83)	1·64 (1·55–1·75)	1·52 (1·40–1·65)	1·45 (1·30–1·60)	3660·2 (3569·5–3758·9)	3589·8 (3510·8–3663·5)	3652·2 (3445·3–3878·2)	3290·0 (2928·9–3719·1)	2551·2 (1954·8–3256·2)	0·8 (0·7–0·8)
Southern Latin America	3·20 (3·11–3·30)	2·97 (2·93–3·01)	1·49 (1·32–1·67)	1·32 (1·10–1·57)	1·23 (0·97–1·53)	673·6 (653·6–693·9)	987·3 (972·7–1001·9)	769·3 (683·8–862·6)	584·3 (452·6–745·4)	293·8 (159·6–482·9)	0·7 (0·6–0·8)
Argentina	3·03 (2·92–3·15)	3·17 (3·11–3·23)	1·52 (1·34–1·72)	1·33 (1·09–1·60)	1·22 (0·91–1·56)	440·7 (424·2–457·7)	683·1 (669·7–696·0)	536·7 (473·3–606·6)	389·6 (284·0–513·3)	173·1 (80·2–310·7)	0·7 (0·6–0·8)
Chile	4·05 (3·94–4·16)	2·59 (2·53–2·65)	1·39 (1·23–1·54)	1·29 (1·09–1·51)	1·24 (0·99–1·51)	188·2 (183·3–193·1)	250·2 (244·2–256·4)	197·2 (175·7–219·6)	169·6 (136·6–210·7)	109·6 (69·1–169·7)	0·7 (0·6–0·8)
Uruguay	2·44 (2·31–2·57)	2·53 (2·47–2·60)	1·47 (1·30–1·64)	1·36 (1·14–1·60)	1·25 (0·97–1·56)	44·8 (42·3–47·1)	53·9 (52·5–55·4)	35·4 (31·5–39·6)	25·1 (19·6–32·2)	11·1 (5·8–19·3)	0·7 (0·6–0·7)
Western Europe	2·41 (2·34–2·47)	1·79 (1·77–1·81)	1·53 (1·44–1·63)	1·44 (1·32–1·57)	1·37 (1·23–1·52)	5617·5 (5459·1–5774·9)	4801·7 (4750·3–4856·9)	4088·4 (3844·3–4353·4)	3757·3 (3360·8–4160·6)	2837·2 (2247·8–3546·1)	0·7 (0·7–0·8)
Andorra	2·79 (2·44–3·18)	1·59 (1·51–1·66)	0·98 (0·91–1·05)	1·02 (0·92–1·11)	1·01 (0·89–1·13)	0·1 (0·1–0·1)	0·5 (0·5–0·5)	0·5 (0·5–0·6)	0·3 (0·3–0·3)	0·1 (0·1–0·1)	0·5 (0·4–0·5)
Austria	2·08 (2·01–2·15)	1·67 (1·63–1·70)	1·46 (1·37–1·55)	1·42 (1·29–1·55)	1·34 (1·18–1·51)	105·8 (102·3–109·7)	91·3 (89·3–93·3)	85·7 (80·5–91·1)	81·0 (71·2–91·5)	63·4 (48·1–80·5)	0·7 (0·7–0·7)
Belgium	2·30 (2·22–2·38)	1·70 (1·66–1·73)	1·56 (1·41–1·72)	1·43 (1·24–1·63)	1·34 (1·13–1·57)	142·4 (137·8–147·2)	123·3 (120·9–125·7)	113·3 (102·2–124·9)	114·6 (95·9–137·7)	99·9 (69·0–140·3)	0·8 (0·7–0·8)
Cyprus	3·96 (3·80–4·11)	2·42 (2·35–2·49)	1·33 (1·15–1·53)	1·18 (0·97–1·43)	1·13 (0·89–1·40)	13·9 (13·4–14·5)	13·4 (13·0–13·8)	15·1 (13·1–17·4)	11·0 (8·5–13·8)	7·6 (4·7–11·6)	0·6 (0·6–0·7)
Denmark	2·54 (2·46–2·63)	1·49 (1·45–1·52)	1·73 (1·63–1·83)	1·57 (1·46–1·69)	1·47 (1·34–1·60)	78·2 (75·8–81·1)	55·3 (53·9–56·7)	63·2 (59·7–66·7)	62·4 (55·2–70·2)	58·0 (46·1–70·9)	0·8 (0·8–0·9)
Finland	3·08 (2·99–3·19)	1·65 (1·60–1·70)	1·44 (1·35–1·53)	1·36 (1·24–1·49)	1·32 (1·18–1·48)	95·6 (92·8–98·9)	63·9 (62·1–65·7)	48·5 (45·3–51·7)	41·9 (36·2–48·5)	30·1 (23·3–38·7)	0·7 (0·7–0·7)
France	2·80 (2·72–2·87)	1·90 (1·85–1·95)	1·75 (1·57–1·93)	1·56 (1·35–1·79)	1·43 (1·19–1·69)	840·4 (817·3–862·6)	795·3 (774·5–816·9)	693·1 (623·0–766·7)	561·9 (448·3–683·9)	348·5 (214·5–542·2)	0·8 (0·8–0·9)
Germany	2·09 (1·94–2·24)	1·52 (1·48–1·55)	1·53 (1·44–1·62)	1·47 (1·35–1·58)	1·40 (1·27–1·53)	1105·0 (1023·7–1188·6)	852·3 (838·8–873·0)	790·3 (742·4–837·6)	742·6 (647·9–832·5)	609·5 (489·2–740·4)	0·7 (0·7–0·8)
Greece	2·50 (2·41–2·60)	1·52 (1·48–1·55)	1·53 (1·44–1·62)	1·47 (1·35–1·58)	1·40 (1·27–1·53)	154·7 (148·6–160·8)	143·4 (140·4–146·8)	82·3 (73·4–92·1)	52·3 (39·8–66·9)	26·1 (15·2–42·2)	0·7 (0·7–0·8)
Iceland	3·81 (3·57–4·08)	2·40 (2·32–2·49)	1·97 (1·81–2·13)	1·73 (1·54–1·93)	1·58 (1·36–1·82)	4·0 (3·8–4·3)	4·3 (4·2–4·5)	4·7 (4·3–5·1)	5·4 (4·5–6·4)	5·4 (3·8–7·5)	0·8 (0·8–0·9)
Ireland	3·18 (3·09–3·28)	3·14 (3·08–3·20)	1·76 (1·65–1·88)	1·54 (1·40–1·70)	1·40 (1·22–1·58)	63·9 (62·1–66·0)	74·1 (72·8–75·4)	57·7 (54·0–61·4)	61·5 (52·5–70·8)	46·8 (34·4–61·9)	0·9 (0·9–1·0)
Israel	3·79 (3·68–3·90)	3·14 (3·08–3·20)	2·90 (2·76–3·05)	2·38 (2·20–2·59)	2·09 (1·86–2·34)	47·0 (45·6–48·4)	95·1 (91·1–99·1)	183·2 (174·1–192·7)	208·6 (174·7–248·4)	231·4 (167·3–315·1)	1·4 (1·3–1·5)
Italy	2·45 (2·37–2·53)	1·63 (1·60–1·66)	1·21 (1·08–1·36)	1·18 (1·00–1·37)	1·09 (0·88–1·32)	882·2 (850·4–912·8)	640·5 (628·7–652·9)	398·2 (354·1–445·2)	285·5 (236·9–343·9)	136·4 (84·0–209·0)	0·6 (0·5–0·7)
Luxembourg	2·00 (1·87–2·15)	1·51 (1·46–1·55)	1·38 (1·28–1·48)	1·30 (1·17–1·44)	1·24 (1·09–1·40)	6·6 (6·1–7·1)	4·2 (4·0–4·3)	6·6 (6·1–7·1)	8·8 (7·7–10·1)	8·8 (6·8–11·1)	0·9 (0·8–0·9)

173

	Total fertility rate					Livebirths (thousands)					Net reproductive rate, 2021
	1950	1980	2021	2050	2100	1950	1980	2021	2050	2100	
(Continued from previous page)											
Malta	4.04 (3.88–4.22)	1.98 (1.91–2.05)	1.53 (1.37–1.71)	1.39 (1.18–1.64)	1.26 (1.01–1.55)	9.8 (9.4–10.2)	5.7 (5.5–6.0)	4.3 (3.9–4.8)	4.8 (3.9–5.9)	4.0 (2.6–6.0)	0.7 (0.7–0.8)
Monaco	2.21 (1.91–2.55)	1.64 (1.43–1.88)	1.52 (1.29–1.80)	1.44 (1.16–1.76)	1.37 (1.06–1.73)	0.3 (0.3–0.3)	0.3 (0.3–0.3)	0.3 (0.2–0.3)	0.2 (0.2–0.3)	0.1 (0.1–0.2)	0.7 (0.6–0.8)
Netherlands	3.12 (3.04–3.22)	1.60 (1.56–1.63)	1.68 (1.58–1.78)	1.54 (1.41–1.67)	1.42 (1.27–1.57)	229.6 (223.4–236.8)	178.6 (174.7–182.6)	177.7 (167.2–188.3)	165.6 (146.4–186.7)	142.0 (112.1–177.0)	0.8 (0.8–0.9)
Norway	2.52 (2.44–2.60)	1.61 (1.57–1.65)	1.55 (1.46–1.64)	1.43 (1.32–1.54)	1.36 (1.24–1.49)	61.9 (60.1–63.9)	47.8 (46.8–48.9)	55.9 (52.8–59.1)	54.8 (48.5–61.5)	46.2 (37.2–57.5)	0.7 (0.7–0.8)
Portugal	3.04 (2.94–3.16)	2.13 (2.09–2.18)	1.30 (1.22–1.39)	1.27 (1.13–1.42)	1.17 (1.00–1.37)	206.3 (199.2–214.4)	154.5 (151.0–158.2)	80.6 (75.2–86.2)	70.9 (59.7–83.9)	46.0 (32.1–63.2)	0.6 (0.6–0.7)
San Marino	2.47 (2.14–2.84)	1.58 (1.48–1.69)	1.30 (1.15–1.48)	1.27 (1.09–1.49)	1.20 (0.99–1.46)	0.3 (0.2–0.3)	0.2 (0.2–0.3)	0.2 (0.2–0.3)	0.2 (0.1–0.2)	0.1 (0.0–0.1)	0.6 (0.5–0.7)
Spain	2.47 (2.38–2.55)	2.13 (2.09–2.17)	1.26 (1.17–1.35)	1.23 (1.10–1.38)	1.11 (0.93–1.30)	560.3 (542.4–579.3)	549.2 (538.5–559.9)	336.7 (312.8–362.0)	377.6 (319.2–439.7)	248.3 (169.5–331.8)	0.6 (0.5–0.7)
Sweden	2.27 (2.20–2.36)	1.65 (1.62–1.69)	1.71 (1.61–1.81)	1.51 (1.39–1.64)	1.38 (1.24–1.53)	113.9 (110.3–118.3)	95.5 (93.4–97.5)	113.9 (107.4–120.7)	135.0 (119.4–151.5)	136.8 (108.5–166.8)	0.8 (0.8–0.9)
Switzerland	2.35 (2.28–2.43)	1.58 (1.54–1.61)	1.48 (1.39–1.59)	1.40 (1.28–1.52)	1.33 (1.20–1.47)	83.2 (80.7–85.8)	75.8 (74.2–77.4)	89.1 (83.5–95.3)	83.8 (74.0–94.7)	68.5 (54.8–84.4)	0.7 (0.7–0.8)
UK	2.19 (2.13–2.25)	1.85 (1.80–1.90)	1.49 (1.33–1.67)	1.38 (1.18–1.58)	1.30 (1.08–1.53)	809.2 (786.2–832.5)	735.5 (715.4–755.5)	683.8 (608.2–762.0)	623.3 (504.8–743.2)	470.8 (303.6–664.1)	0.7 (0.6–0.8)
Latin America and Caribbean	5.82 (5.58–6.06)	4.09 (4.01–4.18)	1.98 (1.83–2.13)	1.57 (1.38–1.79)	1.31 (1.08–1.57)	6278.2 (6037.0–6525.3)	10310.9 (10111.1–10514.4)	9377.7 (8692.9–10090.5)	6763.5 (5627.9–8076.1)	3002.6 (1769.5–4786.3)	0.9 (0.9–1.0)
Andean Latin America	6.72 (6.47–6.95)	4.97 (4.86–5.08)	2.32 (2.14–2.51)	1.80 (1.58–2.05)	1.45 (1.19–1.73)	679.8 (655.9–702.4)	1115.9 (1089.4–1141.9)	1242.6 (1146.2–1345.6)	961.5 (782.6–1184.9)	457.7 (242.3–768.2)	1.1 (1.0–1.2)
Bolivia	6.84 (6.49–7.19)	5.65 (5.45–5.85)	2.53 (2.31–2.77)	1.84 (1.55–2.17)	1.40 (1.07–1.77)	150.5 (143.0–157.8)	216.0 (208.8–223.4)	245.0 (223.2–270.0)	208.5 (162.6–277.0)	113.0 (53.3–210.1)	1.2 (1.1–1.3)
Ecuador	6.09 (5.78–6.44)	4.24 (4.10–4.40)	2.20 (1.95–2.50)	1.74 (1.42–2.10)	1.45 (1.10–1.86)	149.7 (142.2–157.9)	249.6 (241.3–259.0)	321.5 (285.0–363.6)	269.3 (194.5–367.0)	152.8 (66.7–298.3)	1.1 (0.9–1.2)
Peru	6.95 (6.68–7.22)	5.10 (4.96–5.24)	2.30 (2.08–2.55)	1.83 (1.56–2.13)	1.44 (1.14–1.80)	379.7 (366.2–392.8)	650.3 (630.8–669.5)	676.2 (611.2–748.3)	483.7 (374.1–630.9)	192.0 (79.6–384.3)	1.1 (1.0–1.2)
Caribbean	5.02 (4.90–5.14)	3.39 (3.31–3.47)	2.19 (2.02–2.39)	1.77 (1.50–2.08)	1.43 (1.11–1.88)	699.5 (682.6–715.4)	837.0 (818.1–856.6)	797.4 (734.1–868.9)	570.0 (432.5–738.2)	241.7 (98.1–477.6)	1.0 (0.9–1.1)
Antigua and Barbuda	4.63 (4.38–4.88)	2.33 (2.24–2.42)	1.49 (1.33–1.68)	1.30 (1.11–1.52)	1.15 (0.93–1.41)	1.7 (1.6–1.7)	1.2 (1.2–1.3)	1.0 (0.9–1.2)	0.7 (0.5–0.9)	0.3 (0.1–0.5)	0.7 (0.6–0.8)
The Bahamas	3.97 (3.77–4.17)	2.65 (2.56–2.76)	1.23 (1.05–1.45)	1.24 (1.02–1.49)	1.24 (0.99–1.52)	2.6 (2.5–2.7)	5.0 (4.8–5.2)	3.9 (3.3–4.5)	3.1 (2.3–4.2)	1.9 (1.0–3.2)	0.6 (0.5–0.7)
Barbados	[obscured]	1.94 (1.86–2.04)	1.30 (1.09–1.56)	1.18 (0.95–1.47)	1.24 (0.85–1.42)	2.8 (2.7–3.0)	2.6 (2.5–2.7)	2.6 (2.2–3.1)	1.7 (1.1–2.3)	0.7 (0.3–1.3)	0.6 (0.5–0.7)
Belize	[obscured]	5.42 (5.27–5.57)	1.96 (1.74–2.20)	1.58 (1.28–1.90)	1.28 (0.93–1.67)	6.7 (6.4–7.1)	7.6 (2.7–3.0)	7.5 (6.7–8.5)	5.2 (5.5–9.8)	5.2 (2.4–9.0)	0.9 (0.8–1.1)
Bermuda	[obscured]	1.62 (1.55–1.70)	1.28 (1.15–1.43)	1.19 (1.04–1.36)	1.07 (0.88–1.28)	1.1 (1.1–1.2)	0.8 (0.8–0.9)	0.5 (0.4–0.5)	0.3 (0.2–0.4)	0.1 (0.1–0.2)	0.8 (0.8–1.1)

(Table 1 continues on next page)

	Total fertility rate					Livebirths (thousands)					Net reproductive rate, 2021
	1950	1980	2021	2050	2100	1950	1980	2021	2050	2100	
(Continued from previous page)											
Dominica	5·12 (4·88–5·37)	3·50 (3·32–3·69)	1·29 (1·09–1·52)	1·18 (0·96–1·45)	1·13 (0·89–1·42)	1·9 (1·8–2·0)	1·9 (1·8–2·0)	0·6 (0·5–0·7)	0·4 (0·3–0·6)	0·2 (0·1–0·3)	0·6 (0·5–0·7)
Dominican Republic	7·83 (7·60–8·04)	4·72 (4·50–4·94)	2·32 (2·10–2·56)	1·84 (1·55–2·15)	1·51 (1·19–1·86)	132·5 (129·1–135·6)	210·1 (199·5–220·2)	213·5 (192·9–236·2)	159·1 (118·5–211·1)	70·4 (27·8–142·4)	1·1 (1·0–1·2)
Grenada	5·27 (5·05–5·48)	3·57 (3·39–3·75)	1·74 (1·49–2·05)	1·41 (1·09–1·79)	1·19 (0·81–1·62)	3·5 (3·3–3·6)	2·7 (2·5–2·8)	1·4 (1·2–1·6)	0·8 (0·5–1·1)	0·1 (0·0–0·4)	0·8 (0·7–1·0)
Guyana	6·17 (5·96–6·41)	3·91 (3·73–4·09)	2·35 (2·06–2·67)	1·91 (1·54–2·32)	1·58 (1·15–2·04)	19·4 (18·7–20·2)	26·1 (24·8–27·3)	15·3 (13·5–17·4)	8·6 (5·7–12·8)	5·5 (2·0–11·1)	1·1 (1·0–1·2)
Haiti	6·67 (6·36–6·96)	5·98 (5·76–6·18)	3·16 (2·82–3·55)	2·10 (1·68–2·61)	1·44 (0·92–2·05)	175·3 (167·4–182·9)	228·7 (221·2–235·7)	344·4 (308·5–386·7)	271·1 (179·5–381·4)	120·8 (30·5–290·6)	1·4 (1·2–1·5)
Jamaica	4·06 (3·78–4·34)	3·28 (3·18–3·39)	1·37 (1·18–1·56)	1·16 (0·93–1·39)	1·04 (0·79–1·31)	50·1 (46·9–53·6)	58·2 (56·3–60·2)	32·8 (28·4–37·5)	15·8 (11·3–21·6)	2·9 (0·7–6·8)	0·7 (0·6–0·7)
Puerto Rico	5·20 (5·10–5·31)	2·60 (2·53–2·66)	0·90 (0·84–0·97)	0·84 (0·76–0·92)	0·81 (0·72–0·93)	84·9 (83·2–86·8)	71·7 (69·8–73·7)	19·0 (17·7–20·5)	6·7 (5·0–8·5)	1·4 (0·8–2·0)	0·4 (0·4–0·5)
Saint Kitts and Nevis	3·90 (3·73–4·06)	3·32 (3·14–3·52)	1·27 (1·13–1·42)	1·08 (0·79–1·27)	1·00 (0·81–1·20)	1·9 (1·8–1·9)	1·2 (1·1–1·3)	0·6 (0·5–0·6)	0·3 (0·2–0·4)	0·1 (0·0–0·1)	0·6 (0·5–0·7)
Saint Lucia	5·03 (4·80–5·26)	4·24 (4·10–4·38)	1·28 (1·08–1·51)	1·04 (0·79–1·32)	0·87 (0·58–1·19)	2·9 (2·8–3·1)	3·9 (3·8–4·0)	1·7 (1·4–2·0)	1·0 (0·7–1·4)	0·3 (0·1–0·7)	0·6 (0·5–0·7)
Saint Vincent and the Grenadines	4·83 (4·66–4·99)	3·89 (3·76–4·05)	1·60 (1·41–1·82)	1·35 (1·10–1·64)	1·16 (0·87–1·51)	3·0	3·2 (3·1–3·3)	1·3 (1·1–1·5)	0·8 (0·6–1·1)	0·3 (0·1–0·6)	0·8 (0·7–0·9)
Suriname	5·56 (5·33–5·78)	3·76 (3·65–3·88)	2·09 (1·87–2·33)	1·73 (1·41–2·05)	1·39 (1·02–1·78)	7·8 (7·5–8·1)	10·3 (10·0–10·7)	9·0 (8·1–10·0)	7·4 (5·4–9·8)	3·3 (1·1–6·7)	1·0 (0·9–1·1)
Trinidad and Tobago	4·60 (4·44–4·78)	3·29 (3·18–3·40)	1·52 (1·34–1·72)	1·35 (1·13–1·60)	1·19 (0·94–1·49)	23·7 (23·0–24·6)	31·0 (29·9–32·1)	14·7 (13·0–16·7)	6·6 (4·5–8·9)	0·5 (0·0–2·0)	0·7 (0·6–0·8)
Virgin Islands	4·85 (4·61–5·09)	2·91 (2·73–3·08)	1·68 (1·46–1·94)	1·49 (1·28–1·77)	1·37 (1·13–1·69)	0·9 (0·8–0·9)	2·5 (2·3–2·6)	0·8 (0·7–0·9)	0·5 (0·3–0·6)	0·2 (0·1–0·4)	0·8 (0·7–0·9)
Central Latin America	5·73 (5·49–5·99)	4·32 (4·22–4·42)	1·87 (1·68–2·08)	1·47 (1·23–1·74)	1·21 (0·93–1·53)	2327·7 (2229·7–2431·0)	4477·0 (4375·7–4578·5)	3877·3 (3483·8–4308·1)	2704·0 (2091·0–3465·5)	1064·5 (501·2–1993·8)	0·9 (0·8–1·0)
Colombia	5·67 (5·27–6·12)	3·62 (3·41–3·84)	1·67 (1·43–1·96)	1·35 (1·02–1·71)	1·14 (0·77–1·54)	499·9 (466·3–537·1)	823·8 (774·8–875·5)	675·0 (576·7–788·6)	444·7 (296·9–633·1)	176·8 (59·7–379·0)	0·8 (0·7–0·9)
Costa Rica	6·04 (5·87–6·22)	3·60 (3·52–3·70)	1·38 (1·26–1·51)	1·18 (1·02–1·36)	1·03 (0·84–1·26)	38·2 (37·1–39·4)	69·7 (68·0–71·6)	54·6 (49·8–59·7)	33·8 (26·6–42·3)	11·3 (6·2–18·4)	0·7 (0·6–0·7)
El Salvador	6·47 (6·31–6·64)	5·14 (5·02–5·26)	2·05 (1·80–2·32)	1·58 (1·23–1·93)	1·28 (0·86–1·72)	97·8 (95·4–100·5)	181·2 (177·2–185·3)	115·9 (101·7–130·8)	50·9 (30·9–74·0)	[obscured]	1·0 (0·9–1·1)
Guatemala	6·47 (6·38–6·56)	6·66 (6·56–6·77)	2·41 (2·16–2·68)	1·62 (1·26–1·98)	1·16 (0·73–1·61)	146·1 (144·2–148·2)	303·8 (288·8–308·6)	344·7 (309·1–383·9)	228·2 (158·2–314·1)	66·4 (12·7–166·4)	1·1 (1·0–1·3)
Honduras	6·84 (6·49–7·18)	6·38 (6·23–6·52)	2·40 (2·11–2·75)	1·71 (1·35–2·11)	1·27 (0·82–1·76)	[obscured] (151·3–164·0)	[obscured]	220·5 (195·1–252·5)	175·5 (119·4–238·7)	76·9 (23·0–174·0)	1·1 (1·0–1·3)
Mexico	5·66 (5·39–5·95)	4·29 (4·18–4·40)	1·77 (1·61–1·94)	1·39 (1·19–1·62)	1·15 (0·91–1·41)	1277	2772·7	1857·4 (1689·0–2038·3)	1343·9 (1065·2–1696·2)	564·3 (296·0–956·2)	0·9 (0·8–1·0)
Nicaragua	6·12 (5·82–6·43)	6·14 (6·00–6·28)	2·20 (1·93–2·49)	1·65 (1·30–2·01)	1·29 (0·86–1·73)	54·7 (52·0–57·4)	127·7 (122·0–130·3)	126·9 (111·4–143·2)	84·4 (56·0–123·5)	[obscured]	1·0 (0·9–1·1)

175

	Total fertility rate					Livebirths (thousands)					Net reproductive rate, 2021
	1950	1980	2021	2050	2100	1950	1980	2021	2050	2100	
(Continued from previous page)											
Panama	4.04 (3.90–4.20)	3.54 (3.43–3.65)	2.13 (1.91–2.37)	1.76 (1.49–2.05)	1.49 (1.20–1.81)	26.2 (25.3–27.2)	53.9 (52.2–55.5)	69.8 (62.7–77.3)	70.4 (53.4–93.0)	55.5 (31.9–93.2)	1.0 (0.9–1.1)
Venezuela	5.38 (5.22–5.54)	4.09 (3.99–4.20)	2.13 (1.84–2.43)	1.79 (1.43–2.19)	1.51 (1.10–1.97)	219.1 (212.3–225.6)	486.7 (472.9–501.5)	412.7 (355.6–471.4)	272.2 (186.9–399.4)	90.9 (40.0–255.5)	1.0 (0.9–1.1)
Tropical Latin America	5.95 (5.54–6.36)	3.83 (3.72–3.94)	1.94 (1.79–2.12)	1.57 (1.36–1.81)	1.32 (1.08–1.59)	2571.2 (2402.6–2735.9)	3881.0 (3774.3–3985.9)	3460.4 (3188.0–3775.6)	2528.0 (1966.2–3181.6)	1238.7 (691.6–2043.1)	0.9 (0.9–1.0)
Brazil	5.93 (5.51–6.36)	3.81 (3.70–3.92)	1.93 (1.78–2.12)	1.57 (1.35–1.81)	1.31 (1.06–1.59)	2504.7 (2335.7–2669.2)	3773.8 (3670.2–3875.7)	3332.2 (3059.7–3648.5)	2440.4 (1881.9–3096.7)	1207.6 (654.5–2015.8)	0.9 (0.9–1.0)
Paraguay	6.62 (6.35–6.90)	4.90 (4.50–5.29)	2.15 (1.83–2.50)	1.66 (1.25–2.11)	1.39 (0.93–1.89)	66.5 (63.7–69.6)	107.1 (98.7–115.7)	128.2 (109.5–148.5)	87.5 (53.2–131.0)	31.1 (3.6–88.8)	1.0 (0.9–1.2)
North Africa and Middle East	5.93 (5.56–6.31)	6.25 (6.14–6.37)	2.53 (2.33–2.76)	1.94 (1.62–2.28)	1.64 (1.28–2.06)	4777.2 (4479.4–5080.5)	10964.6 (10754.6–11168.9)	12137.4 (11185.8–13232.1)	11415.2 (8900.7–14116.1)	8157.0 (4021.1–14491.3)	1.2 (1.1–1.3)
Afghanistan	6.94 (6.60–7.27)	7.25 (7.04–7.46)	5.39 (5.10–5.72)	3.34 (2.78–3.89)	1.61 (0.90–2.32)	353.5 (336.6–370.1)	616.1 (597.7–632.9)	1211.5 (1147.5–1283.0)	1785.5 (1104.3–2491.9)	1349.7 (348.0–2742.3)	2.3 (2.2–2.4)
Algeria	6.55 (6.18–6.91)	6.82 (6.72–6.91)	2.64 (2.38–2.91)	1.79 (1.37–2.18)	1.48 (1.04–1.89)	415.5 (392.0–438.9)	793.9 (781.7–807.2)	907.7 (818.7–1000.0)	704.6 (502.0–930.0)	342.7 (128.4–657.3)	1.2 (1.1–1.4)
Bahrain	6.15 (5.75–6.56)	4.41 (4.31–4.52)	1.71 (1.52–1.91)	1.39 (1.10–1.68)	1.26 (0.92–1.57)	4.0 (3.7–4.3)	10.0 (9.8–10.3)	16.9 (15.0–18.8)	17.6 (13.1–22.1)	13.3 (6.9–21.5)	0.8 (0.7–0.9)
Egypt	3.54 (3.12–4.02)	5.91 (5.73–6.10)	3.16 (2.82–3.54)	2.38 (1.97–2.82)	2.05 (1.62–2.50)	557.4 (491.3–629.7)	1850.4 (1789.0–1913.1)	2611.0 (2335.5–2921.4)	2968.5 (2235.8–3819.0)	3117.2 (1456.3–5603.2)	1.5 (1.3–1.7)
Iran	6.21 (5.79–6.62)	7.41 (7.32–7.51)	1.52 (1.33–1.73)	1.31 (1.03–1.58)	1.28 (0.97–1.58)	772.2 (721.6–822.6)	1948.0 (1921.2–1973.2)	1027.8 (897.0–1168.0)	776.4 (560.5–1032.3)	456.1 (215.5–786.6)	0.7 (0.6–0.8)
Iraq	6.37 (5.98–6.76)	7.06 (6.83–7.26)	2.87 (2.63–3.16)	1.95 (1.63–2.35)	1.59 (1.25–2.01)	223.0 (209.4–236.5)	606.4 (587.4–624.5)	932.7 (853.6–1028.2)	873.0 (596.0–1223.7)	626.4 (284.1–1129.5)	1.3 (1.2–1.5)
Jordan	8.53 (8.41–8.64)	7.05 (6.96–7.14)	2.33 (2.06–2.62)	1.78 (1.44–2.10)	1.57 (1.20–1.93)	23.4 (23.0–23.7)	91.6 (90.1–93.1)	211.7 (187.4–238.2)	289.6 (219.8–367.5)	362.8 (205.1–553.3)	1.1 (1.0–1.2)
Kuwait	5.21 (4.77–5.67)	5.24 (5.11–5.37)	1.13 (0.98–1.30)	1.07 (0.89–1.30)	1.14 (0.93–1.39)	2.7 (2.5–2.9)	50.2 (48.9–51.6)	50.9 (44.1–59.0)	47.2 (37.1–60.8)	40.3 (26.2–60.8)	0.5 (0.5–0.6)
Lebanon	6.90 (6.55–7.24)	4.25 (3.95–4.55)	1.76 (1.49–2.09)	1.44 (1.12–1.80)	1.33 (0.98–1.73)	59.0 (56.0–61.9)	79.4 (74.3–84.5)	81.3 (69.4–96.1)	49.3 (34.2–68.0)	24.2 (8.6–49.8)	0.8 (0.7–1.0)
Libya	7.60 (7.39–7.81)	7.10 (6.92–7.25)	1.37 (1.14–1.63)	1.13 (0.87–1.43)	1.03 (0.75–1.37)	52.0 (50.6–53.3)	121.6 (118.8–124.4)	79.1 (66.1–94.5)	45.8 (31.7–66.0)	14.9 (4.8–34.7)	0.6 (0.5–0.8)
Morocco	7.18 (6.86–7.49)	5.71 (5.45–5.97)	2.26 (2.05–2.49)	1.36 (1.05–1.70)	1.02 (0.67–1.40)	463.2 (443.0–482.8)	806.7 (771.6–842.5)	646.6 (586.7–714.3)	373.2 (262.4–500.7)	90.9 (20.3–206.9)	1.1 (1.0–1.2)
Oman	7.48 (7.15–7.71)	7.57 (7.39–7.76)	2.48 (2.24–2.73)	1.64 (1.27–2.02)	1.29 (0.88–1.72)	23.9 (23.1–24.7)	59.1 (57.5–60.7)	81.7 (74.1–89.8)	76.9 (56.8–99.4)	53.4 (23.6–95.4)	1.2 (1.1–1.3)
Palestine	7.04 [illegible]	6.75 (6.50–6.98)	2.88 (2.64–3.16)	2.08 (1.79–2.44)	1.77 (1.43–2.15)	36.8 (35.7–38.0)	62.8 (60.4–65.1)	119.8 (109.5–132.2)	108.4 (82.3–139.7)	66.4 (26.4–129.3)	1.4 (1.3–1.5)
Qatar	6.84 (6.53–7.16)	5.35 (5.17–5.54)	1.95 (1.75–2.16)	1.43 (1.17–1.69)	1.29 (1.01–1.57)	1.2 (1.2–1.3)	[illegible]	38.0 (34.4–42.0)	59.8 (47.0–72.7)	58.2 (35.0–…)	0.8
Saudi Arabia	[illegible]	6.79 (6.48–7.09)	1.44 (1.24–1.68)	1.09 (0.80–1.39)	0.97 (0.65–1.31)	131.3 (124.7–137.8)	[illegible]	461.9 (396.5–535.4)	291.3 (195.0–395.8)	128.2 (48.7–242.9)	1.2
Sudan	[illegible]	6.72 (6.51–6.92)	3.38 (3.08–3.72)	1.93 (1.48–2.44)	1.40 (0.93–1.95)	238.8 (229.1–248.2)	[illegible]	1168.4 (1067.7–1281.7)	1011.1 (689.4–1360.9)	504.2 (148.5–1154.4)	1.5 (1.4–1.7)

(Table 1 continues on next page)

176

	Total fertility rate					Livebirths (thousands)					Net reproductive rate, 2021
	1950	1980	2021	2050	2100	1950	1980	2021	2050	2100	
(Continued from previous page)											
Syria	7·68 (7·47–7·88)	6·79 (6·60–6·98)	2·06 (1·76–2·42)	1·57 (1·21–1·98)	1·39 (1·01–1·84)	165·5 (160·5–170·3)	373·0 (360·4–385·6)	196·6 (165·8–234·5)	167·9 (110·2–241·9)	100·5 (38·4–217·1)	1·0 (0·8–1·1)
Tunisia	6·48 (6·15–6·82)	5·07 (4·90–5·23)	1·82 (1·59–2·09)	1·36 (1·02–1·73)	1·19 (0·82–1·59)	166·5 (157·7–175·1)	222·0 (214·0–230·2)	166·5 (145·6–191·5)	99·5 (68·0–136·0)	28·7 (6·9–67·4)	0·9 (0·7–1·0)
Türkiye	5·73 (5·31–6·16)	4·81 (4·61–5·01)	1·67 (1·52–1·85)	1·32 (1·13–1·56)	1·17 (0·95–1·42)	859·4 (797·8–921·8)	1611·4 (1541·0–1680·6)	1052·9 (955·7–1164·2)	634·5 (497·4–793·2)	218·5 (114·1–382·4)	0·8 (0·7–0·9)
United Arab Emirates	7·14 (6·83–7·46)	5·88 (5·69–6·07)	1·90 (1·68–2·14)	1·53 (1·26–1·81)	1·31 (1·00–1·64)	3·6 (3·4–3·7)	35·5 (34·6–36·5)	74·0 (64·1–84·7)	160·2 (122·7–198·1)	155·8 (88·6–234·7)	0·9 (0·8–1·0)
Yemen	7·36 (7·07–7·64)	7·91 (7·77–8·04)	3·87 (3·47–4·31)	1·91 (1·32–2·54)	1·22 (0·54–1·95)	224·0 (214·9–232·8)	513·9 (504·7–522·7)	989·2 (886·4–1105·7)	863·3 (536·7–1288·7)	396·3 (56·2–1154·2)	1·8 (1·6–1·9)
South Asia	6·35 (5·95–6·75)	4·96 (4·74–5·16)	2·07 (1·89–2·28)	1·36 (1·09–1·64)	1·10 (0·80–1·43)	20472·6 (19194·5–21717·6)	31555·9 (30245·2–32782·2)	32043·4 (29175·0–35206·1)	18743·1 (13775·0–24181·6)	5272·8 (1922·0–10462·8)	0·9 (0·9–1·0)
Bangladesh	7·30 (6·99–7·59)	6·03 (5·87–6·18)	1·90 (1·68–2·14)	1·20 (0·84–1·54)	0·97 (0·57–1·37)	2067·5 (1988·9–2140·7)	3641·1 (3563·4–3718·0)	2806·8 (2477·5–3152·8)	1370·6 (828·0–1977·2)	224·3 (6·5–644·2)	0·9 (0·8–1·0)
Bhutan	6·70 (6·35–7·04)	5·89 (5·59–6·18)	1·92 (1·74–2·09)	1·07 (0·73–1·34)	0·69 (0·33–1·00)	8·5 (8·1–8·9)	19·4 (18·5–20·2)	12·6 (11·5–13·8)	6·1 (3·9–8·2)	1·1 (0·2–2·3)	0·9 (0·8–1·0)
India	6·18 (5·75–6·59)	4·60 (4·35–4·83)	1·91 (1·69–2·13)	1·29 (0·97–1·62)	1·04 (0·67–1·42)	16366·5 (15255·4–17463·8)	23512·7 (22306·6–24656·5)	22393·2 (19926·1–25068·0)	13026·2 (8946·1–17555·0)	3792·9 (1086·0–7903·8)	0·9 (0·8–1·0)
Nepal	6·33 (6·03–6·60)	6·17 (5·93–6·41)	2·14 (1·92–2·38)	1·18 (0·80–1·53)	0·82 (0·40–1·22)	416·7 (397·7–436·2)	727·6 (702·1–752·3)	642·2 (576·4–711·9)	273·0 (160·3–402·5)	14·6 (0·0–69·7)	1·0 (0·9–1·1)
Pakistan	7·26 (6·95–7·56)	6·75 (6·54–6·96)	3·22 (2·87–3·62)	1·76 (1·25–2·28)	1·16 (0·59–1·77)	1613·4 (1542·5–1682·1)	3655·1 (3533·0–3773·2)	6188·5 (5530·6–6957·2)	4067·1 (2636·1–5810·4)	1239·9 (85·1–3558·0)	1·4 (1·3–1·6)
Southeast Asia, east Asia, and Oceania	5·76 (5·44–6·09)	2·99 (2·89–3·08)	1·55 (1·44–1·66)	1·37 (1·22–1·54)	1·30 (1·11–1·53)	31218·7 (29613·6–32875·9)	31743·5 (30751·9–32760·5)	22805·8 (21221·6–24442·9)	15544·8 (13337·3–18257·3)	6819·6 (4409·9–10247·2)	0·7 (0·7–0·8)
East Asia	5·57 (5·25–5·90)	2·46 (2·35–2·56)	1·23 (1·12–1·34)	1·14 (0·99–1·30)	1·16 (0·99–1·34)	22400·1 (21213·3–23644·8)	18856·4 (18088·5–19630·1)	11202·9 (10243·8–12246·4)	6621·8 (5397·9–8088·3)	2201·4 (1341·4–3394·0)	0·6 (0·5–0·6)
China	5·55 (5·24–5·89)	2·44 (2·33–2·55)	1·23 (1·12–1·34)	1·14 (0·99–1·31)	1·16 (0·99–1·35)	21609·2 (20451·1–22827·1)	18000·3 (17240·4–18768·2)	10747·2 (9807·6–11774·1)	6360·0 (5139·5–7778·2)	2105·2 (1273·0–3268·7)	0·6 (0·5–0·6)
North Korea	5·41 (5·06–5·77)	3·25 (2·96–3·59)	1·51 (1·32–1·71)	1·24 (1·00–1·48)	1·16 (0·90–1·42)	424·7 (399·0–451·2)	450·7 (408·9–500·1)	299·0 (263·4–339·7)	172·2 (119·0–227·4)	63·4 (27·8–111·8)	0·7 (0·6–0·8)
Taiwan (province of China)	6·82 (6·66–6·98)	2·42 (2·34–2·51)	0·98 (0·87–1·09)	0·90 (0·78–1·04)	0·90 (0·77–1·05)	366·2 (357·7–375·6)	405·5 (391·4–420·2)	156·8 (139·6–175·5)	89·6 (73·8–107·7)	32·8 (22·0–46·8)	0·5 (0·4–0·5)
Oceania	5·36 (5·18–5·53)	4·24 (4·08–4·40)	4·02 (3·68–4·41)	2·93 (2·45–3·46)	1·67 (1·01–2·35)	121·4 (116·7–126·1)	193·5 (186·9–199·5)	430·7 (393·9–472·2)	590·1 (457·1–736·3)	566·7 (224·7–1096·8)	1·8 (1·6–1·9)
American Samoa	5·79 (5·71–5·90)	...	...	...	...	...	...	0·8 (...)	0·6 (0·6–1·0)	0·6 (0·3–1·0)	1·1 (1·0–1·3)
Cook Islands	7·69 (5·49–...)	...	...	...	...	...	...	0·6 (...)	0·2 (0·1–0·2)	0·1 (0·0–0·1)	0·8 (0·7–0·9)
Federated States of Micronesia	5·87 (5·58–6·14)	3·66 (3·48–3·84)	2·37 (2·04–2·78)	1·82 (1·39–2·33)	1·46 (0·96–2·05)	...	18·8 (18·0–19·6)	1·9 (1·6–2·2)	1·4 (0·8–2·0)	0·8 (0·2–1·9)	1·1 (1·0–1·3)
Fiji	3·34 (3·21–3·46)	...	2·42 (2·15–2·73)	1·95 (1·61–2·31)	1·64 (1·28–2·04)	18·8 (18·0–19·6)	16·7 (14·8–18·8)	12·6 (9·3–17·0)	8·7 (4·2–15·8)		1·1 (1·0–1·3)

	Total fertility rate					Livebirths (thousands)					Net reproductive rate, 2021
	1950	1980	2021	2050	2100	1950	1980	2021	2050	2100	
(Continued from previous page)											
Guam	5·38 (5·12–5·68)	3·06 (2·94–3·17)	2·59 (2·30–2·86)	2·07 (1·76–2·38)	1·76 (1·42–2·09)	1·8 (1·7–1·8)	2·9 (2·8–3·1)	2·7 (2·4–3·0)	1·9 (1·4–2·4)	1·4 (0·7–2·4)	1·2 (1·1–1·3)
Kiribati	6·40 (6·25–6·54)	4·81 (4·50–5·12)	2·95 (2·63–3·32)	2·13 (1·70–2·62)	1·67 (1·19–2·21)	1·3 (1·3–1·3)	2·3 (2·1–2·4)	2·9 (2·6–3·3)	2·3 (1·7–3·1)	1·0 (0·2–2·3)	1·3 (1·2–1·5)
Marshall Islands	7·08 (6·77–7·38)	5·25 (5·02–5·50)	2·56 (2·31–2·84)	1·98 (1·67–2·32)	1·65 (1·31–2·02)	0·6 (0·6–0·6)	1·3 (1·3–1·4)	1·2 (1·0–1·3)	1·1 (0·8–1·4)	0·7 (0·4–1·3)	1·2 (1·1–1·3)
Nauru	6·62 (6·45–6·80)	4·95 (4·54–5·35)	3·24 (2·86–3·67)	2·40 (1·93–2·95)	1·91 (1·39–2·51)	0·1 (0·1–0·1)	0·3 (0·3–0·4)	0·3 (0·3–0·3)	0·3 (0·2–0·4)	0·3 (0·1–0·6)	1·5 (1·3–1·6)
Niue	6·36 (6·07–6·69)	4·10 (3·87–4·32)	2·09 (1·84–2·38)	1·71 (1·37–2·08)	1·50 (1·13–1·90)	0·2 (0·2–0·2)	0·1 (0·1–0·1)	0·0 (0·0–0·0)	0·0 (0·0–0·0)	0·0 (0·0–0·0)	0·9 (0·8–1·0)
Northern Mariana Islands	6·06 (5·66–6·46)	2·90 (2·58–3·28)	1·93 (1·68–2·21)	1·67 (1·36–2·01)	1·50 (1·17–1·88)	0·2 (0·2–0·2)	0·4 (0·3–0·4)	0·6 (0·5–0·7)	0·5 (0·4–0·7)	0·3 (0·2–0·6)	0·9 (0·8–1·0)
Palau	5·86 (5·44–6·27)	2·75 (2·44–3·09)	1·93 (1·72–2·15)	1·65 (1·37–1·92)	1·44 (1·14–1·74)	0·3 (0·3–0·3)	0·2 (0·2–0·3)	0·2 (0·2–0·2)	0·1 (0·1–0·2)	0·1 (0·0–0·1)	0·9 (0·8–1·0)
Papua New Guinea	6·73 (6·39–7·06)	5·81 (5·59–6·02)	4·26 (3·86–4·61)	3·03 (2·50–3·58)	1·64 (0·94–2·35)	81·5 (77·4–85·4)	125·1 (120·4–129·4)	345·1 (312·9–381·6)	500·2 (374·6–636·3)	491·1 (180·0–958·2)	1·9 (1·7–2·0)
Samoa	7·45 (7·24–7·64)	5·99 (5·70–6·26)	4·25 (3·91–4·61)	3·18 (2·69–3·68)	2·57 (1·98–3·14)	4·5 (4·4–4·6)	5·8 (5·5–6·0)	6·2 (5·7–6·8)	7·8 (6·1–9·6)	11·5 (5·6–19·0)	2·0 (1·8–2·1)
Solomon Islands	7·10 (6·89–7·30)	6·51 (6·25–6·76)	3·90 (3·61–4·20)	2·51 (2·10–2·90)	1·70 (1·21–2·21)	4·8 (4·7–4·9)	9·9 (9·5–10·2)	20·5 (19·0–22·1)	19·7 (14·8–25·6)	10·5 (3·6–21·0)	1·8 (1·7–1·9)
Tokelau	6·71 (6·46–6·97)	4·18 (3·87–4·49)	1·89 (1·61–2·20)	1·54 (1·17–1·94)	1·34 (0·94–1·78)	0·1 (0·1–0·1)	0·0 (0·0–0·0)	0·0 (0·0–0·0)	0·0 (0·0–0·0)	0·0 (0·0–0·0)	0·8 (0·7–0·9)
Tonga	6·66 (6·47–6·86)	5·88 (5·73–6·03)	4·08 (3·75–4·42)	3·04 (2·58–3·50)	2·45 (1·93–2·98)	2·2 (2·1–2·3)	3·6 (3·5–3·7)	3·0 (2·7–3·2)	3·2 (2·5–4·1)	4·3 (2·3–7·1)	1·9 (1·7–2·0)
Tuvalu	6·69 (6·37–7·01)	5·98 (5·67–6·28)	3·08 (2·74–3·45)	2·20 (1·71–2·70)	1·71 (1·17–2·26)	0·2 (0·2–0·2)	0·4 (0·4–0·4)	0·3 (0·2–0·3)	0·3 (0·2–0·4)	0·2 (0·1–0·4)	1·4 (1·3–1·6)
Vanuatu	7·08 (6·77–7·38)	6·10 (5·88–6·31)	3·52 (3·23–3·84)	2·44 (2·06–2·87)	1·79 (1·33–2·31)	2·1 (2·0–2·2)	5·1 (4·9–5·3)	8·7 (8·0–9·5)	9·8 (7·7–12·5)	8·2 (3·8–15·6)	1·6 (1·5–1·8)
Southeast Asia	6·40 (6·08–6·72)	4·31 (4·20–4·43)	2·05 (1·89–2·23)	1·60 (1·40–1·83)	1·35 (1·14–1·60)	8697·2 (8276·7–9096·0)	12693·6 (12352·2–13033·5)	11172·2 (10297·5–12144·2)	8332·9 (7018·9–10074·5)	4051·6 (2523·7–6469·1)	1·0 (0·9–1·0)
Cambodia	6·60 (6·26–6·93)	5·89 (5·64–6·13)	2·61 (2·39–2·82)	1·65 (1·32–1·93)	1·10 (0·71–1·45)	211·5 (200·4–222·5)	351·8 (337·4–366·1)	372·7 (341·8–403·6)	267·3 (193·9–342·9)	102·9 (35·5–192·8)	1·2 (1·1–1·3)
Indonesia	6·07 (5·71–6·42)	4·28 (4·15–4·41)	1·97 (1·77–2·22)	1·53 (1·25–1·84)	1·29 (0·99–1·63)	3626·7 (3445·3–3804·0)	5175·0 (4954·3–5342·6)	4393·8 (3937·5–4935·6)	3147·3 (2402·1–4049·5)	1453·3 (684·5–2718·1)	0·9 (0·8–1·0)
Laos	6·65 (6·27–7·03)	6·22 (5·88–6·56)	2·76 (2·54–2·98)	1·61 (1·29–1·88)	1·09 (0·73–1·40)	—	—	177·4 (162·5–192·1)	116·7 (88·2–149·0)	32·4 (10·7–63·5)	1·3 (1·0–1·4)
Malaysia	6·89 (6·56–7·22)	3·98 (3·88–4·08)	1·81 (1·62–2·05)	1·39 (1·11–1·70)	1·17 (0·86–1·52)	281·5	—	474·2 (424·4–534·7)	364·6 (271·6–471·1)	203·4 (106·1–366·8)	0·8
Maldives	4·97 (4·69–5·25)	6·46 (6·35–6·57)	1·64 (1·47–1·84)	1·07 (0·79–1·34)	0·77 (0·42–1·11)	(2·5–2·9)	—	6·0 (5·4–6·7)	5·4 (3·9–7·0)	0·8 (0·1–1·9)	0·8

	Total fertility rate					Livebirths (thousands)					Net reproductive rate, 2021
	1950	1980	2021	2050	2100	1950	1980	2021	2050	2100	
(Continued from previous page)											
Mauritius	6·31 (6·17–6·45)	2·61 (2·52–2·71)	1·39 (1·23–1·57)	1·17 (0·94–1·42)	1·03 (0·77–1·32)	23·3 (22·7–23·8)	23·4 (22·6–24·2)	12·7 (11·3–14·3)	6·7 (5·0–9·1)	1·8 (0·6–3·8)	0·7 (0·6–0·8)
Myanmar	6·45 (6·08–6·82)	5·44 (5·18–5·67)	2·40 (2·20–2·62)	1·69 (1·42–1·97)	1·22 (0·89–1·57)	869·3 (819·0–919·4)	1328·9 (1263·1–1389·9)	1073·6 (983·0–1169·8)	754·4 (596·8–943·5)	148·2 (96·8–474·8)	1·1 (1·0–1·2)
Philippines	6·75 (6·43–7·05)	4·77 (4·57–4·98)	2·40 (2·21–2·60)	1·84 (1·61–2·11)	1·50 (1·23–1·79)	937·1 (891·5–982·6)	1767·1 (1681·8–1852·7)	2185·7 (2000·9–2368·9)	1967·3 (1575·7–2425·6)	1254·1 (747·7–2010·5)	1·1 (1·0–1·2)
Seychelles	4·00 (3·75–4·27)	3·55 (3·44–3·68)	2·31 (2·10–2·53)	1·86 (1·60–2·14)	1·60 (1·31–1·91)	1·0 (1·0–1·1)	1·7 (1·6–1·8)	1·6 (1·4–1·7)	1·7 (1·4–2·2)	1·6 (1·0–2·4)	1·1 (1·0–1·2)
Sri Lanka	5·19 (4·94–5·46)	3·39 (3·24–3·53)	1·85 (1·64–2·08)	1·50 (1·24–1·81)	1·30 (0·99–1·66)	306·2 (290·5–323·7)	421·2 (402·2–441·1)	298·6 (265·2–335·8)	179·5 (124·6–245·5)	45·9 (5·8–121·4)	0·9 (0·8–1·0)
Thailand	6·89 (6·58–7·19)	3·15 (3·02–3·27)	1·32 (1·20–1·46)	1·13 (0·96–1·31)	1·04 (0·86–1·24)	1003·1 (956·0–1048·8)	1181·9 (1131·0–1233·1)	573·1 (520·0–635·5)	300·0 (225·5–379·9)	87·3 (44·3–144·5)	0·6 (0·6–0·7)
Timor-Leste	7·00 (6·76–7·26)	6·72 (6·54–6·90)	3·85 (3·43–4·29)	2·27 (1·62–2·90)	1·58 (0·85–2·30)	22·5 (21·6–23·4)	28·8 (27·9–29·6)	41·0 (36·7–45·6)	35·7 (22·7–51·3)	17·5 (4·4–48·6)	1·8 (1·6–1·9)
Viet Nam	6·72 (6·40–7·04)	4·40 (4·25–4·55)	2·06 (1·88–2·28)	1·63 (1·38–1·93)	1·38 (1·10–1·70)	1293·3 (1232·9–1353·8)	1819·8 (1761·6–1875·2)	1546·1 (1416·2–1708·8)	1175·5 (928·2–1496·6)	595·3 (314·7–1084·8)	1·0 (0·9–1·1)
Sub-Saharan Africa	6·94 (6·62–7·25)	6·78 (6·60–6·94)	4·29 (4·03–4·58)	2·72 (2·32–3·15)	1·82 (1·35–2·32)	8850·5 (8455·5–9233·0)	17852·0 (17412·0–18264·8)	37713·3 (35513·3–40151·9)	46344·7 (37509·8–55394·7)	39828·0 (19422·1–69747·3)	1·9 (1·8–2·0)
Central sub-Saharan Africa	7·19 (6·93–7·42)	7·07 (6·84–7·28)	4·44 (4·15–4·72)	2·52 (2·05–2·94)	1·86 (1·37–2·31)	1010·4 (975·5–1042·7)	2065·0 (1997·0–2125·8)	4459·3 (4183·3–4730·0)	5233·7 (3753·5–6919·5)	4873·6 (2153·5–8575·8)	2·0 (1·9–2·1)
Angola	6·94 (6·61–7·26)	7·29 (7·06–7·52)	5·02 (4·66–5·38)	2·76 (2·21–3·35)	1·97 (1·37–2·62)	241·6 (230·2–252·6)	374·6 (361·9–386·9)	1202·7 (1115·3–1294·1)	1594·1 (1152·6–2079·7)	1735·5 (690·4–3385·4)	2·2 (2·1–2·4)
Central African Republic	5·79 (5·46–6·12)	6·47 (6·18–6·74)	4·36 (4·00–4·74)	2·36 (1·86–2·88)	1·35 (0·77–2·03)	59·7 (56·4–62·7)	110·6 (105·9–115·3)	191·1 (176·5–205·8)	142·5 (93·6–203·7)	29·6 (0·0–98·2)	1·8 (1·7–1·9)
Congo (Brazzaville)	6·65 (6·25–7·03)	6·16 (5·88–6·42)	2·95 (2·69–3·23)	1·90 (1·54–2·32)	1·49 (1·11–1·93)	40·8 (38·4–43·1)	76·4 (73·1–79·5)	128·6 (117·3–141·1)	118·9 (86·6–159·7)	78·2 (34·3–146·1)	1·3 (1·2–1·5)
Democratic Republic of the Congo	7·56 (7·27–7·83)	7·16 (6·90–7·40)	4·40 (4·02–4·77)	2·46 (1·82–3·03)	1·76 (1·09–2·38)	639·8 (615·5–662·2)	1459·4 (1404·9–1507·8)	2856·0 (2620·9–3089·5)	3277·7 (1995·4–4613·9)	2910·6 (858·8–5975·8)	2·0 (1·8–2·1)
Equatorial Guinea	7·18 (6·84–7·50)	6·83 (6·50–7·15)	3·09 (2·69–3·57)	2·19 (1·70–2·75)	1·83 (1·29–2·43)	9·6 (9·1–10·0)	14·4 (13·7–15·0)	37·4 (32·6–42·9)	55·9 (39·6–75·8)	82·7 (37·9–154·9)	1·4 (1·2–1·5)
Gabon	6·51 (6·10–6·91)	5·74 (5·37–6·10)	2·84 (2·46–3·30)	1·93 (1·41–2·52)	1·56 (1·02–2·19)	18·9 (17·7–20·0)	29·6 (27·7–31·4)	43·5 (37·7–50·3)	44·7 (29·8–63·8)	36·9 (12·5–80·6)	1·3 (1·1–1·5)
Eastern sub-Saharan Africa	7·15 (6·86–7·45)	7·02 (6·84–7·17)	4·09 (3·80–4·39)	2·50 (2·04–2·96)	1·68 (1·17–2·22)	3378·3 (3239·4–3512·6)	7091·2 (6932·8–7242·3)	13778·4 (12785·2–14858·1)	15968·4 (12317·1–19784·1)	12206·9 (4940·5–23355·8)	1·8 (1·7–1·9)
Burundi	7·14 (6·84–7·43)	6·86 (6·72–6·99)	4·93 (4·55–5·35)	2·74 (2·16–3·31)	1·55 (0·83–2·25)	124·8 (119·4–130·0)	213·9 (209·1–218·4)	468·8 (431·5–510·0)	552·4 (389·3–773·9)	381·8 (97·3–874·8)	2·2 (2·1–2·3)
Comoros	5·53 (5·12–5·90)	7·20 (6·95–7·44)	2·93 (2·55–3·35)	1·73 (1·17–2·33)	1·23 (0·60–1·92)	6·4 (6·0–6·9)	9·5 (9·0–10·0)	17·3 (15·1–19·8)	11·5 (6·5–17·6)	3·5 (0·0–11·1)	1·3 (1·2–1·5)
Djibouti	5·75 (5·35–6·19)	5·18 (4·92–5·44)	2·52 (2·22–2·85)	1·41 (0·92–1·88)	0·95 (0·38–1·51)			25·2 (22·2–28·4)	22·5 (13·9–31·8)	12·8 (2·9–28·1)	1·1 (1·0–1·3)
Eritrea	6·88 (6·52–7·22)	6·64 (6·35–6·90)	3·85 (3·41–4·34)	2·20 (1·52–2·86)	1·28 (0·49–2·09)		118·9 (137·3–237·7)	195·7 (173·8–220·4)	163·7 (88·6–262·8)	66·9 (2·5–221·8)	1·7

(Table 1 continues on next page)

(Continued from previous page)

	Total fertility rate					Livebirths (thousands)					Net reproductive rate, 2021
	1950	1980	2021	2050	2100	1950	1980	2021	2050	2100	
Ethiopia	6·73 (6·35–7·08)	6·93 (6·67–7·17)	4·10 (3·79–4·43)	2·40 (1·86–2·89)	1·29 (0·64–1·87)	868·1 (819·0–914·9)	1786·6 (1715·1–1853·9)	3498·1 (3239·1–3788·0)	3957·1 (2829·4–5150·9)	2375·2 (637·3–4829·0)	1·8 (1·7–2·0)
Kenya	7·64 (7·41–7·86)	7·03 (6·84–7·21)	2·75 (2·43–3·13)	1·84 (1·39–2·35)	1·45 (0·96–2·01)	310·2 (307·7–317·4)	811·8 (792·0–830·5)	1186·7 (1053·2–1340·0)	1050·1 (715·7–1486·9)	551·7 (134·8–1299·0)	1·3 (1·1–1·4)
Madagascar	7·44 (7·12–7·73)	6·72 (6·54–6·89)	3·77 (3·48–4·07)	2·33 (1·91–2·78)	1·70 (1·23–2·22)	230·8 (221·6–239·4)	427·6 (416·9–438·2)	877·1 (815·6–945·5)	958·9 (730·1–1221·2)	735·6 (307·9–1385·5)	1·7 (1·6–1·8)
Malawi	6·17 (5·76–6·57)	7·62 (7·42–7·80)	3·46 (3·07–3·87)	2·03 (1·46–2·57)	1·55 (0·94–2·14)	130·2 (121·2–138·9)	348·4 (339·0–356·9)	574·2 (515·5–639·8)	570·3 (363·3–776·9)	417·2 (95·9–891·8)	1·5 (1·4–1·7)
Mozambique	6·95 (6·69–7·19)	6·67 (6·49–6·85)	4·50 (4·15–4·88)	2·44 (1·91–2·93)	1·55 (0·95–2·14)	337·7 (324·7–348·9)	596·5 (581·4–612·7)	1104·9 (1015·0–1202·2)	1221·8 (875·5–1614·2)	790·1 (242·4–1762·7)	1·9 (1·8–2·1)
Rwanda	7·39 (7·15–7·61)	7·45 (7·35–7·55)	3·55 (3·28–3·84)	1·97 (1·54–2·42)	1·24 (0·76–1·77)	137·3 (132·6–141·8)	267·5 (263·5–271·5)	373·6 (345·4–404·5)	405·7 (303·0–518·7)	298·1 (121·9–552·8)	1·6 (1·5–1·7)
Somalia	7·77 (7·51–8·01)	7·68 (7·50–7·84)	6·54 (6·27–6·81)	4·30 (3·92–4·68)	2·45 (1·92–3·00)	109·7 (105·8–113·3)	334·0 (326·2–341·2)	960·1 (919·1–1004·4)	1464·1 (1008·1–2005·2)	1425·7 (492·7–2833·8)	2·7 (2·6–2·8)
South Sudan	6·13 (5·69–6·56)	6·12 (5·79–6·45)	5·45 (5·04–5·87)	4·09 (3·59–4·64)	1·98 (1·22–2·75)	111·3 (103·6–118·7)	208·7 (196·9–219·7)	384·1 (353·8–414·9)	690·1 (519·9–872·8)	791·2 (304·1–1536·2)	2·2 (2·1–2·3)
Tanzania	7·60 (7·30–7·86)	6·94 (6·71–7·14)	4·04 (3·74–4·37)	2·42 (2·02–2·86)	1·70 (1·23–2·20)	481·7 (463·9–498·1)	943·5 (913·1–972·0)	1902·1 (1762·2–2057·9)	2091·0 (1582·8–2666·8)	1577·3 (661·3–2941·2)	1·8 (1·7–1·9)
Uganda	7·86 (7·60–8·09)	7·53 (7·36–7·69)	4·76 (4·47–5·07)	2·72 (2·26–3·19)	1·98 (1·48–2·50)	339·2 (329·0–348·4)	703·0 (688·9–716·8)	1591·6 (1490·7–1704·3)	2049·6 (1533·6–2610·7)	2014·5 (858·0–3620·6)	2·1 (2·0–2·2)
Zambia	7·58 (7·29–7·86)	7·22 (7·01–7·41)	3·84 (3·52–4·21)	2·39 (1·88–2·91)	1·83 (1·28–2·40)	132·3 (127·4–136·7)	300·2 (292·5–307·8)	606·9 (557·2–668·9)	747·0 (534·7–1007·7)	755·7 (306·5–1475·5)	1·7 (1·6–1·9)
Southern sub-Saharan Africa	6·20 (5·77–6·63)	4·86 (4·69–5·05)	2·42 (2·25–2·61)	1·94 (1·67–2·21)	1·63 (1·29–1·99)	792·2 (739·1–844·6)	1517·8 (1465·6–1572·1)	1626·8 (1518·7–1764·9)	1416·1 (1138·4–1739·9)	876·3 (453·7–1528·0)	1·1 (1·0–1·2)
Botswana	7·01 (6·65–7·35)	6·06 (5·78–6·33)	2·31 (2·05–2·61)	1·70 (1·31–2·12)	1·38 (0·94–1·84)	19·4 (18·4–20·4)	40·8 (38·8–42·7)	48·7 (43·1–55·2)	37·7 (26·2–50·8)	21·1 (7·3–43·8)	1·0 (0·9–1·2)
Eswatini	7·19 (6·84–7·52)	6·17 (5·96–6·38)	2·89 (2·65–3·15)	1·98 (1·62–2·36)	1·53 (1·13–1·95)	12·5 (12·0–13·1)	27·7 (26·8–28·5)	29·4 (27·0–32·1)	21·3 (15·1–28·1)	6·7 (0·7–16·1)	1·3 (1·2–1·3)
Lesotho	6·54 (6·14–6·93)	5·66 (5·46–5·84)	2·61 (2·31–2·93)	1·88 (1·50–2·34)	1·47 (1·03–1·98)	29·9 (28·1–31·7)	55·8 (54·2–57·4)	42·5 (37·8–48·1)	34·6 (23·5–48·4)	16·1 (4·1–39·0)	1·1 (1·0–1·2)
Namibia	7·16 (6·81–7·49)	5·63 (5·42–5·84)	2·80 (2·58–3·08)	2·03 (1·70–2·40)	1·62 (1·24–2·03)	22·1 (21·0–23·1)	40·6 (39·2–41·9)	58·0 (53·3–63·7)	54·7 (40·5–71·4)	39·4 (18·8–69·9)	1·3 (1·2–1·4)
South Africa	5·91 (5·46–6·37)	4·35 (4·16–4·56)	2·07 (1·92–2·23)	1·69 (1·46–1·89)	1·45 (1·20–1·67)	577·2 (529·6–614·5)	1007·6 (963·8–1054·9)	988·1 (913·4–1065·5)	785·7 (619·2–968·1)	470·7 (286·1–706·9)	0·9 (0·9–1·0)
Zimbabwe	7·24 (6·90–7·56)	6·63 (6·50–6·75)	3·60 (3·34–3·89)	2·56 (2·12–3·01)	2·01 (1·52–2·51)	136·0 (129·...–...)	345·3 (337·9–351·1)	470·0 (437·0–506·3)	482·1 (360·8–626·6)	323·3 (197·3–699·7)	1·6 (1·5–1·7)
Western sub-Saharan Africa	6·87 (6·54–7·17)	7·03 (6·83–7·22)	4·79 (4·51–5·09)	3·03 (2·60–3·48)	1·89 (1·39–2·44)	...	...	17838·8 (16834·6–18900·1)	23726·4 (19422·7–28303·1)	21817·2 (10771·0–37177·5)	2·1 (2·0–2·2)
Benin	6·52 (6·12–6·92)	7·00 (6·79–7·19)	5·17 (4·86–5·50)	3·12 (2·65–3·60)	1·58 (0·95–2·18)	...	...	522·3 (488·8–559·3)	724·6 (552·9–910·7)	568·0 (197·5–1084·8)	2·1 (2·0–2·2)
Burkina Faso	6·30 (5·93–6·65)	7·32 (7·17–7·46)	5·52 (5·18–5·86)	3·76 (3·23–4·28)	1·62 (0·89–2·26)	...	879·6 (...–175·6)	950·8 (893·1–1010·0)	1519·4 (1216·6–1833·9)	1197·... (384·0–2996·...)	2·3 (2·0–2·2)

(Table 1 continues...)

	Total fertility rate					Livebirths (thousands)					Net reproductive rate, 2021
	1950	1980	2021	2050	2100	1950	1980	2021	2050	2100	
(Continued from previous page)											
Cabo Verde	5·08 (4·78–5·37)	5·14 (4·99–5·28)	1·78 (1·53–2·04)	1·09 (0·73–1·48)	0·91 (0·51–1·34)	7·0 (6·5–7·4)	10·9 (10·5–11·3)	8·5 (7·4–9·7)	4·3 (2·5–6·6)	1·0 (0·1–2·7)	0·8 (0·7–1·0)
Cameroon	6·40 (5·98–6·80)	6·73 (6·56–6·89)	4·13 (3·76–4·54)	2·44 (1·92–3·03)	1·71 (1·13–2·36)	216·3 (202·6–229·5)	394·4 (385·4–402·9)	1032·5 (940·4–1137·6)	1138·8 (768·0–1579·8)	811·5 (241·3–1828·0)	1·8 (1·7–2·0)
Chad	7·36 (7·03–7·66)	7·60 (7·39–7·80)	6·99 (6·75–7·24)	4·81 (4·45–5·18)	2·15 (1·65–2·71)	127·4 (121·9–132·5)	242·8 (236·2–248·8)	860·2 (829·3–892·5)	1841·1 (1531·6–2177·8)	2491·7 (1487·4–3800·2)	2·9 (2·8–3·0)
Côte d'Ivoire	6·89 (6·52–7·25)	6·95 (6·77–7·11)	4·54 (4·23–4·90)	2·57 (2·11–3·04)	1·44 (0·87–1·99)	127·5 (120·7–133·9)	405·3 (395·4–414·8)	950·1 (879·5–1027·5)	1000·2 (744·1–1262·9)	521·1 (150·7–1089·8)	2·0 (1·9–2·1)
The Gambia	5·90 (5·45–6·35)	6·57 (6·39–6·76)	4·12 (3·89–4·38)	2·21 (1·81–2·61)	1·37 (0·92–1·87)	10·7 (10·0–11·4)	34·0 (33·2–34·9)	77·9 (73·1–83·1)	67·4 (50·8–86·7)	29·8 (9·4–59·0)	1·9 (1·8–1·9)
Ghana	5·37 (4·92–5·84)	6·71 (6·49–6·90)	3·40 (3·01–3·81)	2·12 (1·57–2·71)	1·57 (0·97–2·20)	204·3 (187·1–223·2)	551·2 (532·4–567·7)	966·8 (855·2–1082·9)	922·4 (602·0–1318·0)	636·0 (168·0–1417·0)	1·5 (1·4–1·7)
Guinea	7·05 (6·76–7·34)	6·81 (6·59–7·01)	4·67 (4·33–5·00)	3·02 (2·58–3·43)	1·42 (0·81–2·00)	127·4 (122·3–132·2)	245·1 (238·0–251·7)	495·4 (462·6–528·8)	633·0 (506·6–787·0)	366·2 (114·2–728·3)	2·0 (1·9–2·1)
Guinea-Bissau	7·11 (6·82–7·38)	6·13 (5·86–6·41)	4·42 (4·08–4·78)	2·41 (1·88–2·91)	1·26 (0·63–1·86)	31·2 (29·9–32·4)	37·4 (35·6–39·0)	72·0 (66·1–78·3)	75·6 (52·9–99·7)	35·5 (8·0–81·5)	1·9 (1·8–2·1)
Liberia	6·78 (6·40–7·15)	6·93 (6·74–7·12)	3·81 (3·39–4·26)	2·10 (1·52–2·71)	1·47 (0·85–2·14)	44·2 (41·8–46·6)	100·9 (98·2–103·2)	163·5 (145·6–183·0)	157·0 (100·9–229·0)	101·5 (22·7–247·4)	1·7 (1·5–1·8)
Mali	7·33 (7·00–7·64)	7·51 (7·29–7·71)	6·15 (5·85–6·46)	4·21 (3·83–4·63)	1·85 (1·30–2·42)	182·8 (174·7–190·4)	389·4 (379·0–398·7)	1064·4 (1007·3–1123·0)	1863·5 (1522·4–2237·3)	1675·3 (779·9–2834·3)	2·6 (2·5–2·7)
Mauritania	6·68 (6·29–7·06)	6·70 (6·53–6·88)	4·22 (3·86–4·64)	2·50 (1·98–3·08)	1·66 (1·04–2·34)	33·5 (31·5–35·4)	71·1 (69·1–72·9)	135·3 (122·6–149·5)	153·2 (109·3–206·1)	113·3 (32·7–258·4)	1·9 (1·8–2·1)
Niger	7·64 (7·36–7·89)	7·98 (7·82–8·12)	6·97 (6·71–7·24)	5·15 (4·68–5·64)	2·24 (1·48–2·92)	144·4 (139·4–149·1)	349·4 (342·8–355·8)	1174·8 (1126·7–1224·8)	2766·0 (2211·9–3290·7)	3891·3 (1737·1–6484·1)	3·0 (2·9–3·1)
Nigeria	7·08 (6·72–7·42)	6·99 (6·71–7·24)	4·75 (4·35–5·14)	2·69 (2·06–3·31)	1·87 (1·19–2·54)	1826·3 (1735·3–1911·0)	3200·3 (3085·6–3310·7)	8333·3 (7671·1–8973·3)	9845·1 (6861·8–13037·8)	8949·4 (2670·4–18113·0)	2·0 (1·9–2·2)
São Tomé and Príncipe	6·22 (6·01–6·47)	6·24 (6·03–6·44)	2·84 (2·51–3·19)	1·77 (1·29–2·28)	1·37 (0·83–1·94)	2·4 (2·3–2·5)	3·7 (3·6–3·9)	4·9 (4·3–5·6)	3·1 (1·9–4·6)	0·3 (0·0–1·9)	1·3 (1·2–1·5)
Senegal	7·17 (6·82–7·49)	7·39 (7·27–7·51)	4·02 (3·72–4·34)	2·32 (1·79–2·79)	1·25 (0·60–1·83)	135·9 (129·3–142·0)	303·8 (298·8–308·7)	479·3 (441·8–520·9)	489·6 (354·1–621·1)	233·5 (50·6–499·9)	1·8 (1·7–2·0)
Sierra Leone	6·60 (6·19–7·00)	6·55 (6·27–6·81)	4·20 (3·86–4·56)	2·43 (1·99–2·85)	1·31 (0·78–1·82)	91·7 (86·2–97·0)	159·2 (152·3–164·8)	302·8 (278·5–327·5)	303·3 (228·2–373·7)	144·7 (42·3–292·0)	1·8 (1·7–1·9)
Togo	7·46 (7·16–7·74)	6·93 (6·76–7·08)	3·72 (3·44–4·02)	2·01 (1·61–2·42)	1·24 (0·79–1·72)	75·8 (72·8–78·7)		243·6 (225·8–263·1)	218·3 (157·3–281·1)	107·1 (35·6–216·8)	1·7 (1·6–1·8)

Table 1: Total fertility rate and number of livebirths (thousands) by location in 1950, 1980, and 2021, and for the reference scenario in 2050 and 2100; and net reproductive rate in 2021

Numbers in parentheses are 95% uncertainty intervals. Super-regions, regions, and countries are listed in alphabetical order.
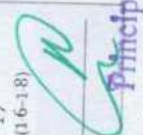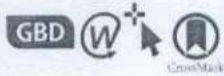
181

Global, regional, and national age-specific progress towards the 2020 milestones of the WHO End TB Strategy: a systematic analysis for the Global Burden of Disease Study 2021

GBD 2021 Tuberculosis Collaborators*

Summary

Background Global evaluations of the progress towards the WHO End TB Strategy 2020 interim milestones on mortality (35% reduction) and incidence (20% reduction) have not been age specific. We aimed to assess global, regional, and national-level burdens of and trends in tuberculosis and its risk factors across five separate age groups, from 1990 to 2021, and to report on age-specific progress between 2015 and 2020.

Methods We used the Global Burden of Diseases, Injuries, and Risk Factors Study 2021 (GBD 2021) analytical framework to compute age-specific tuberculosis mortality and incidence estimates for 204 countries and territories (1990–2021 inclusive). We quantified tuberculosis mortality among individuals without HIV co-infection using 22 603 site-years of vital registration data, 1718 site-years of verbal autopsy data, 825 site-years of sample-based vital registration data, 680 site-years of mortality surveillance data, and 9 site-years of minimally invasive tissue sample (MITS) diagnoses data as inputs into the Cause of Death Ensemble modelling platform. Age-specific HIV and tuberculosis deaths were established with a population attributable fraction approach. We analysed all available population-based data sources, including prevalence surveys, annual case notifications, tuberculin surveys, and tuberculosis mortality, in DisMod-MR 2.1 to produce internally consistent age-specific estimates of tuberculosis incidence, prevalence, and mortality. We also estimated age-specific tuberculosis mortality without HIV co-infection that is attributable to the independent and combined effects of three risk factors (smoking, alcohol use, and diabetes). As a secondary analysis, we examined the potential impact of the COVID-19 pandemic on tuberculosis mortality without HIV co-infection by comparing expected tuberculosis deaths, modelled with trends in tuberculosis deaths from 2015 to 2019 in vital registration data, with observed tuberculosis deaths in 2020 and 2021 for countries with available cause-specific mortality data.

Findings We estimated 9·40 million (95% uncertainty interval [UI] 8·36 to 10·5) tuberculosis incident cases and 1·35 million (1·23 to 1·52) deaths due to tuberculosis in 2021. At the global level, the all-age tuberculosis incidence rate declined by 6·26% (5·27 to 7·25) between 2015 and 2020 (the WHO End TB strategy evaluation period). 15 of 204 countries achieved a 20% decrease in all-age tuberculosis incidence between 2015 and 2020, eight of which were in western sub-Saharan Africa. When stratified by age, global tuberculosis incidence rates decreased by 16·5% (14·8 to 18·4) in children younger than 5 years, 16·2% (14·2 to 17·9) in those aged 5–14 years, 6·29% (5·05 to 7·70) in those aged 15–49 years, 5·72% (4·02 to 7·39) in those aged 50–69 years, and 8·48% (6·74 to 10·4) in those aged 70 years and older, from 2015 to 2020. Global tuberculosis deaths decreased by 11·9% (5·77 to 17·0) from 2015 to 2020. 17 countries attained a 35% reduction in deaths due to tuberculosis between 2015 and 2020, most of which were in eastern Europe (six countries) and central Europe (four countries). There was variable progress by age: a 35·3% (26·7 to 41·7) decrease in tuberculosis deaths in children younger than 5 years, a 29·5% (25·5 to 34·1) decrease in those aged 5–14 years, a 15·2% (10·0 to 20·2) decrease in those aged 15–49 years, a 7·97% (0·472 to 14·1) decrease in those aged 50–69 years, and a 3·29% (−5·56 to 9·07) decrease in those aged 70 years and older. Removing the combined effects of the three attributable risk factors would have reduced the number of all-age tuberculosis deaths from 1·39 million (1·28 to 1·54) to 1·00 million (0·703 to 1·23) in 2020, representing a 36·5% (21·5 to 54·8) reduction in tuberculosis deaths compared to those observed in 2015. 41 countries were included in our analysis of the impact of the COVID-19 pandemic on tuberculosis deaths without HIV co-infection in 2020, and 20 countries were included in the analysis for 2021. In 2020, 50 900 (95% CI 49 700 to 52 400) deaths were expected across all ages, compared to an observed 45 500 deaths, corresponding to 5340 (4070 to 6920) fewer deaths; in 2021, 39 600 (38 300 to 41 100) deaths were expected across all ages compared to an observed 39 000 deaths, corresponding to 657 (−713 to 2180) fewer deaths.

Interpretation Despite accelerated progress in reducing the global burden of tuberculosis in the past decade, the world did not attain the first interim milestones of the WHO End TB Strategy in 2020. The pace of decline has been unequal with respect to age, with older adults (ie, those aged >50 years) having the slowest progress. As countries

refine their national tuberculosis programmes and recalibrate for achieving the 2035 targets, they could consider learning from the strategies of countries that achieved the 2020 milestones, as well as consider targeted interventions to improve outcomes in older age groups.

Introduction

Despite being a preventable and largely curable disease, tuberculosis remains a major contributor to the global burden of disease. Tuberculosis causes more than 1 million deaths annually and was the leading cause of death due to a single infectious agent in 2019.[1] Since the early 1990s, global initiatives to address tuberculosis have grown more prominent, resulting in declines in the global burden of this disease.[2] Recent progress has been unimpressive, however, as global annual rates of decline

Research in context

Evidence before this study

In the context of the WHO End TB Strategy, several groups have generated estimates of tuberculosis incidence and mortality, including the WHO Global Tuberculosis Programme and the Global Burden of Diseases, Injuries, and Risk Factors Study (GBD), to monitor global and national-level progress towards eliminating tuberculosis. 2020 marked a crucial year for evaluating progress as the first quantitative milestones of the End TB Strategy passed. We searched PubMed with the search string "("tuberculosis" OR "TB") AND ("burden" OR "estimates") AND ("End TB") AND ("target*" OR "milestone*")", with no language restrictions, for publications from Jan 1, 2015, to Dec 1, 2023. Our search identified seven studies presenting population-based tuberculosis burden estimates to assess progress towards the End TB targets for subsets of countries; of these, only one study examined differences in progress by age. The single study analysing progress by age used GBD 2019 tuberculosis estimates to evaluate temporal trends in Cambodia. Additionally, the 2022 Global Tuberculosis Report from WHO illustrated that tuberculosis deaths decreased by only 5·9%, while the tuberculosis incidence rate dropped by 10%, between 2015 and 2021, falling well short of the targeted milestones. However, as yet, no global, systematic, age-specific study has been done to investigate progress towards the 2020 End TB Strategy mortality and incidence milestones, which outlined a 35% reduction in tuberculosis deaths and 20% reduction in the tuberculosis incidence rate between 2015 and 2020, with additional assessments of the role of key risk factors in achieving these milestones.

Added value of this study

We comprehensively examined the burden of tuberculosis for five separate age groups in 204 countries and territories from 1990 to 2021. We focused on examining temporal trends in tuberculosis incidence and mortality from 2015 to 2020 to assess global progress towards the End TB Strategy milestones, with an emphasis on exploring progress by age for the first time. We also present age-specific, risk-deleted mortality estimates that represent deaths due to tuberculosis that would have been observed if the combined effects of all evaluated risk factors were removed, to provide insights into the role of addressing risk factors in achieving the End TB targets. Last, we analysed vital registration data only (2015–21 inclusive) to assess the potential impact of the COVID-19 pandemic on age-specific tuberculosis mortality in countries with available cause-specific data.

Implications of all the available evidence

Global tuberculosis control programmes could consider closely examining the 15 countries that achieved the 2020 incidence milestone and the 17 countries that achieved the 2020 mortality milestone, many of which were in western sub-Saharan Africa and eastern Europe, to better understand drivers of their marked progress. Many of these countries have implemented innovative approaches to active case finding while implementing social protection interventions such as advanced tuberculosis surveillance in high-risk areas and economic incentives for patients. We observed unequal progress by age groups and found particularly slow progress in reducing the tuberculosis burden in older adults (aged >50 years), indicating that tuberculosis in this age group should be more widely recognised and monitored to achieve WHO's 2035 End TB Strategy targets. One approach for reducing the tuberculosis burden in older adults and achieving the 2035 End TB targets is addressing risk factors for tuberculosis. Our assessment of risk-deleted mortality suggests that the world would have achieved the 2020 End TB mortality milestone, with a 36% reduction in global tuberculosis deaths and the largest benefits in older adults, if the risk factors of smoking, alcohol use, and diabetes were removed. Although complete elimination of such risk factors is highly unlikely, this assessment illustrates the magnitude of potential improvement. Finally, our secondary analysis of countries with complete vital registration data showed variable impacts of the COVID-19 pandemic on tuberculosis mortality in 2020 and 2021; some countries and age groups reported fewer than expected deaths due to tuberculosis, whereas others reported more deaths than expected. Additional data from countries with a high tuberculosis burden are urgently needed to understand the generalisability of these findings.

183

in tuberculosis incidence over the past 10 years have ranged between 1% and 2%.[14] The WHO End TB Strategy represents a renewed global resolve to accelerate progress by aiming to reduce deaths due to tuberculosis by 95% and cut tuberculosis incidence by 90% between 2015 and 2035, while also seeking to have zero tuberculosis-affected households experiencing catastrophic financial costs due to the disease by 2035.[5] Rigorous evaluations of the trends in the global burden of tuberculosis are therefore crucial for assessing progress towards achieving the End TB Strategy targets and identifying specific drivers of marked national progress.

The year 2020 marked a crucial timepoint for evaluating progress towards eliminating tuberculosis. The first quantitative milestones in the End TB Strategy called for a 35% reduction in deaths due to tuberculosis and a 20% reduction in the tuberculosis incidence rate by 2020.[5] The 2022 Global Tuberculosis Report from WHO illustrated that tuberculosis deaths decreased by only 5·9%, while the tuberculosis incidence rate decreased by 10%, between 2015 and 2021, falling well short of the 2020 milestones.[6] Moreover, studies examining global trends towards WHO targets have yet to fully consider age-specific differences in progress. The current evidence suggests that although the tuberculosis burden remains substantially high in children,[7,8] older age groups generally have the highest rates of tuberculosis mortality and incidence.[9,10] A report of the Global Burden of Diseases, Injuries, and Risk Factors Study 2019 (GBD 2019) based on data from Cambodia also indicated that temporal trends of reductions in the tuberculosis burden become slower with increasing age.[11] Several factors could explain these marked age-related differences, including age-specific diagnostic challenges,[12,13] age-specific mixing patterns,[14] immune senescence[15] and other age-related immune dysfunctions,[16] and comorbidities common in older patients masking tuberculosis symptoms.[17] Although largely unexplored at the global level, age-specific differences in risk factor prevalence might further augment these age-related discrepancies. Identification of age-specific progress towards the End TB Strategy milestones, combined with assessments of the role of key risk factors, could therefore help inform targeted interventions to accelerate progress towards eliminating tuberculosis.

Leveraging the GBD 2021 framework, we aimed to examine the levels and trends in the global burden of tuberculosis to investigate age-specific attainment of the 2020 WHO End TB Strategy mortality and incidence milestones for 204 countries and territories. Considering that modifiable tuberculosis risk factors, such as alcohol consumption, smoking, and diabetes, can augment preventive interventions, we supplemented our analysis by examining age-specific risk-deleted tuberculosis mortality (ie, the tuberculosis mortality rate that would have been observed if risk factors for tuberculosis

mortality were removed) to highlight the need to address reductions in risk factor exposure as part of any holistic response to achieving the End TB Strategy targets. Last, we examined the potential impact of the COVID-19 pandemic on tuberculosis mortality by drawing on vital registration data from those countries with available data. This manuscript was produced as part of the GBD Collaborator Network and in accordance with the GBD Protocol.

Methods

Overview

We have previously published detailed methods of the GBD analytical framework[18,19] and tuberculosis burden estimation in GBD.[1,3,11] Here, we summarise the methodology for estimating tuberculosis mortality and morbidity, as well as key risk factors, with more detailed descriptions of the modelling strategy provided in appendix 1 (pp 3–26). In compliance with the Guidelines for Accurate and Transparent Health Estimates Reporting, input data sources and codes for each step of the estimation process are available on the Global Health Data Exchange.

Tuberculosis mortality

The GBD 2021 Cause of Death database contained all available vital registration, surveillance system, and verbal autopsy data from 1980 to 2020. Leveraging the database, we included 22603 site-years of vital registration data, 825 site-years of sample-based vital registration data, 680 site-years of mortality surveillance data, and 9 site-years of minimally invasive tissue sample (MITS) diagnoses data for modelling tuberculosis mortality among individuals without HIV co-infection. Country-specific data sources and citations are included in the Global Health Data Exchange. We processed raw cause of death data to account for completeness and differences in coding schemes, to redistribute deaths from unspecified codes to more specific underlying causes of death,[20] and to reassign misclassified HIV deaths.

We used the Cause of Death Ensemble modelling (CODEm) strategy to generate tuberculosis mortality estimates in individuals without HIV co-infection by location, year, age, and sex. CODEm is a hierarchical modelling platform that uses an ensemble of different modelling methods for rates or cause fractions with varying choices of covariates (eg, smoking prevalence, alcohol consumption, and Healthcare Access and Quality [HAQ] Index) that perform best with out-of-sample predictive validity testing.[21] Appendix 1 (p 13) provides example countries illustrating that final tuberculosis mortality estimates presented throughout this analysis largely follow trends in input data. Finally, we established age-specific tuberculosis deaths among individuals with HIV infection using a population attributable fraction (PAF) approach (appendix 1 pp 14–15).

184

Tuberculosis morbidity

We simultaneously modelled age-sex-specific tuberculosis incidence, prevalence, and cause-specific mortality using the DisMod-MR 2.1 (disease-model-Bayesian meta-regression) modelling tool. DisMod-MR 2.1 is a Bayesian disease modelling tool that leverages all available morbidity and mortality data, the epidemiological relationships between disease parameters, and spatial relationships to output internally consistent disease burden estimates.[22] We provide details of case definitions, input data sources, and data processing strategies in appendix 1 (pp 2–3. 16–26).

Briefly, we identified all population-based tuberculosis prevalence surveys via comprehensive reviews of the literature. Similarly to previous GBD iterations, we used a Bayesian meta-regression tool[23] to adjust prevalence surveys that used smear-positive tuberculosis as the case definition rather than bacteriologically confirmed tuberculosis. We further recalibrated surveys that used symptoms only as the screening method over both symptoms and chest X-ray (appendix 1 pp 22–23). Next, we maximised data informing DisMod-MR by predicting age-sex-specific incidence for countries with low-quality data ratings for cause of death data. We estimated incidence for these countries through a mortality-to-incidence ratio approach using countries with high-quality data ratings on cause of death data as inputs into a Bayesian meta-regression analysis[23] where the HAQ Index[24] was the primary covariate. We then linked location-specific predicted mortality-to-incidence ratios with tuberculosis death estimates to obtain estimated age-sex-specific incidence (appendix 1 p 20).

We subsequently modelled these data, together with age-sex-specific case notifications for locations with high-quality data ratings on causes of death data, population-based tuberculin surveys, and estimates of tuberculosis excess mortality rate, remission, and cause-specific mortality rate, in DisMod-MR 2.1 to generate all-form tuberculosis morbidity estimates that were internally consistent. To further improve internal consistency of modelling in DisMod, we computed all-age and both-sexes priors of tuberculosis duration using a combination of tuberculosis duration data from a systematic review of studies during the pre-chemotherapy era[25] and the HAQ Index. We then used DisMod's statistical triangulation approach, using the estimated tuberculosis duration priors and age-sex-specific tuberculosis mortality, prevalence, and incidence data, to derive final age-sex-specific tuberculosis duration estimates (appendix 1 pp 27–28). Finally, we disaggregated tuberculosis incidence by HIV status by applying the fraction of new all-form tuberculosis cases that were HIV and tuberculosis co-infections to our all-form tuberculosis cases estimated from DisMod-MR.

Risk factor analysis

GBD has previously published detailed methodology for risk factor estimation.[26] In summary, age-sex-specific

PAFs in adults were computed within the comparative risk assessments framework of GBD with the following inputs: prevalence estimates for exposure to risk factors; the relative risk of tuberculosis mortality as an outcome of exposure to each risk factor; and the theoretical minimum risk exposure level (TMREL), defined as the level of exposure that would minimise risk for each individual in a population. We computed tuberculosis mortality attributable in adults (aged ≥15 years) to each risk factor by multiplying the PAF by the number of tuberculosis deaths for each risk–outcome pair. We subsequently derived risk-deleted mortality rates to quantify tuberculosis deaths that would have been observed had the risk factors been set to their corresponding TMRELs. The risk-deleted tuberculosis mortality rates are therefore computed by multiplying the observed tuberculosis mortality by one minus the PAF for a risk factor or combination of risk factors. The objective of the risk-deleted analysis is to illustrate the potential magnitude of addressing tuberculosis risk factors across countries and age groups. For this analysis, we quantified tuberculosis PAFs for alcohol consumption,[27] smoking,[28] and diabetes[29] among adults without HIV co-infection. We provide complete details of the methods for estimation of the tuberculosis risk factors in appendix 1 (pp 39–67).

Impact of the COVID-19 pandemic on tuberculosis mortality

We evaluated the potential age-specific impact of the COVID-19 pandemic on tuberculosis mortality without HIV co-infection using vital registration data for all countries with available cause-specific mortality data in 2020 and 2021. This secondary analysis included data from 41 countries that reported at least ten tuberculosis deaths in 2019 for each age group of interest, representing four of the seven GBD super-regions (appendix 2 pp 300–04), with 15 countries from the high-income super-region, 14 in central Europe, eastern Europe, and central Asia, ten in Latin America and the Caribbean, and two in southeast Asia, east Asia, and Oceania that had sufficient cause-specific mortality data. Using these data as inputs, we fitted quasi-Poisson regression models to data from 2015 to 2019 with population size as an offset to estimate the expected number of tuberculosis deaths in 2020–21 for each country. The quasi-likelihood was selected to account for overdispersion in count data. This analysis was stratified by adults and children combined (aged <65 years), elderly individuals (≥65 years), and all ages combined. We selected these age groups on the basis of evidence illustrating that global tuberculosis diagnoses during the pandemic declined relatively more in individuals aged 65 years and older than in those younger than 65 years.[30] We subsequently compared age-specific observed tuberculosis deaths to predicted tuberculosis deaths in 2020 and 2021 to identify potential excess tuberculosis deaths. Comparisons were made by computing the difference in observed to

185

expected tuberculosis deaths (excess tuberculosis deaths) and the respective ratio.

Data presentation

We aggregated tuberculosis incidence and mortality estimates by HIV status to present all-form tuberculosis burden estimates for five age groups (<5 years, 5–14 years, 15–49 years, 50–69 years, and ≥70 years) throughout this analysis. Next, we used the GBD world population age standard to derive age-standardised rates for all-form tuberculosis incidence and mortality. For changes over time, we provide annualised rates of change (ARC) as the difference in the natural log of the incidence and mortality rates at the start and end of the time interval divided by the number of years in the interval. We present tuberculosis incidence-specific and mortality-specific ARCs for 1990–2010 and 2010–21. To evaluate attainment of the 2020 WHO End TB interim milestones, we derived percentage changes in all-form tuberculosis rates and counts of both incidence and mortality from 2015 to 2020. At each modelling step described, parameter uncertainty was incorporated by randomly drawing 500 samples from each age-sex-location-year-specific parameter distribution and propagating this uncertainty forward across each step of the analysis. Consistent with the GBD framework, we computed 95% uncertainty intervals (UIs) for all estimates based on the 2·5th and 97·5th percentiles of the final 500 draws. More detailed tuberculosis burden results by HIV status, age, and sex across locations and years are available in the GBD Results Tool. Counts are rounded to three significant figures while rates and percentages are rounded to one decimal place, except where greater precision was needed to differentiate between values.

Role of the funding source

The funder of the study had no role in study design, data collection, data analysis, data interpretation, writing of the report, or the decision to submit the manuscript for publication.

Results

Overview

In 2021, we estimated that there were 9·40 million (95% UI 8·36–10·5) tuberculosis incident cases and 1·35 million (1·23–1·52) deaths due to tuberculosis globally (table 1). HIV and tuberculosis co-infection constituted 1·00 million (0·90–1·13; 10·7% [10·3–11·0]) of the 9·40 million all-form tuberculosis incident cases and 205 000 (158 000–248 000; 15·1% [11·9–17·7]) of the 1·35 million all-form global tuberculosis deaths. The age-standardised incidence rate for all-form tuberculosis was 115 (102–128) per 100 000 population and the age-standardised mortality rate was 16·2 (14·8–18·2) per 100 000 population in 2021 (table 1). From 1990 to 2021, the global age-standardised tuberculosis incidence rate decreased by 37·0% (34·5–39·1), while the global

age-standardised tuberculosis mortality rate decreased by 61·1% (52·6–66·3).

Age-specific tuberculosis burden

The global age distribution for the number of all-form tuberculosis incident cases in 2021 demonstrated a drop-off in cases after age 5 years, but a rapid spike in cases at age 15–24 years, followed by steady decreases until age 70–74 years, after which there was a rapid drop in cases (appendix 2 p 4). The corresponding age distribution of tuberculosis incidence rates showed a similar pattern until age 20–24 years, when the rate levelled off until a rapid increase from age 50–69 years, followed by a small drop (appendix 2 p 5). In 2021, 3·8% (95% UI 3·6–4·2) of incident cases were in those younger than 5 years, 4·7% (3·8–5·9) were in those aged 5–14 years, 54·9% (52·4–58·9) were in those aged 15–49 years, 26·5% (23·4–29·5) were in those aged 50–69 years, and 10·1% (9·2–11·0) were in those aged 70 years and older (table 1).

The age distribution for tuberculosis deaths in 2021 showed a similar drop-off in deaths after age 5 years, with numbers rapidly increasing after age 19 years before levelling off at age 55–69 years and then sharply decreasing (appendix 2 p 4). For the tuberculosis mortality rate distribution, the rate dropped after age 5 years before steadily increasing for the remaining age groups until age 80–84 years when it levelled off (appendix 2 p 5). In 2021, 4·5% (95% UI 3·5–5·0) of global tuberculosis deaths were in children younger than 5 years, 1·5% (1·5–1·6) were in those aged 5–14 years, 36·4% (35·7–35·9) were in those aged 15–49 years, 33·2% (32·8–33·6) were in those aged 50–69 years, and 24·5% (24·6–24·9) were in those aged 70 years and older (table 1).

In 2021, tuberculosis incidence rates were greater than 100 per 100 000 population in children younger than 5 years in 34 countries, and in children aged 5–14 years in 14 countries (appendix 2 pp 6, 8, 20–85). Tuberculosis incidence rates exceeded 500 per 100 000 population in those aged 15–49 years in nine countries, in those aged 50–69 years in 33 countries, and in those aged 70 years and older in 50 countries (appendix 2 pp 10, 12, 14, 20–85).

In 2021, tuberculosis mortality rates exceeded 25 per 100 000 population in children younger than 5 years in 20 countries, in those aged 5–14 years in one country, and in those aged 15–49 years in 37 countries (appendix 2 pp 7, 9, 11, 20–85). Among older adults, tuberculosis mortality rates exceeded 300 per 100 000 in those aged 50–69 years in eight countries and in those aged 70 years and older in 44 countries (appendix 2 pp 13, 15, 20–85).

Our assessment of the global ARC in tuberculosis incidence showed that children younger than 5 years and those aged 5–14 years had the largest ARCs, decreasing by 4·1% (95% UI 3·8–4·3) and 3·7% (3·4–4·0), respectively, between 2010 and 2021, while ARCs in the adult age groups decreased by around 2% in the same period (table 1). Similarly, children younger than 5 years and those aged 5–14 years had the largest ARCs for
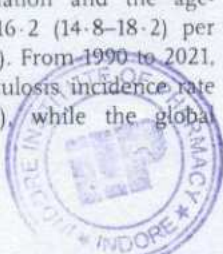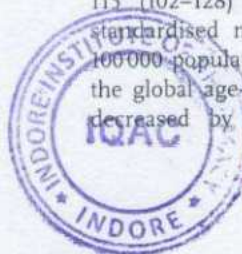
186
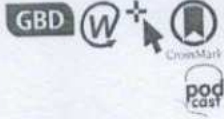
Global, regional, and national burden of disorders affecting the nervous system, 1990–2021: a systematic analysis for the Global Burden of Disease Study 2021

GBD 2021 Nervous System Disorders Collaborators*

Summary

Background Disorders affecting the nervous system are diverse and include neurodevelopmental disorders, late-life neurodegeneration, and newly emergent conditions, such as cognitive impairment following COVID-19. Previous publications from the Global Burden of Disease, Injuries, and Risk Factor Study estimated the burden of 15 neurological conditions in 2015 and 2016, but these analyses did not include neurodevelopmental disorders, as defined by the International Classification of Diseases (ICD)-11, or a subset of cases of congenital, neonatal, and infectious conditions that cause neurological damage. Here, we estimate nervous system health loss caused by 37 unique conditions and their associated risk factors globally, regionally, and nationally from 1990 to 2021.

Methods We estimated mortality, prevalence, years lived with disability (YLDs), years of life lost (YLLs), and disability-adjusted life-years (DALYs), with corresponding 95% uncertainty intervals (UIs), by age and sex in 204 countries and territories, from 1990 to 2021. We included morbidity and deaths due to neurological conditions, for which health loss is directly due to damage to the CNS or peripheral nervous system. We also isolated neurological health loss from conditions for which nervous system morbidity is a consequence, but not the primary feature, including a subset of congenital conditions (ie, chromosomal anomalies and congenital birth defects), neonatal conditions (ie, jaundice, preterm birth, and sepsis), infectious diseases (ie, COVID-19, cystic echinococcosis, malaria, syphilis, and Zika virus disease), and diabetic neuropathy. By conducting a sequela-level analysis of the health outcomes for these conditions, only cases where nervous system damage occurred were included, and YLDs were recalculated to isolate the non-fatal burden directly attributable to nervous system health loss. A comorbidity correction was used to calculate total prevalence of all conditions that affect the nervous system combined.

Findings Globally, the 37 conditions affecting the nervous system were collectively ranked as the leading group cause of DALYs in 2021 (443 million, 95% UI 378–521), affecting 3·40 billion (3·20–3·62) individuals (43·1%, 40·5–45·9 of the global population); global DALY counts attributed to these conditions increased by 18·2% (8·7–26·7) between 1990 and 2021. Age-standardised rates of deaths per 100 000 people attributed to these conditions decreased from 1990 to 2021 by 33·6% (27·6–38·8), and age-standardised rates of DALYs attributed to these conditions decreased by 27·0% (21·5–32·4). Age-standardised prevalence was almost stable, with a change of 1·5% (0·7–2·4). The ten conditions with the highest age-standardised DALYs in 2021 were stroke, neonatal encephalopathy, migraine, Alzheimer's disease and other dementias, diabetic neuropathy, meningitis, epilepsy, neurological complications due to preterm birth, autism spectrum disorder, and nervous system cancer.

Interpretation As the leading cause of overall disease burden in the world, with increasing global DALY counts, effective prevention, treatment, and rehabilitation strategies for disorders affecting the nervous system are needed.

Funding Bill & Melinda Gates Foundation.

Introduction

Conditions can affect the nervous system throughout life, for example by disrupting brain growth; damaging the brain, spinal cord, or peripheral nerves; and impairing cognitive, sensory, socioemotional, and motor function and behaviour. This diverse group of conditions includes congenital and neurodevelopmental disorders, cerebrovascular and neurodegenerative diseases, neurological infections, neurological–immunological disorders, neuromuscular or peripheral nervous system disorders, traumatic injuries, and cancers of the nervous system, for brevity summarised as neurological disorders or nervous system conditions. These disorders vary in cause, symptoms, and course. Some nervous system

Research in context

Evidence before this study
We searched PubMed between Jan 1, 1980, and Oct 22, 2023, to identify studies that assessed trends in nervous system health loss globally, with the search string ("nervous system"[Title] OR "neurological"[Title]) AND ("prevalen*"[Title/Abstract] OR "inciden*"[Title/Abstract] OR "death*"[Title/Abstract] OR "burden"[Title/Abstract]) AND ("global"[Title] OR "international"[Title]). Results yielded studies that either looked at a small subset of conditions, such as only cancers or COVID-19, looked at single geographies, or used Global Burden of Disease, Injuries, and Risk Factors Study (GBD) results. Previous GBD reports on the global, regional, and national burden of neurological disorders covered a period from 1990 to 2016 and were limited to 15 conditions. In 2016, neurological disorders ranked as the leading cause of DALYs and the second-leading cause of death. The largest contributors to DALYs were stroke, migraine, and Alzheimer's disease and other dementias. Other research groups used GBD 2019 results to quantify 18 neurological disorders or smaller geographies. Previous analyses excluded neurodevelopmental conditions that frequently cause lifelong disability, and neurological complications from conditions that affect multiple body systems, such as diabetes, syphilis, malaria, or more recently COVID-19 and Zika virus disease.

Added value of this study
This study extends previous evidence by including important neurological and neurodevelopmental disorders that were previously not considered and by adding consequences of non-neurological conditions that affect the nervous system, bringing the total number of included conditions to 37. This study estimated the proportion of nervous system burden that was potentially avertible by eliminating known risk factors for stroke, Alzheimer's disease and other dementias, multiple sclerosis, Parkinson's disease, encephalitis, meningitis, and idiopathic intellectual disability but also emphasises the scarcity of knowledge about risk factors for nervous system conditions.

Implications of all the available evidence
Until recently, the nervous system has not been a focus of global public health discourse. Quantifying the global burden associated with nervous system health loss aids policy making and helps to lift brain health onto the public health agenda. With the adoption of the *Intersectoral Global Action Plan on Epilepsy and Other Neurological Disorders 2022–2031* by the World Health Assembly, the prevention, early identification, diagnosis, treatment, and rehabilitation of disorders that affect the nervous system have been brought into focus. This study provides the latest evidence to guide ongoing advocacy and awareness efforts. Additional research on modifiable risks, and support for adequate facilities and workforces in managing nervous system conditions, is necessary for equity and access to quality care. As the leading cause of DALYs, affecting more than 40% of the global population, nervous system health loss should be a public health priority.

conditions cause lifelong disability, whereas others are associated with high fatality rates; some are treatable or preventable, whereas for others there is no cure.

Increased life expectancy is arguably one of the greatest achievements of health systems around the world. However, this increase has also led to increases in age-related neurological disorders, such as Alzheimer's disease and other dementias, stroke, and Parkinson's disease, necessitating global health policies not only to focus on survival but also to minimise health loss due to disability by promoting function and independence. Not all neurological burden is associated with population ageing,[1] rendering it important to quantify the overall health loss associated with nervous system conditions throughout the lifespan.[2]

In response to the growing burden of nervous system disorders and conditions worldwide, the World Health Assembly adopted the *Intersectoral Global Action Plan on Epilepsy and Other Neurological Disorders 2022–2031* (IGAP) in May, 2022.[1] The action plan aims to "reduce the stigma, impact and burden of neurological disorders, including their associated mortality, morbidity and disability, and to improve the quality of life of people with neurological disorders, their carers and families".[1]

In the Global Burden of Disease, Injuries, and Risk Factors Study (GBD), nervous system disorders and conditions are spread across many disease groupings. The basic GBD grouping of neurological disorders includes Alzheimer's disease and other dementias, headaches, idiopathic epilepsy, motor neuron disease, multiple sclerosis, Parkinson's disease, and a residual group of other neurological disorders that includes, for instance, muscular dystrophy and Huntington's disease. Using GBD 2015 and 2016 estimates, Feigin and colleagues previously provided more comprehensive estimates of neurological health loss than the basic GBD grouping by also including stroke, meningitis, encephalitis, tetanus, traumatic brain injury, spinal cord injury, and brain and CNS cancers.[1,4] Other researchers used GBD 2019 estimates to look at 18 neurological disorders or specific geographies.[5,6] However, a proportion of global neurological burden stems from neurodevelopmental disorders, which traditionally have been classified in GBD under mental health or neonatal conditions, and from childhood infections. Both infections and neurodevelopmental disorders are often associated with lifelong disability.[7] Furthermore, some peripheral neuropathies were not previously captured within the neurological burden.

Additionally, as shown by the COVID-19 pandemic,[8,9] emerging and re-emerging infectious diseases are becoming an increasing global concern. For example,

vector-borne viruses such as Zika virus,[10] Japanese encephalitis virus,[11] and West Nile virus[12] are increasing their geographical spread owing to climate change and constitute a notable global public health threat. These infections, often targeting the nervous system directly, cause both mortality and neurological morbidity, with an especially high burden in low-income and middle-income countries (LMICs).[13]

This Article aims to create an estimate of the burden of disorders and conditions that affect the nervous system using an expanded group of GBD conditions, cause categories, and disease consequences compared with previous analyses. This manuscript was produced as part of the GBD Collaborator Network and in accordance with the GBD Protocol.

Methods
Overview
GBD 2021 quantifies health loss for 371 diseases in 204 countries and territories, including measures of prevalence, disease severity, and death that together constitute a comprehensive assessment of disease burden. The analysis presented here groups conditions that affect the CNS and peripheral nervous system for which neurological consequences can be isolated in GBD (table 1). The conditions included here are not an exhaustive list; we were unable to include neurological consequences from some conditions, for example HIV or adrenoleukodystrophy, because they could not be explicitly estimated in GBD at this stage. However, this analysis is the most comprehensive attempt to capture neurological health loss to date. Broadly, and as outlined in the IGAP, these conditions include: neurodevelopmental disorders;[14] neurological disorders (eg, stroke or Alzheimer's disease and other dementias); and neurological consequences of other congenital, neonatal, metabolic, or infectious diseases. Neurological consequences captured in this analysis include intellectual disability, cognitive impairment, motor impairment, epilepsy, microcephaly, neuropathy, and sensory deficits resulting from neonatal insults (described by condition in appendix p 5). For example, persistent cognitive symptoms and Guillain–Barré syndrome after COVID-19 were included in the analysis, but ongoing fatigue or respiratory symptoms due to COVID-19 were not included. Methods that were used to isolate nervous system health loss for conditions with neurological and non-neurological outcomes are described later in this section. Other neurological disorders is a residual category (appendix pp 5–6) that encompasses conditions that affect the CNS and peripheral nervous system but are not explicitly modelled as isolated diseases in GBD because of resource constraints. The category broadly includes unspecified disorders of the nervous system, some degenerative or demyelinating diseases, disorders of the autonomic nervous system, some movement disorders,

spinocerebellar diseases, nerve root and plexus disorders, peripheral nerve disorders, some neuromuscular disorders, and muscle diseases, such as myopathies (appendix pp 5–6, 63–64). Epilepsy estimates exclude epilepsy cases that are captured under other conditions to avoid double counting. A Guidelines for Accurate and Transparent Health Estimates Reporting checklist is included in the appendix (pp 2–5).

Prevalence estimates
GBD attempts to acquire all available population-representative studies, large-scale surveys, censuses, insurance claims, and hospital records that catalogue incidence and prevalence for each condition. The number of data sources that inform non-fatal estimates for each condition are summarised in the appendix (pp 6–7). For each condition, a reference case definition and data collection method was set. Data collected with non-reference methods were adjusted to the reference case definition using regression analyses assessing systematic bias. Case definitions and International Classification of Disease (ICD) codes used in non-fatal analyses are described in the appendix (pp 8–16).

For most conditions, Bayesian models were used to estimate incidence and prevalence across time, geography, age, and sex, on the basis of data and relevant predictive covariates. Modelling details vary by condition but generally use a Bayesian meta-regression tool called Disease Modelling Meta-Regression (DisMod-MR) 2.1.[15] Details of Dismod-MR 2.1 are in the GBD 2019 capstone appendix 1, section 4.5 of reference 9,[15] and described in the appendix (p 16). Predictive covariates included in models for individual conditions and details on geographical categories are also described in the appendix (pp 16–18). By including remission rates in the GBD modelling approach, we counted cases as being prevalent only if they were still a case, and we further accounted for transient versus progressive conditions in the case definition (appendix pp 8–14) and assessment of burden. Details of the modelling approach of three conditions with episodic occurrence (ie, migraine, tension-type headaches, and epilepsy) are in the appendix (p 20).

This Article describes prevalence, which reflects incidence and duration. Duration in turn is determined by mortality and remission rates and reflects disease severity and access to care. Total prevalence for each condition was split into more granular categories, termed sequelae, to capture different levels of severities and different possible health outcomes (appendix pp 21–48). For example, Parkinson's disease prevalence was proportionally split between three sequelae (ie, mild, moderate, and severe).[16] For conditions that are not purely neurological, such as COVID-19, only relevant neurological sequelae were included. Further details on non-fatal methods for these conditions and diseases shown in the appendix (pp 5–62).
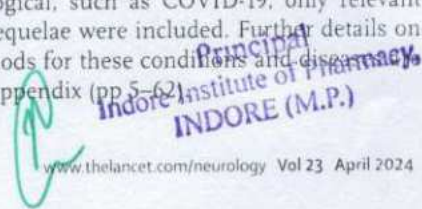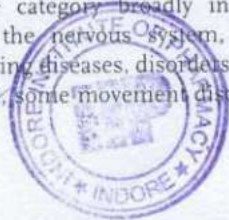
Case aggregation and comorbidity corrections

The total number of prevalent cases for each individual condition was calculated by aggregating cases for all underlying sequelae. For wholly neurological conditions, the aggregate of sequela-level cases equalled the total number of cases for the overall condition. For conditions with both non-neurological and neurological health loss, the aggregate number of cases for sequelae with nervous system health loss was a subset of the total number of cases. For example, only a subset of all individuals with long-term consequences of COVID-19 in 2021 had neurological sequelae captured in GBD, such as cognitive impairment or Guillain–Barré syndrome (details of analysis linking Guillain–Barré syndrome as an outcome from COVID-19 infection are shown in appendix p 62). The total cases of cognitive impairment due to COVID-19 included in this analysis equals the total number of people who had cognitive impairment or Guillain–Barré syndrome attributed to COVID-19, but calculation of years lived with disability (YLDs) excludes any additional health loss in these individuals due to acute COVID-19 symptoms, fatigue, or ongoing respiratory problems.

A comorbidity correction was used to calculate total prevalence of all nervous system conditions and disorders combined, assuming independent comorbidity. Without a comorbidity correction, prevalence would be overestimated because individual conditions or disorders would be assumed to be non-overlapping (ie, one condition or disorder per individual). The total number of people with any nervous system health loss was then calculated by multiplying by the number of people in the population: $prevalence_{total} = 1 - [(1 - prevalence_{condition1}) * (1 - prevalence_{condition2}) * ... (1 - prevalence_{condition37})]$.

YLDs due to nervous system health loss

The YLDs measure of non-fatal burden allows for comparison of relative health effects between disparate diseases. Disability refers to the relative health loss from a condition, as reflected in disability weights that grade severity of health loss from none (ie, disability weight of 0) to severe (ie, disability weight of 1, which is equivalent to death).[17] YLDs account for both prevalence and severity of health loss by multiplying sequela prevalence by a sequela-specific disability weight. For example, although tension-type headaches are highly prevalent, the associated disability weight is relatively low compared with those of many other neurological conditions, which is reflected in the final YLD values. As another example, the disability weight for mild multiple sclerosis is 0·183, and that for severe multiple sclerosis is 0·719 (a description of multiple sclerosis disability weights is shown in appendix pp 55–56). These weights are derived from population and internet surveys where respondents were asked to indicate the person that they believed to be healthier between random pairs of hypothetical people, each with a brief

	Included in GBD 2016 analysis by Feigin and colleagues[1]	Mortality included in this analysis
Alzheimer's disease and other dementias	Yes	Yes
Attention deficit hyperactivity disorder	No	No
Autism spectrum disorder	No	No
Cerebral malaria	No	No
Cognitive impairment or Guillain–Barré syndrome due to COVID-19	No	No
Congenital and adult neurosyphilis	No	No
Diabetic neuropathy	No	No
Encephalitis	Yes	Yes
Epilepsy	Yes (idiopathic)	Yes
Epilepsy due to cystic echinococcosis	No	No
Fetal alcohol syndrome	No	No
Guillain–Barré syndrome	No	Yes*
Idiopathic intellectual disability	No	No
Meningitis	Yes	Yes
Migraine	Yes	No
Motor neuron disease	Yes	Yes
Multiple sclerosis	Yes	Yes
Neonatal encephalopathy	No	Yes
Nervous system cancer (ie, CNS cancers, neuroblastoma, and other peripheral nervous cell tumours; includes paediatric and adult primary cases, and excludes metastases)	Yes (CNS)	Yes
Neural tube defects	No	Yes
Neurocysticercosis	No	Yes
Neurological complications due to congenital birth defects	No	No
Neurological complications due to congenital Zika syndrome	No	No
Neurological complications due to Down syndrome	No	No
Neurological complications due to Klinefelter syndrome	No	No
Neurological complications due to neonatal jaundice	No	No
Neurological complications due to neonatal sepsis	No	No
Neurological complications due to other chromosomal anomalies (excluding Down syndrome, Klinefelter syndrome, and Turner syndrome)	No	No
Neurological complications due to preterm birth	No	No
Other neurological disorders (including degenerative diseases, disorders of the autonomic nervous system, some movement disorders, spinocerebellar diseases, nerve root and plexus disorders, peripheral nerve disorders, neuromuscular disorders, and some muscle diseases such as myopathies; appendix pp 5–6)	Yes	Yes
Parkinson's disease	Yes	Yes
Rabies	No	Yes
Spinal cord injury	Yes	No
Stroke (ie, ischaemic stroke, subarachnoid haemorrhage, and intracerebral haemorrhage)	Yes	Yes
Tension-type headache	Yes	No
Tetanus	Yes	Yes
Traumatic brain injury	Yes	No

*Guillain-Barré syndrome deaths not ascribed to an underlying cause are captured in the category of other neurological disorders.

Table 1: Conditions included in our analysis of nervous system health loss

190

lay description of health states included in GBD. Disability weights and lay descriptions for all health states included in this analysis are described in the appendix (pp 49–61). To account for the fact that individuals can have more than one condition, we did a simulation to produce adjusted disability weights on the basis of the observed combinations of comorbidities generated by the simulation.

For sequelae that include both neurological and non-neurological health loss, YLDs were recalculated to isolate the non-fatal burden attributable to nervous system health loss. For example, sequelae of Down syndrome include severe intellectual disability with congenital heart disease due to Down syndrome (sequela 1) and severe intellectual disability due to Down syndrome (sequela 2). To isolate the neurological component of sequela 1, the adjusted disability weight generated from the comorbidity simulation for sequela 2 was used to recalculate YLDs by multiplying the prevalence of sequela 1 by the adjusted disability weight for sequela 2. This method was used to calculate YLDs for all sequelae with combined neurological and non-neurological health loss to isolate the burden due to nervous system health loss.

Calculating deaths and years of life lost

Deaths were estimated for 15 neurological conditions (table 1). An overview of data and modelling methods is shown in the appendix (pp 62–66). Total sources included for each individual condition are in the appendix (pp 62–63); ICD-9 and ICD-10 mapping for each condition and predictive covariates included in models are in the appendix (pp 63–66).

Causes of death in GBD are mutually exclusive and collectively exhaustive, meaning a given individual is assigned only one underlying cause of death and the sum of all disease-specific deaths adds up to total deaths for a given year. Years of life lost (YLLs) were calculated for each condition by multiplying deaths and remaining standard life expectancy.[15] This measure captures premature death, meaning that a death at a young age, for example from neonatal encephalopathy, leads to more YLLs than a death at older ages, such as from Alzheimer's disease and other dementias. Disability-adjusted life-years (DALYs) were calculated as the sum of YLDs and YLLs by year, age, sex, and location, and represent the combined non-fatal and fatal burden of each condition. For conditions where we did not ascribe deaths (eg, headaches or conditions such as preterm birth where we included only long-term neurological outcomes), DALYs are equal to YLDs. Percentage of deaths and DALYs that occurred in LMICs were calculated using World Bank income levels, which are based on gross national income per capita.

Risk factors

GBD assesses the degree to which risk factors contribute to disease burden by identifying how disease DALYs would change given a theoretical minimum risk exposure level.[17] The contribution of preventable risk factors to

DALYs was quantified for eight conditions: stroke, Alzheimer's disease and other dementias, multiple sclerosis, Parkinson's disease, idiopathic epilepsy, meningitis, encephalitis, and idiopathic intellectual disability. We did not include conditions that are not wholly neurological, for examples diabetes, as we could not ascribe risk contribution specific to neurological health states. The number of risk factors assessed in GBD 2021 varies by condition on the basis of evidence of association and available data. Exposure to a given risk was estimated for each location, age, sex, and year using regression modelling, and relative risk curves were computed by pooling data from studies assessing a given risk–outcome pair, such as intervention, cohort, and case–control studies. For each risk–outcome pair, risk exposure and relative risk analyses were used to calculate population attributable fraction. Attributable DALYs were then calculated, defined as the expected decrease in disease burden if risk exposure had equalled the theoretical minimum risk exposure level. Total attributable burden across all risks for a given outcome accounted for mediation effects but not potential synergistic effects.

Mean estimate, uncertainty, and percentage change calculation

Estimates were calculated 500 times by sampling the posterior distribution of the estimate (termed draws) at each step in the modelling process, and all calculations were performed by draw. Mean estimates for each year, age, sex, and location were taken from the distribution of 100 estimates, and 95% uncertainty intervals (UI) were taken as the 12·5th and 487·5th ordered draws. Age-standardised estimates were calculated using standard GBD population age weights.[15] Percentage change between 1990 and 2021 was calculated by subtracting 1990 estimates from 2021 estimates and dividing the difference by 1990 estimates.

Role of the funding source

The funder of the study had no role in the study design, data collection, data analysis, data interpretation, or writing of the report.

Results

Overview

An estimated 3·40 billion (95% UI 3·20–3·62) individuals had a condition affecting the nervous system in 2021, corresponding to 43·1% (40·5–45·9) of the world population (table 2). These conditions caused 11·1 million (9·75–13·8) deaths and contributed to 168 million (114–243) YLDs and 275 million (247–316) YLLs. With a total of 443 million (378–521) DALYs, this expanded nervous system category was the top-ranked contributor to global DALYs and YLLs in GBD 2021, followed by cardiovascular diseases (excluding stroke; unpublished estimates, GBD 2021 Diseases and Injuries

Collaborators). The grouping of 15 conditions or disorders published in previous analyses' contributed 313 million (260–379) DALYs, or 70·5% (66·9–74·6) of the total neurological DALYs reported here for 2021. Newly added neurological conditions contributed 2·14 million (1·53–2·82) DALYs, or 0·5% (0·4–0·6) of total neurological DALYs; neurodevelopmental and paediatric conditions contributed 80·3 million (69·6–92·5) DALYs, or 18·2% (15·3–21·2); and other conditions that include neurological health loss contributed 48·1 million (34·1–64·8) DALYs, or 10·8% (8·1–13·6) of total neurological DALYs. The percentage contribution of original and newly added groups of conditions to total DALYs is shown in the appendix (p 67). The original category of 15 conditions would have still een the top-ranked contributor to global DALYs in GBD 2021 even without the addition of new conditions. The expanded category was also the first-ranked contributor to global YLDs, followed by musculoskeletal disorders (unpublished estimates, GBD 2021 Diseases and Injuries Collaborators).

For total nervous system health loss, global DALY counts increased by 18·2% (95% UI 8·7 to 26·7), from 375 million (339–419) DALYs in 1990 to 443 million (378–521) DALYs in 2021 (table 2). By contrast, age-standardised DALY rates decreased by 27·0% (21·5 to 32·4), from 7712·5 (6965·3 to 8626·0) per 100000 people in 1990 to 5637·6 (4829·7 to 6587·9) per 100000 people in 2021. Global YLLs remained almost constant, with a change of −3·1% (−11·8 to 7·7) from 284 million (268 to 302) YLLs in 1990 to 275 million (247 to 316) in 2021. By contrast, age-standardised YLL rates decreased 39·0% (33·2 to 44·3), from 5853·3 (5525·9 to 6272·7) per 100000 people in 1990 to 3573·3 (3190·9 to 4134·3) per 100000 people in 2021. Global YLDs increased 85·6% (75·8 to 98·0), from 91·0 million (58·6 to 134) YLDs in 1990 to 168 million (114 to 243) in 2021. Age-standardised YLDs rates increased by 11·2% (7·2 to 16·3), from 1859·4 (1217·7 to 2701·4) per 100000 people in 1990 to 2064·1 (1390·0 to 2983·1) per 100000 people in 2021 (table 2; appendix pp 68–69).

Regionally, age-standardised DALY rates were highest in western sub-Saharan Africa (8190·6 [95% UI 6986·0–9548·9] per 100000 people) and central sub-Saharan Africa (7967·5 [6665·8–9546·6] per 100000 people) and lowest in Australasia (2882·6 [2253·6–3717·3] per 100000 people) and high-income Asia Pacific (2984·6 [2359·4–3768·2] per 100000 people; appendix pp 70–78), with large differences observed for children younger than 5 years. For example, DALY rates for children younger than 5 years were approximately 18-fold higher in western sub-Saharan Africa (29334·5 [23721·8–35170·5]) than in Australasia (1604·1 [1405·5–1846·4]), driven by conditions including neonatal encephalopathy, meningitis, and encephalitis. Age-standardised YLDs were similar between regions, ranging from a minimum in east Asia of 1698·6 (1133·9–2416·0) per 100000 people to a maximum in the

Caribbean of 2327·5 (1571·2–3295·6) per 100000 people. Age-standardised YLLs had greater regional variation, ranging from a minimum in Australasia of 1098·9 (910·3–1456·4) to a maximum in western sub-Saharan Africa of 6163·8 (5131·0–7314·6; appendix pp 70–79). Using World Bank income levels, 81·9% (77·5–84·9; 9·10 million of 11·1 million) of deaths and 84·7% (83·1–86·3; 375 million of 443 million) of DALYs attributable to neurological conditions were in LMICs.

The ten conditions that accounted for the greatest nervous system DALYs in 2021 were stroke, neonatal encephalopathy, migraine, Alzheimer's disease and other dementias, diabetic neuropathy, meningitis, epilepsy, neurological complications due to preterm birth, autism spectrum disorder, and nervous system cancer, with stroke being the greatest contributor globally and in 19 of 21 GBD regions (table 2; figure 1). Notably, four of the top ten conditions were not included in our previous analyses of neurological burden: neonatal encephalopathy, diabetic neuropathy, neurological complications due to preterm birth, and autism spectrum disorder, which emphasises the effects of early life and childhood conditions on total nervous system health loss and the under-recognised effects on the peripheral nervous system.

Regional rankings across conditions were mostly consistent (figure 1). Exceptions included regional variation for meningitis (regional ranking range: third to 22nd), tetanus (range: 11th to 35th), multiple sclerosis (range: 15th to 31st), and motor neuron disease (range: 15th to 34th). Some infectious disease rankings reflected their regional pathogen endemicity (eg, cerebral malaria, neurocysticercosis, and neurological complications due to congenital Zika syndrome).

For children younger than 5 years, the three leading causes of DALYs globally were neonatal encephalopathy (8316·7 [95% UI 7072·6–9991·8] per 100000 people), meningitis (1234·9 [869·5–1741·7] per 100000 people), and neural tube defects (722·6 [580·8–899·4] per 100000 people). For older children and adolescents aged 5–19 years, the three leading causes of DALYs were migraine (380·0 [24·7–946·6] per 100000 people), neurological complications due to preterm birth (234·3 [168·4–305·2] per 100000 people), and epilepsy (185·1 [137·0–261·7] per 100000 people). For adults aged 20–59 years, the leading causes were stroke (1126·1 [1035·5–1218·4] per 100000 people), migraine (750·8 [117·3–1617·8] per 100000 people), and diabetic neuropathy (260·5 [171·9–387·6] per 100000 people), and for adults aged 60–79 years, the leading causes were stroke (8490·9 [7827·5–9108·6] per 100000 people), Alzheimer's disease and other dementias (1504·2 [746·6–3345·6] per 100000 people), and diabetic neuropathy (1397·3 [911·8–1930·8] per 100000 people). For adults aged 80 years and older, the leading causes were stroke (20336·1 [17762·6–22137·4] per 100000 people), Alzheimer's disease and other

Indore Institute of Pharmacy, INDORE (M.P.)

192

	Counts (thousands)		Age-standardised rate (per 100 000 people)				
	2021	Percentage change, 1990–2021	2021	Percentage change, 1990–2021	Females	Males	Female-to-male ratio*
All neurological conditions							
DALYs	443 000 (378 000 to 521 000)	18·2% (8·7 to 26·7)	5637·6 (4829·7 to 6587·9)	−27·0% (−32·4 to −21·5)	5185·8 (4281·2 to 6262·9)	6101·0 (5320·2 to 6982·7)	0·85 (0·78 to 0·93)
YLDs	168 000 (114 000 to 243 000)	85·6% (75·8 to 98·0)	2064·1 (1390·0 to 2983·1)	11·2% (7·2 to 16·3)	2078·2 (1301·3 to 3133·1)	2043·6 (1439·2 to 2832·7)	1·01 (0·88 to 1·14)
YLLs	275 000 (247 000 to 316 000)	−3·1% (−11·8 to 7·7)	3573·3 (3190·9 to 4134·3)	−39·0% (−44·3 to −33·2)	3107·4 (2755·1 to 3604·8)	4057·2 (3574·4 to 4576·6)	0·77 (0·71 to 0·84)
Prevalence	3 400 000 (3 200 000 to 3 620 000)	58·8% (56·3 to 61·5)	41 204·1 (38 654·3 to 43 869·9)	1·5% (0·7 to 2·4)	43 458·5 (40 796·2 to 46 078·7)	38 949·0 (36 503·4 to 41 604·7)	1·12 (1·10 to 1·14)
Deaths	11 100 (9750 to 13 800)	41·2% (28·1 to 58·8)	139·0 (121·3 to 173·3)	−33·6% (−38·8 to −27·6)	125·0 (105·1 to 161·2)	154·6 (136·0 to 186·7)	0·81 (0·73 to 0·90)
Alzheimer's disease and other dementias							
DALYs	36 300 (17 200 to 77 400)	168·7% (156·3 to 179·9)	450·9 (212·9 to 956·8)	1·7% (−2·8 to 5·1)	504·8 (241·5 to 1062·7)	372·4 (170·8 to 806·4)	1·37 (1·26 to 1·46)
YLDs	11 600 (7960 to 15 300)	162·7% (157·0 to 168·0)	141·9 (97·7 to 187·2)	2·6% (1·1 to 3·6)	161·9 (110·7 to 214·8)	114·4 (78·5 to 151·2)	1·42 (1·33 to 1·49)
YLLs	24 700 (6370 to 65 700)	173·4% (153·2 to 192·5)	308·9 (78·9 to 789·0)	1·4% (−4·1 to 7·4)	342·9 (89·2 to 872·0)	258·0 (62·8 to 674·5)	1·36 (1·22 to 1·47)
Prevalence	56 900 (49 400 to 65 000)	160·8% (156·1 to 165·9)	694·0 (602·9 to 794·1)	3·2% (1·7 to 4·2)	769·9 (670·7 to 877·6)	589·5 (507·5 to 678·8)	1·31 (1·28 to 1·35)
Deaths	1950 (503 to 5080)	198·3% (175·2 to 221·8)	25·2 (6·7 to 64·4)	1·5% (−4·0 to 7·1)	27·9 (7·5 to 70·1)	20·7 (5·2 to 55·1)	1·38 (1·24 to 1·49)
Attention deficit hyperactivity disorder							
YLDs	1030 (572 to 1670)	18·7% (14·8 to 22·8)	13·5 (7·4 to 21·9)	−9·6% (−11·9 to −7·3)	7·7 (4·2 to 12·7)	19·0 (10·4 to 30·7)	0·40 (0·38 to 0·43)
Prevalence	84 800 (63 400 to 117 000)	18·8% (14·9 to 23·2)	1108·9 (828·7 to 1536·2)	−9·7% (−11·8 to −7·4)	636·0 (467·9 to 879·0)	1561·7 (1172·5 to 2151·7)	0·41 (0·39 to 0·43)
Autism spectrum disorder							
YLDs	11 500 (7840 to 16 300)	46·7% (44·5 to 48·5)	147·6 (100·2 to 208·1)	2·1% (0·6 to 3·4)	94·5 (64·6 to 133·1)	199·8 (136·3 to 281·7)	0·47 (0·46 to 0·49)
Prevalence	61 800 (52 100 to 72 700)	47·5% (45·1 to 49·4)	788·3 (663·8 to 927·2)	2·0% (0·4 to 3·1)	508·1 (424·6 to 604·3)	1064·7 (898·5 to 1245·7)	0·48 (0·46 to 0·50)
Cerebral malaria							
YLDs	407 (296 to 514)	109·1% (98·6 to 120·1)	5·3 (3·9 to 6·7)	53·6% (45·6 to 61·5)	5·6 (4·1 to 7·1)	5·0 (3·6 to 6·3)	1·12 (1·08 to 1·16)
Prevalence	996 (923 to 1070)	122·2% (116·4 to 128·1)	12·9 (12·0 to 13·9)	63·0% (58·7 to 67·4)	13·8 (12·7 to 14·9)	12·1 (11·2 to 13·1)	1·14 (1·13 to 1·15)
Congenital birth defects†							
YLDs	1450 (676 to 2750)	53·4% (48·3 to 58·4)	18·7 (8·8 to 35·4)	8·9% (5·5 to 12·4)	15·9 (7·4 to 30·4)	21·4 (10·2 to 39·9)	0·74 (0·69 to 0·80)
Prevalence	13 900 (7980 to 21 600)	56·0% (51·6 to 60·4)	180·2 (104·5 to 278·7)	11·4% (8·6 to 14·5)	157·0 (90·4 to 243·6)	203·0 (118·0 to 315·0)	0·77 (0·73 to 0·81)
Congenital Zika syndrome†							
YLDs	0·100 (0·100 to 0·100)	100·0% (100·0 to 100·0)	0·0 (0·0 to 0·0)	100·0% (100·0 to 100·0)	0·0 (0·0 to 0·0)	0·0 (0·0 to 0·0)	0·97 (0·93 to 1·02)
Prevalence	0·100 (0·100 to 0·200)	100·0% (100·0 to 100·0)	0·0 (0·0 to 0·0)	100·0% (100·0 to 100·0)	0·0 (0·0 to 0·0)	0·0 (0·0 to 0·0)	0·97 (0·97 to 0·97)
COVID-19†							
YLDs	2480 (87·2 to 7990)	100% (100 to 100)	29·4 (1·1 to 101·1)	100·0% (100·0 to 100·0)	36·9 (1·0 to 122·8)	19·7 (0·9 to 75·0)	1·84 (0·97 to 3·35)
Prevalence	23 400 (4110 to 72 800)	100% (100 to 100)	288·5 (50·5 to 899·2)	100·0% (100·0 to 100·0)	370·9 (64·3 to 1175·0)	205·7 (35·8 to 608·9)	1·87 (1·32 to 2·61)
Cystic echinococcosis†							
YLDs	4·60 (2·90 to 7·00)	21·1% (−0·3 to 48·3)	0·1 (0·0 to 0·1)	−24·7% (−37·7 to −9·2)	0·1 (0·0 to 0·1)	0·1 (0·0 to 0·1)	1·21 (1·14 to 1·27)

193

	Counts (thousands)		Age-standardised rate (per 100 000 people)				
	2021	Percentage change, 1990–2021	2021	Percentage change, 1990–2021	Females	Males	Female-to-male ratio
(Continued from previous page)							
Prevalence	15·1 (11·5 to 19·3)	45·2% (27·9 to 60·2)	0·2 (0·1 to 0·2)	–10·7% (–19 to –2·0)	0·2 (0·2 to 0·3)	0·2 (0·1 to 0·2)	1·21 (1·14 to 1·27)
Diabetic neuropathy							
YLDs	26 300 (18 000 to 37 400)	309·1% (296·2 to 320·4)	694·0 (602·9 to 794·1)	91·9% (86·3 to 97·3)	769·9 (670·7 to 877·6)	589·5 (507·5 to 678·8)	0·92 (0·89 to 0·94)
Prevalence	206 000 (171 000 to 249 000)	310·5% (297·4 to 322·3)	301·9 (207·0 to 429·4)	92·2% (86·4 to 97·7)	289·7 (198·4 to 410·9)	315·9 (216·4 to 449·9)	0·95 (0·92 to 0·97)
Down syndrome†							
YLDs	135 (89·8 to 194)	–4·5% (–11·8 to 3·0)	1·8 (1·2 to 2·6)	–24·2% (–29·7 to –18·3)	1·7 (1·2 to 2·5)	1·9 (1·2 to 2·7)	0·93 (0·92 to 0·95)
Prevalence	1490 (1240 to 1780)	–5·4% (–12·6 to 2·3)	20·0 (16·7 to 24·0)	–24·6% (–30·2 to –18·6)	19·3 (16·1 to 22·9)	20·7 (17·2 to 25·0)	0·93 (0·91 to 0·94)
Encephalitis							
DALYs	4950 (4150 to 5700)	–17·8% (–33·4 to 4·0)	67·4 (55·7 to 78·3)	–35·7% (–47·8 to –19·0)	67·2 (58·4 to 78·2)	67·7 (50·6 to 83·5)	1·01 (0·76 to 1·26)
YLDs	497 (354 to 658)	5·0% (0·0 to 10·5)	6·2 (4·4 to 8·2)	–29·9% (–33·2 to –26·6)	6·1 (4·3 to 8·1)	6·3 (4·5 to 8·4)	0·96 (0·93 to 1·00)
YLLs	4460 (3690 to 5280)	–19·7% (–36·4 to 4·6)	61·2 (49·9 to 72·9)	–36·2% (–49·1 to –17·9)	61·2 (51·9 to 71·1)	61·4 (44·2 to 76·2)	1·01 (0·74 to 1·31)
Prevalence	4640 (3250 to 6000)	0·7% (–3·0 to 5·3)	57·3 (40·2 to 73·9)	–35·6% (–38·2 to –3·02)	54·7 (38·7 to 70·3)	59·9 (41·7 to 77·7)	0·91 (0·90 to 0·93)
Deaths	92·0 (79·0 to 108)	9·9% (–8·9 to 36·4)	1·2 (1·0 to 1·4)	–26·1% (–38·0 to –8·3)	1·2 (1·0 to 1·4)	1·2 (0·9 to 1·5)	0·98 (0·69 to 1·27)
Epilepsy							
DALYs	14 400 (11 000 to 18 500)	22·5% (7·7 to 38·7)	183·9 (141·0 to 237·2)	–14·6% (–24·6 to –3·9)	160·4 (118·3 to 212·2)	207·2 (161·9 to 262·2)	0·77 (0·67 to 0·86)
YLDs	7760 (4660 to 11 800)	35·6% (7·1 to 67·6)	98·9 (59·8 to 149·8)	–7·1% (–25·8 to 13·7)	94·4 (57·0 to 142·9)	103·6 (62·4 to 157·5)	0·91 (0·89 to 0·94)
YLLs	6610 (5450 to 7340)	10·7% (–0·6 to 24·4)	85·0 (70·7 to 95·0)	–21·6% (–29·6 to –12·5)	66·0 (47·6 to 76·6)	103·6 (84·2 to 117·2)	0·64 (0·45 to 0·78)
Prevalence	24 400 (18 600 to 30 800)	57·4% (30·6 to 85·6)	308·9 (236·2 to 390·1)	6·2% (–10·5 to 24·1)	294·6 (224·6 to 373·7)	323·8 (249·0 to 406·4)	0·91 (0·89 to 0·93)
Deaths	140 (116 to 153)	34·2% (23·3 to 45·8)	1·7 (1·5 to 1·9)	–15·7% (–22·5 to –8·8)	1·4 (1·0 to 1·5)	2·1 (1·8 to 2·4)	0·64 (0·46 to 0·76)
Fetal alcohol syndrome							
YLDs	23·6 (13·8 to 37·0)	24·0% (14·8 to 32·1)	0·3 (0·2 to 0·5)	–11·1% (–17·4 to –5·4)	0·3 (0·2 to 0·5)	0·3 (0·2 to 0·5)	0·91 (0·84 to 0·99)
Prevalence	517 (374 to 677)	33·7% (28·4 to 37·9)	6·7 (4·9 to 8·8)	–4·7% (–8·2 to –1·8)	6·2 (4·7 to 8·0)	7·1 (5·1 to 9·5)	0·88 (0·83 to 0·99)
Guillain–Barré syndrome							
YLDs	49·0 (31·6 to 72·5)	71·3% (61·4 to 81·9)	0·6 (0·4 to 0·9)	5·7% (3·3 to 8·2)	0·6 (0·4 to 0·8)	0·7 (0·4 to 1·0)	0·86 (0·84 to 0·89)
Prevalence	166 (134 to 201)	71·3% (61·4 to 81·9)	2·0 (1·7 to 2·5)	5·7% (3·3 to 8·2)	1·9 (1·5 to 2·3)	2·2 (1·8 to 2·7)	0·86 (0·84 to 0·89)
Idiopathic intellectual disability							
YLDs	3810 (1760 to 6520)	16·3% (10·5 to 22·3)	49·9 (23·2 to 85·4)	–13·6% (–18·0 to –8·4)	51·5 (25·5 to 85·6)	48·3 (20·8 to 84·7)	1·08 (1·00 to 1·20)
Prevalence	88 300 (47 100 to 129 000)	10·2% (5·7 to 13·7)	1157·2 (620·9 to 1688·1)	–18·0% (–21·1 to –15·7)	1204·4 (688·7 to 1708·4)	1110·5 (554·5 to 1667·2)	1·10 (1·02 to 1·24)
Klinefelter syndrome†							
YLDs	3·00 (1·50 to 5·80)	30·5% (24·1 to 37·3)	0·0 (0·0 to 0·0)	2·7% (–1·7 to 6·7)	NA	0·0 (0·0 to 0·1)	NA
Prevalence	230 (158 to 320)	30·2% (25·7 to 34·6)	3·1 (2·1 to 4·3)	2·7% (1·3 to 4·2)	NA	6·1 (4·2 to 8·4)	NA

(Table 2 continues on next page)

	Counts (thousands)		Age-standardised rate (per 100 000 people)				
	2021	Percentage change, 1990–2021	2021	Percentage change, 1990–2021	Females	Males	Female-to-male ratio
(Continued from previous page)							
Meningitis							
DALYs	14 500 (11 500 to 18 700)	−56·0% (−63·6 to −45·5)	208·5 (163·6 to 270·8)	−62·1% (−68·9 to −52·8)	193·3 (155·1 to 245·0)	223·0 (167·7 to 302·2)	0·87 (0·69 to 1·03)
YLDs	603 (425 to 791)	−31·3% (−34·3 to −28·0)	7·8 (5·5 to 10·2)	−51·7% (−53·8 to −49·4)	7·6 (5·4 to 10·0)	7·9 (5·6 to 10·4)	0·97 (0·95 to 1·00)
YLLs	13 900 (11 000 to 18 000)	−56·7% (−64·2 to −45·8)	200·7 (156·5 to 262·5)	−62·5% (−69·3 to −52·9)	185·7 (146·9 to 236·1)	215·1 (160·0 to 294·1)	0·87 (0·68 to 1·03)
Prevalence	7270 (5930 to 9070)	−35·5% (−38·2 to −32·7)	92·3 (75·2 to 114·8)	−56·8% (−58·6 to −55·1)	88·5 (72·5 to 109·7)	96·1 (78·2 to 120·0)	0·92 (0·91 to 0·93)
Deaths	214 (177 to 266)	−49·0% (−56·6 to −38·2)	2·9 (2·4 to 3·7)	−60·2% (−66·3 to −51·7)	2·7 (2·2 to 3·4)	3·2 (2·5 to 4·1)	0·87 (0·70 to 0·99)
Migraine							
YLDs	43 400 (6740 to 95 100)	58·9% (53·7 to 66·0)	532·7 (80·7 to 1167·8)	0·6% (−4·0 to 2·6)	662·8 (93·8 to 1450·9)	403·9 (67·5 to 872·6)	1·62 (1·39 to 1·79)
Prevalence	1 160 000 (996 000 to 1 330 000)	58·2% (54·4 to 62·6)	14 246·5 (12 194·1 to 16 378·7)	1·6% (0·3 to 2·6)	17 902·6 (15 446·0 to 20 487·0)	10 624·2 (9039·5 to 12 297·3)	1·69 (1·65 to 1·73)
Motor neuron disease							
DALYs	1040 (962 to 1120)	105·8% (87·1 to 125·9)	12·2 (11·2 to 13·2)	8·5% (−0·6 to 18·6)	10·1 (9·3 to 11·1)	14·4 (13·0 to 15·7)	0·70 (0·62 to 0·77)
YLDs	57·9 (40·7 to 78·0)	68·4% (61·6 to 75·9)	0·7 (0·5 to 1·0)	−1·4% (−3·4 to 0·7)	0·6 (0·4 to 0·9)	0·8 (0·5 to 1·0)	0·83 (0·81 to 0·86)
YLLs	983 (903 to 1070)	108·6% (88·7 to 130·2)	11·5 (10·5 to 12·4)	9·2% (−0·5 to 20·0)	9·4 (8·7 to 10·5)	13·7 (12·2 to 15·0)	0·69 (0·61 to 0·77)
Prevalence	273 (236 to 314)	68·6% (61·8 to 76·2)	3·3 (2·9 to 3·8)	−1·3% (−3·3 to 0·9)	3·0 (2·6 to 3·5)	3·6 (3·2 to 4·2)	0·83 (0·81 to 0·85)
Deaths	39·1 (35·6 to 42·4)	156·2% (136·0 to 178·6)	0·5 (0·4 to 0·5)	19·9% (10·9 to 30·1)	0·4 (0·3 to 0·4)	0·5 (0·5 to 0·6)	0·69 (0·62 to 0·77)
Multiple sclerosis							
DALYs	973 (836 to 1130)	69·5% (63·5 to 75·6)	11·4 (9·7 to 13·2)	−11·0% (−14 to −8·0)	14·5 (12·4 to 16·9)	8·1 (7·0 to 9·5)	1·80 (1·72 to 1·87)
YLDs	484 (344 to 631)	86·5% (78·9 to 94·5)	5·7 (4·0 to 7·4)	−0·4% (−3·9 to 3·1)	7·5 (5·3 to 9·7)	3·9 (2·7 to 5·1)	1·93 (1·86 to 2·00)
YLLs	490 (465 to 513)	55·7% (47·3 to 63·9)	5·7 (5·4 to 6·0)	−19·5% (−23·5 to −15·1)	7·1 (6·7 to 7·6)	4·2 (4·0 to 4·5)	1·68 (1·54 to 1·80)
Prevalence	1890 (1690 to 2110)	88·1% (80·8 to 95·5)	22·2 (19·8 to 24·8)	−0·3% (−3·6 to 3·3)	29·3 (26·2 to 32·7)	14·7 (13·0 to 16·6)	1·99 (1·94 to 2·05)
Deaths	16·3 (15·3 to 17·0)	79·1% (69·2 to 88·6)	0·2 (0·2 to 0·2)	−12·7% (−17·4 to −8·3)	0·2 (0·2 to 0·2)	0·1 (0·1 to 0·2)	1·59 (1·46 to 1·70)
Neonatal encephalopathy							
DALYs	58 600 (50 100 to 69 000)	−27·5% (−39·5 to −14·5)	932·1 (797·5 to 1101·7)	−26·5% (−38·9 to −13·0)	795·2 (675·1 to 942·3)	1060·2 (889·7 to 1259·1)	0·75 (0·67 to 0·87)
YLDs	4280 (3100 to 5590)	189·1% (61·5 to 348·9)	55·2 (39·9 to 72·1)	107·0% (16·2 to 220·4)	45·3 (32·5 to 59·5)	64·7 (46·7 to 84·3)	0·70 (0·68 to 0·72)
YLLs	54 300 (46 000 to 64 900)	−31·5% (−43·9 to −17·9)	876·9 (743·6 to 1056·6)	−29·2% (−42·0 to −15·3)	749·9 (627·7 to 895·0)	995·6 (824·7 to 1193·6)	0·76 (0·67 to 0·88)
Prevalence	18 600 (16 100 to 21 100)	175·2% (94·9 to 246·8)	238·1 (206·3 to 269·7)	91·2% (37·2 to 139·8)	188·4 (163·5 to 213·3)	286·6 (248·7 to 325·4)	0·66 (0·65 to 0·67)
Deaths	604 (511 to 722)	−31·5% (−44·0 to −17·9)	9·7 (8·3 to 11·7)	−29·2% (−42·0 to −15·3)	8·3 (7·0 to 10·0)	11·1 (9·2 to 13·3)	0·76 (0·67 to 0·88)
Neonatal jaundice†							
YLDs	718 (517 to 917)	80·0% (69·8 to 90·3)	9·3 (6·7 to 11·9)	31·5% (24·3 to 39·0)	9·5 (6·8 to 12·1)	9·2 (6·6 to 11·8)	1·03 (1·01 to 1·05)
Prevalence	1960 (1800 to 2160)	102·7% (95·8 to 109·0)	25·5 (23·4 to 28·2)	48·8% (43·8 to 53·5)	25·6 (23·5 to 28·2)	25·4 (23·3 to 28·1)	1·01 (1·00 to 1·02)

(Table 2 continues on next page)

195

	Counts (thousands)		Age-standardised rate (per 100 000 people)				
	2021	Percentage change, 1990–2021	2021	Percentage change, 1990–2021	Females	Males	Female-to-male ratio
(Continued from previous page)							
Neonatal sepsis†							
YLDs	2490 (1570 to 3590)	136·5% (32·3 to 322·0)	32·3 (20·3 to 46·5)	70·4% (−4·5 to 203·1)	27·0 (17·1 to 38·7)	37·3 (23·5 to 54·0)	0·72 (0·71 to 0·74)
Prevalence	7100 (5140 to 9260)	153·8% (51·5 to 332·6)	92·1 (66·8 to 120·1)	83·3% (9·5 to 212·0)	75·2 (54·7 to 97·7)	108·3 (78·3 to 141·4)	0·69 (0·69 to 0·70)
Nervous system cancer							
DALYs	9200 (7890 to 10 600)	50·2% (29·1 to 69·0)	111·8 (95·5 to 129·3)	−8·9% (−20·8 to 1·5)	96·8 (86·4 to 107·3)	127·5 (97·7 to 162·0)	0·77 (0·60 to 1·00)
YLDs	132 (93·8 to 174)	111·8% (89·2 to 133·2)	1·6 (1·1 to 2·1)	22·5% (9·0 to 34·4)	1·5 (1·0 to 2·0)	1·7 (1·2 to 2·3)	0·86 (0·70 to 1·08)
YLLs	9070 (7750 to 10 500)	49·6% (28·4 to 67·8)	110·3 (93·9 to 127·4)	−9·2% (−21·2 to 1·0)	95·3 (85·1 to 105·7)	125·8 (96·3 to 159·7)	0·77 (0·60 to 1·00)
Prevalence	1030 (907 to 1140)	117·1% (92·0 to 140·4)	12·8 (11·2 to 14·2)	37·7% (22·5 to 51·3)	12·5 (11·1 to 13·9)	13·2 (10·4 to 15·9)	0·95 (0·78 to 1·21)
Deaths	264 (226 to 302)	90·3% (67·8 to 110·7)	3·1 (2·7 to 3·6)	1·3% (−9·8 to 11·9)	2·7 (2·4 to 3·0)	3·6 (2·8 to 4·4)	0·75 (0·59 to 0·96)
Neural tube defects							
DALYs	5300 (4310 to 6510)	−47·3% (−59·0 to −24·7)	83·2 (67·8 to 102·5)	−47·7% (−59·5 to −25·1)	88·2 (64·3 to 118·1)	78·5 (61·6 to 104·5)	1·14 (0·72 to 1·61)
YLDs	333 (229 to 456)	11·8% (5·2 to 18·1)	4·5 (3·1 to 6·2)	−11·0% (−16·3 to −6·2)	4·6 (3·1 to 6·2)	4·4 (3·1 to 6·1)	1·03 (1·00 to 1·06)
YLLs	4970 (3980 to 6430)	−49·1% (−61·3 to −26·5)	78·7 (62·8 to 98·6)	−49·0% (−61·1 to −26·2)	83·7 (60·7 to 114·3)	74·1 (56·9 to 100·2)	1·15 (0·71 to 1·65)
Prevalence	1130 (965 to 1310)	11·2% (4·4 to 17·7)	15·2 (13·0 to 17·6)	−12·2% (−17·1 to −7·6)	15·4 (13·2 to 17·8)	15·0 (12·8 to 17·3)	1·03 (1·00 to 1·06)
Deaths	56·4 (45·3 to 72·8)	−48·6% (−60·9 to −25·7)	0·9 (0·7 to 1·1)	−48·8% (−61·0 to −26·0)	0·9 (0·7 to 1·3)	0·8 (0·6 to 1·1)	1·15 (0·71 to 1·66)
Neurocysticercosis							
DALYs	1240 (788 to 1810)	14·2% (−2·4 to 34·5)	14·6 (9·3 to 21·3)	−38·4% (−46·7 to −28·5)	15·6 (9·9 to 22·5)	13·6 (8·8 to 20·0)	1·15 (1·06 to 1·22)
YLDs	1150 (714 to 1730)	18·5% (0·6 to 41·3)	13·6 (8·4 to 20·2)	−37·3% (−46·2 to −27·0)	14·6 (9·1 to 21·5)	12·6 (7·8 to 18·9)	1·17 (1·09 to 1·24)
YLLs	81·3 (54·1 to 119)	−22·0% (−46·6 to 11·3)	1·0 (0·7 to 1·5)	−48·4% (−65·1 to −25·3)	1·0 (0·5 to 1·5)	1·1 (0·6 to 1·7)	0·94 (0·44 to 1·61)
Prevalence	4360 (3150 to 5720)	43·7% (31·2 to 59·2)	51·3 (37·2 to 67·3)	−25·1% (−29·0 to −19·7)	55·5 (40·3 to 71·9)	46·9 (33·7 to 63·1)	1·19 (1·11 to 1·25)
Deaths	1·60 (1·10 to 2·30)	−16·7% (−43·8 to 17·7)	0·0 (0·0 to 0·0)	−50·0% (−66·2 to −28·5)	0·0 (0·0 to 0·0)	0·0 (0·0 to 0·0)	0·93 (0·48 to 1·53)
Neurosyphilis							
YLDs	64·9 (42·2 to 93·4)	17·3% (4·8 to 31·0)	0·8 (0·5 to 1·2)	−18·5% (−27·0 to −9·4)	0·8 (0·5 to 1·1)	0·9 (0·6 to 1·3)	0·89 (0·83 to 0·94)
Prevalence	696 (563 to 857)	38·5% (25·0 to 53·3)	8·8 (7·1 to 10·8)	−6·1% (−15·5 to 4·0)	8·6 (6·9 to 10·6)	9·0 (7·3 to 11·0)	0·95 (0·93 to 0·97)
Other chromosomal anomalies†							
YLDs	295 (196 to 417)	7·3% (2·3 to 12·4)	4·1 (2·7 to 5·7)	−12·8% (−16·8 to −8·7)	3·3 (2·2 to 4·7)	4·7 (3·1 to 6·9)	0·71 (0·59 to 0·86)
Prevalence	3280 (2880 to 3760)	6·2% (0·9 to 11·2)	45·2 (39·5 to 52·0)	−13·0% (−17·2 to −9·0)	37·0 (32·4 to 43·0)	52·8 (44·2 to 62·9)	0·71 (0·59 to 0·85)
Other neurological disorders							
DALYs	4360 (3630 to 5270)	131·0% (107·3 to 155·5)	54·8 (45·3 to 66·6)	50·7% (35·4 to 65·5)	51·8 (42·7 to 63·2)	57·8 (48·0 to 69·4)	0·90 (0·84 to 0·96)
YLDs	2030 (1330 to 2870)	153·8% (110·9 to 197·8)	25·5 (16·8 to 36·6)	70·6% (43·8 to 98·8)	25·3 (16·6 to 36·2)	25·6 (16·8 to 36·9)	0·99 (0·96 to 1·02)
YLLs	2330 (2080 to 2590)	116·0% (83·3 to 140·8)	29·3 (25·9 to 31·4)	37·6% (18·3 to 52·7)	26·3 (22·7 to 28·9)	32·0 (29·0 to 34·8)	0·82 (0·74 to 0·93)

(Table 2 continues on next page)

196

References
1. Feigin VL, Nichols E, Alam T, et al. Global, regional, and national burden of neurological disorders, 1990–2016: a systematic analysis for the Global Burden of Disease Study 2016. Lancet Neurol 2019; 18: 459–80.
2. WHO. Optimizing brain health across the life course: WHO position paper. Aug 9, 2022. https://www.who.int/publications/i/item/9789240054561 (accessed Nov 16, 2022).
3. WHO. Intersectoral global action plan on epilepsy and other neurological disorders 2022–2031. 2023. https://apps.who.int/iris/handle/10665/371495 (accessed Feb 9, 2024).
4. Feigin VL, Abajobir AA, Abate KH, et al. Global, regional, and national burden of neurological disorders during 1990–2015: a systematic analysis for the Global Burden of Disease Study 2015. Lancet Neurol 2017; 16: 877–97.
5. Kang S, Eum S, Chang Y, et al. Burden of neurological diseases in Asia from 1990 to 2019: a systematic analysis using the Global Burden of Disease Study data. BMJ Open 2022; 12: e059548.
6. Ding C, Wu Y, Chen X, et al. Global, regional, and national burden and attributable risk factors of neurological disorders: the Global Burden of Disease study 1990–2019. Front Public Health 2022; published online Nov 29. https://doi.org/10.3389/fpubh.2022.952161.
7. Newton CR. Global burden of pediatric neurological disorders. Semin Pediatr Neurol 2018; 27: 10–15.
8. WHO. Neurology and COVID-19: scientific brief. 29 September 2021. Sept 29, 2021. https://apps.who.int/iris/handle/10665/345574 (accessed March 14, 2023).
9. Wulf Hanson S, Abbafati C, Aerts JG, et al. Estimated global proportions of individuals with persistent fatigue, cognitive, and respiratory symptom clusters following symptomatic COVID-19 in 2020 and 2021. JAMA 2022; 328: 1604–15.
10. Guerrero Saldivia SE, Unnikrishnan S, Chavarria YY, et al. Zika virus: a systematic review of teratogenesis, congenital anomalies, and child mortality. Cureus 2023; 15: e34735.

197

11 Cheng Y, Tran Minh N, Tran Minh Q, Khandelwal S, Clapham HE. Estimates of Japanese encephalitis mortality and morbidity: a systematic review and modeling analysis. *PLoS Negl Trop Dis* 2022; 16: e0010361.

12 Patel H, Sander B, Nelder MP. Long-term sequelae of West Nile virus-related illness: a systematic review. *Lancet Infect Dis* 2015; 15: 951–59.

13 Muñoz LS, Garcia MA, Gordon-Lipkin E, Parra B, Pardo CA. Emerging viral infections and their impact on the global burden of neurological disease. *Semin Neurol* 2018; 38: 163–75.

14 Olusanya BO, Davis AC, Wertlieb D, et al. Developmental disabilities among children younger than 5 years in 195 countries and territories, 1990–2016: a systematic analysis for the Global Burden of Disease Study 2016. *Lancet Glob Health* 2018; 6: e1100–21.

15 Vos T, Lim SS, Abbafati C, et al. Global burden of 369 diseases and injuries in 204 countries and territories, 1990–2019: a systematic analysis for the Global Burden of Disease Study 2019. *Lancet* 2020; 396: 1204–22.

16 Dorsey ER, Elbaz A, Nichols E, et al. Global, regional, and national burden of Parkinson's disease, 1990–2016: a systematic analysis for the Global Burden of Disease Study 2016. *Lancet Neurol* 2018; 17: 939–53.

17 Murray CJL, Aravkin AY, Zheng P, et al. Global burden of 87 risk factors in 204 countries and territories, 1990–2019: a systematic analysis for the Global Burden of Disease Study 2019. *Lancet* 2020; 396: 1223–49.

18 Feigin VL, Vos T, Nichols E, et al. The global burden of neurological disorders: translating evidence into policy. *Lancet Neurol* 2020; 19: 255–65.

19 Mohammadi D. Neurology in resource-poor countries: fighting for funding. *Lancet Neurol* 2011; 10: 953–54.

20 Patel V, Chisholm D, Dua T, Laxminarayan R, Medina-Mora ME. Mental, neurological, and substance use disorders: disease control priorities, third edition (volume 4) Washington, DC: The International Bank for Reconstruction and Development and The World Bank, 2016.

21 Winkler AS. The growing burden of neurological disorders in low-income and middle-income countries: priorities for policy making. *Lancet Neurol* 2020; 19: 200–02.

22 Feigin VL, Stark BA, Johnson CO, et al. Global, regional, and national burden of stroke and its risk factors, 1990–2019: a systematic analysis for the Global Burden of Disease Study 2019. *Lancet Neurol* 2021; 20: 795–820.

23 Nichols E, Steinmetz JD, Vollset SE, et al. Estimation of the global prevalence of dementia in 2019 and forecasted prevalence in 2050: an analysis for the Global Burden of Disease Study 2019. *Lancet Public Health* 2022; 7: e105–25.

24 Amarenco P, Labreuche J. Lipid management in the prevention of stroke: review and updated meta-analysis of statins for stroke prevention. *Lancet Neurol* 2009; 8: 453–63.

25 Wright JT Jr, Williamson JD, Whelton PK, et al. A randomized trial of intensive versus standard blood-pressure control. *N Engl J Med* 2015; 373: 2103–16.

26 Langhorne P, Ramachandra S. Organised inpatient (stroke unit) care for stroke: network meta-analysis. *Cochrane Database Syst Rev* 2020; 4: CD000197.

27 National Institute of Neurological Disorders and Stroke rt-PA Stroke Study Group. Tissue plasminogen activator for acute ischemic stroke. *N Engl J Med* 1995; 333: 1581–87.

28 Goyal M, Demchuk AM, Menon BK, et al. Randomized assessment of rapid endovascular treatment of ischemic stroke. *N Engl J Med* 2015; 372: 1019–30.

29 de Figueiredo A, Johnston IG, Smith DMD, Agarwal S, Larson HJ, Jones NS. Forecasted trends in vaccination coverage and correlations with socioeconomic factors: a global time-series analysis over 30 years. *Lancet Glob Health* 2016; 4: e726–35.

30 Moore SM. The current burden of Japanese encephalitis and the estimated impacts of vaccination: combining estimates of the spatial distribution and transmission intensity of a zoonotic pathogen. *PLoS Negl Trop Dis* 2021; 15: e0009385.

31 Shlobin NA, LoPresti MA, Du RY, Lam S. Folate fortification and supplementation in prevention of folate-sensitive neural tube defects: a systematic review of policy. *J Neurosurg Pediatr* 2020; 27: 294–310.

32 Ssentongo P, Heilbrunn ES, Ssentongo AE, Ssenyonga LVN, Lekoubou A. Birth prevalence of neural tube defects in eastern Africa: a systematic review and meta-analysis. *BMC Neurol* 2022; 22: 202.

33 Bitew ZW, Worku T, Alebel A, Alemu A. Magnitude and associated factors of neural tube defects in Ethiopia: a systematic review and meta-analysis. *Glob Pediatr Health* 2020; 7: X20939423.

34 Abdullahi A, Candan SA, Soysal Tomruk M, et al. Is Guillain–Barré syndrome associated with COVID-19 infection? A systemic review of the evidence. *Front Neurol* 2021; published online Jan 13. https://doi.org/10.3389/fneur.2020.566308.

35 Luijten LWG, Leonhard SE, van der Eijk AA, et al. Guillain-Barré syndrome after SARS-CoV-2 infection in an international prospective cohort study. *Brain* 2021; 144: 3392–404.

36 Keddie S, Pakpoor J, Mousele C, et al. Epidemiological and cohort study finds no association between COVID-19 and Guillain-Barré syndrome. *Brain* 2021; 144: 682–93.

37 WHO. Parkinson disease: a public health approach: technical brief. June 14, 2022. https://www.who.int/publications-detail-redirect/9789240050983 (accessed March 14, 2023).

38 Ong KL, Stafford LK, McLaughlin SA, et al. Global, regional, and national burden of diabetes from 1990 to 2021, with projections of prevalence to 2050: a systematic analysis for the Global Burden of Disease Study 2021. *Lancet* 2023; 402: 203–34.

39 WHO. Atlas: country resources for neurological disorders, 2nd ed. Jan 1, 2017. https://www.who.int/publications-detail-redirect/9789241565509 (accessed March 14, 2023).

40 O'Donnell MJ, Chin SL, Rangarajan S, et al. Global and regional effects of potentially modifiable risk factors associated with acute stroke in 32 countries (INTERSTROKE): a case-control study. *Lancet* 2016; 388: 761–75.

41 Livingston G, Huntley J, Sommerlad A, et al. Dementia prevention, intervention, and care: 2020 report of the Lancet Commission. *Lancet* 2020; 396: 413–46.

42 van Hecke O, Austin SK, Khan RA, Smith BH, Torrance N. Neuropathic pain in the general population: a systematic review of epidemiological studies. *Pain* 2014; 155: 654–62.

43 Knezevic NN, Candido KD, Vlaeyen JWS, Van Zundert J, Cohen SP. Low back pain. *Lancet* 2021; 398: 78–92.

44 Mahdizade Ari M, Mohamadi MH, Shadab Mehr N, et al. Neurological manifestations in patients with COVID-19: a systematic review and meta-analysis. *J Clin Lab Anal* 2022; 36: e24403.

45 Kiani L. Preventing COVID-19 neurological complications. *Nat Rev Neurol* 2022; 18: 699.

46 Beghi E, Moro E, Davidescu EI, et al. Comparative features and outcomes of major neurological complications of COVID-19. *Eur J Neurol* 2023; 30: 413–33.

47 Wiebers DO, Feigin VL, Winkler AS. Brain health, One Health, and COVID-19. *Neuroepidemiology* 2021; 55: 425–26.

48 Beghi E, Feigin V, Caso V, Santalucia P, Logroscino G. COVID-19 infection and neurological complications: present findings and future predictions. *Neuroepidemiology* 2020; 54: 364–69.

49 Kolappa K, Seeher K, Dua T. Brain health as a global priority. *J Neurol Sci* 2022; 439: 120326.

Principal
Indore Institute of Pharmacy,
INDORE (M.P.)
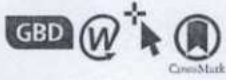
198

Global burden of 288 causes of death and life expectancy decomposition in 204 countries and territories and 811 subnational locations, 1990–2021: a systematic analysis for the Global Burden of Disease Study 2021

GBD 2021 Causes of Death Collaborators*

Summary

Background Regular, detailed reporting on population health by underlying cause of death is fundamental for public health decision making. Cause-specific estimates of mortality and the subsequent effects on life expectancy worldwide are valuable metrics to gauge progress in reducing mortality rates. These estimates are particularly important following large-scale mortality spikes, such as the COVID-19 pandemic. When systematically analysed, mortality rates and life expectancy allow comparisons of the consequences of causes of death globally and over time, providing a nuanced understanding of the effect of these causes on global populations.

Methods The Global Burden of Diseases, Injuries, and Risk Factors Study (GBD) 2021 cause-of-death analysis estimated mortality and years of life lost (YLLs) from 288 causes of death by age-sex-location-year in 204 countries and territories and 811 subnational locations for each year from 1990 until 2021. The analysis used 56604 data sources, including data from vital registration and verbal autopsy as well as surveys, censuses, surveillance systems, and cancer registries, among others. As with previous GBD rounds, cause-specific death rates for most causes were estimated using the Cause of Death Ensemble model—a modelling tool developed for GBD to assess the out-of-sample predictive validity of different statistical models and covariate permutations and combine those results to produce cause-specific mortality estimates—with alternative strategies adapted to model causes with insufficient data, substantial changes in reporting over the study period, or unusual epidemiology. YLLs were computed as the product of the number of deaths for each cause-age-sex-location-year and the standard life expectancy at each age. As part of the modelling process, uncertainty intervals (UIs) were generated using the 2·5th and 97·5th percentiles from a 1000-draw distribution for each metric. We decomposed life expectancy by cause of death, location, and year to show cause-specific effects on life expectancy from 1990 to 2021. We also used the coefficient of variation and the fraction of population affected by 90% of deaths to highlight concentrations of mortality. Findings are reported in counts and age-standardised rates. Methodological improvements for cause-of-death estimates in GBD 2021 include the expansion of under-5-years age group to include four new age groups, enhanced methods to account for stochastic variation of sparse data, and the inclusion of COVID-19 and other pandemic-related mortality—which includes excess mortality associated with the pandemic, excluding COVID-19, lower respiratory infections, measles, malaria, and pertussis. For this analysis, 199 new country-years of vital registration cause-of-death data, 5 country-years of surveillance data, 21 country-years of verbal autopsy data, and 94 country-years of other data types were added to those used in previous GBD rounds.

Findings The leading causes of age-standardised deaths globally were the same in 2019 as they were in 1990; in descending order, these were, ischaemic heart disease, stroke, chronic obstructive pulmonary disease, and lower respiratory infections. In 2021, however, COVID-19 replaced stroke as the second-leading age-standardised cause of death, with 94·0 deaths (95% UI 89·2–100·0) per 100000 population. The COVID-19 pandemic shifted the rankings of the leading five causes, lowering stroke to the third-leading and chronic obstructive pulmonary disease to the fourth-leading position. In 2021, the highest age-standardised death rates from COVID-19 occurred in sub-Saharan Africa (271·0 deaths [250·1–290·7] per 100000 population) and Latin America and the Caribbean (195·4 deaths [182·1–211·4] per 100000 population). The lowest age-standardised death rates from COVID-19 were in the high-income super-region (48·1 deaths [47·4–48·8] per 100000 population) and southeast Asia, east Asia, and Oceania (23·2 deaths [16·3–37·2] per 100000 population). Globally, life expectancy steadily improved between 1990 and 2019 for 18 of the 22 investigated causes. Decomposition of global and regional life expectancy showed the positive effect that reductions in deaths from enteric infections, lower respiratory infections, stroke, and neonatal deaths, among others have contributed to improved survival over the study period. However, a net reduction of 1·6 years occurred in global life expectancy between 2019 and 2021, primarily due to increased death rates from COVID-19 and other pandemic-related mortality. Life expectancy was highly variable between super-regions over the study period, with southeast Asia, east Asia, and Oceania gaining 8·3 years (6·7–9·9) overall, while having the smallest reduction in life expectancy due to COVID-19 (0·4 years). The largest reduction in life expectancy due to COVID-19 occurred in Latin America and the Caribbean (3·6 years). Additionally, 53 of the 288 causes of death were highly concentrated in locations with less than 50% of the global population as of 2021,

199
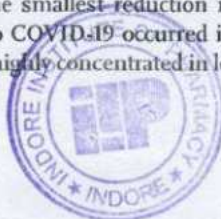
and these causes of death became progressively more concentrated since 1990, when only 44 causes showed this pattern. The concentration phenomenon is discussed heuristically with respect to enteric and lower respiratory infections, malaria, HIV/AIDS, neonatal disorders, tuberculosis, and measles.

Interpretation Long-standing gains in life expectancy and reductions in many of the leading causes of death have been disrupted by the COVID-19 pandemic, the adverse effects of which were spread unevenly among populations. Despite the pandemic, there has been continued progress in combatting several notable causes of death, leading to improved global life expectancy over the study period. Each of the seven GBD super-regions showed an overall improvement from 1990 and 2021, obscuring the negative effect in the years of the pandemic. Additionally, our findings regarding regional variation in causes of death driving increases in life expectancy hold clear policy utility. Analyses of shifting mortality trends reveal that several causes, once widespread globally, are now increasingly concentrated geographically. These changes in mortality concentration, alongside further investigation of changing risks, interventions, and relevant policy, present an important opportunity to deepen our understanding of mortality-reduction strategies. Examining patterns in mortality concentration might reveal areas where successful public health interventions have been implemented. Translating these successes to locations where certain causes of death remain entrenched can inform policies that work to improve life expectancy for people everywhere.

Introduction

For more than three decades, the Global Burden of Diseases, Injuries, and Risk Factors Study (GBD) has been systematically and comprehensively recording and analysing causes of human death stratified by age, sex, and time across the world.[1,2] This information has been used to guide policy solutions, reduce modifiable risk factors, monitor and evaluate national and sub-national health interventions, and ultimately improve health recommendations at both regional and local levels.[1] Assessing trends in cause-specific mortality is essential to inform health policy that must continuously evolve to account for rapid changes to the global health landscape, such as the COVID-19 pandemic.[3] Comprehensive updates to levels and trends in causes of death give insight into emerging global health challenges and can facilitate benchmarking in the case of a new pandemic or other events that can lead to a staggering loss of life. Therefore, documenting novel changes to mortality, such as an emerging pandemic, in real time, is important.

Causes of death are not uniformly distributed between populations; rather, large variability in the leading causes often reflects important social and geographical differences.[4] These differences can include access to and quality of health care, timeliness of health system responsiveness, and exposure to causes that are endemic to specific geographical locations.[4] Mortality patterns continually evolve, as some areas become successful in their reduction efforts, whereas other causes persist within specific locations. The past 30 years have seen improvements among many causes of mortality, some of which have considerably narrowed in geographical range and are now concentrated within smaller areas worldwide. This change enables us to identify the resulting areas of concentrated mortality— areas where deaths from that cause are occurring within

a limited subset of the global population. Our analysis provides an opportunity to answer important epidemiological questions that have been at the forefront of global and public health discourse—eg, which causes have contributed to the largest increase or decrease in life expectancy, which locations are experiencing greater concentrations of preventable causes of death, and how has COVID-19 and other pandemic-related mortality (OPRM) affected life expectancy and the overall fatal burden of diseases? Regional variation in many of the leading causes of death remains evident in these most recent estimates, representing important opportunities for creating tailored health policy to improve disparities and alleviate concentrations of mortality.

GBD 2021 provides an updated, comprehensive set of the fatal burden of disease summarised with cause-specific mortality metrics and years-of-life-lost (YLLs) metrics for 288 causes by age and sex across 204 countries and territories from 1990 to 2021, an update from the previously published estimates covering 1990–2019. In this study, we present mortality concentrations and a decomposition analysis of life expectancy due to different causes of death and illustrate the impact of causes of death on global, regional, and country-specific life expectancy, as well as highlighting locations that are most affected by concentrated geographical mortality burden. As with previous iterations of GBD, this cycle incorporates newly available data sources and improved methodological approaches to re-estimate the entire time series, providing updated estimates that supersede all previous GBD cause-of-death publications. GBD 2021 includes an estimation of several different models for disease and injury outcomes. This manuscript was produced as part of the GBD Collaborator Network and in accordance with the GBD Protocol.[5]

Principal
Indore Institute of Pharmacy,
INDORE (M.P.)

200

Research in context

Evidence before this study

The Global Burden of Diseases, Injuries, and Risk Factors Study (GBD) has provided regular updates on the complex patterns and trends in population health around the world since the first GBD publication in 1993. With each subsequent iteration, there have been important methodological updates, new datasets included, and an expanded list of causes, risk factors, and locations for which estimates of the burden of disease are produced. In 1993, mortality and years of life lost (YLLs) were reported for 107 categories of diseases that covered all possible causes of death, for eight regions. In the last GBD cycle—GBD 2019—estimates of mortality and YLLs were produced for 286 causes of death in 204 countries and territories, including all WHO member states, and for subnational locations in 21 countries and territories, for every year from 1990 to 2019. Although many groups have reported on national-level, cause-specific mortality and other population-health metrics, including the WHO World Health Statistics reports, GBD is the most detailed and transparent research effort to date. Further, estimates of COVID-19-related deaths in 2020 and 2021 have been reported by several sources, including GBD studies that have quantified excess mortality due to the pandemic within a subset of GBD locations. However, no previous publications have quantified the effect of COVID-19 on life expectancy, while considering the full spectrum of disease mortality over the past three decades, across all countries and territories. This study presents, for the first time, 288 causes of death from 1990 to 2021, complementary to the all-cause mortality findings presented in the GBD 2021 Demographics analysis. Combined, these studies provide a comprehensive view of all-cause and cause-specific mortality from 1990 to 2021.

Added value of this study

Alongside the all-cause mortality and life-expectancy assessments in companion publications for GBD 2021, this analysis delineates cause-specific mortality and its effect on life expectancy. This study includes a comprehensive decomposition analysis elucidating the primary cause of death influencing life expectancy on a global, regional, and national level. Additionally, we present causes of death and YLLs for all countries and territories, providing policy makers with valuable insights into variations in cause-specific mortality. This study is also the first of its kind to publish 2021 estimates of COVID-19-related deaths and YLLs for 204 countries and territories in the context of the global burden of disease. Although other publications have estimated deaths due to COVID-19, those deaths have not previously been compared with deaths from other causes. By modelling COVID-19 deaths within a hierarchy

of mutually exclusive and collectively exhaustive causes of death, this study provides policy makers with information that is essential for setting health priorities around the world. To obtain more comprehensive insights from life expectancy, it is necessary to break it down into age-specific mortality, which is influenced by cause-specific mortality rates. We examined the effect of COVID-19 and other causes of death on life expectancy by decomposing death counts into different cause-specific mortality rates across various dimensions, including country or territory, region, super-region, and five distinct time periods: 1990–2000, 2000–2010, 2010–2019, 2019–2021, and 1990–2021. We could therefore systematically calibrate the COVID-19 pandemic against other causes of mortality over the period 1990–2021. Finally, our study identified several causes of death that exhibited increased geographical concentration over time—ie, causes with a disproportionate impact within a specific geographical area compared with the rest of the global observations. This analysis provides policy makers important information on regional variation and inequalities in cause-specific mortality. Also new to GBD 2021, we report on 12 additional causes of death: COVID-19 and other pandemic-related mortality, pulmonary arterial hypertension, and nine cancer types—hepatoblastoma, Burkitt lymphoma, other non-Hodgkin lymphoma, eye cancer, retinoblastoma, other eye cancers, soft tissue and other extraosseous sarcomas, malignant neoplasm of bone and articular cartilage, and neuroblastoma and other peripheral nervous-cell tumours. Granularity of the estimation of deaths in children younger than 5 years was enhanced by the addition of four new age groups: 1–5 months, 6–11 months, 12–23 months, and 2–4 years.

### Implications of all the available evidence

Our study provides a full analysis of causes of death worldwide and across time, alongside the changing patterns in life expectancy precipitated by those causes. Increasing geographical concentration of mortality was observed for many causes of death, highlighting disparities between regions and substantial differences in cause-specific contributions to life expectancy. On a global scale, this information provides an opportunity to examine whether reductions in mortality were resilient to the onset of a novel pandemic. On a regional level, the estimates generated by our study provide important detail on the evolving impact of causes of death among countries, allowing crucial insight into differential success by geography, time, and cause. The comprehensive nature of GBD 2021 cause-of-death estimation provides valuable opportunities to learn from mortality gains and losses, helping to accelerate progress in reducing mortality.

Methods

Overview

In GBD 2021, we produced estimates for each epidemiological quantity of interest for 288 causes of death by age-sex-location-year for 25 age groups from birth to 95 years and older; for males, females, and both sexes combined; in 204 countries and territories grouped into 21 regions and seven super-regions, and for every year from 1990 to 2021. GBD 2021 also includes subnational analyses for 21 countries and territories
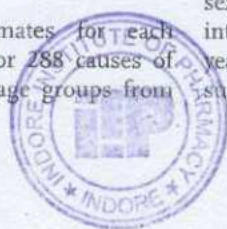
201

(appendix 1 section 2.1). An international network of collaborators provides, reviews, and analyses the available data to generate these metrics; GBD 2021 drew on the expertise of more than 11 000 collaborators from more than 160 countries and territories.

The methods used to generate these estimates closely followed those for GBD 2019.[6] These methods have been extensively peer reviewed over previous rounds of the GBD study[4–9] and as part of the peer-review process for GBD 2021. Here, we provide an overview of the methods with an emphasis on the main methodology changes since GBD 2019; a comprehensive description of the analytical methods for GBD 2021 is provided in appendix 1. Detailed descriptions of analytical methods and models for each cause of death are also available in a searchable online tool.

The GBD 2021 cause-of-death estimates described here include cause-specific mortality and the premature death metric (YLLs). We calculated YLLs as the number of deaths for each cause-age-sex-location-year multiplied by the standard life expectancy at each age (appendix 1 section 6.3). Standard life expectancy is calculated from the lowest age-specific mortality rate between countries.[10] Briefly, we estimated cause-specific death rates for 209 causes using the Cause of Death Ensemble model (CODEm), and we used alternative strategies to model causes with little data, substantial changes in reporting over the study period, or unusual epidemiology. The modelling strategy used for all causes of death can be found in appendix 1 (table S10). CODEm is a modelling tool developed specifically for GBD that assesses the out-of-sample predictive validity of different statistical models and covariate permutations and then combines the results from those assessments to produce cause-specific estimates of the burden of mortality. Methodological improvements for cause-of-death estimates in the present round of estimation focused on several key areas. First, cause-of-death data were updated to include age data for the following age groups younger than 5 years: 1–5 months, 6–11 months, 12–23 months, and 2–4 years. Second, we implemented enhanced methods to account for stochastic variation in cause-of-death data and improve the estimation of small cause fractions present in less common causes of death. Third, we added 199 new country-years of vital registration cause-of-death data, 5 country-years of surveillance data, 21 country-years of verbal autopsy data, and 94 country-years of other data types. Lastly, we incorporated COVID-19 and OPRM, which includes excess mortality associated with the COVID-19 pandemic, excluding deaths from COVID-19, lower respiratory infections, measles, malaria, and pertussis.

The GBD disease and injury hierarchy
GBD classifies diseases and injuries into a hierarchy with four levels that include both fatal and non-fatal causes. Level 1 causes include three broad aggregate categories (communicable, maternal, neonatal, and nutritional [CMNN] diseases; non-communicable diseases [NCDs]; and injuries) and Level 2 disaggregates those categories into 22 clusters of causes, which are further disaggregated into Level 3 and Level 4 causes. At the most detailed level, 288 fatal causes are estimated. For a full list of causes of death by level, see appendix 1 (table S2). For GBD 2021, we separately report on 12 causes of death for the first time: COVID-19, OPRM, pulmonary arterial hypertension, and nine cancer types: hepatoblastoma, Burkitt lymphoma, other non-Hodgkin lymphoma, eye cancer, retinoblastoma, other eye cancers, soft tissue and other extraosseous sarcomas, malignant neoplasm of bone and articular cartilage, and neuroblastoma and other peripheral nervous cell tumours.

## Data sources, processing, and assessing for completeness
The GBD 2021 cause-of-death database included data sources identified in previous rounds of estimation in addition to 9248 new sources (appendix 1 table S5). We included multiple data types to capture the widest array of information, including vital registration and verbal autopsy for all 288 causes as well as survey, census, surveillance, cancer registry, police records, open-source databases, and minimally invasive tissue sampling. To standardise these data so that they can be compared by cause, age, sex, location, and time, we applied a set of data processing corrections. First, deaths with insufficient age data to estimate the GBD age groups or missing age and sex data underwent age and sex splitting to assign GBD age groups as well as sex (appendix 1 section 3.5). Additionally, garbage codes, which are non-specific, implausible, or intermediate, rather than underlying cause of death codes from the International Classification of Diseases, were redistributed to appropriate targets to assign the underlying cause of death.[11] We excluded data sources with more than 50% of all deaths assigned to major garbage codes (class 1 or class 2 garbage codes) in a given year for a specific location (location-year) to mitigate the potential for bias from these sources (appendix 1 section 3.7). For GBD 2021, we established a buffer system so that location-years that were included in the previous GBD cycle would not be dropped from the current cycle as long as less than 55% of all deaths were assigned to major garbage codes. This 5% buffer ensured greater consistency in data source inclusion from one cycle to the next.

Assessing data completeness illustrates the coverage from a data source on overall mortality for the country. Vital registration and verbal autopsy data completeness—a source-specific estimate of the percentage of total cause-specific deaths that are reported in a given location and year—was assessed by location-year, and sources with less than 50% completeness were excluded. We excluded 142 country-years of data because of completeness. As with garbage codes, we used a

Principal
Indore Institute of Pharmacy,
INDORE (M.P.)

2103

202
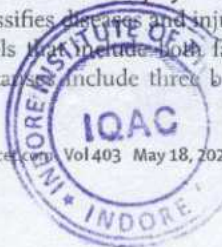
5% buffer so that sources included in the previous GBD cycle would not be excluded from the current cycle if they had at least 45% completeness, allowing us to retain 24 country-years that had previously been dropped. We then multiplied the estimated all-cause mortality for each age-sex-location-year by the cause fraction for the corresponding age-sex-location-year to adjust all included sources to 100% completeness. Verbal autopsy and vital registration data availability, completeness, and quality rating for each location-year are available in appendix 1 (section 3), as well as full details on all data processing corrections.

Improvements in GBD 2021 to cause of death data processing and estimation

Adjustments for stochastic variation

In GBD 2021, we made two primary improvements to the methods used to reduce stochastic variation, most affecting causes of death with small sample sizes. First, we updated the Bayesian algorithm used in the noise reduction of these data to improve the preservation of real trends in data with large sample sizes, and imparted additional information from regional trends for data with small sample sizes. Second, the non-zero floor, a method that addresses distorted data shapes and nonsensical trends caused by small numbers when transformed to log space, was updated to be time-invariant and independent of demographic inputs. The full details of these two key improvements, as well as other improvements that address stochastic variation, can be found in appendix 1 (section 3.14).

COVID-19 and OPRM estimation

We derived COVID-19 and OPRM estimates from an analysis of the overall excess mortality due to the COVID-19 pandemic from January 1, 2020, to December 31, 2021. Full details of the estimation of excess mortality, COVID-19 deaths, and OPRM are provided in appendix 1 (section 5). To estimate excess mortality, we first developed a database of all-cause mortality by week and month after accounting for reporting lags, anomalies such as heat waves, and under-registration of deaths. Next, we developed an ensemble model to predict expected deaths in the absence of the COVID-19 pandemic for the years 2020 and 2021. In location and time combinations with data used for these models, we estimated excess mortality as observed mortality minus expected mortality. To estimate excess mortality for location-years without data, we developed a statistical model to directly predict the excess mortality due to COVID-19, using covariates that pertained to both the COVID-19 pandemic and background population-health-related metrics at the population level before SARS-CoV-2 emerged. Uncertainty was propagated through each step of this estimation procedure.[12] To produce the final estimates of COVID-19 deaths used in GBD 2021, we used a counterfactual approach.

The counterfactual estimates the number of deaths if infection detection rates were at the highest observed value for each location-year. Using the ratio of counterfactual over estimated excess deaths and the ratio of reported COVID-19 deaths over excess deaths, we calculated the ratio of total COVID-19 deaths over reported COVID-19 deaths and multiplied this figure by the number of reported COVID-19 deaths for our final estimates of COVID-19 deaths.[12]

To account for increases in excess mortality in 2020 and 2021 that could not be attributed to particular causes, we introduced a residual cause, OPRM. We identified four causes of death—lower respiratory infections, measles, malaria, and pertussis—as related to the COVID-19 pandemic and having reliable enough estimates to not contribute to OPRM. Thus, we calculated OPRM as the difference between excess mortality and the sum of deaths due to COVID-19 and these four causes.[12]

Presentation of cause-specific mortality estimates

Cause-specific mortality estimates for 2021 are given in death counts and age-standardised rates per 100 000 population, calculated using the GBD standard-population structure.[10] For changes over time, we present percentage changes over the period 1990–2021, and annualised rates of change as the difference in the natural log of the values at the start and end of the time interval divided by the number of years in the interval. We computed uncertainty intervals (UIs) for all metrics using the mean estimate across 1000 draws (appendix 1 sections 2–3), and 95% UIs are given as the 2·5th and 97·5th percentiles of that distribution.

Life-expectancy decomposition

The objective of life-expectancy decomposition is to analyse the difference in life expectancy by age and location, quantifying contributions from specific causes (appendix 1 section 7). We examined temporal trends in causes over continuous time periods across different locations. We aimed to identify the effect of causes of death on life expectancy by using three main decomposition steps. For this study, we investigated the top-20 Level 2 and Level 3 GBD causes contributing to change in life expectancy. The remaining causes were then combined as "other communicable and maternal disorders" or "other NCDs". The first step involved decomposing the difference in life expectancy by age. We calculated age-specific contributions to understand the variation in life expectancy across different age groups. In the second step, each age-specific contribution was further decomposed into cause-age-specific contributions. This analysis allowed for the identification of the specific causes of death that contributed to the differences in life expectancy within each age group. Finally, we aggregated the cause-age-specific contributions across age groups to produce cause-specific contributions to the overall difference

203

in life expectancy. This aggregation provided a comprehensive understanding of how different causes of death contributed to the observed variations in life expectancy. By applying this decomposition approach, we gain insights into the relative effect of different causes of death on changes in life expectancy by age and location.

Calculation of mortality concentration

Concentrated causes in GBD refer to causes that exhibit a disproportionate impact in a specific geographical subset of the data compared with the rest of the global observations. In GBD 2021, we used two different methods to identify these concentrated causes: coefficient of variation and mortality concentration.

Coefficient of variation

For each GBD cause, we calculated a coefficient of variation using standard statistical methods. This measure assesses the variability of a population relative to its mean.[13] The observations considered for this calculation were national, age-standardised, both-sex mortality rates, using the mean mortality rate between 2019 and 2021. Causes with larger coefficients of

variation have data that are less centred around the mean and indicate a greater likelihood of a concentrated cause.

Mortality concentration

To identify concentrations of mortality—geographical locations or groups of locations with populations that are disproportionately affected by a particular cause—we first calculated the total number of all-age, both-sex deaths in 2021 by cause in each of the 811 subnational locations and sorted these locations by number of deaths in descending order. We then calculated the cumulative percentage of deaths by dividing location-specific cumulative deaths by the number of global deaths for each cause. When the cumulative percentage reached or exceeded 90% for a given cause, we divided the population of the geographical subset included in that cumulative percentage by the total global population in 2021, using population estimates from the GBD population model described in previous publications.[10,12] This identification of geographical subsets that contain at least 90% of deaths from a given cause but represent a comparatively small share of the global population was used to identify potential inequalities in the

Leading causes 1990	Age-standardised rate of deaths per 100 000, 1990	Leading causes 2019	Age-standardised rate of deaths per 100 000, 2019	Leading causes 2021	Age-standardised rate of deaths per 100 000, 2021
1 Ischaemic heart disease	158·9 (147·4 to 165·4)	1 Ischaemic heart disease	110·9 (102·5 to 116·9)	1 Ischaemic heart disease	108·7 (99·8 to 115·6)
2 Stroke	144·3 (134·0 to 152·3)	2 Stroke	89·3 (81·6 to 95·6)	2 COVID-19	94·0 (89·2 to 100·0)
3 COPD	71·9 (64·6 to 77·5)	3 COPD	46·1 (42·0 to 49·8)	3 Stroke	87·4 (79·5 to 94·4)
4 Lower respiratory infections	61·8 (57·0 to 66·8)	4 Lower respiratory infections	34·7 (31·5 to 37·5)	4 COPD	45·2 (40·7 to 49·8)
5 Diarrhoeal diseases	60·6 (46·7 to 79·6)	5 Neonatal disorders	30·7 (26·8 to 35·3)	5 Other pandemic-related death	32·3 (24·8 to 43·3)
6 Neonatal disorders	46·0 (43·5 to 48·9)	6 Alzheimer's and other dementias	25·0 (6·2 to 65·0)	6 Neonatal disorders	29·6 (25·3 to 34·4)
7 Tuberculosis	40·0 (34·1 to 44·6)	7 Lung cancer	23·7 (21·8 to 25·8)	7 Lower respiratory infections	28·7 (26·0 to 31·1)
8 Lung cancer	27·6 (26·1 to 29·0)	8 Diabetes	19·8 (18·5 to 20·8)	8 Alzheimer's and other dementias	25·2 (6·4 to 65·6)
9 Alzheimer's and other dementias	25·1 (6·0 to 66·1)	9 Chronic kidney disease	18·6 (16·9 to 19·8)	9 Lung cancer	23·5 (21·2 to 25·9)
10 Cirrhosis	24·4 (22·3 to 27·5)	10 Diarrhoeal diseases	17·1 (12·4 to 23·2)	10 Diabetes	19·6 (18·2 to 20·8)
11 Stomach cancer	22·0 (20·1 to 24·0)	11 Cirrhosis	17·1 (15·9 to 18·5)	11 Chronic kidney disease	18·5 (16·7 to 19·9)
12 Road injuries	21·8 (20·9 to 22·8)	12 Hypertensive heart disease	16·9 (14·1 to 18·6)	12 Cirrhosis liver	16·6 (15·2 to 18·2)
13 Hypertensive heart disease	20·9 (17·1 to 23·3)	13 Road injuries	15·1 (14·2 to 16·0)	13 Hypertensive heart disease	16·3 (13·7 to 18·1)
14 Diabetes	18·2 (17·0 to 19·1)	14 Tuberculosis	14·9 (13·7 to 16·4)	14 Diarrheal diseases	15·4 (10·9 to 20·9)
15 Colorectal cancer	15·6 (14·5 to 16·3)	15 Colorectal cancer	12·6 (11·6 to 13·4)	15 Road injuries	14·6 (13·6 to 15·6)
16 Congenital defects	15·2 (9·6 to 19·7)	16 Stomach cancer	11·5 (9·9 to 12·9)	16 Tuberculosis	14·0 (12·6 to 15·8)
17 Self-harm	14·9 (12·8 to 15·8)	17 Falls	10·3 (8·8 to 11·2)	17 Colorectal cancer	12·4 (11·2 to 13·4)
18 Chronic kidney disease	14·9 (13·7 to 16·4)	18 HIV/AIDS	9·8 (9·0 to 11·0)	18 Stomach cancer	11·2 (9·6 to 12·6)
19 Malaria	12·5 (6·1 to 26·0)	19 Malaria	9·3 (3·7 to 18·3)	19 Malaria	10·5 (3·9 to 21·4)
20 Measles	11·0 (3·9 to 22·6)	20 Self-harm	9·2 (8·6 to 9·7)	20 Falls	9·9 (8·5 to 10·8)
21 Falls	10·9 (9·8 to 11·8)	21 Congenital defects	8·9 (7·7 to 10·9)	21 Self-harm	9·0 (8·3 to 9·6)
34 HIV/AIDS	5·9 (4·5 to 7·8)	67 Measles	1·4 (0·5 to 3·0)	22 HIV/AIDS	8·7 (8·1 to 9·6)

☐ Non-communicable diseases
☐ Communicable, maternal, neonatal, and nutritional causes
☐ Injuries

Figure 1: Leading causes of global deaths and age-standardised death rate per 100 000 population for males and females combined, 1990, 2019, and 2021
Figure shows the 20 leading causes of death in descending order. Causes are connected by lines between time periods; solid lines represent an increase or lateral shift in ranking and dashed lines are decreases in rank. COPD=chronic obstructive pulmonary disease. Lung cancer=tracheal, bronchus, and lung cancer.
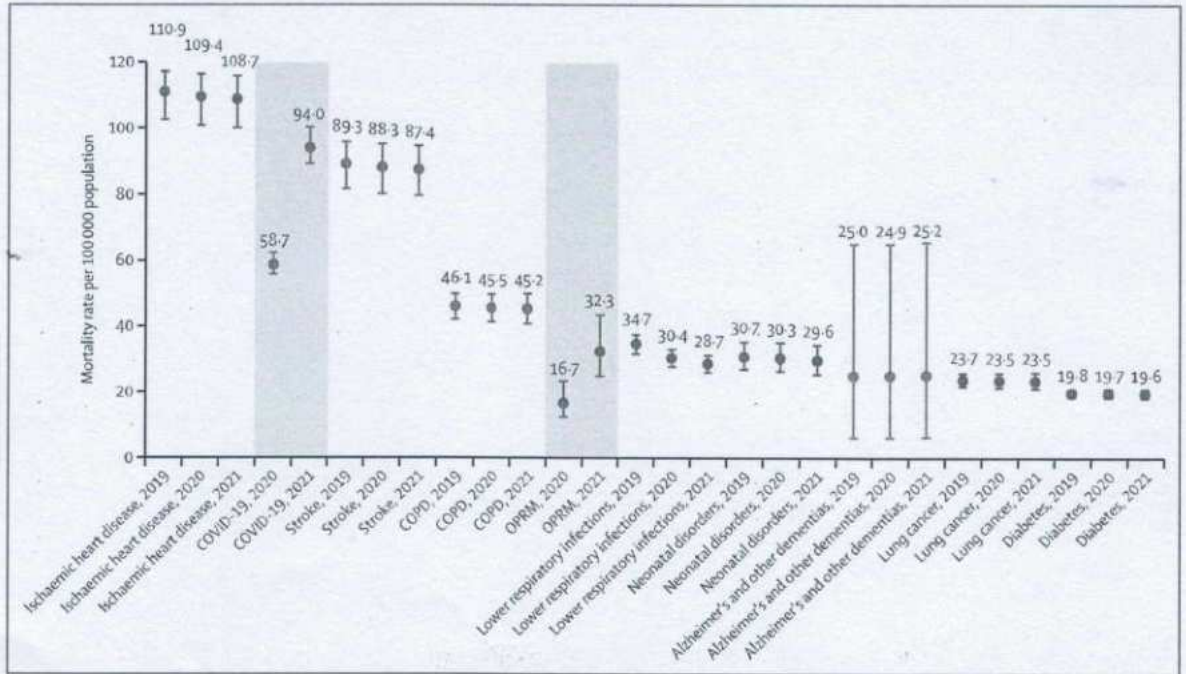
204

Figure 2: Age-standardised mortality rate per 100 000 population for the ten leading Level 3 causes of death globally, 2019–21
Whisker plot in which the y-axis represents the age-standardised mortality rate and the x-axis represents a selected cause-year. Causes are arranged from highest to lowest age-standardised mortality rate, with each cause assigned a distinct colour for identification. The whiskers represent the 95% uncertainty interval. COPD=chronic obstructive pulmonary disease. OPRM=other pandemic-related mortality.

incidence of mortality between locations and populations. In addition to identifying these concentrations of mortality in 2021, we repeated this same analysis for 1990. By comparing the respective proportions of affected global population in these two years, we were able to differentiate causes that showed increased, decreased, or unchanged concentrations of mortality. The causes highlighted in this study were those characterised by an age-standardised mortality rate greater than 0·5 per 100 000 population. The purpose of presenting mortality concentrations is to illustrate causes that are disproportionately affecting specific populations, when previously that cause affected large swaths of the population. Thus, we did not calculate the mortality concentration for causes that are endemic to certain regions, as the mortality rate is already known to be concentrated among specific parts of the global population. We excluded two endemic causes, Ebola virus disease and Chagas disease, from this calculation.

GBD research and reporting practices

This research is compliant with the Guidelines for Accurate and Transparent Health Estimates Reporting recommendations (GATHER; appendix 1 table S4).[14] Software packages used in the cause-of-death analysis for GBD 2021 were Python (version 3.10.4), Stata (version 13.1), and R (version 4.2.1). Statistical code used for GBD estimation is publicly available online.

Role of the funding source

The funder of this study had no role in study design, data collection, data analysis, data interpretation, or the writing of the report.

Results

Estimates described in the Article are viewable in appendix 2. Detailed results for each cause of death in the analysis are available in downloadable form through the GBD Results tool and via visual exploration through the online tool GBD Compare. Summaries of results for each cause of death included in the analysis are available online.

Global causes of death

From 1990 to 2019, the annual rate of change in global deaths from all causes ranged from –0·9% (95% UI –2·7 to 0·8) to 2·4% (0·1 to 4·7; appendix 2 figure S1). The corresponding annual rates of change in the global age-standardised mortality rate ranged from –3·3% (–5·0 to –1·6) to 0·4% (–1·9 to 2·5). In 2020, however, the total number of deaths worldwide increased by 10·8% (6·4 to 15·4) compared with 2019, from 57·0 million deaths (54·9 to 59·5) in 2019 to 63·1 million deaths (60·6 to 65·9) in 2020. This trend persisted in 2021, with an increase of 7·5% (3·1 to 12·4) relative to 2020, to 67·9 million (65·0 to 70·8) deaths. The age-standardised mortality rate followed a similar pattern, increasing by 8·1% (3·9 to 12·4) in 2020 and
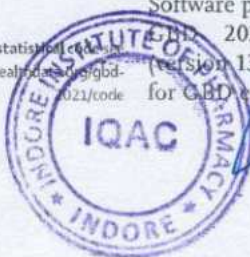
	Global	Central Europe, eastern Europe, and central Asia	High income	Latin America and Caribbean	North Africa and Middle East	South Asia	Southeast Asia, east Asia, and Oceania	Sub-Saharan Africa
2020								
1								
Cause	Ischaemic heart disease	Ischaemic heart disease	Ischaemic heart disease	COVID-19	Ischaemic heart disease	Ischaemic heart disease	Stroke	COVID-19
Age-standardised rate (per 100 000 population)	109·4 (100·7–116·1)	215·3 (199·2–225·7)	51·4 (45·1–54·6)	133·7 (121·5–145·3)	205·2 (182·7–225·6)	150·3 (139·7–162·2)	142·8 (123·9–159·8)	158·9 (148·5–170·0)
Number	8 840 000 (8 180 000– 9 360 000)	1 410 000 (1 310 000– 1 480 000)	1 290 000 (1 110 000– 1 390 000)	799 000 (725 000– 869 000)	760 000 (681 000– 838 000	1 960 000 (1 820 000– 2 110 000)	3 460 000 (3 030 000– 3 880 000)	659 000 (615 000– 706 000)
2								
Cause	Stroke	Stroke	COVID-19	Ischaemic heart disease	COVID-19	Chronic obstructive pulmonary disease	Ischaemic heart disease	Stroke
Age-standardised rate (per 100 000 population)	88·3 (80·2–95·0)	110·7 (102·7–115·6)	41·8 (40·8–42·8)	84·3 (77·2–89·4)	123·9 (106·8–137·1)	104·1 (92·3–117·0)	110·8 (97·3–124·6)	126·2 (113·4–140·4)
Number	7 140 000 (6 500 000– 7 680 000)	726 000 (675 000– 758 000)	930 000 (908 000– 952 000)	496 000 (454 000– 525 000)	483 000 (415 000– 537 000)	1 230 000 (1 090 000– 1 370 000)	2 570 000 (2 260 000– 2 880 000)	481 000 (432 000– 538 000)
3								
Cause	COVID-19	COVID-19	Stroke	Stroke	Stroke	COVID-19	Chronic obstructive pulmonary disease	Ischaemic heart disease
Age-standardised rate (per 100 000 population)	58·7 (55·8–62·4)	72·9 (64·1–81·7)	29·0 (24·7–31·2)	47·5 (43·4–50·5)	103·8 (92·0–115·6)	101·8 (95·0–108·5)	66·9 (57·4–77·0)	92·9 (83·1–103·0)
Number	4 800 000 (4 560 000– 5 110 000)	467 000 (411 000– 523 000)	764 000 (636 000– 830 000)	278 000 (255 000– 296 000)	370 000 (329 000– 414 000)	1 320 000 (1 230 000– 1 400 000)	1 500 000 (1 290 000– 1 730 000)	346 000 (309 000– 388 000)
4								
Cause	Chronic obstructive pulmonary disease	Other COVID-19 pandemic-related outcomes	Alzheimer's disease and other dementias	Diabetes mellitus	Hypertensive heart disease	Stroke	Tracheal, bronchus, and lung cancer	Lower respiratory infections
Age-standardised rate (per 100 000 population)	45·5 (41·2–49·6)	41·0 (32·9–51·9)	26·5 (6·74–65·1)	36·5 (33·9–38·9)	40·2 (32·0–46·7)	83·3 (75·7–90·4)	34·8 (29·0–41·0)	88·5 (77·8–98·2)
Number	3 650 000 (3 320 000– 3 970 000)	264 000 (212 000– 333 000)	774 000 (198 000– 1 900 000)	217 000 (202 000– 231 000)	138 000 (110 000– 160 000)	1 060 000 (969 000– 1 150 000)	938 000 (783 000– 1 110 000)	588 000 (494 000– 686 000)
5								
Cause	Lower respiratory infections	Tracheal, bronchus, and lung cancer	Tracheal, bronchus, and lung cancer	Lower respiratory infections	Chronic kidney disease	Diarrhoeal diseases	Alzheimer's disease and other dementias	Malaria
Age-standardised rate (per 100 000 population)	30·4 (27·7–32·9)	25·5 (24·4–26·5)	25·9 (23·8–27·0)	32·8 (29·6–35·1)	37·9 (33·3–42·4)	50·2 (32·0–79·4)	27·9 (6·76–74·8)	67·9 (22·6–145·0)
Number	2 280 000 (2 080 000– 2 460 000)	168 000 (161 000– 174 000)	581 000 (526 000– 610 000)	187 000 (169 000– 200 000)	142 000 (125 000– 159 000)	591 000 (381 000– 940 000)	562 000 (136 000– 1 490 000)	713 000 (251 000– 1 480 000)
6								
Cause	Neonatal disorders	Cirrhosis and other chronic liver diseases	Chronic obstructive pulmonary disease	Chronic kidney disease	Other COVID-19 pandemic-related outcomes	Neonatal disorders	Lower respiratory infections	Tuberculosis
Age-standardised rate (per 100 000 population)	30·3 (26·3–35·0)	22·5 (21·7–23·3)	19·2 (16·9–20·3)	30·9 (28·3–33·1)	30·4 (11·4–52·0)	43·8 (37·2–51·6)	21·2 (18·9–23·6)	67·3 (56·7–77·8)
Number	1 910 000 (1 650 000– 2 200 000)	131 000 (127 000– 136 000)	490 000 (424 000– 522 000)	184 000 (169 000– 197 000)	121 000 (46 500– 207 000)	672 000 (571 000– 792 000)	424 000 (378 000– 469 000)	378 000 (313 000– 442 000)

(Table 1 continues on next page)

206

	Global	Central Europe, eastern Europe, and central Asia	High income	Latin America and Caribbean	North Africa and Middle East	South Asia	Southeast Asia, east Asia, and Oceania	Sub-Saharan Africa
(Continued from previous page)								
7								
Cause	Alzheimer's disease and other dementias	Alzheimer's disease and other dementias	Colon and rectum cancer	Chronic obstructive pulmonary disease	Diabetes mellitus	Lower respiratory infections	Hypertensive heart disease	HIV/AIDS
Age-standardised rate (per 100 000 population)	24·9 (6·16–65·0)	20·8 (4·88–55·3)	14·7 (13·2–15·6)	25·0 (22·5–26·5)	29·4 (26·4–32·3)	40·0 (35·8–44·7)	20·1 (14·1–24·8)	65·8 (59·9–73·2)
Number	1 890 000 (470 000–4 940 000)	136 000 (32 100–362 000)	344 000 (300 000–367 000)	144 000 (130 000–152 000)	113 000 (101 000–124 000)	522 000 (465 000–582 000)	459 000 (320 000–562 000)	539 000 (487 000–612 000)
8								
Cause	Tracheal, bronchus, and lung cancer	Lower respiratory infections	Chronic kidney disease	Interpersonal violence	Chronic obstructive pulmonary disease	Tuberculosis	Stomach cancer	Diarrhoeal diseases
Age-standardised rate (per 100 000 population)	23·5 (21·3–25·8)	19·5 (18·3–20·8)	14·0 (12·1–15·3)	23·5 (22·4–24·8)	26·9 (23·9–29·7)	34·2 (30·1–40·1)	18·4 (14·2–22·0)	57·0 (36·2–79·4)
Number	1 970 000 (1 780 000–2 160 000)	96 200 (91 200–101 000)	364 000 (307 000–399 000)	147 000 (140 000–155 000)	92 400 (82 500–102 000)	509 000 (450 000–597 000)	491 000 (380 000–589 000)	452 000 (324 000–588 000)
9								
Cause	Diabetes mellitus	Cardiomyopathy and myocarditis	Lower respiratory infections	Other COVID-19 pandemic-related outcomes	Alzheimer's disease and other dementias	Diabetes mellitus	Road injuries	Other COVID-19 pandemic-related outcomes
Age-standardised rate (per 100 000 population)	19·7 (18·4–20·9)	19·2 (17·9–20·4)	13·6 (11·8–14·6)	20·9 (10·3–33·3)	25·7 (6·30–67·6)	33·1 (29·8–36·0)	15·7 (13·9–17·6)	50·5 (31·3–70·8)
Number	1 630 000 (1 520 000–1 720 000)	113 000 (105 000–121 000)	361 000 (306 000–390 000)	125 000 (59 600–199 000)	73 600 (17 900–198 000)	419 000 (378 000–457 000)	380 000 (335 000–429 000)	245 000 (159 000–339 000)
10								
Cause	Chronic kidney disease	Colon and rectum cancer	Self-harm	Alzheimer's disease and other dementias	Lower respiratory infections	Other COVID-19 pandemic-related outcomes	Chronic kidney disease	Neonatal disorders
Age-standardised rate (per 100 000 population)	18·6 (16·9–19·9)	18·6 (17·6–19·4)	10·9 (10·5–11·2)	20·8 (5·14–53·8)	25·4 (22·4–28·5)	28·2 (18·5–39·5)	15·3 (13·4–17·0)	50·0 (42·1–59·2)
Number	1 500 000 (1 360 000–1 610 000)	122 000 (115 000–127 000)	149 000 (142 000–153 000)	119 000 (29 200–308 000)	103 000 (91 000–116 000)	370 000 (246 000–514 000)	376 000 (333 000–420 000)	889 000 (749 000–1 050 000)
2021								
1								
Cause	Ischaemic heart disease	Ischaemic heart disease	Ischaemic heart disease	COVID-19	Ischaemic heart disease	COVID-19	Stroke	COVID-19
Age-standardised rate (per 100 000 population)	108·7 (99·8–115·6)	213·6 (196·1–229·1)	51·0 (44·9–54·2)	195·4 (182·1–211·4)	202·8 (179·7–225·9)	156·5 (150·4–164·4)	141·1 (123·2–159·7)	271·0 (250·1–290·7)
Number	8 990 000 (8 290 000–9 550 000)	1 410 000 (1 290 000–1 510 000)	1 310 000 (1 120 000–1 400 000)	1 200 000 (1 110 000–1 290 000)	769 000 (679 000–863 000)	2 060 000 (1 980 000–2 170 000)	3 550 000 (3 100 000–4 020 000)	1 150 000 (1 060 000–1 240 000)
2								
Cause	COVID-19	COVID-19	COVID-19	Ischaemic heart disease	COVID-19	Ischaemic heart disease	Ischaemic heart disease	Stroke
Age-standardised rate (per 100 000 population)	94·0 (89·2–100·0)	168·8 (150·6–186·1)	48·1 (47·4–48·8)	83·8 (75·9–90·6)	172·4 (150·3–191·5)	149·1 (136·4–161·8)	110·4 (94·9–124·6)	124·7 (111·8–138·6)
Number	7 890 000 (7 490 000–8 400 000)	1 100 000 (982 000–1 210 000)	1 070 000 (1 060 000–1 090 000)	504 000 (457 000–545 000)	698 000 (608 000–777 000)	1 990 000 (1 820 000–2 160 000)	2 660 000 (2 290 000–3 000 000)	484 000 (432 000–544 000)

(Table 1 continues on next page)

207

	Global	Central Europe, eastern Europe, and central Asia	High income	Latin America and Caribbean	North Africa and Middle East	South Asia	Southeast Asia, east Asia, and Oceania	Sub-Saharan Africa
(Continued from previous page)								
3								
Cause	Stroke	Stroke	Stroke	Stroke	Stroke	Chronic obstructive pulmonary disease	Chronic obstructive pulmonary disease	Other COVID-19 pandemic-related outcomes
Age-standardised rate (per 100 000 population)	87·4 (79·5–94·4)	109·8 (101·6–116·6)	28·8 (24·5–30·9)	46·7 (42·3–50·2)	101·9 (89·2–114·4)	101·6 (90·3–114·2)	66·6 (56·2–77·7)	123·9 (87·7–159·5)
Number	7 250 000 (6 600 000–7 820 000)	725 000 (671 000–770 000)	771 000 (641 000–838 000)	279 000 (254 000–301 000)	372 000 (325 000–421 000)	1 230 000 (1 100 000–1 380 000)	1 560 000 (1 310 000–1 820 000)	584 000 (418 000–757 000)
4								
Cause	Chronic obstructive pulmonary disease	Other COVID-19 pandemic-related outcomes	Alzheimer's disease and other dementias	Other COVID-19 pandemic-related outcomes	Other COVID-19 pandemic-related outcomes	Stroke	Tracheal, bronchus, and lung cancer	Ischaemic heart disease
Age-standardised rate (per 100 000 population)	45·2 (40·7–49·8)	50·0 (34·8–68·7)	26·5 (6·74–64·8)	39·0 (22·5–58·4)	64·5 (34·4–100·6)	81·8 (74·2–89·6)	34·8 (28·8–41·1)	92·8 (83·3–103·5)
Number	3 720 000 (3 360 000–4 090 000)	321 000 (223 000–438 000)	792 000 (203 000–1 940 000)	236 000 (135 000–355 000)	265 000 (139 000–414 000)	1 070 000 (968 000–1 170 000)	970 000 (800 000–1 150 000)	352 000 (316 000–396 000)
5								
Cause	Other COVID-19 pandemic-related outcomes	Tracheal, bronchus, and lung cancer	Tracheal, bronchus, and lung cancer	Diabetes mellitus	Hypertensive heart disease	Other COVID-19 pandemic-related outcomes	Alzheimer's disease and other dementias	Lower respiratory infections
Age-standardised rate (per 100 000 population)	32·3 (24·8–43·3)	25·1 (23·7–26·6)	25·9 (23·8–27·0)	36·3 (33·2–39·3)	39·5 (31·3–46·3)	63·3 (50·4–77·2)	28·9 (7·41–78·6)	85·4 (75·3–95·0)
Number	2 690 000 (2 060 000–3 610 000)	167 000 (157 000–176 000)	591 000 (537 000–620 000)	221 000 (202 000–239 000)	138 000 (109 000–162 000)	838 000 (674 000–1 020 000)	608 000 (155 000–1 670 000)	563 000 (472 000–655 000)
6								
Cause	Neonatal disorders	Cirrhosis and other chronic liver diseases	Chronic obstructive pulmonary disease	Chronic kidney disease	Chronic kidney disease	Diarrhoeal diseases	COVID-19	Malaria
Age-standardised rate (per 100 000 population)	29·6 (25·3–34·4)	22·3 (21·0–23·5)	19·1 (16·8–20·2)	30·7 (27·8–33·5)	37·7 (32·7–42·8)	47·8 (30·2–75·7)	23·2 (16·3–37·2)	65·9 (23·6–136·7)
Number	1 830 000 (1 570 000–2 130 000)	131 000 (123 000–138 000)	495 000 (428 000–527 000)	187 000 (170 000–204 000)	145 000 (126 000–164 000)	573 000 (372 000–908 000)	606 000 (425 000–974 000)	704 000 (265 000–1 400 000)
7								
Cause	Lower respiratory infections	Alzheimer's disease and other dementias	Colon and rectum cancer	Lower respiratory infections	Diabetes mellitus	Neonatal disorders	Lower respiratory infections	Tuberculosis
Age-standardised rate (per 100 000 population)	28·7 (26·0–31·1)	20·8 (4·94–55·6)	14·7 (13·1–15·5)	30·4 (27·0–33·3)	29·3 (25·9–32·5)	42·0 (35·6–50·2)	20·9 (18·6–23·4)	65·8 (56·1–76·9)
Number	2 180 000 (1 980 000–2 360 000)	137 000 (32 500–370 000)	348 000 (304 000–372 000)	177 000 (157 000–194 000)	116 000 (102 000–129 000)	636 000 (538 000–760 000)	431 000 (384 000–482 000)	373 000 (313 000–439 000)
8								
Cause	Alzheimer's disease and other dementias	Cardiomyopathy and myocarditis	Chronic kidney disease	Chronic obstructive pulmonary disease	Chronic obstructive pulmonary disease	Lower respiratory infections	Hypertensive heart disease	HIV/AIDS
Age-standardised rate (per 100 000 population)	25·2 (6·36–65·6)	19·1 (17·5–20·7)	13·9 (12·0–15·1)	24·7 (22·1–26·4)	26·4 (23·2–29·6)	39·2 (34·2–44·6)	19·8 (14·0–24·3)	61·4 (55·8–68·5)
Number	1 960 000 (499 000–5 120 000)	112 000 (103 000–122 000)	368 000 (310 000–402 000)	145 000 (130 000–156 000)	92 700 (82 000–104 000)	516 000 (451 000–584 000)	470 000 (333 000–575 000)	515 000 (467 000–583 000)

(Table 1 continues on next page)

Principal
Indore Institute of Pharmacy,
INDORE (M.P.)

2109

208

Global age-sex-specific mortality, life expectancy, and population estimates in 204 countries and territories and 811 subnational locations, 1950–2021, and the impact of the COVID-19 pandemic: a comprehensive demographic analysis for the Global Burden of Disease Study 2021

GBD 2021 Demographics Collaborators*

Summary

Background Estimates of demographic metrics are crucial to assess levels and trends of population health outcomes. The profound impact of the COVID-19 pandemic on populations worldwide has underscored the need for timely estimates to understand this unprecedented event within the context of long-term population health trends. The Global Burden of Diseases, Injuries, and Risk Factors Study (GBD) 2021 provides new demographic estimates for 204 countries and territories and 811 additional subnational locations from 1950 to 2021, with a particular emphasis on changes in mortality and life expectancy that occurred during the 2020–21 COVID-19 pandemic period.

Methods 22 223 data sources from vital registration, sample registration, surveys, censuses, and other sources were used to estimate mortality, with a subset of these sources used exclusively to estimate excess mortality due to the COVID-19 pandemic. 2026 data sources were used for population estimation. Additional sources were used to estimate migration; the effects of the HIV epidemic; and demographic discontinuities due to conflicts, famines, natural disasters, and pandemics, which are used as inputs for estimating mortality and population. Spatiotemporal Gaussian process regression (ST-GPR) was used to generate under-5 mortality rates, which synthesised 30 763 location-years of vital registration and sample registration data, 1365 surveys and censuses, and 80 other sources. ST-GPR was also used to estimate adult mortality (between ages 15 and 59 years) based on information from 31 642 location-years of vital registration and sample registration data, 355 surveys and censuses, and 24 other sources. Estimates of child and adult mortality rates were then used to generate life tables with a relational model life table system. For countries with large HIV epidemics, life tables were adjusted using independent estimates of HIV-specific mortality generated via an epidemiological analysis of HIV prevalence surveys, antenatal clinic serosurveillance, and other data sources. Excess mortality due to the COVID-19 pandemic in 2020 and 2021 was determined by subtracting observed all-cause mortality (adjusted for late registration and mortality anomalies) from the mortality expected in the absence of the pandemic. Expected mortality was calculated based on historical trends using an ensemble of models. In location-years where all-cause mortality data were unavailable, we estimated excess mortality rates using a regression model with covariates pertaining to the pandemic. Population size was computed using a Bayesian hierarchical cohort component model. Life expectancy was calculated using age-specific mortality rates and standard demographic methods. Uncertainty intervals (UIs) were calculated for every metric using the 25th and 975th ordered values from a 1000-draw posterior distribution.

Findings Global all-cause mortality followed two distinct patterns over the study period: age-standardised mortality rates declined between 1950 and 2019 (a 62·8% [95% UI 60·5–65·1] decline), and increased during the COVID-19 pandemic period (2020–21; 5·1% [0·9–9·6] increase). In contrast with the overall reverse in mortality trends during the pandemic period, child mortality continued to decline, with 4·66 million (3·98–5·50) global deaths in children younger than 5 years in 2021 compared with 5·21 million (4·50–6·01) in 2019. An estimated 131 million (126–137) people died globally from all causes in 2020 and 2021 combined, of which 15·9 million (14·7–17·2) were due to the COVID-19 pandemic (measured by excess mortality, which includes deaths directly due to SARS-CoV-2 infection and those indirectly due to other social, economic, or behavioural changes associated with the pandemic). Excess mortality rates exceeded 150 deaths per 100 000 population during at least one year of the pandemic in 80 countries and territories, whereas 20 nations had a negative excess mortality rate in 2020 or 2021, indicating that all-cause mortality in these countries was lower during the pandemic than expected based on historical trends. Between 1950 and 2021, global life expectancy at birth increased by 22·7 years (20·8–24·8), from 49·0 years (46·7–51·3) to 71·7 years (70·9–72·5). Global life expectancy at birth declined by 1·6 years (1·0–2·2) between 2019 and 2021, reversing historical trends. An increase in life expectancy was only observed in 32 (15·7%) of 204 countries and territories between 2019 and 2021. The global population reached 7·89 billion (7·67–8·13) people in 2021, by which time 56 of 204 countries and territories had peaked and subsequently populations have declined. The largest proportion of

population growth between 2020 and 2021 was in sub-Saharan Africa (39·5% [28·4–52·7]) and south Asia (26·3% [9·0–44·7]). From 2000 to 2021, the ratio of the population aged 65 years and older to the population aged younger than 15 years increased in 188 (92·2%) of 204 nations.

Interpretation Global adult mortality rates markedly increased during the COVID-19 pandemic in 2020 and 2021, reversing past decreasing trends, while child mortality rates continued to decline, albeit more slowly than in earlier years. Although COVID-19 had a substantial impact on many demographic indicators during the first 2 years of the pandemic, overall global health progress over the 72 years evaluated has been profound, with considerable improvements in mortality and life expectancy. Additionally, we observed a deceleration of global population growth since 2017, despite steady or increasing growth in lower-income countries, combined with a continued global shift of population age structures towards older ages. These demographic changes will likely present future challenges to health systems, economies, and societies. The comprehensive demographic estimates reported here will enable researchers, policy makers, health practitioners, and other key stakeholders to better understand and address the profound changes that have occurred in the global health landscape following the first 2 years of the COVID-19 pandemic, and longer-term trends beyond the pandemic.

Introduction

Understanding mortality and population trends over time and across locations, age groups, and sexes is crucial for planning population-specific public health policies. Age-specific mortality rates can indicate the emergence of new adverse health risks in specific locations, while population counts can inform resource allocation and aid in planning future development. The COVID-19 pandemic has highlighted the importance of demography in understanding disease and injury burden[1] and the roles health policy and infrastructure have in health and demographic outcomes.[1,2] As the COVID-19 pandemic enters an endemic phase in some locations, demographic indicators can provide important context for understanding and addressing COVID-19, long COVID-19,[3] and the interaction between COVID-19 and other diseases and injuries. Furthermore, demographic trends in the decades before the COVID-19 pandemic and reversals in those trends during the first 2 years of the COVID-19 pandemic (2020–21) can provide insights into potential long-term effects of the pandemic. These shifts in demographic patterns, including in population growth and age distribution, can help policy makers and public health experts better understand how the pandemic has impacted different groups within society and inform strategies for future pandemic preparedness and health-care planning.

The Global Burden of Diseases, Injuries, and Risk Factors Study (GBD) is an evolving research effort that quantifies the state of global health.[4] The scope of the study has historically included estimating key demographic metrics and comprehensive health metrics for a set of national and subnational locations that has expanded over time. Mortality has been estimated as part of GBD since the first GBD estimates were published in the 1993 World Bank World Development Report, and

mortality estimates have been included in each update since GBD 2010.[5–10] A comprehensive, internally consistent modelling strategy for estimating population and fertility was introduced in GBD 2017, greatly improving the consistency of results.[11] Previously, GBD drew on population estimates from the UN Population Division of the Department of Economic and Social Affairs (UNPD).[12,13] In GBD 2019, the demographic analysis used population, fertility, and mortality estimates to produce a typology that better helped to specify phases of demographic transition.[10] The GBD demography framework is part of the greater GBD enterprise; thus, it differs from other demographic research initiatives by using estimates of disease and injury burden to inform population and mortality estimates, and vice versa. Attempting to estimate the effects of the pandemic is now a major focus of GBD and other demographic research efforts.[12,14–16]

The GBD 2021 demographic analysis improved on GBD 2019 by using additional data sources and refined methods to generate updated estimates of mortality, life expectancy, and population size at the global, regional, national, and subnational levels for each year from 1950 to 2021. GBD 2021 is the first round to incorporate the COVID-19 pandemic into the modelling process through the estimation of excess mortality due to the pandemic, defined as the net difference between the number of deaths that occurred between 2020 and 2021 and the number of deaths that would be expected over the same period based on previous trends in all-cause mortality.[16] The unified approach to estimate all-cause mortality and excess mortality in GBD 2021 is an innovation in current demographic research methods. This facilitates analysis of the interplay between wider demographic processes and the COVID-19 pandemic. In this iteration of the GBD demographic analysis, we aim to

210
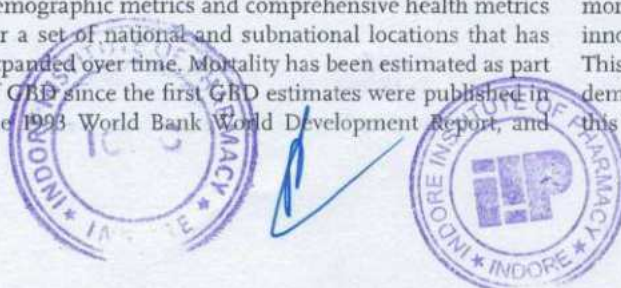
Research in context

Evidence before this study

The UN Population Division of the Department of Economic and Social Affairs (UNPD) produces estimates and projections of global, regional, and national demographic metrics that are updated biannually. Their latest findings, published in the World Population Prospects 2022 revision, incorporated WHO estimates of excess mortality due to the COVID-19 pandemic in 2020 and 2021. Estimates of excess mortality during the pandemic have also been generated by the Institute for Health Metrics and Evaluation and the World Mortality Dataset. The International Database of the US Census Bureau reports population estimates and projections for more than 200 countries and areas, of which a subset are updated every year. Organisations including WHO, the Organisation for Economic Co-operation and Development, and the European Union release demographic estimates less regularly and typically only for select metrics or locations. Some national statistics offices also produce their own demographic indicators. The Global Burden of Diseases, Injuries, and Risk Factors Study (GBD) generates regularly updated and globally comparable health metrics, including mortality, life expectancy, and population estimates for past years, and forecasts up to the year 2100. The current GBD 2021 cycle is directly preceded by GBD 2019, which reported demographic estimates for 204 countries and territories for each year from 1950 through 2019. While each of these studies represent important efforts to provide insights into demographic estimates and the COVID-19 pandemic, only GBD estimates comply with the Guidelines for Accurate and Transparent Health Estimates Reporting, which identifies best practices for reporting global health estimates.

Added value of this study

GBD 2021 is one of the first studies to fully evaluate demographic trends in the context of the first 2 years of the COVID-19 pandemic. The study employed a unified framework to calculate excess mortality rates due to the COVID-19 pandemic along with a comprehensive set of demographic metrics including all-cause mortality, life expectancy, and

population counts for 204 countries and territories and 811 subnational locations. This allowed estimates of all-cause mortality to inform estimates of excess mortality due to the pandemic, and vice versa. In contrast, the demographic estimates published by UNPD for 2020 and 2021, although based on data available during the pandemic, did not use a unified framework for all-cause and excess mortality. Additionally, while the US Census Bureau published population estimates for 2020 and 2021, the estimates were adjusted to reflect the effects of the pandemic for only a subset of locations. GBD 2021 utilised a suite of customised and validated data processing and modelling tools, systematically analysing thousands of data sources to produce global, regional, national, and subnational demographic estimates by age, sex, and Sociodemographic Index (SDI) level for each year from 1950 to 2021. Compared with GBD 2019, GBD 2021 utilised 5296 additional data sources. Additionally, the model life table system used in GBD 2021 was improved to provide more accurate mortality estimates for older age groups. All estimates are packaged within freely accessible data-sharing and visualisation tools.

Implications of all the available evidence

Our study highlights the impact of the first 2 years of the COVID-19 pandemic at a novel level of granularity, demonstrating unprecedented reversals in adult mortality and life expectancy trends at the global, regional, and national levels. Furthermore, globally comparable measures of excess mortality due to the pandemic show substantial variation in the burden experienced by different countries and territories. Our comprehensive set of demographic estimates provides a rich description of evolving long-term trends in mortality and life expectancy across age groups, sexes, and SDI levels, and our population analyses reveal changing dynamics and age structures with implications for the future of health-care systems, economies, and societies. Collectively, the estimates reported here provide an integrated demographic framework for GBD and a valuable foundation for policy evaluation, development, and implementation around the world.

provide policy makers and the public with the information needed to gain a better understanding of the demographic context of disease and injury burden since 1950 and during the COVID-19 pandemic in 2020–21 specifically.

Methods

Overview

For each new GBD iteration, recently available data and improved methods are used to update the full time series of demographic estimates from 1950 to the latest year of analysis; GBD 2021 demographic estimates therefore supersede all previous estimates.

The GBD 2021 demographic methods closely followed those used in GBD 2019.[10] Improvements for GBD 2021

centred on a single framework to estimate both all-cause mortality and excess mortality due to the COVID-19 pandemic. The analytical process for computing internally consistent demographic estimates included six main components: (1) estimating age-specific fertility rates; (2) estimating under-5 and adult (age 15–59 years) mortality rates; (3) estimating age-specific mortality rates using a relational model life table system with HIV adjustments; (4) estimating excess mortality due to the COVID-19 pandemic and adjusting all-cause mortality estimates accordingly; (5) accounting for fatal discontinuities such as wars, famines, and natural disasters; and (6) estimating population sizes. To resolve discrepancies due to the inherent interdependent nature of population, mortality,

Principal
Indore Institute of Pharmacy,
INDORE (M.P.)

and fertility estimates, the estimation process was run twice: first to generate preliminary numbers, and second to refine all estimates and ensure internal consistency. A detailed description of all methods and analytical flowcharts for all-cause mortality, fertility, and population estimation are available in appendix 1 (sections 2–6, 8).

This study complies with the Guidelines for Accurate and Transparent Health Estimates Reporting (GATHER);[17] a completed GATHER checklist is provided in appendix 1 (section 8). Python (version 3.8.17 and 3.10.4), Stata (version 15.1), and R (version 3.5 and 4.2) were used for statistical analysis This manuscript was produced with the GBD Collaborator Network and in accordance with the GBD Protocol.[18] An international network of collaborators provides, reviews, and analyses the available data to generate health metrics; the 2021 GBD round drew on the expertise of more than 11 000 collaborators across more than 160 countries and territories.

Data sources and processing

The GBD 2021 analysis used a range of data types for mortality and population estimation that were identified from a systematic search of available data from government websites, statistical annuals, demographic compendia, large-scale surveys, and collaborator input; comprehensive details on the sources of input data are available online via the GBD 2021 Sources Tool. Under-5 mortality rates (U5MRs), defined as the probability of death from birth to age 5 years, were estimated using 30 526 location-years of vital registration data (3179 new location-years for GBD 2021 compared with GBD 2019),[10] 237 location-years of sample vital registration data, and 1445 other sources (including 57 new surveys, one new census, and ten other new sources; appendix 1 section 8). Adult mortality, defined as the probability of death before age 60 years assuming survival to age 15 years, was estimated using 30 207 location-years of vital registration data (3150 new location-years for GBD 2021 compared with GBD 2019), 1435 location-years of sample vital registration data, 75 censuses, 280 surveys (including 65 sources of household death data and 167 sources of sibling history data), and 24 other sources (appendix 1 section 8). Age-specific mortality was estimated using 43 758 empirical life tables for 1950–2021 (compared with 35 406 in GBD 2019; appendix 1 section 8). Prevalence surveys, antenatal clinic serosurveillance, and vital registration were used to adjust for the impact of the HIV epidemic due to its exceptional impact on age-specific mortality. Fatal discontinuities were accounted for using 2235 location-years from vital registration and 237 other sources (compared with 1812 from vital registration and 174 other sources in GBD 2019). Estimation of excess mortality due to the COVID-19 pandemic utilised an additional 146 139 datapoints of all-cause mortality data at either weekly or monthly intervals from vital registration and surveillance reports that were assessed for completeness of registration (compared with

our previous excess mortality estimation,[16] GBD 2021 used 1389 additional weeks or months of data).

Population estimates utilised national and subnational censuses (1277 overall; 25 new), population registries (749 location-years of data), and post-enumeration surveys (161 in total). Additionally, migration data on refugee movements from the UN High Commissioner for Refugees and datasets for select countries (primarily Gulf States and nations in the EU) were used to inform migration estimates.

All-cause mortality estimation

GBD 2021 all-cause mortality estimation followed the analytical framework for mortality analysis used in GBD 2019.[10] Point estimates from surveys were generated using both direct and indirect estimation methods for U5MR, while for adult mortality, they were generated from sibling history data with methods that correct for inherent biases such as zero-survivor and recall bias. Time series estimates of the completeness of adult vital registration data were generated using the same modelling process as GBD 2019, which used a combination of five death distribution methods, and point estimates were adjusted accordingly.

Time series of under-5 and adult mortality without fatal discontinuities were estimated using spatiotemporal Gaussian process regression (ST-GPR), including a bias-adjustment process for U5MR, to correct for systematic differences in the data sources and smooth results across time and location. Education, HIV, and lag-distributed income were included as covariates, along with U5MR for adult mortality. These estimates were used as inputs for the GBD relational model life table system with adjustments for older-age mortality to estimate HIV-free age-specific mortality rates. HIV mortality was modelled with a combination of ST-GPR, the Estimation and Projection Package Age-Sex Model,[19] and Spectrum,[20] and subsequently used to produce life tables that included HIV mortality. These abridged life tables were used to generate full life tables by single year age groups with further detailed age groups under the age of 1 year. Sex-redistributed and age-redistributed fatal discontinuities by cause were aggregated by age and sex and added to the estimated mortality from the previous step to generate the final all-cause mortality life tables by location, year, sex, and age. We recalculated abridged life tables, including fatal discontinuities for each location, year, and sex combination, and then calculated the final envelope from these abridged life tables. Detailed methods for estimating each mortality component are available in appendix 1 (section 2).

Excess mortality due to the COVID-19 pandemic estimation

Excess mortality due to the COVID-19 pandemic in 2020 and 2021 is defined as the observed all-cause mortality minus the mortality that would be expected had

212

the pandemic not occurred, based on historical trends. Excess deaths are those attributed to the COVID-19 pandemic as a whole, both from SARS-CoV-2 infection and from other pandemic-related factors such as deferred care seeking.[21,22] Excess mortality was calculated using similar methods as in Wang et al (2022),[16] with several key improvements. We included yearly observed deaths from vital registration to supplement daily, weekly, and monthly observed death data. We then used five variants of the spline for weekly seasonal patterns that set the second-to-last knot at 18, 24, 36, 48, or 60 months to allow for more stable trends. To select covariates, we used Rover, a method developed at the Institute for Health Metrics and Evaluation based on Bayesian model averaging. Rover is conceptually similar to the Bayesian model averaging method, which is widely used to explore the parameter space and aggregate estimates across candidate models based on performance metrics.[23] The main difference is that while Bayesian model averaging uses marginal likelihood, Rover focuses on out-of-sample performance. We included covariates pertaining to the COVID-19 pandemic, such as seroprevalence, and background population health metrics, such as the Healthcare Access and Quality Index.[24] With the best model selected, we ran a prediction process using 100 draws for each covariate and 100 draws of estimated coefficients and residuals, estimated from the regressions run at the draw level using draw-level input data on both excess mortality and covariates. Mean values and 95% uncertainty intervals (UIs) were then generated at national, regional, and global levels. Out-of-sample predictive validity testing was conducted based on our final model specification. Complete excess mortality methodology is detailed in appendix 1 (section 2.8).

To determine age-specific and sex-specific excess mortality, we estimated all-cause mortality twice: once with data from during the pandemic in 2020 and 2021 included and once without. For location-years with vital registration data from during the pandemic, we computed the difference in estimated age-sex-specific mortality between the two sets of estimates. We then applied this distribution to our excess mortality estimates to calculate age-specific and sex-specific excess mortality. Due to instability in age-sex distributions and implausible patterns, we used the global age-sex distribution for locations with fewer than 75 000 excess deaths, unless otherwise noted (appendix 1 section 2.8). Other pandemic-related mortality (OPRM) was estimated by calculating the difference between excess mortality and the sum of deaths due directly to COVID-19 infection and indirect deaths due to lower respiratory infections, measles, and pertussis. For locations with a negative OPRM, we adjusted the non-pandemic mortality estimates downward accordingly. We redistributed small discrepancies that remained between the mortality estimates that used vital registration age-sex-specific data from during the pandemic and the non-pandemic

mortality estimates plus age-sex-specific excess mortality to ensure that the final mortality estimates including mortality shocks were consistent with observed high-quality vital registration data.

Population estimation

We used the Bayesian hierarchical cohort component model for population projection (BCCMP) from GBD 2019 to produce age-specific population estimates.[19] This method used age-specific fertility estimates from GBD 2021 (appendix 1 section 3), the previously described age-specific mortality estimates, and available census and registry data as inputs. Auxiliary refugee and migration data were used to inform the prior distribution on net migration in countries with substantial migration or reliable data. The model estimates an age-specific 1950 baseline population, age-specific net migration, and age-specific population estimates that are fully consistent with the input fertility and mortality estimates. Complete population estimation methodology is in appendix 1 (section 4).

Expected mortality based on Socio-demographic Index (SDI) estimation

We analysed the relationship between age-specific log mortality rates and SDI using MR-BRT (meta-regression-Bayesian regularised trimmed),[25] a meta-regression programme (appendix 1 section 6.1). SDI is a composite indicator of a country's lag-distributed income per capita,
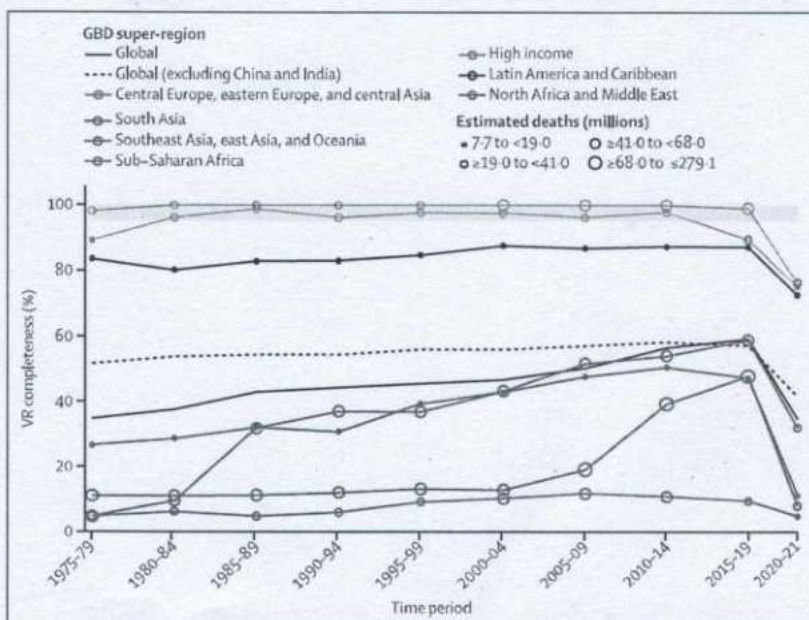

Figure 1: Completeness of VR systems in GBD super-regions, 1975–2021
Completeness is defined as the total number of deaths registered in all VR systems within a super-region during a 5-year period divided by the total number of estimated deaths within that super-region and period, with 100% completeness indicating that all deaths were registered. The size of the datapoints represents the number of estimated deaths. The solid black line shows the global completeness, the dashed black line indicates global completeness excluding China and India, and other coloured lines indicate GBD super-regions. The green box indicates complete registration (defined as >95%). GBD=Global Burden of Diseases, Injuries, and Risk Factors study. VR=vital registration.

1993

213

average years of schooling, and the total fertility rate in females younger than age 25 years (appendix 1 section 5). MR-BRT defines a linear mixed-effects model with a B-spline specification for the relationship between outcomes of interest and SDI. We used a cubic spline with five knots between 0 and 1, with left-most and right-most spline segments enforced to be linear, and with slopes matching adjacent interior segments. To ensure that the results were not sensitive to the choice of spline knots, we used a model ensemble of over 50 cubic spline models, as described above. For each model, interior knot placement was randomly generated to be between 0·1 and 0·9, with minimum inter-knot distance of 0·1 and maximum inter-knot distance of 1·0. The final predictions were obtained using the ensemble aggregate over these 50 models. This model was performed separately for each GBD age-sex group. Expected mortality rates for each age-sex group based on SDI were used to estimate expected life expectancy. A similar analysis was done for excess mortality rates due to the COVID-19 pandemic, with the exception that two-degree splines were used.

Geographical units, age groups, and time periods

We produced estimates for each demographic metric by age-sex-location-year for 25 age groups: early neonatal (0–6 days), late neonatal (7–27 days), 1–5 months, 6–11 months, 12–23 months, 2–4 years, 5–9 years, every 5-year age group up to 95 years, and 95 years and older (fertility estimated for 5-year age groups between ages 10 years and 54 years); for males, females, and all sexes combined; for 204 countries and territories grouped into 21 regions and seven super-regions; and for every year from 1950 to 2021. We also included subnational analyses for 21 countries and territories (Brazil, China, Ethiopia, India, Indonesia, Iran, Italy, Japan, Kenya, Mexico, New Zealand, Nigeria, Norway, Pakistan, the Philippines, Poland, Russia, South Africa, Sweden, the UK, and the USA) and estimates by SDI quintile. All countries and territories were assigned an SDI value ranging from 0 (lowest income and educational attainment and highest fertility) to 100 and then grouped into quintiles from low SDI to high SDI.

Uncertainty analysis

Uncertainty was propagated throughout the estimation process. For under-5 and adult mortality, ST-GPR generated 1000 draws for every location, year, and sex combination; 1000 draws were also produced for the crude death rate associated with HIV estimates. The 100 draws of excess mortality due to the COVID-19 pandemic were repeated ten times to generate 1000 draws. These draw-level inputs were then used to create 1000 draws of all-cause mortality estimates and draw-level estimates of fatal discontinuities. Mean estimates and 95% UIs (the 25th and 975th ranked values from the 1000 draws) were generated for all demographic

metrics using the draw-level estimates. The uncertainty associated with fertility and mortality estimates was included as inputs in the BCCMP model to produce 1000 draws of population estimates.

Role of the funding source

The funders of this study had no role in study design, data collection, data analysis, data interpretation, or the writing of the report

Results

This section presents global, regional, and national-level results for key demographic metrics; given space constraints, estimates at the subnational level are presented in appendix 2 and are also available in downloadable form through the GBD Results tool. All subnational locations are listed in appendix 1 (section 8).

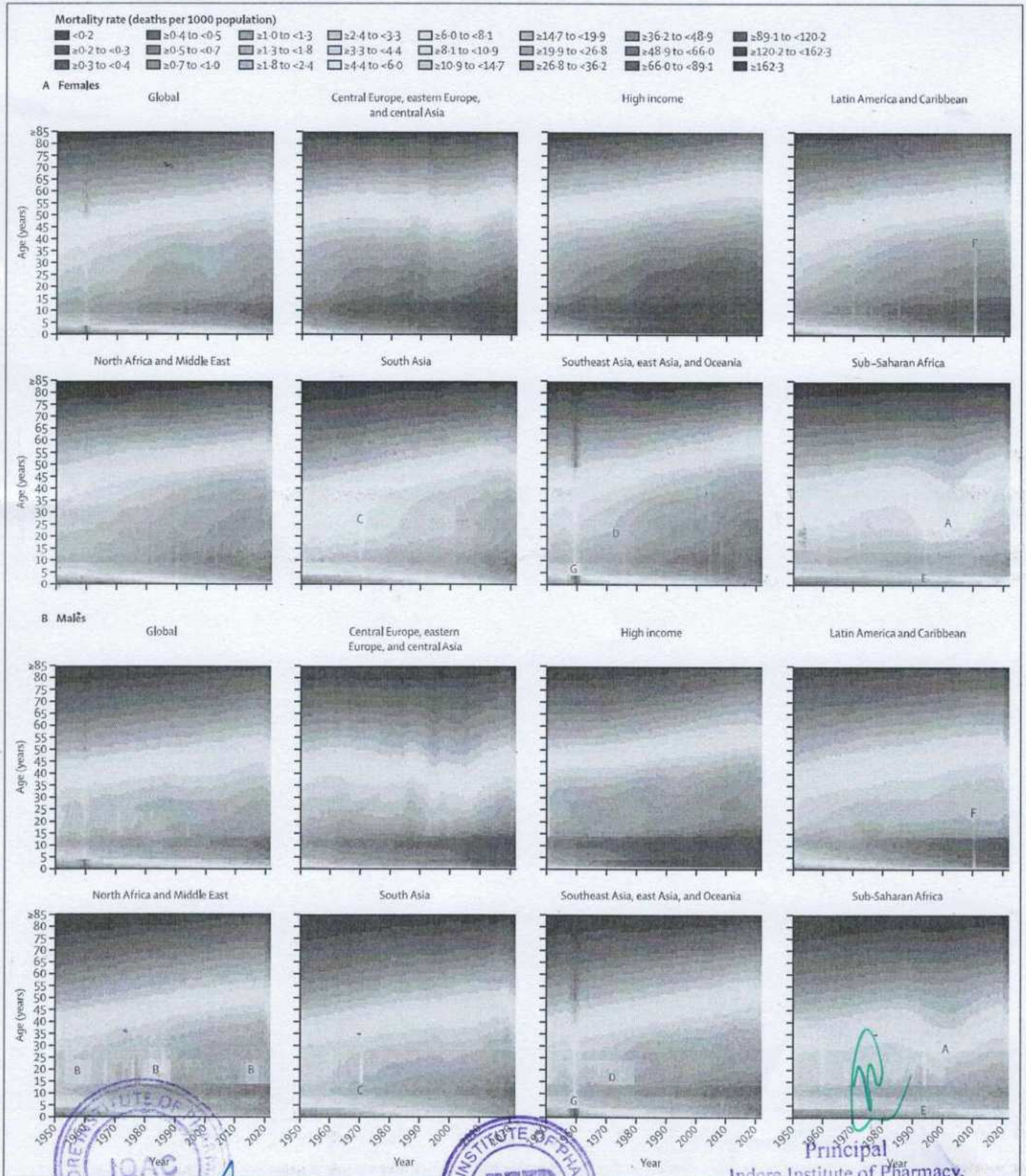### Civil registration and vital statistics completeness

The proportion of deaths registered in vital registration systems increased substantially at the global level during the study period, from 30·3% in 1975 to a peak of 61·1% in 2016, before declining in subsequent years due to lags in reporting (figure 1). Completeness of death registration in vital registration systems varied markedly between regions, however, most progress in completeness was observed in China (where completeness peaked at 71·2% in 2018) and India (where completeness peaked at 80·1% in 2019; appendix 2 table S1). The Indian Sample Registration System is considered complete for the sample population it covers. Outside of China and India, progress in death registration has been slow, with only a 10·3 percentage point increase observed in the rest of the world between 1975 and the peak in 2016. This increase was concentrated in north Africa and the Middle East, which improved from 20·6% completeness in 1975 to a peak of 56·0% in 2016. While registration has been complete (defined as >95%) since 1975 for nearly all countries in the high-income super-region and central Europe, eastern Europe, and central Asia, in sub-Saharan Africa peak completeness of only 8·7% was reached in 2008 and completeness has declined since then. Death registration in Latin America and the Caribbean was more variable: countries such as Costa Rica, Cuba, and Argentina have been complete for many years; registration in countries such as Peru and Ecuador has remained around 60–90% complete, and

Figure 2: Global and GBD super-region all-cause mortality rates across the lifespan in females (A) and males (B), 1950–2021
Mortality rates are expressed as the number of deaths per 1000 population. Fatal discontinuities are indicated by the following letters: A=HIV epidemic; B=conflicts in the Middle East; C=war and genocide in India, Pakistan, and Bangladesh in 1971; D=war and genocide in Cambodia in the 1970s; E=Rwandan genocide in 1994; F=earthquake in Haiti in 2010; G=famine between 1959 and 1961. GBD=Global Burden of Diseases, Injuries, and Risk Factors Study.

214

Mortality rate (deaths per 1000 population)

- <0·2
- ≥0·2 to <0·3
- ≥0·3 to <0·4
- ≥0·4 to <0·5
- ≥0·5 to <0·7
- ≥0·7 to <1·0
- ≥1·0 to <1·3
- ≥1·3 to <1·8
- ≥1·8 to <2·4
- ≥2·4 to <3·3
- ≥3·3 to <4·4
- ≥4·4 to <6·0
- ≥6·0 to <8·1
- ≥8·1 to <10·9
- ≥10·9 to <14·7
- ≥14·7 to <19·9
- ≥19·9 to <26·8
- ≥26·8 to <36·2
- ≥36·2 to <48·9
- ≥48·9 to <66·0
- ≥66·0 to <89·1
- ≥89·1 to <120·2
- ≥120·2 to <162·3
- ≥162·3

A Females

Global — Central Europe, eastern Europe, and central Asia — High income — Latin America and Caribbean

North Africa and Middle East — South Asia — Southeast Asia, east Asia, and Oceania — Sub–Saharan Africa

B Males

Global — Central Europe, eastern Europe, and central Asia — High income — Latin America and Caribbean

North Africa and Middle East — South Asia — Southeast Asia, east Asia, and Oceania — Sub-Saharan Africa

215

others, such as Bolivia, continue to lack registration data. At the national level, 96 countries and territories had at least 1 year of complete death registration between 2010 and 2021; 29 countries and territories without complete death registration had at least 1 year of registering more than 75% of deaths; and 47 countries and territories had no vital registration data in the GBD 2021 mortality database. Registration was incomplete or non-existent in many countries with large numbers of deaths in 2021, especially in sub-Saharan Africa, including Nigeria and Democratic Republic of Congo. In the 2020–21 period, super-regions had varying degrees of lowered completeness indicative of lags in reporting (figure 1).

Mortality and life expectancy

Between 1950 and 2019, global age-standardised all-cause mortality rates per 100 000 population broadly declined, from 1980·5 age-standardised deaths (95% UI 1855·5–2115·0) in 1950 to 736·1 (700·1–772·8) in 2019 (appendix 2 table S3A), which equates to a 62·8% (60·5–65·1) decline in mortality during the entire period. Global all-cause mortality rates across the human lifespan for the younger than 15 years and older than 40 years age groups broadly improved for both females and males between 1950 and 2019 (figure 2). This pattern was relatively consistent across super-regions, with the exception of increased mortality in sub-Saharan Africa during the HIV epidemic and a fluctuating pattern in the central Europe, eastern Europe, and central Asia super-region. However, substantial variation in mortality levels and trends across super-regions and over time were observed in the 15–39-years age group. This age group

was particularly susceptible to mortality shocks such as famine in China between 1959 and 1961; conflicts in the Middle East during multiple time periods; war in India, Pakistan, and Bangladesh and genocide in Bangladesh in 1971; war and genocide in Cambodia in the 1970s; the Rwandan genocide in 1994; and the earthquake in Haiti in 2010 (figure 2). Conflict and war had a larger impact on mortality rates in males than females. Furthermore, the HIV epidemic had an especially large impact on this age group in sub-Saharan Africa and a lesser impact in southeast Asia, east Asia, and Oceania, with a larger impact on females than males. Additionally, male mortality rates increased in Latin America and the Caribbean during the 2000s, to varying extents in countries such as El Salvador, Peru, Guatemala, Honduras, Mexico, Venezuela, and Brazil (appendix 2 figure S5). An increase in male and female mortality was observed in the high-income super-region during the late 2010s, which was most notable in the USA, Canada, and Spain (appendix 2 figure S5).

During the COVID-19 pandemic in 2020 and 2021, global age-standardised all-cause mortality rates increased by 21·9% (95% UI 13·6–31·1) for males aged 15 years and older compared with 2019 and 16·6% (10·0–23·4) for females in the same age group and time period, reversing trends in mortality observed before the pandemic (appendix 2 table S3). In contrast, during 2020 and 2021, global mortality rates for both males and females generally remained constant or further decreased for age groups younger than 15 years (figure 2). In particular, between 2019 and 2021, global U5MR decreased by 7·0% (2·3–11·1). This continued reduction in child mortality was consistent across all super-regions (figure 2).
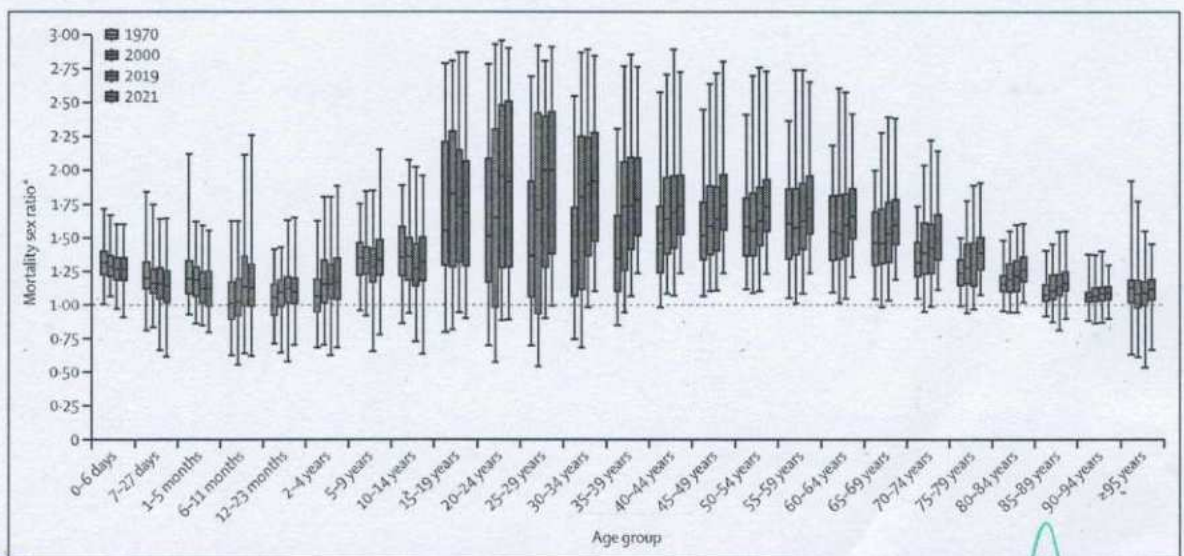

Figure 3: Distribution of the mortality sex ratio by age in 1970, 2000, 2019, and 2021
The distributions are for the mortality sex ratio calculated across all 204 countries and territories included in this study. The boxes represent the middle 50% of the distribution (25th and 75th percentiles), the horizontal line in boxes indicates the mean, and the whiskers show the middle 95% of the distribution (2·5th and 97·5th percentiles). *The ratio of male to female mortality rates, computed by dividing the male mortality rate by the female mortality rate for each age group and year.

216

	Under-5 mortality		Probability of death between ages 15 and 59 years, 2021		Life expectancy at birth in 2021 (years)			Total deaths in 2021 (thousands)	Total deaths among children younger than 5 years in 2021 (thousands)	Excess deaths due to COVID-19 in 2020 (thousands)	Excess deaths due to COVID-19 in 2021 (thousands)	Excess mortality rate due to COVID-19, 2020–21 (deaths per 1000)
	Mortality rate in 2021 (deaths per 1000)	Annualised rate of change, 2000–21	Females	Males	Females	Males	Both sexes					
Global	35.7 (30.5 to 42.0)	–3.3% (–4.0 to –2.5)	0.12 (0.11 to 0.12)	0.19 (0.18 to 0.20)	74.8 (74.0 to 75.5)	69.0 (68.0 to 69.9)	71.7 (70.9 to 72.5)	67900.0 (65000.0 to 70800.0)	4660.0 (3980.0 to 5500.0)	5890 (5480 to 6440)	9970 (9260 to 10900)	1.04 (0.96 to 1.13)
Central Europe, eastern Europe, and Central Asia	12.0 (10.5 to 13.7)	–3.8% (–4.4 to –3.2)	0.11 (0.11 to 0.12)	0.25 (0.24 to 0.26)	75.5 (75.0 to 75.9)	67.4 (66.9 to 67.9)	71.5 (71.0 to 71.8)	5950.0 (5790.0 to 6130.0)	59.0 (51.7 to 67.6)	740 (681 to 801)	1400 (1300 to 1520)	2.70 (2.50 to 2.90)
Central Asia	20.9 (17.6 to 24.6)	–4.1% (–4.8 to –3.2)	0.11 (0.10 to 0.12)	0.22 (0.21 to 0.24)	74.3 (73.3 to 75.2)	67.4 (66.4 to 68.5)	70.8 (69.8 to 71.8)	724.0 (671.0 to 779.0)	42.6 (36.0 to 50.4)	108 (80 to 133)	150 (102 to 186)	1.46 (1.06 to 1.80)
Armenia	11.1 (9.0 to 13.8)	–4.8% (–6.0 to –3.6)	0.07 (0.06 to 0.07)	0.18 (0.16 to 0.19)	78.6 (77.8 to 79.4)	71.3 (70.3 to 72.4)	75.0 (74.1 to 76.0)	31.3 (28.9 to 33.8)	0.4 (0.3 to 0.5)	7 (5 to 9)	5 (3 to 6)	2.08 (1.43 to 2.61)
Azerbaijan	28.6 (23.4 to 34.7)	–4.0% (–5.0 to –3.0)	0.10 (0.09 to 0.11)	0.21 (0.19 to 0.23)	73.4 (72.5 to 74.3)	67.0 (66.0 to 68.2)	70.1 (69.2 to 71.2)	89.3 (81.9 to 96.4)	3.9 (3.2 to 4.7)	21 (17 to 24)	25 (20 to 30)	2.31 (1.83 to 2.67)
Georgia	9.7 (7.7 to 12.2)	–6.1% (–7.2 to –5.0)	0.10 (0.10 to 0.10)	0.25 (0.25 to 0.26)	75.8 (75.5 to 76.2)	67.3 (67.0 to 67.5)	71.5 (71.2 to 71.7)	59.6 (58.6 to 60.5)	0.4 (0.3 to 0.6)	6 (4 to 7)	17 (11 to 21)	3.29 (2.22 to 4.19)
Kazakhstan	10.2 (8.4 to 12.3)	–6.1% (–7.0 to –5.1)	0.13 (0.12 to 0.14)	0.28 (0.26 to 0.30)	73.9 (73.1 to 74.7)	65.3 (64.4 to 66.2)	69.6 (68.7 to 70.4)	181.0 (169.0 to 194.0)	4.1 (3.4 to 5.0)	30 (23 to 36)	51 (41 to 60)	2.36 (1.87 to 2.76)
Kyrgyzstan	17.0 (14.9 to 19.0)	–4.4% (–5.2 to –3.7)	0.10 (0.09 to 0.12)	0.23 (0.20 to 0.26)	76.1 (74.7 to 77.6)	68.4 (66.6 to 70.2)	72.3 (70.7 to 73.9)	38.9 (34.2 to 43.6)	2.7 (2.3 to 3.0)	7 (5 to 9)	6 (4 to 9)	1.06 (0.74 to 1.38)
Mongolia	16.9 (14.0 to 20.5)	–5.6% (–6.6 to –4.6)	0.12 (0.10 to 0.13)	0.29 (0.26 to 0.32)	74.6 (73.5 to 75.7)	65.7 (64.3 to 67.1)	70.0 (69.1 to 71.0)	21.5 (19.9 to 23.0)	1.3 (1.1 to 1.6)	–2 (–5 to 1)	1 (–3 to 4)	–0.17 (–1.15 to 0.74)
Tajikistan	34.5 (28.5 to 42.2)	–3.1% (–4.1 to –2.1)	0.13 (0.11 to 0.15)	0.21 (0.18 to 0.24)	72.1 (70.4 to 73.7)	66.9 (65.1 to 69.1)	69.3 (67.8 to 71.0)	59.1 (52.2 to 65.6)	9.7 (8.0 to 11.9)	12 (9 to 15)	16 (11 to 20)	1.46 (1.06 to 1.79)
Turkmenistan	27.5 (22.2 to 33.5)	–3.7% (–4.6 to –2.6)	0.15 (0.12 to 0.19)	0.28 (0.24 to 0.34)	71.5 (69.4 to 73.7)	64.3 (62.0 to 66.8)	67.8 (65.5 to 70.1)	43.6 (36.5 to 51.2)	3.0 (2.4 to 3.7)	6 (5 to 8)	8 (6 to 10)	1.46 (1.06 to 1.79)
Uzbekistan	21.5 (17.7 to 26.0)	–3.5% (–4.4 to –2.5)	0.10 (0.09 to 0.12)	0.18 (0.15 to 0.20)	75.1 (73.6 to 76.6)	69.9 (68.1 to 71.7)	72.5 (70.8 to 74.2)	200.0 (175.0 to 227.0)	17.0 (14.0 to 20.7)	22 (12 to 30)	21 (7 to 31)	0.69 (0.30 to 0.98)
Central Europe	5.0 (4.5 to 5.6)	–4.7% (–5.1 to –4.2)	0.08 (0.08 to 0.08)	0.18 (0.18 to 0.18)	78.3 (78.2 to 78.5)	71.3 (71.1 to 71.4)	74.7 (74.5 to 74.8)	1760.0 (1740.0 to 1780.0)	5.3 (4.8 to 5.9)	195 (140 to 243)	353 (268 to 422)	2.54 (1.89 to 3.05)
Albania	13.1 (10.7 to 16.0)	–3.7% (–4.8 to –2.6)	0.06 (0.05 to 0.07)	0.13 (0.11 to 0.15)	78.7 (77.6 to 79.9)	73.6 (72.1 to 75.3)	76.0 (74.7 to 77.5)	30.1 (26.5 to 33.6)	0.4 (0.3 to 0.4)	5 (2 to 8)	7 (3 to 10)	2.36 (1.05 to 3.63)
Bosnia and Herzegovina	5.2 (4.4 to 6.3)	–3.6% (–4.4 to –2.7)	0.07 (0.06 to 0.09)	0.15 (0.12 to 0.17)	78.3 (76.9 to 79.8)	72.6 (70.8 to 74.6)	75.4 (73.8 to 77.0)	46.4 (39.7 to 53.0)	0.1 (0.1 to 0.2)	5 (1 to 9)	8 (3 to 14)	2.05 (0.80 to 3.47)
Bulgaria	6.6 (5.9 to 7.4)	–4.6% (–5.2 to –4.1)	0.13 (0.13 to 0.14)	0.26 (0.25 to 0.27)	73.7 (73.3 to 74.1)	66.4 (65.9 to 67.0)	69.0 (64.0 to 70.3)	169.0 (164.0 to 173.0)	0.4 (0.3 to 0.4)	20 (11 to 26)	47 (36 to 56)	5.21 (3.82 to 6.30)
Croatia	4.6 (3.8 to 5.4)	–2.7% (–3.5 to –1.8)	0.06 (0.05 to 0.06)	0.13 (0.12 to 0.13)	80.3 (80.0 to 80.6)	74.1 (73.8 to 74.4)	62.4 (60.6 to 64.0)	62.4 (60.6 to 64.0)	0.2 (0.1 to 0.2)	5 (2 to 7)	10 (6 to 14)	1.84 (1.03 to 2.61)
Czechia	2.7 (2.3 to 3.1)	–3.2% (–4.0 to –2.4)	0.06 (0.06 to 0.06)	0.12 (0.12 to 0.13)	80.9 (80.6 to 81.1)	74.4 (74.2 to 74.6)	77.8 (77.6 to 77.8)	138.0 (136.0 to 141.0)	0.3 (0.2 to 0.3)	15 (8 to 22)	23 (12 to 32)	1.88 (1.00 to 2.57)
Hungary	4.0 (3.4 to 4.7)	–4.6% (–5.3 to –3.8)	0.09 (0.09 to 0.10)	0.19 (0.19 to 0.19)	78.0 (77.8 to 78.2)	70.9 (70.7 to 71.1)	74.3 (74.1 to 74.6)	154.0 (152.0 to 156.0)	0.4 (0.3 to 0.4)	12 (3 to 18)	26 (14 to 35)	2.02 (0.96 to 2.84)

(Table 1 continues on next page)

217

(Continued from previous page)

	Under-5 mortality		Probability of death between ages 15 and 59 years, 2021		Life expectancy at birth in 2021 (years)			Total deaths in 2021 (thousands)	Total deaths among children younger than 5 years in 2021 (thousands)	Excess deaths due to COVID-19 in 2020 (thousands)	Excess deaths due to COVID-19 in 2021 (thousands)	Excess mortality rate due to COVID-19, 2020–21 (deaths per 1000)
	Mortality rate in 2021 (deaths per 1000)	Annualised rate of change, 2000–21	Females	Males	Females	Males	Both sexes					
Montenegro	3.9 (3.2 to 4.7)	−5.5% (−6.5 to −4.5)	0.08 (0.08 to 0.09)	0.18 (0.17 to 0.19)	76.0 (75.4 to 76.6)	69.8 (69.0 to 70.5)	72.7 (72.1 to 73.3)	9.9 (9.4 to 10.4)	0.0 (0.0 to 0.0)	1 (1 to 1)	3 (3 to 3)	3.35 (2.78 to 3.90)
North Macedonia	5.6 (4.9 to 6.3)	−4.9% (−5.5 to −4.2)	0.11 (0.09 to 0.12)	0.19 (0.17 to 0.22)	74.2 (73.2 to 75.3)	69.2 (68.0 to 70.4)	71.5 (70.4 to 72.7)	32.7 (29.3 to 36.3)	0.1 (0.1 to 0.1)	7 (5 to 8)	10 (8 to 12)	4.86 (3.79 to 5.66)
Poland	4.4 (3.9 to 5.0)	−3.7% (−4.3 to −3.1)	0.07 (0.07 to 0.07)	0.18 (0.18 to 0.18)	79.7 (79.6 to 79.8)	71.8 (71.7 to 71.9)	75.7 (75.6 to 75.8)	517.0 (514.0 to 520.0)	1.5 (1.3 to 1.7)	65 (48 to 78)	101 (72 to 122)	2.28 (1.81 to 2.72)
Romania	6.7 (6.1 to 7.4)	−5.7% (−6.2 to −5.3)	0.10 (0.10 to 0.10)	0.22 (0.22 to 0.22)	76.8 (76.7 to 77.0)	69.2 (69.1 to 69.4)	72.9 (72.8 to 73.0)	334.0 (332.0 to 337.0)	1.2 (1.1 to 1.3)	38 (25 to 51)	72 (49 to 90)	3.00 (2.06 to 3.85)
Serbia	4.7 (4.2 to 5.2)	−5.4% (−6.3 to −4.6)	0.08 (0.08 to 0.09)	0.16 (0.16 to 0.16)	76.7 (76.5 to 76.9)	71.7 (71.5 to 71.8)	74.1 (74.0 to 74.3)	149.0 (147.0 to 151.0)	0.3 (0.3 to 0.4)	15 (5 to 27)	26 (6 to 44)	2.52 (0.61 to 4.24)
Slovakia	5.8 (5.1 to 6.4)	−2.6% (−3.2 to −2.0)	0.08 (0.08 to 0.08)	0.17 (0.17 to 0.18)	78.3 (78.1 to 78.6)	71.3 (71.0 to 71.5)	74.7 (74.6 to 74.9)	72.6 (71.5 to 73.6)	0.3 (0.3 to 0.4)	5 (2 to 8)	18 (13 to 22)	2.23 (1.38 to 2.88)
Slovenia	2.2 (2.0 to 2.5)	−4.2% (−4.8 to −3.6)	0.04 (0.04 to 0.04)	0.10 (0.09 to 0.10)	84.0 (83.4 to 84.6)	77.6 (77.2 to 78.1)	80.8 (80.4 to 81.3)	23.0 (22.0 to 23.9)	0.0 (0.0 to 0.0)	3 (1 to 4)	2 (0 to 4)	1.20 (0.31 to 1.88)
Eastern Europe	6.1 (5.6 to 6.5)	−5.2% (−5.6 to −4.8)	0.13 (0.12 to 0.14)	0.30 (0.28 to 0.32)	74.9 (74.2 to 75.5)	65.8 (65.0 to 66.6)	70.4 (69.8 to 70.9)	3470.0 (3340.0 to 3610.0)	11.1 (10.3 to 11.9)	436 (398 to 467)	899 (854 to 940)	3.33 (3.15 to 3.46)
Belarus	4.0 (3.1 to 5.3)	−6.9% (−8.2 to −5.5)	0.11 (0.10 to 0.13)	0.29 (0.25 to 0.33)	76.0 (74.4 to 77.5)	66.0 (64.2 to 67.8)	71.0 (69.2 to 72.7)	162.0 (141.0 to 186.0)	0.3 (0.3 to 0.4)	23 (17 to 29)	42 (32 to 54)	3.67 (2.78 to 4.77)
Estonia	2.5 (2.2 to 2.9)	−7.1% (−7.8 to −6.4)	0.07 (0.06 to 0.07)	0.17 (0.17 to 0.18)	81.2 (80.6 to 81.8)	72.4 (71.9 to 72.9)	76.9 (76.5 to 77.3)	18.6 (18.0 to 19.2)	0.0 (0.0 to 0.0)	0 (−1 to 1)	3 (2 to 5)	1.44 (0.59 to 2.33)
Latvia	3.7 (3.2 to 4.3)	−6.1% (−6.9 to −5.4)	0.10 (0.09 to 0.10)	0.26 (0.25 to 0.27)	78.1 (77.7 to 78.5)	68.3 (67.9 to 68.7)	73.2 (73.0 to 73.5)	34.2 (33.4 to 35.0)	0.1 (0.1 to 0.1)	1 (0 to 3)	7 (5 to 9)	2.35 (1.36 to 3.41)
Lithuania	3.5 (3.1 to 3.9)	−5.3% (−5.9 to −4.7)	0.09 (0.09 to 0.10)	0.24 (0.23 to 0.24)	78.9 (78.5 to 79.3)	69.2 (68.8 to 69.5)	74.1 (73.8 to 74.4)	47.2 (46.2 to 48.2)	0.1 (0.1 to 0.1)	5 (3 to 8)	10 (6 to 13)	2.84 (1.91 to 3.89)
Moldova	10.9 (8.2 to 14.4)	−4.4% (−5.7 to −3.0)	0.11 (0.10 to 0.12)	0.25 (0.23 to 0.27)	76.4 (75.4 to 77.3)	67.9 (66.7 to 69.0)	72.1 (71.0 to 73.2)	50.1 (47.0 to 53.6)	0.3 (0.2 to 0.4)	5 (3 to 6)	10 (10 to 11)	2.29 (2.21 to 2.38)
Russia	5.8 (5.5 to 6.2)	−5.6% (−5.9 to −5.2)	0.14 (0.14 to 0.14)	0.31 (0.31 to 0.31)	74.3 (74.3 to 74.4)	65.5 (65.5 to 65.6)	70.0 (69.9 to 70.0)	2410.0 (2410.0 to 2420.0)	8.1 (7.6 to 8.6)	357 (355 to 360)	690 (687 to 693)	3.70 (3.68 to 3.72)
Ukraine	7.8 (6.2 to 9.2)	−3.3% (−4.3 to −2.4)	0.11 (0.08 to 0.15)	0.29 (0.22 to 0.37)	75.7 (72.7 to 78.6)	66.3 (62.7 to 70.1)	71.0 (68.5 to 73.6)	745.0 (614.0 to 880.0)	2.2 (1.7 to 2.6)	44 (9 to 77)	137 (96 to 179)	2.18 (1.45 to 2.93)
High income	4.6 (4.2 to 5.0)	−2.4% (−2.8 to −2.0)	0.06 (0.06 to 0.06)	0.11 (0.11 to 0.11)	83.3 (83.3 to 83.4)	77.9 (77.8 to 78.0)	80.6 (80.5 to 80.7)	10900.0 (10800.0 to 10900.0)	47.9 (44.0 to 52.2)	971 (939 to 1000)	947 (907 to 985)	0.90 (0.87 to 0.93)
Australia	3.3 (2.8 to 3.8)	−3.3% (−4.0 to −2.5)	0.04 (0.04 to 0.04)	0.08 (0.08 to 0.08)	85.3 (85.3 to 85.4)	81.2 (81.1 to 81.3)	83.4 (83.3 to 83.5)	210.0 (209.0 to 210.0)	1.2 (1.0 to 1.4)	−5 (−6 to −5)	4 (3 to 5)	−0.03 (−0.06 to −0.00)
Australia	3.0 (2.5 to 3.6)	−3.6% (−4.4 to −2.7)	0.04 (0.04 to 0.04)	0.08 (0.08 to 0.08)	85.6 (85.5 to 85.7)	81.2 (81.1 to 81.3)	83.4 (83.1 to 83.5)	175.0 (174.0 to 176.0)	0.9 (0.7 to 1.0)	−3 (−4 to −3)	4 (3 to 4)	0.01 (−0.02 to 0.03)

(Table 1 continues on next page)

218

RESEARCH ARTICLE

Unlocking the Immunomodulatory Potential of Rosmarinic Acid Isolated from *Punica granatum* L. using Bioactivity-Guided Approach: *In Silico*, *In Vitro*, and *In Vivo* Approaches

Rupesh K. Gautam[1,2,#], Shailesh Mani Tripathi[3,#], Shopnil Akash[4], Sanjay Sharma[5], Komal Sharma[6], Swapnil Goyal[7], Sahar Behzad[8], Rohit Gundamaraju[9,10], Dinesh Kumar Mishra[11], Yingbo Zhang[1], Bairong Shen[1,*], Sandeep Sundriyal[3,*] and Rajeev K. Singla[1,12,*]

[1]*Joint Laboratory of Artificial Intelligence for Critical Care Medicine, Department of Critical Care Medicine and Institutes for Systems Genetics, Frontiers Science Center for Disease-related Molecular Network, West China Hospital, Sichuan University, Chengdu, China;* [2]*Indore Institute of Pharmacy, IIST Campus, Rau, Indore, 453331, (M.P.), India;* [3]*Department of Pharmacy, Birla Institute of Technology and Science Pilani, Pilani Campus, Rajasthan, 333031, India;* [4]*Department of Pharmacy, Daffodil International University, Daffodil Smart City, Ashulia, Savar, Dhaka, 1207, Bangladesh;* [5]*Department of Quality Assurance, Shobhaben Pratapbhai Patel School of Pharmacy & Technology Management, SVKMs NMIMS, V.L. Mehta Road, Vile Parle (W), Mumbai, Maharashtra, 400056, India;* [6]*Bhupal Nobles' College of Pharmacy, Bhopal Noble's University, Udaipur, 313001, India;* [7]*Faculty of Pharmacy, Mandsaur University, Mandsaur, 458001, India;* [8]*Evidence-based Phytotherapy and Complementary Medicine Research Center, Alborz University of Medical Sciences, Karaj, Iran;* [9]*ER Stress and Mucosal Immunology lab, School of Health Sciences, University of Tasmania, Launceston, Tasmania, Australia;* [10]*School of Medicine, University of California San Francisco, San Francisco, California, United States of America;* [11]*Department of Pharmacy, Guru Ghasidas Vishwavidyalaya (A Central University) Koni, Bilaspur (C.G.), 495009, India;* [12]*School of Pharmaceutical Sciences, Lovely Professional University, Phagwara, Punjab, 144411, India*

Abstract: *Background:* *Punica granatum* L. is well-known for its multifaceted therapeutic potential, including anti-inflammatory and immunomodulatory activities.

Aim: This study aimed to characterize an immunomodulatory compound isolated from *Punica granatum* L. using a bioactivity-guided approach.

Methods: Chromatographic techniques were adopted for isolation and purification of secondary metabolites. *In silico*, *in vitro*, and *in vivo* methods were performed to characterize the therapeutic potential of the isolated compound.

Results: Using preparative thin-layer chromatography, rosmarinic acid was isolated from F4 (column chromatography product obtained from a butanolic fraction of the extract). The impact of rosmarinic acid was assessed in rats using the neutrophil adhesion test, DTH response, and phagocytic index. In immunized rats, rosmarinic acid demonstrated significant immunomodulatory potential. Computational experiments, like molecular docking and molecular dynamics, were also conducted against two targeted receptors, Cereblon (PDB ID: 8AOQ) and human CD22 (PDB ID: 5VKM). Computational studies suggested that an increase in phagocytic index by rosmarinic acid could be attributed to inhibiting Cereblon and CD22. Pharmacokinetics and toxicity prediction also suggested the drug-likeness of rosmarinic acid.

Conclusion: Rosmarinic acid is a potential candidate, but extensive research needs to be done to translate this molecule from bench to bedside.

*Address correspondence to these authors at the Joint Laboratory of Artificial Intelligence for Critical Care Medicine, Department of Critical Care Medicine and Institutes for Systems Genetics, Frontiers Science Center for Disease-related Molecular Network, West China Hospital, Sichuan University, Chengdu, China; E-mails: bairong.shen@scu.edu.cn; rajeevsingla26@gmail.com, rajeevkumar@scu.edu.cn; Department of Pharmacy, Birla Institute of Technology and Science Pilani, Pilani Campus, Rajasthan 333031, India; E-mail: sandeep.sundriyal@pilani.bits-pilani.ac.in

#These authors contributed equally to this work.

1. INTRODUCTION

A disease-free state may be achieved in a living organism by stimulating or inhibiting the immune response [1]. A different system of medicines exists for managing diverse diseases and provides a massive scope of research and discovery of various potent herbs and shrubs as natural therapy [2-9]. Many herbs/shrubs that produce immunomodulatory effects either in single or combination have been explored [10].

With the help of various immunomodulators, the immune system can perform better. Wide varieties of medicinal plants are available to improve the natural resistance of living organisms against various pathogenic attacks and are scientifically reported for their immuno-

modulatory activities. Currently, medicinal flora is exhaustively being explored for high-quality and mighty immunomodulatory compounds [10-13].

Punica granatum L. is also commonly known as pomegranate. Hepatic injury, cerebral ischemia-reperfusion injury, neurological diseases, ulcers, and many other ailments are traditionally treated using various parts of *P. granatum* L. [14, 15]. Previous researchers using various models have proved its anti-inflammatory and immunomodulatory activities [16-18]. In our earlier study on arthritic rats, the anti-arthritic potential of the butanolic fraction of *P. granatum* L. rind extract was evaluated, and a significant effect was observed [19]. As of January 12, 2024, there were 9 articles on
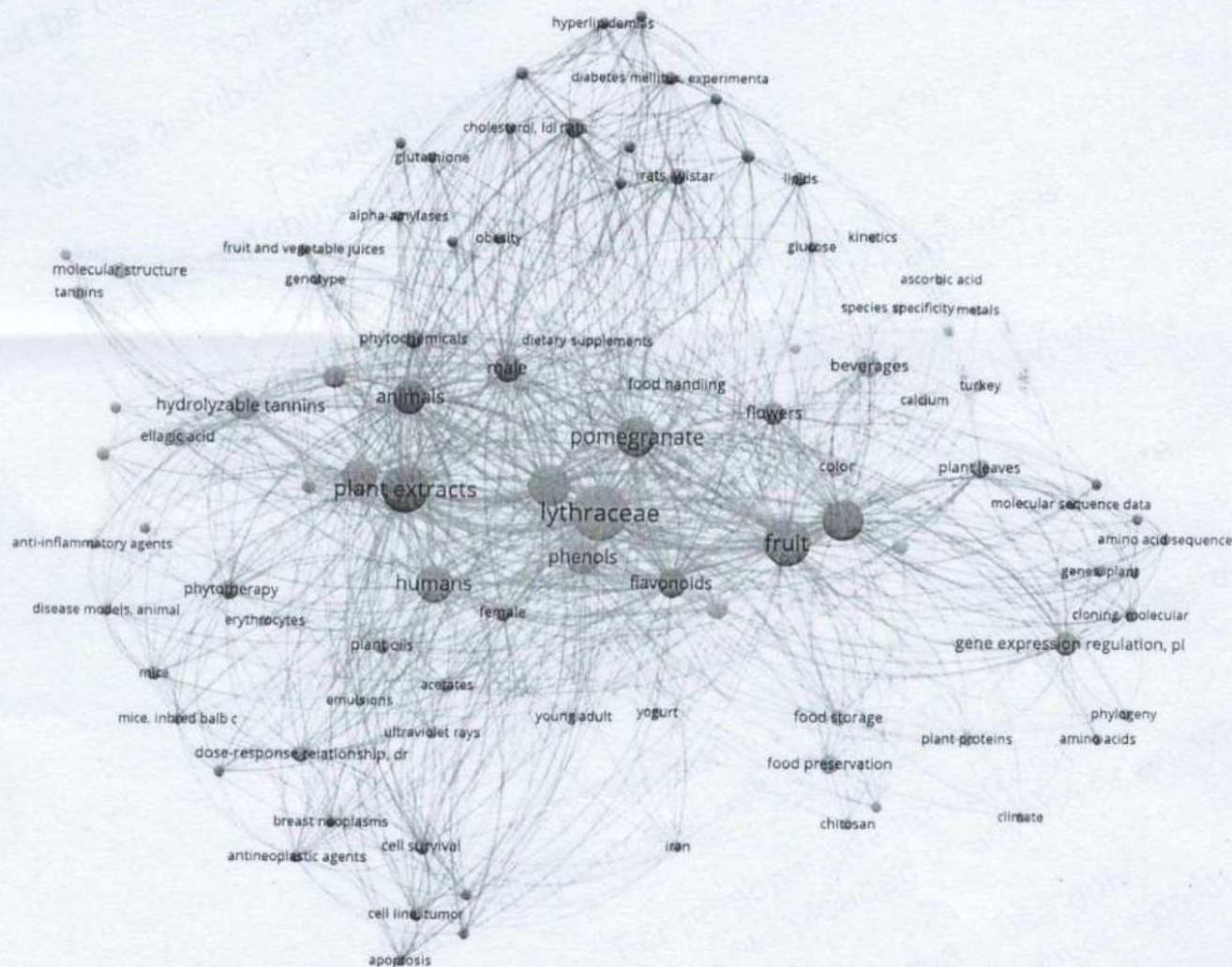
Fig. (1). Interactive mapping between various co-occurring MeSH terms associated with the literature obtained from PubMed related to *Punica granatum* L. and flavone/flavanol/carotenoid/flavonoid/alkaloid/terpene/terpenoid/glycoside/saponin/polyphenol/anthocyanin/steroid. Metadata from PubMed was processed in VOSviewer. (*A higher resolution / colour version of this figure is available in the electronic copy of the article*).

Principal
Indore Institute of Pharmacy,
INDORE (M.P.)

220

PubMed when we used search terms like "*Punica granatum* (title) AND Immunomodulat* (title/abstract)." When we explored PubMed for articles having "*Punica granatum*" in their title and other search terms, like "flavone/flavanol/carotenoid/flavonoid/alkaloid/terpene/terpenoid/glycoside/saponin/polyphenol/anthocyanin/steroid" in their title/abstract, it resulted in 109 articles, as on January 12, 2024, including 7 review articles. Interestingly, 5 out of 7 reviews were published in 2023, reflecting the sudden surge and interest of researchers. VOSviewer is a tool that is widely used for bibliometric analysis [20-22]. We processed metadata and abstracts from these 109 articles in VOSviewer and observed 306 MeSH terms. 99 of the MeSH terms co-occurred in a minimum of 2 publications. Fig. (**1**) illustrates the interactive mapping between these 99 co-occurring MeSH terms. Some of the top co-occurring MeSH terms were "Lythraceae," "plant extracts," "fruit," "antioxidants," "anthocyanins," "polyphenols," "phenols," "flavonoids," "hydrolysable tannins," "seeds," and "flowers." Ellagic acid is one of the most studied molecules, and it seems to be mainly discussed with "antioxidants" and animal studies (Fig. **1**). The interactive analysis also suggested that *P. granatum* L. has been explored for various kinds of phytochemical classes, including flavonoids, phytosterols, tannins (including hydrolysable tannins), alkaloids, plant oils, and amino acids. MeSH terms related to many pharmacological activities were also visible in the interactive mapping. Some of those were related to diabetes, obesity, inflammation, cancer, and infections. Further, clinical studies on *P. granatum* L. and some of its major compounds, like ellagic acid, signify its translational potential [23-25].

Continuing the above perspective, this study aimed to characterize the immunomodulatory compound from *P. granatum*. In this current investigation, we have used *in vitro*, *in vivo*, and *in silico* study protocols to evaluate pharmacological efficiency. We have utilized chromatographic and spectroscopic techniques to isolate and characterize the bioactive constituent of *P. granatum*. L. Protein denaturation assay was adopted for preliminary screening and bioactivity-guided isolation approach. It was then followed by neutrophil adhesion test, DTH response, HA titer, as well as a phagocytic assay to ascertain the immunomodulatory activity. Molecular docking, MD simulation, and MM/PBSA binding free energy calculations were performed to ascertain the binding capabilities of isolated compound with selected targets. Further, ADME profile and toxicity were also predicted for drug-likeness assessment.

2. MATERIALS AND METHODS

2.1. Chemicals and Solvents

Analytical grade solvents (procured from S.D. Fine Chemicals, India) were used in our study. A precoated Thin Layer Chromatography (TLC) plate of 0.2 mm thickness procured from Merck, Germany, was also utilized.

2.2. Extraction, Fractionation, and Isolation by Bioactivity-guided Approach

The extraction, fractionation, and isolation of the compound were carried out according to our previous study, *i.e.*, bioactivity-guided isolation procedure [26]. Briefly, 90% methanolic extract was obtained from 250 g of powdered *P. granatum* L., and it was further fractionated using various solvents. A preliminary phytochemical screening of all the fractions had been performed previously to determine the presence of several active phytocompounds [19, 27, 28]. The inhibition of protein denaturation method has been used to preliminary determine the anti-inflammatory potential of F1 to F5 (collected fractions). Among all fractions, fraction F4 exhibited potent activity and, based on TLC, it showed two spots/bands [26]. Both spots (F4A and F4B) were scratched out and evaluated using a protein denaturation assay [29]. Both scratched spots were characterized using spectral methods (1H-NMR, 13C-NMR, IR, and mass spectrometry) to determine their structural identity.

2.3. Animals

Healthy and untreated Wistar albino rats (body weight ranging between 180-200 g) were used in the pharmacological evaluation of the isolated compound. They were maintained under standard laboratory conditions at $25 \pm 2°C$, relative humidity ($50 \pm 15\%$), and regular photoperiod (12-hour light-dark cycle) throughout the experimental period. A standard pellet diet with *water ad libitum* has been provided to all animals according to standard guidelines provided by the CPCSEA (The Committee for the Purpose of Control and Supervision of Experiments on Animals). The study protocol was followed after getting approval from the IAEC (Institutional Animal Ethics Committee) (protocol no.: 192/PhD/2012/IAEC/BRNCP/12-13/Mandsaur). The rats were subjectively separated as per the models, and six animals were included in each group.

1) The sample size was taken as 6 rats per group.

2) The experimental animals were purchased from a CPCSEA-approved vendor, *i.e.*, Indian Veterinary Research Institute, Izatnagar, India.

Principal
Indore Institute of Pharmacy,
INDORE (M.P.)

221

2.4. Immunomodulatory Activity of Rosmarinic Acid

2.4.1. Neutrophil Adhesion Test (NAT)

As per the Wilkinson method (1978), three groups were prepared. Group 1 included normal rats treated with normal saline, whereas rats of groups II and III were orally given rosmarinic acid (25 and 50 mg/kg, respectively). The rosmarinic acid was given till the 14th day, and on the last day of the experiment, Total Leukocyte Count (TLC) and Differential Leukocyte Count (DLC) were evaluated from the sample (which was collected into heparinized vials) [30-33].

The below formula has been used to calculate the percent neutrophil adhesion:

$$\text{Neutrophil adhesion (\%)} = \frac{\text{NIu (untreated blood sample) - NIt (treated blood sample)}}{\text{NIu (untreated blood sample)}} \times 100 \quad \textbf{(Eq. 1)}$$

2.4.2. Hemagglutinating Antibody (HA) Titer

Rosmarinic acid (25 and 50 mg/kg, orally) was administered to the drug-treated rat groups for 14 days. Simultaneously, Sheep Red Blood Cells (SRBC) were used to immunize all control and drug-treated groups. The day on which immunization was induced was considered as day zero and the drug was continued until 14 days. On the last day of the experiment, blood was collected from each rat, and the titer value was examined through titrating serum dilution method. Antibody titer was considered as hemagglutination using a minimum volume of serum [34].

2.4.3. Delayed-type Hypersensitivity (DTH) Response

Rats were divided into three groups, and every group included six rats. Group I was treated as a control, while groups II and III were administered the test drug (rosmarinic acid). All rats from each group were treated with 0.5×109 cells SRBCs (acting as an antigen) in the pad of the right hind foot. The immunization day was considered zero, and rosmarinic acid was given for seven days. The differences in the paw thickness obtained using pre- and post-challenge thicknesses in the foot were considered for assessing delayed-type hypersensitivity reaction and measured in mm [35].

2.4.4. Phagocytic Response

The methodology proposed by Cheng *et al.* in 2005 was adopted to determine phagocytic response [36-38]. From day 0 to day 7, animals were exposed to varying concentrations of rosmarinic acid (25 and 50 mg/kg, re-

spectively). On the 7th day, each animal received a 0.3 ml/30 g intravenous injection of pre-warmed Indian ink dispersion. Blood samples (50 µl) were taken from each animal at a time interval of 2 and 10 minutes post-injection *via* retro-orbital bleeding. These samples were combined with a 0.1% sodium carbonate solution to break down the red blood cells. The absorbance of these samples was determined at 675 nm using a spectrophotometer. After the final blood collection at 10 minutes, animals were euthanized, and their livers and spleens were harvested and weighed [38]. The K value was determined as follows:

$$\text{Carbon clearance (K)} = \frac{\log OD2 - \log OD10}{T2 - T1} \quad \textbf{(Eq. 2)}$$

$$\text{Phagocytic index (α)} = (K1/3 \times \text{body wt of animal})/(\text{liver wt + spleen wt})$$

OD2 is the log absorbance of blood at 2 min; OD10 is the log absorbance of blood at 10 min; T2 is the last time point of blood collection; T1 is the first time point of blood collection [38].

2.5. Statistical Analysis

The values have been expressed in mean ± SEM. Statistical analysis between treated and control groups was performed using one-way ANOVA and multiple comparison tests to calculate significant differences. The differences were measured as significant when p values were 0.001, 0.01, and 0.05, respectively.

2.6. Computational Studies for Mechanistic Insights and ADME Prediction

2.6.1. Ligand Preparation

The 3D structure of the co-crystallized ligand was extracted from the crystal structure of the target protein, and the rosmarinic acid structure was sourced from PubChem. Both the ligands underwent optimization using the LigPrep tool in the Schrödinger Suite [39], utilizing the OPLS 2005 force field [40]. The Epik algorithm was applied at pH 7.0 ± 2.0 to explore the potential protonation states of all molecules [41]. Throughout the process, the original chirality of the structures was preserved, and tautomeric states were created.

2.6.2. Protein Preparation

Cereblon (CRBN) is an essential target for immunomodulatory drugs and also has antiproliferative potential [42, 43]. Cereblon negatively regulates phagocytosis [44]. Similarly, CD22 is well-recognized for its inhi-

222

2.4. Immunomodulatory Activity of Rosmarinic Acid

2.4.1. Neutrophil Adhesion Test (NAT)

As per the Wilkinson method (1978), three groups were prepared. Group I included normal rats treated with normal saline, whereas rats of groups II and III were orally given rosmarinic acid (25 and 50 mg/kg, respectively). The rosmarinic acid was given till the 14th day, and on the last day of the experiment, Total Leukocyte Count (TLC) and Differential Leukocyte Count (DLC) were evaluated from the sample (which was collected into heparinized vials) [30-33].

The below formula has been used to calculate the percent neutrophil adhesion:

$$\text{Neutrophil adhesion (\%)} = \frac{\text{NIu (untreated blood sample)} - \text{NIt (treated blood sample)}}{\text{NIu (untreated blood sample)}} \times 100 \quad \text{(Eq. 1)}$$

2.4.2. Hemagglutinating Antibody (HA) Titer

Rosmarinic acid (25 and 50 mg/kg, orally) was administered to the drug-treated rat groups for 14 days. Simultaneously, Sheep Red Blood Cells (SRBC) were used to immunize all control and drug-treated groups. The day on which immunization was induced was considered as day zero and the drug was continued until 14 days. On the last day of the experiment, blood was collected from each rat, and the titer value was examined through titrating serum dilution method. Antibody titer was considered as hemagglutination using a minimum volume of serum [34].

2.4.3. Delayed-type Hypersensitivity (DTH) Response

Rats were divided into three groups, and every group included six rats. Group I was treated as a control, while groups II and III were administered the test drug (rosmarinic acid). All rats from each group were treated with 0.5×109 cells SRBCs (acting as an antigen) in the pad of the right hind foot. The immunization day was considered zero, and rosmarinic acid was given for seven days. The differences in the paw thickness obtained using pre- and post-challenge thicknesses in the foot were considered for assessing delayed--type hypersensitivity reaction and measured in mm [35].

2.4.4. Phagocytic Response

The methodology proposed by Cheng *et al.* in 2005 was adopted to determine phagocytic response [36-38]. From day 0 to day 7, animals were exposed to varying concentrations of rosmarinic acid (25 and 50 mg/kg, re-spectively). On the 7th day, each animal received a 0.3 ml/30 g intravenous injection of pre-warmed Indian ink dispersion. Blood samples (50 µl) were taken from each animal at a time interval of 2 and 10 minutes post-injection *via* retro-orbital bleeding. These samples were combined with a 0.1% sodium carbonate solution to break down the red blood cells. The absorbance of these samples was determined at 675 nm using a spectrophotometer. After the final blood collection at 10 minutes, animals were euthanized, and their livers and spleens were harvested and weighed [38]. The K value was determined as follows:

$$\text{Carbon clearance (K)} = \frac{\log OD2 - \log OD10}{T2 - T1} \quad \text{(Eq. 2)}$$

Phagocytic index (α) = (K1/3 × body wt of animal)/(liver wt + spleen wt)

OD2 is the log absorbance of blood at 2 min; OD10 is the log absorbance of blood at 10 min; T2 is the last time point of blood collection; T1 is the first time point of blood collection [38].

2.5. Statistical Analysis

The values have been expressed in mean ± SEM. Statistical analysis between treated and control groups was performed using one-way ANOVA and multiple comparison tests to calculate significant differences. The differences were measured as significant when p values were 0.001, 0.01, and 0.05, respectively.

2.6. Computational Studies for Mechanistic Insights and ADME Prediction

2.6.1. Ligand Preparation

The 3D structure of the co-crystallized ligand was extracted from the crystal structure of the target protein, and the rosmarinic acid structure was sourced from PubChem. Both the ligands underwent optimization using the LigPrep tool in the Schrödinger Suite [39], utilizing the OPLS 2005 force field [40]. The Epik algorithm was applied at pH 7.0 ± 2.0 to explore the potential protonation states of all molecules [41]. Throughout the process, the original chirality of the structures was preserved, and tautomeric states were created.

2.6.2. Protein Preparation

Cereblon (CRBN) is an essential target for immunomodulatory drugs and also has antiproliferative potential [42, 43]. Cereblon negatively regulates phagocytosis [44]. Similarly, CD22 is well-recognized for its inhi-

223

bition of phagocytosis and is a promising option for targeted immunotherapy [45-48]. Considering these findings, we have selected two targets, Cereblon and human CD22, for the computational studies to assess the molecular mechanism of rosmarinic acid's immunomodulatory action and to understand if rosmarinic acid induces phagocytosis by inhibiting these targets. The crystal structures of Cereblon in complex with 3-[(phenylsulfonyl)methyl]piperidine-2,6-dione (PDB ID: 8AOQ) and human CD22 in complex with alpha 2-6 sialy lactose (PDB ID: 5VKM) were acquired from the RCSB protein data bank [49, 50]. The protein preparation workflow tool in the Schrödinger Suite 2022 was utilized to prepare the structures to be utilized for computational studies [51]. This involved adding hydrogens, assigning charges, refining bond orders, and removing all non-standard residues (including water molecules) from the PDB files. Subsequently, the protein's minimization was performed using the OPLS 2005 force field, which was followed by adding any missing side chains using Prime [51]. For docking simulations, the receptor grid was generated with its center points set at X = 25.76, Y = 19.44, and Z = -7.78 for Cereblon, while X = -53.65, Y = 10.62, and Z = 18.47 for human CD22. Dimensions were defined as X = 10 Å, Y = 10 Å, and Z = 10 Å. Considering the protein's substrate-binding region, these dimensions were determined to ensure an appropriate grid box size.

2.6.3. Re-docking and Free Binding Energy Calculation

To assess the reliability of Glide, which was employed for docking, we conducted re-docking experiments using co-crystallized ligands. The co-crystallized ligand structures of Cereblon (PDB ID: 8AOQ, ligand 3-[(phenylsulfonyl)methyl]piperidine-2,6-dione) and human CD22 (PDB ID: 5VKM, ligand alpha 2-6 sialyl lactose) were redocked into the active site using the standard precision mode [52]. The RMSD values were 0.3512 Å for Cereblon and 0.5907 Å for human CD22, respectively. These results confirmed the robustness and accuracy of the applied methodology. Furthermore, the docked pose of both ligands aligned perfectly with their respective conformations in the crystal structures. Afterward, rosmarinic acid was subjected to docking against both these targets.

2.6.4. Molecular Dynamics (MD) Simulations

As reported earlier, the stability of various protein-ligand complexes resulting from molecular docking was investigated using explicit solvent MD simulations [53]. A protein-ligand complex was simulated for 100 nanoseconds using GROMACS version 2019.4 while employing the charmm36-jul2021 force field [54]. The force field and parameter files for ligands were generated using the CGenFF (CHARMM General Force Field) [55]. The complexes were solvated in cubic boxes with periodic boundary conditions to conduct the simulations. The TIP3P water model was used, and a minimum distance of 10Å was maintained between the box and the solute. To achieve a neutral charge, sodium and chloride ions were added at a concentration of 0.15 M, with a gradient tolerance of less than 10 kJ/mol/nm. Before the actual dynamics simulations, the systems underwent 50,000 steps of energy minimization using the steepest descent method. The LINCS-like algorithm and Particle Mesh Ewald (PME) method were employed to restrain all atoms and handle long-range electrostatic interactions to control the dynamics during simulations. Short-range Van der Waals interactions were considered within a cutoff distance of 10 Å. The equilibration of the systems was performed in two phases, involving 100 picoseconds each, under the NVT (constant Number of particles, Volume, and Temperature) and NPT (constant Number of particles, Pressure, and Temperature) ensembles. A V-rescale thermostat and Parrinello-Rahman barostat were used to control 300 K temperature and 1 bar pressure during equilibration. Following equilibration, a production run of 100 nanoseconds was carried out using the NPT ensemble. The resulting trajectories of the simulated systems were then saved for the detailed analysis. Built-in features of GROMACS, such as gmx rms, rmsf, and hbond, were utilized to analyze various properties throughout the trajectory, including Root Mean Square Deviation (RMSD), Root Mean Square Fluctuation (RMSF), and hydrogen bonds. PYMOL and VMD software were employed for visualization purposes so as to examine and interpret the structures of interest [56, 57].

2.6.5. Binding Energy Calculations using MM/PBSA

The MM/PBSA protocol was employed to determine the relative binding energies of specific protein-ligand pairs. The following equations were utilized to calculate the free binding energies for each complex:

$$\Delta G \text{ bind} = G_{RL} - (G_R + G_L) \qquad \text{(Eq. 3)}$$

Here, G_{RL} represents the binding free energy of the receptor-ligand complex, while G_R and G_L correspond to the binding free energies of receptor and ligand, respectively. Every 500 frames from the last 50 ns of the trajectory were used. The detailed methodology adopted was resourced from our previous work [58], employing the g_mmpbsa tool compiled with GROMACS to calculate the binding free energy of the ligands [59].

2.6.6. Pharmacokinetics and Toxicity Prediction

The SwissADME tool was used to predict the pharmacokinetics and drug-likeness of rosmarinic acid [60]. Various parameters considered in the current study include Log Po/w (iLOGP), Log Po/w (XLOG-P3), Log S (ESOL), GI absorption, BBB permeant, P-gp substrate, CYP1A2 inhibitor, CYP2C19 inhibitor, CYP2C9 inhibitor, CYP2D6 inhibitor, CYP3A4 inhibitor, Log Kp (skin permeation), Lipinski, and bioavailability score. ProTox-II webserver was used for toxicity prediction [61]. Toxicological parameters taken into consideration were hepatotoxicity, carcinogenicity, immunotoxicity, mutagenicity, cytotoxicity, Aryl Hydrocarbon Receptor (AhR), Androgen Receptor (AR), Androgen Receptor Ligand Binding Domain (AR-LBD), aromatase, Estrogen Receptor alpha (ER), Estrogen Receptor Ligand Binding Domain (ER-LBD), Peroxisome Proliferator-activated Receptor Gamma (P-PAR-Gamma), Nuclear factor (erythroid-derived 2)--like 2/Antioxidant Responsive Element (nrf2/ARE), Heat Shock factor response Element (HSE), Mitochondrial Membrane Potential (MMP), phosphoprotein (tumor suppressor) p53, and ATPase family AAA domain containing protein 5 (ATAD5).

3. RESULTS AND DISCUSSION

3.1. *In Vitro* Evaluation of Subfractions

Based on the results of the protein denaturation assay, sub-fractions (F1-F5, concentrations ranging from 10 to 500 µg/ml) significantly inhibited protein denaturation. Our study revealed that F4 sub-fraction exhibited more potent inhibition than F1, F2, F3, and F5 (Fig. 2), leading us to conclude F4 as the most potent sub--fraction out of all these tested sub-fractions.

3.2. *In Vitro* Evaluation of Scratched Samples (F4A and F4B)

The protein denaturation assay revealed that the sub-fractions F4A and F4B, isolated from F4, exhibited significant inhibition of protein denaturation at concentrations ranging from 10 to 500 µg/ml. We evaluated each sub-fraction and found F4B to be significantly better (Fig. 3).

3.3. Characterization of the Isolated Compound

After isolating the compound, we performed TLC and found the Retention factor (Rf) value to be 0.63. We tested various solvents to determine solubility and observed that the isolated compound was freely soluble in methanol and water. The isolated compound appeared as a light gray colored powder. Based on the UV, FTIR, NMR, and mass spectra, we deduced the molecular formula of $C_{18}H_{16}O_8$ and the compound as rosmarinic acid after validating our results with the published literature [62].
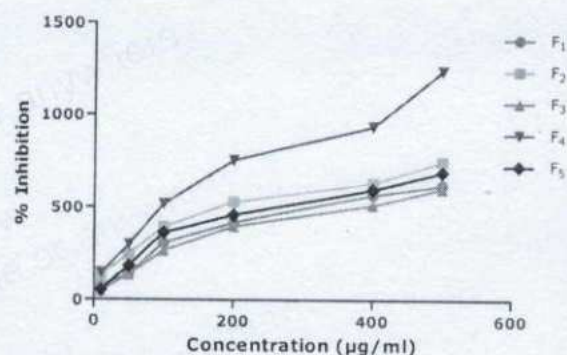
Fig. (2). Comparative inhibitory effect (compared to the standard diclofenac sodium) of different sub-fractions obtained from the butanolic fraction of the methanolic extract of *P. granatum* L. against protein denaturation. (*A higher resolution / colour version of this figure is available in the electronic copy of the article*).
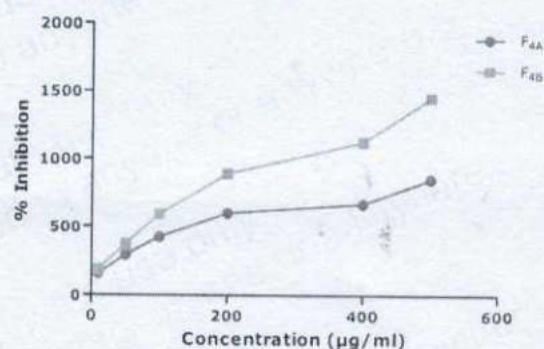
Fig. (3). Comparative inhibitory effect (compared to the standard diclofenac sodium) of scratched samples (F4A and F4B) observed in the protein denaturation assay. (*A higher resolution / colour version of this figure is available in the electronic copy of the article*).

Our previous study showed that rosmarinic acid (500 mg/kg orally) did not produce any toxic symptoms, behavioral changes, or mortality in the tested animals [26]. According to do Nascimento *et al.*, LD50 of rosmarinic acid is around 2500 mg/kg [63], so safety seems not to be an issue for rosmarinic acid.

3.4. Evaluation of Immunomodulatory Activity

3.4.1. Neutrophil Adhesion Test

At 25 and 50 mg/kg, rosmarinic acid produced a highly significant increase in neutrophil adhesion. An increase in neutrophil count in the blood of both treated groups was also observed. However, rosmarinic acid showed a dose-dependent percentage rise in neutrophil adhesion. The results are tabulated in Table 1.

225

Table 1. Effect of rosmarinic acid on neutrophil count. RA: rosmarinic acid; TLC: total leukocyte count; UB, untreated blood; NFTB, nylon fiber treated blood. Values are expressed as mean±SEM, with *n*=6 in each group; ** *p*<0.01, compared to disease control. ****p*<0.001, compared to disease control.

Treatments	TLC (10^3/mm3) (A)		Neutrophil% (B)		Neutrophil Index (A×B)		Neutrophil Adhesion (%)
	UB	NFTB	UB	NFTB	UB	NFTB	
Disease control	6.7± 0.14	6.8±0.17	27.4± 0.71	24.6±0.6	177.82±5.4	174.92±6.6	1.62
RA (25 mg/kg)	7.6± 0.65	6.7±0.52	26.4± 1.25	16.7±1.5**	211.72±5.6	118.68±8.5***	44.47***
RA (50 mg/kg)	8.8± 0.56	7.6±0.15	28.1± 1.32	17.5±1.1***	253.3±6.5	138.6±6.8***	45.73***

Table 2. Effect of rosmarinic acid on Delayed-Type Hypersensitivity (DTH) and Hemagglutinating Antibody (HA) titer in rats. Values are expressed as mean±SEM, with *n*=6 in each group; ** *p*<0.01, compared to disease control. ****p*<0.001, compared to disease control.

S. No.	Treatments	Delayed Type Hypersensitivity Response (mm) at 24 hrs	Delayed Type Hypersensitivity Response (mm) at 48 hrs	HA Titer
1	Normal control (10 ml/kg)	0.29±0.03	0.23±0.03	23.35 ± 0.12
2	RA (25 mg/kg)	0.58±0.03**	0.46±0.03**	41.21 ± 2.21**
3	RA (50 mg/kg)	0.82±0.04***	0.68±0.07***	79.42 ± 2.45***

3.4.2. DTH Response and HA Titer using SRBC as Antigen

Rosmarinic acid demonstrated a dose-dependent increase in DTH reactivity in animals (Table **2**). At a dose of 50 mg/kg, rosmarinic acid produced a highly significant ($p< 0.001$) increase in DTH response activity, indicating its potential as an immunomodulatory agent.
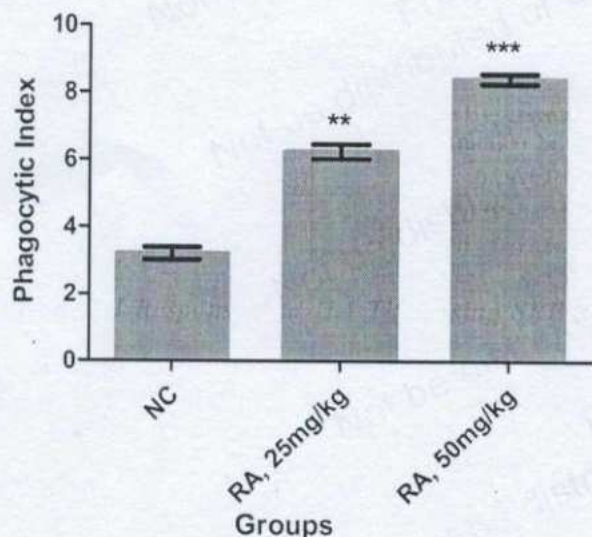

Fig. (4). Effect of rosmarinic acid on phagocytic index in rats. (*A higher resolution / colour version of this figure is available in the electronic copy of the article*).

Furthermore, after immunization with SRBCs, treatment with rosmarinic acid resulted in a noticeable increase ($p <0.01$, $p <0.001$) in the HA titer, which continued to rise with increasing doses (Table **2**). The results suggest that rosmarinic acid positively affects the immune system and can enhance the body's ability to fight infections. Overall, the findings of this study provide important insights into the potential therapeutic applications of rosmarinic acid in immunomodulation, and warrant further investigation.

3.4.3. Phagocytic Response

Rosmarinic acid at both doses enhanced ($p<0.01$, $p<0.001$) phagocytic index significantly (Fig. **4**). An enhancement in the clearance of colloidal carbon was also observed due to rosmarinic acid.

3.5. Molecular Docking against Immunomodulatory Receptor

The results of the docking and the free binding energies calculated using Molecular Mechanics with Generalised Born and Surface Area solvation (MMGBSA) prime for both targets are presented in Table **3** and Fig. (**5**) [64]. The comparison between the docking scores and MMGBSA energies indicated that rosmarinic acid bound less strongly to both targets than the co-crystallized ligands. However, in the case of Cerebolon (Fig. **5B**), rosmarinic acid displayed H-bond interactions with the critical active site residues, TYR 101 and PHE 77, as also observed in the case of the co-crystallized inhibitor. Additionally, rosmarinic acid formed a hydrogen bond with GLU 76 and engaged in pi-pi stacking with TRP 85 and TRP 99. In the case of CD22 (Fig. **5D**), rosmarinic acid exhibited an interac-

226

Table 1. Effect of rosmarinic acid on neutrophil count. RA: rosmarinic acid; TLC: total leukocyte count; UB, untreated blood; NFTB, nylon fiber treated blood. Values are expressed as mean±SEM, with *n*=6 in each group; ** *p*<0.01, compared to disease control. ***p<0.001, compared to disease control.

Treatments	TLC (10^3/mm3) (A)		Neutrophil% (B)		Neutrophil Index (A×B)		Neutrophil Adhesion (%)
	UB	NFTB	UB	NFTB	UB	NFTB	
Disease control	6.7± 0.14	6.8±0.17	27.4± 0.71	24.6±0.6	177.82±5.4	174.92±6.6	1.62
RA (25 mg/kg)	7.6± 0.65	6.7±0.52	26.4± 1.25	16.7±1.5**	211.72±5.6	118.68±8.5***	44.47***
RA (50 mg/kg)	8.8± 0.56	7.6±0.15	28.1± 1.32	17.5±1.1***	253.3±6.5	138.6±6.8***	45.73***

Table 2. Effect of rosmarinic acid on Delayed-Type Hypersensitivity (DTH) and Hemagglutinating Antibody (HA) titer in rats. Values are expressed as mean±SEM, with *n*=6 in each group; ** *p*<0.01, compared to disease control. ***p<0.001, compared to disease control.

S. No.	Treatments	Delayed Type Hypersensitivity Response (mm) at 24 hrs	Delayed Type Hypersensitivity Response (mm) at 48 hrs	HA Titer
1	Normal control (10 ml/kg)	0.29±0.03	0.23±0.03	23.35 ± 0.12
2	RA (25 mg/kg)	0.58±0.03**	0.46±0.03**	41.21 ± 2.21**
3	RA (50 mg/kg)	0.82±0.04***	0.68±0.07***	79.42 ± 2.45***

3.4.2. DTH Response and HA Titer using SRBC as Antigen

Rosmarinic acid demonstrated a dose-dependent increase in DTH reactivity in animals (Table **2**). At a dose of 50 mg/kg, rosmarinic acid produced a highly significant ($p< 0.001$) increase in DTH response activity, indicating its potential as an immunomodulatory agent.

Fig. (4). Effect of rosmarinic acid on phagocytic index in rats. (*A higher resolution / colour version of this figure is available in the electronic copy of the article*).

Furthermore, after immunization with SRBCs, treatment with rosmarinic acid resulted in a noticeable in-

crease ($p <0.01$, $p <0.001$) in the HA titer, which continued to rise with increasing doses (Table **2**). The results suggest that rosmarinic acid positively affects the immune system and can enhance the body's ability to fight infections. Overall, the findings of this study provide important insights into the potential therapeutic applications of rosmarinic acid in immunomodulation, and warrant further investigation.

3.4.3. Phagocytic Response

Rosmarinic acid at both doses enhanced ($p<0.01$, $p<0.001$) phagocytic index significantly (Fig. **4**). An enhancement in the clearance of colloidal carbon was also observed due to rosmarinic acid.

3.5. Molecular Docking against Immunomodulatory Receptor

The results of the docking and the free binding energies calculated using Molecular Mechanics with Generalised Born and Surface Area solvation (MMGBSA) prime for both targets are presented in Table **3** and Fig. (**5**) [64]. The comparison between the docking scores and MMGBSA energies indicated that rosmarinic acid bound less strongly to both targets than the co-crystallized ligands. However, in the case of Cerebolon (Fig. **5B**), rosmarinic acid displayed H-bond interactions with the critical active site residues, TYR 101 and PHE 77, as also observed in the case of the co-crystallized inhibitor. Additionally, rosmarinic acid formed a hydrogen bond with GLU 76 and engaged in pi-pi stacking with TRP 85 and TRP 99. In the case of CD22 (Fig. **5D**), rosmarinic acid exhibited an interac-

227

tion pattern similar to the co-crystallized ligand alpha 2-6 sialyl lactose, involving H-bond interactions with ARG 120, MET 129, and ARG 131. The MD simula-

tions were performed to further understand the stability and interaction pattern of the docked rosmarinic acid complexes.
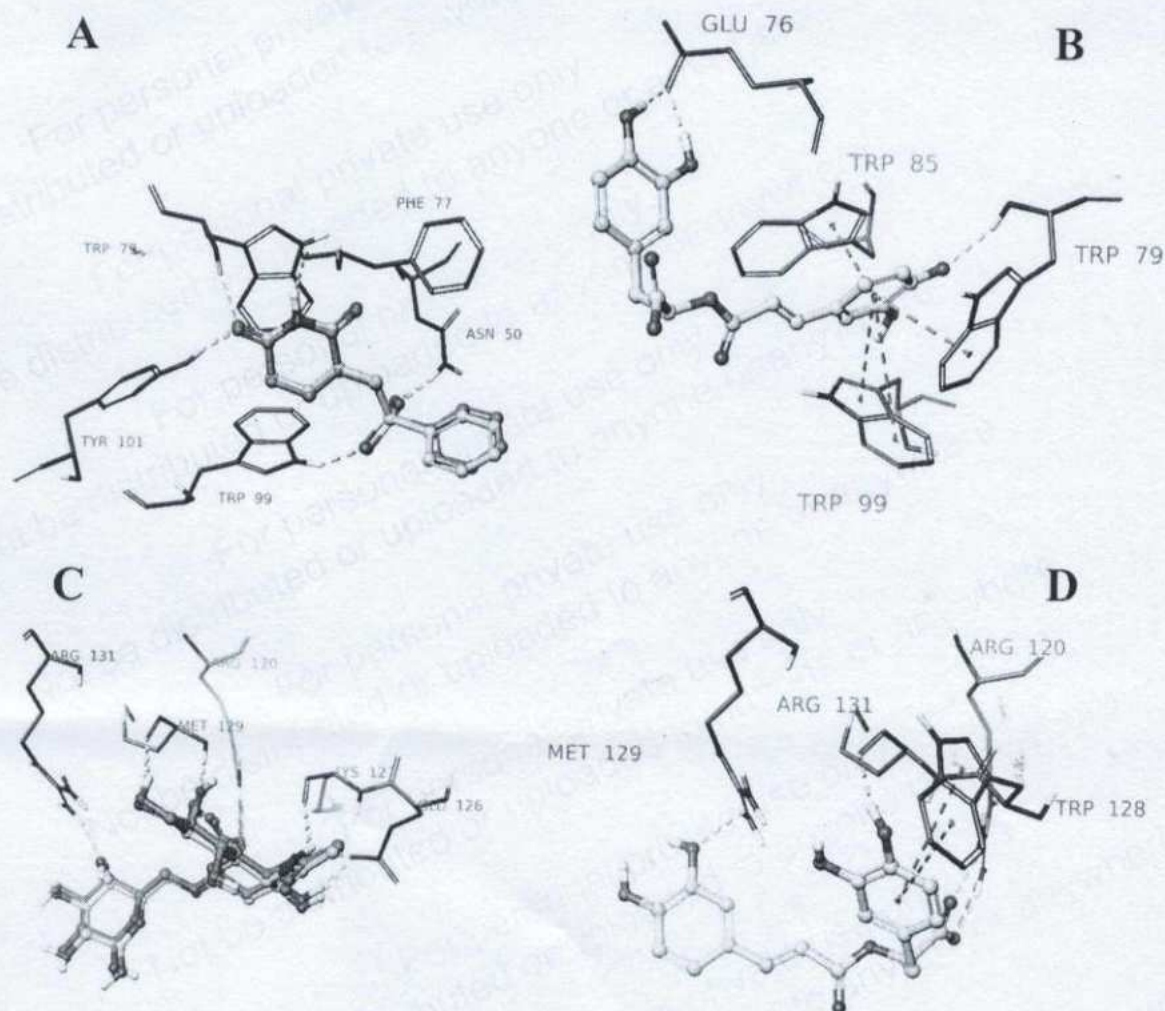

Fig. (5). (A) 3D superposition and binding interactions of docked pose with native co-crystallized ligand in complex with Cereblon (PDB ID: 8AOQ). **(B)** Binding interactions of rosmarinic acid in complex with Cereblon. **(C)** Superposition of docked pose with native co-crystallized ligand and binding interactions in complex with human CD22 (PDB ID: 5VKM), and **(D)** Binding interactions of rosmarinic acid in complex with human CD22. (*A higher resolution / colour version of this figure is available in the electronic copy of the article*).

Table 3. Docking score and MMGBSA energy against Cereblon and human CD22.

Target	Compound	Docking Score	MMGBSA (kcal/mol)
Cereblon (PDB ID: 8AOQ)	3-[(phenylsulfonyl)methyl]piperidine-2,6-dione (co-crystallized ligand)	-9.112	-72.10
Cereblon (PDB ID: 8AOQ)	Rosmarinic acid	-6.467	-53.07
CD22 (PDB ID: 5VKM)	2-6 sialyl lactose (co-crystallized ligand)	-5.867	-73.91
CD22 (PDB ID: 5VKM)	Rosmarinic acid	-4.077	-42.57

Principal
Indore Institute of Pharmacy,
INDORE (M.P.)

228

3.6. MD Simulation

The study aimed to assess the stability and accuracy of different protein-ligand complexes obtained from docking studies by subjecting them to 100 ns MD simulations (Fig. 6). The RMSD data for the ligand binding to Cereblon (Fig. 6A) revealed that co-crystallized ligand and rosmarinic acid converged at approximately 0.15 and 0.35 nm, respectively. These values remained constant throughout the MD simulation, indicating a highly stable and robust binding of the ligands to the target's active site.

On the other hand, the RMSD graph for human CD22 (Fig. 6B) indicated that rosmarinic acid initially exhibited a gradual rise in RMSD up to 20 ns, after which it reached convergence at around 0.9 nm. This deviation was significant, likely due to the increased conformational space of certain linear portions of the ligands, such as the 4-vinylbenzene-1,2-diol. Nevertheless, the ligand predominantly remained within the protein binding cavity, suggesting a stable interaction. The rosmarinic acid in the complex with Cereblon demonstrated better stability than rosmarinic acid-human CD22 docked complexes.
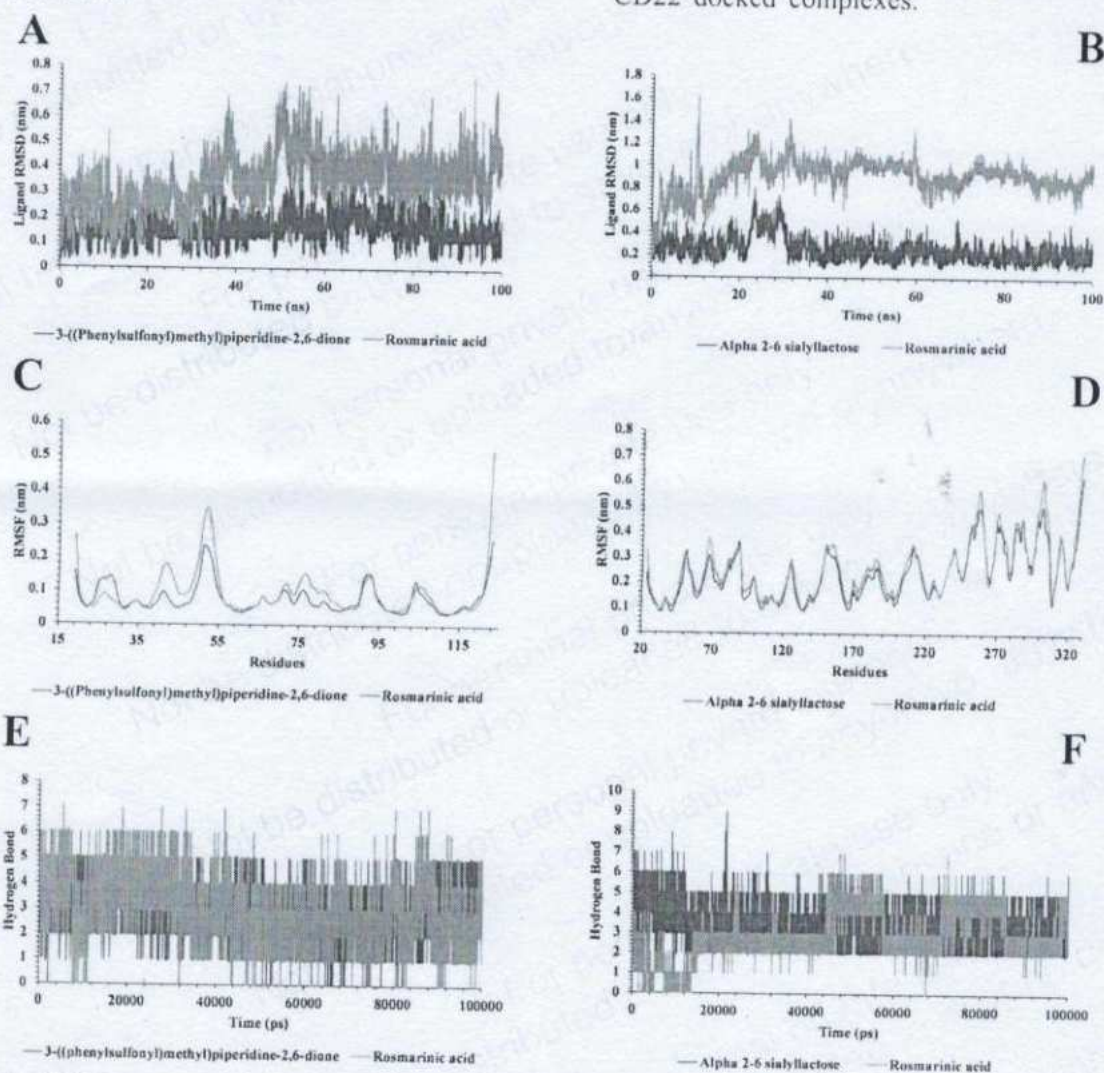
Fig. (6). (**A**) RMSD plot for 3-[(phenylsulfonyl)methyl]piperidine-2,6-dione and rosmarinic acid in complex with Cereblon. (**B**) RMSD plot for alpha 2-6 sialyl lactose and rosmarinic acid in complex with human CD22. (**C**) RMSF plot for 3-[(phenylsulfonyl)methyl]piperidine-2,6-dione and rosmarinic acid in complex with Cereblon. (**D**) RMSF plot for alpha 2-6 sialyl lactose and rosmarinic acid in complex with human CD22. (**E**) H-bond plot for 3-[(phenylsulfonyl)methyl]piperidine-2,6-dione and rosmarinic acid in complex with Cereblon. (**F**) H-bond plot for alpha 2-6 sialyl lactose and rosmarinic acid in complex with human CD22 throughout the 100 ns MD simulation. (*A higher resolution / colour version of this figure is available in the electronic copy of the article*).

229
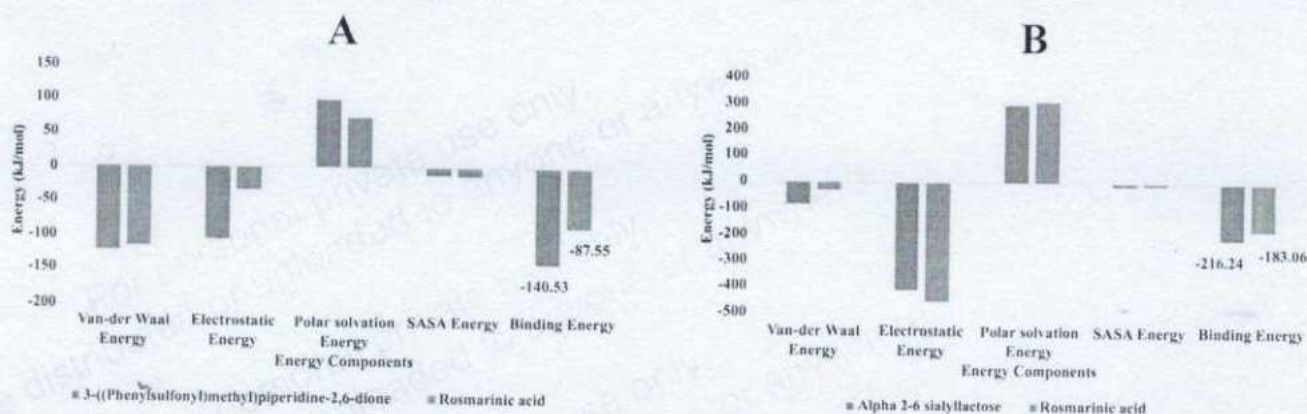
Fig. (7). Contribution of individual interaction components and binding free energy of Cereblon and CD22 inhibitors. (**A**). Data related to interactions with Cereblon; (**B**). Data related to interactions with human CD22. (*A higher resolution / colour version of this figure is available in the electronic copy of the article*).

The variability in the residues' flexibility was assessed by calculating the RMSF of the co-crystallized ligand and rosmarinic acid when bound to Cereblon and human CD22. The RMSF values of 3-[(phenylsulfonyl)methyl]piperidine-2,6-dione and rosmarinic acid in complex with Cereblon (Fig. **6C**), as well as alpha 2-6 sialyl lactose and rosmarinic acid in complex with human CD22 (Fig. **6D**), demonstrated relatively stable fluctuations. These fluctuations displayed a similar pattern to that of the co-crystallized ligands.

Further calculations were conducted to better understand the nature of H-bonds, which exhibited primary stabilizing interactions between two molecules at the inhibitory site. The formation of H-bonds within a 5 Å distance was analyzed during the simulations. As a result, it was found that the complex of 3-[(phenylsulfonyl)methyl]piperidine-2,6-dione and rosmarinic acid with Cereblon formed an average of 3.165 and 2.975 H-bonds, respectively (Fig. **6E**). On the other hand, the complex of alpha 2-6 sialyl lactose and rosmarinic acid with human CD22 exhibited an average of 3.505 and 2.579 H-bonds (Fig. **6F**).

3.7. MM/PBSA Binding Free Energy Calculations

The MM/PBSA (Molecular Mechanics energies combined with the Poisson-Boltzmann and Surface Area continuum solvation) based method can more accurately determine all complexes' free binding energy [65]. This binding free energy accounts for various non-bonded interactions between the receptor and ligand during the MD simulation. These interactions encompass Van der Waals forces, electrostatic interactions, polar solvation effects, and SASA (Solvent-accessible Surface Area) energies. A lower binding free energy value indicates a stronger affinity between the ligand and receptor.

Using a 100ns MD trajectory, the binding free energies of docked ligands were calculated. Specifically, 3-[(phenylsulfonyl)methyl]piperidine-2,6-dione and rosmarinic acid exhibited a binding free energy of -140.53 ± 2.13 kJ/mol and -87.55 ± 4.070 kJ/mol, respectively, towards the inhibitory receptor site of Cereblon (Fig. **7A**). On the other hand, alpha 2-6 sialyl lactose and rosmarinic acid, when interacting with human CD22, demonstrated a binding free energy of -216.24 ± 4.58 kJ/mol and -183.06 ± 7.28 kJ/mol, respectively (Fig. **7B**). The observed data suggest that both Van der Waals and electrostatic interactions contributed to the stability of all complexes, while the polar solvation energy exhibited an inverse relationship.

3.8. ADME and Toxicity Prediction of Rosmarinic Acid

SwissADME and Protox-II web-based servers were used for the ADME and toxicity predictions. Table 4 showcases the pharmacokinetic features of rosmarinic acid as predicted by the SwissADME. In line with our findings, rosmarinic acid was predicted to be water soluble and suitable for making oral formulations. Further, rosmarinic acid was predicted not to cross the Blood-Brain Barrier (BBB), being favorable to avoid any CNS-related adverse events. However, this BBB impermeability prediction contradicts the literature where rosmarinic acid has been validated for antidepressant activity [66]. Hitl and the team, in their review article, documented various routes for administering rosmarinic acid, including topical, pulmonary, intra-nasally, and intravenous, with peroral as the main route [67]. They have also indicated the metabolism of rosmarinic acid by gut microflora, which should also be considered [67]. SwissADME also predicted that rosmarinic acid might not be an inhibitor of CYP1A2,

230

CYP2C19, CYP2C9, CYP2D6, and CYP3A4, suggesting lower chances for the CYP-associated drug-drug interactions. However, this is contrary to the study published by Kim and the team, where they found that rosmarinic acid weakly inhibited CYP2C19 and CYP2E1. They further indicated mixed inhibition in the case of CYP2C19 and competitive inhibition in the case of CYP2E1 [68]. Further, looking into this article, we could observe that rosmarinic acid also had a slight inhibitory effect on CYP1A2. However, SwissADME prediction in the case of CYP3A4 seems to be accurate and adheres to the experimental results of Kim and the team [68].

Toxicity prediction (Table 5 and Fig. 8) by Protox II indicated the LD50 value for rosmarinic acid to be 5000mg/kg, corroborating with our previously performed acute toxicity studies [26]. Except for immunotoxicity, for all other toxicological endpoints, rosmarinic acid was predicted to be safe (Table 5 and Fig. 8). Our experiments also validate the immunotoxicity as immunomodulatory activity has been observed. As per the ProTox II prediction, rosmarinic acid was not found to be hepatotoxic, which agrees with the previous studies [59-62]. The results of the studies by Yao and the team [69], Yu and the team [70], Jafaripour and the team [71], and Elufioye and the team proved these predictions to be accurate [72], as these studies validate hepatoprotective effects of rosmarinic acid. Renzulli and the team indicated the protective effect of rosmarinic acid against aflatoxin B(1)-induced carcinogenicity in a human hepatoma cell line (Hep G2) [73], which proved the prediction of Protox-II for rosmarinic acid to be non-carcinogenic as accurate. Furtado and the team indicated antimutagenicity of ros-

marinic acid in Swiss mice [74]. Han and the team, through their experiments, proved that rosmarinic acid activated PPAR-gamma [75], again proving the reliability of the prediction of Protox-II that rosmarinic acid is not a PPAR-gamma inhibitor. Along with many other predictions, ProTox-II also suggested rosmarinic acid to not be an inhibitor of Nuclear factor (erythroid-derived 2)-like 2/Antioxidant Responsive Element (Nrf2/ARE). Experiments by Chen and the team and Fetoni and the team validate it as rosmarinic acid has been reported to activate or upregulate the Keap1-Nrf2-ARE antioxidant system [76, 77].

Table 4. Prediction of pharmacokinetics and drug-likeness of rosmarinic acid.

Parameters	Predicted Value
Log Po/w (iLOGP)	1.17
Log Po/w (XLOGP3)	2.36
Log S (ESOL)	-3.44
Solubility	1.31e-01 mg/ml ; 3.63e-04 mol/l
Water solubility class	Soluble
GI absorption	Low
BBB permeant	No
P-gp substrate	No
CYP1A2 inhibitor	No
CYP2C19 inhibitor	No
CYP2C9 inhibitor	No
CYP2D6 inhibitor	No
CYP3A4 inhibitor	No
Log Kp (skin permeation)	-6.82 cm/s
Drug likeness as per Lipinski's rule of five	Yes, 0 violation
Bioavailability score	0.56

Table 5. Toxicity prediction of rosmarinic acid.

Classification	Target	Prediction	Probability
Oral toxicity	Predicted LD50	5000mg/kg	-
Organ toxicity	Hepatotoxicity	Inactive	0.62
Toxicity end-point	Carcinogenicity	Inactive	0.66
Toxicity end-point	Immunotoxicity	Active	0.93
Toxicity end-point	Mutagenicity	Inactive	0.85
Toxicity end-point	Cytotoxicity	Inactive	0.90
Tox21 nuclear receptor signaling pathways	Aryl hydrocarbon Receptor (AhR)	Inactive	0.82
Tox21 nuclear receptor signaling pathways	Androgen Receptor (AR)	Inactive	0.94
Tox21 nuclear receptor signaling pathways	Androgen Receptor Ligand Binding Domain (AR-LBD)	Inactive	0.99
Tox21 nuclear receptor signaling pathways	Aromatase	Inactive	0.96
Tox21 nuclear receptor signaling pathways	Estrogen Receptor alpha (ER)	Inactive	0.74
Tox21 nuclear receptor signaling pathways	Estrogen Receptor Ligand Binding Domain (ER-LBD)	Inactive	0.72
Tox21 nuclear receptor signaling pathways	Peroxisome Proliferator-Activated Receptor Gamma (PPAR-Gamma)	Inactive	0.80

(Table 5) contd....

Principal
Indore Institute of Pharmacy,
INDORE (M.P.)

231

Classification	Target	Prediction	Probability
Tox21 stress response pathways	Nuclear factor (erythroid-derived 2)-like 2/Antioxidant Responsive Element (nrf2/ARE)	Inactive	0.88
Tox21 stress response pathways	Heat Shock factor response Element (HSE)	Inactive	0.88
Tox21 stress response pathways	Mitochondrial Membrane Potential (MMP)	Inactive	0.67
Tox21 stress response pathways	Phosphoprotein (Tumor Suppressor) p53	Inactive	0.73
Tox21 stress response pathways	ATPase family AAA Domain-containing protein 5 (ATAD5)	Inactive	0.86
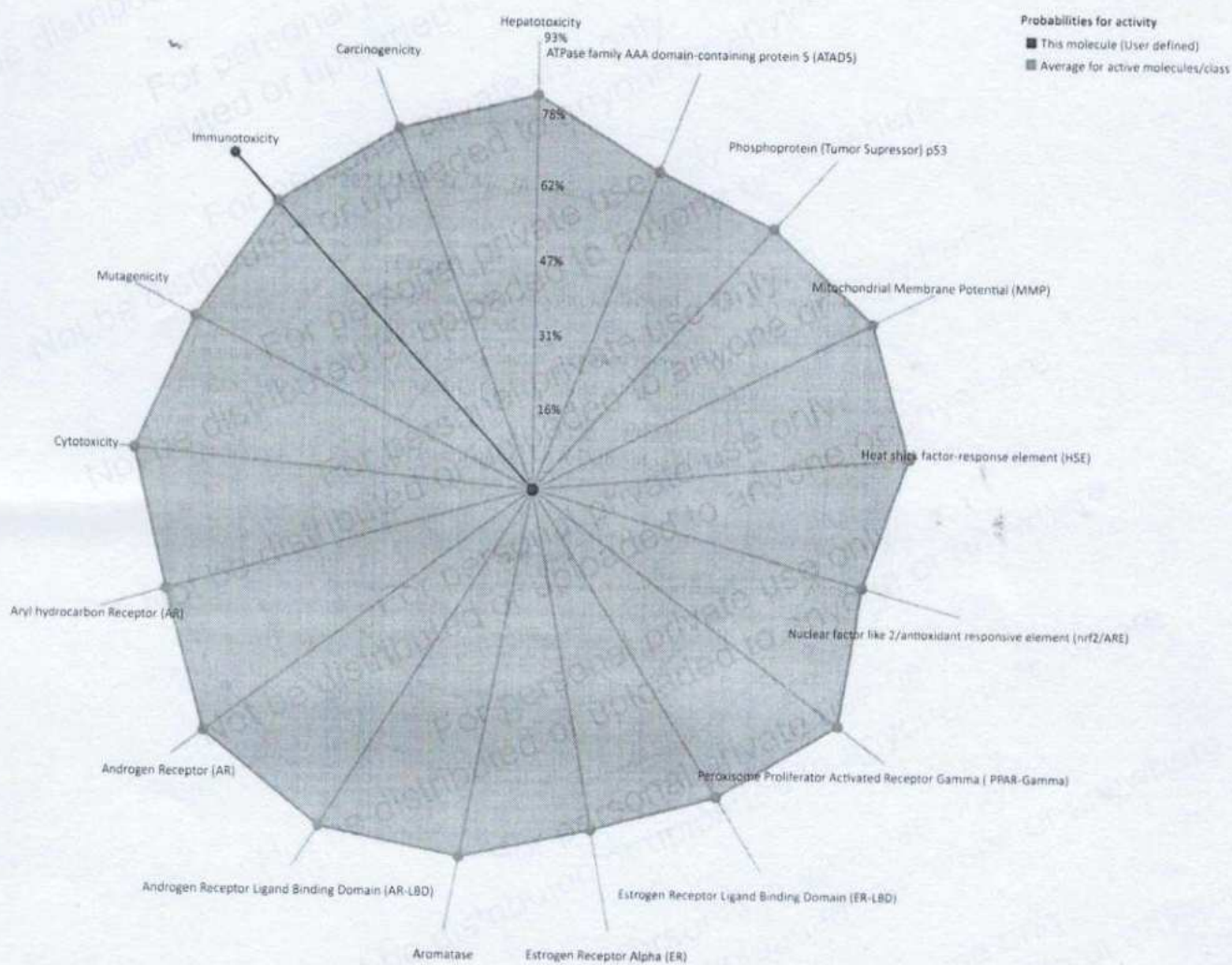
Fig. (8). Toxicity radar plot indicating the probability of toxicity induced by rosmarinic acid. Immunotoxicity was the only positive indication. (*A higher resolution / colour version of this figure is available in the electronic copy of the article*).

Synthetic drugs are often associated with undesirable side effects, leading to a growing interest in natural products with significant therapeutic potential and negligible side effects. In this study, we aimed to isolate the active compound, rosmarinic acid, using a bioactivity-guided approach for its immunomodulatory activity [78, 79]. Through this approach, we collected sub-fractions (F1-F5) and evaluated their inhibitory effect on protein denaturation. Our findings revealed that the F4 fraction exhibited a promising effect compared to other fractions and diclofenac sodium, a reference standard [26]. The observed pharmacological effect of

Principal
Indore Institute of Pharmacy,
INDORE (M.P.)

232

the F4 fraction may be attributed to the presence of flavonoids and phenolics, as identified through phytochemical screening. These phytoconstituents have been previously reported for their anti-arthritic activity and may be responsible for the observed effect of *P. granatum* L. [31, 34-36, 62, 78]. Our study provides evidence for the immunomodulatory potential of rosmarinic acid and highlights the importance of natural products in drug discovery. The F4 fraction of *P. granatum* L. may serve as a potential natural source of anti-arthritic compounds with negligible side effects. However, the experiments conducted in this direction are very preliminary and more exhaustive studies should be conducted to validate our hypothesis. Further research is warranted to elucidate the mechanism of action and potential clinical applications of the F4 fraction.

Using a preparative thin-layer chromatography approach, we collected two samples (F4A and F4B) and evaluated their *in vitro* acute anti-inflammatory activity. Our results showed fraction F4B to be more effective than F4A. Thus, we selected F4B for further characterization using spectral analysis to identify the active compound. Based on the spectral comparison and distinction from the current biomarker, we successfully identified the isolated compound as rosmarinic acid.

Rosmarinic acid and its related compounds are commonly called "Labiatengerbstoff". It was initially identified in *Rosmarinus officinalis* L. (rosemary) and is a natural phenolic compound found in various species of *Boraginaceae* and other plants [79]. Other biosustainable sources for rosmarinic acid include *Thunbergia laurifolia* Lindl [80], *Mentha arvense* [81], *Mentha piperita* [81], *Melissa officinalis* L [82], *Blechnum brasiliense* [83], *Rabdosia serra* (MAXIM.) HARA [84], *Coleus blumei* Benth [85], *Salviae miltiorrhizae* [86], *Perilla frutescens* Britton Var. *acuta* f. *viridis* [87], and *Salvia limbata* C.A. Meyer [88]. Rosmarinic acid has various pharmacological activities, including antioxidant and anti-inflammatory effects [79, 89]. Costa and the team have shown the immunomodulatory and antiallergic potential of rosmarinic acid, mediated by a decrease in total inflammatory cells, eosinophils, and IL-4 levels [90, 91]. Zhao and the team have proven the anti-inflammatory potential of rosmarinic acid by evaluating the DD-induced colitis model. According to their studies, possible mechanisms shown by the rosmarinic acid were mediated by the downregulation of COX-2, iNOS, NF-κBp65, and pSTAT3, as well as by the upregulation of IL-1β, IL-6, and IL-22

[91, 92]. do Nascimento and the team have indicated that rosmarinic acid could prevent gastric cancer *via* multiple pathways, including sulfhydryl groups reinforcement, oxidative stress-mediated and immunomodulatory effects (reduction of pro-inflammatory cytokines TNF-α and IL-1β levels) [63]. Shakeri and the team evaluated the immunomodulatory and anti-inflammatory effects of rosmarinic acid in asthmatic rats. They observed decreased IL-4, IgE, PLA2, IFN-γ, and TP levels in rosmarinic acid-treated asthmatic rats [93].

Exploring PubMed (dated 09.08.2023) for the articles with rosmarinic acid in their title resulted in 881 articles. These included 10 trials, 9 randomized trials, and 29 review articles. However, when we explored PubMed (dated 09.08.2023) for the articles having rosmarinic acid in their title and "immuno*" as the MeSH term, it resulted in 54 articles. PubMed metadata for these 54 articles was then exported to VOSviewer for further analysis of co-occurring MeSH terms and their interactions. 463 co-occurring MesH keywords were observed in these articles and 147 had been repeated in at least two publications. These MeSH-related results may somehow improve the understanding of readers about the kinds of studies that have been conducted in a particular domain. Some MeSH terms were removed, including "animals", "humans", "mice", "male", "disease models, animals", "female", "plant extracts", "mice, inbred BALB c", "rats", " cell culture", "blotting, western", "phytotherapy", "immunohistochemistry", "rats, Wistar", "reverse transcriptase polymerase chain reaction", "signal transduction, enzyme-linked immunosorbent assay", "cell line, tumor", "rabbits", "*in vitro* techniques", "cell line", "models, chemical", "middle-aged", "adult", "rats, Sprague-Dawley", "time factors", "enzyme inhibitors", "double-blind method", "reproducibility of results", "real-time polymerase chain reaction", "immunoblotting", "flow cytometry", "comet assay", and other such terms having no or poor significance with immuno-related results and most probably not being insightful for readers. Interactions between remaining MeSH terms are visualized in Fig. (**9**). The top-most co-occurring MeSH terms with high "total link strengths" and with significant occurrences were "depsides", "cinnamates", "cytokines", "NF-Kappa B", "lymphocyte activation", "interleukin 2", "chemokine CCL11", "tumor necrosis factor-alpha", and "anti-inflammatory agents, non-steroidal". All such studies have validated the strong potential of rosmarinic acid, and extensive studies are further required for its translation to bedside.
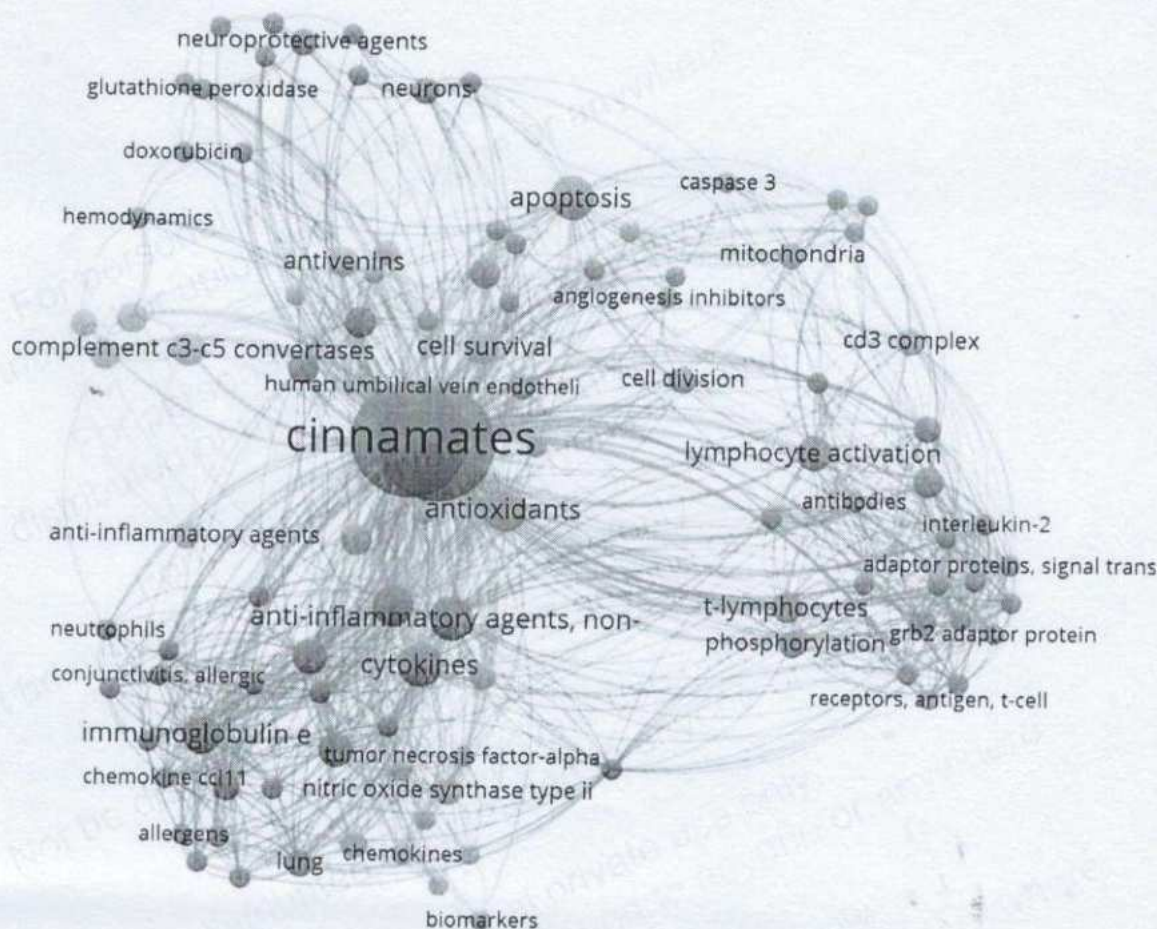
Fig. (9). Interactive mapping between co-occurring MeSH terms based on the literature obtained from PubMed using the search term as rosmarinic acid. Metadata from PubMed has been processed using VOSviewer. (*A higher resolution / colour version of this figure is available in the electronic copy of the article*).

Our previous study has evaluated the anti-arthritic activity of the isolated compound F4B, identified as rosmarinic acid from *P. granatum* [26]. The findings of our previous study have highlighted the potential of rosmarinic acid as a natural anti-arthritic agent, adding to the growing body of evidence supporting the pharmacological activities of this compound.

Our immune system's primary and secondary defense mechanisms co-exist to combat foreign particles and various antigens. The neutrophils are the central part of the primary defense mechanism and, in continuation, have limited capacity to divide and induce protein synthesis [26, 94-96]. In our study, rosmarinic acid at a dose of 25-50 mg/kg by oral route provoked a considerable enhancement in the percentage of neutrophils. Increasing the total neutrophil count improved the body's defense against microbial infection [26].

Antibodies are the molecules that may play a role in humoral or antibody-mediated immune responses and the creation of B-lymphocytes and plasma cells. In humans, the chief immunoglobulins are IgG and IgM. The chief role of immunoglobulins has been considered in activating the complement system and neutralizing various endogenous and exogenous toxins [26]. In our study, the increase in the antibody titer was significantly enhanced by rosmarinic acid. The proposed mechanism may be the increased T and B lymphocyte responsiveness that may be concerned with the synthesis of antibodies, but it needs to be experimentally validated [26].

The cells of cell-mediated immunity activate a defense mechanism against various infectious organisms, foreign particles, transplanted organs, and different types of hypersensitivity reactions [26]. Therefore, in our study, delayed-type hypersensitivity reaction has been found to be dependent on T cells. Rosmarinic acid has been found to have a stimulatory effect on an antigen being T cell-dependent.

234

Phagocytes are the defense cells of our body that mediate the phagocytosis process. Through this process, cells' phagocytes digest various microorganisms, cancerous cells, inflammatory cells, and certain inorganic particles [26]. In our study, rosmarinic acid increased phagocytic activity by enlarging the cells of the reticule endothelial system.

CONCLUSION

In this research, we have successfully isolated, characterized, and evaluated the immunomodulatory activity of rosmarinic acid, isolated from the butanolic fraction of the methanolic extract obtained from the rind of *P. granatum* L. We have observed rosmarinic acid to have significant immunomodulatory potential. Molecular docking and molecular dynamics studies have indicated that interactions with Cereblon and human CD22 might be some of the possible mechanisms behind the phagocytosis activity of rosmarinic acid. ADME and toxicological predictions have affirmed rosmarinic acid's drug-likeness and its safety profile.

More exhaustive animal studies, along with cell line-based studies, are needed and may reflect the limitations of this work. Moreover, experimental validation of the binding affinity of rosmarinic acid with Cereblon and human CD22 is required to ascertain the computational results. Moreover, cytoskeletal rearrangement, crawling, transmigration, and superoxide production may be evaluated to further ascertain the immunomodulatory activity of rosmarinic acid.

AUTHORS' CONTRIBUTIONS

R.K.G., S.S., and R.K.S. contributed to the study conception and design. Material preparation, data collection, and analysis were performed by R.K.G., S.A., S.M.T., S.S., K.S., S.G., D.K.M., S.B., R.G., S.S., B.S., Y.Z., and R.K.S. The first draft of the manuscript was written by R.K.G., S.S., and R.K.S., and all authors have commented on previous versions of the manuscript. All authors have read and approved the final manuscript.

LIST OF ABBREVIATIONS

PG	= *Punica granatum* L.
TLC	= Thin Layer Chromatography
13-CNMR	= 13-Carbon Nuclear Magnetic Resonance Spectroscopy
1H-NMR	= Proton Nuclear Magnetic Resonance
IR	= Infrared
TNF	= Tumor Necrosis Factor IL - Interleukin
RA	= Rheumatoid Arthritis
FT-IR	= Fourier Transform Infrared
Hz	= Hertz
MHz	= Megahertz
Ppm	= Parts Per Million
MeOH	= Methanol
ESI-MS	= Electrospray Ionization-mass Spectroscopy
PGME	= *Punica granatum* L. Methanolic Extract
IUPAC	= International Union of Pure and Applied Chemistry
IAEC	= Institutional Animal Ethical Committee
ANOVA	= Analysis of Variance

ETHICS APPROVAL AND CONSENT TO PARTICIPATE

The study protocol was carried out after getting clearance from the IAEC (protocol no.: 192/PhD/2012/IAEC/BRNCP/12-13/Mandsaur).

HUMAN AND ANIMAL RIGHTS

All the procedures involving animals were performed according to the US Public Health Service's "Policy on Human Care and Use of Laboratory Animals," and "Guide for the Care and Use of Laboratory Animals" in accordance with ARRIVE guidelines.

CONSENT FOR PUBLICATION

Not applicable.

AVAILABILITY OF DATA AND MATERIALS

All data generated or analyzed during this study are included in this published article. Further inquiries can be resolved if routed through proper and official channels.

FUNDING

None.

CONFLICT OF INTEREST

The authors declare no conflict of interest, financial or otherwise.

Principal
Indore Institute of Pharmacy,
INDORE (M.P.)

235

ACKNOWLEDGEMENTS

REFERENCES

[1] Wagner, H.; Hikino, H.; Farnsworth, N. *Economic and Medicinal Plant Research*, 3rd ed.; Elsevier, **1989**.

[2] Singla, R.K.; Guimarães, A.G.; Zengin, G. Editorial: Application of plant secondary metabolites to pain neuromodulation, volume III. *Front. Pharmacol.*, **2023**, *14*, 1166272.
http://dx.doi.org/10.3389/fphar.2023.1166272 PMID: 36895948

[3] Singla, R.K.; Joon, S.; Sinha, B.; Kamal, M.A.; Simal-Gandara, J.; Xiao, J.; Shen, B. Current trends in natural products for the treatment and management of dementia: Computational to clinical studies. *Neurosci. Biobehav. Rev.*, **2023**, *147*, 105106.
http://dx.doi.org/10.1016/j.neubiorev.2023.105106 PMID: 36828163

[4] Babbar, R.; Kaur, R.; Rana, P.; Arora, S.; Behl, T.; Albratty, M.; Najmi, A.; Meraya, A.M.; Alhazmi, H.A.; Singla, R.K.; Parajuli, N. The current landscape of bioactive molecules against DENV: A systematic review. *Evid. Based Complement. Alternat. Med.*, **2023**, *2023*, 1-17.
http://dx.doi.org/10.1155/2023/2236210 PMID: 36818227

[5] Kumar, D.; Singla, R.K.; Sharma, R.; Sharma, P.; Kumar, L.; Kaur, N.; Dhawan, R.K.; Sharma, S.; Dua, K. Phytochemistry and polypharmacological potential of *Colebrookea oppositifolia* smith. *Curr. Top. Med. Chem.*, **2023**, *23*(5), 334-348.
http://dx.doi.org/10.2174/1568026623666221202112414 PMID: 36476430

[6] Singla, R.K.; De, R.; Efferth, T.; Mezzetti, B.; Sahab Uddin. M. The International Natural Product Sciences Taskforce (INPST) and the power of Twitter networking exemplified through #INPST hashtag analysis. *Phytomedicine*, **2023**, *108*, 154520.

[7] Singla, R.K.; Dubey, A.K. Phytochemical profiling, GC-MS analysis and α-amylase inhibitory potential of ethanolic extract of *Cocos nucifera* linn. endocarp. *Endocr. Metab. Immune Disord. Drug Targets*, **2019**, *19*(4), 419-442.
http://dx.doi.org/10.2174/1871530319666181128100206 PMID: 30484412

[8] Marzocco, S.; Singla, R.K.; Capasso, A. Multifaceted effects of lycopene: A boulevard to the multitarget-based treatment for cancer. *Molecules*, **2021**, *26*(17), 5333.
http://dx.doi.org/10.3390/molecules26175333 PMID: 34500768

[9] Singla, R.K.; Sai, C.S.; Chopra, H.; Behzad, S.; Bansal, H.; Goyal, R.; Gautam, R.K.; Tsagkaris, C.; Joon, S.; Singla, S.; Shen, B. Natural products for the management of castration-resistant prostate cancer: Special focus on nanoparticles based studies. *Front. Cell Dev. Biol.*, **2021**, *9*, 745177.
http://dx.doi.org/10.3389/fcell.2021.745177 PMID: 34805155

[10] Patel, P.; Asdaq. S.M.B. Immunomodulatory activity of methanolic fruit extract of *Aegle marmelos* in experimental animals. *Saudi Pharm. J.*, **2010**, *18*(3), 161-165.
http://dx.doi.org/10.1016/j.jsps.2010.05.006 PMID: 23964175

[11] Neelam Balekar, S.B.; Mohan, V.; Prasad, A. Modulatory activity of a polyphenolic fraction of *Cinnamomum zeylanicum* L. bark on multiple arms of immunity in normal and immunocompromised mice. *J. Appl. Pharm. Sci.*, **2014**, *4*(7), 114-122.

[12] Alhazmi, H.A.; Najmi, A.; Javed, S.A.; Sultana, S.; Al Bratty, M.; Makeen, H.A.; Meraya, A.M.; Ahsan, W.; Mohan, S.; Taha, M.M.E.; Khalid, A. Medicinal plants and isolated molecules demonstrating immunomodulation activity as potential alternative therapies for viral diseases including COVID-19. *Front. Immunol.*, **2021**, *12*, 637553.

[13] Zebeaman, M.; Tadesse, M.G.; Bachheti, R.K.; Bachheti, A.; Gebeyhu, R.; Chaubey, K.K.; Li, M.H. Plants and plant-derived molecules as natural immunomodulators. *BioMed Res. Int.*, **2023**, *2023*, 1-14.
http://dx.doi.org/10.1155/2023/7711297 PMID: 37313550

[14] Satyavati, G.V.; Gupta, A.K.; Tandon, N.; Seth, S.D. *Medicinal Plants of India*; Indian Council of Medical Research, **1987**, 2, p. 262.

[15] Morzelle, M.C.; Salgado, J.M.; Telles, M.; Mourelle, D.; Bachiega, P.; Buck, H.S.; Viel, T.A. Neuroprotective effects of pomegranate peel extract after chronic infusion with amyloid-β peptide in mice. *PLoS One*, **2016**, *11*(11), e0166123.
http://dx.doi.org/10.1371/journal.pone.0166123 PMID: 27829013

[16] Venkatrao, N.; Koroth, S.M.; Satyanarayana, S.; Hemamalini, K.; Kumar, S.M.S. Antidiarrhoeal and anti-inflammatory activity of fruit rind extracts of *Punica granatum*. *Indian Drugs*, **2007**, *44*(12), 909-914.

[17] Das, S.; Singh, S.R.; Ahmed, S.; Kanodia, L. Analgesic and anti-inflammatory activities of ethanolic extract of leaves of *Punica granatum* L. on experimental animal models. *Pharmacologyonline*, **2011**, *3*, 379-385.

[18] Labsi, M.; Khelifi, L.; Mezioug, D.; Soufli, I.; Touil-Boukoffa, C. Antihydatic and immunomodulatory effects of *Punica granatum* peel aqueous extract in a murine model of echinococcosis. *Asian Pac. J. Trop. Med.*, **2016**, *9*(3), 211-220.
http://dx.doi.org/10.1016/j.apjtm.2016.01.038 PMID: 26972390

[19] Tiwari, P.; Kumar, B.; Kaur, M.; Kaur, G.; Kaur, H. Phytochemical screening and extraction: A review. *Int. Pharm. Sci.*, **2011**, *1*(1), 98-106.

[20] Wang, J.; Rani, N.; Jakhar, S.; Redhu, R.; Kumar, S.; Kumar, S.; Kumar, S.; Devi, B.; Simal-Gandara, J.; Shen, B.; Singla, R.K. *Opuntia ficus-indica* (L.) Mill. - anticancer properties and phytochemicals: current trends and future perspectives. *Front. Plant Sci.*, **2023**, *14*, 1236123.
http://dx.doi.org/10.3389/fpls.2023.1236123

[21] Singla, R.K.; Singh, D.; Verma, R.; Kaushik, D.; Echeverría, J.; Garg, V.; Gupta, P.; Rahman, M.A.; Sharma, A.; Mittal, V.; Shen, B. Fermented formulation of silybum marianum seeds: Optimization, heavy metal analysis, and hepatoprotective assessment. *Phytomedicine*. **2023**.
PMID: 38241906

[22] Singla, R.K.; Zhang, Y.; Singla, S.; Shen, B. Bibliometric and temporal trend analysis of nipah virus- an emerging zoonotic disease: what do we know so far. *bioRxiv*, **2023**.
http://dx.doi.org/10.1101/2023.10.17.562837

[23] Hajiluian, G.; Karegar, S.J.; Shidfar, F.; Aryaeian, N.; Salehi, M.; Lotfi, T.; Farhangnia, P.; Heshmati, J.; Delbandi, A.A. The effects of Ellagic acid supplementation on neurotrophic, inflammation, and oxidative stress factors, and indoleamine 2, 3-dioxygenase gene expression in multiple sclerosis patients with mild to moderate depressive symp-

236

toms: A randomized, triple-blind, placebo-controlled trial. *Phytomedicine*, **2023**, *121*, 155094.
http://dx.doi.org/10.1016/j.phymed.2023.155094 PMID: 37806153

[24] Ghadimi, M.; Foroughi, F.; Hashemipour, S.; Nooshabadi, R.M.; Ahmadi, M.H.; Ahadi Nezhad, B.; Khadem Haghighian, H. Randomized double-blind clinical trial examining the Ellagic acid effects on glycemic status, insulin resistance, antioxidant, and inflammatory factors in patients with type 2 diabetes. *Phytother. Res.*, **2021**, *35*(2), 1023-1032.
http://dx.doi.org/10.1002/ptr.6867 PMID: 32909365

[25] Barghchi, H.; Milkarizi, N.; Belyani, S.; Norouzian Ostad, A.; Askari, V.R.; Rajabzadeh, F.; Goshayeshi, L.; Ghelichi Kheyrabadi, S.Y.; Razavidarmian, M.; Dehnavi, Z.; Sobhani, S.R.; Nematy, M. Pomegranate *(Punica granatum L.)* peel extract ameliorates metabolic syndrome risk factors in patients with non-alcoholic fatty liver disease: A randomized double-blind clinical trial. *Nutr. J.*, **2023**, *22*(1), 40.
http://dx.doi.org/10.1186/s12937-023-00869-2 PMID: 37605174

[26] Gautam, R.K.; Gupta, G.; Sharma, S.; Hatware, K.; Patil, K.; Sharma, K.; Goyal, S.; Chellappan, D.K.; Dua, K. Rosmarinic acid attenuates inflammation in experimentally induced arthritis in Wistar rats, using Freund's complete adjuvant. *Int. J. Rheum. Dis.*, **2019**, *22*(7), 1247-1254.
http://dx.doi.org/10.1111/1756-185X.13602 PMID: 31155849

[27] Kokate, C.K.; Purohit, A.P.; Gohkale, S.B. Pharmacognosy, 21 ed.; Nirali Prakashan: Pune, India, *Med. J.*, **2002**, *43*(2), pp. 007-085.

[28] Yadav, R.; Agarwala, M. Phytochemical analysis of some medicinal plants. *J. Phytol.*, **2011**, *3*(12), 10-14.

[29] Gautam, R.K.; Sharma, S.; Sharma, K. Comparative evaluation of anti-arthritic activity of *Salvadora persica linn.* and *Asparagus racemosus* willd: an *in-vitro* study. *IAJPR*, **2013**, *3*(10), 8222-8227.

[30] Wilkinson, P. Neutrophil adhesion test. In: *In Handbook of experimental pharmacology, I*, 1ˢᵗ ed.; Springer: Berlin, **1978**; p. 109.

[31] Choudhary, M.; Kumar, V.; Malhotra, H.; Singh, S. Medicinal plants with potential anti-arthritic activity. *J. Intercult. Ethnopharmacol.*, **2015**, *4*(2), 147-179.
http://dx.doi.org/10.5455/jice.20150313021918 PMID: 26401403

[32] Rajput, K.; Dubey, R.C.; Kumar, A. Probiotic potential and immunomodulatory properties in *Enterococcus faecium* GMB24 and *Enterococcus hirae* SMB16 isolated from goat and sheep milk. *Arch. Microbiol.*, **2022**, *204*(10), 619.
http://dx.doi.org/10.1007/s00203-022-03217-w PMID: 36098848

[33] Kumar, H.; Vasudeva, N. Immunomodulatory potential of *Nyctanthes abrortristis* stem bark. *J. Ayurveda Integr. Med.*, **2022**, *13*(2), 100556.
http://dx.doi.org/10.1016/j.jaim.2022.100556 PMID: 35653920

[34] Shen, X.; Zeng, Y.; Li, J.; Tang, C.; Zhang, Y.; Meng, X. The anti-arthritic activity of total glycosides from *Pterocephalus hookeri*, a traditional Tibetan herbal medicine. *Pharm. Biol.*, **2017**, *55*(1), 560-570.
http://dx.doi.org/10.1080/13880209.2016.1263869 PMID: 27937009

[35] Upadhyay, R.K. Anti-arthritic potential of plant natural products; its use in joint pain medications and anti-inflammatory drug formulations. *Int. J. Green. Pharm.*, **2016**, *10*(3), S120-S130.

[36] Muthuraman, A.; Sood, S.; Singla, S.K. The antiinflammatory potential of phenolic compounds from *Emblica officinalis L.* in rat. *Inflammopharmacology*, **2011**, *19*(6), 327-334.
http://dx.doi.org/10.1007/s10787-010-0041-9 PMID: 20596897

[37] Cheng, W.; Li, J.; You, T.; Hu, C. Anti-inflammatory and immunomodulatory activities of the extracts from the inflorescence of *Chrysanthemum indicum* Linné. *J. Ethnopharmacol.*, **2005**, *101*(1-3), 334-337.
http://dx.doi.org/10.1016/j.jep.2005.04.035 PMID: 16029939

[38] Shukla, S.; Mehta, A.; John, J.; Mehta, P.; Vyas, S.P.; Shukla, S. Immunomodulatory activities of the ethanolic extract of *Caesalpinia bonducella* seeds. *J. Ethnopharmacol.*, **2009**, *125*(2), 252-256.
http://dx.doi.org/10.1016/j.jep.2009.07.002 PMID: 19607900

[39] Anonymous Schrödinger Release. **2023**. Available from: https://www.schrodinger.com/citations#LigPrep

[40] Jorgensen, W.L.; Tirado-Rives, J. The OPLS [optimized potentials for liquid simulations] potential functions for proteins, energy minimizations for crystals of cyclic peptides and crambin. *J. Am. Chem. Soc.*, **1988**, *110*(6), 1657-1666.
http://dx.doi.org/10.1021/ja00214a001 PMID: 27557051

[41] Anonymous Schrödinger Release. Available from: https://www.schrodinger.com/citations#Epik

[42] Lopez-Girona, A.; Mendy, D.; Ito, T.; Miller, K.; Gandhi, A.K.; Kang, J.; Karasawa, S.; Carmel, G.; Jackson, P.; Abbasian, M.; Mahmoudi, A.; Cathers, B.; Rychak, E.; Gaidarova, S.; Chen, R.; Schafer, P.H.; Handa, H.; Daniel, T.O.; Evans, J.F.; Chopra, R. Cereblon is a direct protein target for immunomodulatory and antiproliferative activities of lenalidomide and pomalidomide. *Leukemia*, **2012**, *26*(11), 2326-2335.
http://dx.doi.org/10.1038/leu.2012.119 PMID: 22552008

[43] Carrancio, S.; Groocock, L.; Janardhanan, P.; Jankeel, D.; Galasso, R.; Guarinos, C.; Narla, R.K.; Groza, M.; Leisten, J.; Pierce, D.W.; Rolfe, M.; Lopez-Girona, A. CC-99282 is a novel cereblon (CRBN) E3 Ligase Modulator (CELMoD) agent with enhanced tumoricidal activity in preclinical models of lymphoma. *Blood*, **2021**, *138*(S1), 1200-1200.
http://dx.doi.org/10.1182/blood-2021-148068

[44] Moon, H.; Min, C.; Kim, G.; Kim, D.; Kim, K.; Lee, S.A.; Moon, B.; Yang, S.; Lee, J.; Yang, S.J.; Cho, S.K.; Lee, G.; Lee, C.S.; Park, C.S.; Park, D. Crbn modulates calcium influx by regulating Orai1 during efferocytosis. *Nat. Commun.*, **2020**, *11*(1), 5489.
http://dx.doi.org/10.1038/s41467-020-19272-0 PMID: 33127885

[45] Pluvinage, J.V.; Haney, M.S.; Smith, B.A.H.; Sun, J.; Iram, T.; Bonanno, L.; Li, L.; Lee, D.P.; Morgens, D.W.; Yang, A.C.; Shuken, S.R.; Gate, D.; Scott, M.; Khatri, P.; Luo, J.; Bertozzi, C.R.; Bassik, M.C.; Wyss-Coray, T. CD22 blockade restores homeostatic microglial phagocytosis in ageing brains. *Nature*, **2019**, *568*(7751), 187-192.
http://dx.doi.org/10.1038/s41586-019-1088-4 PMID: 30944478

[46] Aires, V.; Coulon-Bainier, C.; Pavlovic, A.; Ebeling, M.; Schmucki, R.; Schweitzer, C.; Kueng, E.; Gutbier, S.;

Harde, E. CD22 blockage restores age-related impairments of microglia surveillance capacity. *Front. Immunol.*, **2021**, *12*, 684430.
http://dx.doi.org/10.3389/fimmu.2021.684430 PMID: 34140954

[47] Rossi, E.A.; Goldenberg, D.M.; Michel, R.; Rossi, D.L.; Wallace, D.J.; Chang, C.H. Trogocytosis of multiple B-cell surface markers by CD22 targeting with epratuzumab. *Blood*, **2013**, *122*(17), 3020-3029.
http://dx.doi.org/10.1182/blood-2012-12-473744 PMID: 23821660

[48] Enterina, J.R.; Jung, J.; Macauley, M.S. Coordinated roles for glycans in regulating the inhibitory function of CD22 on B cells. *Biomed. J.*, **2019**, *42*(4), 218-232.
http://dx.doi.org/10.1016/j.bj.2019.07.010 PMID: 31627864

[49] Krasavin, M.; Adamchik, M.; Bubyrev, A.; Heim, C.; Maiwald, S.; Zhukovsky, D.; Zhmurov, P.; Bunev, A.; Hartmann, M.D. Synthesis of novel glutarimide ligands for the E3 ligase substrate receptor Cereblon (CRBN): Investigation of their binding mode and antiproliferative effects against myeloma cell lines. *Eur. J. Med. Chem.*, **2023**, *246*, 114990.
http://dx.doi.org/10.1016/j.ejmech.2022.114990 PMID: 36476642

[50] Ereño-Orbea, J.; Sicard, T.; Cui, H.; Mazhab-Jafari, M.T.; Benlekbir, S.; Guarné, A.; Rubinstein, J.L.; Julien, J.P. Molecular basis of human CD22 function and therapeutic targeting. *Nat. Commun.*, **2017**, *8*(1), 764.
http://dx.doi.org/10.1038/s41467-017-00836-6 PMID: 28970495

[51] Madhavi Sastry, G.; Adzhigirey, M.; Day, T.; Annabhimoju, R.; Sherman, W. Protein and ligand preparation: Parameters, protocols, and influence on virtual screening enrichments. *J. Comput. Aided Mol. Des.*, **2013**, *27*(3), 221-234.
http://dx.doi.org/10.1007/s10822-013-9644-8 PMID: 23579614

[52] Friesner, R.A.; Banks, J.L.; Murphy, R.B.; Halgren, T.A.; Klicic, J.J.; Mainz, D.T.; Repasky, M.P.; Knoll, E.H.; Shelley, M.; Perry, J.K.; Shaw, D.E.; Francis, P.; Shenkin, P.S. Glide: A new approach for rapid, accurate docking and scoring. 1. Method and assessment of docking accuracy. *J. Med. Chem.*, **2004**, *47*(7), 1739-1749.
http://dx.doi.org/10.1021/jm0306430 PMID: 15027865

[53] Raj, P.; Selvam, K.; Roy, K.; Mani Tripathi, S.; Kesharwani, S.; Gopal, B.; Varshney, U.; Sundriyal, S. Identification of a new and diverse set of *Mycobacterium tuberculosis* uracil-DNA glycosylase (MtUng) inhibitors using structure-based virtual screening: Experimental validation and molecular dynamics studies. *Bioorg. Med. Chem. Lett.*, **2022**, *76*, 129008.
http://dx.doi.org/10.1016/j.bmcl.2022.129008 PMID: 36174837

[54] Van Der Spoel, D.; Lindahl, E.; Hess, B.; Groenhof, G.; Mark, A.E.; Berendsen, H.J.C. GROMACS: Fast, flexible, and free. *J. Comput. Chem.*, **2005**, *26*(16), 1701-1718.
http://dx.doi.org/10.1002/jcc.20291 PMID: 16211538

[55] Vanommeslaeghe, K.; MacKerell, A.D., Jr. Automation of the CHARMM General Force Field (CGenFF) I: Bond perception and atom typing. *J. Chem. Inf. Model.*, **2012**, *52*(12), 3144-3154.
http://dx.doi.org/10.1021/ci300363c PMID: 23146088

[56] Humphrey, W.; Dalke, A.; Schulten, K. VMD: Visual molecular dynamics. *J. Mol. Graph.*, **1996**, *14*(1), 33-38, 27-28.

http://dx.doi.org/10.1016/0263-7855(96)00018-5 PMID: 8744570

[57] Schiffrin, B.; Radford, S.E.; Brockwell, D.J.; Calabrese, A.N. PYXLINKVIEWER : A flexible tool for visualization of protein chemical crosslinking data within the PYMOL molecular graphics system. *Protein Sci.*, **2020**, *29*(8), 1851-1857.
http://dx.doi.org/10.1002/pro.3902 PMID: 32557917

[58] Tripathi, S.M.; Akash, S.; Rahman, M.A.; Sundriyal, S. Identification of synthetically tractable MERS-CoV main protease inhibitors using structure-based virtual screening and molecular dynamics potential of mean force (PMF) calculations. *J. Biomol. Struct. Dyn.*, **2023**, 1-11.
http://dx.doi.org/10.1080/07391102.2023.2283780 PMID: 37978909

[59] Kumari, R.; Kumar, R.; Lynn, A. g_mmpbsa--a GROMACS tool for high-throughput MM-PBSA calculations. *J. Chem. Inf. Model.*, **2014**, *54*(7), 1951-1962.
http://dx.doi.org/10.1021/ci500020m PMID: 24850022

[60] Daina, A.; Michielin, O.; Zoete, V. SwissADME: A free web tool to evaluate pharmacokinetics, drug-likeness and medicinal chemistry friendliness of small molecules. *Sci. Rep.*, **2017**, *7*(1), 42717.
http://dx.doi.org/10.1038/srep42717 PMID: 28256516

[61] Banerjee, P.; Eckert, A.O.; Schrey, A.K.; Preissner, R. ProTox-II: A webserver for the prediction of toxicity of chemicals. *Nucleic Acids Res.*, **2018**, *46*(W1), W257-W263.
http://dx.doi.org/10.1093/nar/gky318 PMID: 29718510

[62] Ambriz-Perez, D.L.; Leyva-Lopez, N.; Gutierrez-Grijalva, E.P.; Heredia, J.B.; Yildiz, F. Phenolic compounds: Natural alternative in inflammation treatment. A Review. *Cogent Food Agric.*, **2016**, *2*(1), 1131412.

[63] do Nascimento, R.F.; de Oliveira Formiga, R.; Machado, F.D.F.; de Sales, I.R.P.; de Lima, G.M.; Alves Júnior, E.B.; Vieira, G.C.; Pereira, R.F.; de Araújo, A.A.; de Araújo Junior, R.F.; Barbosa Filho, J.M.; Batista, L.M. Rosmarinic acid prevents gastric ulcers *via* sulfhydryl groups reinforcement, antioxidant and immunomodulatory effects. *Naunyn Schmiedebergs Arch. Pharmacol.*, **2020**, *393*(12), 2265-2278.
http://dx.doi.org/10.1007/s00210-020-01894-2 PMID: 32642876

[64] Wang, E.; Sun, H.; Wang, J.; Wang, Z.; Liu, H.; Zhang, J.Z.H.; Hou, T. End-point binding free energy calculation with MM/PBSA and MM/GBSA: Strategies and applications in drug design. *Chem. Rev.*, **2019**, *119*(16), 9478-9508.
http://dx.doi.org/10.1021/acs.chemrev.9b00055 PMID: 31244000

[65] Genheden, S.; Ryde, U. The MM/PBSA and MM/GBSA methods to estimate ligand-binding affinities. *Expert Opin. Drug Discov.*, **2015**, *10*(5), 449-461.
http://dx.doi.org/10.1517/17460441.2015.1032936 PMID: 25835573

[66] Lataliza, A.A.B.; de Assis, P.M.; da Rocha Laurindo, L.; Gonçalves, E.C.D.; Raposo, N.R.B.; Dutra, R.C. Antidepressant-like effect of rosmarinic acid during LPS -induced neuroinflammatory model: The potential role of cannabinoid receptors/ PPAR -γ signaling pathway. *Phytother. Res.*, **2021**, *35*(12), 6974-6989.
http://dx.doi.org/10.1002/ptr.7318 PMID: 34709695

[67] Hitl, M.; Kladar, N.; Gavarić, N.; Božin, B. Rosmarinic acid-human pharmacokinetics and health benefits. *Planta Med.*, **2021**, *87*(4), 273-282.
http://dx.doi.org/10.1055/a-1301-8648 PMID: 33285599

238
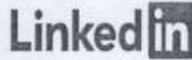
Article Details

PREPARATION AND CHARACTERIZATION OF MICROSPHERES UTILIZING RATE-CONTROLLING MEMBRANES FOR THE MANAGEMENT OF DIABETES MELLITUS

Nitu Patidar[a], Nadeem A. Farooqui[a], Darshan Jamindar[a,b], Dinesh K. Mishra[c], Rajat Goyal[c], Hitesh Chopra[e] and Rupesh K. Gautam[a]

[a] Department of Pharmaceutics, Indore Institute of Pharmacy, IIST Campus, Rau-Indore-453 331, Madhya Pradesh, India
[b] Department of Pharmaceutics, Madhyanchal Professional University, Bhopal – 462 044, Madhya Pradesh, India
[c] Department of Pharmacy, Guru Ghasidas Vishwavidalaya, Bilaspur-495 009, Chhattisgarh, India
[d] MM College of Pharmacy, Maharishi Markandeshwar (Deemed to be University), Mullana-Ambala -133 207, Haryana, India
[e] Department of Biosciences, Saveetha School of Engineering, Saveetha Institute of Medical and Technical Sciences, Chennai-602 105, Tamil Nadu, India
* For Correspondence: E-mail: drrupeshgautam@gmail.com

ABSTRACT

The present research work aimed at the formulation of film-coated microspheres incorporating glibenclamide drug and their evaluation for the management of diabetes mellitus (DM). Microspheres were prepared by solvent evaporation methodology by the usage of ethyl cellulose as polymer, ethanol and dichloromethane as solvents and Tween 80® as a non-ionic surfactant. The film-coated membrane was prepared by pan coating method, incorporating ethyl cellulose, isopropyl alcohol, diethyl phthalate and sodium lauryl sulfate. This film membrane was coated on microspheres with the help of a spray gun. The efficiency of entrapment of the film coated microspheres of F5* batch, among different formulations, is highest and comes out to be in the range of 76.65±0.58. The percentage yield was observed to be 73.32±0.14. Morphological studies conducted by scanning electron microscope show spherical microspheres of uniform size. In vitro drug release study conducted of the coated microspheres of glibenclamide shows the highest amount of release of 97.44% in the F5*batch. The best-fit model was determined by the highest R^2 value. Further, the developed formulation helps in reduction in dose dumping, with better patient compliance, and also masks the bitter taste of the drug.

DOWNLOAD ARTICLE

Principal
Indore Institute of Pharmacy,
INDORE (M.P.)

Insights on aspects of apoptosis in neurodegenerative disorders: a comprehensive review

Rajat Goyal[1], Kashish Wilson[1], Anjali Saharan[2], Rupesh K. Gautam[3*], Hitesh Chopra[4], Sumeet Gupta[1], Mohammad Amjad Kamal[4,5,6,7,8]

[1]MM College of Pharmacy, Maharishi Markandeshwar (Deemed to be University), Mullana-Ambala 133207, Haryana, India

[2]Department of Pharmaceutical Sciences, Maharishi Dayanand University, Rohtak 124001, Haryana, India

[3]Department of Pharmacology, Indore Institute of Pharmacy, Indore 453331, Madhya Pradesh, India

[4]Department of Biosciences, Saveetha School of Engineering, Saveetha Institute of Medical and Technical Sciences, Chennai 602105, Tamil Nadu, India

[5]Institutes for Systems Genetics, Frontiers Science Center for Disease-related Molecular Network, West China Hospital, Sichuan University, Chengdu 610065, Sichuan, China

[6]King Fahd Medical Research Center, King Abdulaziz University, Jeddah 21589, Saudi Arabia

[7]Department of Pharmacy, Faculty of Allied Health Sciences, Daffodil International University, Dhaka 1207, Bangladesh

[8]Enzymoics, 7 Peterlee Place, Novel Global Community Educational Foundation, Hebersham 2770, Australia

*Correspondence: Rupesh K. Gautam, Department of Pharmacology, Indore Institute of Pharmacy, IIST Campus, Opposite IIM Indore, Rau-Pithampur Road, Indore 453331, Madhya Pradesh, India. rupeshgautammmu@gmail.com

Academic Editor: Hua Su, University of California, USA

Received: October 14, 2023 Accepted: November 8, 2023 Published: February 28, 2024

Abstract

Nerve cell death is the central aspect of human neurodegenerative disorders. Neuronal death in results leads to the onset of various human neurological disorders such as Alzheimer's disease, Parkinson's disease, Huntington's disease, amyotrophic lateral sclerosis, and stroke. In developing neurons, apoptosis is assumed to provide a counterbalance to overexuberant cell replication. Numerous signals may induce apoptosis in neurons, such as the absence of neurotrophic factor support, increased levels of metabolic and oxidative stress, and overstimulation of glutamate receptors (leading to the calcium influx). Cell death and neurological disorders have been related to oxidative stress, which creates an imbalance between antioxidant defenses and free radical production. In this paper, a summary of the engrossment of oxidative stress, neuronal apoptosis, and mitochondrial dysfunction in neurodegenerative disorders has been discussed. Antioxidant therapy's potential assistance for neurodegenerative illnesses in human beings is still up for dispute, despite encouraging pre-clinical research findings. One elucidation for this disparity could be the non-existence of an accurate way to assess oxidative stress in the brain. The explosion in research on apoptosis in neurodegeneration has stemmed from the conception that persuading neuronal apoptotic death may be crucial to the progression of a disease and that anti-apoptotic approaches may be useful in the prevention of neurodegenerative processes. A deeper understanding of the role that apoptosis plays in neurodegenerative processes will serve as the foundation for future research into the development of focused, effective treatment modalities.

Principal
Indore Institute of Pharmacy,
INDORE (M.P.)

240

Keywords

Introduction

Apoptosis is a phenomenon of programmed cell death, in which cells die sequentially at the end. The central nervous system is at fatal risk during both acute and chronic neurodegenerative disorders (NDs) [1]. The onset and prevalence of NDs such as Parkinson's disease (PD), Alzheimer's disease (AD), and stroke lead to an alarming rate of increase in the number of people suffering from it. These disorders cause the degeneration of neurons oxidative stress and excessive cell-mediated proteolysis [2].

Degenerating neurons exhibit oxidative stress and excessive calcium-mediated proteolysis at the cellular level, which eventually results in apoptosis. In apoptosis, the cell and nucleus shrink and form blebbing, causing chromatin fragmentation, loss of adhesion, and rapid engulfment by phagocytosis [3]. Apoptosis also causes several biochemical changes along with morphological alterations such as DNA fragmentation, plasma membrane depolarization, lysosome permeability, and enhanced formation of reactive oxygen species (ROS) [4]. Induction of apoptosis is achieved by many methods depending on their pathways such as internal and external stimuli. Internal stimuli are triggered by activating intrinsic pathways such as abnormalities in the DNA and external stimuli are activated by cytokines such as extrinsic signaling pathways [5]. The description of normal apoptotic pathways by Guerin et al. [6] is depicted in Figure 1.

Figure 1. The description of the general apoptosis pathway of a cell

Principal
Indore Institute of Pharmacy.
INDORE (M.P.)

241

The apoptosis pathways elaborated in Figure 1 show different phases such as shrinking of the cell, membrane blebbing, the collapse of the nucleus, normal apoptotic body, and at the end leads to lysis of the apoptotic body. The descriptive pathways include two different methods of apoptosis such as intrinsic and extrinsic pathways for cascades, as depicted in Figure 2.
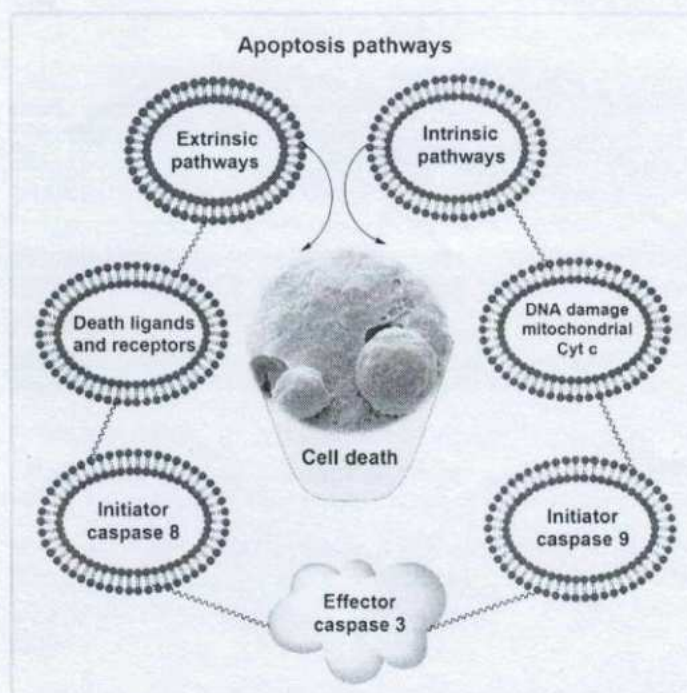

Figure 2. Intrinsic and extrinsic apoptosis pathways. Cyt c: cytochrome c

Intrinsic apoptosis

The non-receptor-mediated intracellular signals that are part of the intrinsic signaling pathway for programmed cell death include the numerous mitochondrial processes that start apoptosis [7]. The intrinsic pathway for programmed cell death can also be activated by damage to cellular DNA. Pro-apoptotic proteins set off caspases, which then regulate several cell death pathways. These proteins also enter the cellular nucleus where they trigger apoptosis and DNA damage. The removal of growth factor supplements from culture media, exposure to ultraviolet (UV) light, or cell stressors are examples of situations that can start the intrinsic pathway (for instance osmotic or metabolic). In the end, these circumstances result in DNA cell damage. When exposed to UV radiation, thymine base pairs adsorb UVB photon, which then joins together to generate pyrimidine dimers. ROS production may rise in response to growth factor withdrawal or other stressful circumstances. ROS can harm DNA through several mechanisms, including base modification [8].

The literature has reported that several diseases, including hypoxia, irreversible DNA damage, oxidative stress, and viral infections are triggered by intrinsic pathways, which will cause the alteration in the release of cytochrome from mitochondria, and form the complexes with the apoptotic protease activating factor-1 (Apaf-1) and procaspase [9].

Extrinsic apoptosis

Transmembrane death receptors, which are the products of the tumor necrosis factor (*TNF*) receptor gene, are a component of the extrinsic signaling cascade that results in apoptosis [10]. These receptors interact with extrinsic ligands to bind and translate intracellular signals that lead to cell death. It works on the active receptor and subsequently l binds procaspase-8 and *TNF* R1 (receptor type 1). Procaspase-8 is

242

activated by this multiprotein complex, which starts apoptosis, or the process of cell death. Several caspases, which are proteases with specific biological targets, are involved in the signal transduction of the extrinsic pathway. The activation of caspases affects a variety of cellular processes and plays a significant part in the process that results in cell death [11].

Prompts of apoptosis: oxidative stress and Ca^{2+}

Oxidative stress

A high level of ROS such as hydrogen peroxide radicals ($\bullet H_2O_2$), hydroxyl radicals ($\bullet OH$), and superoxide anion and an imbalance of antioxidant enzymes contribute to oxidative stress, which is a detrimental factor in memory dysfunctions [12]. Oxidative stress may be associated with cell membrane mutilation from lipid peroxidation, vicissitudes in protein structure and function, and structural damage to DNA. As the brain is one of the most metabolically active organs in the body, it is particularly susceptible to oxidative stress for the reasons listed below: First, its high oxygen demand (20% of the body's oxygen intake). Second, the brain is full of redox-active metals like copper and iron, which constantly accelerate ROS production. Third, the membranes of brain cells contain substantial amounts of polyunsaturated fatty acids, that act as substrates for lipid peroxidation. Fourth, the brain has comparatively low levels of GSH, which functions as an endogenous antioxidant that helps in eliminating ROS [13].

It was evident from a research study that showed a prompt increase in oxidative stress levels as compared to neurologically impaired patients with aging factors. From the immunohistological examination, it was evident the increased protein oxidation, and lipid peroxidation in brain areas having neurofibrillary tangles and plaques. In AD, the cerebrospinal fluid had increased lipid peroxidation levels such as 4-hydroxynonenal [14]. Variations in the antioxidant enzymes catalase, Cu/Zn-superoxide dismutase (SOD), and Mn-SOD are caused by the increased oxidative stress in AD. These enzymes present in the neurons in the membrane cause lipid peroxidation with an increase in the secretion of toxic aldehydes such as 4-hydroxynonenal or malondi-aldehyde. These aldehydes disturb cellular Ca^{2+} homeostasis by interfering with the activity of the adenosine triphosphatases (ATPases), glucose, and glutamate transporters. Oxidative stress accumulation leads to the generation of ROS, which causes mitochondrial dysfunctions [15].

Nitric oxide (NO), which functions as a second messenger and can combine with superoxide anion to generate peroxynitrite [ONOO(-)], produces an interesting concept concerning oxidative stress in neurons. It has been demonstrated that ONOO(-) is neurotoxic and induces apoptosis in leukemic cells [16]. Several substances including vitamin E, estrogens, uric acid, and glutathione, are utilized to alleviate oxidative stress. They have been reported to prevent cellular injury, and membrane lipid or protein damage. Through the tumor protein (p53), poly(ADP-ribose) polymerase (PARP), or the ataxia telangiectasia mutant (ATM), ROS can cause DNA damage, which triggers lethal apoptotic signaling [17]. It was evident that oxidative stress in AD has scavenging free radicals which are used as a neuroprotective therapy for the disease. Moreover, prophylactic treatment with free radical scavengers such as vitamin E may reduce the risk of AD.

Perturbed Ca^{2+} homeostasis

The alteration and dysfunction in the Ca^{2+} regulation have been reported in various clinical studies on patients with AD. The neurofibrillary changes are exhibited by calpain-II which gets activated by the activation of Ca^{2+}-dependent protease [18]. The oxidative stress or greater intracellular calcium levels can activate cysteine proteases called caspases, such as calpain linked to neuronal cell death. Some conditions, such as cerebral ischemia, epilepsy, and traumatic brain injury, affect the calcium homeostasis of neurons and overstimulate capillaries [19].

To maintain cellular ion homeostasis and cell viability, calpain depends on a variety of substrates, including membrane receptors, kinases, phosphatases, cytoskeletal proteins, and transporters. Increased levels of calpains or the endogenous calpain inhibitor, calpastatin, have been connected to neuron loss in several neurodegenerative illnesses, including amyotrophic lateral sclerosis (ALS), PD, and AD [20]. Calpain

Prinzipal
Indore Institute of Pharmacy.
INDORE (M.P.)

243

inhibitors inhibited neuronal cell death in a variety of experimental scenarios, supporting the idea that calpains are crucial in the regulation of apoptosis and necrosis. The existence of higher Ca^{2+} binding proteins such as calretinin and calbindin, which are resistant to neurofibrillary degeneration, has been found to promote neurodegeneration in AD illness [21].

It is widely known that the cytotoxic buildup of intracellular calcium plays a crucial role in neuronal cell death as well as other stress conditions like toxicity. The cytotoxic intracellular Ca^{2+} is mediated via the stimulation of glutamate receptors. This strengthens the voltage-dependent Ca^{2+} channels, metabotropic glutamate receptors, and Ca^{2+} permeable α-amino-3-hydroxy-5-methyl-4-isoxazole propionic acid (AMPA) receptors [22]. The lethal accumulation of Ca^{2+} in apoptotic cells is caused due to the over-activation of glutamate receptors. This fatal result arises due to the cleavage of ion pumps due to variability in the physiological environment which supports the pumping out of Ca^{2+} to maintain a stable state of cytosolic calcium [23]. On exposure to apoptotic damage, the caspases or calpains become activated and cleave the ion pumps. This lets the Ca^{2+} ion pump remove huge amounts of calcium that have accumulated in the cytosol. Because of this, calcium homeostasis is upset, which ultimately causes apoptotic signaling to change to necrosis.

It reveals that the signaling pathways of apoptosis are crucial for the development and control of illness. There are still a large number of proteins that are unknown and are involved in various signaling pathways. The purpose of that unidentified protein would be as a linker protein, which would be able to treat or stop the aberrant loss of neural cells in neurodegenerative illnesses. One of the key goals of current science is to understand the mechanism of proteins in the signaling pathways of apoptosis and anti-apoptosis [24].

Pathogenesis of neurogenerative disorders

Proteopathies are diseases in which some proteins develop aberrant structural characteristics, which are aggregated at various cellular levels and in tissues causing the interruption of their activities [25]. The proteopathies comprise several NDs in which peculiarly accumulated proteins seem to play a vital role [26]. When the misfolded or atypical proteins accumulate in the nuclear, cytoplasmic, and extracellular enclosures, it leads to disruption of organelle and synaptic dysfunction in the nervous system. Neuronal apoptosis in neurodegenerative illnesses can be induced via oxidative stress, disruption of calcium homeostasis, and metabolic impairment, at the cellular level. The anti-apoptotic or neuroprotective signaling pathways comprising neurotrophic factors, cytokines, and conditioning responses may offset the aging effects and hereditary predisposition in the experimental models of NDs [27].

Free radical production, activation of the pathway for NO synthesis, disruption of cellular calcium homeostasis, and programmed cell death are all factors that contribute to the progression of neurodegenerative illnesses associated with glutamatergic dysfunction [28, 29]. These methods may induce mutilation of proteins, nucleic acids, and lipids, as well as open the pores of mitochondrial permeability transition, which may increase the ROS generation, energy failure degeneration, and proclamation of proapoptotic substances like Cyt c in the cytoplasm [30]. The overproduction of ROS and downregulation of antioxidant defense cause the death of NDs' neuronal cells [31]. A variety of neurodegenerative illnesses are linked to inappropriate regulation of Wnt/β-catenin (WβC) signaling [32]. Degenerative nerve diseases are thought to contribute to the deterioration of various vital bodily functions, including memory, breathing, balance, speech, movement, and heartbeat [29]. The factors for the pathogenesis of neurogenerative disorders by Mehta et al. [33] are illustrated in Figure 3.

Apoptosis involvement in NDs

Apoptosis is a fundamental physiologic process that contributes to cellular homeostasis. Apoptosis (programmed cell death) is a type of physiological cellular suicide that occurs in several biological processes, including immune response, synaptogenesis, embryogenesis, and normal tissue and organ involvement. Normal brain development depends on programmed cell death. It affects the quantity and
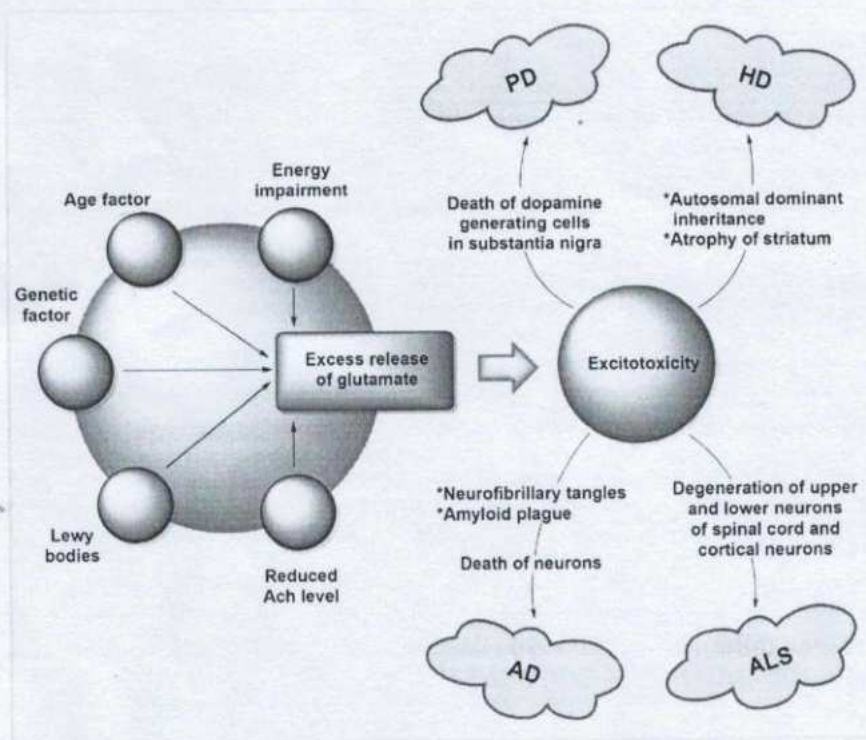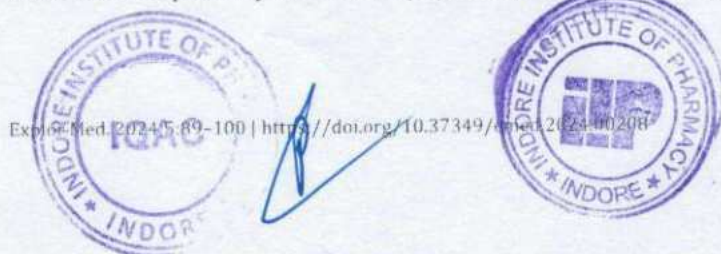
Principal
Indore Institute of Pharmacy.
INDORE (M.P.)

244

Figure 3. Pathogenesis of NDs. HD: Huntington's disease

type of cells in the growing brain and spinal cord and is essential for the development of a functional neural network. In pathological circumstances, it is also partly accountable for physiological aging and the death of neurons linked to NDs [27]. Apoptotic cell death is well characterized via a sequence of morphological variations that comprise attenuation of nuclear and cytoplasmic compartments, condensation of chromatin, DNA degradation into fragments of oligonucleosomes, and an assortment of nuclear material into the vesicular apoptotic bodies [34].

Neurodegenerative disorders cause neuronal death at the cellular level as a result of oxidative stress, DNA damage as a result of endoplasmic reticulum (ER) stress, and disruption of cellular calcium homeostasis. The apparent upsurge in the lifespan of individuals and the normal age of the population is tactlessly allied to a liberal intensification in the vast number of persons having NDs [35]. Apoptosis induction via pathogenic proteins of NDs by Yang et al. [36] is described in Figure 4.

Mitochondrial apoptotic signaling

Mitochondrial dysfunction plays a crucial role in the etiology of NDs. Numerous fragments of data suggest that NDs have profoundly impaired mitochondrial activity. The mitochondria are highly vulnerable to oxidative stress as it has the primary organelles for the production of ATP and are the main source of ROS generation [37]. The release of Cyt c, which occupies center stage as the starting point and mediator of the apoptosis cascade, is the major paradigm in mitochondria-mediated apoptotic signaling. Cyt c acts as a molecular adaptor that couples the procaspase-9 and Apaf-1 to produce the apoptosome complex during the activation of the death protease, caspase-3. Cyt c is released from the mitochondria into the cytosol either by non-specifically expanding and rupturing the mitochondria or by opening a particular channel or permeability transition pore in the mitochondrial membrane. Members of the pro- and anti-apoptotic subfamilies of B-cell lymphoma 2 (Bcl-2) are the guardians of channel-mediated Cyt c release within mitochondria. This ROS mechanism of apoptosis signaling is probably going to be crucial in reperfusion-induced neuronal cell death since post-ischemic mitochondria can produce more ROS [34]. This mitochondrial pathway of cellular apoptosis is illustrated in Figure 5.
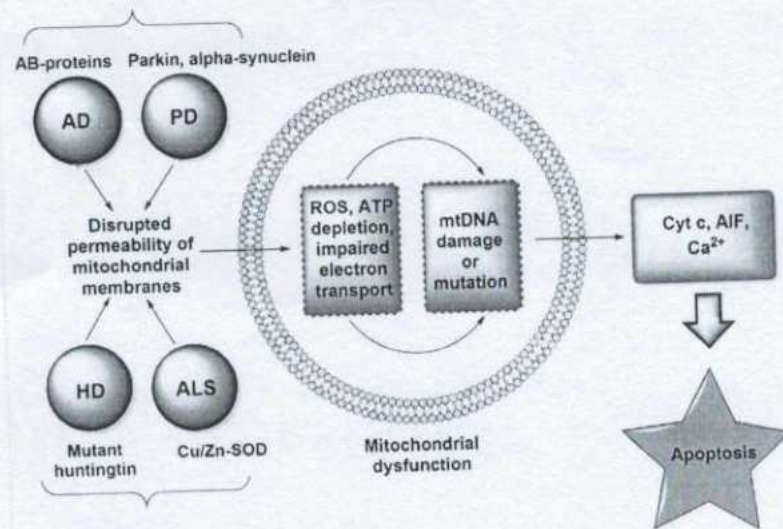
Figure 4. Induction of apoptosis by pathogenic proteins of NDs. ATP: adenosine triphosphate; mtDNA: mitochondrial DNA; AIF: apoptosis-inducing factor
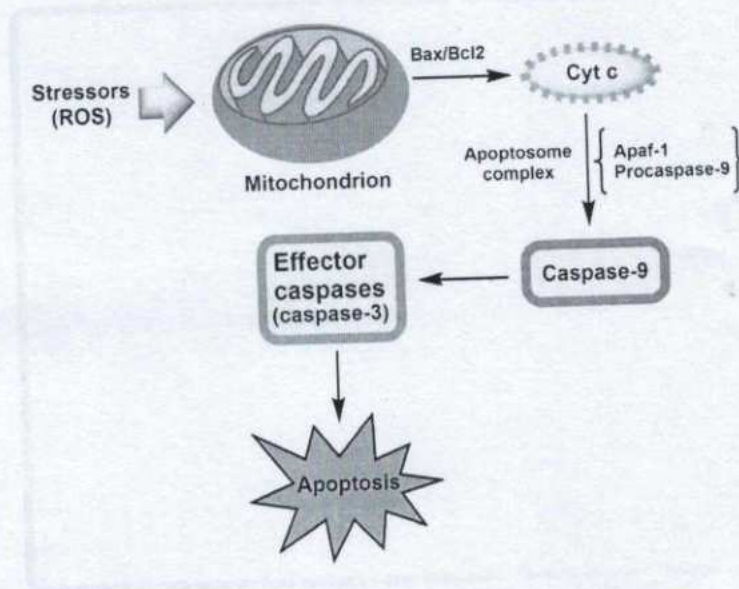

Figure 5. The mitochondrial pathway of cellular apoptosis. Bax: Bcl-2-associated X protein

Novel strategies for preventing neuronal apoptosis/anti-apoptotic strategies

The apoptosis induction in tumor cells affects the anti-tumor efficacy of radiotherapy and chemotherapy. However, the significant adverse impact of those pro-apoptotic therapies has prompted researchers to seek out other ways to promote tumor apoptosis [38]. Antioxidants or medications that block glutamate receptors or calcium channels have traditionally been used to reduce neuronal death in NDs. Anti-inflammatory medicines and caspase inhibitors are also being utilized. The biology of neural stem cells and the "anti-aging" enzyme telomerase have also been utilized to create two distinct strategies for avoiding apoptosis and replacing damaged or dead neurons. The six-base DNA repeat sequence (TTAGGG) is added to chromosomal ends by the telomerase reverse transcriptase (TERT) enzyme, which has recently attracted a lot of attention due to its purported "anti-aging" capabilities. TERT may assist an anti-apoptotic activity in neurons by suppressing the TERT expressions or activity, which makes them more vulnerable to oxidative and excitotoxic stimuli. Conversely, overexpression of TERT protects the neurons from apoptosis [39].

Acetylcholine (Ach) is a parasympathetic neurotransmitter that also enhances synaptogenesis in living cells to influence memory and learning in people. With three approved medications (donepezil, galantamine, and rivastigmine), acetylcholinesterase inhibitors (AChEIs) are the most well-researched medications and the first-choice treatment for NDs globally. Nevertheless, the AChEIs are less valuable in the advanced stages as they necessitate a higher dose which also upsurges the risk of adverse effects. Over the years, many potential candidates like metrifonate and tesofensine came under clinical trial as AChEIs but failed at certain stages mainly due to their safety profile. Altogether, this evidence indicates an awful and unmet necessity for the development of novel AChEIs [40].

Some potent apoptotic medications used for the treatment of NDs are described in Table 1.

Table 1. Some potent apoptotic medications used for the treatment of NDs

Sr. No.	Drugs	Mechanism of action	Model used	References
1.	Minocycline	Inhibition of the generation of free radicals and the neurotoxicity caused by 6-OHDA in rat CGN.	Cultured rat CGN	[41, 42]
2.	Rasagiline	This causes MAO-B inhibition, which may decrease oxidation and the buildup of free radicals while simultaneously increasing the amount of monoamines in the brain through the suppression of their catabolism.	Aged male C57Bl/6J mice	[43, 44]
3.	Resveratrol	Present in red wine, grapes, and other fruits that inhibit oxidative stress via attenuation of 6-OHDA-induced oxidative damage and dopamine depletion.	6-OHDA-induced PD rat model	[45, 46]
4.	Coenzyme Q_{10}	By reducing oxidative stress and activating the P13K pathway, amyloid beta-induced neuronal cell death can be prevented.	Amyloid beta$_{25-35}$-induced rat cortical neurons	[47]
5.	Metformin	By lowering the transcription of Nrf2 and neurotrophic factors, the brain is protected against neurodegeneration without suffering cognitive impairment.	Aged male C57Bl/6J mice	[48]
9.	*Mucuna pruriens*	Its treatment significantly reduced nitrite levels, lipid peroxidation, and iNOS expression, indicating that it lowers NO in PD.	PQ-induced PD mouse model	[49]
10.	Ursolic acid	Reduction of oxidative stress in nigrostriatal tissue and enhancement of neurobehavioral functioning in PD patients.	MPTP-induced Parkinsonian mouse model	[50]

Sr. No.: serial number; 6-OHDA: 6-hydroxydopamine; CGN: cerebellar granule neurons; MAO-B: monoamine oxidase B; P13K: phosphoinositide 3-kinase; C57Bl/6J: parentral substrain of mice; Nrf2: nuclear factor erythroid 2–related factor 2; PQ: paraquat; iNOS: inducible NO synthase; MPTP: 1-methyl-4-phenyl-1,2,3,6-tetrahydropyridine

Discussion

When subjected to excessive oxidative stress, neurons may respond adaptively to overcome the stress, or they may activate a programmed cell death pathway called apoptosis. Alterations in the ER and mitochondria, as well as the activation of cysteine proteases known as caspases, are the characteristics of apoptosis. There is mounting evidence that neurodegenerative diseases cause malfunction and neuronal death due to apoptotic biochemical pathways. Indeed, the notion that neuronal apoptotic death induction plays a crucial role in the progression of the disease, the recent advances in basic apoptosis research, and the recognition that apoptosis has a broad range of clinical applications, have prompted much of the research into investigations of intervention tactics directed at the apoptosis control or apoptosis induction in the neuronal apoptotic death program. Potential remedies can be inferred from the hypothesis that oxidative stress is shared by multiple illnesses involving increasing cell death. Among these, using neurotrophic growth factors and antioxidant molecules could be a common strategy to shield neurons from oxidative damage.

Conclusions

The field of apoptosis research has recently gained exciting additional insights into the mechanics of cell death programs that may perhaps contribute to the degeneration and death of neurons after acute brain trauma and the evolution of neurodegenerative diseases. The focus of this review paper will be on

Principal
Indore Institute of Pharmacy

247

contemporary ideas that are important for comprehending the apoptotic death program, the mediators and regulators of cellular apoptosis, and the connection between aberrant apoptosis and the emergence of neurodegenerative illnesses. A deeper comprehension of the mechanisms underlying apoptosis may open the door to more advanced therapeutic approaches and treatment modalities that aim to regulate the neuronal apoptotic death pathway. To date, caspases and the Bcl-2 protein family are two members of the apoptotic machinery that have been the subject of much investigation. Future treatment modalities that emerge from research to more precisely identify the redox-sensitive molecular components of the neuronal apoptotic death machinery and their regulation in the various acute and chronic neurodegenerative pathologies should be challenged by the successes of these current approaches. More apoptotic inhibitors will probably be added to physicians' daily toolkits in the coming years for treating neurologic conditions involving caspase-mediated cell malfunction and cell death.

Abbreviations

6-OHDA: 6-hydroxydopamine

AChEIs: acetylcholinesterase inhibitors

AD: Alzheimer's disease

ALS: amyotrophic lateral sclerosis

Apaf-1: apoptotic protease activating factor-1

Bcl-2: B-cell lymphoma 2

Cyt c: cytochrome c

DNA: deoxyribonucleic acid

NDs: neurodegenerative disorders

NO: nitric oxide

PD: Parkinson's disease

ROS: reactive oxygen species

SOD: superoxide dismutase

TERT: telomerase reverse transcriptase

UV: ultraviolet

Declarations

Acknowledgments

Authors are thankful to their organizations for their support.

Author contributions

RG and KW: Writing—original draft, Writing—review & editing, Visualization. AS and HC: Supervision, Investigation, Conceptualization, Writing—review & editing. RKG and SG: Formal analysis, Resources, Visualization. MAK: Writing—review & editing, Supervision, Methodology. All the authors have equally contributed to conceiving this paper and participated in its revisions. All authors read and approved the final manuscript.

Conflicts of interest

The authors declare that they have no conflicts of interest.

Ethical approval

Not applicable.

Principal
Indore Institute of Pharmacy,
INDORE (M.P.)

Consent to participate

Not applicable.

Consent to publication

Not applicable.

Availability of data and materials

Not applicable.

Funding

Not applicable.

Copyright

© The Author(s) 2024.

References

1. Sankari SL, Masthan KM, Babu NA, Bhattacharjee T, Elumalai M. Apoptosis in cancer-an update. Asian Pac J Cancer Prev. 2012;13:4873–8.
2. Rahman MA, Sultan MT, Islam MR. Apoptosis and cancer: insights molecular mechanisms and treatments. Int J Biomol Biomed. 2012;2:1–6.
3. Cheung HH, Liu X, Rennert OM. Apoptosis: reprogramming and the fate of mature cells. Int Sch Res Not. 2012;2012:685852.
4. Rahbar Saadat Y, Saeidi N, Zununi Vahed S, Barzegari A, Barar J. An update to DNA ladder assay for apoptosis detection. Bioimpacts. 2015;5:25–8.
5. Shirjang S, Mansoori B, Asghari S, Duijf PH, Mohammadi A, Gjerstorff M, et al. MicroRNAs in cancer cell death pathways: apoptosis and necroptosis. Free Radic Biol Med. 2019;139:1–15.
6. Guerin MB, McKernan DP, O'Brien CJ, Cotter TG. Retinal ganglion cells: dying to survive. Int J Dev Biol. 2006;50:665–74.
7. Kim MA, Lee HE, Lee HS, Yang HK, Kim WH. Expression of apoptosis-related proteins and its clinical implication in surgically resected gastric carcinoma. Virchows Archiv. 2011;459:503–10.
8. Franklin JL. Redox regulation of the intrinsic pathway in neuronal apoptosis. Antioxid Redox Signal. 2011;14:1437–48.
9. Loreto C, La Rocca G, Anzalone R, Caltabiano R, Vespasiani G, Castorina S, et al. The role of intrinsic pathway in apoptosis activation and progression in Peyronie's disease. Bio Med Res Int. 2014;2014: 616149.
10. Nair P, Lu M, Petersen S, Ashkenazi A. Apoptosis initiation through the cell-extrinsic pathway. Methods Enzymol. 2014;544:99–128.
11. Ashkenazi A. Targeting the extrinsic apoptotic pathway in cancer: lessons learned and future directions. J Clin Invest. 2015;125:487–9.
12. Tripathi PN, Srivastava P, Sharma P, Tripathi MK, Seth A, Tripathi A, et al. Biphenyl-3-oxo-1, 2, 4-triazine linked piperazine derivatives as potential cholinesterase inhibitors with anti-oxidant property to improve the learning and memory. Bioorg Chem. 2019;85:82–96.
13. Kim GH, Kim JE, Rhie SJ, Yoon S. The role of oxidative stress in neurodegenerative diseases. Exp Neurobiol. 2015;24:325–40.
14. Giorgi C, Baldassari F, Bononi A, Bonora M, De Marchi E, Marchi S, et al. Mitochondrial Ca^{2+} and apoptosis. Cell Calcium. 2012;52:36–43.
15. Tian H, Qu S, Wang Y, Lu Z, Zhang M, Gan Y, et al. Calcium and oxidative stress mediate perillaldehyde-induced apoptosis in *Candida albicans*. Appl Microbiol Biotechnol. 2017;101:3335–45.

Principal
Indore Institute of Pharmacy.

16. Gorman AM, McGowan A, O'Neill C, Cotter T. Oxidative stress and apoptosis in neurodegeneration. J Neurol Sci. 1996;139:45–52.

17. Ly LD, Xu S, Choi SK, Ha CM, Thoudam T, Cha SK, et al. Oxidative stress and calcium dysregulation by palmitate in type 2 diabetes. Exp Mol Med. 2017;49:e291.

18. Resende R, Pereira C, Agostinho P, Vieira AP, Malva JO, Oliveira CR. Susceptibility of hippocampal neurons to Aβ peptide toxicity is associated with perturbation of Ca^{2+} homeostasis. Brain Res. 2007; 1143:11–21.

19. Giorgi C, Bonora M, Sorrentino G, Missiroli S, Poletti F, Suski JM, et al. p53 at the endoplasmic reticulum regulates apoptosis in a Ca^{2+}-dependent manner. Proc Natl Acad Sci. 2015;112:1779–84.

20. Cook NL, Viola HM, Sharov VS, Hool LC, Schöneich C, Davies MJ. Myeloperoxidase-derived oxidants inhibit sarco/endoplasmic reticulum Ca^{2+}-ATPase activity and perturb Ca^{2+} homeostasis in human coronary artery endothelial cells. Free Radic Biol Med. 2012;52:951–61.

21. Vergun O, Keelan J, Khodorov BI, Duchen MR. Glutamate-induced mitochondrial depolarisation and perturbation of calcium homeostasis in cultured rat hippocampal neurones. J Physiol. 1999;519: 451–66.

22. Florea AM. Toxicity of alkylated derivatives of arsenic, antimony, and tin *in vitro*: cellular uptake, cytotoxicity, genotoxic effects, perturbation of Ca^{2+} homeostasis, and cell death [dissertation]. Essen: University of Duisburg-Essen; 2005.

23. Bandara S, Malmersjö S, Meyer T. Regulators of calcium homeostasis identified by inference of kinetic model parameters from live single cells perturbed by siRNA. Sci Signal. 2013;6:ra56.

24. Zhou X, Hao W, Shi H, Hou Y, Xu Q. Calcium homeostasis disruption-a bridge connecting cadmium-induced apoptosis, autophagy and tumorigenesis. Oncol Res Treat. 2015;38:311–5.

25. Luheshi LM, Crowther DC, Dobson CM. Protein misfolding and disease: from the test tube to the organism. Current Opin Chem Biol. 2008;12:25–31.

26. Xilouri M, Stefanis L. Autophagy in the central nervous system: implications for neurodegenerative disorders. CNS Neurol Disord Drug Targets. 2010;9:701–19.

27. Ghavami S, Shojaei S, Yeganeh B, Ande SR, Jangamreddy JR, Mehrpour M, et al. Autophagy and apoptosis dysfunction in neurodegenerative disorders. Prog Neurobiol. 2014;112:24–49.

28. Maragakis NJ, Rothstein JD. Mechanisms of disease: astrocytes in neurodegenerative disease. Nat Clin Pract Neurol. 2006;2:679–89.

29. Lee HG, Zhu X, Casadesus G, Pallàs M, Camins A, O'Neill MJ, et al. The effect of mGluR2 activation on signal transduction pathways and neuronal cell survival. Brain Res. 2009;1249:244–50.

30. Nicholls DG. Mitochondrial dysfunction and glutamate excitotoxicity studied in primary neuronal cultures. Current Mol Med. 2004;4:149–77.

31. Farooqui T, Farooqui AA. Aging: an important factor for the pathogenesis of neurodegenerative diseases. Mech Ageing Dev. 2009;130:203–15.

32. Ramakrishna K, Nalla LV, Naresh D, Venkateswarlu K, Viswanadh MK, Nalluri BN, et al. WNT-β catenin signaling as a potential therapeutic target for neurodegenerative diseases: current status and future perspective. Diseases. 2023;11:89.

33. Mehta A, Prabhakar M, Kumar P, Deshmukh R, Sharma PL. Excitotoxicity: bridge to various triggers in neurodegenerative disorders. Eur J Pharmacol. 2013;698:6–18.

34. Ekshyyan O, Aw TY. Apoptosis: a key in neurodegenerative disorders. Curr Neurovasc Res. 2004;1: 355–71.

35. Culmsee C, Landshamer S. Molecular insights into mechanisms of the cell death program: role in the progression of neurodegenerative disorders. Curr Alzheimer Res. 2006;3:269–83.

36. Yang JL, Weissman L, Bohr VA, Mattson MP. Mitochondrial DNA damage and repair in neurodegenerative disorders. DNA Repair. 2008;7:1110–20.

Principal
Indore Institute of Pharmacy.
INDORE (M.P.)

37. Rai SN, Singh C, Singh A, Singh MP, Singh BK. Mitochondrial dysfunction: a potential therapeutic target to treat Alzheimer's disease. Mol Neurobiol. 2020;57:3075–88.

38. Mazarakis ND, Edwards AD, Mehmet H. Apoptosis in neural development and disease. Arch Dis Child Fetal Neonatal Ed. 1997;77:F165–70.

39. Mattson MP, Duan W, Pedersen WA, Culmsee C. Neurodegenerative disorders and ischemic brain diseases. Apoptosis. 2001;6:69–81.

40. Srivastava P, Tripathi PN, Sharma P, Rai SN, Singh SP, Srivastava RK, et al. Design and development of some phenyl benzoxazole derivatives as a potent acetylcholinesterase inhibitor with antioxidant property to enhance learning and memory. Eur J Med Chem. 2019;163:116–35.

41. Kim HS, Suh YH. Minocycline and neurodegenerative diseases. Behav Brain Res. 200;196:168–79.

42. Lin S, Wei X, Xu Y, Yan C, Dodel R, Zhang Y, et al. Minocycline blocks 6-hydroxydopamine-induced neurotoxicity and free radical production in rat cerebellar granule neurons. Life Sci. 2003;72: 1635–41.

43. Youdim MB, Bar Am O, Yogev-Falach M, Weinreb O, Maruyama W, Naoi M, et al. Rasagiline: neurodegeneration, neuroprotection, and mitochondrial permeability transition. J Neurosci Res. 2005; 79:172–9.

44. Weinreb O, Badinter F, Amit T, Bar-Am O, Youdim MB. Effect of long-term treatment with rasagiline on cognitive deficits and related molecular cascades in aged mice. Neurobiol Aging. 2015;36:2628–36.

45. Khan MM, Ahmad A, Ishrat T, Khan MB, Hoda MN, Khuwaja G, et al. Resveratrol attenuates 6-hydroxydopamine-induced oxidative damage and dopamine depletion in rat model of Parkinson's disease. Brain Res. 2010;1328:139–51.

46. Allard JS, Perez EJ, Fukui K, Carpenter P, Ingram DK, de Cabo R. Prolonged metformin treatment leads to reduced transcription of Nrf2 and neurotrophic factors without cognitive impairment in older C57BL/6J mice. Behav Brain Res. 2016;301:1–9.

47. Choi H, Park HH, Koh SH, Choi NY, Yu HJ, Park J, et al. Coenzyme Q10 protects against amyloid beta-induced neuronal cell death by inhibiting oxidative stress and activating the P13K pathway. Neurotoxicology. 2012;33:85–90.

48. Wahlqvist ML, Lee MS, Hsu CC, Chuang SY, Lee JT, Tsai HN. Metformin-inclusive sulfonylurea therapy reduces the risk of Parkinson's disease occurring with Type 2 diabetes in a Taiwanese population cohort. Parkinsonism Relat Disord. 2012;18:753–8.

49. Yadav SK, Rai SN, Singh SP. *Mucuna pruriens* reduces inducible nitric oxide synthase expression in Parkinsonian mice model. J Chem Neuroanat. 2017;80:1–10.

50. Rai SN, Yadav SK, Singh D, Singh SP. Ursolic acid attenuates oxidative stress in nigrostriatal tissue and improves neurobehavioral activity in MPTP-induced Parkinsonian mouse model. J Chem Neuroanat. 2016;71:41–9.

251

Review

Unlocking β-cell restoration: The crucial role of PDX1 in diabetes therapy

Deepali Siwan [a], Mukesh Nandave [a] ✉, Ritu Gilhotra [b], Waleed Hassan Almalki [c], Gaurav Gupta [d e g], Rupesh K Gautam [f] ✉

Show more ∨

⚯ Share ⁹⁹ Cite

Abstract

Diabetes has been a significant healthcare problem worldwide for a considerable period. The primary objective of diabetic treatment plans is to control the symptoms associated with the pathology. To effectively combat diabetes, it is crucial to comprehend the disease's etiology, essential factors, and the relevant processes involving β-cells. The development of the pancreas, maturation, and maintenance of β-cells, and their role in regular insulin function are all regulated by PDX1. Therefore, understanding the regulation of PDX1 and its interactions with signaling pathways involved in β-cell differentiation and proliferation are crucial elements of alternative diabetes treatment strategies. The present review aims to explore the protective role of PDX1 in β-cell proliferation through signaling pathways. The main keywords chosen for this review include "PDX1 for β-cell mass," "β-cell proliferation," "β-cell restoration via PDX1," and "mechanism of PDX1 in β-cells." A comprehensive literature search was conducted using various internet search engines, such as PubMed, Science Direct, and other publication databases. We summarize several approaches to generating β-cells from alternative cell sources, employing PDX1 under various modified growth conditions and different transcriptional factors. Our analysis highlights the unique potential of PDX1 as a promising target in molecular and cell-based therapies for diabetes.

252
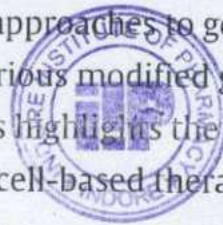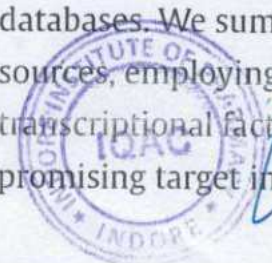
Introduction

The endocrine pancreas has four types of cells: PP-cells, which create pancreatic polypeptide; δ-cells make somatostatin; α-cells make glucagon; and β-cells, which result in insulin. Islet pancreatic β cells have formed the transcription, production, and stimulation of insulin according to the disposition of blood sugar levels. While β-cells make between 70 to 80% of the bulk of an islet, the islet itself only makes up around 1% of the overall mass of the pancreas [1]. β-cell malfunction and its reductions cause the onset of diabetes [2]. Thus, it is essential for our comprehension of the etiology of diabetes to clarify the molecular processes governing the death of β-cells.

A β-cell function is commonly regulated by PDX1, known as pancreatic duodenal homeobox 1. Pdx1 plays an essential role as the insulin gene in the pancreas, where it also controls the development and differentiation of pancreatic growth factors in the gut [1], [3]. On mouse chromosome 5, the Pdx1 gene is a part of the mammalian Parahox gene cluster. Its name refers to a group of essential genes for early embryogenesis that is not a part of the conventional Hox (homeobox) gene cluster [4]. Genes involved, Gsh1, Pdx1, and Cdx2/3, which are all outlined in a certain kind of pancreatic cell, make up the Parahox cluster [3], [4], [5]. The dominant human mutation ortholog of the Pdx1 gene similarly causes the same severe phenotype in humans [6], highlighting the importance of Pdx1 seems to be essential for the developed β-cell's functionality. Heterozygous missense and frameshift mutation of the PDX1 gene cause impaired insulin production and the onset of one variant of maturity-onset diabetic of the young 4 (MODY4) [7], [8], [9], [10].

Similarly, the etiology of type 2 diabetes (T2D) in animal studies illustrated that β-cell failure might be connected to the downregulation of Pdx1 transcription in the β-cell [11]. As a result, Pdx1 contributes to pancreatic islet development and β-cell survival in animals. Although Pdx1 has a well-defined involvement in creating specific types in the developing pancreatic islets, it is less known how Pdx1 controls β-cell viability and functioning in adult pancreatic islets. This review describes regulating Pdx1 synthesis and signaling pathways to maintain the pancreatic β cell mass via PDX1.
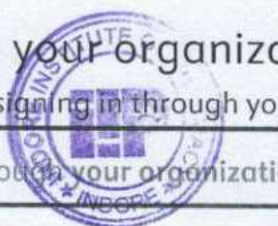
Section snippets

Physiological characteristics of PDX1

PDX1 is synonymous with insulin promoter factor 1, a transcriptional factor at the ParaHox gene cluster. PDX1 activity may be observed in mice at the 5–6 somite stage as early as embryonic stage 8.5 (E8.5). However, humans do not see it until the fourth week after pregnancy. According to the case report, a 5-year-old white girl has a deletion of a single homozygous nucleotide in the PDX1 gene, which causes pancreatic agenesis [12]. This suggests that PDX1 is necessary for the early stages of ...

Regulation of PDX1 gene

PDX1 gene expression is controlled from transcription up to 6kb (Fig. 1). The ubiquitous bHLH protein USF-1 is bound by a downstream E box at around −104 [16], [17]. HNF3, a transcription factor with forkhead wings, may also bind to other sites [18], [16], [17], [19]. This family of organisms can reach regulatory sequences by opening up chromatin. Hence, HNF3β could set the stage for other transcription factors to express the PDX1 gene. One of the HNF3β locations where PDX-1 binds has a TAAT ...

### Regulation of expression of PDX1 in β-cell

The nuclear mesoderm protein PDX1 was initially identified as being made by the pancreatic islets and duodenal epithelium [22]. Later, it was discovered that PDX1 was responsible for binding and activating promoters for insulin gene expression [23]. Some pancreas-related genes are activated by PDX1, such as glucose kinase (GCK), HNF1B (HNF1 homeobox B), somatostatin (SST), islet amyloid polypeptide (IAPP), regulatory factor X6 (RFX6) [24].

Unlike other species, the human PDX1 gene is relatively ...

PDX1 stimulates pancreatic development and islet β cell proliferation

Every endocrine cell develops from endocrine progenitors that express Neurogenin 3 (Ngn3), which is critical for triggering the differentiation of endocrine islet cells from embryonic pancreatic progenitors [52]. Ngn 3 expressions are directly regulated by PDX-1 [53]. One of the most crucial transcription factors for pancreatic maturation and directed development is PDX-1. PDX-1 encourages the primary expansion of the pancreas and beta cell differentiation during embryonic development, a marker ...

254
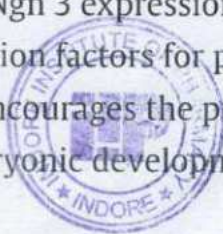
Conclusion

Diabetes management is a systematic and intricate procedure. Conventional medicine can only slow the spread of a disease; it cannot cure it. The primary transcription factor controlling islet cells is PDX-1, and cell division, growth, and differentiation are necessary for the synthesis of insulin, transcription of the insulin gene, and other purposes. As a result, PDX-1-targeted medication, depending on the pertinent PDX-1 mechanism, offers a path to treating diabetes. Yet, after the ...

Author contributions

All authors listed have significantly contributed to this article's development and writing. ...

Additional information

CRediT authorship contribution statement

Nandave Mukesh: Writing – original draft, Validation, Supervision. **Siwan Deepali:** Writing – review & editing, Supervision. **Gilhotra Ritu:** Conceptualization, Data curation, Formal analysis. **Gautam Rupesh K:** Software, Data curation. **Gupta Gaurav:** Validation, Project administration, Formal analysis. **Almalki Waleed Hassan:** Supervision, Project administration. ...

Declaration of Competing Interest

The authors declare that they have no known competing financial interests or personal relationships that could have appeared to influence the work reported in this paper. ...

Recommended articles

References (151)

A. Rosanas-Urgell et al.
Pdx1-related homeodomain transcription factors are distinctly expressed in mouse adult pancreatic islets

255

Mol. Cell Endocrinol. (2005)

S.W. Li et al.

Pancreatic duodenal homeobox 1 protein is a novel β-cell-specific autoantigen for type I diabetes

Lab Investig. (2010)

S. Sharma et al.

Pancreatic islet expression of the homeobox factor STF-1 relies on an E- box motif that binds USF

J. Biol. Chem. (1996)

K. Gerrish et al.

Pancreatic β cell-specific transcription of the pdx-1 gene. The role of conserved upstream control regions and their he-patic nuclear factor 3b sites

J. Biol. Chem. (2000)

X. Wang et al.

Genome-wide analysis of PDX1 target genes in human pancreatic progenitors

Mol. Metab. (2018)

M. Stoffel et al.

Localization of human homeodomain transcription factor insulin promoter factor 1 (IPF1) to chromosome band 13q12.1

Genomics (1995)

S. Sharma et al.

Pancreatic islet expression of the homeobox factor STF-1 relies on an E-box motif that binds USF

J. Biol. Chem. (1996)

K. Gerrish et al.

Pancreatic β cell-specific transcription of the pdx-1 gene. The role of conserved upstream control regions and their hepatic nuclear factor 3β sites

J. Biol. Chem. (2000)

J.C. Van Velkinburgh et al.

Interactions between areas I and II direct pdx-1 expression specifically to islet cell types of the mature and developing pancreas

J. Biol. Chem. (2005)

M. Stolovich-Rain et al.

Weaning triggers a maturation step of pancreatic β cells

Principal
Indore Institute of Pharmacy,
INDORE (M.P.)

256

Identification and evaluation of antimicrobial and anti-arthritis activities of hydroethanolic extract of *Rubus ellipticus* leaves

Anjana Kumari[1], Vinit Prakash[2], Dinesh Gupta[3], Lokender Kashyap[4], Rajat Goyal[5], Hitesh Chopra[6], **Rupesh K. Gautam**[7], Sandip Chakraborty[8], Deepak Chandran[9] and Kuldeep Dhama[10]

[1]Department of Applied Sciences and Humanities, Ambala College of Enginnering and Applied Research, Devsthali, Ambala, India; [2]Department of Applied Sciences, Global Group of Institutes, Amritsar, India; [3]Department of Silviculture and Forestry, University of Agriculture and Technology, Banda, India; [4]Department of Agriculture, Maharishi Markandeshwar (Deemed to be University), Ambala, India; [5]MM College of Pharmacy, Maharishi Markandeshwar (Deemed to be University), Ambala, India; [6]Chitkara College of Pharmacy, Chitkara University, Rajpura, India; [7]Indore Institute of Pharmacy, IIST Campus, Indore, India; [8]Department of Veterinary Microbiology, College of Veterinary Sciences and Animal Husbandry, Agartala, India; [9]Department of Veterinary Sciences and Animal Husbandry, Amrita School of Agricultural Sciences, Amrita Vishwa Vidyapeetham University, Coimbatore, India; [10]Division of Pathology, ICAR-Indian Veterinary Research Institute, Bareilly, India

*Corresponding author: rupeshgautammmu@gmail.com

Abstract

Rubus ellipticus is a native plant to India's tropical and subtropical regions and has been used as a traditional medicinal. The aim of study was to identify and evaluate the antimicrobial and anti-arthritis activities of hydroethanolic extract of *R. ellipticus* leaves (HEERE). The leaves were collected from the Narkanda Valley, India and were shade-dried and finely ground to produce the powder. The hydroethanolic extract was utilized for phytochemical analysis to determine the existence of carbohydrate, phenolic, terpenoid, flavonoid, saponin, glycoside, tannin, protein, and alkaloid. The HEERE was futher analyzed by gas chromatography mass spectrometry (GC-MS) for the characterization of the phytoconstituents. The antimicrobial activity was tested against *Escherichia coli*, *Staphylococcus aureus* as well as *Aspergillus niger*. To assess its anti-arthritic activities, different doses of HEERE were given orally to complete Freund's adjuvant (CFA)-induced albino Wistar rats for twenty-one days. The GC-MS analysis of hydroethanolic extracts from leaves detected and identified the presence of 33 phytochemical compounds. HEERE showed significant effects against *E. coli*, *S. aureus*, and *A. niger* strains at 600 ppm. Our data indicated that HEERE 200 mg/kg was more effective than 50 mg/kg as anti-arthritis. Paw volume, ankle joint diameter, the number leucocytes, and erythrocyte sedimentation rate (ESR) were all significantly reduced in experimental rats. Furthermore, when compared to respective standard drugs, the body weight, erythrocyte, hemoglobin, and synobium healing effect have all improved. These data demonstrated the potential of *R. ellipticus* for the long-term investigation of antimicrobial and anti-arthritic properties.

Keywords: *Rubus ellipticus*, phytochemical, GC-MS, antimicrobial, anti-arthritis

Introduction

While chemical-based synthetic medications are approached cautiously due to their adverse effects, traditional herbs are gaining attention for being naturally derived, environmentally friendly, and minimal adverse effects. Consequently, despite the advantages and disadvantages

of modern synthetic medications, people increasingly opt for plant-based herbal remedies [1]. Medicinal plants, such as traditional herbs, contain a high concentration of bioactive compounds, which have been linked to several therapeutic potentials such as antimicrobial, antioxidant, anti-inflammatory, and anticancer properties [2-6].

The increasing utilization of bioactive derivatives for managing various diseases necessitates a critical examination of their perspective. Medicinal plants are a complex blend of various phytochemicals that are typically derived from crude plant extracts [7]. Many species of plants contain a large number of bioactive compounds, however, only a small fraction of them have been studied and proven to significantly contribute to bioactive mediators. The usage of the appropriate methodology of screening is crucial in the discovery of novel compounds [8]. Extraction and characterization of numerous bioactive compounds from various medicinal plants have led to the development of stable medicinal agents with higher therapeutic profiles [9]. Gas chromatography-mass spectrometry (GC-MS) techniques have been employed in the initial screening of herbal plants, assisting in the identification of bioactive compounds found in the plants [10,11].

The Rosaceae family contains around 750 species and has primarily been employed as traditional medicinal, and ornamental plants in various Asian regions. *Rubus ellipticus (R. ellipticus)*, belonging to the Rosaceae berry plant family, is a plant species native to India's tropical and subtropical regions, exhibiting potential antimicrobial and anti-arthritic properties [12,13,14]. The aim of this study was to identify and evaluate the antimicrobial and anti-arthritis activities of the hydroethanolic extract of *R. ellipticus* leaves (HEERE).

Methods

Plant material
R. ellipticus leaves were collected in the Narkanda Valley, India, in August 2020 and were identified by the Himachal Pradesh State Biodiversity Board, Shimla, India, under the specimen number HPSBB/3055, and the specimen was finally acquiesced at the Biodiversity Board in Herbarium Department, Shimla, India.

Extraction of *R. ellipticus* leaves
R. ellipticus leaves were shade-dried and finely ground to produce a powder of 800 grams by utilizing hydroethanolic (4:6) via a Soxhlet extractor for around 72 hours, following the standard protocol [15]. Afterward, the extract was concentrated with a rotary evaporator using Rotavapor (BUCHI, Flawil, Switzerland) and kept in a glass vial sealed with a Teflon-coated cap at 4°C in the refrigerator for further investigation.

Photochemical analysis
The phytochemical analysis of HEERE was performed following the standard procedures outlined in previous studies [3,15]. The existence of carbohydrates, phenolic, terpenoids, flavonoids, saponins, glycosides, tannins, proteins, and alkaloids was determined in the crude extract.

Gas chromatography-mass spectrometry (GC-MS)
The Agilent 7890B gas chromatograph and Agilent 5977B mass detector (Agilent Tech, California, USA) were employed for the GC-MS analysis. The equipment was equipped with an auto-injector and a fused silica capillary column. Samples were injected at a split ratio of 50:1, with helium serving as the carrier gas at a rate value of 1 ml/minute. The injector's temperature was fixed to 280°C. The temperature of the oven was primarily set at 80°C for 2 minutes, then changed to 220°C at 10°C/minute with no hold and augmented to 310°C at 20°C/min held for 10 minutes and with a solvent delay of five minutes. The flow rate of the column was set at 1 ml/minute. The chromatography of a single sample took 30 minutes. The following parameters were set for the mass spectrometer's operation, namely ion source temperature of 230°C, electron energy (70eV), MS Quad temperature of 150°C, and scanning range of m/z 25–1000 amu. Matching fragmentation patterns and library searches were used to identify the metabolites.

258

Antimicrobial activity evaluation

The well-diffusion method was used to assess antimicrobial activity [16]. The Microbial Type Culture Collection (MTCC) from the Institute of Microbial Technology, Chandigarh, India, provided two bacterial strains of *Escherichia coli* (MTCC 452) and *Staphylococcus aureus* (MTCC 737), and one fungal strain of *Aspergillus niger* (MTCC 1344). These strains were kept in the freezer at 4°C until they were utilized. Potato dextrose agar (PDA) and nutrient agar (NA) were used in the study. The bacterial inoculum was made by growing the freeze-dried cells in NA for 24 hours at 37°C, and the fungal strain was made by growing freeze-dried cells in PDA for 72 hours at 30°C. The test organisms were inoculated on a solidified agar plate with a micropipette and dried for about 10 minutes. A sterilized steel borer was utilized to make the 4-wells in each Petri dish containing agar and then filled with the test compound and standard solutions. The solvent used for the sample preparation was dimethyl sulfoxide (DMSO). The test sample was prepared in DMSO at various concentrations (i.e., 200, 400, and 600 ppm). Ciprofloxacin and fluconazole (both from the Central Drug House Pvt. Ltd., India) were used as positive controls, respectively for bacteria and fungus. The negative control was DMSO, and positive reference standards were ciprofloxacin/fluconazole at 100 ppm for all selected strains.

For the microbial assay, all work was done under aseptic conditions. The bacteria plates underwent incubation at 37 ± 1°C for 24 hours, whereas the fungal plates underwent incubation at 30 ± 1°C for 72 hours. The anti-microbial potential of the test compounds was calculated using the average diameter of the zone of inhibition surrounding the wells in millimeters (mm). Each antimicrobial activity was replicated three times, and the standard deviation of the bacterial and fungal growths corresponding to a specific sample was reported.

Animal preparation and oral acute toxicity test

Albino rats (Wistar strain) of *Rattus norvegicus* from both genders, with a weight range of 200–250 grams, were employed in the study as test samples and housed in standard temperature conditions (24–28°C), and in a relatively humid environment (60–70%) with a 12:12 light and dark cycle. The animals were fed a standard pellet diet and an unlimited supply of water. The protocol was approved by the Institute of Animal Ethics Committee of MM College of Pharmacy (deemed to be University), Maharishi Markandeshwar, India, following the guidelines of the Committee for the Purpose of Control and Supervision on Experimental Animals (CPSCEA).

The test samples of various doses (50, 100, and 200 mg/kg) of HEERE were dissolved in 0.2% w/v carboxy methyl cellulose and 2% Tween 80. Methotrexate (0.5 mg/kg) was also given orally as a standard drug in the form of a suspension [17]. The rats were divided into six groups with six rats from each group. Group I: normally operated + normal saline (0.9% normal saline orally); Group II: complete Freund's adjuvant (CFA) 0.1 ml, injected subcutaneously; Group III: CFA + methotrexate (0.5 mg/kg, orally); Group IV: CFA + HEERE (50 mg/kg body weight, once a day, orally); Group V: CFA + HEERE (100 mg/kg body weight, once a day, orally) and Group VI: CFA + HEERE (200 mg/kg body weight, once a day, orally). Group I acted as the negative control, while Group II served as the arthritic control.

The Organization for Economic Cooperation and Development (OECD) guideline 42518 was employed to test acute oral toxicity in the rats. The rats fasted for 16 hours before the experiment and had unlimited access to water. Six groups of rats were given the test samples orally at doses of 50 mg/kg, 500 mg/kg, and 2,000 mg/kg, respectively. The rats were continuously observed for 3 hours to detect any behavioral changes and for 7 days to look for signs of critical and short-term toxicological indications such as coma, respiratory depression, diarrhea, salivation, convulsion, and perspiration [18].

Anti-arthritis activity evaluation

The condition of arthritis was induced in all groups of rats via subcutaneous injection of 0.1 ml (0.1% w/v) suspension of killed *M. tuberculosis* bacteria, homogenized in the liquid paraffin into the left hind paw (except the normal control group). Intraperitoneal injection of thiopentone sodium (40 mg/kg) [18] was used to anesthetize the rats. The drug treatment began on the 1ˢᵗ day and lasted until the twenty-first. The paw volume was measured by a digital plethysmometer Model 7140 (UGO Basile, Gemonio, Italy) on the first, seventh, fourteenth, and twenty-first days.

An anti-inflammatory response was defined as the percentage inhibition of edema as that of normal control. Methotrexate (0.5 mg/kg, once daily) [18] was used as a controlled drug. The ankle-joint diameter and body weight were measured using a verniercaliper and a digital weighing balance AUX220 (Shimadzu, Kyoto, Japan) on the first, sixth, eleventh, sixteenth, and twenty-first days [19].

For the biochemical evaluation, the rats with were anesthetized with thiopentone sodium (60 mg/kg) and sacrificed at the end of the protocol. The blood samples were collected from each rat by retro-orbital plexus puncture and placed in vials containing ethylenediaminetetraacetic acid (EDTA) for biochemical analysis such as red blood cells (RBC), white blood cells (WBC), hemoglobin (Hb), and erythrocyte sedimentation rate (ESR) count [19].

After the sacrifice, the rat's knee joints were separated and well-preserved in 10% formalin for histopathology examination of the synovium. After the fixation and decalcification, the sample was cut into 45 m pieces and provided staining with eosin and hematoxylin for microscopic estimation [20,21].

Statistical analysis

The data were accessible as the mean standard deviation of the mean (SEM). ANOVA test was utilized for comparison of the statistical significance of the means, followed by Tukey's multiple comparison tests. The $p < 0.05$ was considered to be statistically significant. All statistical analysis was performed on SPSS version 20 (SPPS, IBM Inc, New York, US).

Results

Phytochemical analysis

The existence of flavonoids, tannins, phenols, carbohydrates, saponins, terpenoids, phenolic compounds, proteins, oil, and fats was observed in the phytochemical analysis of the HEERE (**Table 1**). Phytochemicals of alkaloids and glycosides were not found.

Table 1. Phytochemical constituents of HEERE

Phytochemical compounds	Chemical tests	Hydroethanolic extract
Alkaloids	Dragendorff's test	---
	Wagner's test	---
Glycosides	Legal's test	---
	Keller-Killiani test	---
Flavonoids	Shinoda's test	+++
	Alkaloid's test	+++
Tannins and Phenols	Ferric chloride test	+++
Carbohydrates	Fehling's test	-+
	Molisch's test	---
Protein	Ninhydrin test	--+
	Biuret's test	-++
Terpenoids	Hager's test	-++
Saponins	Froth test	+++
Oil and fats	Saponification test	---

---: Absent; --+: slightly present; -++: moderately present; +++: intensely present

Gas chromatography-mass spectrometry (GC-MS) analysis

A total of 33 phhytochemical constituents were found in HEERE. The most prominent compound found in the HEERE were gallic acid (13.69%), protocatechuicacid (10.12%), quercetin (6.09%), glyceric acid (5.10%), malic acid (4.19%), 4-coumaric acid (3.91%), 2-butene-dioic acid (3.88), erythritol (3.82%), galactaric acid (3.55%), and palmitic acid (3.39%) (**Table 2**).

Table 2. Gas chromatography-mass spectrometry (GC-MS) analysis of HEERE

Peak no	Retention time (minute)	Compound name	Area (%)	Molecular weight (ug)
1	5.778	1,3-Propanediol	0.30	76
2	6.084	Glycolic acid	0.27	76
3	8.381	4-Hydroxybutanoic acid	0.15	104
4	8.592	Benzoic acid	0.12	122

Principal
Indore Institute of Pharmacy,
INDORE (M.P.)

260

Peak no	Retention time (minute)	Compound name	Area (%)	Molecular weight (ug)
5	8.865	Glycerol	4.27	92
6	9.22	L-Proline	3.19	115
7	9.476	Butanedioic acid	0.80	118
8	9.643	Glyceric acid	5.10	106
9	9.966	2-Butenedioic acid	3.88	144
10	10.127	Pipecolic acid	0.67	129
11	10.956	β-Alanine	0.22	89
12	11.389	Decanoic acid	0.17	172
13	11.495	Citramalic acid	0.11	148
14	11.723	Malic acid	4.89	134
15	11.834	Erythritol	4.82	122
16	12.118	Aspartic acid	0.42	133
17	12.157	5-Oxoproline	0.69	129
18	12.363	2,3,4-Trihydroxybutyric acid	0.71	136
19	13.481	Levoglucosan	3.51	161
20	13.731	Dodecanoic acid	0.09	200
21	14.415	Arabitol	2.86	152
22	15.505	Citric acid	4.62	192
23	15.544	Protocatechoic acid	10.12	154
24	16.823	4-Coumaric acid	3.91	164
25	16.923	Gallic acid	13.69	170
26	17.663	Galactaric acid	3.55	210
27	17.78	Palmitic Acid	3.39	256
28	18.047	Myo-Inositol	0.66	180
29	18.441	Caffeic acid	0.42	180
30	19.142	Stearic acid	0.69	284
31	20.838	1-Monopalmitin	0.77	330
32	21.628	Glycerol monostearate	0.54	358
33	23.569	Quercetin	6.09	302

Antimicrobial activity

All tested microorganisms were inhibited by the HEERE, with the zone of inhibition ranging from 1.9±0.2 to 8.0±0.15 mm for bacterial strains and 1.4±0.4 to 4.5±0.1 mm for fungal strains. The HEERE was more effective againts *S. aureus* (8.0±0.15 mm) than *E. coli* (6.4±0.4mm) at 600 ppm concentration. While at the same concentration, a maximum zone of inhibition 4.5±0.1mm was observed for the fungal strain (*A. niger*) (**Table 3**).

Table 3. Antimicrobial activity of HEERE using well-diffusion method

Samples	HEERE doses (ppm)	Zone of inhibition Mean±SD (mm)
E. coli	200	1.9±0.2
	400	3.1±0.11
	600	6.4±0.4
S. aureus	200	2.8±0.19
	400	4.2±0.4
	600	8.0±0.15
A. niger	200	1.4±0.2
	400	2.9±0.31
	600	4.5±0.1
Ciprofloxacin	100	20.8±0.1
Fluconazole	100	18.3±0.1

Anti-arthritis activity

Acute toxicity studies have demonstrated that the HEERE was risk-free. The treated rats appeared normal, with no significant changes in behavioral or neurological responses up to 2,000 mg/kg body weight of HEERE. Similarly, no change in body weight, adaptation, mortality, or toxicity reaction was observed at any of the doses until the study's conclusion. As a result, therapeutic doses of *R. ellipticus* of 50, 100, and 200 mg/kg were chosen. In the chronic CFA model, swelling and redness were observed in the injected paw after 24 hours. From the seventh day until the end of the study, the methotrexate-treated group had a decrease in paw volume. All HEERE doses of 50, 100, and 200 mg/kg decreased paw volume and thickness throughout the 21st day of the study. The 200 mg/kg dose of HEERE outperformed the 100 and 50 mg/kg doses

and was almost identical to methotrexate. From the first day to the end of the research investigation, the CFA-induced paw volume gradually increases (**Table 4** and **Table 5**).

Table 4. Effect of HEERE on paw thickness

Groups	o day	1st day	6th day	11th day	16th day	21st day
Negative control	0.40± 0.05	0.40± 0.03	0.45± 0.08	0.41± 0.06***	0.42± 0.05***	0.40± 0.09***
Arthritic control (CFA)	0.42± 0.018	0.78± 0.031	1.64± 0.84	1.89± 0.36	2.07± 0.15	2.26± 0.09
CFA+methotrexate 0.5mg/kg)	0.36± 0.05	0.80± 0.04	1.89± 0.53	1.57± 0.80**	0.86± 0.11***	0.47± 0.19***
CFA+HEERE 50 mg/kg	0.34± 0.06	0.82± 0.14	2.36± 0.53	2.08± 0.22	1.89± 0.15	1.66± 0.91*
CFA+HEERE 100 mg/kg	0.36± 0.10	0.81± 0.03	2.22± 0.80	1.83± 0.16	1.54± 0.13**	1.29± 0.11***
CFA+HEERE 200 mg/kg	0.37± 0.03	0.80± 0.37	2.13± 0.50	1.67± 0.20*	1.27± 0.11***	0.85± 0.05***

Data was presented in mean±SD and analyzed by one-way ANOVA which is followed by Tukey's multiple comparison test. All treated groups and the normal group were compared with the Arthritic control group.
* Statistically significant at $p<0.05$
** Statistically significant at $p<0.01$
*** Statistically significant at $p<0.001$

Table 5. Effect of HEERE on paw volume

Groups	o day	1st day	7th day	14th day	21st day
Negative control	1.83±0.05	1.81±0.08	1.79±0.79***	1.82±0.55***	1.14±0.74***
Arthritic control (CFA)	1.84±0.07	1.99±0.05	2.29±0.11	2.46±0.87	2.62±0.89
CFA + methotrexate 0.5mg/kg	1.85±0.06	2.14±0.12	1.90±0.32*	1.70±0.43**	1.21±0.07***
CFA + HEERE 50 mg/kg	1.86±0.01	2.34±0.13	2.22±0.45 ns	2.16±0.39 ns	2.06±0.48**
CFA+HEERE 100 mg/kg	1.87±0.05	2.23±0.15	2.17±0.90 ns	2.13±0.80 ns	2.01±0.16**
CFA+HEERE 200 mg/kg	1.86±0.04	2.21±0.12	2.14±0.38 ns	1.90±0.63*	1.32±0.24***

Data was presented in mean±SD and analyzed by one-way ANOVA which is followed by Tukey's multiple comparison test. All treated groups and the normal group were compared with the arthritic control group.
* Statistically significant at $p<0.05$
** Statistically significant at $p<0.01$
*** Statistically significant at $p<0.001$

The WBC and ESR levels increased in the arthritic control group, while Hb and RBC levels decreased. In hematological analysis, all HEERE doses (50, 100, and 200 mg/kg) exhibited significant results ($p<0.05$, $p<0.01$, and $p<0.001$). The HEERE at 200 mg/kg produced the best results, with lower WBC and ESR levels and higher Hb and RBC levels (**Table 6**).

Table 6. Effect of HEERE on hematology parameters

Groups	Hb (g/dl)	WBC (10^9/L)	RBC (million/µl)	ESR (mm)
Negative Control	14.18±0.51***	8.46±0.59***	6.88±0.11***	3.29±0.47***
Arthritic Control (CFA)	7.79±0.42	14.96±0.49	3.06±0.58	10.23±0.15
CFA+Standard (Methotrexate 0.5mg/kg)	13.30±0.54***	8.09±0.72***	6.97±0.49***	3.65±0.10***
CFA+HEERE 50 mg/kg	9.55±0.10 ns	13.03±0.52 ns	4.92±0.43 ns	7.74±0.1****
CFA+HEERE 100 mg/kg	11.03±0.75*	12.84±0.43**	5.46±0.84*	5.48±0.38***
CFA+HEERE 200 mg/kg	12.55±0.82**	9.93±0.70***	6.31±0.1***	5.48±0.38***

Data was articulated in mean±SD and analyzed by one-way ANOVA which is followed by Tukey's multiple comparison test. All treated groups and the normal group were compared with the arthritic control group.
* Statistically significant at $p<0.05$
** Statistically significant at $p<0.01$
*** Statistically significant at $p<0.001$

Histopathology

Histopathology of the ankle joint of negative control and arthritic control rats exposed intact synovium and synovial lining morphology, without inflammation, and the influx of inflammatory

Principal
Indore Institute of Pharmacy,
INDORE (M.P.)

cells. HEERE at 200 mg/kg inhibited all histological findings of arthritis significantly more than at 100 and 50 mg/kg (**Figure 1**).
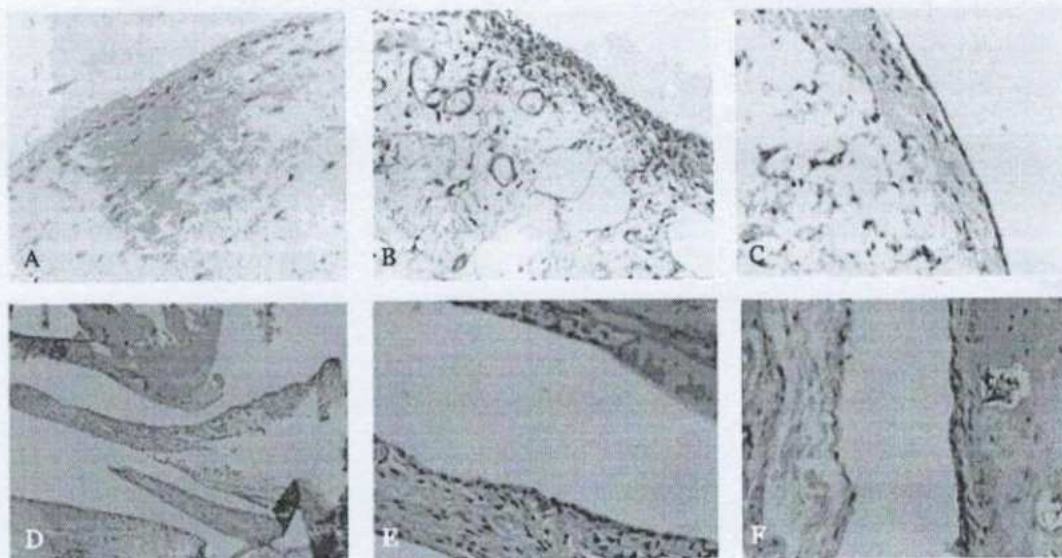

Figure 1. Histopathology of ankle-joint of Wistar rats (A) Group I: normally operated + normal saline; (B) Group II: Complete Freund's adjuvant (CFA) 0.1 ml, injected subcutaneously); (C) Group III: CFA + methotrexate (0.5 mg/kg, orally) standard; (D) Group IV: CFA + HEERE (50 mg/kg body weight, once a day, orally); (E) Group V: CFA + HEERE (100 mg/kg body weight, once a day, orally); and (F) CFA+ HEERE (200 mg/kg body weight, once a day, orally. Original magnification 40×, DXIT 1200, Nikon, Japan.

Discussion

The present study investigated phytochemical constituents and in-vivo anti arthritis activity of HEERE. Phytochemical analysis was done by the GC-MS. Several studies confirmed similar phytochemical constituents found in *R. ellipticus* [17,18]. In line the study's findings, thirty-three phytochemical constituents were identified in *R. ellipticus* leaves by GC-MS analysis in previous studies [22,23,24]. The HEERE was found to have the highest levels of gallic acid, protocatechoic acid, and quercetin in our study. However, these constituents have already been reported from the genus *Rubus* by numerous studies [12,22-26].

The HEERE have shown antimicrobial activities against *E. coli*, *S. aureus*, and *A. niger*. The maximum zone of inhabitation was observed in *S. aureus*, rather than *E. coli*, and *A. niger* due to phenols and flavonoids as a major constituent Phenols and flavonoids are responsible for the destruction of the membrane of microorganisms first and making the cells more delicate. Resulted in impairment of proton pumps and loss of H+- ATPase in damaged membranes can disrupt the normal cellular function of the microorganism ultimately lead to cell death. The antimicrobial activity findings of this study also aligns with several other prior studies [17,18,27]. Several herbal plants deliver relief from the various maladies and symptoms that are similar to those provided by traditional medicinal agents [28]. The CFA or Adjuvant induced arthritis in a tested rat model was chosen for the study because it is a common and widely employed animal model for inflammation and arthritis [29]. Reduced paw swelling is the most important factor in determining the degree of inflammation, and activity of anti-inflammatory and anti-arthritic drugs [30, 31]. It is also one of the simplest, most sensitive, and fastest methods. The decrease in paw thickness is thought to be due to a decline in the release of inflammatory mediators, and it is evidence of any drug's anti-inflammatory and anti-arthritic action in CFA-induced arthritis [32]

R. ellipticus is commonly employed in traditional medicines to treat inflammation [33]. As a result, the current study has been confirming the efficacy of *R. ellipticus* in reducing paw swelling as well as regulating the synobium cell line. Previous research has confirmed that the phenolic, flavonoids [34-36] have a broad range of anti-arthritic activity due to the presence of

Principal
Indore Institute of Pharmacy,
INDORE (M.P.)

gallic acid, procatechoic acid, p-coumaric acid, Quercetin, and Kaempferol,which is similar to our findings [37-39].

Conclusion

A total of 33 phytochemical constituents were found in the hydroethanolic extract of *R. ellipticus* leaves. The HEERE demonstrated potential antimicrobial properties with the zone of inhibition ranging from 1.9 ± 0.2 to 8.0 ± 0.15 mm for bacterial strains and 1.4 ± 0.4 to 4.5 ± 0.1 mm for fungal strains. The acute toxicity studies have demonstrated that the HEERE was risk-free with no significant changes in behavioral or neurological responses up to 2,000 mg/kg body weight of HEERE. All HEERE doses of 50, 100, and 200 mg/kg decreased paw volume and thickness throughout the study. The 200 mg/kg dose of HEERE was almost identical to methotrexate for anti-anthritis activity.

Ethical approval

The protocol was approved by the Institute of Animal Ethics Committee (MMCP-IAEC-85) and the guidelines of the Committee for the Purpose of Control and Supervision on Experimental Animals (CPSCEA) were followed.

Competing interests

The authors declare that there is no conflict of interest.

Acknowledgments

All authors are thankful to their organizations for their full support during the research work.

Funding

Underlying data

All data underlying the results are available as part of the article and no additional source data are required.

How to cite

Kumari A, Prakash V, Gupta D, et al. Identification and evaluation of antimicrobial and anti-arthritis activities of hydroethanolic extract of *Rubus ellipticus* leaves. Narra J 2023; 3 (3): e152 - http://doi.org/10.52225/narra.v3i3.152.

References

1. Konappa N, Udayashankar AC, Krishnamurthy S, et al. GC-MS analysis of phytoconstituents from Amomum nilgiricum and molecular docking interactions of bioactive serverogenin acetate with target proteins. Sci Rep 2020; KR: 1 - 13.

2. Prakash V, Kumari A, Kaur H, et al. Chemical constituents and biological activities of genus picrorhiza: An update. Indian J Pharm Sci 2020; 82(4) 562-577.

3. Prakash V, Kumari A, Kaur H, et al. Green synthesis, characterization and antimicrobial activities of copper nanoparticles from the rhizomes extract of Picrorhiza kurroa. Pharm Nanotechnol 2021; 9(4) 298-306.

4. Prakash V, Kumari A, Kaur H, et al. Chemical composition and anti-microbial activity of essential oil from aerial parts of Origanum vulgare L. from North-Western Himalayas. J Essent Oil-Bear Plants 2021; 24 (2) 177-196.

5. Prakash V, Kaur H, Kumari A, et al. Phytochemicals and biological studies on cycas revolute thumb: A review. Adv Trad Med 2021; 21(3) 389-404.

6. Maiongane F, McGaw LJ, Mudau FN. The synergistic potential of various teas, herbs and therapeutic drugs in health improvement: A review. J Sci Food Agri 2017; 97:4679-4689.

7. Pandey MM, Rastogi S, Rawat AK. Indian herbal healthcare: An overview. Intern J Green Med

Principal
Indore Institute of Pharmacy,
INDORE (M.P.)

8. Keskes H, Belhadj S, Jlail L, et al. LC-MS-MS and GC-MS analyses of biologically active extracts and fractions from Tunisian Juniperusphoeniceleaves. PharmBiol 2017;55:88-95.

9. Yadav R, Khare RK, Singhal A. Qualitative phytochemical screening of some selected medicinal plants of Shivpuri District (MP). Int J Life SciSci Res 2017;3:844-847.

10. Satapute P, Murali KP, Kurjogi M, et al. Physiological adaptation and spectral annotation of arsenic and cadmium in new metal-resistant and susceptible strain Pseudomonas taiwanensis. Environ Pollut 2019;251:555-563.

11. Juszczak AM, Zovko-Koncic M, Tomczyk M. Recent trends in the application of chromatographic techniques in the analysis of Luteolin and its derivatives. Biomol 2019;9:731.

12. Badhani A, Rawat S, Bhatt ID, et al. Variation in chemical constituents and antioxidant activity in yellow himalayan (Rubus ellipticus Smith) and hill raspberry (Rubus niveusThunb.). J Food Biochem 2015;39:663-672.

13. Vadivelan R, Bhadra S, Ravi AVS, et al. Evaluation of anti-inflammatory and membrane stabilizing property of ethanol root extract of Rubus ellipticus Smith in Albino rats. J NatRemedies 2009;3:74-76.

14. Graham J, Woodhead M. Rubus. in wild crop relatives: Genetic, genomic and breeding resources. C. Kole. Ed. 2011;6:179-187.

15. Kaur H, Kumar A, Kumar M, et al. Phytochemicals analysis of sarcotesta layer of Cycas revolutea Thunb. fruit through GC-MS. Int J Adv Sci 2020;29:5111-5118.

16. Sethi P, Khare R, Choudhary R. Complexes of pyrimidine thiones: Mechanochemical synthesis and biological evaluation. Asian J Chem2020;32(10):2594-600.

17. Ringmichon CL, Gopalkrishnan B, Dixit AP. Ethno-pharmacognostical studies on root bark of Rubus ellipticus Smith from Manipur. Int J Pharmacogn Phytochem 2013;2(2):233-226.

18. Prasanth SC, Chandran P. Phytochemical and antimicrobial analysis of leaf samples of different Rubus species. Int J Chem Tech Res 2017;10(4):359-368.

19. Kumar S, Bhatia M, Garg LN, et al. Acute and chronic inflammation studies of Shorea robusta resin cleave extract on rat model. Inflammo pharmacology 2013;21(3):233-239.

20. Mbiantcha M, Almas J, Shabana SU, et al. Anti-arthritic property of crude extracts of Phyllanthusniruri altemifolium (Mimosaceae) in complete Freund's adjuvant-induced arthritis in rats. BMC Complement Altern Med 2017;17(1):111.

21. Parasuraman S, Raveendran R, Kesavan R. Blood sample collection in small laboratory animals. J Pharmacol Pharmacother 2001;1(2):87-93.

22. Krauze-Baranowska M, Głod D, Kula M, et al. Chemical composition and biological activity of Rubus idaeus shoots a traditional herbal remedy of Eastern Europe. BMC Complement Altern Med 2014;14:1-12.

23. Tallini LR, Pedrazza GP, de Bordignon SA, et al. Analysis of flavonoids in Rubuserythroclados and Morus nigra leaves extracts by liquid chromatography and capillary electrophoresis. Rev BrasFarmacogn 2015;25:219-227.

24. Muniyandi K, George E, Sathyanarayanan S, et al. Phenolics, tannins, flavonoids and anthocyanins contents influenced antioxidant and anticancer activities of Rubus fruits from Western Ghats, India. Food Sci Hum Wellness 2019;8:73-81.

25. Belwal T, Pandey A, Bhatt ID, et al. Trends of polyphenolics and anthocyanins accumulation along ripening stages of wild edible fruits of Indian Himalayan region. Sci Rep 2019;9:1-11.

26. Sparzak B, Merino-Arevalo M, Vander Heyden Y, et al. HPLC analysis of polyphenols in the fruits of Rubusidaeus L. (Rosaceae) Nat Prod Res2010;24:1811-1822.

27. Latha R, Sarkar T, Janu RS, et al. Evaluation of antimicrobial efficacy and alpha-glucosidase inhibition of Rubus ellipticus smith Leaf extracts and its phytochemical analysis. Asian J Pharm Clin Res 2015;8:70-322-421.

28. Verpoorte R. Exploration of nature's chemodiversity: The role of secondary metabolites as leads in drug development. Drug Discov 2019;3:232-238.

29. Arulmozhi S, Mazumder PM, Sathyanarayanan L, et al. Anti-arthritic and antioxidant activity of leaves of Alstoniascholaris Linn. R.Br. Eur J Integr Med 2011;3:83-90.

30. Patil KS, Suryavanshi J. Effect of Celastrus paniculatus Willd. seed on adjuvant induced arthritis in rats. Pharmacogn Mag 2007;3(11):177.

31. Ekambaram S, Perumal SS, Subramanian V. Evaluation of antiarthritic activity of Strychnos potatorum Linn seeds in Freund's adjuvant induced arthritic rat model. BMC Complement Altern Med 2010;10:56.

32. Paval J, Kaithen S, Potu B, et al. Comparing the anti-arthritic activities of the plants Justiciagendarussaburm. F. and Withania somniferalinn. Int J Green Pharm2009;3:281.

33. Pandey Y, Bhatt SS. Overview of Himalayan yellow raspberry (Rubus ellipticus Smith): A nutraceutical plant. J Nat AppliSci 2016;8(1):494-499.

34. Elisha IL, Dzoyem JP, McGaw LJ, et al. The anti-arthritic, anti-inflammatory, antioxidant activity and relationships with total phenolics and total flavonoids of nine South African plants used traditionally to treat arthritis. BMC ComplemAlter Med2016;16(1):1-10.

35. Shokry AA, El-Shiekh RA, Kamel G, et al. Anti-arthritic activity of the flavonoids fraction of ivy leaves (Hedera helix L.) standardized extract in adjuvant induced arthritis model in rats in relation to its metabolite profile using LC/MS. BiomedPharmacother 2022;145:112456.

36. Ticona LA, Serban AM, Ticona DA, et al. Anti-inflammatory and anti-arthritic activities of aqueous extract and flavonoids from Tripodanthus acutifolius leaves in mice paw oedema. Planta Medica International Open 2021;8(2):e43-55.

37. Jean-Gilles D, Li L, Ma H, et al. Anti-inflammatory effects of polyphenolic-enriched red raspberry extract in an antigen-induced arthritis rat model. J Agric Food Chem2012;60(23):5755-5762.

38. Kroes BV, Van den Berg AJ, Van Ufford HQ, et al. Anti-inflammatory activity of gallic acid. Planta Med 1992;58(06):499-504.

39. Saleem A, Saleem M, Akhtar MF. Antioxidant, anti-inflammatory and antiarthritic potential of Moringa oleifera Lam: An ethnomedicinal plant of Moringaceae family. S Afr J Bot2020;128:246-256.

Principal
Indore Institute of Pharmacy
INDORE (M.P.)

266

RESEARCH ARTICLE

Diuretic Activity of Hydroalcoholic Extract of *Peristrophe bicalyculata* (R.) Nees. Leaves in Saline Loaded Rats

Sumeet Dwivedi[1*], Mahavir Chhajed[2], Gurmeet Chabra[3], Sujit A Jadhav[4], Gaurav Goyanar[5] Navin K Choudhary[6]

[1]Acropolis Institute of Pharmaceutical Education & Research, Indore, Madhya Pradesh, India
[2]Vidyasagar College of Pharmacy, Indore, Madhya Pradesh, India
[3]Indore Institute of Pharmacy, Indore, Madhya Pradesh, India
[4]R.G. Sapkal College of Pharmacy, Anjaneri, Nashik, Maharashtra, India
[5]Institute of Pharmaceutical Sciences, SAGE University, Indore, Madhya Pradesh, India
[6]Faculty of Pharmacy, B.R. Nahata College of Pharmacy, Mandsaur University, Mandsaur, Madhya Pradesh, India

ABSTRACT

Peristrophe bicalyculata (R.) Nees. (PB) is one of the most widely medicinal plants used in ancient folklore to treat a number of diseases. In the present investigation, the diuretic activity of hydroalcoholic extract of leaves of selected plant was evaluated in saline-loaded rats. Rats weighing in between 180 to 200 gm of either sex were taken for the present study and concentration of urinary NA^+K^+ and Cl^- was determined to access the memorandum of association (MOA). The hydroalcoholic extract of PB leaves at the test dose of 250 mg/kg bw showed significant diuresis in 3 hours while at the test dose of 500 mg/kg bw produced substantial diuresis at the end of 4 hours.

Keywords: *Peristrophe bicalyculata*, Diuresis, Leaves, Rat, Extract.

INTRODUCTION

From ancient cultures, herbs have been used to treat several human disorders, even in developing countries; a majority of the population depends on medicinal plants for the treatment of various human ailments.[1] Diuresis is one of the most important fields where there is a tremendous possibility to use MP's and their products so as to get good effects of drug and patient will feel comfortable.[2]

The plant *Peristrophe bicalyculata* (R.) Nees. (PB) family Acanthaceae is a short sub-shrub having a height of 4 to 6 feet. The various part of the plant is used medicinally. The plant is widely used as an antioxidant, anti-cancer, anti-inflammatory, etc. Literature has reported the dieresis action of this plant,[3] therefore an attempt was made to screen the anti-diuretic activity of the plant.

MATERIAL AND METHODS

Plant Material

The leaves of *P. bicalyculata* (R.) Nees. Was collected from the Malwa region and was made authenticated by Botanist, Voucher No. J./Bot./PBL-038.

Animal

Rats of wither sex weighing 180 to 200 gm were selected for the present study. The protocols were approved by IAEC.

Plant Extraction

In 250 gm off dried powdered coarsely plant material was subject to extraction in soxhlet using ethanol and water (90:10), after extraction extract was dried. HAEPBL is a hydroalcoholic extract on leaves extract of *P. bicalyculata* (R.).[4]

Animal Group and Dosing

Rats were divided in different groups. Oral treatment vehicle 2 mL/1-mL was given as negative control, and standard drug furosemide at the dose of 10 mg/kg was taken in reconstitution 2 mL/100 gm distilled water. The other two groups received plant extract at the test dose of 250 and 500 mg/kg bw. (The dose was received from previous findings)

Diuretic activity

The activity was performed using animal fasting overnight and the treatment with NaCl i.e., normal saline, oral dose of 15 mL/kg for uniformity in water and salt load. The groups

*Author for Correspondence: sumeet_dwivedi2002@yahoo.com

267

Table 1: Effects of hydroalcoholic extract on leaves extract of *P. bicalyculata* (R.) Nees. on urine volume

Group	Volume (mL) after 5 hour	%Urine Excretion	Diuretic action	Diuretic Activity
Control	2.87 ± 0.16	51.39	1	-
Standard-10 mg/ kgbw	6.93 ± 0.18	101.36	1.97	1
HAEPBL-250 mg/kgbw	4.76 ± 0.28	80.27	1.56	0.79
HAEPBL-500 mg/kgbw	5.14 ± 0.28	91.28	1.77	0.89

Table 2: Effect of hydroalcoholic extract on leaves extract of *P. bicalyculata* (R.) Nees. on urinary electrolyte

Group	Electrolyte Conc. Urinary (mmol/L)		
	Na^+	K^+	Cl^-
Control	25.32 ± 1.12	22.18 ± 2.42	41.82 ± 4.14
Standard-10 mg/kgbw	65.32 ± 4.14***	60.14 ± 3.08***	77.28 ± 4.48***
HAEPBL-250 mg/kgbw	43.29 ± 3.17***	64.46 ± 3.19***	53.28 ± 2.25***
HAEPBL-500 mg/kgbw	48.23 ± 87***	70.46 ± 2.71***	66.24 ± 4.15***

Note: Reading are expressed as X + SEM from data six and found significant ***$p < 0.001$
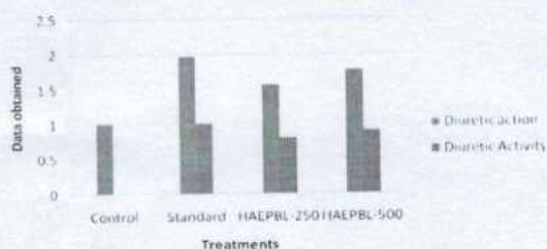
Graph 1: Diuretic action of leaves extract of PB
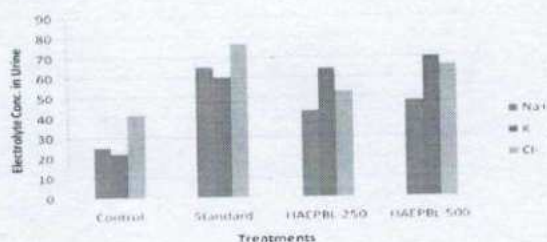
Graph 2: Urinary Electrolyte Concentration in leaves extract of *P. bicalyculata* (R.) Nees. on urinary electrolyte

were given with standard drug and another test dose. Urine was collected and further pH and electrolyte analysis was estimated. Statistically, the results were compared using ANOVA and expressed in mean ± SEM.[5-7]

RESULTS AND DISCUSSION

The diuretic activity of hydroalcoholic extract on leaves extract of *P. bicalyculata* (R.) was screened on saline-loaded rats. From the results obtained it was found that the diuretic action of HAEPBL having dose 500 mg/kgbw is 1.77 which is more than that of HAEPBL having 250 mg/kgbw (1.56). %Urine excretion is more in HAEPBL 500 mg/kg be and was found to be 91.28. The diuretic activity of HAEPBL -250 mg/kg bw was found to be 0.79 and HAEPBL-500 mg/kg bw was found to be 0.89 (Table 1 and Graph 1). The results for urinary electrolytes wad presented in Table 2 and Graph 2.

CONCLUSION

From the results obtained, it was revealed that the hydroalcoholic extract on leaves extract of *P. bicalyculata* (R.) possess diuretic activity at both dose i.e., 250 and 500 mg/kg bw. At higher doses the results were more better than lower doses. The results of urinary electrolyte concentration suggest that the extract has several MOA and the study will provide the traditional and folklore claims of the plant as a diuretic agent.

ACKNOWLEDGEMENT

REFERENCES

1. Sumeet D. Status survey of medicinal plants wealth of Malwa region of Madhya Pradesh with special reference to conservation of vulnerable and endangered species. Journal of Economic and Taxonomic Botany. 2009;33(2):443-52.

2. Wright CI, Van-Buren L, Kroner CI, Koning MM. Herbal medicines as diuretics: a review of the scientific evidence. Journal of Ethnopharmacology. 2007 Oct 8;114(1):1-31.

3. Dwivedi S, Dwivedi A, Dwivedi SN. Folk lore uses of some plants by the tribes of Madhya Pradesh with special reference to their conservation. Ethnobotanical Leaflets. 2008; 1:105.

4. Shriwas S, Chouksey R, Dwivedi S. Anti-Candida activity of few India Medicinal herbs used in the treatment of Gynecological disorders. Research Journal of Pharmacy and Technology. 2021; 14(4):2185-7.

5. Bhat R, Shanbhag P, Shabaraya AR. Diuretic Activity of Ethanolic Extract of Bauhinia tomentosa Linn Roots. International Journal of Pharmaceutical and Phytopharmacological Research (eIJPPR). 2023 Apr; 13(2):25-9.

6. Ngamlai EV, Pradhan RB, Lalbiaknii PC, Ralte V, Lalnunmawia F, Vanlalhluna PC, Mehta SK. Diuretic activity evaluation and chemical composition analysis of Hedyotis scandens extract from Mizoram, India, in rat models. Journal of Ethnopharmacology. 2024 Jan 30; 319:117079.

7. Konan BA, Kpahé ZF, Koko KB, Adepo YP. Diuretic activities of root bark aqueous and ethanolic extracts of Parquetina nigrescens: I-effects on urinary excretion in wistar rat. Journal of Drug Delivery and Therapeutics. 2022 May 15; 12(3):57-61.

Principal
Indore Institute of Pharmacy,
INDORE (M.P.)

268